The Development of Small Molecule Autophagy Inducers in Cervical Cancer Cells and Antiviral Modified Nucleosides Against COVID-19

by

Shaziyaparveen Khairunnasar Siddiqui
10CC17A26009

A thesis submitted to the
Academy of Scientific & Innovative Research
for the award of the degree of
DOCTOR OF PHILOSOPHY
in
SCIENCE

Under the supervision of
Dr. C. V. Ramana

CSIR- National Chemical Laboratory(NCL), Pune

Academy of Scientific and Innovative Research
AcSIR Headquarters, CSIR-HRDC campus
Sector 19, Kamla Nehru Nagar,
Ghaziabad, U.P. – 201 002, India

January 2024

Certificate

This is to certify that the work incorporated in this Ph.D. thesis entitled "***The Development of Small Molecule Autophagy Inducers in Cervical Cancer Cells and Antiviral Modified Nucleosides Against COVID-19***." submitted by ***Ms. Shaziyaparveen Khairunnasar Siddiqui*** to the Academy of Scientific and Innovative Research (AcSIR), in partial fulfillment of the requirements for the award of the Degree of *Doctor of Philosophy in Science*, embodies original research work carried-out by the student. We, further certify that this work has not been submitted to any other University or Institution in part or full for the award of any degree or diploma. Research material(s) obtained from other source(s) and used in this research work has/have been duly acknowledged in the thesis. Image(s), illustration(s), figure(s), table(s) *etc*., used in the thesis from other source(s), have also been duly cited and acknowledged.

S.K. Siddiqui

Shaziyaparveen Khairunnasar Siddiqui

Research Student

Date: 05/01/2024

Dr. C. V. Ramana

Research Supervisor

Date: 05/01/2024

STATEMENTS OF ACADEMIC INTEGRITY

I, Ms. Shaziyaparveen Khairunnasar Siddiqui, a Ph.D. student of the Academy of Scientific and Innovative Research (AcSIR) with Registration No. 10CC17A26009 hereby undertake that, the thesis entitled "**The Development of Small Molecule Autophagy Inducers in Cervical Cancer Cells and Antiviral Modified Nucleosides Against COVID-19.**" has been prepared by me and that the document reports original work carried out by me and is free of any plagiarism in compliance with the UGC Regulations on *"Promotion of Academic Integrity and Prevention of Plagiarism in Higher Educational Institutions (2018)"* and the CSIR Guidelines for "*Ethics in Research and in Governance (2020)*".

S.K. Siddiqui

Signature of the Student

Date : 05/01/2024

Place : Pune

It is hereby certified that the work done by the student, under my/our supervision, is plagiarism-free in accordance with the UGC Regulations on *"Promotion of Academic Integrity and Prevention of Plagiarism in Higher Educational Institutions (2018)"* and the CSIR Guidelines for "*Ethics in Research and in Governance (2020)*".

Signature of the Supervisor

Name : Dr. C. V. Ramana

Date : 05/01/2024

Place : Pune

DECLARATION

The research work embodied in this thesis has been carried out at CSIR–National Chemical Laboratory, Pune under the supervision of **Dr. C. V. Ramana**, Organic Chemistry Division, CSIR–National Chemical Laboratory, Pune – 411 008. This work is original and has not been submitted in part or full, for any degree or diploma of this or any other university.

S.K. Siddiqui

Date:-05/01/2024

Shaziyaparveen Khairunnasar Siddiqui
Organic Chemistry Division
CSIR–National Chemical Laboratory
Pune – 411 008

Dedicated to

My beloved Mother

(Shehnazbegum)

ACKNOWLEDGEMENT

I would like to take this opportunity to express my gratitude to all those infinite people associated with the path of my research career who have supported and taught me so many things throughout my life. I would like to acknowledge all those who have contributed directly or indirectly for the success of the thesis.

First of all, I'd like to convey my gratitude to my honorific supervisor ***Dr. C. V. Ramana****, for allowing me to work under his guidance. His guidance, blessings, and encouragement are the key to my success in research. Words cannot express my gratitude to him for understanding and supporting me in all the highs and lows of work as well as life. I have also been inspired by his passion, enthusiasm, motivation, dedication, patience, and calmness which helped me to handle difficult situations. I would like to thank him for giving me an opportunity to work in the field of medicinal chemistry. His scientific curiosity in teaching the students in the form of conducting group meetings has inspired and driven me to learn many aspects of chemistry. I will carry on the work ethic and discipline he instilled in me for the rest of my life.*

I would like to express my deepest appreciation to my DAC members, Dr. Santosh Mhaske, Dr. Pradip Maity, and Dr, Sailaja Krishnamurty for their constant encouragement and insightful comments and suggestions throughout these six years. I am extremely grateful to the people in various parts of the institute, Mrs. Katharine Raphel, Mrs. Dipika, and the others from the OCD office, Komal, Vijaya, Vaishali, Mrs. Kolhe, and other SACC office staff for their cooperation. Help from the spectroscopy, analytical, and mass groups is gratefully acknowledged. I sincerely thank the support staff from the NMR division especially Mr. Dinesh Shinde, Mr. Satish Pandole, Ms. Minakshi, and Mrs. Deepali Jadhav whereas, Dr. Santha Kumari, Mr. Bhushan and Mr. Ganesh Sevi (HRMS) for their unhesitant support and assistance. I also thank the former and current HOD, the Division of Organic Chemistry. It's my privilege to thank the Director, NCL for giving me this opportunity and providing all necessary infrastructure and facilities.

I am also thankful to Dr. Pandian G. N., Dr. Dan V. M., Dr. SahayaSheela V. J., Dr. Santhoshkumar T. R., and Dr. Gonnade R. G. for the biological study. I am also thankful to Dr. Koteshwar Rao and Mr. Shahaji for the antimicrobial study.

This endeavor not have been possible without I sincerely acknowledge Dr. Sankala C. and Dr. Kadu V. from Punyashlok Ahilyadevi Holkar Solapur University, Solapur who taught me the first lessons in Practical Organic Chemistry. Thanks should also go to Dr, Bhosale R. B., Dr. Ghanwat A., Dr. Peerzade N., Dr. Malegaonkar, Dr. Mhamane N., Dr. Salunkhe P., Dr. Mali, and all the other teachers and staff from Punyashlok Ahilyadevi Holkar Solapur University, Solapur (M.Sc.). Also, I'm thankful to Dr. Ubale, Prof. Nimkar, Prof. Gawali, Prof. Basutkar, Prof. Jadhav, Prof. Pujari, Prof. Deshmukh, Prof. Rajmane and all the other teachers and staff from Dept. of Chemistry, D. B. F. Dayanand college of arts and science, Solapur (B.Sc.) for their motivated teaching, advice and encouragement.

The training and support extended by my senior colleague at the beginning and during my tenure of Ph.D., is worth mentioning, to express my thanks to Dr. Srinivas Kolluru. I would also express my gratitude to Dr. Dinesh Paymode, Dr. Suparna Roy, Dr. Rajendra Rohokale, and Dr. Ganesh More. I would like to thank Dr. Mahesh Shinde and Dr. Mullapudi V. (Babu sir) for teaching various skills and techniques throughout my Ph.D. tenure.

I am immensely thankful to my seniors and colleagues Rupali, Anand, Pushpa, Sibadatta, Pawan, Swapnil, Virendra, Chaitra, Kiran, Krishna, Dr. Sudhakar Gaikwad, Amit, Kishor (Pund & Thete), Pooja (Sarode, Jain, Pawar), Manoj, Harish, Pariksha, Nivedita, Nidhi, Sarvani, Iram, Anil, Hemant, Tushar, Vinay, also the MSc trainees Shreya, Pandhari, Gauri, Laxmi, & Rutik for supporting and maintaining cheerful and healthy work environment inside as well as outside the Lab.

ACKNOWLEDGEMENT

I sincerely thank my NCL friends Amrita, Ambrish, Rahul (Jagtap & Choudhary) Sangram, Sairam, Akash, Madhukar, J. Sabne, Nitin J, Digambar, Sagar, Ashwini, Shubhangi, Priyanka, Abha, Vishal, Suhag and many others for their irreplaceable cooperation.

I express my heartfelt thanks to my family members, particularly my late father, mother, and sisters, thank you for your love, support, and unwavering belief in me. Whatever I am and whatever I will be in the future is because of their enormous blessings, commitments to my ambitions, selfless sacrifices, and cheering atmosphere in my home. I want to thank Adil (nephew) and Adira (niece) for their unconditional love towards their aunt. I consider myself extremely fortunate to have such a supportive family who has always been with me through thick and thin. I also want to thank my brother-in-law, uncles, and aunts for their support in critical situations. I am especially thankful to my mother-in-law Mrs. Gaziya and sister-in-laws who understand each situation and support me all the time.

*I want to thank and give lots of blessings to my daughter **Ayzal** for making my life full of happiness. Last but not least, I'd like to express my deepest gratitude to my loving husband **Tousif** whose love and persistent confidence in me, has taken the load off my shoulder. Your unwavering faith has propelled me forward in times of challenge. If I had written down everything I ever wanted in a life partner, I would not have believed I could meet someone better!*

I am also thankful to DST-INSPIRE for the financial assistance in the form of a fellowship. Finally, my acknowledgement would not be complete without thanking the Almighty, for the strength and determination to put my chin up when faced with hardships in life.

Shaziyaparveen K. Siddiqui

ABBREVIATIONS

Ac	Acetyl
Ac_2O	Acetic anhydride
CH_2Cl_2	Dichloromethane
$CHCl_3$	Chloroform
CH_3CN	Acetonitrile
Conc.	Concentrated
DCE	1,2-Dichloroethane
DMF	*N,N*-Dimethylformamide
DMAP	*N,N'*-Dimethylaminopyridine
DMSO	Dimethyl sulfoxide
PTSA	*p*-toluene sulfonic acid
EtOAc	Ethyl acetate
Et_3N	Triethylamine
$Pd(PPh_3)_4$	Palladium-tetrakis(triphenylphosphine)
CuI	Copper iodide
HRMS	High Resolution Mass Spectrometry
K_2CO_3	Potassium carbonate
AcOH	Acetic acid
Me	Methyl
NMR	Nuclear Magnetic Resonance
NaH	Sodiumhydride
OB reagent	Ohira-Bestman reagent
Im	Imidazole
MeOH	Methanol
BSA	N,O-bis(trimethylsilyl)acetamide
Ph	Phenyl
TMSOTf	Trimethylsilyl trifluoromethanesulfonate
$Rh(PPh_3)_3Cl$	Chlorotris(triphenylphosphine)rhodium(I)
TBSCl	*tert*-Butyldimethylsilyl chloride
br	Branched
PPh_3	Triphenylphosphine
rt	Room Temperature

ABBREVIATIONS

sat.	Saturated
IBX	2-Iodoxybenzoic acid
TBAF	Tetra-n-butylammonium fluoride
THF	Tetrahydrofuran
HRP	Horse radish peroxidase
ELISA	Enzyme linked immunosorbent assay
PBS	Phosphate buffer saline
PBST	Phosphate buffer saline with 0.05% Tween 20
Ct	Cycle threshold
DMEM	Dulbecco's Modified Eagle Medium
FBS	Fetal bovine serum
BSA	Bovine serum albumin
MOI	multiplicity of infection
TMB	3,3′,5,5′-Tetramethylbenzidine.

Abbreviations used for NMR spectral informations:

br	broad	s	singlet	dt	doublet of triplets
d	doublet	t	triplet	ddd	doublet of doublet of doublets
m	multiplet	q	quartet	ddt	doublet of doublet of triplets
quint	quintet	sept	septet	tt	triplet of triplets

GENERAL REMARKS

- All the moisture and air sensitive reactions have been carried out in anhydrous solvents under argon atmosphere in oven-dried glassware. The anhydrous solvents were distilled prior to use: CH_2Cl_2 and DMF from CaH_2; methanol from Mg cake; THF on Na/benzophenone; triethylamine and pyridine over KOH; acetic anhydride from sodium acetate.

- ^1H NMR spectra were recorded on AV–200 MHz, AV–400 MHz, JEOL AL- 400 (400 MHz) and DRX–500 MHz spectrometer using tetramethylsilane (TMS) as an internal standard. Chemical shifts have been expressed in ppm units downfield from TMS.

- ^{13}C NMR spectra were recorded on AV–50 MHz, AV–100 MHz, JEOL AL- 100 (100 MHz) and DRX–125 MHz spectrometer.

- High-resolution mass spectra (HRMS) were recorded on a Thermo Scientific Q-Exactive, Accela 1250 pump and also EI Mass spectra were recorded on Finngan MAT–1020 spectrometer at 70 *eV* using a direct inlet system.

- All reactions are monitored by Thin Layer Chromatography (TLC) carried out on 0.25 mm E-Merck silica gel plates (60F–254) with UV light, I2, and anisaldehyde in ethanol as developing agents.

- All evaporations were carried out under reduced pressure on Buchi rotary evaporator below 50 °C unless otherwise specified.

- Silica gel (60–120), (100–200), and (230–400) mesh were used for column chromatography.

CONTENTS

SYNOPSIS

AcSIR	**Synopsis of the thesis to be submitted to the Academy of Scientific and Innovative Research for the award of the degree of Doctor of Philosophy in Chemical Science**
Name of the Candidate	Ms. Shaziyaparveen K. Siddiqui
Enrollment No. and Date	10CC17A26009; August 2017
Laboratory	Division of Organic Chemistry, CSIR-NCL, Pune
Title of the Thesis	**The Development of Small Molecule Autophagy Inducers in Cervical Cancer Cells and Antiviral Modified Nucleosides Against COVID-19**
Research Supervisor	Dr. C. V. Ramana

Keywords: Autophagy, benzofuranylindoles, antiviral agents, COVID-19, modified nucleosides, cyclotrimerization

1. **Introduction:** The thesis describes studies directed towards the development of small molecule autophagy inducers in cervical cancer cells and antiviral modified nucleosides against COVID-19. The current thesis is categorized into two chapters. Each chapter comprises of a brief introduction, results and discussion, experimental and the spectral data followed by the references. The first chapter deals with discovery of 3-(benzofuran-2-ylmethyl)-1*H*-indole derivatives as potential autophagy inducers in cervical cancer cells. The second chapter comprises of synthesis of modified nucleosides - indene fused sugar nucleosides and 7-[(2-hydroxyethoxy)methyl]pyrrolo[2,3-*d*]pyrimidine derivatives and their screening as potential antiviral agents against SARS-CoV-2.
2. **Statement of the problem:** Cervical cancer is a leading cause of cancer-related deaths in women and is one of the global health concerns. Amongst the various cellular processes of the Cervical cancer cells, the autophagy (a process that regulates cell death and recycling of damaged or unnecessary cellular components) has been shown to play a crucial role in cervical cancer cell survival and resistance to therapy. One of the purposes of this research is to develop small molecule autophagy inhibitors with potential therapeutic value for cervical cancer treatment.

In the initial phases of COVID-19 pandemic, lot of efforts have been focused on the development or the deployment of new and know nucleoside based small molecules for identifying potential small molecules to target SARS-CoV-2. Nucleoside analogues are structural mimics of naturally occurring nucleosides and can interfere with viral replication by inhibiting the activity of viral polymerases. Remdesivir, a nucleoside analogue, is one of the first drugs to be approved for the treatment of COVID-19 patients in some countries, but its efficacy and side effects warrant further investigation. Apart from this rapid evolution of SARS-CoV-2 mutants posed a significant challenge to the vaccination programs though they played a major role in containing this pandemic. Thus, the development of novel nucleoside analogues tailored specifically to target SARS-CoV-2 presents a significant opportunity to enhance antiviral therapy for COVID-19 and this constitutes as the second objective of this thesis.

3. Objectives:

- Development of small molecule autophagy inhibitors for cervical cancer.
- Design and synthesis of nucleoside analogues for developing new antiviral candidates for COVID-19.

4. Methodology and Results:

Chapter 1. Discovery of 3-(Benzofuran-2-ylmethyl)-1*H*-Indole Derivatives as Potential Autophagy Inducers in Cervical Cancer Cells

Introduction: Cancer pathophysiology is correlated to metabolic dysfunctions and genetic abnormalities. Autophagy is a key physiological regulatory process that occurs through the breaking down of cellular components like proteins, cytoplasmic organelles and macromolecules, for energy and building blocks, along with recycling of the broken down products.[1] Autophagy plays an essential role in maintaining cellular homeostasis, which, when disrupted, can lead to tumorigenesis or other clinical issues.[2] The correlation of cancer to autophagy is complex and primarily depends on the type and stage of cancer. It is generally accepted that autophagy can trigger tumor suppression, as many autophagy-related genes are also known as tumor suppressors.[3] Considering the role of autophagy as an underlying cause in many diseases, including cancer, autophagy modulation has accumulated interest among researchers as a potential therapeutic target.[4]

Cervical cancer, a major health concern in many developing countries, is often associated to human papillomavirus infection (HPV). HPV infection alters autophagy in keratinocytes, thereby establishing a viral life cycle in the host cell. Even though cervical cancer management has advanced into newer treatment modalities with the help of targeted drugs, the clinical achievement of these modern drugs has failed to show the expected success. This lag in the growth of cervical cancer treatment is often related to clonal/genetic heterogeneity and the complex pattern of associated cell signaling pathways. Such shortcomings in cervical cancer further warrant the need for employing molecules that can induce cell death pathways like autophagy, which is less explored in cervical cancer treatment.

In this regard, we document the design and development of 3-(benzofuran-2-ylmethyl)-1*H*-indole derivatives as potential autophagy inducers in cervical cancer cells. The design of targeted compounds was based on the natural products having bisindolylmethane and benzofuran scaffolds with diverse biological activities such as antimicrobial, antibacterial, antitumor, anti-inflammatory, antidiabetic, antineophobic and anticonvulsant. We have designed the new analogues with a simple hypothesis that the combination of two different heterocyclic scaffolds can be a promising approach for identifying new small molecule probes. A focused small molecule library designed around this scaffold has been synthesized and screening against various cancer cells led to the identification of **3eb** and **3ec** with a promising inhibition against the Siha cell line. The morphological features of the cells after treatment with this set of compounds indicated autophagy as a reason for the observed inhibition.

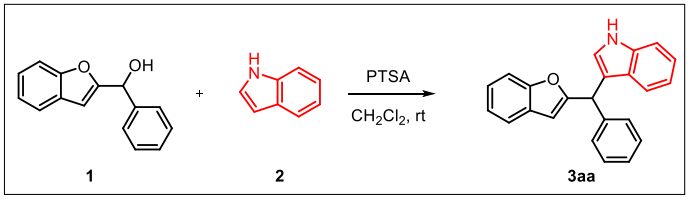

Scheme 1: Synthesis of target molecule

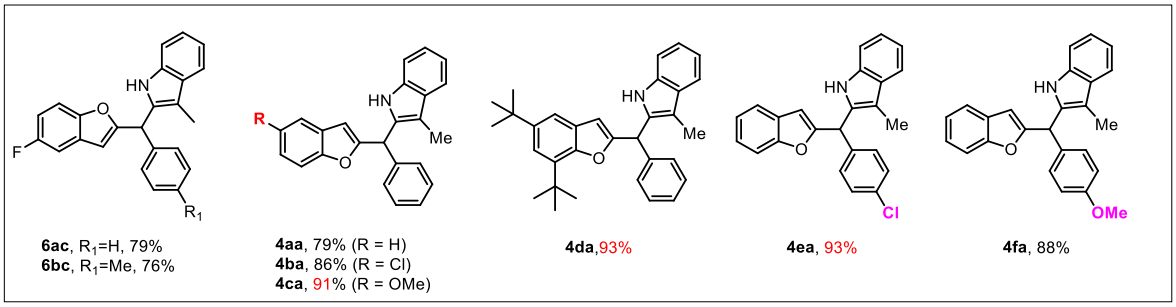

6ac, R_1=H, 79%
6bc, R_1=Me, 76%

4aa, 79% (R = H)
4ba, 86% (R = Cl)
4ca, 91% (R = OMe)

4da,93%

4ea, 93%

4fa, 88%

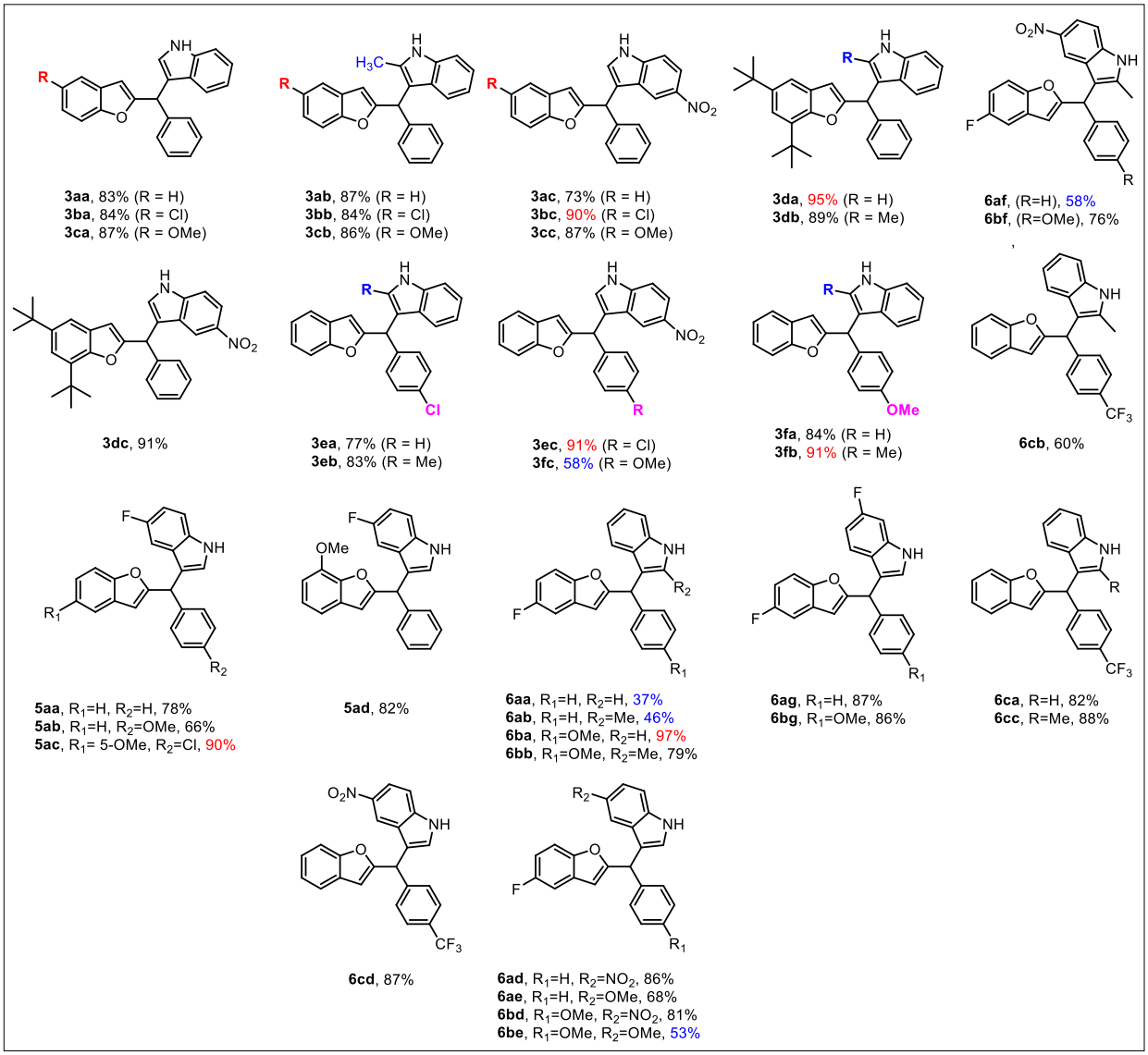

Scheme 2: Substrate Scope (C2 and C3 alkylation products)

Next, compounds **3eb** and **3ec** were subjected for further analysis of the progressive conversion of LC3I to LC3II as a positive indicator of autophagy. Compounds **3eb** and **3ec** show GFP-LC3 Puncta formation and confirmed the induction of autophagy.

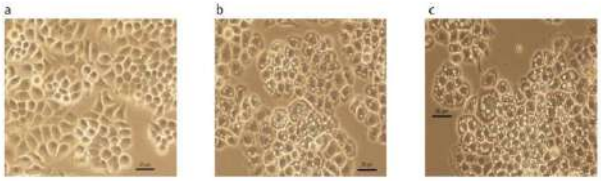

Figure 1: Morphological changes of SiHa cells treated with compounds **3eb** and **3ec** (a) Control SiHa cell line. Presence of autophagic vacuoles in SiHa cell line at 24 h of treatment b) with **3eb** and c) with **3ec**

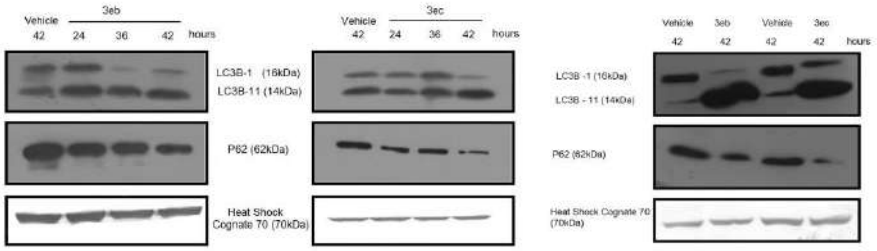

Figure 2: Representative of western blot, **3eb** (30 µm) and **3ec** (30 µm) induces LC3I to LC3II conversion. Similarly, p62 showed decreasing pattern of expression with time, thereby confirming autophagy in the SiHa cell line and C33a cell line.

Chapter 2 (Part I): Design and Synthesis of Indene Fused Sugar Nucleosides as Potential Antiviral Agents for COVID-19

Introduction: In 2019, when the COVID (Corona virus Disease) outbreak occurred, everyone witnessed the huge disaster caused by a small virus, and ever since then the whole world is fighting against this deadly virus. The corona virus has been continuously evolving over the past two years, unleashing itself in mutated forms after certain intervals in the form of new variants, which have higher transmission capabilities thus causing a large number of deaths. For the treatment of these deadly viruses, various sugar nucleosides were tested which exhibited very good results.[6]

Nucleosides are the structural subunits of nucleic acids such as DNA and RNA. A nucleoside is composed of nucleobases which is either a pyrimidine base (cytosine, thymine or uracil), or a purine base (adenine or guanine), and a five-carbon sugar which is either ribose or a deoxyribose. The nucleoside analogues mimic natural nucleotides (**fig. 3**) to be incorporated into nascent viral RNA chains and due to structural differences, nucleoside analogues block the elongation of nascent RNA molecules by serving as chain terminators and thus inhibit virus replication. In this context, Remdesivir, Ribavirin and EIDD-1931 are the representative antiviral

nucleoside analogues that successfully crossed the clinical trials and entered into the market (**fig. 3**).

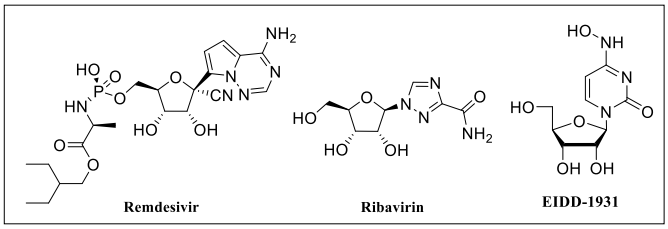

Figure 3. Antiviral nucleosides used for the treatment of COVID-19

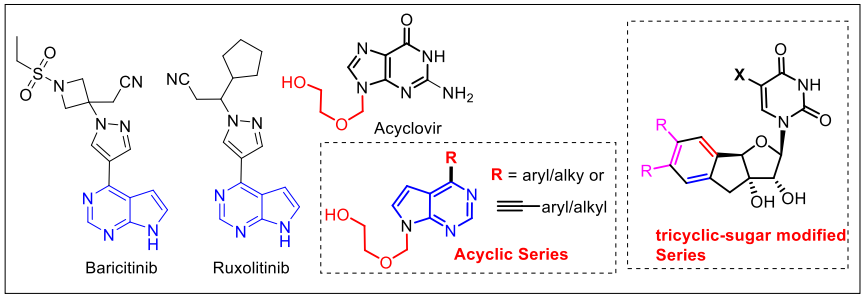

Scheme 3. Anti-viral agents

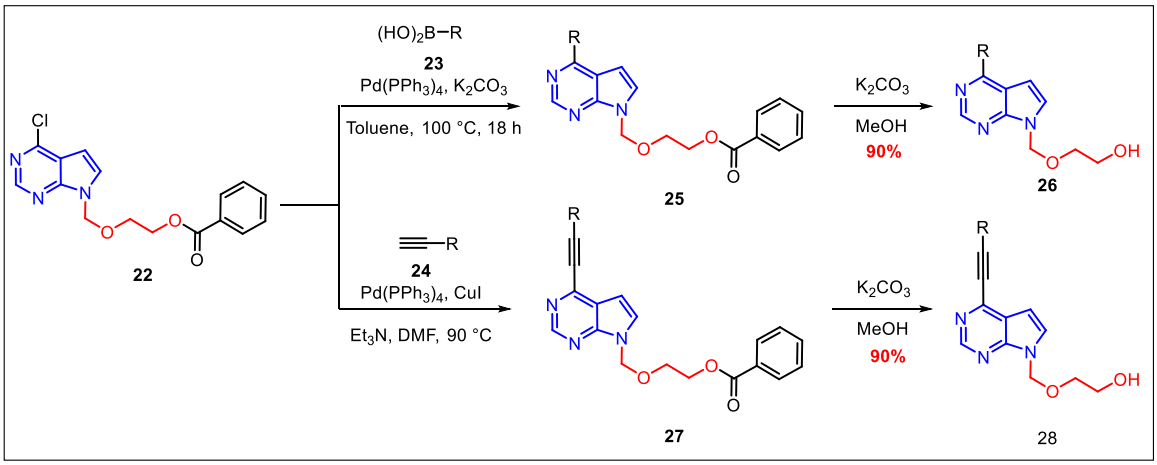

Scheme 4: Synthetic strategy for the target compound

In the context of COVID-19, and as a part of the newly initiated antiviral drug discovery program, we have come up with two different scaffolds. The first series is funded upon integrating structural feature of the acyclovir and JAK-2 kinase inhibitors Ruxolitinib and Baricitinib. As this series [**Scheme 4** provides the details of synthesis] was found to be not promising in terms of the anti-viral activity against SARS-CoV-2, we have come up with a new design and strategy that provided a rapid access to the sugar-modified tricyclic nucleoside

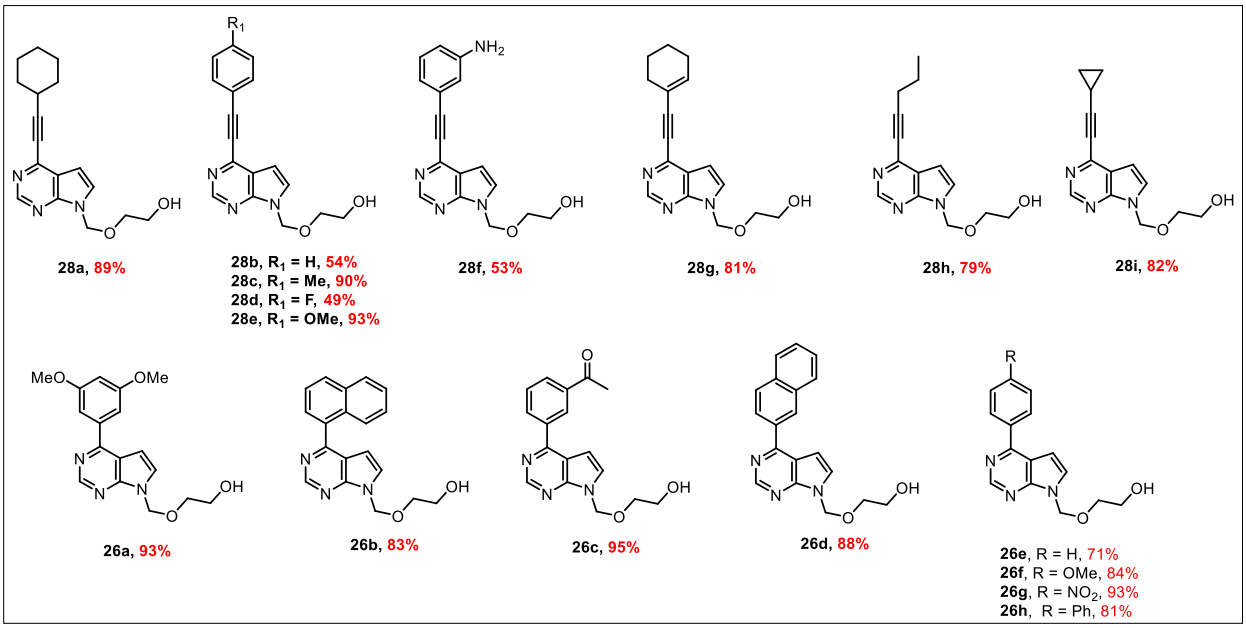

Scheme 5: Substrate Scope

derivatives. As shown in Scheme 6, we have employed cyclotrimerization of the diyne 17 (derived from D-glucose) as a key reaction at the penultimate stages to fuse the indene ring and

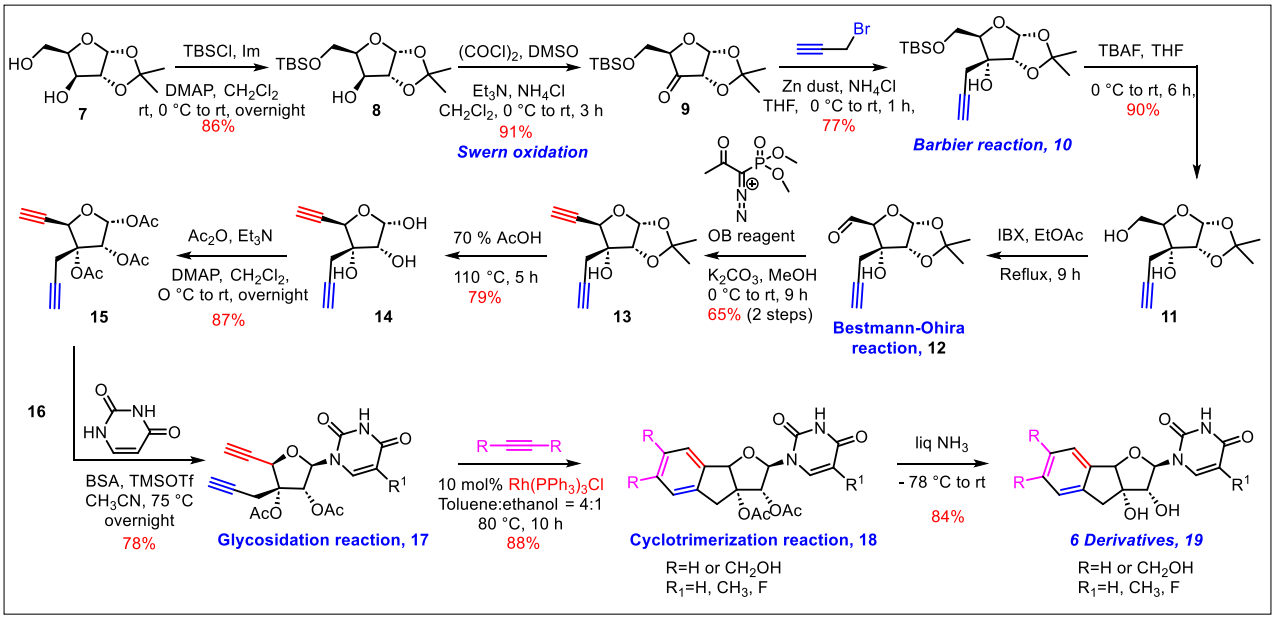

arrive at the modified nucleosides **19a**–**19f**.

Scheme 6: Synthesis of indene conjugated sugar nucleosides

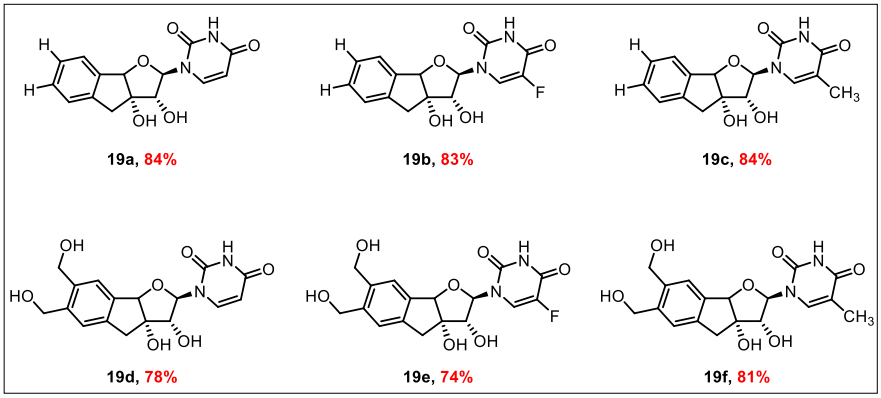

Scheme 7: Substrate scope

The synthesized compounds were tested for their anti-SARS-CoV-2 activity and found to be moderately active.

Compounds	SARS-CoV-2 inactivation 10uM (%)		SARS-CoV-2 inactivation 1uM (%)	
	FAM	HEX	FAM	HEX
6d	N/A	0	99.99	0
6b	0	98	0	0
6e	ND	ND	ND	ND

Conclusions:

- Novel autophagy inducers in cervical cancer were synthesized successfully, which was confirmed by progressive conversion of LC3I to LC3II and down regulation of p62 in SiHa and C33a cells.
- Antiviral Modified sugar nucleosides were designed and synthesized.
- The library of pyrrolo[2,3-*d*]pyrimidine acyclic nucleoside analogues were synthesized and screened for their biological activity.

Future Directions:

- The synthesis of 3-(Benzofuran-2-ylmethyl)-1*H*-Indole was done in few steps and with very good yield. So, in the future we will focus on the synthesis of natural products having similar tricyclic system.
- The synthesis of indene fused sugar nucleoside is quite impressive and future work will focus on modifying the structure of sugar nucleosides to increase the antiviral activity.
- New library of 7-[(2-Hydroxyethoxy)Methyl]Pyrrolo[2,3-*d*]Pyrimidine derivatives will be designed to increase the biological activity.
- Synthesized compound will be further screened for biological activities.

Publications:

1. Srinivas K, Siddiqui SK, Mudaliar JK, Ramana CV. *J. Org. Chem.* 2019;84 (9): 50565066.

2. Siddiqui SK, SahayaSheela VJ, Kolluru S, Pandian GN, Santhoshkumar TR, Dan VM, Ramana CV. *Bioorganic & Medicinal Chemistry Letters.* 2020;30 (19):127431.

3. Siddiqui SK, Ramana CV, Gonnade RG. *Acta Crystallographica Section E.* 2023;79(7):633-636.

References:

1) Bhat P, Kriel J, Shubha Priya B, Basappa, Shivananju NS, Loos B. Modulating autophagy in cancer therapy: Advancements and challenges for cancer cell death sensitization. *Biochem. Pharmacol*. 2018;147:170–182.
2) Mizushima N, Komatsu M. Autophagy: Renovation of Cells and Tissues. *Cell*. 2011;147(4):728–741.
3) Yang Y, Hu L, Zheng H, et al. Application and interpretation of current autophagy inhibitors and activators. *Acta Pharmacol Sin*. 2013;34(5):625.
4) a) Takamura A, Komatsu M, Hara T, et al. Autophagy-deficient mice develop multiple liver tumors. *Genes Dev*. 2011;25(8):795–800.

5) Ueda K, Okado Y, Shigetomi K, Ubukata M. Novel autophagy modulators: Design and synthesis of (+)-epogymnolactam analogues and structure-activity relationship. *Bioorg med chem*. 2018;26(18):5159–5168.
6) Pruijssers AJ, Denison MR. Nucleoside analogues for the treatment of coronavirus infections. *Curr Opin Virol*. 2019;35:57-62.

Chapter I

Discovery of 3-(Benzofuran-2-ylmethyl)-1*H*-Indole Derivatives as Potential Autophagy Inducers in Cervical Cancer Cells

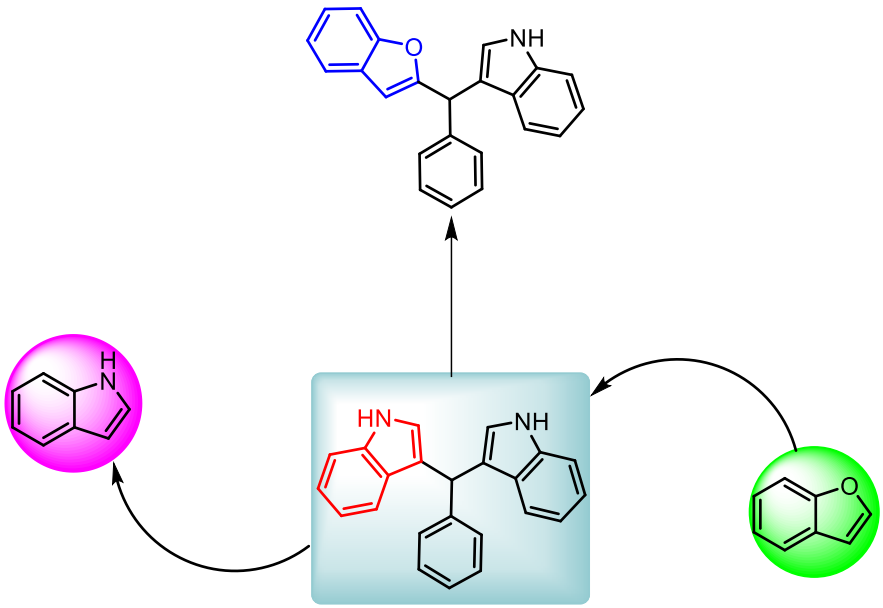

1.1 Introduction to Cancer

Cancer is a term used for a group of diseases that can affect any part of the body by abnormal cell growth. It is renowned for its uncontrollable cell division and capacity to infiltrate other tissues, either directly through invasion into nearby tissue or indirectly by metastasis into distant places (**Fig. F1.1**). Human cells typically divide to create new cells through a process known as cell growth and multiplication where the old or damaged cells die, and new ones replace them. This methodical procedure can occasionally go wrong, leading to the proliferation of damaged or abnormal cells against their planned course and the formation of a tumor that may or may not be malignant. The body's ability to remove cells with damaged DNA decreases as people age, which is another possible cause of cancer. As a result, there is a higher chance of cancer as the person becomes older.

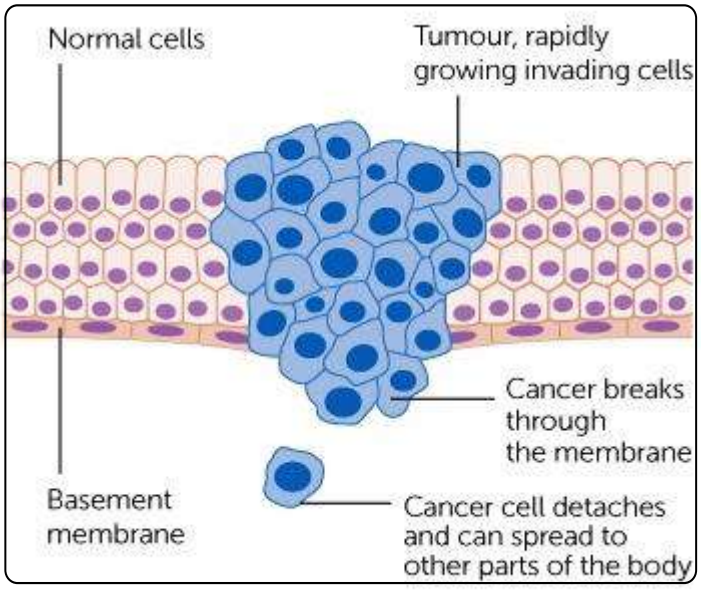

Figure F1.1: *Spreading of cancer (cancer Research UK)*

According to Cancer Research UK, more than 200 types of cancers are reported including breast, colorectal, lung, bronchus, and prostate. The most commonly found cancers in women are cervical squamous cell carcinoma, breast invasive carcinoma, uterine corpus endometrial carcinoma, endocervical adenocarcinoma, uterine carcinosarcoma, and ovarian serous cystadenocarcinoma.[1] The main causes of cancer are tobacco, low fruit, and vegetable intake, poor diet, obesity, excessive alcohol consumption,

insufficient physical activity, ionization radiation, infections (such as human papillomavirus infection), genetics, and environmental toxins.[2] Every individual's cancer has a unique set of genetic mutations, and as the disease spreads, more changes will occur. Different genetic changes can occur in different cells, even within the same tumor.

Cancer ranks as the second most common cause of mortality globally as a result of age, population increase, and socioeconomic progress.[3] According to the International Agency for Research on Cancer, 1 in 5 people worldwide will develop cancer during their lifetime while 1 in 8 men and 1 in 11 women are estimated to die due to this disease. According to GLOBOCAN 2020, around 9.9 million cancer-related deaths and 19 million new cancer cases have been reported in 2020.[4] When compared to the numbers from 2018, this was quite concerning, because 1.8 million people died and 9.5 million new cases were documented.[5] According to the National Council of Medical Research (ICMR), the estimated cases of cancer in 2020 were 1.3 million which increased to 1.42 million in 2021 followed by 1.465 million in 2022, and the estimated cancer-related deaths were 0.77 million in 2020,0.78 million in 2021 and 0.8 million in 2022.

According to WHO studies, worldwide 7.9 million people die due to cancer and among them, 5.5 million i.e. 70% of deaths occur in developing countries. This indicates that the costs of cancer treatment affect not just the wealthy but also the poor. Thus, there is a dire need for novel, efficient, and affordable medication to treat deadly diseases.

Classification of cancer: Cells which experience uncontrolled growth damage the genes which are responsible for cell division which in turn damage the DNA that eventually causes mutations. There are four major types of genes that are responsible for the process of cell division.

i) Oncogenes control the division of cells.

ii) Tumor suppressor genes inform cells when to stop dividing.

iii) Apoptosis is regulated by suicide genes, which instruct the cell to commit suicide if something goes wrong.

iv) DNA-repair genes direct a cell to fix damaged DNA.

When the gene alterations in a cell prevent it from repairing the DNA damage or from committing suicide, cancer starts developing. In the same way, mutations that prevent

oncogene and tumor suppressor gene activity cause cancer, which results in an uncontrollable cell growth.

The classification of cancer is divided into five major categories.

- Carcinoma: Cancers like lung, breast, and colon are examples of carcinomas, which are characterized by cells that cover both internal and external body regions.
- Sarcoma: Cells found in cartilage, bone, connective tissue, fat, muscle, and other supportive tissues are what define sarcomas.
- Lymphoma: Lymphomas are malignancies that start in the immune system's tissues and lymph nodes.
- Leukemia: Cancers called leukemias usually start in the bone marrow and frequently spread to the bloodstream.
- Adenoma: Adenomas are tumors that develop in the pituitary gland, thyroid, adrenal gland, and other glandular tissues.

1.2. Treatment:

Chemotherapy and radiation therapy were used to treat cancer in the 19th century, and after that various types of treatments were discovered. Depending on the patient's condition and the type and stage of their cancer, they may receive just one treatment or almost all types of treatments. Different types of cancer treatments are mentioned below.[6]

- Surgery
- Chemotherapy
- Radiation Therapy
- Targeted Therapy (small-molecule drugs or monoclonal antibodies)
- ImmunoTherapy
- Hyperthermia
- Stem cell transplant or bone marrow transplant
- Laser treatment
- Photodynamic Therapy
- Hormone Therapy

According to Cancer Research UK, surgery, chemotherapy, and radiation therapy have a variety of side effects, including bleeding and bruising, a decrease in bone density, nerve problems, heart problems, hypertension, and lung issues (chemotherapy and radiation therapy to the chest may result in lung failure), endocrine system issues, male hormone issues, infertility in both men and women, bone, joint, and soft tissue issues, dental and oral health issues, vision problems, digestion issues, and fatigue. Due to these adverse side effects, there is an urgent need of target specific drugs for the treatment of deep-seated malignancies in a consistent manner with the fewest possible adverse effects.[7] As a result of this, targeted therapy has gained importance over the past few years, thus pushing researchers to come up with better and more effective drugs.

With the exception of hormone therapies, almost all cancer treatments up to the late 1990s killed cancer cells that were in the process of splitting into two new cells by replicating their DNA. Although some normal cells were also eliminated by these chemotherapy drugs, they had a greater impact on cancer cells. In targeted therapy, the drugs work by affecting the processes that govern the development, division, and spread of cancer cells while also affecting the signals that lead to the natural death of cancer cells (much like healthy cells do when they get damaged or old). Targeted therapy is divided into the following types.

- Small molecule drugs
- Monoclonal antibodies

Small compounds that enter the cytoplasm have an impact on DNA repair systems, polymerase inhibitors (PARP), and tyrosine kinases (PI3K/AKT/mTOR pathways). On the other hand, monoclonal antibodies specifically attach to ligands and receptors on the cell surface without entering the cells themselves, thereby killing cancer cells *via* an effect known as Antibody-Dependent Cellular Cytotoxicity (ADCC). Monoclonal antibody therapy has various advantages such as target specific treatment, fast-acting, and potential for long-term immunity. Despite these benefits, the monoclonal antibody therapy suffers from the risk of side effects and limitations such as potential resistance and possible mutation, insufficient accessibility and availability, the detection and intervention at an early stage while also being expensive, which restricts the treatment to very few people.[8]

Since past two decades we have seen a surge in the research carried out for the development of small molecule drugs as they are much safer and effective than the traditional chemotherapeutic drugs used for the treatment of cancer.[9] Targeted therapies operate through various modes of operation such as apoptosis-inducing drugs, angiogenesis inhibitors, and growth signal blockers just to name a few. In 2001, the first tyrosine kinase inhibitor (TKI) imatinib was approved by the Food and Drug Administration (FDA) which commenced the golden era of the targeted drug therapies. Since then, more than 90 drugs have been approved as anti-cancer drugs and the scope of these drugs covers a large area including epigenetic regulatory proteins, kinases, proteasomes, and DNA damage repair enzymes. As a result of these developments, adjuvant therapies such as autophagy, that target the metabolic irregularities in cancer have piqued the interest of researchers.[10]

1.3. Introduction to Autophagy:

The term Autophagy (derived from Greek meaning self-eating) was first coined by Christian de Duve in 1963 on the occasion of the Siba Foundation Symposium, that took place in London.[11] The mechanism of Autophagy was discovered by Yoshinori Ohsumi and for this contribution, he was awarded the Nobel Prize for Physiology and Medicine in 2016. Autophagy is a key physiological process that involves the degradation of cellular constituents such as proteins, cytoplasmic organelles, and macromolecules, for energy and building blocks as well as for recycling of the broken-down products.[12] Autophagy plays an important role in maintaining cellular homeostasis, which, on disruption can cause tumorigenesis or other clinical issues.[13] Furthermore, it eliminates invasive bacteria to shield our body against a range of infectious diseases as well as other conditions including cancer.

There are three types of Autophagy. 1) Chaperone-mediated autophagy; 2) Microautophagy and 3) Macroautophagy. Depending upon how and which target (lysosome, RdRp, endosome etc) are subjected to lysosomal degradation, the type and mode of action varies. In chaperone-mediated autophagy, the chaperone Hsc70 recognizes the substrate with the targeting motif KFERQ and then lysosomal degradation of individual protein substrate takes place.[14] On the other hand in microautophagy, the

cytoplasmic content degrades via via direct lysosome invagination.[15] While in macroautophagy (i.e. autophagy), the degradation and recycling process takes place in the following four steps (**Fig. F1.2**).[16, 17]

1. Initiation step
2. Nucleation step
3. Elongation step
4. Fusion and degradation step

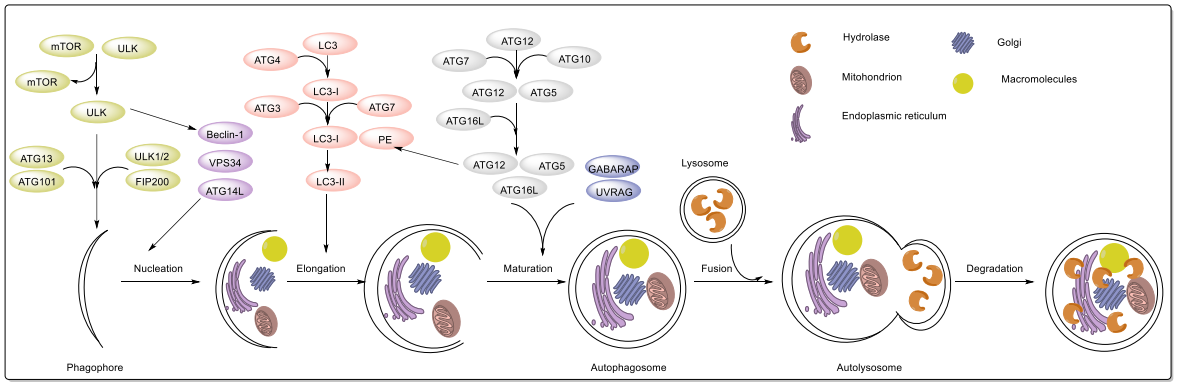

Figure F1.2: *Process of Autophagy*

- **Initiation Step**: In the first i.e. initiation step, a multi-protein complex known as ULK complex governs the initiation of phagophore formation. The autophagic process is then triggered by the integration of the ULK complex with the upstream nutritional and energy status. Each ULK complex protein has a distinct function. Serine-threonine protein kinase ULK1, for instance, is crucial to the scaffold assembly of the ULK1-ATG13-FIP200 complex. ATG13 is an adaptor protein that mediates the connection between the FIP200 and ULK1 complex and also directly binds to LC3. The ULK complex subunit ATG101 is necessary for autophagy because it attracts downstream Atg proteins.

- **Nucleation Step**: Phagophore production in the nucleation step of autophagy begins with the nucleation complex—a protein complex made up of Vps34, Beclin1, ATG14, and p150—coordinating with one another. Other autophagy protein components including WIPI-1, DFCP1, ATG5, and LC3 are recruited during nucleation in part by

vesicular sorting protein 34 and its enzymatic product, phosphatidylinositol-3-phosphate. During this procedure, Vps34's interaction with the phagophore membrane is anchored by myristic acid through p150. Numerous distinct binding partners have an impact on Beclin-1's activity, which is the third crucial element for phospholipid kinase activity. Beclin1 separates from the anti-apoptotic factor Bcl2 in order to activate Vps34. The relationship between Beclin1 and Vps34 is stabilized by the UV radiation-associated resistance gene and the beclin-1-associated autophagy-related essential regulator.

- **Elongation Step**: This stage involves the development of the autophagosome through the assistance of two ubiquitin-like conjugation mechanisms. Initially, Atg12 is triggered by Atg7 and then moved to Atg10, where it forms a covalent bond with Atg5. Atg12-Atg5 conjugate combines with Atg16L to generate the autophagy elongation complex. Apart from the thioester linkage formation with the active site Cys residues of Atg5 and Atg10, the amide linkage with the Lys residue of Atg5 is also facilitated by the carboxy-terminal Gly residue of Atg12. The elongation stage involves the creation of an elongation complex in the form of a dimer, which serves as the location for LC3 lipidation, an essential step for LC3's attachment to the autophagosome membrane. Atg12 creates a ubiquitin-like structure that is involved in the elongation stage, despite the fact that it differs from ubiquitin. Lipidation of LC3 is critical for autophagosome maturation. There are several steps involved in this LC3 lipidation, which functions as a second ubiquitin-like conjugation.
- **Fusion and Degradation**: For the purpose of meeting their needs, all living cells break down and recycle their constituent parts. Maturated autophagosomes fuse with lysosomes and multivescular endosomes during the fusion process. Vps34/SKD1 and Rab11 are two of the proteins required for the degradation of cytosolic components and the achievement of autophagosome-lysosome fusion. Once the autophagosome's inner membrane merges, the cargo is hydrolyzed to destruction, and the lysosomes acquire the cytosolic proteins.

1.4. Autophagy Modulators for the Treatment of Cancer:

The use of pharmaceutical drugs to modulate autophagy in the treatment of cancer has increased in recent years. Numerous small compounds, including as ULK kinase inhibitors, Vps34 inhibitors, ATG4 inhibitors, elongation inhibitors, chloroquine, and

hydroxyl chloroquine, etc., impede initiation, nucleation, elongation, and lysosome fusion, according to pre-clinical and clinical research. Furthermore, it has been demonstrated that a variety of tiny compounds, such as rapamycin analogs or adenosine 5'-monophosphate-activated protein kinase (like sulforaphane), can induce autophagy.[17,18] Studies of the literature indicate that there are still a number of druggable targets in the autophagy pathway that may be utilized to create novel cancer treatments.

1.4.1: mTOR inhibitor: The catalytic subunit of two distinct protein complexes, mTOR Complex 1 (mTORC1) and mTOR Complex 2 (mTORC2), which are involved in multiple oncogenic signaling pathways, is formed by the serine/threonine protein kinase mTOR (mechanistic target of rapamycin), a member of the PI3K-related kinase (PIKK) family. mTOR is a key player in the regulation of cell growth, proliferation, metabolism, and survival.[19] As mTOR is a common feature in many human malignancies, targeting or blocking mTOR has emerged as a promising new avenue for cancer treatment. The compound Rapamycin, which has two binding moieties—one that binds to FKBP12 and the other that binds to mTOR—is the first generation mTOR inhibitor. Temsirolimus, one of the several rapamycin analogs created by substituting other moieties for C-40-O, was approved by the FDA to treat cancer. (**Fig. F1.3**).

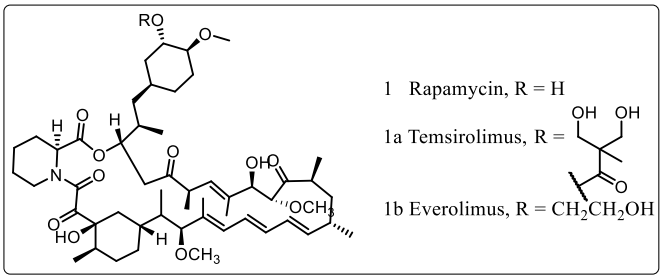

Figure F1.3: *mTOR inhibitors*

1.4.2: Pan-PI3K inhibitors: Phosphatidylinositol 3-kinases is a subunit of the PI3-AKT-mTOR pathway and a family of enzymes involved in many cellular processes, including cell growth, differentiation, proliferation, survival, motility, and intracellular trafficking, these processes are all linked to cancer. Since activation of PI3K-AKT-mTOR has been

identified in a number of cancers, including glioblastoma, juvenile high-grade glioma, diffused intrinsic pontine glioma, cutaneous melanoma, and breast cancer, PI3K inhibition has become a major focus in these diseases. Pan-phosphoinositide 3-kinase (Pan-PI3K) inhibitors is a class of pharmaceuticals that are mainly used to treat advanced malignancies. These inhibitors selectively target pI3K by blocking the activity of PI3K which can help in decreasing the growth and spread of cancer cells (**Fig. F1.4**).[17]

1.2 Introduction to Cancer

Cancer is a term used for a group of diseases that can affect any part of the body by abnormal cell growth. It is renowned for its uncontrollable cell division and capacity to infiltrate other tissues, either directly through invasion into nearby tissue or indirectly by metastasis into distant places (**Fig. F1.1**). Human cells typically divide to create new cells through a process known as cell growth and multiplication where the old or damaged cells die, and new ones replace them. This methodical procedure can occasionally go wrong, leading to the proliferation of damaged or abnormal cells against their planned course and the formation of a tumor that may or may not be malignant. The body's ability to remove cells with damaged DNA decreases as people age, which is another possible cause of cancer. As a result, there is a higher chance of cancer as the person becomes older.

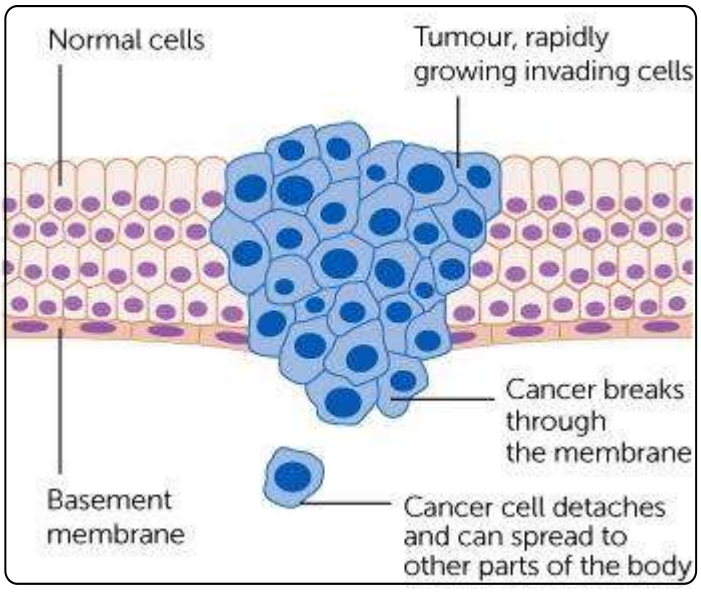

Figure F1.1: *Spreading of cancer (cancer Research UK)*

According to Cancer Research UK, more than 200 types of cancers are reported including breast, colorectal, lung, bronchus, and prostate. The most commonly found cancers in women are cervical squamous cell carcinoma, breast invasive carcinoma, uterine corpus endometrial carcinoma, endocervical adenocarcinoma, uterine carcinosarcoma, and ovarian serous cystadenocarcinoma.[1] The main causes of cancer are tobacco, low fruit, and vegetable intake, poor diet, obesity, excessive alcohol consumption, insufficient physical activity, ionization radiation, infections (such as human papillomavirus infection), genetics, and environmental toxins.[2] Every individual's cancer has a unique set of genetic mutations, and as the disease spreads, more changes will occur. Different genetic changes can occur in different cells, even within the same tumor.

Cancer ranks as the second most common cause of mortality globally as a result of age, population increase, and socioeconomic progress.[3] According to the International Agency for Research on Cancer, 1 in 5 people worldwide will develop cancer during their lifetime while 1 in 8 men and 1 in 11 women are estimated to die due to this disease. According to GLOBOCAN 2020, around 9.9 million cancer-related deaths and 19 million new cancer cases have been reported in 2020.[4] When compared to the numbers from 2018, this was quite concerning, because 1.8 million people died and 9.5 million new cases were documented.[5] According to the National Council of Medical Research (ICMR), the estimated cases of cancer in 2020 were 1.3 million which increased to 1.42 million in 2021 followed by 1.465 million in 2022, and the estimated cancer-related deaths were 0.77 million in 2020,0.78 million in 2021 and 0.8 million in 2022.

According to WHO studies, worldwide 7.9 million people die due to cancer and among them, 5.5 million i.e. 70% of deaths occur in developing countries. This indicates that the costs of cancer treatment affect not just the wealthy but also the poor. Thus, there is a dire need for novel, efficient, and affordable medication to treat deadly diseases.

Classification of cancer: Cells which experience uncontrolled growth damage the genes which are responsible for cell division which in turn damage the DNA that eventually causes mutations. There are four major types of genes that are responsible for the process of cell division.

v) Oncogenes control the division of cells.

vi) Tumor suppressor genes inform cells when to stop dividing.

vii) Apoptosis is regulated by suicide genes, which instruct the cell to commit suicide if something goes wrong.

viii) DNA-repair genes direct a cell to fix damaged DNA.

When the gene alterations in a cell prevent it from repairing the DNA damage or from committing suicide, cancer starts developing. In the same way, mutations that prevent oncogene and tumor suppressor gene activity cause cancer, which results in an uncontrollable cell growth.

The classification of cancer is divided into five major categories.

- Carcinoma: Cancers like lung, breast, and colon are examples of carcinomas, which are characterized by cells that cover both internal and external body regions.
- Sarcoma: Cells found in cartilage, bone, connective tissue, fat, muscle, and other supportive tissues are what define sarcomas.
- Lymphoma: Lymphomas are malignancies that start in the immune system's tissues and lymph nodes.
- Leukemia: Cancers called leukemias usually start in the bone marrow and frequently spread to the bloodstream.
- Adenoma: Adenomas are tumors that develop in the pituitary gland, thyroid, adrenal gland, and other glandular tissues.

1.2. Treatment:

Chemotherapy and radiation therapy were used to treat cancer in the 19th century, and after that various types of treatments were discovered. Depending on the patient's condition and the type and stage of their cancer, they may receive just one treatment or almost all types of treatments. Different types of cancer treatments are mentioned below.[6]

- Surgery
- Chemotherapy
- Radiation Therapy

- Targeted Therapy (small-molecule drugs or monoclonal antibodies)
- ImmunoTherapy
- Hyperthermia
- Stem cell transplant or bone marrow transplant
- Laser treatment
- Photodynamic Therapy
- Hormone Therapy

According to Cancer Research UK, surgery, chemotherapy, and radiation therapy have a variety of side effects, including bleeding and bruising, a decrease in bone density, nerve problems, heart problems, hypertension, and lung issues (chemotherapy and radiation therapy to the chest may result in lung failure), endocrine system issues, male hormone issues, infertility in both men and women, bone, joint, and soft tissue issues, dental and oral health issues, vision problems, digestion issues, and fatigue. Due to these adverse side effects, there is an urgent need of target specific drugs for the treatment of deep-seated malignancies in a consistent manner with the fewest possible adverse effects.[7] As a result of this, targeted therapy has gained importance over the past few years, thus pushing researchers to come up with better and more effective drugs.

With the exception of hormone therapies, almost all cancer treatments up to the late 1990s killed cancer cells that were in the process of splitting into two new cells by replicating their DNA. Although some normal cells were also eliminated by these chemotherapy drugs, they had a greater impact on cancer cells. In targeted therapy, the drugs work by affecting the processes that govern the development, division, and spread of cancer cells while also affecting the signals that lead to the natural death of cancer cells (much like healthy cells do when they get damaged or old). Targeted therapy is divided into the following types.

- Small molecule drugs
- Monoclonal antibodies

Small compounds that enter the cytoplasm have an impact on DNA repair systems, polymerase inhibitors (PARP), and tyrosine kinases (PI3K/AKT/mTOR pathways). On the

other hand, monoclonal antibodies specifically attach to ligands and receptors on the cell surface without entering the cells themselves, thereby killing cancer cells *via* an effect known as Antibody-Dependent Cellular Cytotoxicity (ADCC). Monoclonal antibody therapy has various advantages such as target specific treatment, fast-acting, and potential for long-term immunity. Despite these benefits, the monoclonal antibody therapy suffers from the risk of side effects and limitations such as potential resistance and possible mutation, insufficient accessibility and availability, the detection and intervention at an early stage while also being expensive, which restricts the treatment to very few people.[8]

Since past two decades we have seen a surge in the research carried out for the development of small molecule drugs as they are much safer and effective than the traditional chemotherapeutic drugs used for the treatment of cancer.[9] Targeted therapies operate through various modes of operation such as apoptosis-inducing drugs, angiogenesis inhibitors, and growth signal blockers just to name a few. In 2001, the first tyrosine kinase inhibitor (TKI) imatinib was approved by the Food and Drug Administration (FDA) which commenced the golden era of the targeted drug therapies. Since then, more than 90 drugs have been approved as anti-cancer drugs and the scope of these drugs covers a large area including epigenetic regulatory proteins, kinases, proteasomes, and DNA damage repair enzymes. As a result of these developments, adjuvant therapies such as autophagy, that target the metabolic irregularities in cancer have piqued the interest of researchers.[10]

1.3. Introduction to Autophagy:

The term Autophagy (derived from Greek meaning self-eating) was first coined by Christian de Duve in 1963 on the occasion of the Siba Foundation Symposium, that took place in London.[11] The mechanism of Autophagy was discovered by Yoshinori Ohsumi and for this contribution, he was awarded the Nobel Prize for Physiology and Medicine in 2016. Autophagy is a key physiological process that involves the degradation of cellular constituents such as proteins, cytoplasmic organelles, and macromolecules, for energy and building blocks as well as for recycling of the broken-down products.[12] Autophagy plays an important role in maintaining cellular homeostasis, which, on disruption can cause tumorigenesis or other clinical issues.[13] Furthermore, it eliminates invasive bacteria to

shield our body against a range of infectious diseases as well as other conditions including cancer.

There are three types of Autophagy. 1) Chaperone-mediated autophagy; 2) Microautophagy and 3) Macroautophagy. Depending upon how and which target (lysosome, RdRp, endosome etc) are subjected to lysosomal degradation, the type and mode of action varies. In chaperone-mediated autophagy, the chaperone Hsc70 recognizes the substrate with the targeting motif KFERQ and then lysosomal degradation of individual protein substrate takes place.[14] On the other hand in microautophagy, the cytoplasmic content degrades via via direct lysosome invagination.[15] While in macroautophagy (i.e. autophagy), the degradation and recycling process takes place in the following four steps (**Fig. F1.2**).[16, 17]

5. Initiation step
6. Nucleation step
7. Elongation step
8. Fusion and degradation step

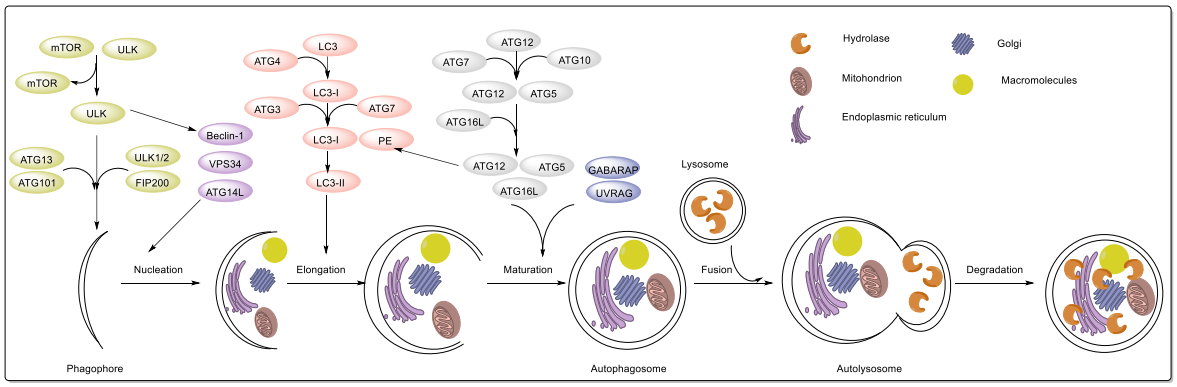

Figure F1.2: *Process of Autophagy*

- **Initiation Step**: In the first i.e. initiation step, a multi-protein complex known as ULK complex governs the initiation of phagophore formation. The autophagic process is then triggered by the integration of the ULK complex with the upstream nutritional and energy status. Each ULK complex protein has a distinct function. Serine-threonine protein

kinase ULK1, for instance, is crucial to the scaffold assembly of the ULK1-ATG13-FIP200 complex. ATG13 is an adaptor protein that mediates the connection between the FIP200 and ULK1 complex and also directly binds to LC3. The ULK complex subunit ATG101 is necessary for autophagy because it attracts downstream Atg proteins.

- **Nucleation Step**: Phagophore production in the nucleation step of autophagy begins with the nucleation complex a protein complex made up of Vps34, Beclin1, ATG14, and p150 coordinating with one another. Other autophagy protein components including WIPI-1, DFCP1, ATG5, and LC3 are recruited during nucleation in part by vesicular sorting protein 34 and its enzymatic product, phosphatidylinositol-3-phosphate. During this procedure, Vps34's interaction with the phagophore membrane is anchored by myristic acid through p150. Numerous distinct binding partners have an impact on Beclin-1's activity, which is the third crucial element for phospholipid kinase activity. Beclin1 separates from the anti-apoptotic factor Bcl2 in order to activate Vps34. The relationship between Beclin1 and Vps34 is stabilized by the UV radiation-associated resistance gene and the beclin-1-associated autophagy-related essential regulator.
- **Elongation Step**: This stage involves the development of the autophagosome through the assistance of two ubiquitin-like conjugation mechanisms. Initially, Atg12 is triggered by Atg7 and then moved to Atg10, where it forms a covalent bond with Atg5. Atg12-Atg5 conjugate combines with Atg16L to generate the autophagy elongation complex. Apart from the thioester linkage formation with the active site Cys residues of Atg5 and Atg10, the amide linkage with the Lys residue of Atg5 is also facilitated by the carboxy-terminal Gly residue of Atg12. The elongation stage involves the creation of an elongation complex in the form of a dimer, which serves as the location for LC3 lipidation, an essential step for LC3's attachment to the autophagosome membrane. Atg12 creates a ubiquitin-like structure that is involved in the elongation stage, despite the fact that it differs from ubiquitin. Lipidation of LC3 is critical for autophagosome maturation. There are several steps involved in this LC3 lipidation, which functions as a second ubiquitin-like conjugation.
- **Fusion and Degradation**: For the purpose of meeting their needs, all living cells break down and recycle their constituent parts. Maturated autophagosomes fuse with

lysosomes and multivescular endosomes during the fusion process. Vps34/SKD1 and Rab11 are two of the proteins required for the degradation of cytosolic components and the achievement of autophagosome-lysosome fusion. Once the autophagosome's inner membrane merges, the cargo is hydrolyzed to destruction, and the lysosomes acquire the cytosolic proteins.

1.4. Autophagy Modulators for the Treatment of Cancer:

The use of pharmaceutical drugs to modulate autophagy in the treatment of cancer has increased in recent years. Numerous small compounds, including as ULK kinase inhibitors, Vps34 inhibitors, ATG4 inhibitors, elongation inhibitors, chloroquine, and hydroxyl chloroquine, etc., impede initiation, nucleation, elongation, and lysosome fusion, according to pre-clinical and clinical research. Furthermore, it has been demonstrated that a variety of tiny compounds, such as rapamycin analogs or adenosine 5'-monophosphate-activated protein kinase (like sulforaphane), can induce autophagy.[17,18] Studies of the literature indicate that there are still a number of druggable targets in the autophagy pathway that may be utilized to create novel cancer treatments.

1.4.1: mTOR inhibitor: The catalytic subunit of two distinct protein complexes, mTOR Complex 1 (mTORC1) and mTOR Complex 2 (mTORC2), which are involved in multiple oncogenic signaling pathways, is formed by the serine/threonine protein kinase mTOR (mechanistic target of rapamycin), a member of the PI3K-related kinase (PIKK) family. mTOR is a key player in the regulation of cell growth, proliferation, metabolism, and survival.[19] As mTOR is a common feature in many human malignancies, targeting or blocking mTOR has emerged as a promising new avenue for cancer treatment. The compound Rapamycin, which has two binding moieties one that binds to FKBP12 and the other that binds to mTOR is the first generation mTOR inhibitor. Temsirolimus, one of the several rapamycin analogs created by substituting other moieties for C-40-O, was approved by the FDA to treat cancer. (**Fig. F1.3**).

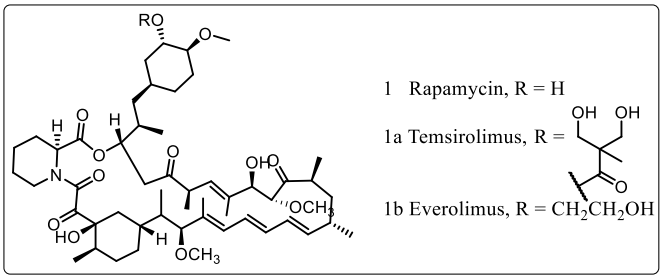

Figure F1.3: *mTOR inhibitors*

1.4.2: Pan-PI3K inhibitors: Phosphatidylinositol 3-kinases is a subunit of the PI3-AKT-mTOR pathway and a family of enzymes involved in many cellular processes, including cell growth, differentiation, proliferation, survival, motility, and intracellular trafficking, these processes are all linked to cancer. Since activation of PI3K-AKT-mTOR has been identified in a number of cancers, including glioblastoma, juvenile high-grade glioma, diffused intrinsic pontine glioma, cutaneous melanoma, and breast cancer, PI3K inhibition has become a major focus in these diseases. Pan-phosphoinositide 3-kinase (Pan-PI3K) inhibitors is a class of pharmaceuticals that are mainly used to treat advanced malignancies. These inhibitors selectively target pI3K by blocking the activity of PI3K which can help in decreasing the growth and spread of cancer cells (**Fig. F1.4**).[17]

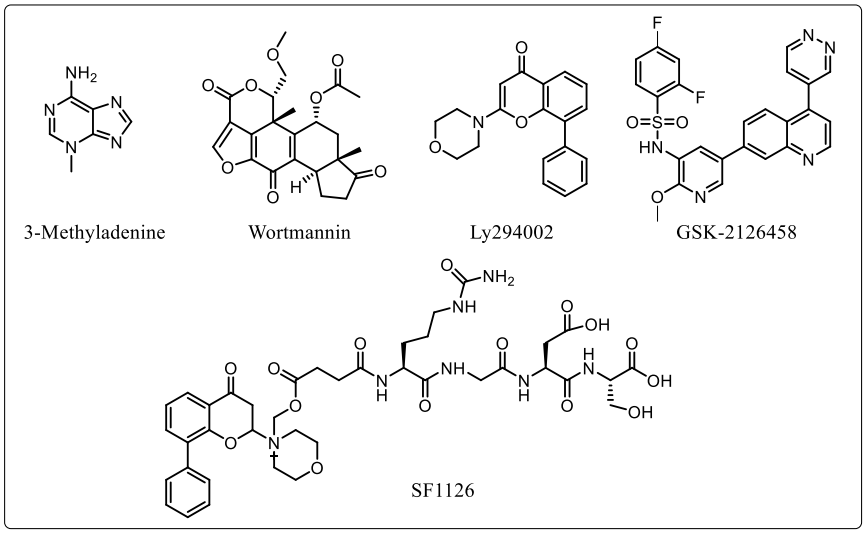

Figure F1.4: *Pan-PI3K inhibitors*

1.4.3: Pan-mTORC inhibitors: In many cancers, mTORC1 and mTORC2 get activated which regulate cell growth, proliferation, survival, apoptosis resistance and migration.

Thus Pan-mTOR inhibitors target mTOR dysregulation and inhibit the kinase domain of both mTORC1 and mTORC2 and work better than rapalogs (**Fig. F1.5**).[20]

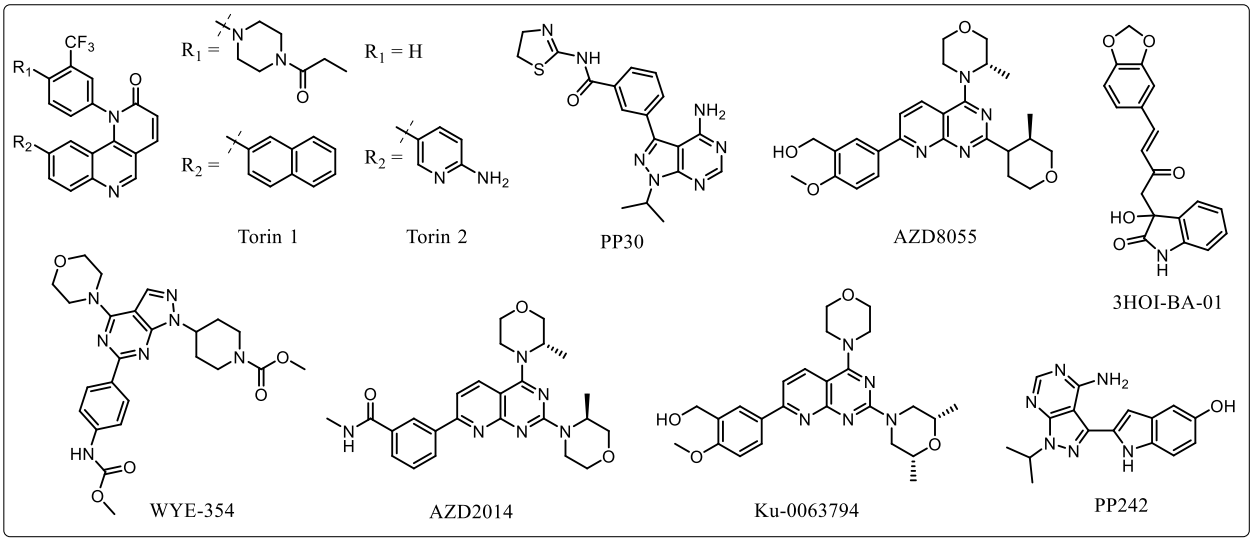

Figure F1.5: *Pan-mTORC inhibitors*

1.4.4: PI3K/mTOR inhibitors: PI3K and mTOR belong to the same superfamily of kinases i.e. PIKK in which mTOR and PI3K show homology in the hinge region. In order to control autophagy, certain small drugs disrupt the PI3K/AKT/mTOR pathway and simultaneously target mTOR and PI3K. In some cases, these inhibitors also affect other kinases with similar structures (**Fig. F1.6**).[17, 18]

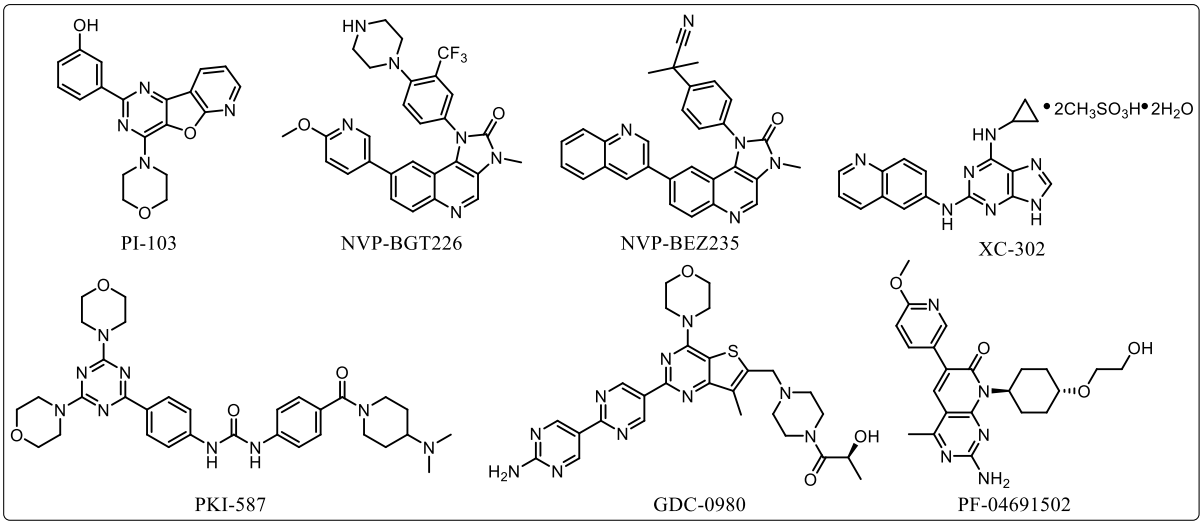

Figure F1.6: *Dual PI3K/mTOR inhibitors*

1.4.5: Unc-51-like kinases inhibitor: ULK, a member of the serine/threonine kinase family of proteins, is crucial in the regulation of autophagy. Among the four ULK kinases (ULK1, ULK2, ULK3, and ULK4) present in humans, ULK1 is a thoroughly studied kinase because it is essential for initiation of autophagy. In the process of autophagy initiation, ULK1 gets activated by upstream signals such as AMPK, etc. and then various proteins such as FIP200, ATG101, and ATG13 for the ULK complex get recruited. Under nutrient deficiency, ULK1 and other proteins of the ULK complex play an important role in cell survival mechanisms. As the process of autophagy helps in cell survival and tumor progression by providing energy and nutrient to cancer cells, disruption of ULK1 and other ULK protein complexes lead to inhibition of autophagy and death of cancer cell. Thus, designing small molecules that can inhibit ULK protein kinase became an attractive approach for the treatment of cancer (**Fig. F1.7**).[21]

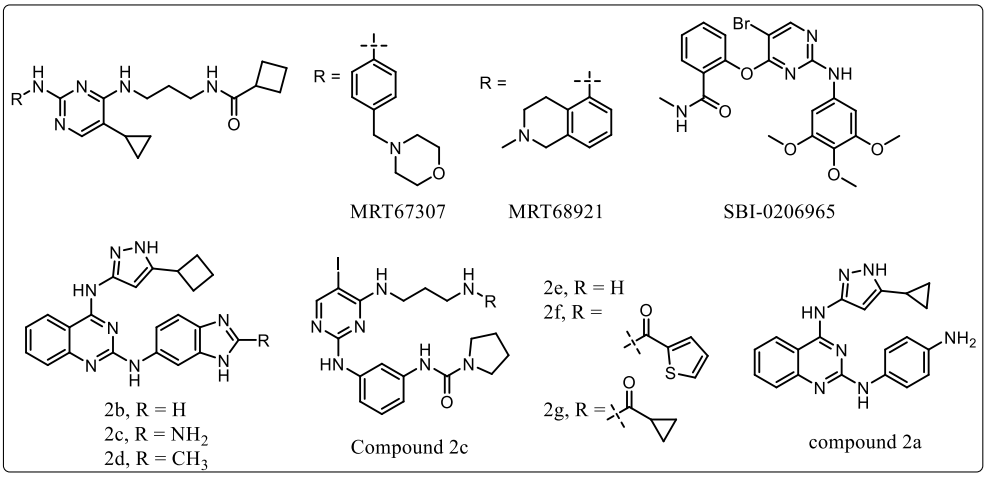

Figure F1.7: *ULK1 inhibitors*

1.4.6: Vacuolar protein sorting (Vps) 34 inhibitors: The protein known as Vps34 was first identified by Emr and co-workers in the year 1990, in Saccharomyces cerevisiae (budding yeast) as a part of the screen for vacuolar protein sorting mutants. Vps34 is a member of the class III PI3K family of lipid kinase protein. Depending on substrate and structure specificity Vps34 divided. Due to its presence in multiple complexes, it is involved in various cellular functions, such as endocytic traffic, phagocytosis, and autophagy. Vps43 forms Vps34 complex I (i.e., Vps34, Vps15, Beclin1, and Atg14L) after interaction with a number of protein subunits, and catalyzes the PtdIns to PtdIns3P phosphorylation and finally anchors with intracellular membrane.[22] In the next step, PtdIns3P with FYVE, PX, or WD40 domain-containing proteins gets involved in vesicle trafficking

and autophagy system. Therefore during nutrient deprivation, Vps34 works as an essential protein that initiates or induces autophagy through mTOR pathway regulation. Thus, to inhibit autophagy and cell death, Vps34 has to be disrupted and thus inhibition of Vps34 has become an important target for the treatment of cancer. There are various inhibitors reported in the literature and some of them have reached the clinical studies stage (**Fig. F1.8**).[23]

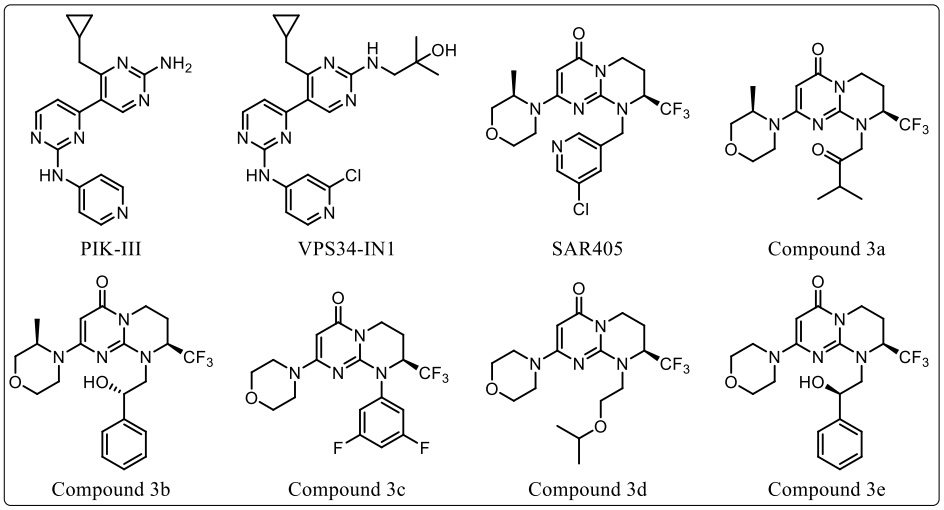

Figure F1.8: *Representative Vps34 inhibitors*

1.4.7: Lysosomotrophic agents: Lysosome is a membrane-bound cytoplasmic organelle that is responsible for metabolic homeostasis, cell signal transduction, and the degradation of protein, carbohydrates, lipids, and nucleic acids. Different autophagy-related diseases, like Alzheimer's disease, can develop as a result of lysosomal dysfunction. The lysosome has a dual function; in addition to being necessary for autophagy breakdown, it also affects autophagy via the Rag/RRAG GTPase pathway. Thus, lysosome inhibitors not only suppress autophagy but also inhibit autophagy. In addition to hydroxychloroquine, which is being studied as an autophagy modulator in Stage II/III cancer therapy trials, chloroquine is a commonly used drug to block the last step of autophagy.[24]

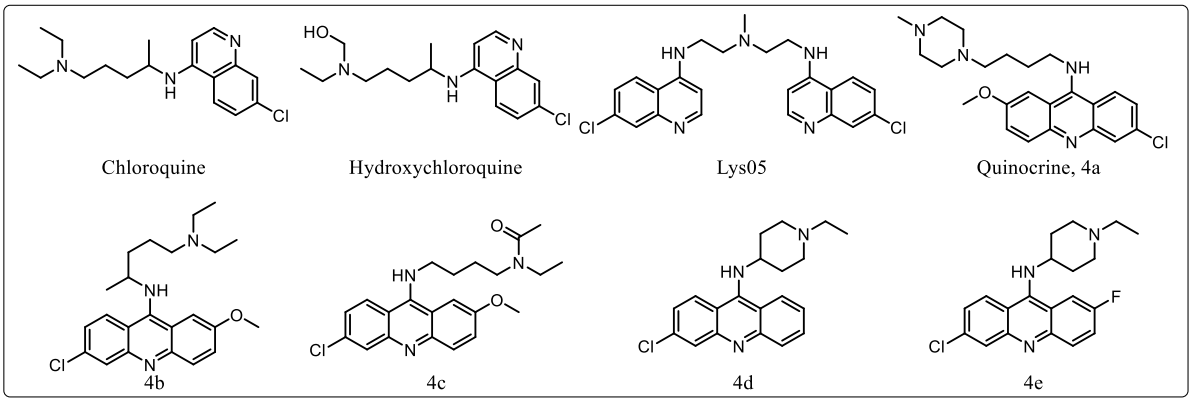

Figure F1.9: *Lysosome inhibitors*

1.5: Cervical Cancer:

Cervical cancer is one of the important types of cancer in which the abnormal cells from the lining of the cervix grow uncontrollably. The cervix is situated in the bottom part of the womb and it is a component of the female reproductive system. The Human Papillomavirus (HPV), which can be spread through sexual relations, is the leading cause of cervical cancer. Squamous cell carcinomas and adenocarcinomas are the two predominant kinds of cervical cancer, accounting for roughly 80–90% and 10–20%, respectively, of all cases. In the host cell, HPV infection establishes a viral life cycle, by altering autophagy in keratinocytes. The phosphorylation of protein kinase B (Akt) and the mammalian target of rapamycin (mTOR) is activated as a result of interactions between HPV proteins and other cellular proteins.[25] The process of inhibition of autophagy is self-regulated by the mTOR complex by activation of mTOR. The resultant activation of the aforementioned protein activates protein synthesis and, when combined with impaired autophagy, it successfully infects keratinocytes by HPV, and ensures the onset and development of cervical cancer.[25] In order to suppress autophagy, the HPV viral proteins E5, E6, and E7 either upregulate other important genes or transcriptionally repress genes associated with autophagy.[26]

One woman dies from cervical cancer every two minutes, making it the fourth most prevalent cancer in women. In 2020, the estimated number of new cases was 6,04,127, and 3,41,831 deaths were reported worldwide.[27] This number is probably going to increase, especially in underprivileged and vulnerable populations. According to current data, 90% of cervical cancer diagnoses and fatalities occur in low- and middle-income countries,

mostly because of limited access to screening, early detection, and cancer and pre-cancer therapy.[28]

1.6: Treatment of cervical cancer:

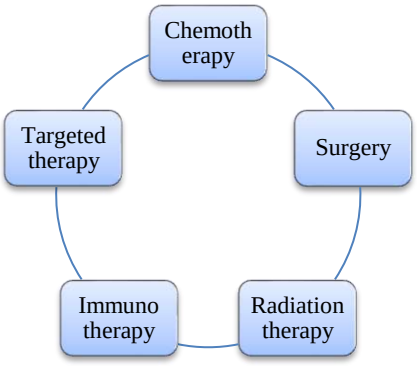

The treatment of cervical cancer includes surgery (hysterectomy, conization or LEEP, radical hysterectomy, pelvic exenteration), radiation therapy (brachytherapy, external beam radiation), targeted therapy, and chemotherapy**.** Depending on the type of cervical cancer, and cancer's stage, there are several different ways to treat cervical cancer.

Precancerous lesions: Treatment options include thermal cryotherapy, LLETZ, and tissue-removal therapy known as ablation.

Advanced cervical cancer: Radiotherapy, either in combination with or without chemotherapy, is frequently used to treat cervical cancer when it has developed further. Treatments can sometimes have long-lasting effects, such as removing the womb, infertility, and premature menopause.

Early-stage cervical cancer: When cervical cancer is found and identified early, it is frequently treated with radiation, surgery, or a combination of the two.

Palliating cervical cancer: There are treatments available to delay the spread of cervical cancer, ease discomfort, lengthen life, and enhance the quality of life when it cannot be cured.

1.7: Drugs used for the treatment of cervical cancer: Targeted drug therapy is an important approach in the treatment of cervical cancer and various other cancers. These

drugs are designed to specifically target and interfere with the mechanisms that cancer cells use to grow and survive. They can work in several ways, including blocking specific proteins or signaling pathways that promote cancer cell growth by enhancing the body's immune response against cancer cells. Some targeted therapies, like monoclonal antibodies, not only directly target cancer cells but also have immunomodulatory effects. These medications can be considered a form of immunotherapy because they can stimulate the immune system to recognize and attack cancer cells. Immunotherapy aims to enhance the body's natural immune response against cancer, which can be particularly effective in cases where the immune system needs a boost to recognize and attack cancer cells effectively.

It's important to note that targeted therapies and immunotherapies often have different side effect profiles compared to traditional chemotherapy. Since they are more specific in their action, they may cause fewer side effects associated with non-specific damage to healthy cells. However, they can still have side effects, which may vary depending on the specific drug and individual patient factors. The development of targeted therapies and immunotherapies has led to significant advancements in cancer treatment, including cervical cancer, and they are often used in combination with other treatment modalities to improve outcomes for patients. Treatment decisions are made based on the type and stage of cancer, as well as individual patient characteristics, and are typically determined by a medical oncologist in consultation with the patient. Cervical cancer can be treated with a variety of targeted medication therapies.[29]

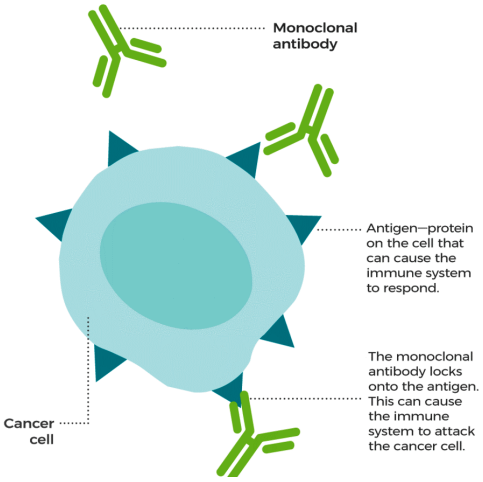

Figure F1.10: *Working of monoclonal antibodies (cancer.gov)*

1.7.1. Vascular Endothelial Growth Factor (VEGF/VEGFR) Directed Therapy:

A class of drugs known as angiogenesis inhibitors is created to obstruct this process by selectively targeting VEGF and its receptors. These inhibitors function in a variety of ways. Some medications prevent the generation of VEGF in the tumor cells, which lowers the quantity of VEGF that is available to promote angiogenesis. Other medications bind specifically to VEGF molecules in the blood, blocking them from binding to endothelial cells' receptors. Endothelial cells are the cells that line blood vessels. As a result, the signaling chain that triggers the growth of new blood vessels is inhibited. Some inhibitors go after the endothelial cells' receptors that VEGF binds to. They obstruct the signal that promotes the development of new blood vessels in this way.

Angiogenesis inhibitors can reduce or even stop the formation of blood vessels in the tumor by inhibiting the activity of VEGF, potentially lowering the tumor's nutrition supply and halting its growth. Particularly for malignancies known to be heavily dependent on angiogenesis for their progression, these drugs are an essential component of cancer treatment.

a) Alymsys (Bevacizumab, Avastin, Mvasi, Zirabev):

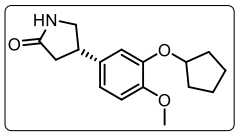

Advanced cervical cancer can be treated with bevacizumab, an angiogenesis inhibitor. It is a monoclonal antibody, or a synthetic variation of a certain immune system protein, that specifically targets VEGF. Occasionally, this medication is used along with chemo. If the cancer responds, the chemotherapy may be halted and bevacizumab is administered alone until the cancer begins to recur.

It is used for the treatment of various types of cancers as first-line therapy including cervical cancer, colorectal cancer, lung cancer, breast cancer, renal cancer, brain cancer, ovarian cancer, and eye disease.[30]

b) Pazopanib (Votrient):

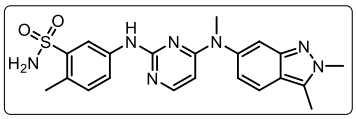

Pazopanib is a multitargeted and broad-spectrum inhibitor of receptor tyrosine kinases, including VEGFR-1, VEGFR-2, VEGFR-3, PDGFR-a/b, and c-kit, which inhibit in a powerful, and selective manner for decreasing the growth of tumor. It has been used for the treatment of patients with cervical cancer, recurrent glioblastoma, soft tissue sarcomas, ovarian cancer, breast cancer, nasopharyngeal carcinoma, and thyroid cancer.[31]

c) Sunitinib (Sutent):

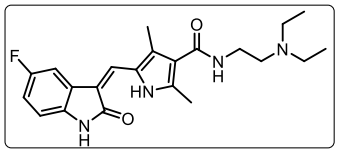

In January 2006, the FDA approved the use of sunitinib as a multiple-targeted, small-molecule receptor tyrosine kinase (RTK) inhibitor for the treatment of imatinib-resistant gastrointestinal stromal tumor (GIST) and advanced renal cell carcinoma (RCC). Targeting a variety of receptor tyrosine kinases (RTKs), sunitinib reduces cellular signaling, which includes vascular endothelial growth factor receptors (VEGFRs) and platelet-derived growth factor (PDGF-Rs). These two receptors are important for cell proliferation and tumor angiogenesis. Therefore, by simultaneously inhibiting these targets, tumor vascularization is decreased, induces cancer cell apoptosis, and consequently causes tumor cell shrinkage. It stops cancer cells from spreading and, as a result, stops the proliferation of cancer cells by blocking the aberrant protein from triggering the formation of cancer cells.[32]

d) Nintedanib (Ofev, Vargatef):

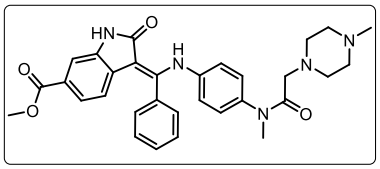

Orally administered nintedanib is used to treat idiopathic pulmonary fibrosis; in some cases, it is used in combination with other medications to treat non-small-cell lung cancer. It received approval in the US in March 2020 for the management of progressive phenotypic chronic fibrosing interstitial lung disease. It is the first medication for this type of progressive fibrosing lung disorders that has been approved by the U.S. Food and Drug Administration (FDA). Targets of this small molecule tyrosine kinase inhibitor include the fibroblast growth factor receptor, platelet-derived growth factor receptor, and vascular endothelial growth factor receptor. Nintedanib competitively

inhibits receptor tyrosine kinases (RTKs) as well as nonreceptor tyrosine kinases (nRTKs). Among the nRTK targets of neintedanib are Lyn, Src, and Lck. RTK targets of neintedanib include fibroblast growth factor receptors (FGFR) 1, 2, and 3, platelet-derived growth factor receptors (PDGFR) 1, 2, FLT3, and vascular endothelial growth factor receptors (VEGFR) 1, 2, and 3. Because it inhibits PDGFR, FGFR, and VEGFR three proteins that encourage fibroblast migration, proliferation, and transformation it is an effective treatment for IPF.[33]

e) Brivanib:

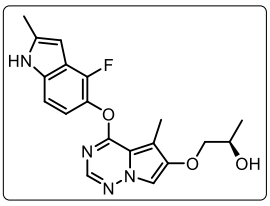

It is an oral tyrosine kinase inhibitor that primarily targets vascular endothelial growth factor (VEGF) receptors and fibroblast growth factor (FGFR). Cell signaling, cell proliferation, and angiogenesis are all impacted by FGFRs. These pathways can be interfered with by FGFR inhibition, which can therefore have anti-cancer effects. It was designed and developed as a potential anti-cancer agent, primarily to treat solid tumors and cancers that depend on angiogenesis (the creation and dissemination of new blood vessels) for growth and progression.[34]

f) Cediranib (AZD 2171, Recentin):

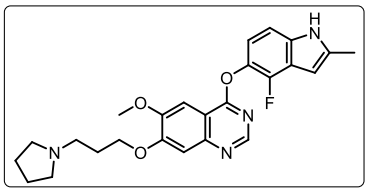

Vascular endothelial growth factor (VEGF) receptor tyrosine kinases are effectively inhibited by cediranib. AstraZeneca is working on the medication as a potential oral chemotherapeutic agent for treating cancer. When cediranib forms a blockade at VEGF receptors, it restricts the development of new blood vessels, which are necessary for supporting tumor growth. Without enough blood supply, tumor cells become starved for nutrients, which can slow or stop the growth of the tumor and possibly increase the effectiveness of other treatments.[35]

1.7.2: Epidermal growth factor receptor (EGFR): The epidermal growth factor receptor (EGFR), commonly referred to as ErbB1 or HER1 (human epidermal growth factor receptor 1), is a cell surface receptor that is a member of the ErbB family of receptor

tyrosine kinases. Controlling cell proliferation, growth, and differentiation in various tissues, such as the gastrointestinal system, lungs, and skin, requires EGFR. The extracellular ligand-binding domain, the transmembrane domain, and the intracellular tyrosine kinase domain comprise the transmembrane protein structure of EGFR. Its structure allows it to transmit messages from the extracellular environment to the cell's interior. The EGFR can be activated by a number of ligands, such as transforming growth factor alpha (TGF-alpha) and epidermal growth factor (EGF). Receptor dimerization, or the pairing of two EGFR molecules, results from these ligands binding to the receptor and activating the EGFR's intrinsic tyrosine kinase activity.

Tyrosine residues in the EGFR's intracellular domain are autophosphorylated as a result of EGFR activation. A series of intracellular signaling processes are triggered by these phosphorylated tyrosine residues, which act as docking sites for numerous downstream signaling proteins. These pathways play a role in controlling cell migration, differentiation, survival, and proliferation. EGFR signaling dysregulation is frequently seen in cancer. A variety of malignancies, including non-small cell lung cancer, colorectal cancer, and head and neck cancer, can arise and advance as a result of EGFR mutations or overexpression, which can cause uncontrolled growth of cells. To stop EGFR signaling in cancer cells, targeted medicines including EGFR inhibitors like gefitinib and erlotinib have been developed. Certain tumors with EGFR mutations or overexpression have been treated with EGFR inhibitors. These medications stop EGFR from functioning, which slows or prevents the growth of cancer cells. The efficiency of these inhibitors, however, may differ based on the particular cancer type and the presence of certain EGFR mutations. In-depth research on EGFR and its function in cancer biology resulted in the creation of targeted medicines, which have enhanced the therapy options for some cancer patients.

a) Gefitinib (Iressa):

Gefitinib is a member of the class of drugs known as EGFR (epidermal growth factor receptor) inhibitors. It is mostly employed to treat specific varieties of non-small cell lung cancer (NSCLC), a prevalent sort of lung cancer. The EGFR pathway, which is frequently dysregulated in NSCLC, is precisely the target of gefitinib. Similar to erlotinib, gefitinib is

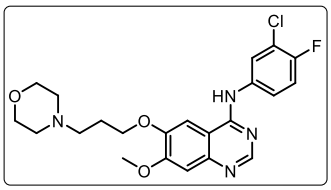

an EGFR inhibitor that prevents signaling through EGFR in target cells which affects the growth, proliferation, and survival of cancer cells. As a result, it is only beneficial in tumors with mutant and hyperactive EGFR, though additional mutations can cause resistance to gefitinib. It is used to treat some forms of breast, lung, and other malignancies.[36]

b) Cetuximab (Erbitux):

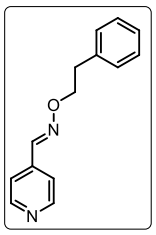

A monoclonal antibody drug called cetuximab is used to treat cancer. It particularly targets and inhibits the EGFR protein, which is involved in controlling cell growth and proliferation. Cetuximab disrupts the signaling pathways that support cancer cell proliferation by inhibiting EGFR. Most commonly, metastatic colorectal cancer, head and neck cancer, and other cancers are treated with cetuximab. cetuximab interacts with the EGFR protein found on the surface of cancer cells which stops EGFR from being activated and interferes with the signaling pathways that support the growth and survival of cancer cells.[37]

c) Erlotinib (Tarceva): As a tyrosine kinase inhibitor, erlotinib is a medicine used to

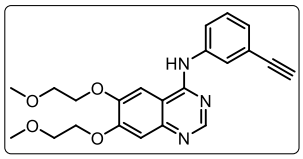

treat cancer. It is mostly used to treat pancreatic cancer and non-small cell lung cancer (NSCLC). The medicine erlotinib is a member of the EGFR inhibitors subclass of medications. Erlotinib disrupts the signaling pathways by inhibiting the EGFR, a cell surface receptor that controls the development and proliferation of cells.

Erlotinib targets the epidermal growth factor receptor (EGFR) tyrosine kinase, which is typically overexpressed and mutated in many forms of cancer. It attaches itself reversibly to the adenosine triphosphate (ATP) binding site of the receptor. To transmit the signal, two EGFR molecules must come together to form a homodimer. Using the ATP molecule to trans-phosphorylate each other on tyrosine residues, these then enlist the phosphotyrosine-binding proteins to EGFR to construct protein complexes that transduce signal cascades to the nucleus or activate other cellular metabolic processes. Erlotinib stops

phosphotyrosine residues in EGFR from being synthesized, which stops signal cascades from starting.[38]

1.7.3: BCAR4 amplification/HER2: Breast cancer has been linked to the long non-coding RNA (lncRNA) gene known as BCAR4 (Breast Cancer Anti-Estrogen Resistance 4). An increase in the number of copies of the BCAR4 gene in cancer cells is referred to as amplification. Gene amplification can result in the overexpression of a gene's RNA or protein output, which could aid in the emergence and spread of cancer. Targeted therapeutics that can inhibit BCAR4 action or its aftereffects are still being developed through research. These treatments might enhance the prognosis for people with breast cancers amplified by BCAR4.

a) Lapatinib (Tykerb and Tyverb):

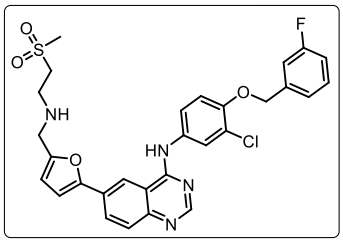

Lapatinib is a drug that is used in the form of lapatinib ditosylate used to treat cancer, notably some forms of breast cancer. As a tyrosine kinase inhibitor, it is primarily used to target particular proteins involved in the growth and spread of cancer cells. Human epidermal growth factor receptor 2 (HER2) and epidermal growth factor receptor (EGFR) are two related proteins that lapatinib inhibits in order to function. Cell surface receptors HER2 and EGFR are both involved in the development and proliferation of cells. The proliferation of cancer cells that rely on these pathways can be slowed or stopped by inhibiting their receptors.[31]

1.7.4. mTOR (mammalian target of rapamycin): A protein kinase known as the mammalian target of rapamycin (mTOR) is essential for controlling cell growth, proliferation, and survival. It is an essential part of signaling pathways that react to numerous environmental and cellular inputs, including energy status, growth factor signaling, and nutrition availability. Autophagy, which is the process of breaking down and recycling cellular components, ribosome biogenesis, protein synthesis, and lipid metabolism are all regulated by mTOR. It performs the function of a central regulator, integrating information from many sources to decide whether the cell should divide,

expand, or go through other cellular processes. mTOR is part of the mTOR Complex 1 (mTORC1) and mTOR Complex 2 (mTORC2) protein complexes, each of which has unique roles and downstream targets. These complexes control various facets of cell biology.

mTOR signaling dysregulation is frequently seen in cancer. Mutations in the genes connected to this pathway can result in the uncontrolled proliferation of cells and support the growth of cancer. Certain malignancies are treated with targeted treatments that block mTOR or its upstream regulators. mTOR is very responsive to the availability of nutrients, particularly glucose and amino acids. When nutrients are in plenty, mTOR signaling is triggered, which promotes anabolic processes and cell development. On the other hand, when nutrients are in short supply, mTOR signaling is suppressed, which promotes catabolic activities like autophagy. Numerous studies have been conducted on mTOR in the areas of cell biology, cancer biology, and aging. The development of targeted therapeutics and insights into the molecular mechanisms underlying various diseases have both been made possible by our growing understanding of their regulation and function.[39]

a) Temsirolimus (Torisel):

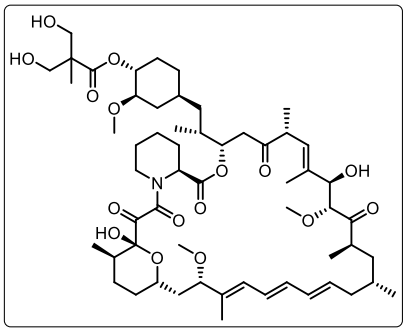

Temsirolimus belongs to the class of medications known as mTOR (mammalian target of rapamycin) inhibitors. Temsirolimus is a drug used to treat cancer, specifically as a targeted therapy for specific cancer types. The protein kinase mTOR, which is essential for cell growth, proliferation, and survival, is inhibited by temsirolimus. Temsirolimus interferes with the signaling pathways that support the development of cancer cells by inhibiting mTOR. Even though temsirolimus exhibits activity on its own, it can also be transformed in vivo into sirolimus (rapamycin) As a result, despite what the manufacturer may state, the prodrug's metabolite may really be more responsible for its activity than the prodrug itself. Even though temsirolimus exhibits activity on its own, it can also be transformed in vivo into sirolimus (rapamycin). As a result, despite what the producer may state, the prodrug's metabolite may really be

more responsible for its activity than the prodrug itself. Temsirolimus therapy causes cell cycle arrest in the G1 phase and prevents tumor angiogenesis by lowering VEGF production. For some cancer types, particularly renal cell carcinoma, temsirolimus is a significant therapeutic option.[40]

1.7.5. Histone deacetylases (HDAC):

Histone deacetylase, often known as HDAC, is an enzyme that controls how genes are expressed and how chromatin is organized in living cells. proteins, known as histones, which assist in packing and compacting DNA into a structure within the cell nucleus, are modified by these enzymes, and this alteration is critical. HDACs may be overactive in cancer cells, which would silence tumor suppressor genes and encourage the proliferation of cancer cells. HDAC inhibitors are a class of medications created to limit the function of HDACs, increasing histone acetylation and perhaps reactivating tumor suppressor genes that have been silenced. HDAC inhibitors are utilized in several cancer treatments and have been investigated for their potential in cancer therapy.

a) Valproic acid (Valproate, VPA):

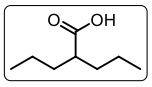

Valproic acid is a drug primarily used to treat bipolar disorder and epilepsy. It is a mood stabilizer and an anticonvulsant. Valproic acid's precise mode of action is unknown, however, it is believed to involve a number of processes. Gamma-aminobutyric acid (GABA), a neurotransmitter that suppresses neuronal activity and can help avoid seizures (partial seizures, absence seizures, and generalized seizures), is known to rise in the body because of valproic acid. Ion channels and other neurotransmitter systems in the brain may potentially be impacted by valproic acid. Prophylaxis for migraines is one of VPA's therapeutic applications.[41]

1.7.6. Poly (ADP-ribose) polymerase [PARP]:

A family of enzymes known as PARP is involved in a number of crucial biological functions, such as DNA repair, genomic integrity, and cell death. These enzymes are essential for preserving genomic integrity and are located in the nucleus of cells. The

human body has many PARP enzymes, although PARP-1 and PARP-2 are the most thoroughly researched. The primary function of PARP enzymes is the restoration of DNA that has been damaged. The PARP proteins are activated and assist in recruiting repair proteins to the location of DNA damage when a cell experiences environmental stressors such as radiation, toxins, or other environmental stresses.

In recent years, a new family of anti-cancer medications called PARP inhibitors has emerged. These inhibitors are made to prevent the PARP enzymes from working, especially PARP-1 and PARP-2. Cancer cells with specific DNA repair deficiencies (such as mutations in the BRCA genes) are less able to repair DNA damage when PARP is inhibited, which causes DNA errors to accumulate and ultimately results in cell death. Several cancers, including ovarian cancer, breast cancer, and prostate cancer, are treated with PARP inhibitors.

a) Veliparib:

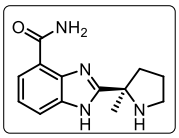

The drug Veliparib is categorized as a PARP (poly (ADP-ribose) polymerase) inhibitor. The drug Veliparib is categorized as a PARP (poly (ADP-ribose) polymerase) inhibitor. Veliparib and other PARP inhibitors are used to treat cancer, particularly ovarian and breast malignancies. The PARP enzymes, especially PARP-1 and PARP-2, are inhibited by Veliparib. In order to repair damaged DNA in cells, PARP enzymes are necessary. Cancer cells with abnormalities in other DNA repair mechanisms, such as those brought on by mutations in the BRCA genes, are less able to repair DNA damage when PARP is blocked. As a result, DNA errors start to accumulate, which ultimately causes cell death.[42]

b) Olaparib (Lynparza):

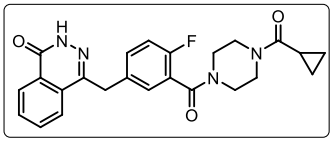

Adults with advanced BRCA-mutated ovarian cancer can use the drug Olaparib. It is a poly ADP ribose polymerase (PARP) inhibitor, that inhibits the poly ADP ribose polymerase enzyme, preventing the enzyme from repairing DNA. It works against some ovarian, breast, and prostate cancers in those with genetic BRCA1 or BRCA2 mutations. BRCA1/2

mutations may be resistant to various cancer treatments and genetically predisposed to the development of some cancers. These tumors do, however, occasionally have a special susceptibility since the cancer cells rely more heavily on PARP to fix their DNA and keep them dividing. This indicates that if the malignancies are responsive to this treatment, then medications that specifically block PARP may be advantageous.[43]

1.7.7. Immune Checkpoint Inhibitor:

Immune checkpoint inhibitors are a type of therapy that uses the immune system's power to combat cancer. To improve the body's immune response and control the immunological responses against cancer cells, these inhibitors specifically target proteins on immune cells known as checkpoints. The checkpoints, such as PD-1 and CTLA-4 operate as "brakes" on the immune system to avoid overactivation. These checkpoints can be used by cancer cells to circumvent the immune system. Immune checkpoint drugs disengage these brakes, allowing the immune system to more accurately identify and combat cancer cells. These inhibitors are used to treat a number of cancers, including Hodgkin lymphoma, lung cancer, melanoma, kidney cancer, bladder cancer, and more. In certain cases, they have been approved for both advanced and early-stage malignancies.[44]

a) Pembrolizumab (Keytruda):

Pembrolizumab is an immune checkpoint inhibitor that is primarily used to treat different tumors. An immune checkpoint inhibitor called pembrolizumab specifically targets the T cell-surface PD-1/programmed cell death protein 1 (PD-1) receptor. Immune cells' surface protein called PD-1 is involved in controlling the immune response. The PD-1 pathway can be used by some cancer cells as a means of immune system evasion. By blocking PD-1, pembrolizumab stops cancer cells from avoiding immune identification and attack. Pembrolizumab is a humanized antibody used to treat a number of malignancies, such as

non-small cell lung cancer (NSCLC), cancer of head and neck squamous cell, melanoma, Hodgkin lymphoma, Merkel cell tumor, kidney cancer, urethral cancer, gastric cancer, and more. It uses the immune system's strength to target and attack. Pembrolizumab "releases the brakes" by blocking PD-1 on the immune system, which allows it to effectively identify and attack cancer cells.[45]

1.7.8. Immune checkpoint Inhibitor in adjuvant treatment:

Immune checkpoint inhibitors are being researched extensively as adjuvant therapies for specific forms, types, and stages of cancer. In order to lower the chance of cancer recurrence, adjuvant therapy is a treatment provided after the initial treatment (such as surgery or radiation therapy). Immune checkpoint inhibitors are used as adjuvant therapy to help the body's immune system get rid of any cancer cells that the primary therapy may not have entirely destroyed or in situations where the tumor has traits that make it more amenable to immunotherapy.

Immune checkpoint inhibitors, including pembrolizumab and nivolumab, have been authorized for use as adjuvant therapy for high-risk melanoma. After the main tumor has been surgically removed, these treatments are used to lower the likelihood of melanoma recurrence. Adjuvant therapy with checkpoint inhibitors like durvalumab may be explored in some cases of early-stage non-small cell lung cancer (NSCLC), particularly when the tumor has been entirely removed. In patients with renal cell carcinoma (kidney cancer) who are at high risk of recurrence following surgery, adjuvant therapy with immune checkpoint inhibitors, such as nivolumab, is being explored. Atezolizumab has been investigated as adjuvant therapy for surgically treated individuals with muscle-invasive bladder cancer. Immune checkpoint inhibitors may be used as adjuvant therapy following initial therapy in select cases of Hodgkin lymphoma.

Investigations are continuing to determine if immune checkpoint inhibitors are effective as adjuvant treatments for various cancer types. The effectiveness and safety of these medicines in various patient populations are mostly determined by clinical trials. Immune checkpoint inhibitors have the potential to lower the risk of cancer recurrence in

some patients, but they can also cause immune-related adverse events (irAEs), which may need close observation and therapy. When choosing to use these medications as adjuvant therapy, the possible advantages and hazards should be considered carefully.

a) Ipilimumab (Yervoy):

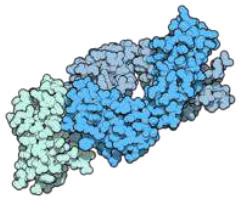

A drug called ipilimumab is used in cancer immunotherapy. Instead of directly attacking the disease, it works by boosting the body's natural immune response to work against cancer cells. It is primarily used to treat specific cancers and is categorized as a checkpoint inhibitor. Ipilimumab targets the CTLA-4 protein receptor, which is present on the surface of T cells, an immune cell subtype, which is known to produce cytotoxic T lymphocytes. The immune response is downregulated by CTLA-4, which functions as a checkpoint inhibitor to stop the immune system from becoming overactive. However, CTLA-4 can be used by cancer cells as a means of immune system evasion. Ipilimumab inhibits CTLA-4, enabling the immune system to react more robustly to cancer cells. Skin cancer called melanoma is primarily treated with ipilimumab. It has received approval for the treatment of advanced melanoma as well as for use as an adjuvant therapy in individuals who are at high risk of developing the disease again after surgery.[46]

1.7.9. Other drugs used for the treatment of cervical cancer:

a) Bleomycin Sulfate: A class of water-soluble basic glycopeptides antibiotics derived from “Streptomyces verticillus” referred to as “bleomycin” is employed as both antibiotics and cancer drugs.[45] All bleomycins share the same basic structure. The sole structural difference among bleomycin is the functional group joined to the terminal amine. It is supposed to degrade DNA by sequence selective DNA binding and cleavage. Bleomycin also prevents thymidine from being incorporated into DNA. In vitro, Oxygen

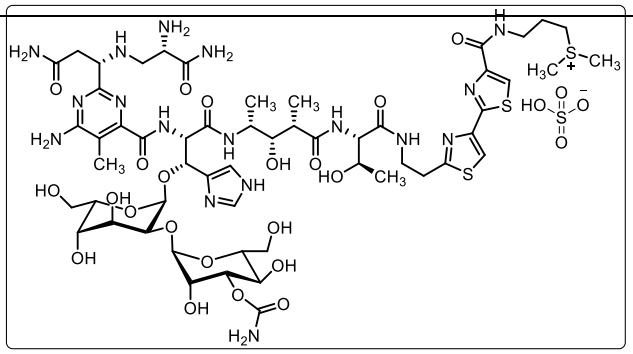

and metal ions, such as iron, are required for bleomycin-induced DNA breakdown. When iron is chelated by bleomycin, a pseudoenzyme is produced that releases superoxide and hydroxide free radicals, which then break DNA. Oxygen and metal ions, such as iron, are required for bleomycin-induced DNA breakdown in vitro. When iron is chelated by bleomycin, a pseudoenzyme is produced that releases superoxide and hydroxide free radicals, which then break DNA. Topoisomerase II enzyme inhibition, lipid peroxidation, and oxidative RNA degradation are other mechanisms that contribute to bleomycin-induced cytotoxicity. According to a different theory, bleomycin can bind to specific DNA strand locations and cause scission by removing the hydrogen atom from the base, leading to strand cleavage as the base goes through a Criegee-type rearrangement or creates an alkali-labile lesion. Cancers of the testicles, ovary, breast, and cervix are all treated with bleomycin. It is also used to treat Hodgkin and non-Hodgkin lymphomas.[47]

b) Hycamtin (Topotecan Hydrochloride): A semi-synthetic camptothecin derivative called topotecan hydrochloride has anti-tumor properties as well as topoisomerase I-inhibitory activity. It is used to treat specific forms of cervical cancer, small-cell lung cancer, and ovarian cancer.

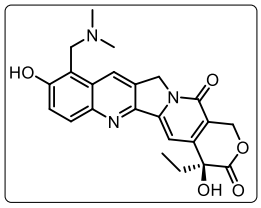

By causing reversible single-strand breaks, topoisomerase I reduces torsional stress in DNA. Topotecan blocks the religation of these single strand breaks by attaching to the topoisomerase I-DNA complex. Topotecan's cytotoxicity is hypothesized to be due to interactions between replication enzymes and the ternary complex generated by topotecan, topoisomerase I, and DNA, which results in double-strand DNA damage produced during DNA synthesis. These double strand breaks cannot be effectively repaired by mammalian cells.[48]

1.7.10. Future Treatment of Cervical Cancer using Autophagy: In order to combat human diseases, such as cervical cancer, disregulation of autophagy is emerging as a

crucial biological mechanism. Additionally, homeostasis has been linked to autophagy, a process that involves the breakdown of cellular organelles and cytoplasm in lysosomes. Depending on the type of cell or tissue, autophagic flux can change, which can change a cell's fate under stress and cause it to either survive or die. In turn, autophagy may control tumor spread and ensuing carcinogenesis. Cancer is noted for having an inflammatory phenotype. Vascular insufficiency in malignancies, particularly cervical tissue, results in the loss of glucose and/or oxygen, disrupting the osmotic gradient, and extracellular acidosis in the tumor microenvironment, which may ultimately lead to autophagy. Therefore, in the near future, selective modulation of complicated autophagic signals may be a creative method for identifying clinically significant biomarkers for cervical cancer.[49] Autophagy modulation is a promising field of research that could lead to the development of novel therapeutic modalities for the treatment of cervical cancer in the future.

1.8 Present Work:

Heterocyclic compounds constitute an essential class of chemicals because they are found in many pharmaceuticals, natural products, and other bioactive molecules. Heterocyclic compounds contain at least one non-carbon element such as nitrogen, oxygen, or sulfur which accounts for their biological activity and due to this, their wide range of chemical and biological characteristics are well studied and in order to create novel molecules with a variety of biological functions. One important aspect of the biological activity of heterocyclic compounds is their reversible binding to proteins. Researchers have taken the advantage of this feature while designing drugs since substances with the ability to attach to target proteins both selectively and reversibly may be therapeutically useful. Heterocyclic compounds are important in the treatment of cancer because they have been used in the synthesis of several chemotherapy drugs. While designing specific cancer medicines, heterocyclic chemicals are frequently employed. Targeting chemicals or pathways that are essential to the development and spread of cancer cells is the specific aim of these medications. These medications can hinder the growth of cancer cells while causing the least amount of harm to healthy cells by blocking particular targets.

There are some heterocyclic compounds, like indoles, that can mimic the structure of peptides, which are vital biomolecules. Because of their structural similarities, these substances can interact with proteins and enzymes to produce specific biological effects.

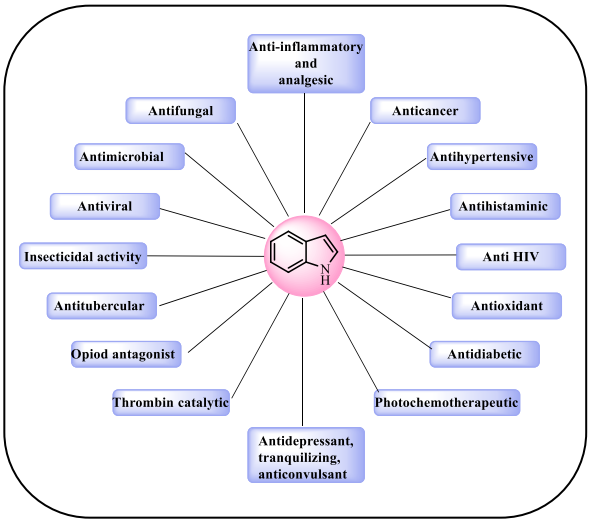

Figure F1.11: *Biological activities of indole*

In Medicinal Chemistry, indole is a commonly used pharmacophore - a component of a molecule that is responsible for its biological activity. This versatile heterocyclic molecule has a broad range of biological functions **(Fig. F1.11)** and is present in many medications and natural products.[50] Therapeutic applications are frequently linked to the existence of an indole nucleus. Because of its potential applications in medicine, indoles have sparked the curiosity of scientists who are interested in synthesizing novel medications. To create molecules with better pharmacological qualities or to target particular illnesses or conditions, researchers frequently modify the indole structure.

Several natural products, chemicals, and molecules that have shown anti-cancer activities contain indole as a structural element. Known by several names, including DIM or 3,3'-diindolyl methane, the bis-indolyl methane is a naturally occurring substance that is simple one found in the indole class of natural products. During digestion, a variety of plants and vegetables, including cabbage, broccoli, and Brussels sprouts, emit bis-indolyl methane. When it comes to hormone-related diseases like breast, prostate, and cervical cancer, DIM is a well-known anti-cancer agent[51] that has drawn attention for its possible health benefits, which include its application in cancer prevention and treatment **(Fig. F1.12)**.[52] Through the STAT3 pathway, 3,3'-diindolylmethane increases chemotherapy sensitivity and reduces the viability of ovarian cancer cells.[53]

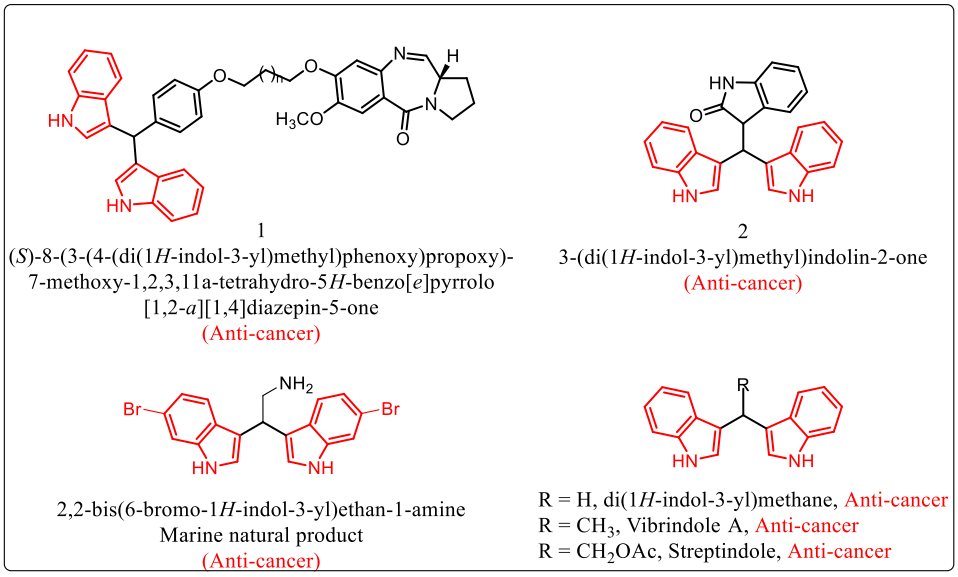

Figure F1.12: *Pharmacological importance of bioactive 3,3'-BIMs based molecules, and natural products.*

As discussed in the introduction, among various types of cancer, the fourth most commonly found cancer in women is cervical cancer, which affects the woman's reproductive system. Depending on the stage of the disease, there are several treatment options for cervical cancer. When compared to chemotherapy or radiation therapy, targeted therapy may have fewer adverse effects for certain patients, making it a better choice for them. Treatment solutions that enable procedures that spare fertility should be taken into consideration for younger individuals who want to maintain their fertility. In such circumstances, targeted therapy might be useful.

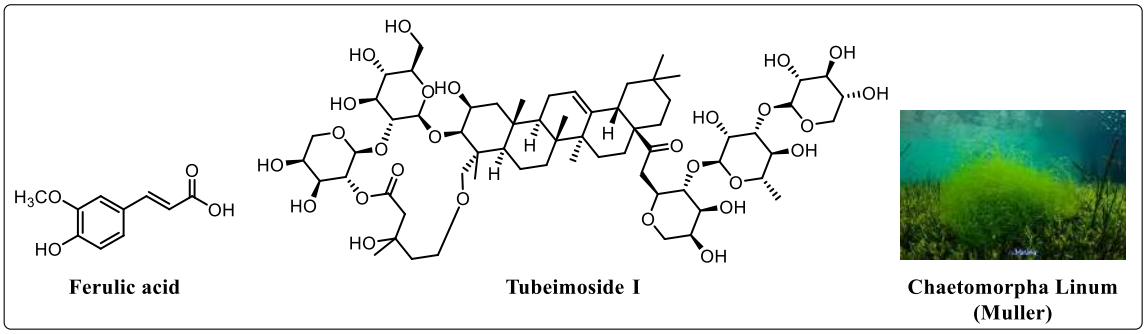

Figure F1.13: *Process of Autophagy*

With the help of targeted medications, cervical cancer management has progressed into novel therapy methods; nonetheless, the clinical achievement of these contemporary therapies has not demonstrated the anticipated effectiveness.[54] Clonal/genetic heterogeneity and the intricate network of related cell signaling pathways are frequently linked to this slow growth in cervical cancer treatment **(Fig. F1.13)**.[55] These cervical cancer deficiencies make it even more imperative to use chemicals that trigger cell death pathways, such as autophagy, which is not as well studied in cervical cancer treatment.

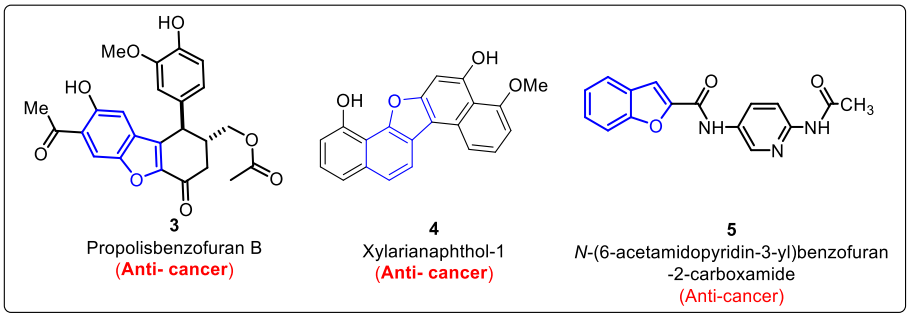

Figure F1.14: *Representative examples of drugs containing benzofuran structural core*

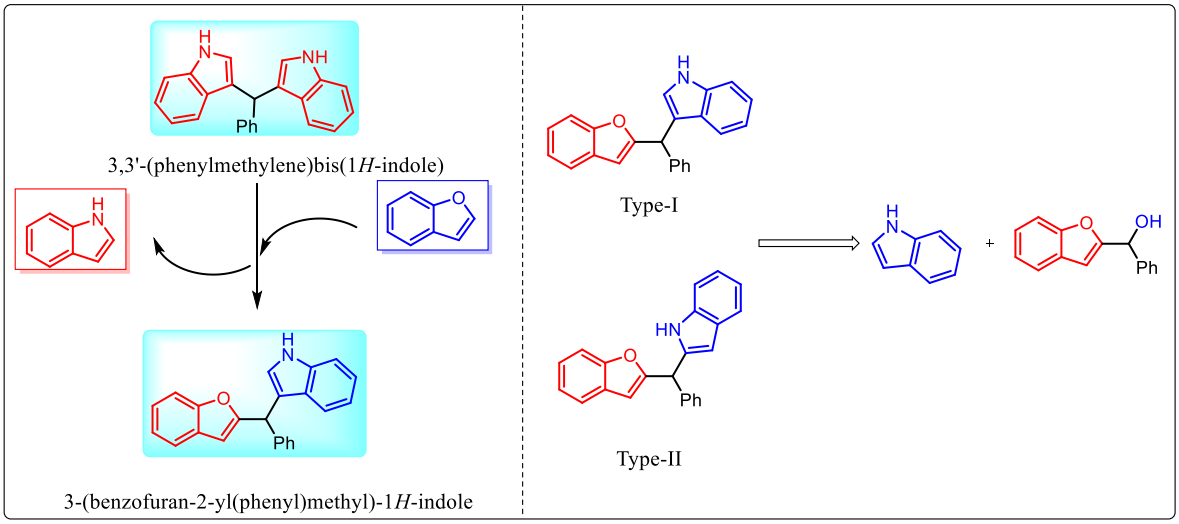

Figure F1.15: *Designing the targeted compounds by displacing one of the indoles from bis indolyl methane and synthesis of two types of newly designed scaffolds*

Motivated by the necessity to find new synthetic and natural medications that might cause autophagy to be induced in cervical cancer cells, we describe here the discovery of novel 3-(benzofuran-2-ylmethyl)-1H-indole derivatives as putative inducers of autophagy in cervical cancer cells. These compounds were designed by integrating the bisindolylmethane[56] and benzofuran scaffolds[57-64] found in natural products, which have a variety of biological activities, including antimicrobial, antibacterial, and anticancer **(Fig. F1.14)**, anti-inflammatory, antidiabetic, antineophobic, and anticonvulsant properties. These compounds were designed based on the notion that combining two distinct heterocyclic scaffolds can be a useful strategy for discovering novel small molecule probes. In this context, we designed the compounds in such a way that in type I, the indolyly unit is substituted at C3 position, where as in type II, substitution is at the C2 position. These two classes of compounds have been designed as potential candidates for anti-cancer screenings (**Fig. F1.15**).

1.9. Chemistry:

1.9.1 Synthesis of 3-(benzofuran-2-yl(phenyl)methyl)-1*H*-indole derivatives:

The adopted approach employs a simple Friedel-Crafts-like alkylation of indole (**2a**) with benzofuran-2-yl(phenyl)methanol (**1a**), which is made by reducing the corresponding 2-aroyl benzofurans with $NaBH_4$.[65] The structures of the resulting

compounds was confirmed by using spectral and analytical data (^{1}H, ^{13}C, and HRMS). In the ^{1}H NMR spectrum of **1a**, the characteristic peak of OH appeared at δ 5.91 ppm as a broad singlet and in the product, the OH peak disappeared and the C2-H proton from the indole group resonated at δ 5.73 ppm. The four benzene protons were seen to resonate at δ 6.73 ppm as a doublet with J = 0.8 Hz and another one at δ 6.96 ppm as a triplet with J = 7.3 Hz. The remaining two benzene protons appear to have fused with other aromatic protons and the NH proton resonated at δ 7.95 ppm as a singlet. In the 13C NMR spectrum of the **1a**, CH-OH carbon appeared at δ 70 ppm, whereas in the 3aa, it resonated at δ 43 ppm, and in the NMR of 3aa, C2 carbon from indole appeared at δ 136.5 ppm and the 6 benzene carbons were seen to resonate at δ 120.6, 119.6, 119.5, 116.7, 113.5, 111.1 ppm. Thus, satisfying the alkylation product (3aa) formation. In the HRMS, the exact mass calculated for the product 3aa was $C_{19}H_{16}O_4Na$ $[M+H]^+$: 324.1383, and it was found to be 324.1380. Thus, from ^{1}H, ^{13}C, and the HRMS spectrum, the formation of the alkylation product **3aa** was confirmed.

Subsequently experiments were performed to check the feasibility of the proposed alkylation which then led to the identification of the compatible solvents and Lewis acids for the alkylation. For the optimization studies the experiments were divided into two parts, in the first part, the solvent, i.e. dichloromethane was kept constant because starting materials were easily soluble in dichloromethane and most of the Lewis acids are soluble in this solvent. Whereas, in the second part, the reagent was kept constant. In the case of $AlCl_3$ (Table T1.1, entry 1) and $Sc(OTf)_3$ (Table T1.1, entry 2), the product **3aa** was isolated in more than 40% yield. When the $Cu(OTf)_2$ (Table T1.1, entry 3) was employed as catalysts, no product was isolated from the reaction mixture. In the presence of $ZnCl_2$ (Table T1.1, entry 4) 42% of product was observed. In the case of $BF_3.OEt_2$ (Table T1.1, entry 5) complex mixture was formed. The increase in the product formation was observed in the case of PTSA (Table T1.1, entry 6), where the product **3aa** formed in 83% yield.

Table T1. 1. *Optimization Studies*

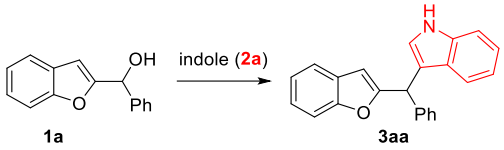

1a 3aa

Sr. No.	Lewis acid	Solvent	Yield % (3aa)
1	$AlCl_3$	CH_2Cl_2	41%
2	$Sc(OTf)_3$	CH_2Cl_2	45%
3	$Cu(OTf)_2$	CH_2Cl_2	[c]No reaction
4	$ZnCl_2$	CH_2Cl_2	42%
5	$BF_3.OEt_2$	CH_2Cl_2	[d]Complex mixture
6	**PTSA**	**CH_2Cl_2**	**[e]83%**
7	PTSA	DCE	71%
8	PTSA	Toluene	68%
9	PTSA	DMF	69%
10	PTSA	THF	54%
11	PTSA	Chloroform	56%
12	PTSA	Methanol	59%
13	PTSA	Acetone	69%
14	PTSA	Acetonitrile	71%

[a]Reaction Conditions: 1a (1 equi), 2a (1.5 equi), (1.2 equi), at rt for 2 h. [b]isolated yield after chromatographic purification. [c]no reaction, unreacted starting material recovered. [d]formation of complex mixture. [e]clean reaction.

For the next series of compounds, catalytic (PTSA) was kept constant and different solvents were screened for the optimization studies. As shown in Table T1.1, when DCE (Table T1.1, entry 7) was used, 71% of the product was obtained. In the presence of toluene (Table T1.1, entry 8) and DMF (Table T1.1, entry 9), the product 3aa was isolated in more than 65% of yield. When THF (Table T1.1, entry 10), Chloroform (Table T1.1, entry 11), and methanol (Table T1.1, entry 12) were employed as solvents, more than 50% of the product was isolated. However, in the presence of Acetone (Table T1.1, entry 13), the alkylated product **3aa** was obtained in more than 65% yield, whereas solvent CH_3CN (Table T1.1, entry 14) gave the final product **3aa** in more than 70% yield. Optimization studies reveal that PTSA and CH_2Cl_2 gave the best results.

After getting the best results in hand, the amount of reagent was optimized using different equivalents of the PTSA. When 0.1 equivalents of PTSA was used, only small amount of product, i.e. 10% of the product was observed (Table T1.2, entry 1). Then 0.5 equivalents of reagent were used, but only 54% of the product was observed (Table T1.2, entry 2). At the 0.7 equivalent, 60% of the product was isolated (Table T1.2, entry 3). Results were satisfying at 1 equivalent, where 74% of the product was obtained (Table T1.2, entry 4) and after that we thought about further increasing the equivalents of the PTSA. And for our delight we got good results i.e. 83% of yield at 1.2 equivalents (Table T1.2, entry 5). When the equivalents of the reagent were increased further to 1.5 equivalents, no remarkable difference was observed and the product was isolated in 83.2% (Table T1.2, entry 6). So, we further moved with the 1.2 equivalents of the PTSA for scope of reaction.

Sr. No.	Amount (in equi.)	Time (h)	Yield (%)
1	0.1	3	10
2	0.5	3	54
3	1	2	74
4	1.2	2	83
5	1.5	2	83.2

Table T1.2: *Optimization of the weight of the reagent*

1.9.2 Exploring the scope of reaction:

Once the ideal conditions were reached, the three aryl rings' substituents were changed to investigate the reaction's scope. Different electron donating and withdrawing groups were used for the substitution. Overall, the reactions went effectively and produced

good to excellent yields of the corresponding 3-(benzofuran-2-ylmethyl)-1*H*-indole derivatives. C3 alkylation products were isolated in good to excellent yields. Along with simple indoles, 3 substituted indoles were also used for C2 alkylation.

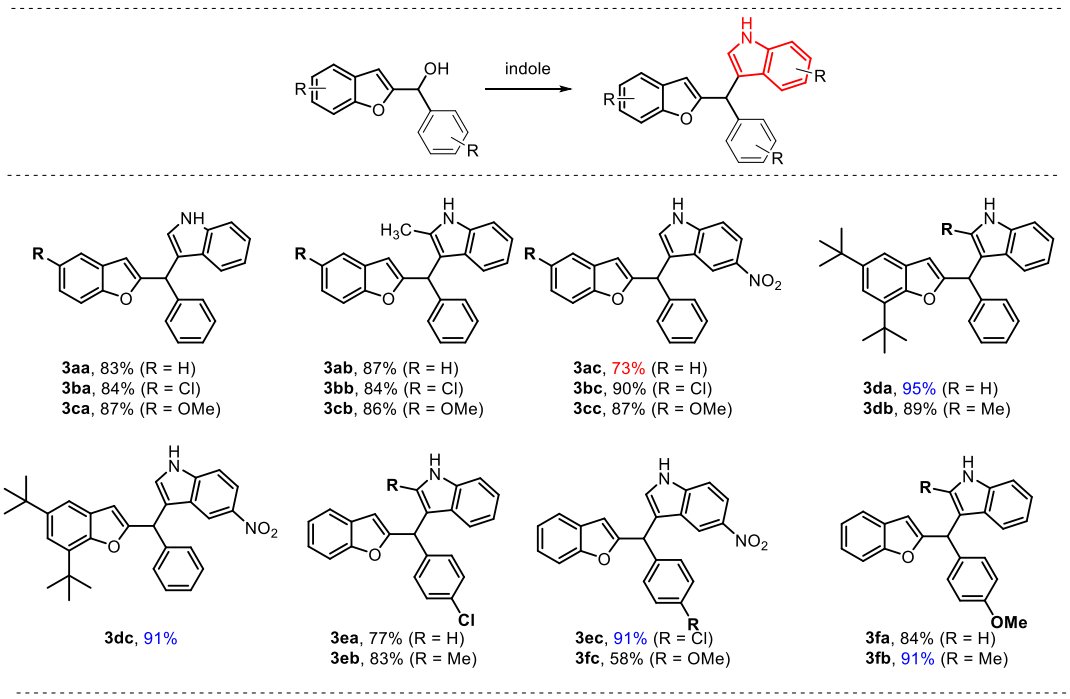

Scheme S1.1: *C3 alkylation products*

Furthermore, we have investigated the possibility of C2 alkylation of 3-methyl indole, which results in the 2-(benzofuran-2-ylmethyl)-3-methyl-1*H*-indole derivatives (**4aa-4fa**). To our delight, the C2-alkylated product also was formed in good to excellent yield.

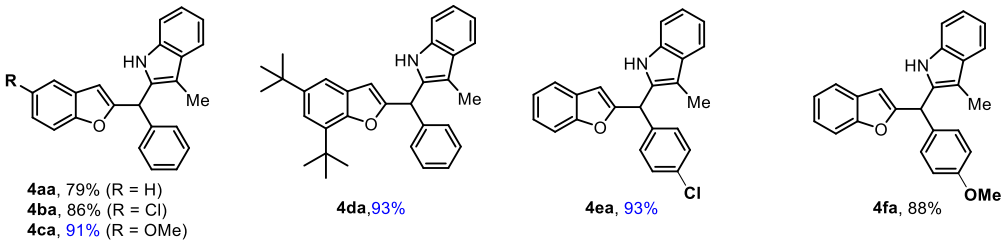

Scheme S1.2: *C2 alkylation products*

1.10 Biology:

Since most of the compounds examined formed vacuoles in the treated SiHa cell line, screening all of the synthesized compounds for biological activity and morphological changes with the treatment suggested the induction of autophagy. It's crucial to remember that earlier research linked certain cell morphological characteristics to the start of autophagy in response to outside stimulation.[68-70] Five compounds, from the panel of compounds were selected, which showcased the lowest IC50 on treatment with Siha and were eventually tested in another cervical cancer cell line, C33a (**Table T1.3**). It's interesting to note that the isomeric series' compounds **4aa**–**4fa** were determined to be inert, and the biological screening of **5aa** to **6cc** is going on.

Table T1.3: *IC_{50} values of **3aa** to **4fa***

Entry	**Compound**	IC_{50} (μM±SE)	
		SiHa	C33a
1	**3aa**	71.12±5.95	
2	**3ba**	58.01±1.24	
3	**3ca**	>100	
4	**3ab**	56.47±6.44	
5	**3bb**	47.52±1.92	38.74±6.12
6	**3cb**	>100	
7	**3ac**	40.43±3.17	35.17±4.88
8	**3bc**	>100	
9	**3cb**	>100	
10	**3da**	61.58±2.15	
11	**3db**	72.00±5.22	
12	**3dc**	48.21±6.15	
13	**3ea**	49.81±2.95	34.21±6.53
14	**3eb**	35.85±3.23	31.23±3.31
15	**3ec**	36.87±3.85	29.44±1.66
16	**3fa**	>100	
17	**3fb**	>100	
18	**3fc**	>100	
19	**4aa**	>100	
20	**4ba**	77.87±3.22	
21	**4ca**	>100	
22	**4da**	>100	
23	**4ea**	72.49±2.50	

24	**4fa**	>100	

1.10.1 % Viability Assay:

Compounds **3eb** and **3ec** were then examined for the % viability assay, which is performed by using a MTT assay. Interestingly, the (**Fig. F1.17**) graphs illustrate that the compounds **3eb** and **3ec** are highly viable on squamous cell carcinoma and cervical carcinoma cell lines at a concentration of 10 µg. As a result, these results motivated more studies into these two chemicals.

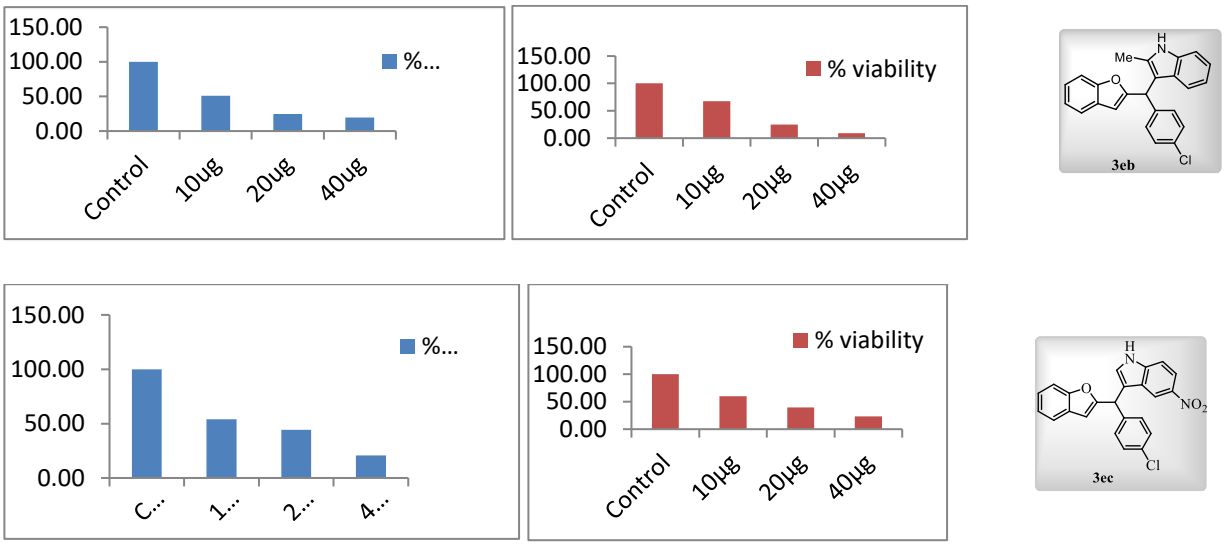

Figure F1.17: [a]compounds 3eb and 3ec were tested for % viability using two different cell lines.

- **Cell Lines screened**

SiHa (ATCC® HTB-35™) squamous cell carcinoma

C33a (ATCC® HTB-31™) cervical carcinoma

- **Performed by MTT Assay**

Blue Graph indicates activity against C33a

Red Graph indicates activity against SiHa

1.10.2 Evidence of Autophagy: Confirming Cellular Self-Digestion in SiHa cell line:

The process of autophagy has been studied in this experiment using two commonly employed methods: (1) cell staining, and (2) morphological changes.

(1) Cell Staining: Compounds **3eb** and **3ec** were then examined in more detail in order to determine whether the increasing conversion of LC3I to LC3II is a sign of autophagy.[71] A ubiquitin-like protein linked to autophagosomes that leads to selective autophagy is called LC3 (microtubule-associated protein 1 light chain 3). LC3 is cleaved at its carboxy-terminal to generate the cytosolic variation known as LC3I during the autophagic process. The glycine at the carboxy-terminus region then associates with phosphatidylethanolamine to form an LC3-phosphatidylethanolamine complex, also referred to as LC3II.25. Since both cell lines treated with compounds **3eb** and **3ec** showed a progressive conversion of LC3I to LC3II, this suggests that autophagy is occurring (**Figures F1.18 and F1.19**). An additional protein linked to autophagy, p62 is a ubiquitin-binding scaffold protein with an LC3 binding region. The protein declines with increasing autophagy and accumulates upon autophagic inhibition.[72] Autophagy induction was further validated by the timely reduction of p62 expression observed with increased incubation with the compounds (**Figures F1.18 and F1.19**). As a result of the autophagosome and lysosome fusion during the autophagy process, LC3 becomes degraded or dissociated and is reduced in quantity in the autolysosome membrane (**Fig. F1.19**).

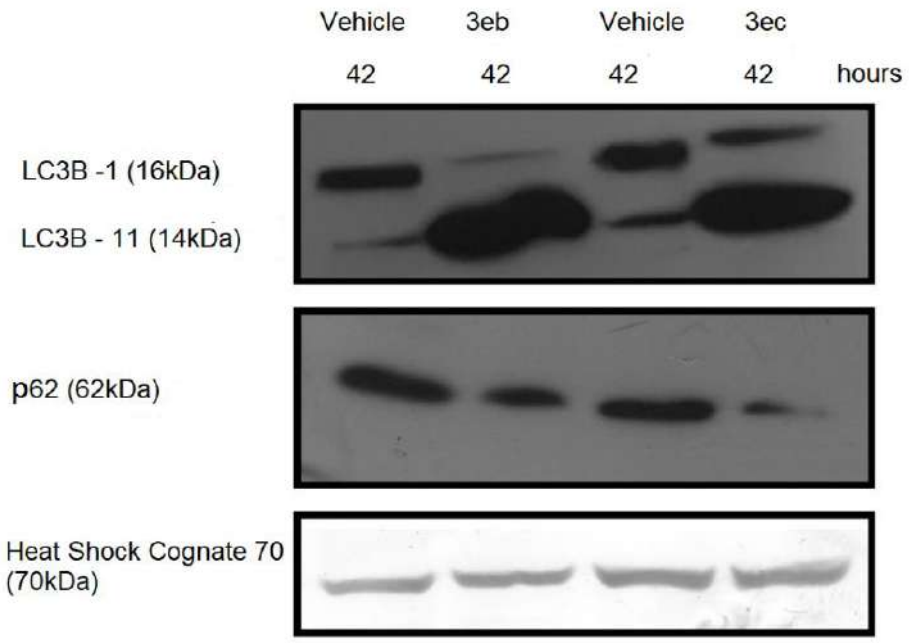

Figure F1.18: *Induction of Autophagy by **3eb** (30 µM) and **3ec** (30 µM) was also observed in C33a cell line by LC31 to LC311 cleavage and reduction in p62 levels.*

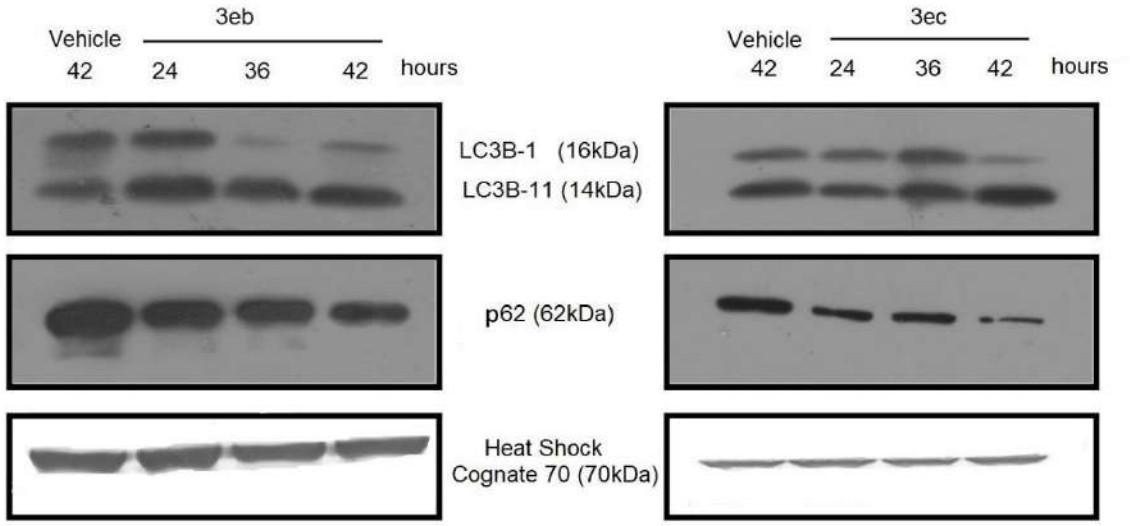

Figure F1.19: *Representative of western blot, **3eb** (30 µm) and **3ec** (30 µm) induces LC3I to LC3II conversion. Similarly, p62 showed decreasing pattern of expression with time, thereby confirming autophagy in the SiHa cell line.*

(2) Morphological Changes: Light microscopy observation exhibits that compounds **3eb** and **3ec** induced morphological changes in the Siha cell line viz., rounding up of cells and seem to be detached from the surface of the culture plate as shown in Figure F1.20b and Figure F1.20c. The morphology of compounds **3eb** and **3ec** treated Siha cells are completely different from the control Siha cells as shown in Figure F1.20a-c. The presence of autophagic vacuoles is clearly seen in treated cells that are not observed in the control group. Further, the treated cells show a significant amount of membrane blebs, which are unable to be seen from untreated cells demonstrating the significance of Autophagy in a cellular pathway. Moreover, promising blisters are clearly seen from **3ec** compounds treated cells as compared to **3eb** treated cells indicating the significant impact of compound **3ec** on the Autophagy pathway as shown in Figure F1.20. Interestingly, blisters are unable to be observed from untreated cells. Overall, the observation of autophagic vacuoles, membrane blebs, blisters, and morphological changes demonstrated cell apoptosis. Especially, vacuole formation inside the cytoplasm indicates the possibility of autophagy.

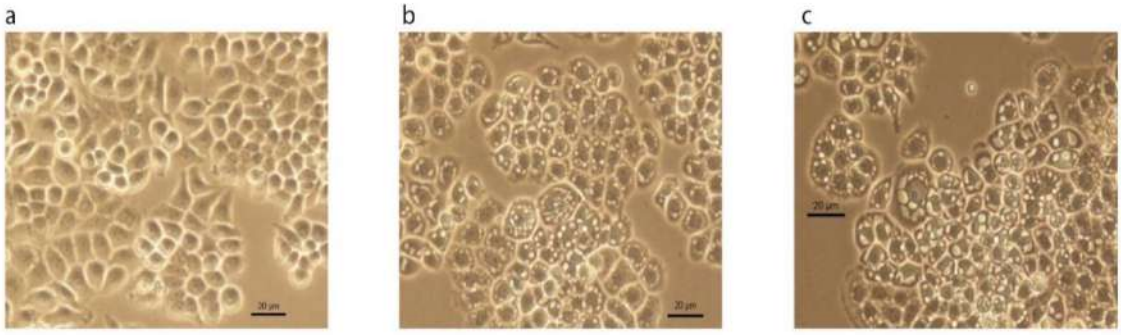

Figure F1.20: *Morphological changes of SiHa cells treated with compounds **3eb** and **3ec** (a) Control SiHa cell line. Presence of autophagic vacuoles in SiHa cell line at 24 h of treatment b) with **3eb** and c) with **3ec***

LC3 protein staining is a well-known analysis for oxygen deficiency that stimulates autophagy to confirm cell apoptosis via visualizing the intracellular distribution of LC3 using a GFP-LC3 fusion protein. Using fluorescence microscopy to capture punctate signals was made easier by the use of a green fluorescent protein (GFP). Oxygen deprivation caused a decrease in the presence of LC3 form indicating the stimulation of autophagy. These punctate marks clearly indicated the presence of autophagosomes and

isolation membranes, which is indicative of autophagy.[73-74] **3eb** compounds treated cells show maximum appearance of LC3 as compared to 3ec compound treated cells that is further higher than the control cells representing the promising effect of 3eb compounds on autophagy that causes the oxygen deficiency cell apoptosis (see Figure F1.21), these GFP-LC3 Puncta formation, which is demonstrated in Figure, validate the induction of autophagy.

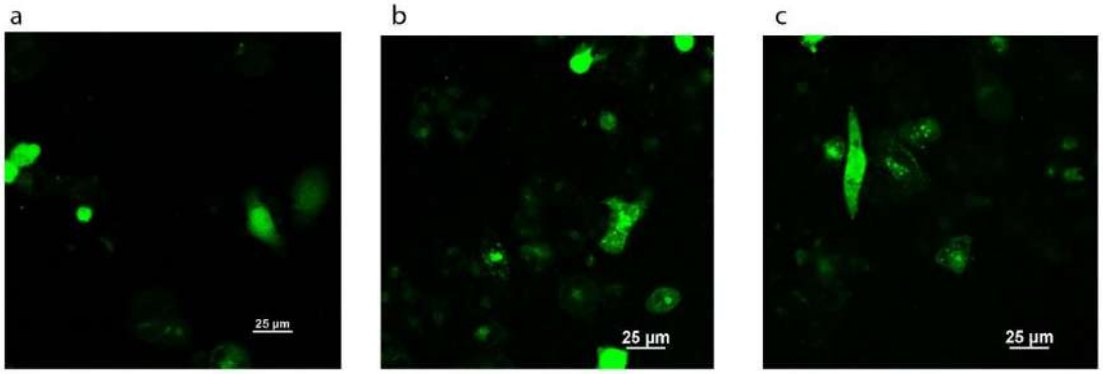

Figure F1.21: *Detection of GFP-LC3 puncta in SiHa cells. (a) control cells (b) treated with **3eb** and (c) treated with **3ec.***

After having identified potential autophagy inhibitors, we intended to incorporate the F and CF_3 groups in the designed molecule considering its ability to improve a variety of pharmacokinetic and physicochemical properties, including enhanced metabolic stability and membrane permeation.[75] Nearly 40% of drugs consist of fluorine as a substitute because it forms strong hydrogen bonds with enzymes and bio-molecules. There are couple of investigational drugs having benzofuran and fluorine in their core exhibiting very good anticancer activity (**Fig. F1. 16**).[66-67]

Following the similar protocols that we have established earliers, about 22 compounds having CF_3 and F groups at different positions of three aryl rings in combination with other electron donating and withdrawing substituents have been synthesized and subjected for the preliminary screening for the formation of vacuoles in the treated SiHa cell lines keeping **3eb** and **3ec** as control substrates. However, as none of these compounds were found to be as good as the control substrates. Hence, the further evaluation of these compounds has been not pursued.

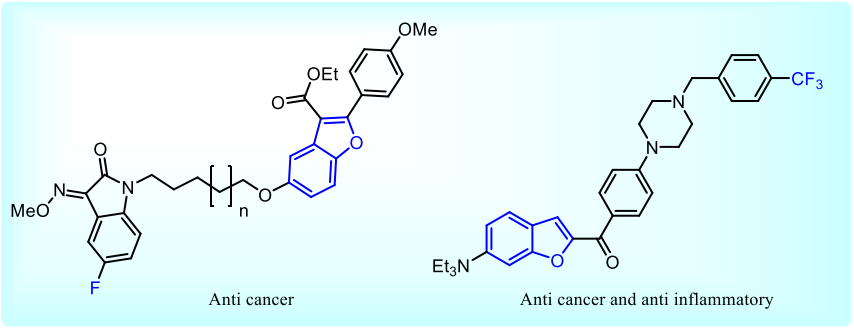

Figure F1.16: *Fluorine and benzofuran containing anticancer agents*

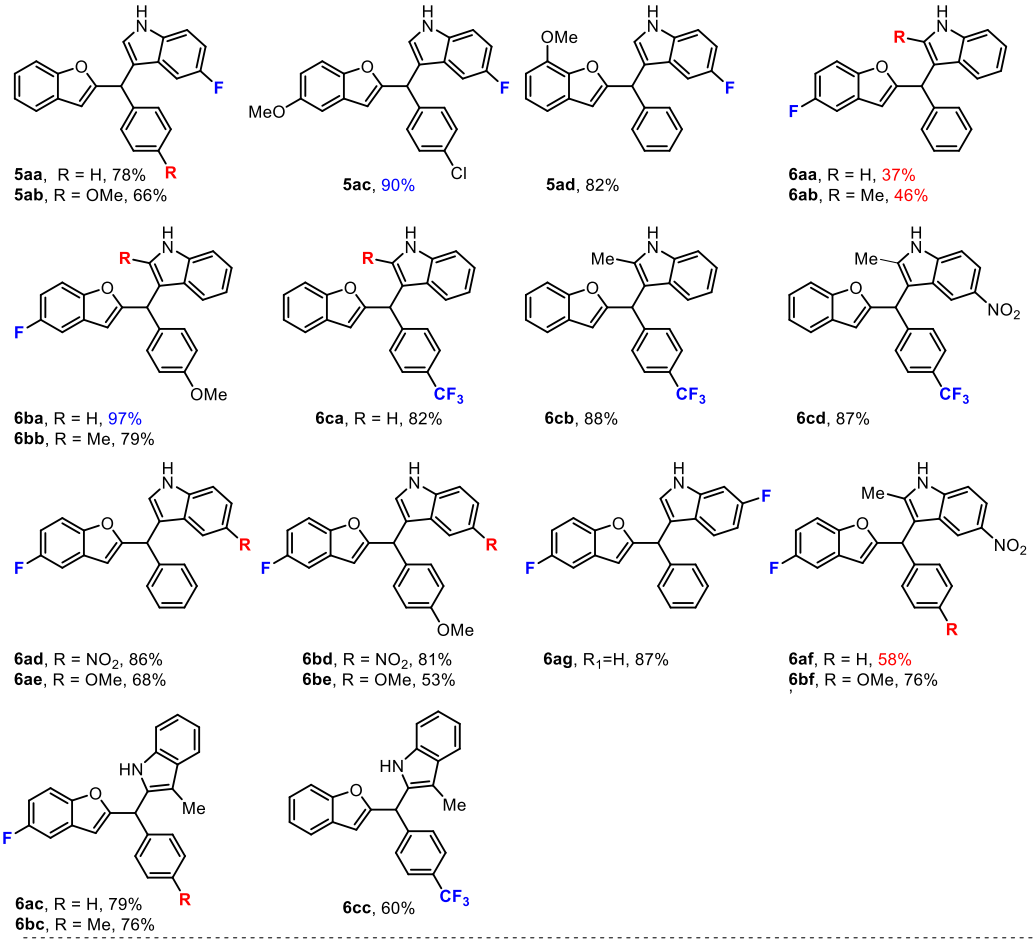

Scheme S1.3: *F and CF3 substituted C2 and C3 alkylated products*

1.11 Conclusions:

In conclusion, novel small molecule scaffolds were identified that effectively induce autophagy in cervical cancer cell lines, resulting in programmed cell death. A total of 46 novel conjugates were synthesized and tested for cytotoxicity against two cervical cancer cell lines, SiHa and C33a. Five of them had IC_{50} values less than 40 M, with compounds **3eb** and **3ec** being the most effective. The compound efficiently induced autophagy in SiHa and C33a cells, as evidenced by the progressive conversion of LC3I to LC3II and the downregulation of p62. The accessibility of obtaining these compounds from simple building blocks, as well as the therapeutic potential of autophagy inducers in the treatment of cervical cancer, open new avenues for expanding the scope of identifying the potential therapeutic candidates. Future research will concentrate on this topic, alongside determining the precise mechanism of cytotoxicity generated by these compounds.

Materials and Methods

Cell cultures: The cell lines used in the study were human origin cervical cancer cell lines. Siha is human papillomavirus (HPV) positive while C33a is negative for HPV DNA. The cell lines were procured from ATCC, work were carried out within 3–4 passage numbers after revival. Cells were grown and maintained in Dulbecco's Modified Eagle's Medium (DMEM) added with 10% fetal bovine serum (Pan life sciences, USA) and antibiotics (Streptomycin 0.1 mg/ml).

Proliferation assay

The IC_{50} of the panel of compounds were determined employing the method by Edmondson *et al.*[1] 3-[4,5-dimethylthiazole-2-yl]-2,5-diphenyltetrazolium bromide (MTT) **was used at a final concentration of 0.5 mg/mL. The absorbance was taken at 570nm.**

Western blot analysis

Total protein was isolated from control and treated cancer cell lines after different incubation periods (24 h, 36 h and 42 h). RIPA buffer(50 mM Tris-HCL, pH 8.0, with 150 mM sodium chloride, 1.0% Igepal CA-630 (NP-40), 0.5% sodium deoxychlorate, and 0.1% sodium dodecyl sulfate) with combination of protease inhibitor (500 mM phenylmethylsulfonyl fluoride) was employed for protein isolation. Bradford reagent was used for finding protein concentration. Protein obtained further denatured and ran in SDS-PAGE and transferred to PVDF membrane. To avoid nonspecific binding of antibodies on membrane, blocking was done with 5% skim milk powder dissolved in Tris buffer saline containing Tween 20. The blocked membrane was probed against specific antibodies for 12 hours in cold condition and then washed thrice for 10 min in appropriate buffer. Secondary antibody was probed for 2 h in ambient conditions. The membrane was washed and developed in dark room.

Antibodies

The antibodies for LC3, p62 and Beclin 1 were procured from Cell Signalling Technology. HSC70 from Santacruz

General Experimental Procedure:

In general, all reactions are carried out employing respective benzofuran-2-yl(phenyl)methanol **1** (100 mg) and the product yields provided are with respect to the substrate. Representative procedure was given below.

3-(Benzofuran-2-yl(phenyl)methyl)-1*H*-indole (3aa):

To a solution of benzofuran-2-yl(phenyl)methanol **1a** (100 mg, 0.45 mmol) and indole **2a** (78 mg, 0.67 mmol) in CH_2Cl_2 (5 ml) was added PTSA (101 mg, 0.53 mmol) and stirred at rt. After completion of the reaction (2 h) as indicated by TLC, the reaction mixture was diluted with CH_2Cl_2 (25 ml) and washed with water, dried (Na_2SO_4) and concentrated under reduced pressure. The residue was purified by column chromatography (petroleum ether/ethyl acetate = 85:15, R_f = 0.5) to obtain compound **3aa** (121 mg, 83%) as a brown solid. MP: 143–145 °C; ^{1}H NMR (500 MHz, $CDCl_3$): δ 7.95 (br. s., 1H), 7.37 (d, J = 7.5 Hz, 1H), 7.34 (d, J = 8.1 Hz, 2H), 7.23–7.30 (m, 5H), 7.09–7.19 (m, 4H), 6.96 (t, J = 7.3 Hz, 1H), 6.73 (d, J = 0.8 Hz, 1H), 6.27 (s, 1H), 5.73 (s, 1H); ^{13}C NMR (125 MHz, $CDCl_3$): δ 160.0, 155.0, 141.0, 136.5, 128.6 (2C), 128.5 (2C), 126.9, 126.6, 123.5 (2C), 122.5, 122.2, 120.6, 119.6, 119.5, 116.7, 113.5, 111.2, 111.1, 104.6, 43.0; HRMS (ESI) calcd for $C_{23}H_{18}NO$ $[M+H]^+$: 324.1383; found: 324.1380.

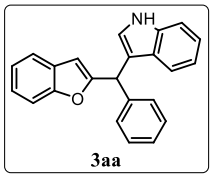

3aa

3–(Benzofuran–2–yl(phenyl)methyl)–2–methyl–1*H*–indole (3ab): Yield: 132 mg, 87%; R_f = 0.4 (petroleum ether/ethyl acetate = 90:10); Brown solid; MP: 63–65 °C; ^{1}H NMR (500 MHz, $CDCl_3$): δ 7.76 (br. s., 1H), 7.36–7.38 (m, 1H), 7.31–7.33 (m, 1H), 7.22 (s, 1H), 7.22 (s, 1H), 7.21 (s, 1H), 7.18–7.19 (m, 1H), 7.13–7.16 (m, 3H), 7.11 (d, 1H), 7.09 (d, 1H), 6.98–7.02 (ddd, J = 7.7, 6.9, 1.0 Hz, 1H), 6.83–6.87 (ddd, J = 7.0, 0.9, 8.0 Hz, 1H), 6.24 (m, 1H), 5.74 (s, 1H), 2.21 (s, 3H); ^{13}C NMR (125 MHz, $CDCl_3$): δ 160.1, 155.0, 141.2, 135.1, 132.2, 128.6, 128.5 (2C), 128.4 (2C), 128.1, 126.6, 123.5, 122.5, 121.0, 120.5, 119.5, 119.1, 111.1, 111.1, 110.2, 105.1, 42.3,12.2; HRMS (ESI) calcd for $C_{24}H_{19}ONNa$ $[M+Na]^+$: 360.1359; found: 360.1352.

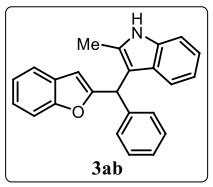

3ab

3-(Benzofuran-2-yl(phenyl)methyl)-5-nitro-1*H*-indole (3ac): Yield: 120 mg, 73%; R_f = 0.5 (petroleum ether/ethyl acetate = 90:10); Yellow solid; MP: 210–212 °C; ^{1}H NMR (500 MHz, $CDCl_3$): δ 8.46 (br. s., 1H), 8.41 (s, 1H), 8.12 (br. d, J = 9.0 Hz, 1H), 7.48 (d, J = 7.6 Hz, 1H), 7.43 (dd, J = 5.7, 8.4 Hz, 2H), 7.35–7.36 (m, 4H), 7.31–7.33 (m, 1H), 7.19–7.25 (m, 2H), 7.05 (s, 1H), 6.37 (s, 1H), 5.85 (s, 1H); ^{13}C NMR (125 MHz, $CDCl_3$): δ 158.9, 155.0, 141.8, 140.1, 139.4, 128.8 (2C), 128.4 (2C), 128.3, 127.4, 126.5, 126.1, 123.9, 122.7, 120.8, 119.3, 118.1, 116.8, 111.2 (2C), 104.9, 42.7; HRMS (ESI) calcd for $C_{23}H_{16}O_3N_2Na$ $[M+Na]^+$: 391.1053; found: 391.1047.

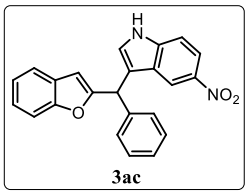

3ac

3-((5-Chlorobenzofuran-2-yl)(phenyl)methyl)-1*H*-indole (3ba): Yield: 117 mg, 84%; R_f = 0.4 (petroleum ether/ethyl acetate = 85:15); Brown solid; MP: 74–76 °C; ^{1}H NMR (400 MHz, $CDCl_3$) δ 7.88 (br. s., 1H), 7.29–7.31 (m, 2H), 7.23–7.25 (m, 5H), 7.18–7.21 (m, 2H), 7.10–7.13 (m, 1H), 7.06 (dd, J = 2.2, 8.7, 1H), 6.93–6.97 (m, 1H), 6.65 (d, J = 2.4 Hz, 1H), 6.19 (s, 1H), 5.68 (s, 1H); ^{13}C NMR (125 MHz, $CDCl_3$): δ 161.7, 153.4, 140.6, 136.5, 130.0, 128.6 (2C), 128.5 (2C), 128.1, 127.0, 126.5, 123.7, 123.5, 122.3, 120.2, 119.7, 119.4, 116.3, 112.0, 111.2, 104.3, 43.1; HRMS (ESI) calcd for $C_{23}H_{17}ONCl[M+H]^+$: 358.0993; found: 358.0987.

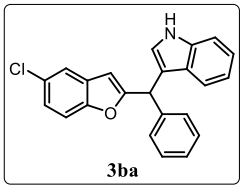

3ba

3-((5-Chlorobenzofuran-2-yl)(phenyl)methyl)-2-methyl-1*H*-indole (3bb): Yield: 122 mg 84%,; R_f = 0.25 (petroleum ether/ethyl acetate = 90:10); Brown solid, MP: 55–57 °C; ^{1}H NMR (500 MHz, $CDCl_3$) δ 7.71 (br. s., 1H), 7.30 (d, J = 2.0 Hz, 1H), 7.19 (s, 1H), 7.19 (s, 2H), 7.15–7.17 (m, 3H), 7.07–7.11 (m, 2H), 7.05 (dd, J = 8.7, 2.0 Hz, 1H), 6.97 (d, J = 7.7 Hz, 1H), 6.82–6.85(m, 1H), 6.17 (s, 1H), 5.69 (s, 1H), 2.16 (s, 3H); ^{13}C NMR (125 MHz, $CDCl_3$) δ 161.8, 153.3, 140.8, 135.1, 132.2, 130.0, 128.5 (2C), 128.4 (2C), 128.0, 127.9, 126.8, 123.6, 121.1, 120.1, 119.6, 118.9, 112.1, 110.7, 110.3, 104.7, 42.3, 12.1; HRMS (ESI) calcd for $C_{24}H_{19}ONCl$ $[M+H]^+$: 372.1150; found: 372.1144.

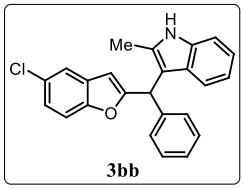

3bb

3-((5-Chlorobenzofuran-2-yl)(phenyl)methyl)-5-nitro-1*H*-indole (3bc): Yield: 141 mg, 90%; R_f = 0.4 (petroleum ether/ethyl acetate = 85:15); Yellow solid, MP: 180–182 °C; ^{1}H NMR (400 MHz, DMSO-d_6) δ 11.68 (br. s., 1H), 8.29 (s, 1H), 7.94 (d, J = 8.9 Hz, 1H),

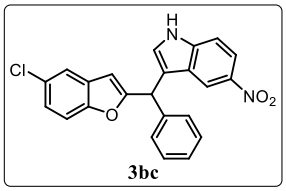

3bc

7.48–7.51 (m, 2H), 7.40 (d, *J* = 8.7 Hz, 1H), 7.28–7.34 (m, 4H), 7.23 (d, *J* = 6.8 Hz, 1H), 7.14–7.17 (m, 2H), 6.43 (s, 1H), 5.95 (s, 1H); ^{13}C NMR (100 MHz, DMSO-d_6) δ 161.2, 153.0, 140.6, 140.4, 139.7, 129.7, 128.5 (2C), 128.2 (2C), 127.7, 127.4, 127.0, 125.5, 123.7, 120.2, 117.1, 116.8, 115.9, 112.2, 112.1, 104.1, 41.9; HRMS (ESI) calcd for $C_{23}H_{15}O_3N_2ClNa$ $[M+Na]^+$: 425.0663; found: 425.0660.

3-((5-Methoxybenzofuran-2-yl)(phenyl)methyl)-1*H*-indole (3ca): Yield: 121 mg, 87%; R_f = 0.6 (petroleum ether/ethyl acetate = 90:10); Brown solid; MP: 108–110 °C; ^{1}H NMR (400 MHz, $CDCl_3$) δ 7.97 (br. s., 1H), 7.48 (d, *J* = 7.7 Hz, 1H), 7.39–7.41 (m, 3H), 7.35–7.37 (m, 2H), 7.33 (d, *J* = 7.7 Hz, 2H), 7.23 (t, *J* = 7.1 Hz, 1H), 7.10 (t, *J* = 7.3 Hz, 1H), 6.96 (d, *J* = 2.5 Hz, 1H), 6.88 (m, 1H), 6.75 (s, 1H), 6.33 (s, 1H), 5.83 (s, 1H), 3.84 (s, 3H); ^{13}C NMR (100 MHz, $CDCl_3$) δ 160.9, 155.8, 150.0, 141.0, 136.5, 129.2, 128.6 (2C), 128.5 (2C), 126.9, 126.7, 123.5, 122.2, 119.6, 119.5, 116.7, 111.9, 111.5, 111.2, 104.8, 103.5, 55.9, 43.2; HRMS (ESI) calcd for $C_{24}H_{19}O_2NNa$ $[M+Na]^+$: 376.1308; found: 376.1306.

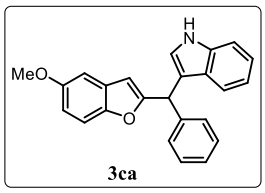

3ca

3-((5-Methoxybenzofuran-2-yl)(phenyl)methyl)-2-methyl-1*H*-indole (3cb): Yield: 125 mg, 86%; R_f = 0.4 (petroleum ether/ethyl acetate = 90:10); Brown solid; MP: 146–148 °C; ^{1}H NMR (400 MHz, $CDCl_3$) δ 7.78 (br. s., 1H), 7.31–7.39 (m, 2H), 7.13–7.21 (m, 5H), 7.10–7.12 (m, 1H), 7.00 (m, 1H), 6.84–6.88 (m, 1H), 6.75–6.77 (m, 2H), 6.24 (s, 1H), 5.69 (s, 1H), 3.71 (s, 3H), 2.21 (s, 3H); ^{13}C NMR (125 MHz, $CDCl_3$) δ 161.0, 155.8, 150.0, 141.3, 135.2, 132.2, 129.2, 128.6 (2C), 128.3 (2C), 128.1, 126.6, 121.1, 119.5, 119.1, 111.9, 111.5, 111.1, 110.2, 105.3, 103.4, 55.9, 42.4, 12.1; HRMS (ESI) calcd for $C_{25}H_{21}O_2NNa$ $[M+Na]^+$: 390.1465; found: 390.1463.

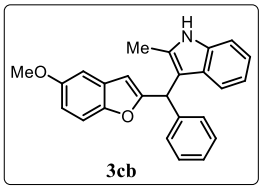

3cb

3-((5-Methoxybenzofuran-2-yl)(phenyl)methyl)-5-nitro-1*H*-indole (3cc): Yield: 137 mg, 87%; R_f = 0.4 (petroleum ether/ethyl acetate = 90:10); Yellow solid; mp: 172–174 °C; ^{1}H NMR (400 MHz, DMSO–d_6) δ 8.66 (br. s., 1H), 8.41 (s, 1H), 8.12 (dd, *J* = 8.9, 2.0 Hz, 1H), 7.42 (d, *J* = 9.1 Hz, 1H), 7.36–7.37 (m, 4H), 7.33 (d, *J* = 8.7 Hz, 2H), 7.05 (s, 1H), 6.97 (d, *J* = 2.4 Hz, 1H), 6.87 (dd, *J* = 8.8, 2.5 Hz, 1H), 6.33 (s, 1H), 5.82 (s, 1H), 3.83 (s,

3H); ^{13}C NMR (101 MHz, DMSO–d$_6$) δ 159.8, 155.9, 150.0, 141.7, 140.1, 139.4, 128.9, 128.7 (2C), 128.4 (2C), 127.3, 126.6, 126.1, 119.2, 118.0, 116.7, 112.3, 111.5, 111.3, 105.0, 103.5, 55.9, 42.8; HRMS (ESI) calcd for $C_{24}H_{18}O_4N_2Na$ [M+Na]$^+$: 421.1159; found: 421.1156.

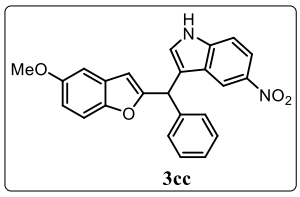

((5,7-Di-*tert*-butylbenzofuran-2-yl)(phenyl)methyl)-1*H*-indole (3da): Yield: 111 mg, 85%; R_f = 0.5 (petroleum ether/ethyl acetate = 90:10); Brown solid; MP: 68–70 °C; ^{1}H NMR (500 MHz, $CDCl_3$) δ 7.91 (br. s., 1H), 7.29–7.31 (m, 2H), 7.27–7.28 (m, 2H), 7.24 (d, *J* = 1.9 Hz, 1H), 7.19–7.22 (m, 2H), 7.15–7.17 (m, 1H), 7.11 (d, *J* = 2.0 Hz, 1H), 7.08–7.09 (m, 1H), 6.92–6.95 (m, 1H), 6.80 (d, *J* = 2.1 Hz, 1H), 6.23 (s, 1H), 5.71 (s, 1H), 1.35 (s, 9H), 1.27 (s, 9H); ^{13}C NMR (126 MHz, $CDCl_3$): δ 159.0, 151.3, 145.2, 141.5, 136.4, 133.6, 128.6 (2C), 128.3 (2C), 126.7, 126.7, 123.3, 122.1, 120.7, 119.7, 119.5, 118.1, 117.1, 114.7, 111.0, 104.3, 43.2, 34.8, 34.4, 31.9 (3C), 29.9 (3C); HRMS (ESI) calcd for $C_{31}H_{33}ONNa$ [M+Na]$^+$: 458.2454; found: 458.2449.

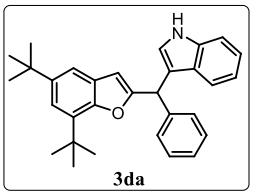

3-((5,7-Di-*tert*-butylbenzofuran-2-yl)(phenyl)methyl)-2-methyl-1*H*-indole (3db): Yield: 119 mg, 89%; R_f = 0.5 (petroleum ether/ethyl acetate = 90:10); Brown solid, MP: 72–74 °C; ^{1}H NMR (400 MHz, $CDCl_3$) δ 7.84 (br. s., 1H), 1.37 (s, 9H), 7.32 (d, *J* = 1.9 Hz, 1H), 7.30–7.31 (m, 3H), 7.28–7.28 (m, 2H), 7.26–7.27 (m, 1H), 7.25 (s, 1H), 7.22 (d, *J* = 4.4Hz, 1H), 7.20 (d, *J* = 2 Hz, 1H), 7.07–7.11 (m, 1H), 6.93–6.97 (m, 1H), 6.33 (s, 1H), 5.85 (s, 1H), 2.30 (s, 3H), 1.42 (s, 9H); ^{13}C NMR (101 MHz, $CDCl_3$): δ 158.6, 151.3, 145.1, 141.7, 137.4, 135.1, 133.6, 132.1, 128.6, 128.5 (2C), 128.1 (2C), 126.4, 120.9, 119.4, 119.3, 118.1, 114.6, 111.6, 110.0, 104.8, 42.0, 34.8, 34.4, 31.9 (3C), 29.8 (3C), 12.2; HRMS (ESI) calcd for $C_{32}H_{35}ONNa$ [M+Na]$^+$: 472.2611; found: 472.2605.

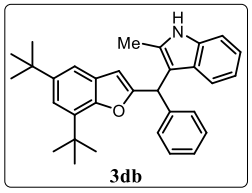

3-((5,7-Di-*tert*-butylbenzofuran-2-yl)(phenyl)methyl)-5-nitro-1*H*-indole (3dc): Yield 131 mg, 91%; R_f = 0.5 (petroleum ether/ethyl acetate = 90:10); Yellow solid; MP: 194–196 °C; ^{1}H NMR (500 MHz, DMSO-*d*$_6$) δ 11.78 (br. s., 1H), 8.34 (d, *J* = 2.3 Hz, 1H), 7.98 (dd, *J* = 9.0, 2.2 Hz, 1H), 7.55 (d, *J* = 8.9 Hz, 1H), 7.38–7.40 (m, 4H), 7.33–7.36 (m, 2H), 7.24–7.27 (m, 1H), 7.12 (d, *J* = 1.7 Hz, 1H), 6.54 (s, 1H), 6.10 (s, 1H), 1.34 (s, 9H), 1.30

(s, 9H); ^{13}C NMR (101 MHz, $CDCl_3$) δ 157.8, 151.4, 145.5, 141.8, 140.5, 139.3, 133.7, 128.6 (2C), 128.4 (2C), 127.2 (2C), 126.2, 119.7, 118.5 (2C), 118.0, 117.0, 114.8, 111.1, 104.6, 42.9, 34.8, 34.4, 31.9 (3C), 29.8 (3C); HRMS (ESI) calcd for $C_{31}H_{32}O_3N_2Na$ $[M+Na]^+$: 503.2305; found: 503.2299.

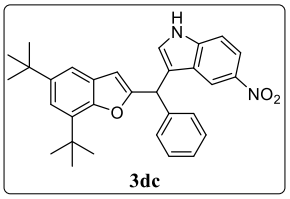

3-(Benzofuran-2-yl(4-chlorophenyl)methyl)-1*H*-indole (3ea):

Yield: 107 mg. 77%; R_f = 0.4 (petroleum ether/ethyl acetate = 90:10); MP: 58–60 °C; Brown solid; ^{1}H NMR (500 MHz, $CDCl_3$): δ 7.84 (br. s., 1 H), 7.34 (d, J = 7.4 Hz, 1H), 7.31 (d, J = 8.2 Hz, 1H), 7.28 (d, J = 8.0 Hz, 1H), 7.23 (d, J = 8.2 Hz, 1H), 7.14–7.19 (m, 4H), 7.07–7.12 (m, 3H), 6.93–6.96 (m, 1H), 6.65 (d, J = 2.3 Hz, 1H), 6.24 (s, 1H), 5.66 (s, 1H); ^{13}C NMR (125 MHz, $CDCl_3$): δ 159.4, 155.0, 139.5, 136.5, 132.7, 129.9 (2C), 128.6 (2C), 128.5, 126.4, 123.7, 123.5, 122.6, 122.4, 120.7, 119.7, 119.4, 116.1, 111.3, 111.1, 104.8, 42.5; HRMS (ESI) calcd for $C_{23}H_{17}ClON$ $[M+H]^+$: 356.0837; found: 356.0834.

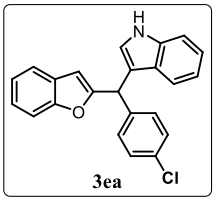

3-(Benzofuran-2-yl(4-chlorophenyl)methyl)-2-methyl-1*H*-indole(3eb): Yield: 120 mg 83%; R_f = 0.2 (petroleum ether/ethyl acetate = 90:10); Brown solid; MP: 70–72 °C; ^{1}H NMR (400 MHz, $CDCl_3$) δ 7.79 (br. s., 1H), 7.36–7.38 (m, 1H), 7.31–7.33 (m, 1H), 7.10–7.21 (m, 8H), 6.99–7.03 (m, 1H), 6.84–6.88 (m, 1H), 6.24 (s, 1H), 5.69 (s, 1H), 2.21 (s, 3H); ^{13}C NMR (100 MHz, $CDCl_3$): δ 159.4, 155.0, 139.8, 135.1, 132.4, 132.2, 130.0, 129.9 (2C), 128.5 (2C), 127.8, 123.7, 122.6, 121.2, 120.6, 119.6, 119.0, 111.1, 110.6, 110.3, 105.2, 41.6, 12.1; HRMS (ESI) calcd for $C_{24}H_{19}ONCl$ $[M+H]^+$: 372.1150; found: 372.1149.

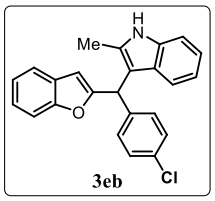

3-(Benzofuran-2-yl(4-chlorophenyl)methyl)-5-nitro-1*H*-indole (3ec): Yield: 142 mg, 91%; R_f = 0.3 (petroleum ether/ethyl acetate = 90:10); Yellow solid; MP: 118–220 °C; ^{1}H NMR (400 MHz, DMSO–d_6) δ 11.85 (br. s., 1H), 8.40 (d, J = 2.3 Hz, 1H), 7.98–8.01 (m, 1H), 7.55–7.58 (m, 2H), 7.50 (d, J = 8.2 Hz, 1H), 7.42 (s, 4H), 7.35 (d, J = 2.2 Hz, 1H), 7.18–7.26 (m, 2H), 6.55 (s, 1H), 6.17 (s, 1H); ^{13}C NMR (101 MHz, DMSO-d_6) δ 159.2, 154.4, 140.5, 140.1, 139.6, 131.6, 130.1 (2C), 128.6 (2C), 128.0, 124.0, 122.9, 121.0, 117.1,

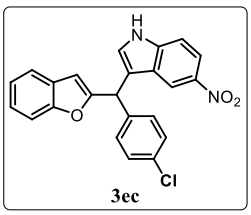

116.8, 115.9, 112.3, 111.8, 111.0, 104.4, 103.9, 40.7; HRMS (ESI) calcd for $C_{23}H_{15}ClO_3N_2Na$ $[M+Na]^+$: 425.0663; found: 425.0663.

3-(Benzofuran-2-yl(4-methoxyphenyl)methyl)-1*H*-indole (3fa): Yield: 117 mg, 84%; R_f = 0.3 (petroleum ether/ethyl acetate = 90:10); Brown solid; MP: 90–92 °C; ^{1}H NMR (400 MHz, $CDCl_3$) δ 8.03 (br. s., 1H), 7.39–7.43 (m, 3H), 7.37 (d, *J* = 8.2 Hz, 1H), 7.26 (d, *J* = 8.3 Hz, 2H), 7.20–7.23 (m, 1H), 7.18–7.19 (m, 1H), 7.15–7.17 (m, 1H), 7.01–7.05 (m, 1H), 6.84–6.87 (m, 2H), 6.81 (d, *J* = 2.4 Hz, 1H), 6.32 (s, 1H), 5.75 (s, 1H), 3.79 (s, 3H); ^{13}C NMR (101 MHz, $CDCl_3$) δ 160.4, 158.5, 155.0, 136.5, 133.1, 129.5 (2C), 128.6, 126.6, 123.4 (2C), 122.5, 122.2, 120.6, 119.6 (2C), 117.0, 113.9 (2C), 111.1, 111.1, 104.5, 55.2, 42.2; HRMS (ESI) calcd for $C_{24}H_{19}O_2NNa$ $[M+Na]^+$: 376.1308; found: 376.1306

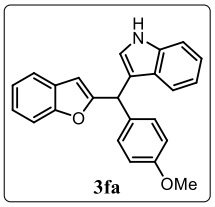

3-(Benzofuran-2-yl(4-methoxyphenyl)methyl)-2-methyl-1*H*-indole (3fb): Yield 91%, 132 mg; R_f = 0.5 (petroleum ether/ethyl acetate = 90:10); Brown gum; ^{1}H NMR (500 MHz, $CDCl_3$) δ 7.87 (br. s., 1H), 7.48(d , *J* = 7.5 Hz, 1H), 7.42(d , *J* = 7.8 Hz, 1H), 7.29–7.31 (m, 1H), 7.24–7.26 (m, 3H), 7.19–7.23 (m, 2H), 7.09–7.12 (m, 1H), 6.95–6.98 (m, 1H), 6.86 (d, *J* = 8.8 Hz, 2H), 6.34 (s, 1H), 5.79 (s, 1H), 3.81 (s, 3H), 2.31 (s, 3H); ^{13}C NMR (126 MHz, $CDCl_3$) δ 160.5, 158.3, 155.0, 135.2, 133.4, 132.1, 129.5 (2C), 128.7, 128.1, 123.4, 122.5, 121.0, 120.5, 119.5, 119.1, 113.7 (2C), 111.3, 111.1, 110.2, 104.9, 55.2, 41.5, 12.1; HRMS (ESI) calcd for $C_{25}H_{21}O_2NNa$ $[M+Na]^+$: 390.1465; found: 390.1462.

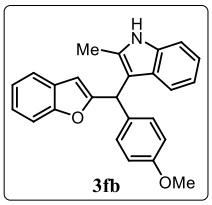

3-(Benzofuran-2-yl(4-methoxyphenyl)methyl)-5-nitro-1*H*-indole (3fc): Yield: 91 mg, 58%; R_f = 0.36 (petroleum ether/ethyl acetate = 90:10); Yellow solid; MP: 218–220 °C;^{1}H NMR (400 MHz, DMSO d_6) δ 11.68 (s, 1H), 8.32 (d, *J* = 2.3 Hz, 1H), 7.95 (dd, *J* = 9.0, 2.3 Hz, 1H), 7.48–7.52 (m, 2H), 7.42 (d, *J* = 7.8 Hz, 1H), 7.27 (d, *J* = 8.4 Hz, 2H), 7.13–7.21 (m, 3H), 6.87 (d, *J* = 8.5 Hz, 2H), 6.43 (s, 1H), 5.94 (s, 1H), 3.72 (s, 3H); ^{13}C NMR (101 MHz, DMSO–d6) δ 158.1, 156.3, 152.6, 138.6, 137.8, 130.9, 127.4 (2C), 126.3, 125.7, 123.7, 121.8, 120.7, 118.8, 116.0, 114.8, 114.1, 112.0 (2C), 110.2, 109.0, 102.1, 53.1, 39.1; HRMS (ESI) calcd for $C_{24}H_{18}O_4N_2Na$ $[M+Na]^+$: 421.1159; found: 421.1157.

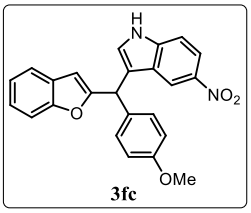

2–(Benzofuran–2–yl(phenyl)methyl)–3–methyl–1*H*–indole (4aa): Yield: 121 mg, 79%; R_f = 0.5 (petroleum ether/ethyl acetate = 90:10); Brown solid; MP: 68–70 °C; ^{1}H NMR (500 MHz, $CDCl_3$): δ 7.93 (br. s., 1H), 7.63 (d, J = 7.7 Hz, 1H), 7.57 (d, J = 7.8Hz, 1H), 7.51 (d, J = 8.0 Hz, 1H), 7.34–7.41 (m, 3H), 7.31 (d, 2H), 7.28–7.29 (m, 3H), 7.18–7.23 (m, 2H), 6.54 (s, 1H), 5.93 (s, 1H), 2.35 (s, 3H); ^{13}C NMR (125 MHz, $CDCl_3$): δ 157.5, 155.2, 139.3, 135.4, 132.2, 129.1, 128.2, 128.8 (2C), 128.2 (2C), 127.3, 124.0, 122.9, 121.8, 120.8, 119.3, 118.6, 111.3, 110.7, 108.7, 105.5, 42.8, 8.5; HRMS (ESI) calcd for $C_{24}H_{20}ON$ $[M+H]^+$: 338.1539; found: 338.1535.

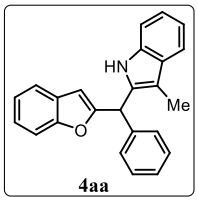

4aa

2-((5-Chlorobenzofuran-2-yl)(phenyl)methyl)-3-methyl-1*H*-indole (4ba): Yield: 124 mg, 86%; R_f = 0.45 (petroleum ether/ethyl acetate = 90:10); Brown solid, MP: 53–55 °C; ^{1}H NMR (400 MHz, $CDCl_3$): δ 7.71 (br. s., 1H), 7.46 (d, J = 7.3 Hz, 1H), 7.34 (s, 1H), 7.18–7.24 (m, 4H), 7.07–7.14 (m, 4H), 7.01–7.05 (m, 2H), 6.30 (s, 1H), 5.74 (s, 1H), 2.18 (s, 3H); ^{13}C NMR (100 MHz, $CDCl_3$) δ 159.1, 153.5, 138.9, 135.4, 131.7, 129.6, 129.0, 128.9 (2C), 128.4, 128.2 (2C), 127.5, 124.2, 121.9, 120.4, 119.3, 118.6, 112.2, 110.7, 108.9, 105.1, 42.8, 8.5; HRMS (ESI) calcd for $C_{24}H_{19}ONCl$ $[M+H]^+$: 372.1150; found: 372.1144.

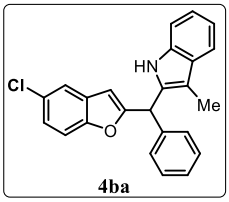

4ba

2-((5-Methoxybenzofuran-2-yl)(phenyl)methyl)-3-methyl-1*H*-indole (4ca): Yield: 132 mg, 91%; R_f = 0.4 (petroleum ether/ethyl acetate = 90:10); Brown gum; ^{1}H NMR (400 MHz, $CDCl_3$) δ 7.79 (br. s., 1H), 7.45–7.46 (m, 1H), 7.15–7.21 (m, 4H), 7.08–7.12 (m, 3H), 6.98–7.05 (m, 2H), 6.83 (d, J = 2.5 Hz, 1H), 6.73 (dd, J = 9, 2.4 Hz, 1H), 6.29 (s, 1H), 5.72 (s, 1H), 3.68 (s, 3H), 2.17 (s, 3H); ^{13}C NMR (101 MHz, $CDCl_3$) δ 158.3, 156.0, 150.1, 139.3, 135.4, 132.2, 128.8 (2C), 128.2 (2C), 121.7, 119.2, 119.0, 118.7, 118.6, 112.5, 111.6, 110.9, 110.7, 108.6, 105.6, 103.5, 55.9, 42.9, 8.5; HRMS (ESI) calcd for $C_{25}H_{22}O_2N$ $[M+H]^+$: 368.1645; found: 368.1642.

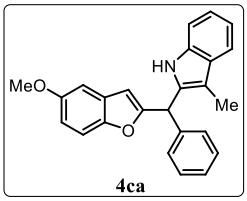

4ca

2-((5,7-Di-*tert*-butylbenzofuran-2-yl)(phenyl)methyl)-3-methyl-1*H*-indole (4da): Yield: 187 mg, 93%; R_f = 0.45 (petroleum ether/ethyl acetate = 90:10); Brown solid, MP: 123–125 °C; ^{1}H NMR (400 MHz, $CDCl_3$) δ 7.87 (br. s., 1H), 7.54–7.58 (m, 1H), 7.37 (d, J = 2.1

Hz, 1H), 7.31–7.33 (m, 1H), 7.29–7.30 (m, 1H), 7.27–7.28 (m, 1H), 7.25 (d, *J* = 2.4 Hz, 2H), 7.21–7.24 (m, 2H), 7.11–7.16 (m, 2H), 6.44 (s, 1H), 5.86 (s, 1H), 2.27 (s, 3H), 1.45 (s, 9H), 1.37 (s, 9H); ^{13}C NMR (101 MHz, $CDCl_3$) δ 156.4, 151.5, 145.7, 139.8, 135.3, 133.7, 132.7, 129.1, 128.6 (2C), 128.3, 128.3 (2C), 127.1, 121.6, 119.2, 118.7, 118.5, 114.9, 110.6, 108.5, 105.4, 42.9, 34.8, 34.4, 31.9 (3C), 29.9 (3C), 8.6; HRMS (ESI) calcd for $C_{32}H_{36}ON$ $[M+H]^+$: 450.2791; found: 450.2787.

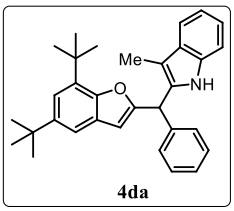

2-(Benzofuran-2-yl(4-chlorophenyl)methyl)-3-methyl-1*H*-indole (4ea): Yield: 135 mg, 93%; R_f = 0.4 (petroleum ether/ethyl acetate = 90:10); Brown solid; MP: 50–52 °C; ^{1}H NMR (400 MHz, $CDCl_3$): δ 7.72 (br. s., 1H), 7.29–7.44 (m, 3H), 6.98–7.06 (m, 9H), 6.32 (s, 1H), 5.68 (s, 1H), 2.13 (s, 3H); ^{13}C NMR (100 MHz, $CDCl_3$): δ 156.9, 155.1, 137.8, 135.4, 133.2, 131.6, 129.5 (2C), 129.0, 128.9 (2C), 128.1, 124.2, 123.0, 121.9, 120.9, 119.4, 118.6, 111.2, 110.8, 108.9, 105.6, 42.2, 8.50; HRMS (ESI) calcd for $C_{24}H_{19}ONCl$ $[M+H]^+$: 372.1150; found: 372.1148.

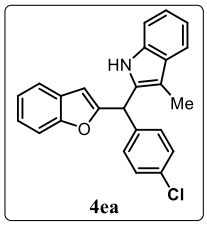

2-(Benzofuran-2-yl(4-methoxyphenyl)methyl)-3-methyl-1*H*-indole (4fa): Yield: 128 mg, 88%; R_f = 0.5 (petroleum ether/ethyl acetate = 90:10); Brown oil; ^{1}H NMR (400 MHz, $CDCl_3$) δ 7.75 (br. s., 1H), 7.46 (d, *J* = 7.4 Hz, 1H), 7.38 (d, *J* = 7.2 Hz, 1H), 7.33 (d, *J* = 7.9 Hz, 1H), 7.13 (d, *J* = 8.2 Hz, 2H), 7.08–7.10 (m, 1H), 6.99–7.03 (m, 4H), 6.73–6.79 (m, 2H), 6.33 (s, 1H), 5.70 (s, 1H), 3.66 (s, 3H), 2.17 (s, 3H); ^{13}C NMR (101 MHz, $CDCl_3$) δ 158.8, 157.9, 155.1, 135.3, 132.5, 131.3, 129.3 (2C), 128.3, 124.0, 122.8, 121.8, 120.8, 119.2, 119.0, 118.5, 114.2 (2C), 111.2, 110.7, 108.5, 105.3, 55.2, 42.1, 8.5; HRMS (ESI) calcd for $C_{25}H_{22}O_2N$ $[M+H]^+$: 368.1645; found: 368.1642.

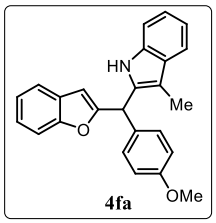

3-(benzofuran-2-yl(phenyl)methyl)-5-fluoro-1*H*-indole (5aa): Yield: 120 mg, 78%; R_f = 0.6 (petroleum ether/ethyl acetate = 80:20); Brown solid; MP: 129–131 °C; ^{1}H NMR (400 MHz, $CDCl_3$) δ 7.75 (br. s., 1H), 7.31–7.33 (m, 1H), 7.26–7.28 (m, 1H), 7.17–7.19 (m, 3H), 7.12–7.16 (m, 1H), 7.01–7.12 (m, 4H), 6.92 (dd, *J* = 9.6, 2.4 Hz, 1H), 6.77 (td, *J* = 9.1, 2.5 Hz, 1H), 6.63 (d, *J* = 2.3 Hz, 1H), 6.21 (s, 1 H), 5.58 (s, 1 H); ^{13}C NMR (101 MHz, $CDCl_3$) δ

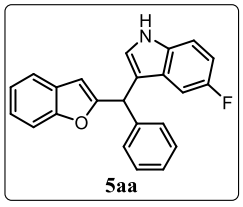

159.6 (s), 157.6 (d, $J_{C–F}$ = 234.7 Hz), 155.0 (s), 140.6 (s), 132.9 (s), 128.5 (d, 2C), 128.5 (d, 3C), 127.0 (d),126.9 (d, $J_{C–F}$ = 9.4 Hz), 125.2 (d), 123.6 (d), 122.6 (d), 120.7 (d), 116.6 (d, $J_{C–F}$ = 5.1 Hz), 111.9 (d, $J_{C–F}$ = 9.4 Hz), 111.1 (d), 110.5 (d, $J_{C–F}$ = 26.1 Hz), 104.6 (d), 104.3 (d, $J_{C–F}$ = 24 Hz), 43.0 (q); HRMS (ESI) calcd for $C_{23}H_{16}NOFNa$ $[M+Na]^+$: 364.1108; found: 364.1108.

3-(benzofuran-2-yl(4-methoxyphenyl)methyl)-5-fluoro-1*H*-indole (5ab): Yield: 96 mg, 66%; R_f = 0.3 (petroleum ether/ethyl acetate = 80:20); Reddish brown semi solid; ^{1}H NMR (400 MHz, $CDCl_3$) δ 8.05 (br. s., 1H), 7.42–7.48 (m, 2H), 7.28–7.30 (m, 1H), 7.25–7.27 (m, 2H), 7.17–7.24 (m, 2H), 7.03 (dd, J = 9.6, 2.5 Hz, 1H), 6.94 (td, J = 9.1, 2.5 Hz, 1H), 6.88–6.89 (m, 2H), 6.86–6.87 (m, 1H), 6.34 (t, J = 0.9 Hz, 1H), 5.69 (s, 1H), 3.81 (s, 3H); ^{13}C NMR (101 MHz, $CDCl_3$) δ 160.0 (s), 157.6 (d, $J_{C–F}$ = 235.0 Hz), 158.6 (s), 155.0 (s), 133.0 (d), 132.8 (d), 129.5 (d, 2C), 128.5 (s), 127 (d, $J_{C–F}$ = 9.9 Hz), 125.1 (d), 123.6 (d), 122.5 (d), 120.6 (d),117.2 (d, $J_{C–F}$ = 4.6 Hz), 113.9 (d, 2C), 111.7 (d, $J_{C–F}$ = 9.2 Hz), 111.1 (d), 110.6 (d, $J_{C–F}$ = 27 Hz), 104.7 (d, $J_{C–F}$ = 23.7 Hz), 104.5 (d), 55.3 (d), 42.2 (q); HRMS (ESI) calcd for $C_{24}H_{18}NO_2FNa$ $[M+Na]^+$: 394.1214; found: 394.1217.

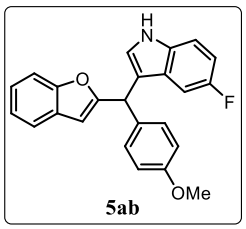

5ab

3-((4-chlorophenyl)(5-methoxybenzofuran-2-yl)methyl)-5-fluoro-1*H*-indole (5ac): Yield: 126 mg, 90%; R_f = 0.4 (petroleum ether/ethyl acetate = 85:15); White solid; MP: 95–97 °C; ^{1}H NMR (400 MHz, $CDCl_3$) δ 8.00 (br. s., 1H), 7.14–7.21 (m, 6H), 6.91 (dd, J = 9.6, 2.5 Hz, 1H), 6.81–6.86 (m, 2H), 6.73–6.76 (m, 2H), 6.19 (s, 1H), 5.57 (s, 1H), 3.71 (s, 3H); ^{13}C NMR (101 MHz, $CDCl_3$) δ 159.8 (s), 157.6 (d, $J_{C–F}$ = 235.4 Hz), 155.8 (s), 150.0 (s), 139.2 (s), 133.0 (d), 132.8 (d), 129.8 (d, 2C), 128.9 (s), 128.7 (d, 2C), 126.8 (d, $J_{C–F}$ = 9.5 Hz), 125.2 (d), 116.2 (d, $J_{C–F}$ = 5.1 Hz), 112.3 (d), 111.9 (d, $J_{C–F}$ = 9.5 Hz), 111.5 (d), 110.9 (d, $J_{C–F}$ = 26.9 Hz), 105.0 (d), 104.5 (d, $J_{C–F}$ = 24 Hz), 103.5 (d), 55.9 (d), 42.5 (q); HRMS (ESI) calcd for $C_{24}H_{18}NO_2FCl$ $[M+H]^+$: 406.1005; found: 406.1004.

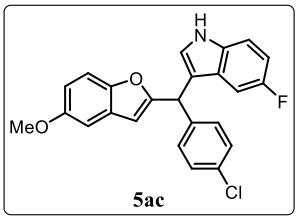

5ac

5-fluoro-3-((7-methoxybenzofuran-2-yl)(phenyl)methyl)-1*H*-indole (5ad): Yield: 120 mg, 82%; R_f = 0.4 (petroleum ether/ethyl acetate = 90:10); White solid; MP: 116–118 °C; ^{1}H NMR (400 MHz, $CDCl_3$) δ 8.18 (br. s., 1H), 7.43–7.46 (m, 4H), 7.38–7.40 (m, 1H), 7.34 (dd, J = 8.8, 4.3 Hz, 1H), 7.24 (d, J = 7.8 Hz, 1H), 7.18–7.21 (m, 1H), 7.14 (dd, J = 9.6, 2.4 Hz, 1H), 7.03 (td, J = 9, 2.4 Hz 1H), 6.92 (d, J = 2.5 Hz, 1H), 6.89 (dd, J = 7.8, 0.9 Hz, 1H), 6.45 (s, 1H), 5.88 (s, 1H), 4.08 (s, 3H); ^{13}C NMR (101 MHz, $CDCl_3$) δ 159.9 (s), 157.6 (d, $J_{C–F}$ = 234.7 Hz), 145.1 (s), 144.1 (s), 140.6 (s), 133.0 (s), 130.2 (s), 128.5 (d, 2C), 128.5 (d, 2C), 127.0 (s), 126.9 (d), 125.3 (d), 123.2 (d), 116.8 (d, $J_{C–F}$ = 4.4 Hz), 113.1 (d), 111.8 (d, $J_{C–F}$ = 10.2 Hz), 110.5 (d, $J_{C–F}$ = 26.2 Hz), 106.0 (d), 105.1 (d), 104.3 (d, $J_{C–F}$ = 24 Hz), 55.9 (q), 43.0 (d); HRMS (ESI) calcd for $C_{24}H_{19}NO_2F$ $[M+H]^+$: 372.1394; found: 372.1396.

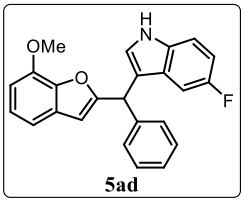

5ad

3-((5-fluorobenzofuran-2-yl)(phenyl)methyl)-1*H*-indole (6aa) : Yield: 52 mg, 37%; R_f = 0.4 (petroleum ether/ethyl acetate = 85:15); Yellowish brown semi solid; ^{1}H NMR (400 MHz, $CDCl_3$) δ 8.02 (br. s., 1H), 7.45 (d, J = 8.0 Hz, 1H), 7.37–7.40 (m, 5H), 7.31–7.35 (m, 2H), 7.24 (t, J = 7.6 Hz, 1H), 7.07–7.15 (m, 2H), 6.96 (td, J = 9.1, 2.6 Hz, 1H), 6.81 (d, J = 2.4 Hz, 1H), 6.36 (s, 1H), 5.82 (s, 1H); ^{13}C NMR (101 MHz, $CDCl_3$) δ 162.0 (s), 159.2 (d, $J_{C–F}$ = 237.6 Hz), 151.2 (s), 140.7 (s), 136.5 (s), 129.4 (d, $J_{C–F}$ = 10.9 Hz), 128.5 (d, 2C), 128.5 (d, 2C), 127.0 (d), 126.6 (s), 123.5 (d), 122.3 (d), 119.7 (d), 119.4 (d), 116.4 (s), 111.6 (d, $J_{C–F}$ = 9.4 Hz), 111.2 (d), 111.2 (d, $J_{C–F}$ = 26.2 Hz), 106.2 (d, $J_{C–F}$ = 24.7 Hz), 104.9 (d, $J_{C–F}$ = 3.6 Hz), 43.2 (s); HRMS (ESI) calcd for $C_{23}H_{16}NOFNa$ $[M+Na]^+$: 364.1108; found: 3364.1098.

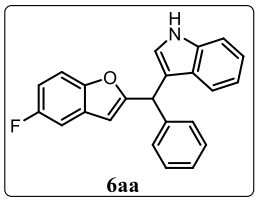

6aa

3-((5-fluorobenzofuran-2-yl)(phenyl)methyl)-2-methyl-1*H*-indole (6ab): Yield: 64 mg, 46%; R_f = 0.4 (petroleum ether/ethyl acetate = 90:10); Reddish brown semi solid; ^{1}H NMR (400 MHz, $CDCl_3$) δ 7.86 (br. s., 1H), 7.28–7.32 (m, 6H), 7.22–7.26 (m, 2H), 7.09–7.13 (m, 2H), 6.91–6.98 (m, 2H), 6.31 (s, 1H), 5.81 (s, 1H), 2.31 (s, 3H); ^{13}C NMR (101 MHz, $CDCl_3$) δ 162.1 (s), 159.2 (d, $J_{C–F}$ = 236.9 Hz), 151.2 (s), 140.9 (s), 135.1 (s), 132.2 (s), 129.4 (d, $J_{C–F}$ = 10.9 Hz), 128.6 (d), 128.5 (d, 2C), 128.4 (d, 2C), 128.0 (s), 126.8 (d),

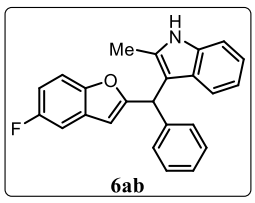

6ab

121.1 (d), 119.5 (d), 119.0 (d), 111.6 (d, $J_{C–F}$ = 9.4 Hz), 110.9 (d, $J_{C–F}$ = 25.9 Hz), 110.3 (d), 106.1 (d, $J_{C–F}$ = 25.4 Hz), 105.3 (d, $J_{C–F}$ = 4.4 Hz), 42.3 (d), 12.1 (q); HRMS (ESI) calcd for $C_{24}H_{19}NOF$ $[M+H]^+$: 356.1445; found: 356.1444.

2-((5-fluorobenzofuran-2-yl)(phenyl)methyl)-3-methyl-1*H*-indole (6ac): Yield: 116 mg, 79%; R_f = 0.6 (petroleum ether/ethyl acetate = 85:15); Red semi solid; ^{1}H NMR (400 MHz, $CDCl_3$) δ 7.85 (br. s., 1H), 7.57–7.59 (m, 1H), 7.34–7.38 (m, 3H), 7.31–7.34 (m, 1H), 7.27–7.31 (m, 1H), 7.22–7.24 (m, 2H), 7.11–7.19 (m, 3H), 6.99 (td, J = 9.1, 2.6 Hz, 1 H), 6.46 (s, 1H), 5.87 (s, 1H), 2.30 (q, 3H); ^{13}C NMR (101 MHz, $CDCl_3$) δ 159.2 (d, $J_{C–F}$ = 238.0 Hz), 159.5 (s), 151.4 (s), 139.0 (s), 135.4 (s), 131.9 (s), 129.1 (d, $J_{C–F}$ = 10.7 Hz), 129.1 (s), 128.9 (d, 2C), 128.2 (d, 2C), 127.5 (d), 121.9 (d), 119.4 (d), 118.6 (d), 111.9 (d, $J_{C–F}$ = 9.2 Hz), 111.5 (d, $J_{C–F}$ = 25.9 Hz), 110.7 (d), 108.9 (s), 106.5 (d, $J_{C–F}$ = 25.2 Hz), 105.7 (d, $J_{C–F}$ = 3.8 Hz), 42.9 (d), 8.5 (q); HRMS (ESI) calcd for $C_{24}H_{19}NOF$ $[M+H]^+$: 356.1445; found: 356.1438.

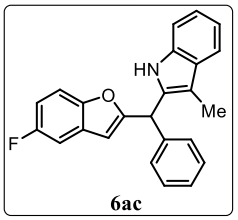

6ac

3-((5-fluorobenzofuran-2-yl)(phenyl)methyl)-5-nitro-1*H*-indole (6ad): Yield: 137 mg, 86%; R_f = 0.4 (petroleum ether/ethyl acetate = 80:20); Yellow solid; MP: 154–156 °C; ^{1}H NMR (400 MHz, $CDCl_3$) δ 8.49 (br. s., 1H), 8.30 (d, J = 2.3 Hz, 1H), 8.02 (dd, J = 8.9, 2.3 Hz, 1H), 7.34 (d, J = 9.0 Hz, 1H), 7.21–7.30 (m, 6H), 7.04 (dd, J = 8.5, 2.6 Hz, 1H), 6.96 (dd, J = 2.4, 0.8 Hz, 1H), 6.87 (td, J = 9.1, 2.6 Hz, 1H), 6.26 (t, J = 0.8 Hz, 1H), 5.73 (s, 1H); ^{13}C NMR (101 MHz, $CDCl_3$) δ 160.9 (s), 159.1 (d, $J_{C–F}$ = 237.3 Hz), 151.3 (s), 141.8 (s), 139.8 (s), 139.4 (s), 129.2 (d, $J_{C–F}$ = 10.7 Hz), 128.8 (d, 2C), 128.4 (d, 2C), 127.4 (d), 126.6 (d), 126.0 (s), 119.0 (s), 118.1 (d), 116.7 (d), 111.7 (d, $J_{C–F}$ = 9.9 Hz), 111.6 (d), 111.3 (d), 106.4 (d, $J_{C–F}$ = 25.2 Hz), 105.1 (d, $J_{C–F}$ = 3.8 Hz), 42.8 (d); HRMS (ESI) calcd for $C_{23}H_{16}N_2O_3F$ $[M+H]^+$: 387.1139; found: 387.1143.

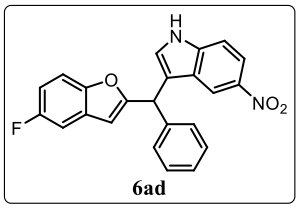

6ad

3-((5-fluorobenzofuran-2-yl)(phenyl)methyl)-5-methoxy-1*H*-indole (6ae) : Yield: 105 mg, 68%; R_f = 0.6 (petroleum ether/ethyl acetate = 80:20); Yellow semi solid; ^{1}H NMR (400 MHz, $CDCl_3$) δ 7.96 (br. s., 1H), 7.28–7.34 (m, 6H), 7.25 (d, J = 2.3 Hz 1H), 7.10 (dd, J = 8.6, 2.6 Hz 1H), 6.93 (td, J = 9.1, 2.6 Hz, 1H), 6.86 (dd, J = 8.8, 2.4 Hz, 1H), 6.78

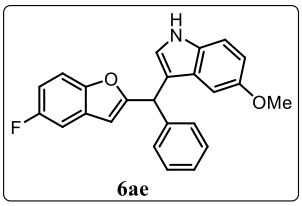

6ae

(t, J = 2.3 Hz, 2H), 6.33 (s, 1H), 5.73 (s, 1H), 3.70 (s, 3H); ^{13}C NMR (101 MHz, $CDCl_3$) δ 161.9 (s), 159.1 (d, $J_{C–F}$ = 237.6 Hz), 154.0 (s), 151.3 (s), 140.7 (s), 131.6 (s), 129.4 (d, $J_{C–F}$ = 10.2 Hz), 128.7 (d), 128.6 (d, 2C), 128.5 (d, 2C), 127.0 (d, $J_{C–F}$ = 2.2 Hz), 124.3 (d), 116.1 (s), 112.4 (d), 111.9 (d), 111.6 (d, $J_{C–F}$ = 9.5 Hz), 111.1 (d, $J_{C–F}$ = 26.2 Hz), 106.3 (d, $J_{C–F}$ = 25.4 Hz), 104.9 (d, $J_{C–F}$ = 3.6 Hz), 101.3 (s), 55.8 (q), 43.2 (d); HRMS (ESI) calcd for $C_{24}H_{19}NO_2F$ $[M+H]^+$: 372.1394; found: 372.1396.

3-((5-fluorobenzofuran-2-yl)(phenyl)methyl)-2-methyl-5-nitro-1*H*-indole (6af): Yield: 96 mg, 58%; R_f = 0.3 (petroleum ether/ethyl acetate = 80:20); Yellow solid; MP: 154–156 °C; ^{1}H NMR (400 MHz, $CDCl_3$) δ 8.27 (br. s., 1H), 8.08 (d, J = 2.1 Hz, 1H), 7.90 (dd, J = 8.9, 2.2 Hz, 1H), 7.15–7.23 (m, 7H), 7.02 (dd, J = 8.6, 2.6 Hz, 1H), 6.83 (td, J = 9.1, 2.7 Hz, 1H), 6.23 (t, J = 0.9 Hz, 1H), 5.72 (s, 1H), 2.22 (s, 3H); ^{13}C NMR (101 MHz, $CDCl_3$) δ 160.8 (s), 159.2 (d, $J_{C–F}$ = 238 Hz), 151.2 (s), 141.7 (s), 139.9 (s), 138.3 (s), 135.9 (s), 129.1 (d, $J_{C–F}$ = 10.7 Hz), 128.7 (d, 2C), 128.3 (d, 2C), 127.5 (s), 127.2 (d), 117.1 (d), 116.1 (d), 113.2 (s), 111.7 (d, $J_{C–F}$ = 9.9 Hz), 111.4 (d, $J_{C–F}$ = 26.7 Hz), 110.2 (d), 106.3 (d, $J_{C–F}$ = 25.2 Hz), 105.6 (d, $J_{C–F}$ = 3.8 Hz), 42.1 (q), 12.3 (d); HRMS (ESI) calcd for $C_{24}H_{18}N_2O_3F$ $[M+H]^+$: 401.1296; found: 401.1300.

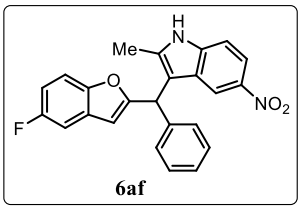

6af

6-fluoro-3-((5-fluorobenzofuran-2-yl)(phenyl)methyl)-1*H*-indole (6ag): Yield: 130 mg, 87%; R_f = 0.3 (petroleum ether/ethyl acetate = 85:15); White solid; MP: 130–132 °C; ^{1}H NMR (400 MHz, $CDCl_3$) δ 7.91 (br. s., 1H), 7.16–7.25 (m, 7H), 7.02 (dt, J = 8.5, 2.7 Hz, 1H), 6.95 (d, J = 9.6 Hz, 1H), 6.82–6.87 (m, 1H), 6.69–6.74 (m, 2H), 6.23 (s, 1H), 5.65 (s, 1H); ^{13}C NMR (101 MHz, $CDCl_3$) δ 161.7 (s), 160.2 (d, $J_{C–F}$ = 238.3 Hz), 159.1 (d, $J_{C–F}$ = 237.6 Hz), 151.2 (s), 140.5 (s), 136.5 (d, $J_{C–F}$ = 12.4 Hz), 129.3 (d, $J_{C–F}$ = 10.9 Hz), 128.6 (d, 2C), 128.5 (d, 2C), 127.1 (d), 123.8 (d), 123.2 (s), 120.3 (d, $J_{C–F}$ = 10.2 Hz), 116.5 (d), 111.7 (d, $J_{C–F}$ = 9.5 Hz), 111.3 (d, $J_{C–F}$ = 26.2 Hz), 108.5 (d, $J_{C–F}$ = 24 Hz),

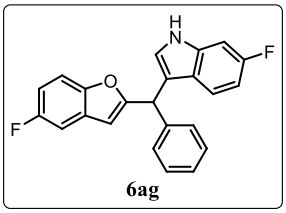

6ag

106.3 (d, $J_{C–F}$ = 24.7 Hz), 104.9 (d, $J_{C–F}$ = 2.9 Hz), 97.6 (d, $J_{C–F}$ = 26.2 Hz), 43.1 (d); HRMS (ESI) calcd for $C_{23}H_{16}NOF_2$ $[M+H]^+$: 358.1038; found: 358.1052.

3-((5-fluorobenzofuran-2-yl)(4-methoxyphenyl)methyl)-1*H*-indole (6ba): Yield: 132 mg, 97%; R_f = 0.4 (petroleum ether/ethyl acetate = 75:25); White solid; MP: 110–112 °C; ^{1}H NMR (400 MHz, $CDCl_3$) δ 8.06 (br. s., 1H), 7.38–7.41 (m, 2H), 7.33 (dd, J = 8.9, 4.1 Hz, 1H), 7.26–7.27 (m, 1H), 7.25–7.26 (m, 1H), 7.20 (ddd, J = 8.2, 7.2, 1.1 Hz, 1H), 7.10 (dd, J = 8.6, 2.6 Hz, 1H), 7.05 (ddd, J = 8.1, 7.1, 0.9 Hz, 1H), 6.93 (td, J = 9.1, 2.6 Hz, 1H), 6.86–6.89 (m, 2H), 6.83 (dd, J = 2.4, 0.9 Hz, 1H), 6.32 (t, J = 0.8 Hz, 1H), 5.74 (s, 1H), 3.81 (s, 3H); ^{13}C NMR (101 MHz, $CDCl_3$) δ 162.4 (s), 160.3 (d, $J_{C–F}$ = 237.3 Hz), 158.6 (s), 151.2 (s), 136.5 (s), 132.9 (s), 129.5 (d, 2C), 129.4 (s), 126.6 (s), 123.4 (d), 122.3 (d), 119.7 (d), 119.5 (d), 116.8 (s), 113.9 (d, 2C), 111.6 (d, $J_{C–F}$ = 9.9 Hz), 111.2 (d), 110.9 (d, $J_{C–F}$ = 25.9 Hz), 106.1 (d, $J_{C–F}$ = 25.2 Hz), 104.6 (d, $J_{C–F}$ = 3.8 Hz), 55.3 (q), 42.4 (d); HRMS (ESI) calcd for $C_{24}H_{18}NO_2FNa$ $[M+Na]^+$: 394.1214; found: 394.1217.

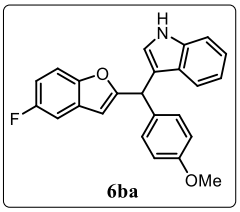

6ba

3-((5-fluorobenzofuran-2-yl)(4-methoxyphenyl)methyl)-2-methyl-1*H*-indole (6bb): Yield: 112 mg, 79%; R_f = 0.6 (petroleum ether/ethyl acetate = 80:20); White solid; MP: 152–154 °C; ^{1}H NMR (400 MHz, $CDCl_3$) δ 7.87 (br. s., 1H), 7.28–7.32 (m, 2H), 7.20–7.23 (m, 3H), 7.07–7.11 (m, 2H), 6.92–6.97 (m, 2H), 6.83–6.86 (m, 2H), 6.30 (s, 1H), 5.75 (s, 1H), 3.80 (s, 3H), 2.30 (s, 3H); ^{13}C NMR (101 MHz, $CDCl_3$) δ 161.5 (d, $J_{C–F}$ = 220.5 Hz), 158.4 (s), 151.2 (s), 135.1 (s), 133.0 (s), 132.1 (s), 129.5 (d, 2C), 129.3 (s), 128.0 (s), 121.9 (s), 121.1 (d), 120.4 (s), 119.5 (d), 119.0 (d), 113.8 (d, 2C), 111.6 (d, $J_{C–F}$ = 9.9 Hz), 110.9 (d, $J_{C–F}$ = 25.9 Hz), 110.2 (d), 106.1 (d, $J_{C–F}$ = 25.2 Hz), 105.2 (d, $J_{C–F}$ = 3.8 Hz), 55.2 (q), 41.6 (d), 12.1 (q); HRMS (ESI) calcd for $C_{25}H_{20}NO_2FNa$ $[M+Na]^+$: 408.1370; found: 408.1375

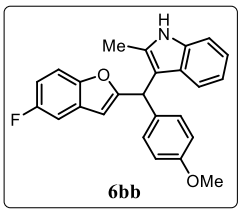

6bb

2-((5-fluorobenzofuran-2-yl)(p-tolyl)methyl)-3-methyl-1*H*-indole (6bc): Yield: 108 mg, 76%; R_f = 0.8 (petroleum ether/ethyl acetate = 80:20); Orange semi solid; ^{1}H NMR (400 MHz, $CDCl_3$) δ 7.73 (br. s., 1H), 7.48 (d, J = 7.8 Hz, 1H), 7.24–7.27 (m, 1H), 7.17 (d, J = 8.4 Hz,

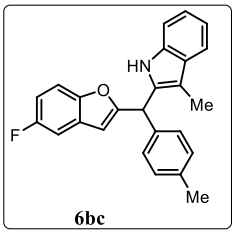

6bc

1H), 7.02–7.08 (m, 5H), 6.85–6.90 (m, 1H), 6.79 (dd, *J* = 8.6, 1.7 Hz, 2H), 6.34 (s, 1H), 5.71 (s, 1H), 3.71 (s, 3H), 2.19 (s, 3H); ^{13}C NMR (101 MHz, $CDCl_3$) δ 159.2 (d, J_{C-F} = 238.0 Hz), 159.8 (s), 158.9 (s), 151.3 (s), 135.3 (s), 132.2 (s), 131.0 (s), 129.2 (d, 2C), 121.8 (d), 119.31 (d), 118.9 (d, J_{C-F} = 28.2 Hz), 118.6 (d), 114.25 (d, 2C), 111.8 (d, J_{C-F} = 9.2 Hz), 111.75 (d, J_{C-F} = 26.2 Hz), 110.89 (d), 110.71 (d), 108.67 (s), 106.3 (d, J_{C-F} = 25.2 Hz), 105.5 (d, J_{C-F} = 3.8 Hz), 55.3 (d), 42.1 (q), 8.5 (q); HRMS (ESI) calcd for $C_{25}H_{21}NO_2F$ $[M+H]^+$: 386.1551; found: 386.1549.

3-((5-fluorobenzofuran-2-yl)(4-methoxyphenyl)methyl)-5-nitro-1*H*-indole (6bd):

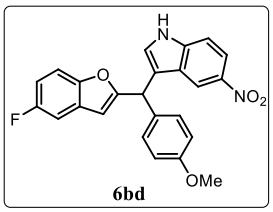

6bd

Yield: 124 mg, 81%; R_f = 0.4 (petroleum ether/ethyl acetate = 85:15); Yellow solid; MP: 200–202 °C; ^{1}H NMR (400 MHz, $CDCl_3$) δ 8.44 (br. s., 1H), 8.30 (d, *J* = 2.1 Hz, 1H), 8.03 (dd, *J* = 9.0, 2.3 Hz, 1H), 7.34 (d, *J* = 9.0 Hz, 1H), 7.25 (dd, *J* = 9.0, 4.1 Hz, 1H), 7.15–7.19 (m, 2H), 7.04 (dd, *J* = 8.6, 2.6 Hz, 1H), 6.95 (dd, *J* = 2.4, 0.8 Hz, 1H), 6.87 (td, *J*=9.1, 2.7 Hz, 1H), 6.78–6.83 (m, 2H), 6.24 (s, 1H), 5.68 (s, 1H), 3.73 (s, 3H); ^{13}C NMR (101 MHz, $CDCl_3$) δ 160.4 (s), 160.1 (d, J_{C-F} = 241.8 Hz), 151.3 (s), 141.9 (s), 139.5 (s), 131.9 (s), 129.4 (d, 2C), 129.2 (s), 129.1 (s), 126.4 (d), 126.0 (s), 119.4 (s), 118.1 (d), 116.7 (d), 114.2 (d, 2C), 111.7 (d, J_{C-F} = 9.9 Hz), 111.5 (d), 111.3 (d), 106.2 (d, J_{C-F} = 24.4 Hz), 104.9 (d, J_{C-F} = 3.8 Hz), 55.3 (q), 42.1 (d); HRMS (ESI) calcd for $C_{24}H_{18}N_2O_4F$ $[M+H]^+$: 417.1245; found: 417.1239.

3-((5-fluorobenzofuran-2-yl)(4-methoxyphenyl)methyl)-5-methoxy-1*H*-indole (6be):

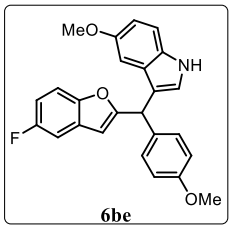

6be

Yield: 78 mg, 53%; R_f = 0.3 (petroleum ether/ethyl acetate = 80:20); Brown semi solid; ^{1}H NMR (400 MHz, $CDCl_3$) δ 7.86 (br. s., 1H), 7.23 (dd, *J* = 8.9, 4.1 Hz, 1H), 7.14–7.18 (m, 3H), 7.01 (dd, *J* = 8.6, 2.6 Hz, 1H), 6.83 (td, *J* = 9.1, 2.7 Hz, 1H), 6.74–6.81 (m, 3H), 6.72 (d, *J* = 2.4 Hz, 1H), 6.70 (d, *J* = 2.3 Hz, 1H), 6.23 (s, 1H), 5.59 (s, 1H), 3.71 (s, 3H), 3.62 (s, 3H); ^{13}C NMR (101 MHz, $CDCl_3$) δ 162.3 (s), 158.8 (d, J_{C-F} = 237.3 Hz), 158.5 (s), 154.0 (s), 151.2 (s), 132.9 (s), 131.7 (s), 129.5 (d, 2C), 129.4 (d, J_{C-F} = 10.7 Hz), 127.0 (s), 124.2 (d), 116.4 (s), 113.9 (d, 2C), 112.3 (d), 111.9 (d), 111.6 (d, J_{C-F} = 9.9 Hz), 111.1 (d, J_{C-F} = 25.9 Hz), 106.2 (d, J_{C-F} = 25.2 Hz), 104.7 (d, J_{C-F} = 3.8 Hz), 101.4 (d),

55.8 (q), 55.2 (q), 42.4 (d); HRMS (ESI) calcd for $C_{25}H_{21}NO_3F$ $[M+H]^+$: 402.1500; found: 402.1502.

3-((5-fluorobenzofuran-2-yl)(4-methoxyphenyl)methyl)-2-methyl-5-nitro-1*H*-indole (6bf): Yield: 120 mg, 76%; R_f = 0.3 (petroleum ether/ethyl acetate = 75:25); Yellow solid; MP: 183–185 °C; ^{1}H NMR (400 MHz, $CDCl_3$) δ 8.37 (s, 1H), 8.20 (d, J = 2.1 Hz, 1H), 8.02 (dd, J = 8.9, 2.1 Hz, 1H), 7.29–7.34 (m, 2H), 7.18–7.21 (m, 2H), 7.13 (dd, J = 8.6, 2.6 Hz, 1H), 6.94 (td, J = 9.1, 2.6 Hz, 1H), 6.86–6.89 (m, 2H), 6.34 (s, 1H), 5.79 (s, 1H), 3.81 (s, 3H), 2.33 (s, 3H); ^{13}C NMR (101 MHz, $CDCl_3$) δ 161.2 (s), 159.1 (d, J_{C-F} = 238.0 Hz), 158.7 (s), 151.2 (s), 141.7 (s), 138.3 (s), 135.7 (s), 131.9 (s), 129.4 (d, 2C), 129.1 (d, J_{C-F} = 10.7 Hz), 127.5 (s), 117.1 (d), 116.1 (d), 114.1 (d, 2C), 113.5 (s), 111.7 (d, J_{C-F} = 9.9 Hz), 111.3 (d, J_{C-F} = 25.9 Hz), 110.2 (d), 106.2 (d, J_{C-F} = 25.2 Hz), 105.5 (d, J_{C-F} = 3.8 Hz), 55.3 (d), 41.3 (q), 12.3 (q); HRMS (ESI) calcd for $C_{25}H_{20}N_2O_4F$ $[M+H]^+$: 431.1402; found: 431.1408.

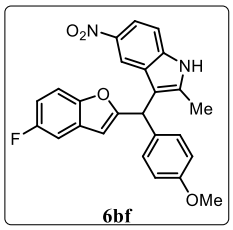

3-(benzofuran-2-yl(4-(trifluoromethyl)phenyl)methyl)-1*H*-indole (6ca): Yield: 110 mg, 82%; R_f = 0.2 (petroleum ether/ethyl acetate = 85:15); Yellowish brown semi solid; ^{1}H NMR (400 MHz, $CDCl_3$) δ 7.99 (br. s., 1H), 7.49 (d, J = 8.1 Hz, 2H), 7.38 (d, J = 8.1 Hz, 3H), 7.34 (d, J = 8.3 Hz, 1H), 7.30 (dd, J = 8.2, 2.7 Hz, 2H), 7.10–7.17 (m, 3H), 6.95–7.00 (m, 1H), 6.74 (d, J = 1.8 Hz, 1H), 6.29 (s, 1H), 5.77 (s, 1H); ^{13}C NMR (101 MHz, $CDCl_3$) δ 158.9 (s), 155.1 (s), 145.1 (s), 136.5 (s), 129.4 (s), 129.0 (d), 128.9 (d, 2C), 128.4 (s), 126.4 (s), 125.5 (q), 123.8 (d), 123.5 (d), 122.8 (d), 122.7 (d), 122.5 (d), 120.7 (d), 119.8 (d), 119.3 (d), 115.8 (s), 111.3 (d), 111.1 (d), 105.0 (d), 42.9 (d); HRMS (ESI) calcd for $C_{24}H_{17}NOF_3$ $[M+H]^+$: 390.1100; found: 390.1116.

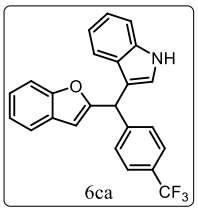

3-(benzofuran-2-yl(4-(trifluoromethyl)phenyl)methyl)-2-methyl-1*H*-indole (6cb): Yield: 122 mg, 88%; R_f = 0.5 (petroleum ether/ethyl acetate = 80:20); Yellowish brown semi solid; ^{1}H NMR (400 MHz, $CDCl_3$) δ 7.91 (br. s., 1H), 7.56 (d, J = 8.3 Hz, 2H), 7.48 (d, J = 6.9 Hz, 1H), 7.43 (d, J = 8.5 Hz, 3H), 7.31 (d, J = 8.0 Hz, 1H), 7.19–7.25 (m, 3H), 7.12 (t, J = 7.6 Hz, 1H), 6.97 (t, J = 7.9 Hz, 1H), 6.36 (s, 1H), 5.87 (s, 1H), 2.33 (s, 3H);

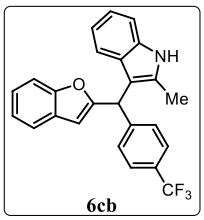

6cb

^{13}C NMR (101 MHz, $CDCl_3$) δ 158.8 (s), 155.0 (s), 145.4 (s), 135.2 (s), 132.3 (s), 129.1 (s), 128.9 (d, 2C), 128.7 (d), 128.4 (s), 127.7 (s), 125.4 (q), 123.8 (d), 122.9 (d), 122.7 (d), 121.3 (d), 120.7 (d), 119.7 (d), 118.9 (d), 111.2 (d), 110.4 (d), 110.3 (s), 105.4 (d), 42.1 (d), 12.2 (q); HRMS (ESI) calcd for $C_{25}H_{19}NOF_3$ $[M+H]^+$: 406.1413; found: 406.1407.

2-(benzofuran-2-yl(4-(trifluoromethyl)phenyl)methyl)-3-methyl-1*H*-indole (6cc): Yield: 84 mg, 60%; R_f = 0.3 (petroleum ether/ethyl acetate = 80:20); Red semi solid; ^{1}H NMR (400 MHz, $CDCl_3$) δ 7.93 (br. s., 1H), 7.61 (d, J = 7.4 Hz, 3H), 7.56 (d, J = 7.3 Hz, 1H), 7.49 (d, J = 7.9 Hz, 1H), 7.29–7.37 (m, 5H), 7.16–7.23 (m, 2H), 6.55 (s, 1H), 5.94 (s, 1H), 2.33 (s, 3H); ^{13}C NMR (101 MHz, $CDCl_3$) δ 156.4 (s), 155.2 (s), 143.4 (s), 135.5 (s), 131.2 (s), 129.8 (s), 129.5 (s), 129.0 (s), 128.6 (d, 2C), 128.0 (s), 125.7 (q), 125.4 (d), 124.4 (d), 123.1 (d), 122.1 (d), 121.0 (d), 119.5 (d), 118.7 (d), 111.3 (d), 110.8 (d), 109.2 (s), 105.8 (d), 42.6 (d), 8.5 (q); HRMS (ESI) calcd for $C_{25}H_{19}NOF_3$ $[M+H]^+$: 406.1413; found: 406.1401.

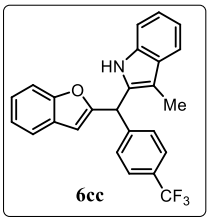

6cc

3-(benzofuran-2-yl(4-(trifluoromethyl)phenyl)methyl)-2-methyl-5-nitro-1*H*-indole (6cd): Yield: 130 mg, 87%; R_f = 0.4 (petroleum ether/ethyl acetate = 70:30); Yellow solid; MP: 170–172 °C; ^{1}H NMR (400 MHz, $CDCl_3$) δ 8.32 (br. s., 1H), 8.14 (d, J = 2.1 Hz, 1H), 7.95 (dd, J = 8.9, 2.2 Hz, 1H), 7.51 (d, J = 8.3 Hz, 2H), 7.40–7.43 (m, 1H), 7.31–7.34 (m, 3H), 7.24 (d, J = 8.9 Hz, 1H), 7.12–7.19 (m, 2H), 6.32 (s, 1H), 5.82 (s, 1H), 2.26 (s, 3H); ^{13}C NMR (101 MHz, $CDCl_3$) δ 157.6 (s), 155.0 (s), 144.3 (s), 141.8 (s), 138.3 (s), 136.0 (s), 128.9 (d), 128.7 (d, 2C), 128.1 (s), 127.3 (s), 125.7 (q), 125.4 (d), 124.2 (d), 123.0 (d), 122.7 (s), 120.9 (d), 117.3 (d), 115.9 (d), 112.6 (s), 111.2 (d), 110.3 (d), 105.7 (d), 41.8 (d), 12.3 (q); HRMS (ESI) calcd for $C_{25}H_{18}N_2O_3F_3Na$ $[M+H]^+$: 459.0927; found: 459.0918.

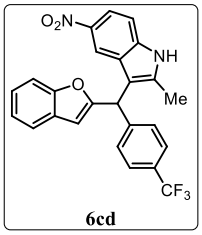

6cd

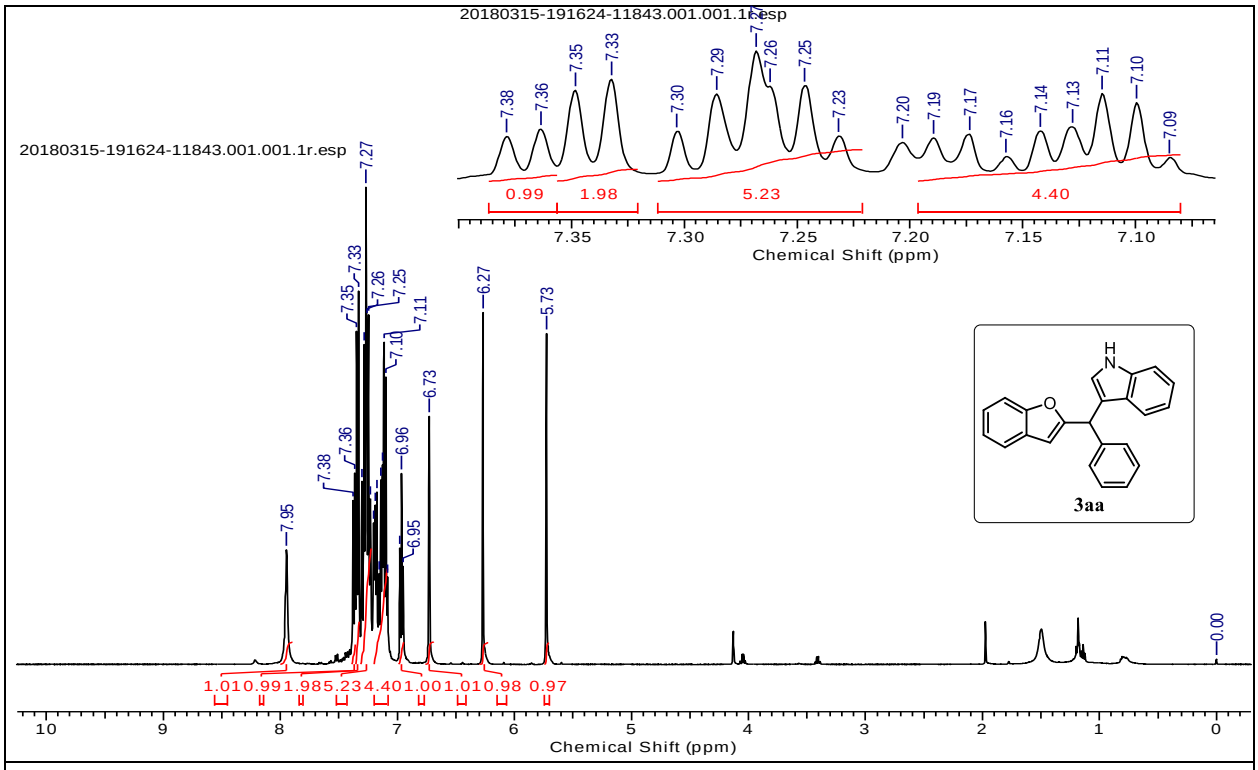

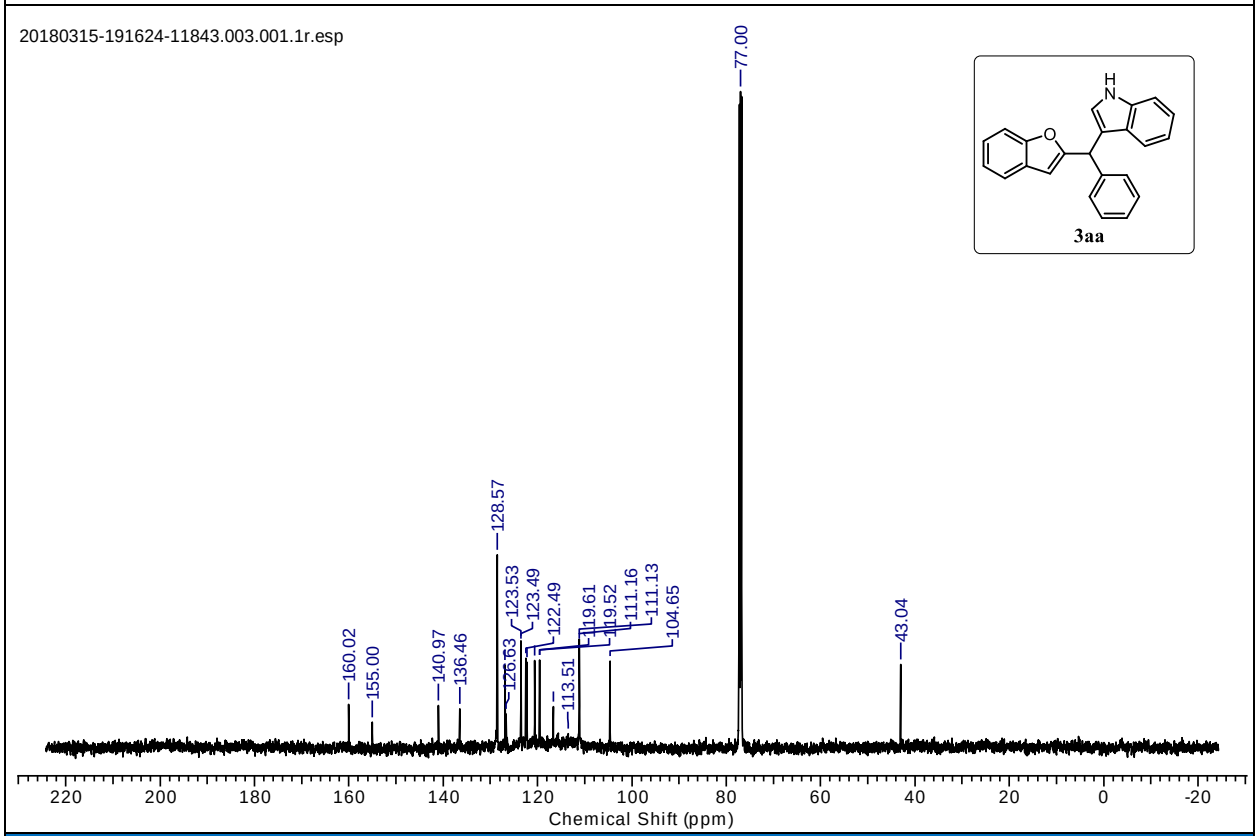

^{1}H /^{13}C NMR Spectrum of 3aa in $CDCl_3$

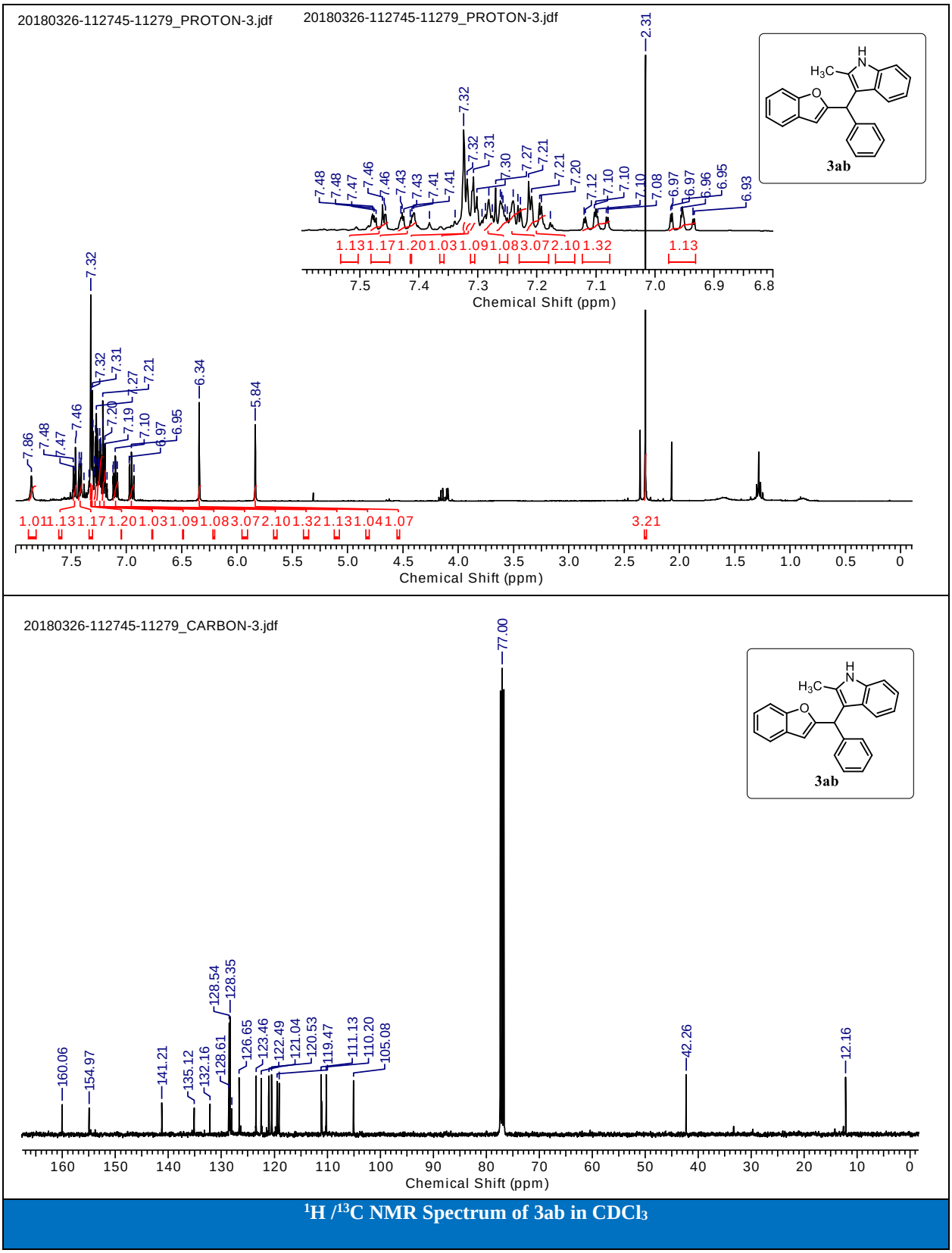

^{1}H /^{13}C NMR Spectrum of 3ab in $CDCl_3$

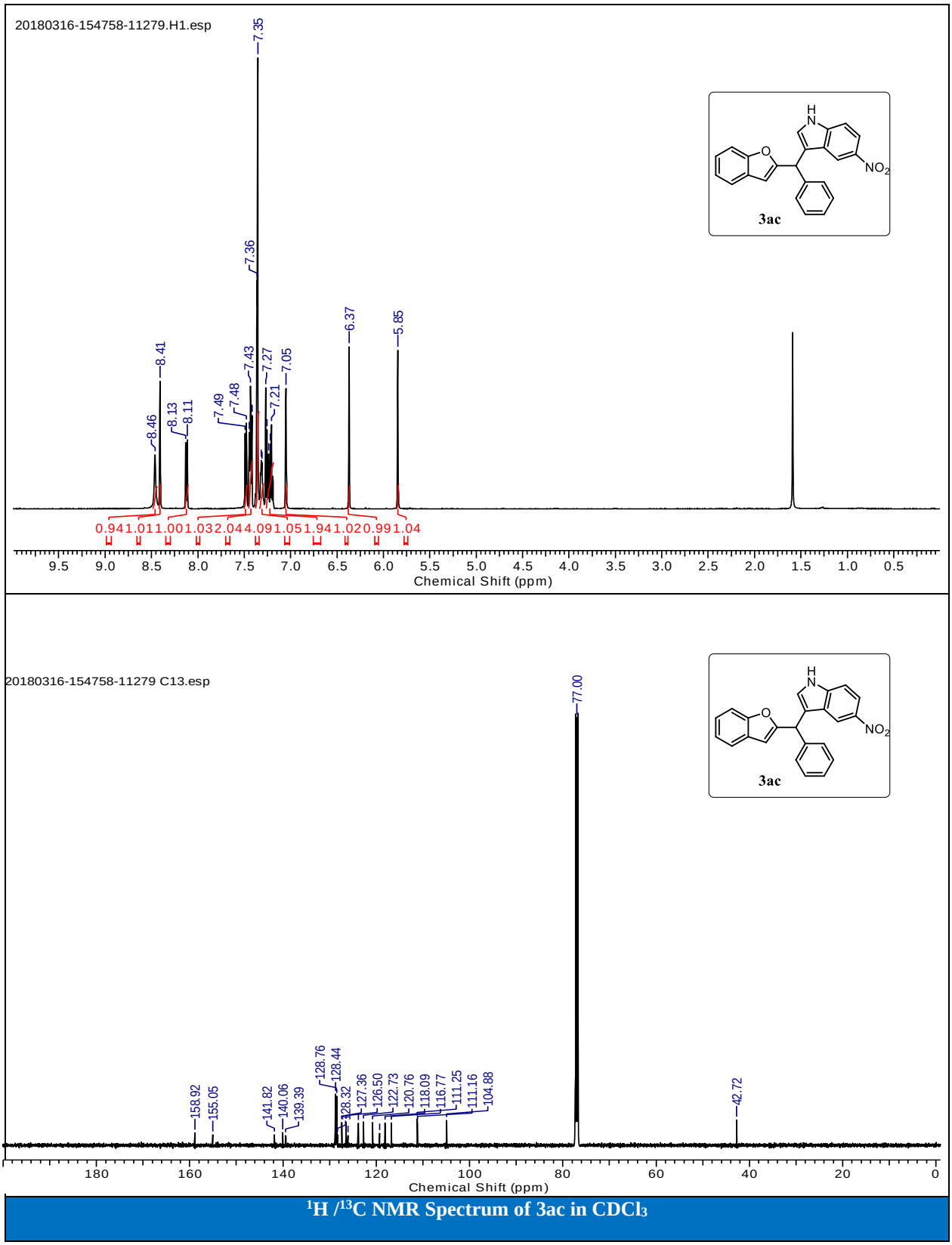

^{1}H /^{13}C NMR Spectrum of 3ac in $CDCl_3$

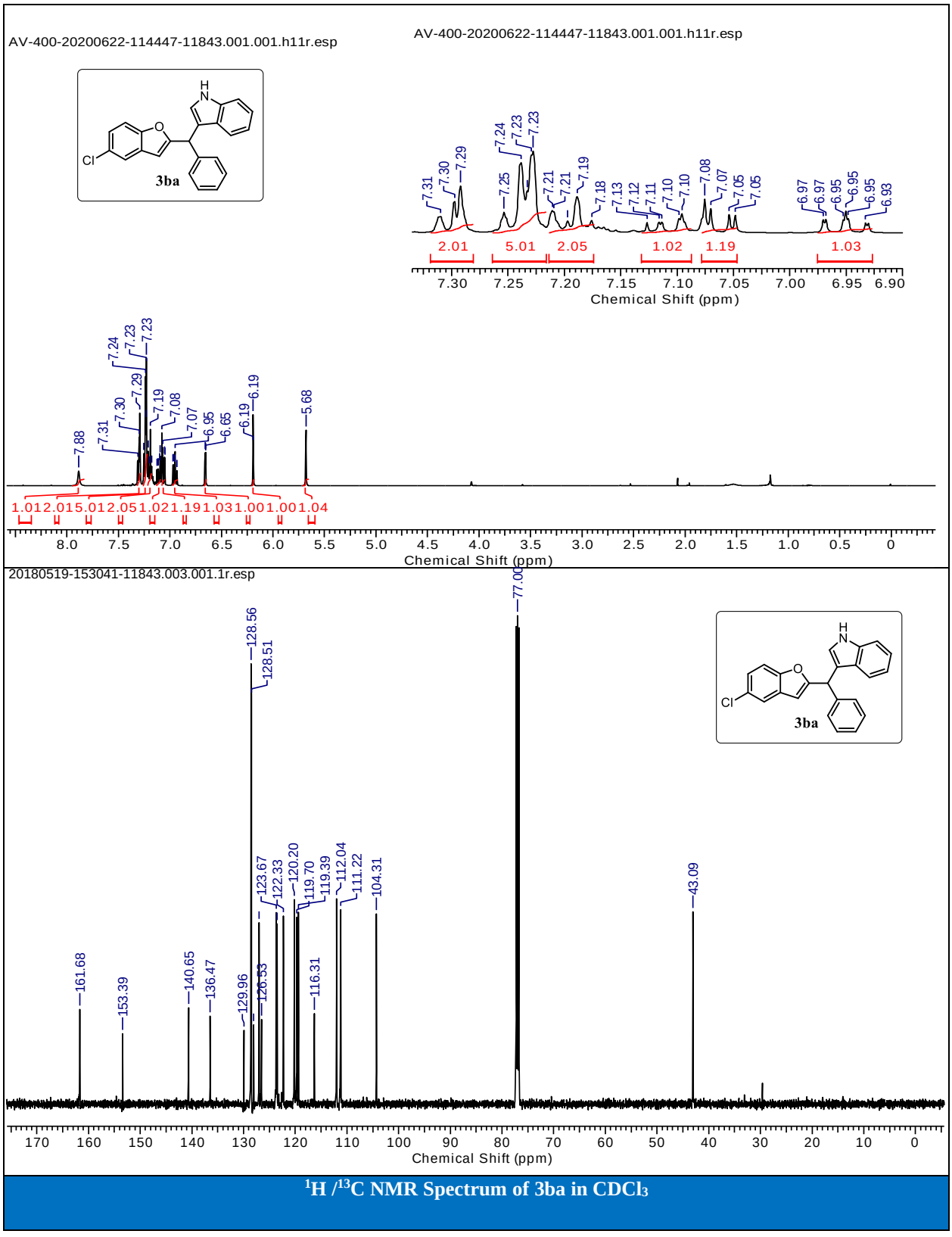

^{1}H /^{13}C NMR Spectrum of 3ba in $CDCl_3$

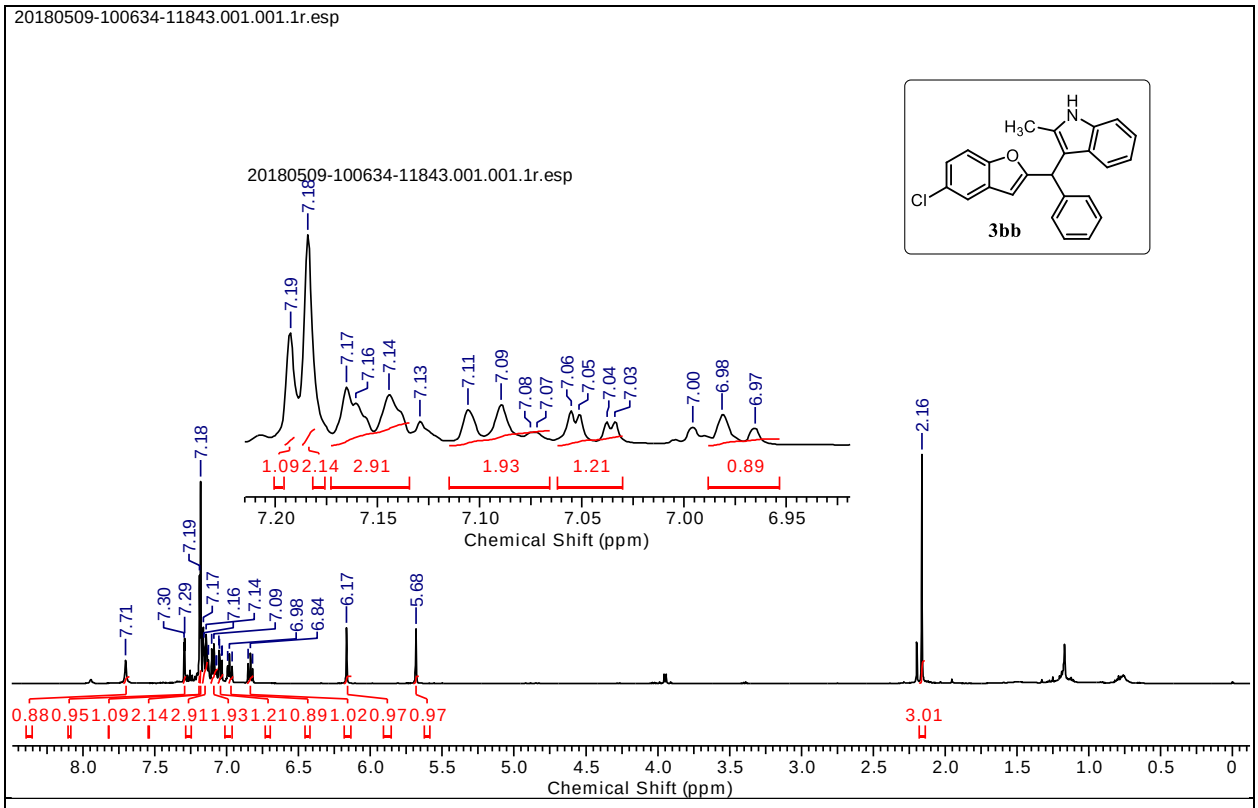

^{1}H /^{13}C NMR Spectrum of 3bb in $CDCl_3$

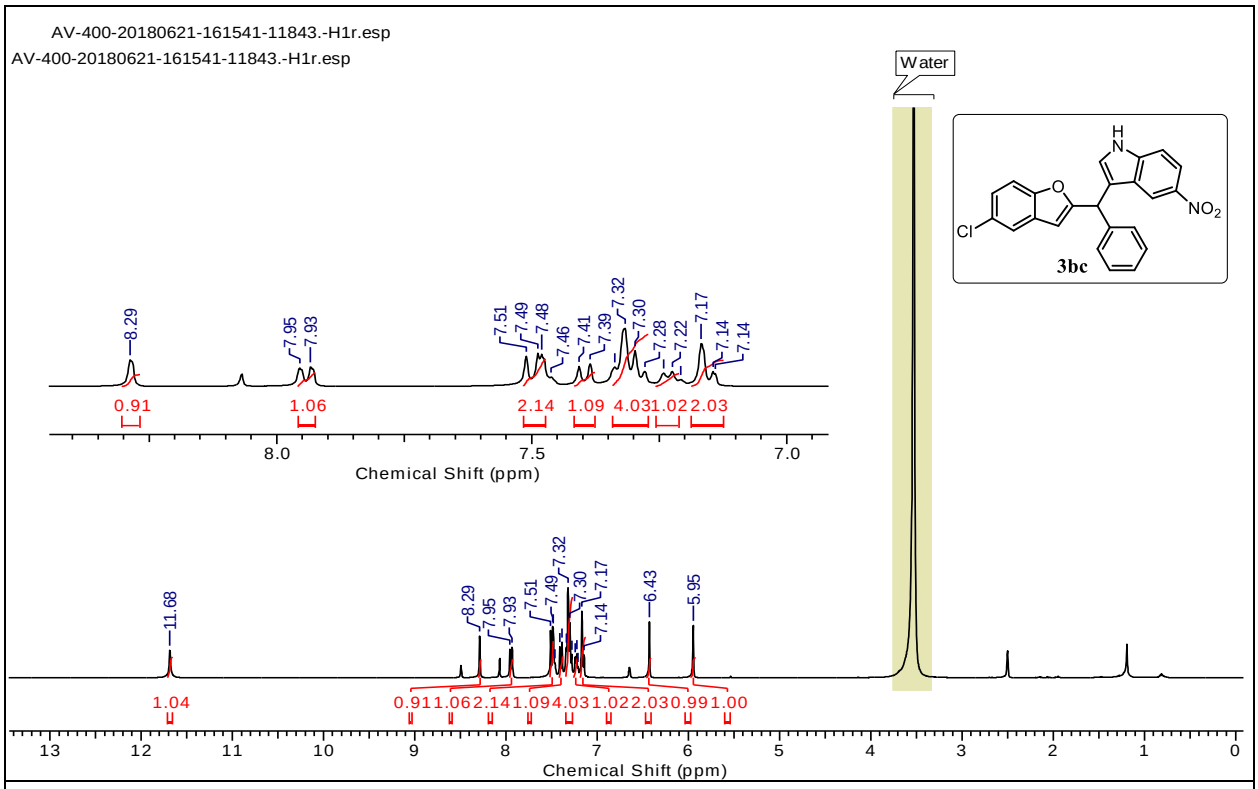

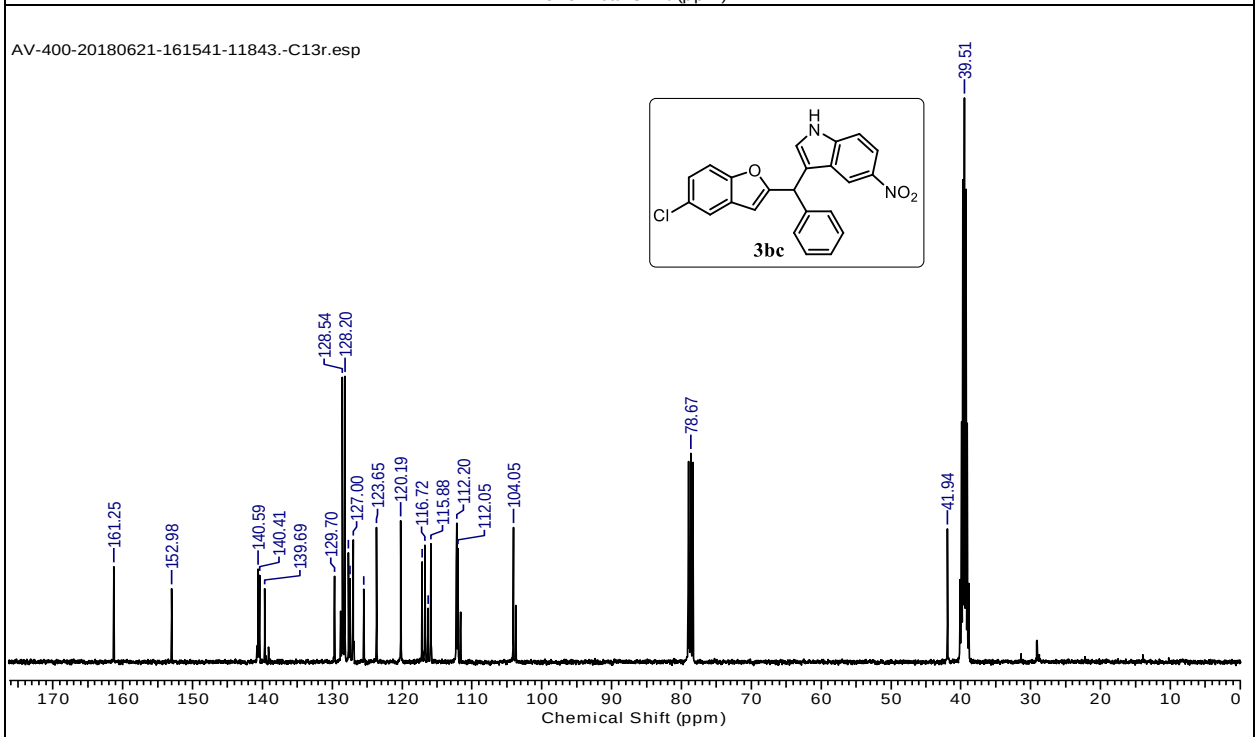

^{1}H /^{13}C NMR Spectrum of 3bc in $CDCl_3$

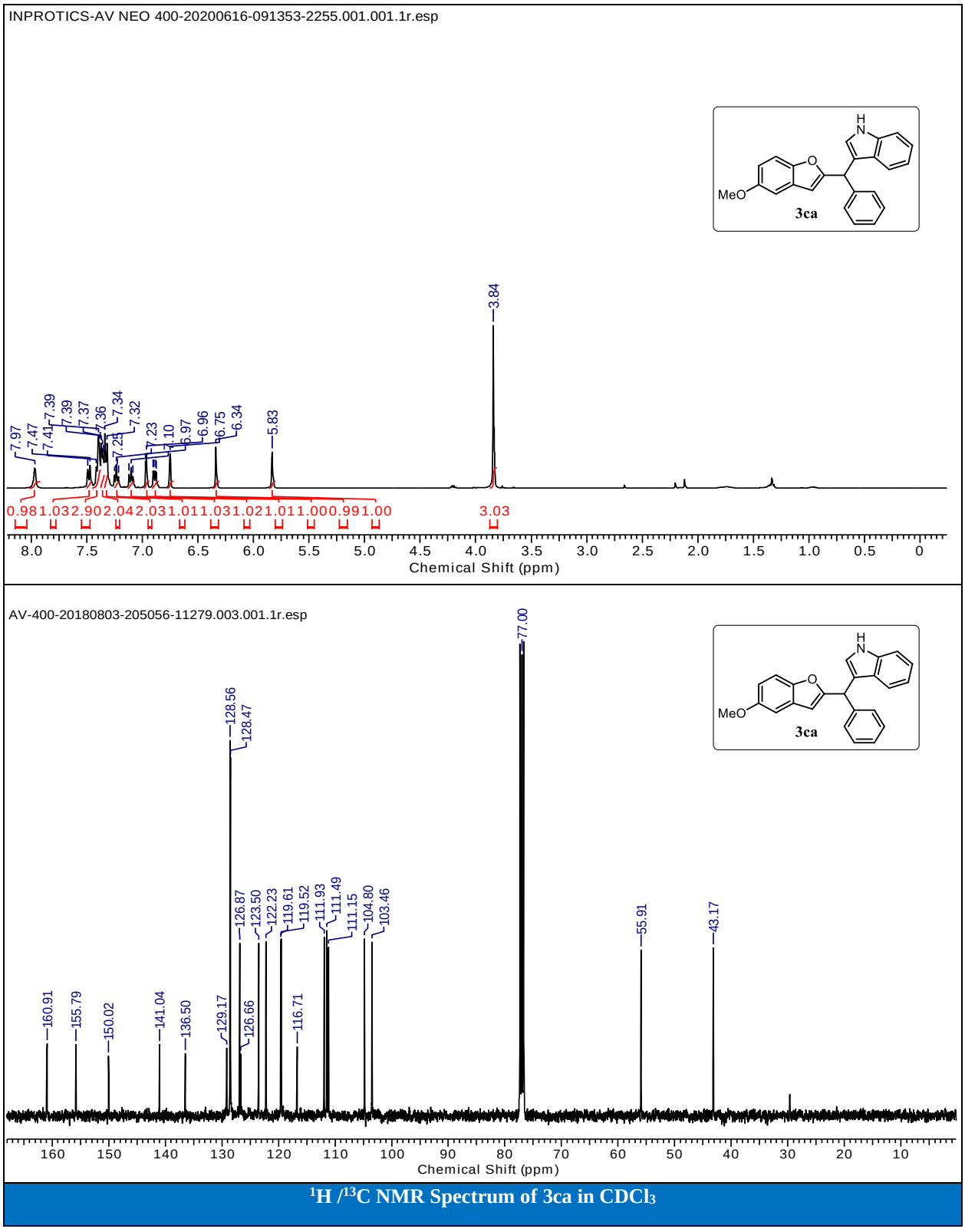

^{1}H /^{13}C NMR Spectrum of 3ca in $CDCl_3$

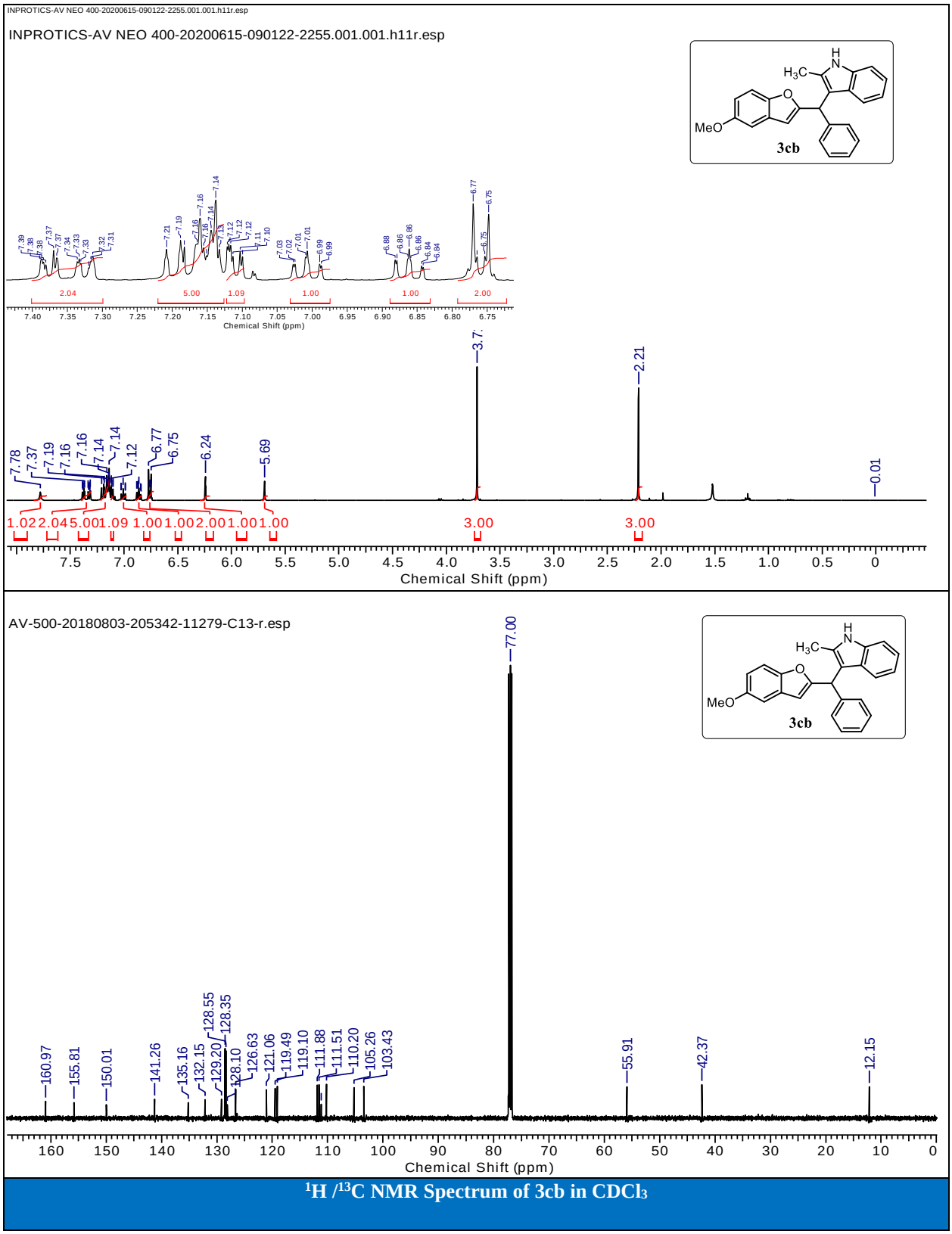

^{1}H /^{13}C NMR Spectrum of 3cb in $CDCl_3$

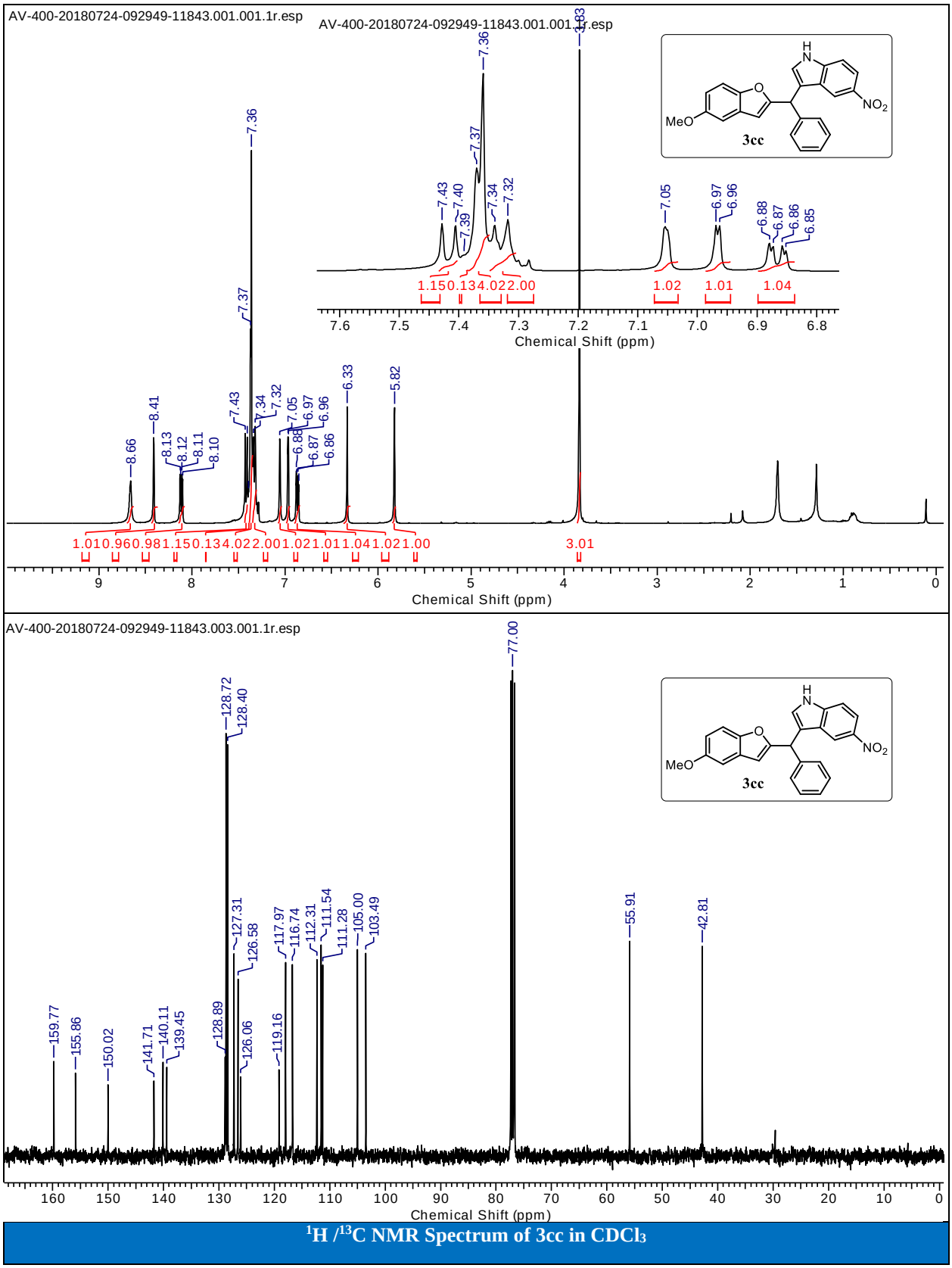

^{1}H /^{13}C NMR Spectrum of 3cc in $CDCl_3$

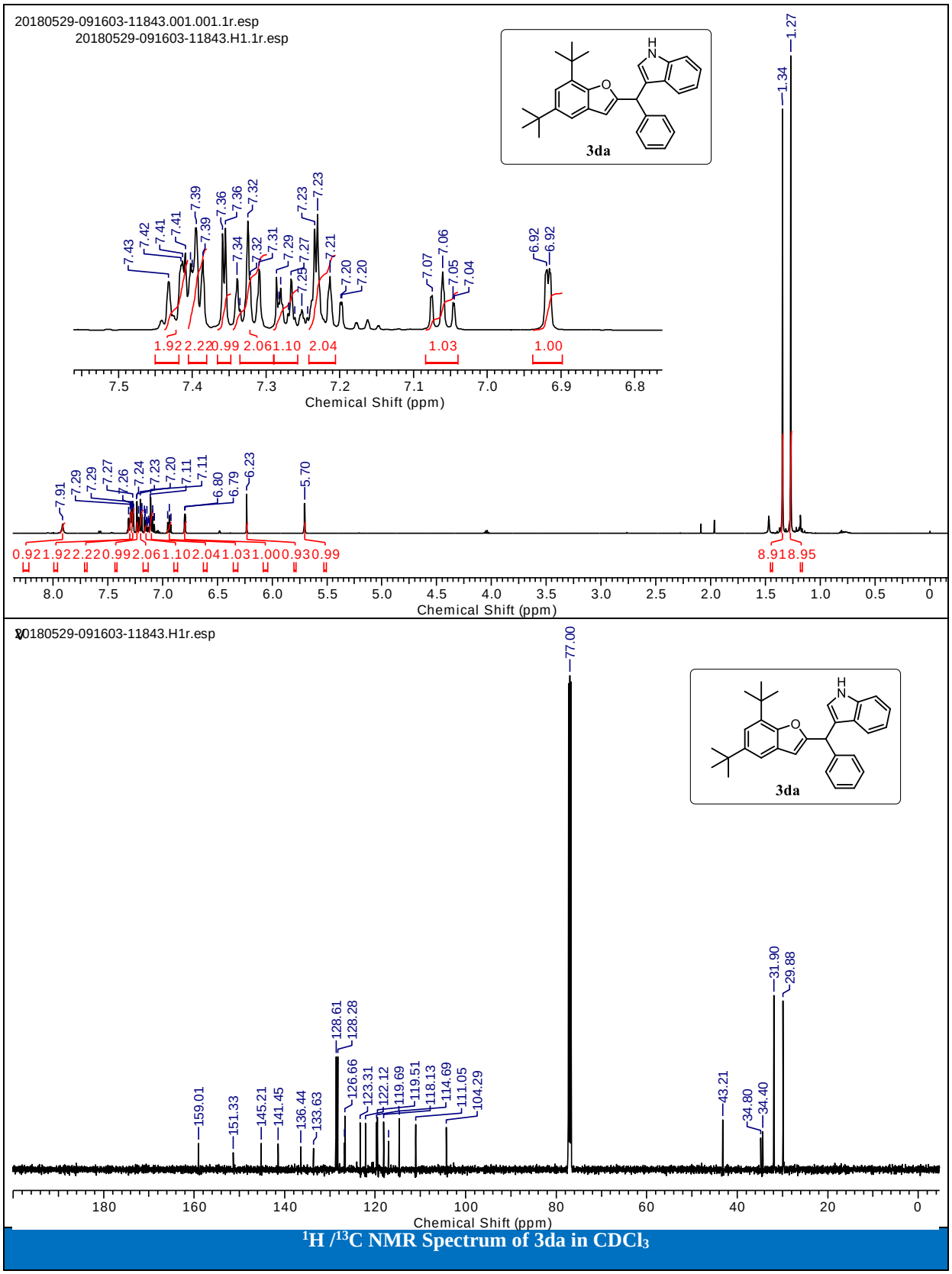

^{1}H /^{13}C NMR Spectrum of 3da in $CDCl_3$

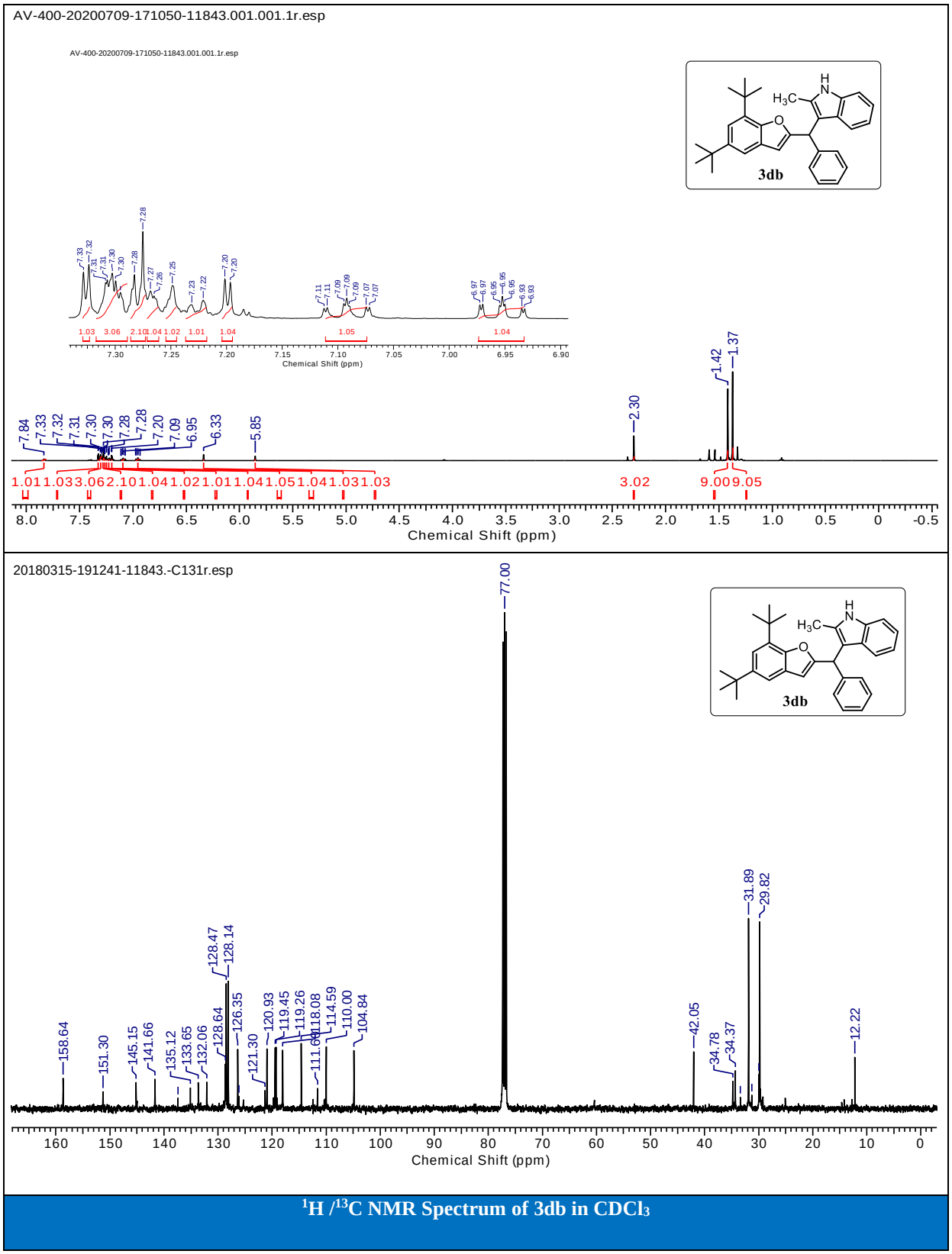

^{1}H /^{13}C NMR Spectrum of 3db in $CDCl_3$

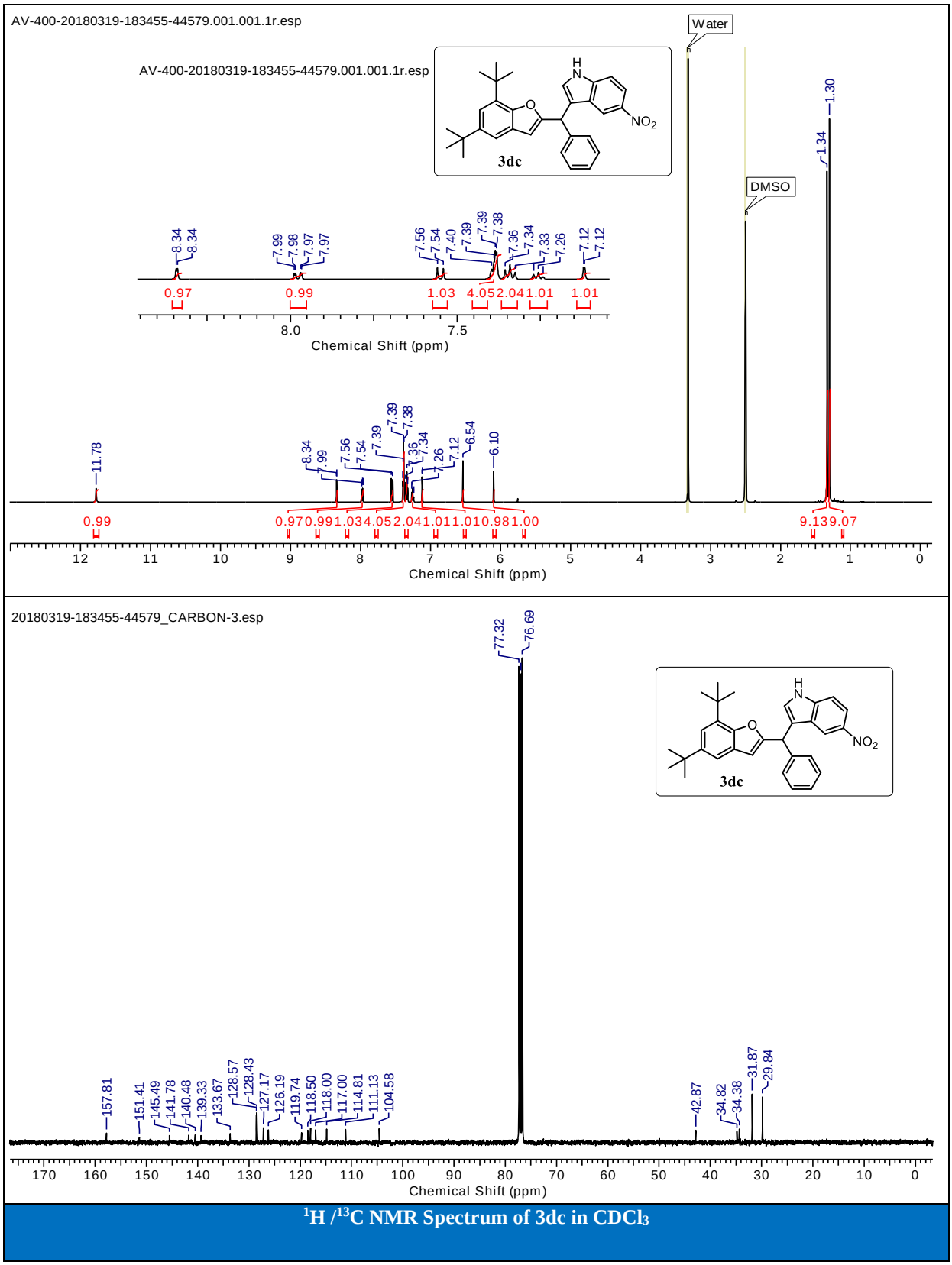

^{1}H /^{13}C NMR Spectrum of 3dc in $CDCl_3$

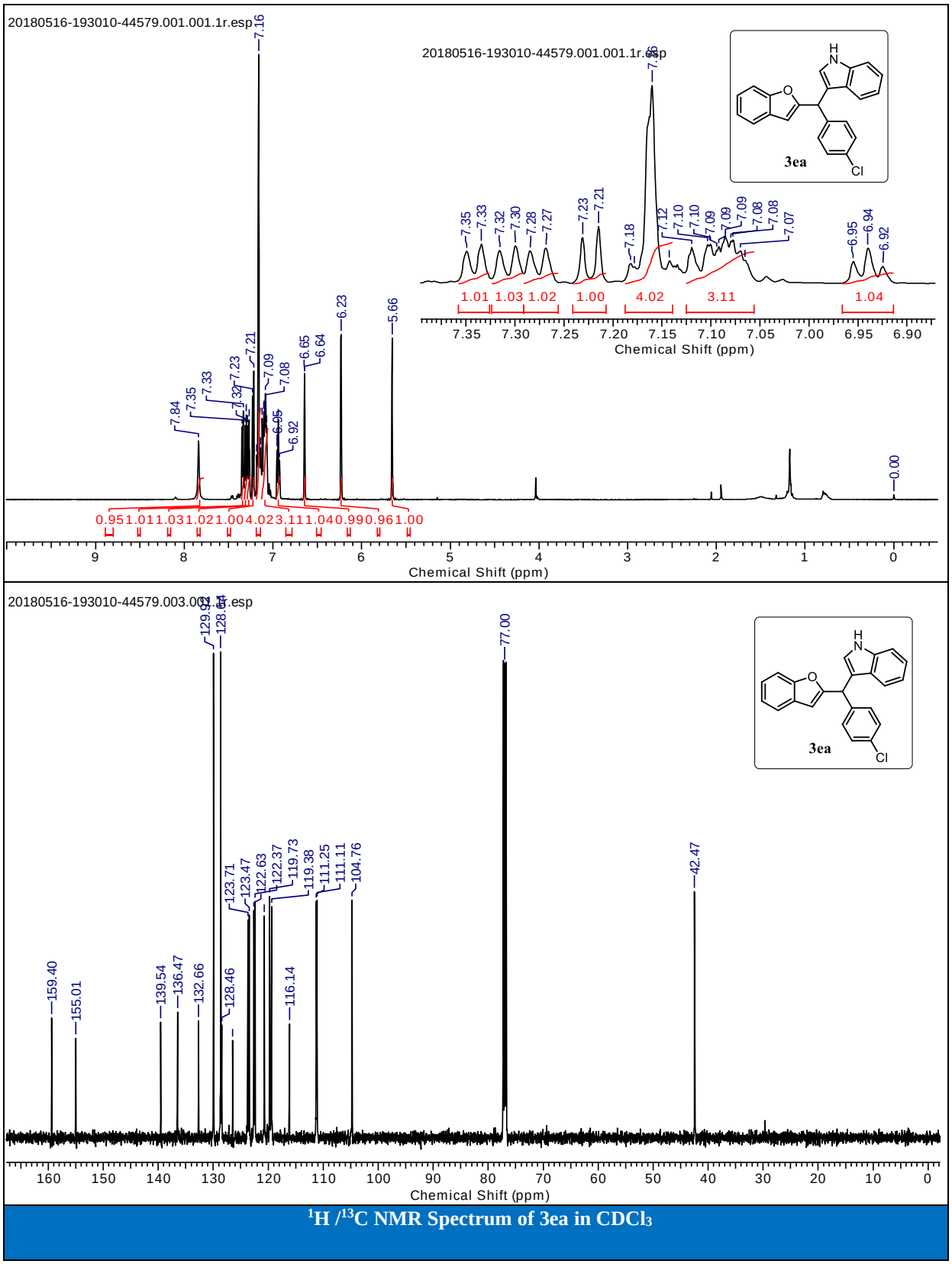

^{1}H /^{13}C NMR Spectrum of 3ea in $CDCl_3$

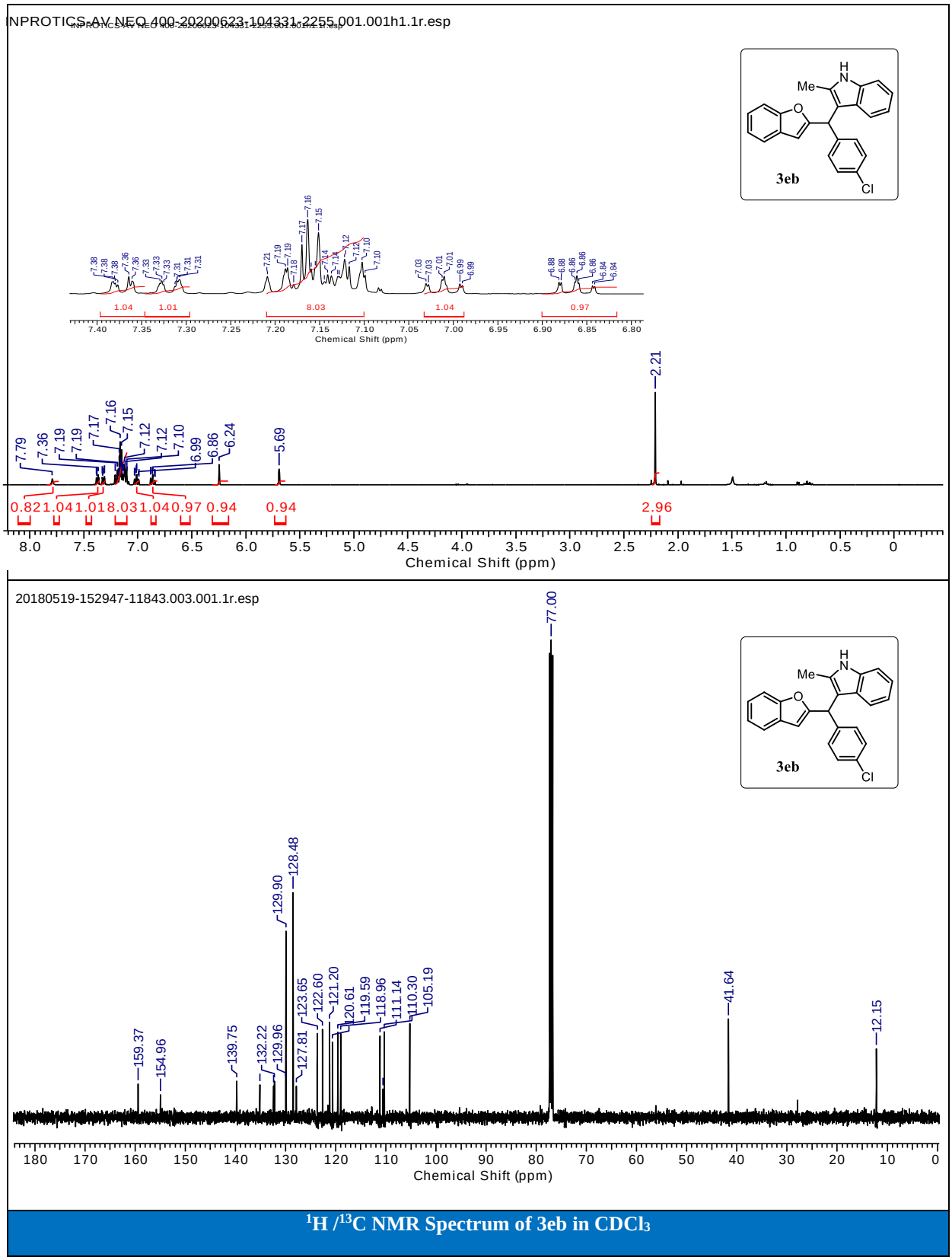

^{1}H /^{13}C NMR Spectrum of 3eb in $CDCl_3$

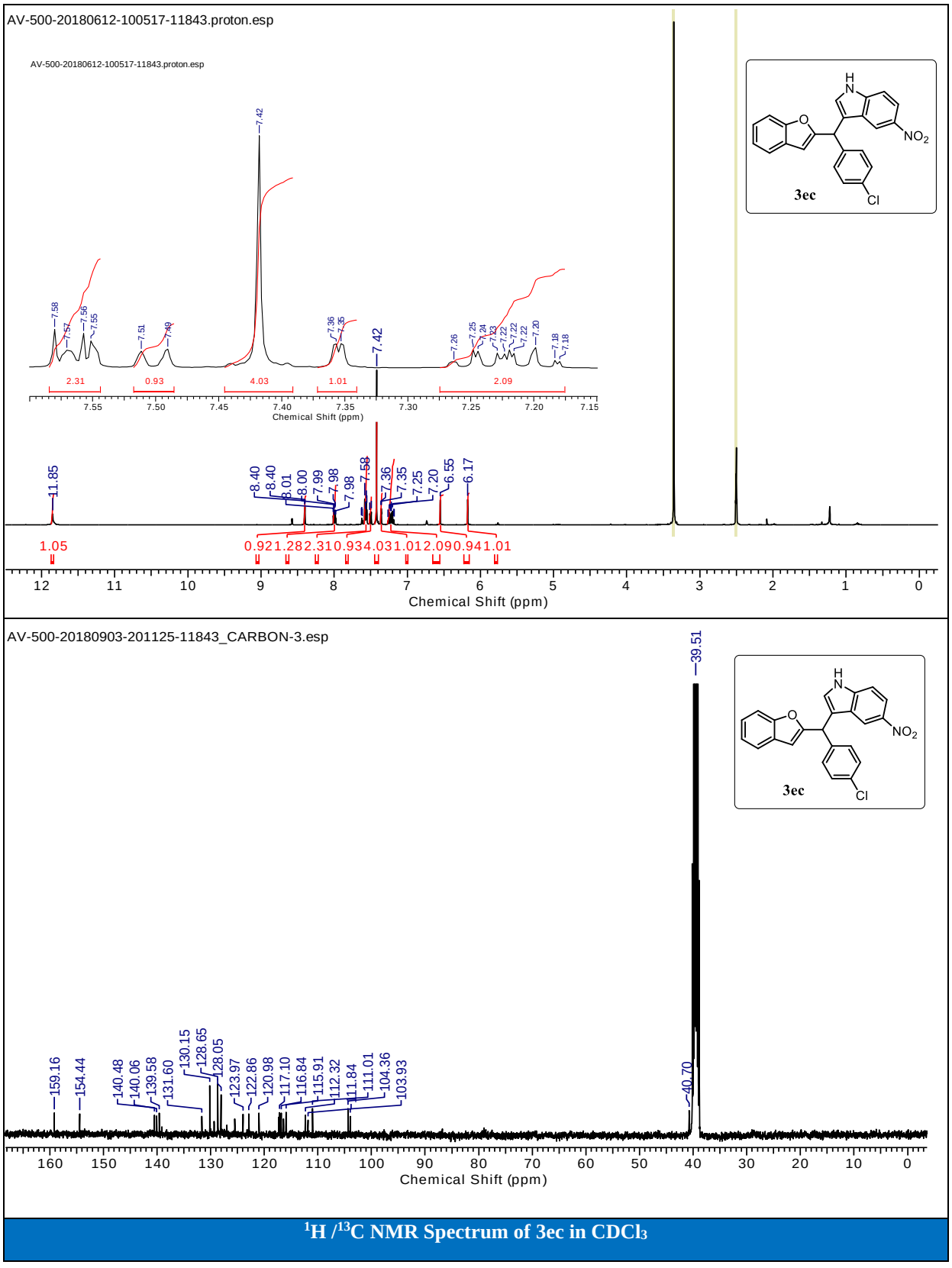

^{1}H /^{13}C NMR Spectrum of 3ec in $CDCl_3$

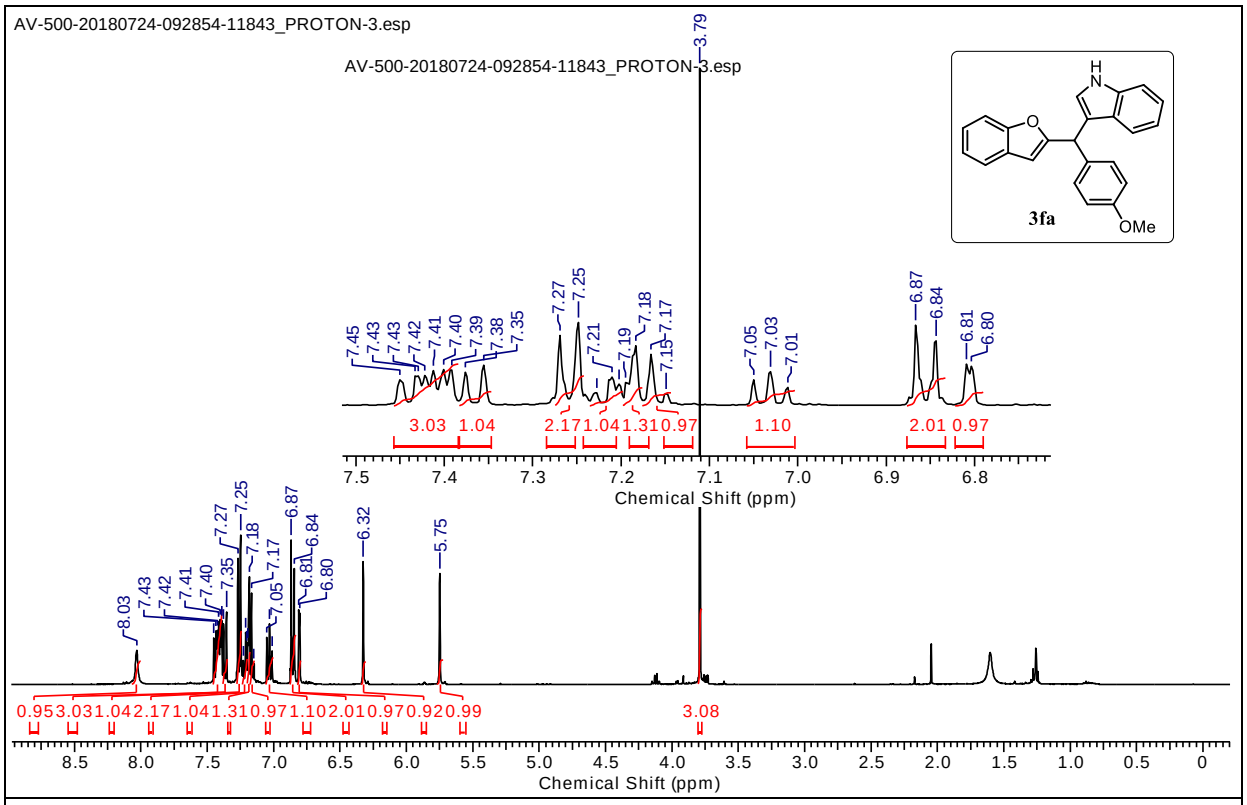

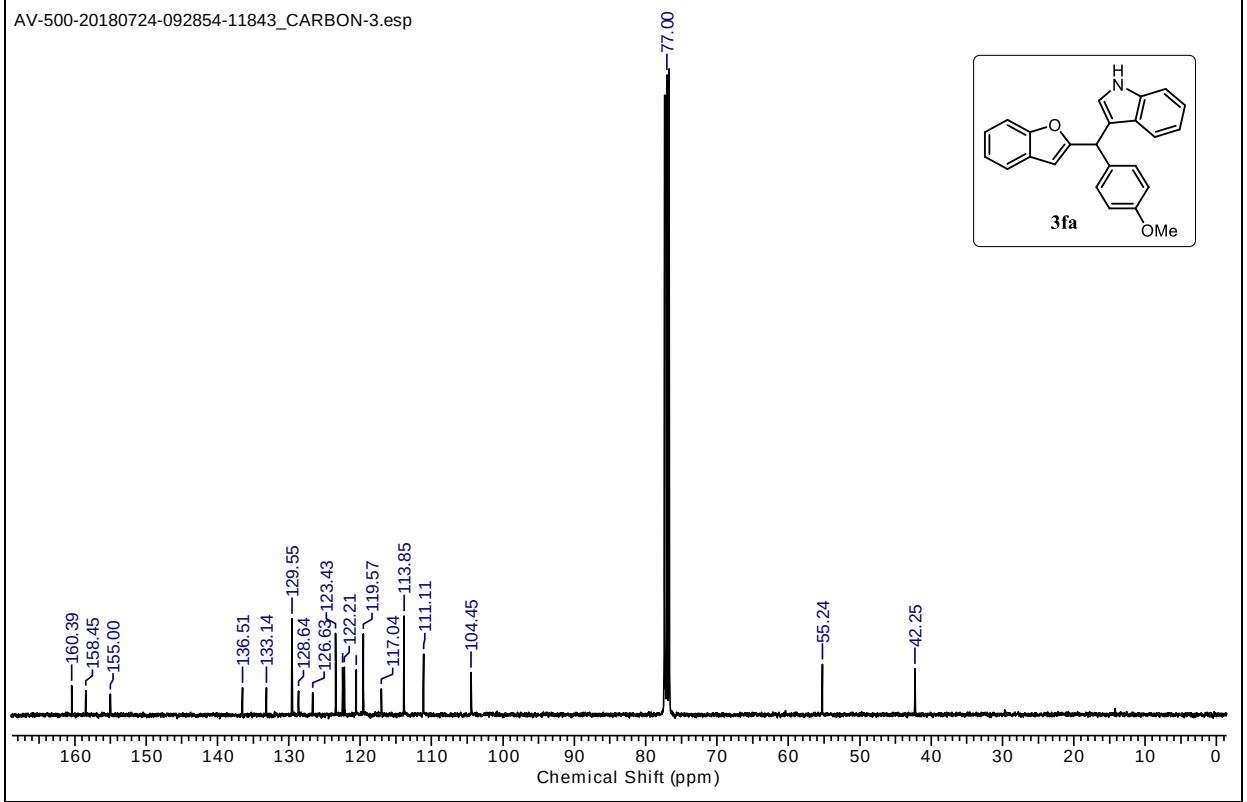

^{1}H /^{13}C NMR Spectrum of 3fa in $CDCl_3$

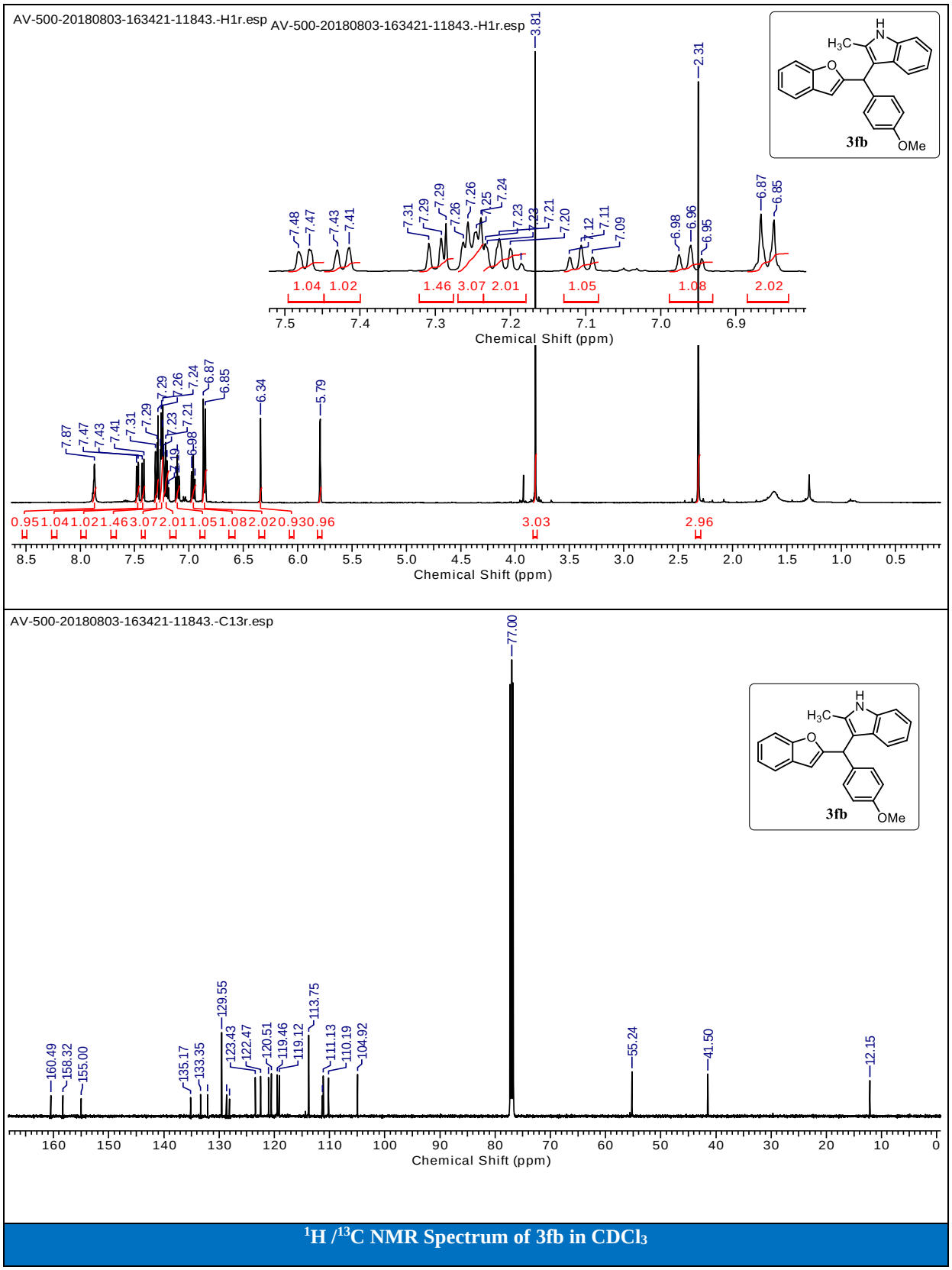

^{1}H /^{13}C NMR Spectrum of 3fb in $CDCl_3$

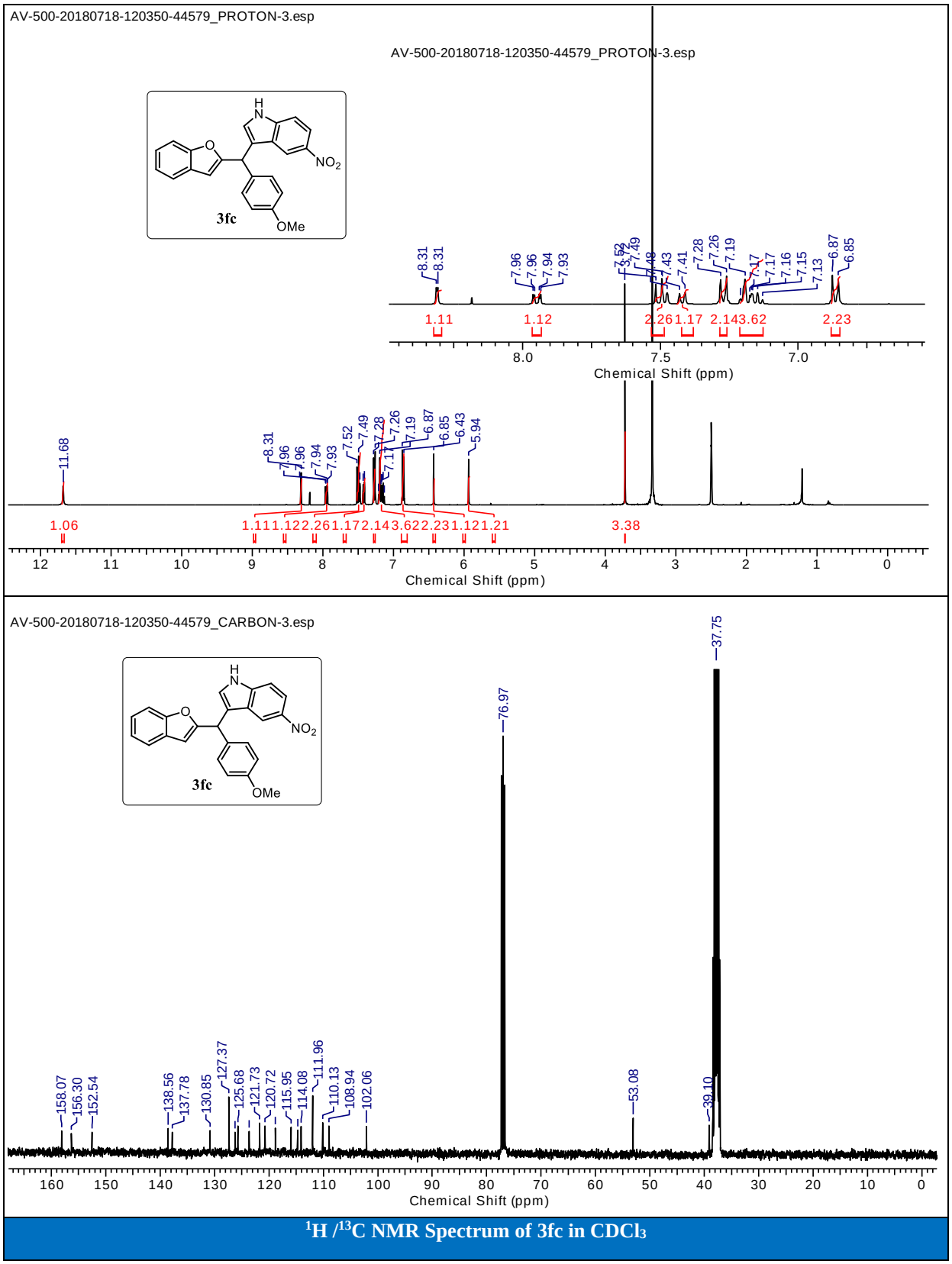

^{1}H /^{13}C NMR Spectrum of 3fc in $CDCl_3$

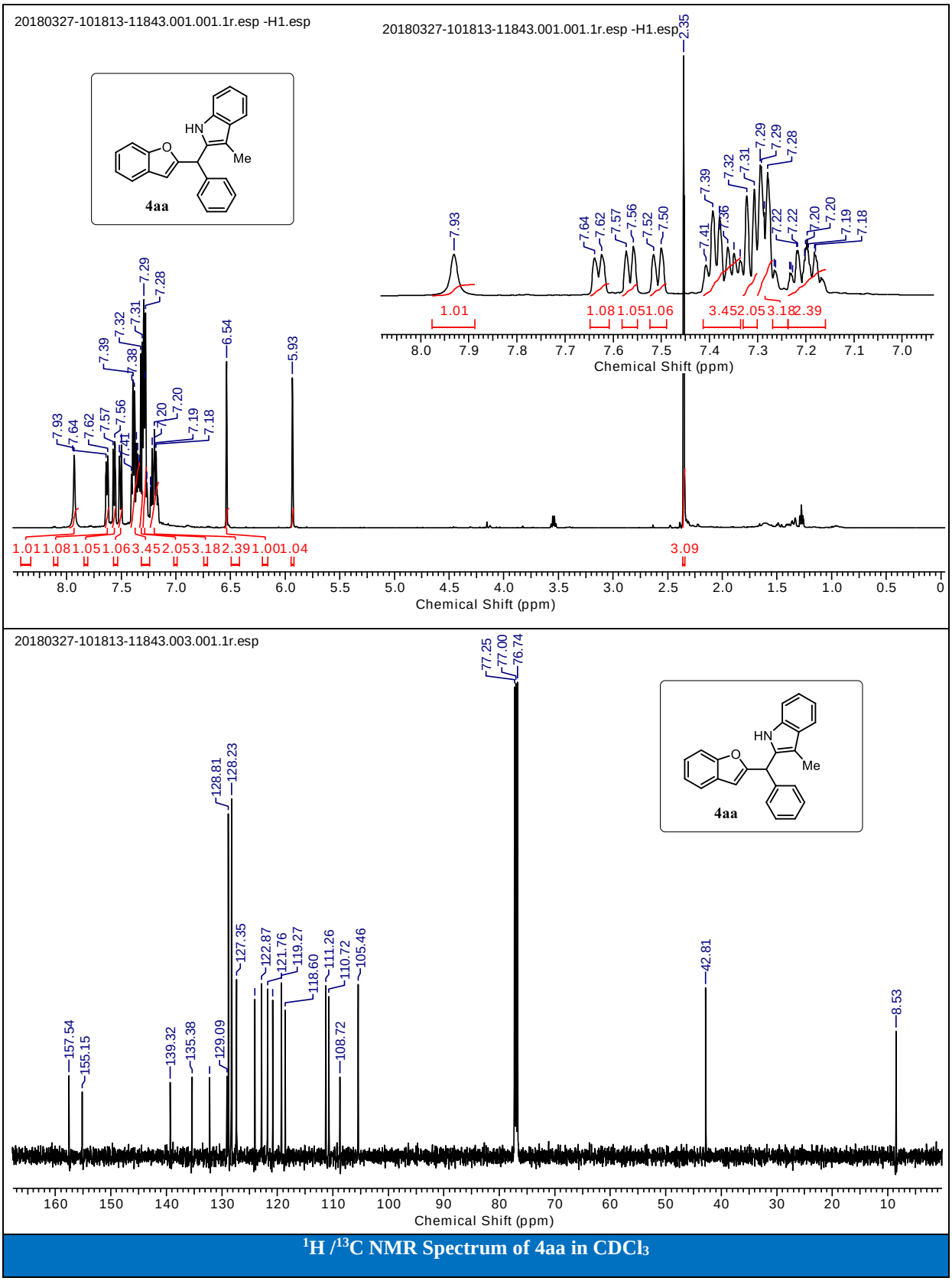

^{1}H /^{13}C NMR Spectrum of 4aa in $CDCl_3$

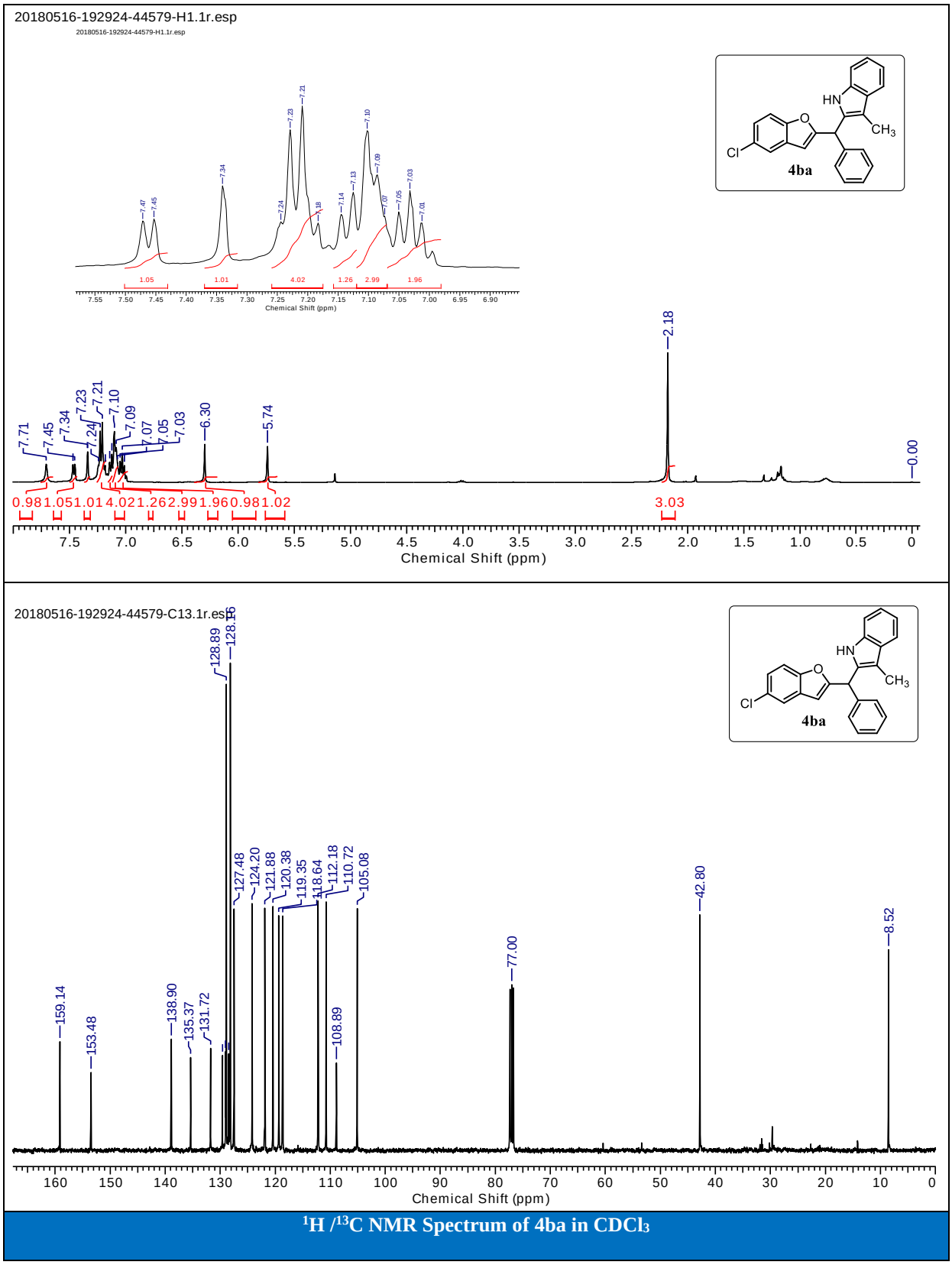

^{1}H /^{13}C NMR Spectrum of 4ba in $CDCl_3$

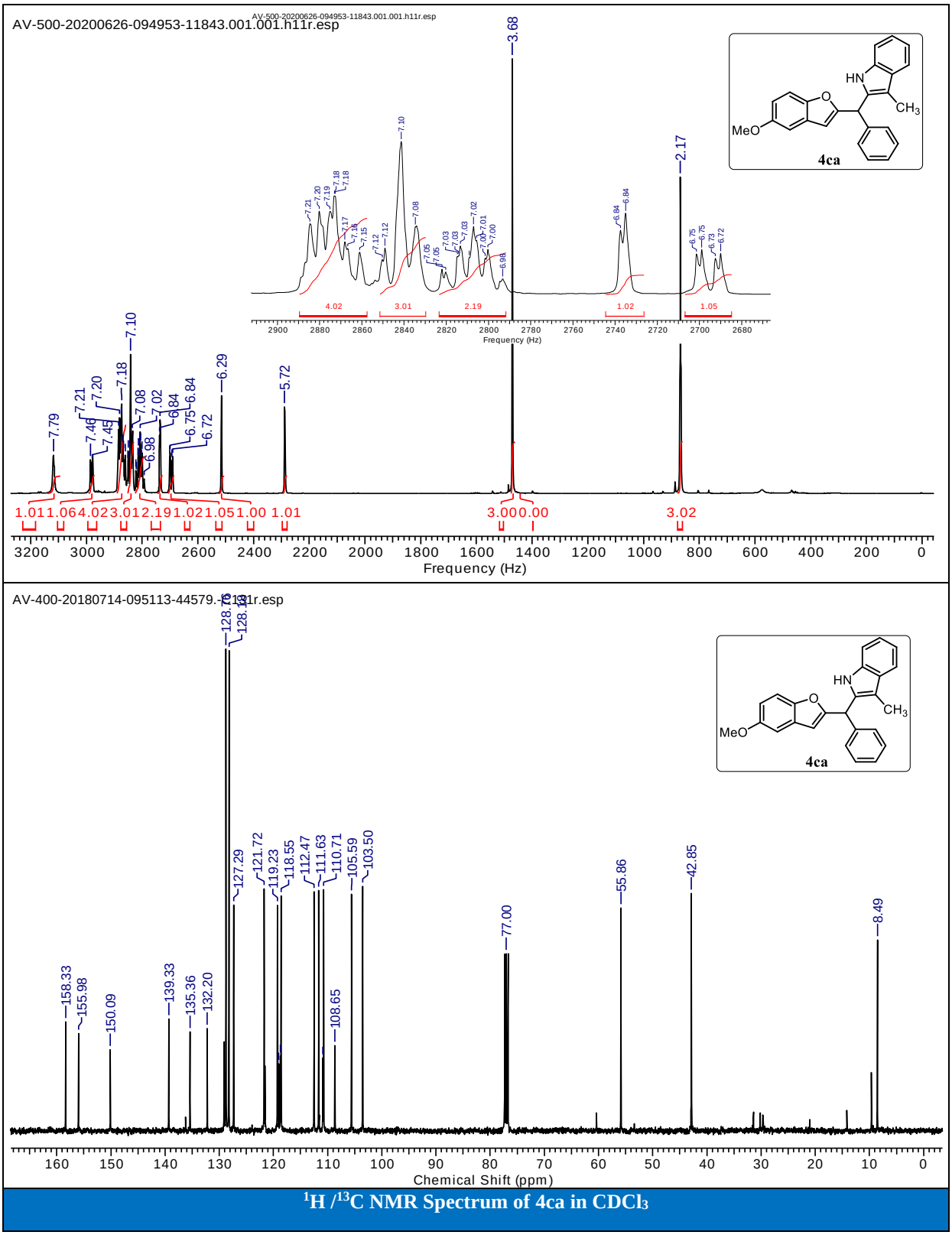

^{1}H /^{13}C NMR Spectrum of 4ca in $CDCl_3$

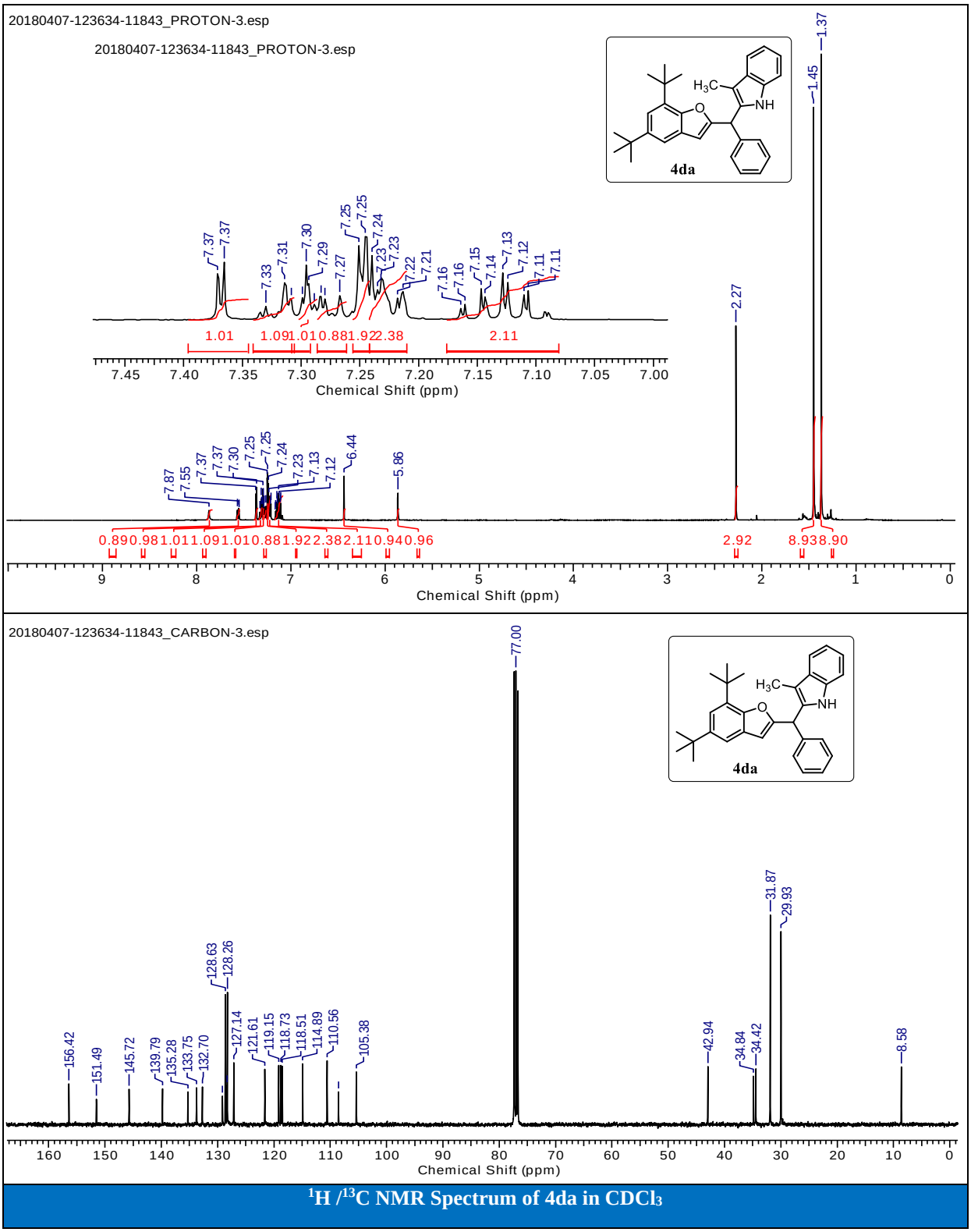

^{1}H /^{13}C NMR Spectrum of 4da in $CDCl_3$

20180529-091513-11843.001.001.1r.esp

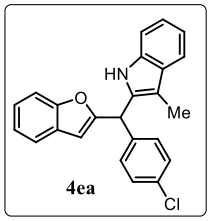

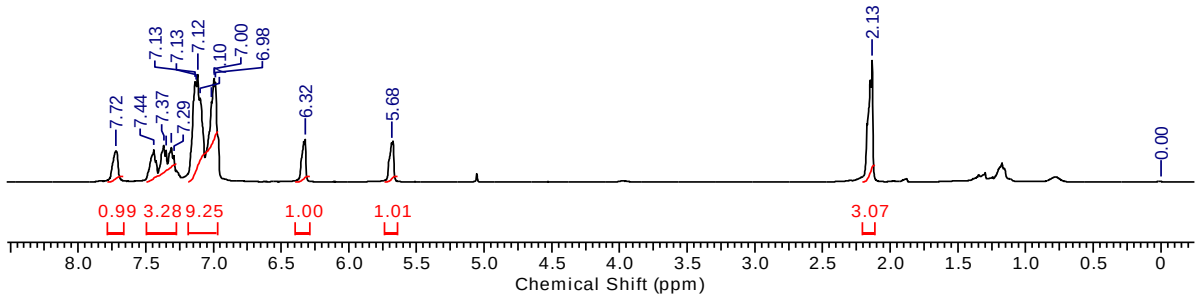

20180529-091513-11843.C13r.esp

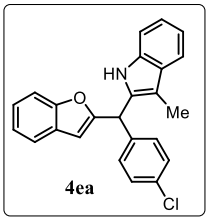

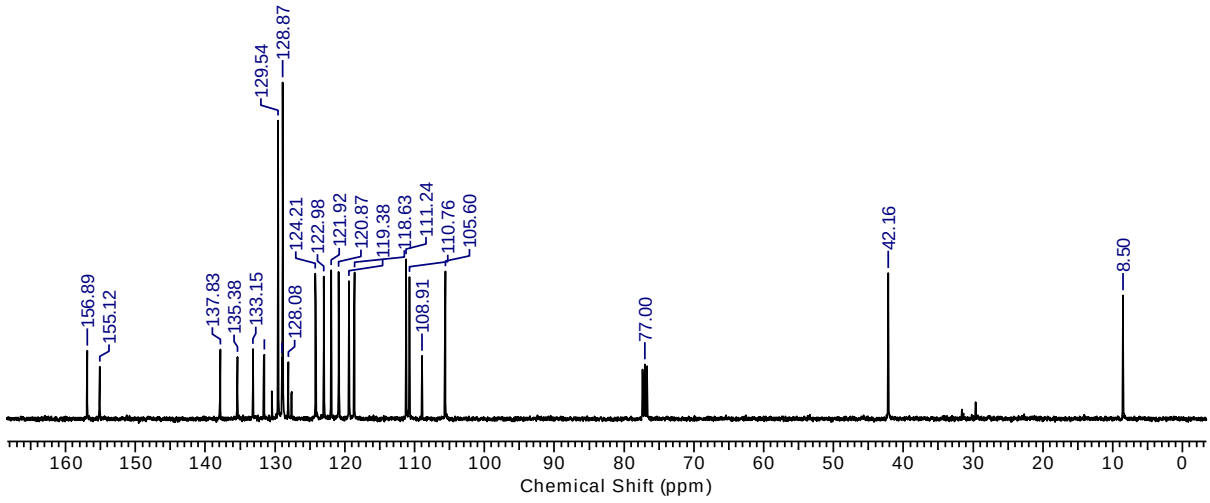

^{1}H /^{13}C NMR Spectrum of 4ea in $CDCl_3$

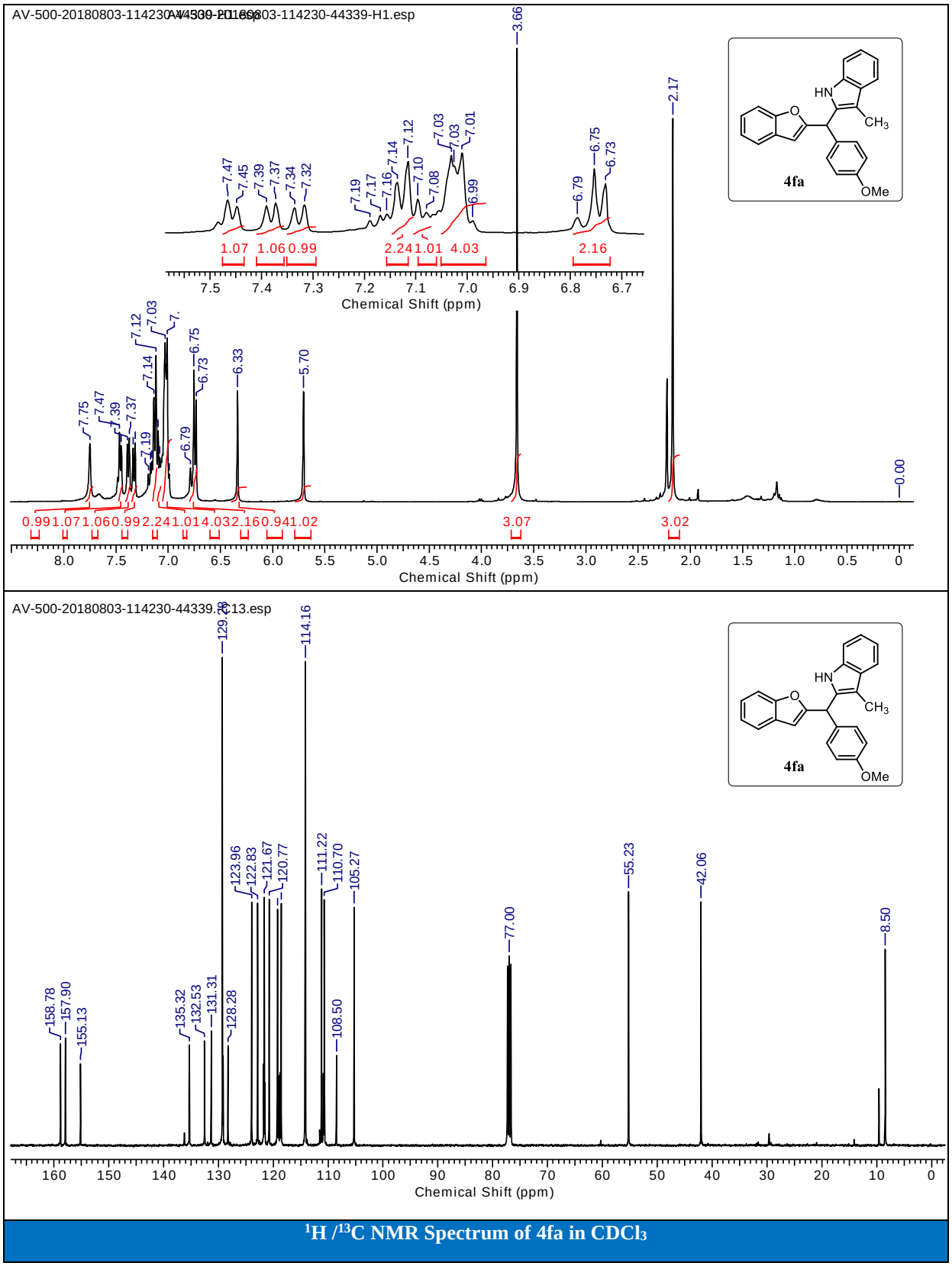

^{1}H /^{13}C NMR Spectrum of 4fa in $CDCl_3$

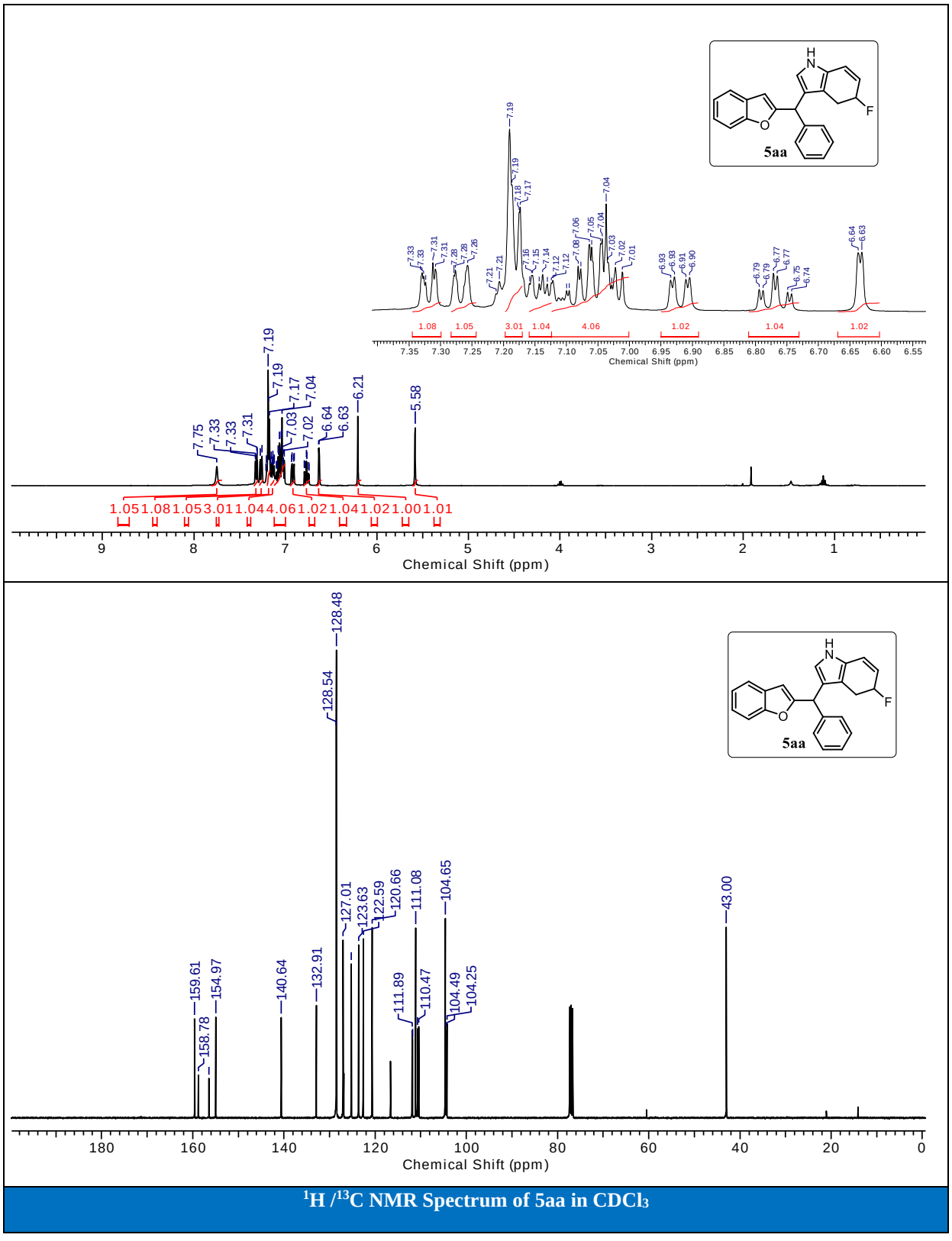

^{1}H /^{13}C NMR Spectrum of 5aa in $CDCl_3$

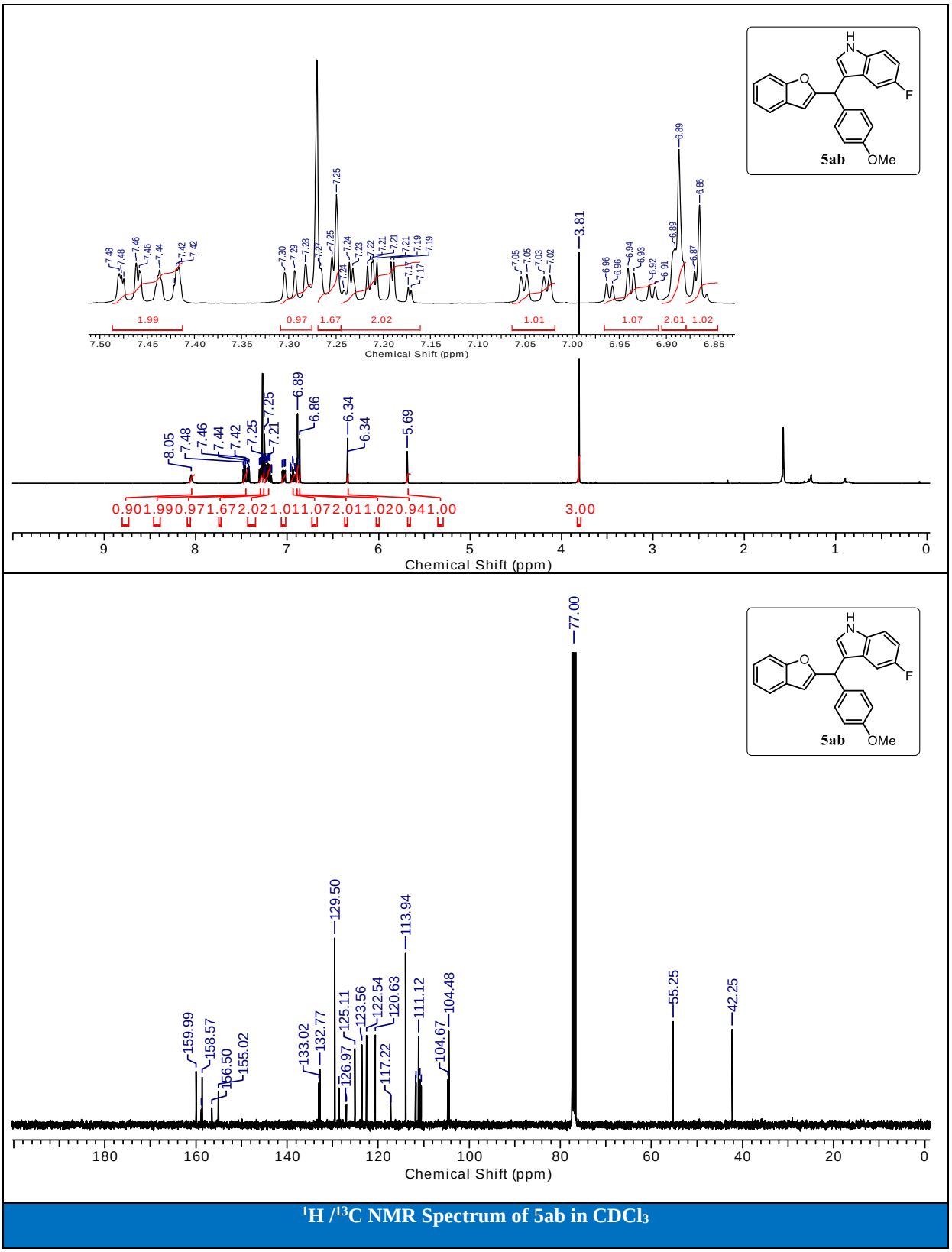

^{1}H /^{13}C NMR Spectrum of 5ab in $CDCl_3$

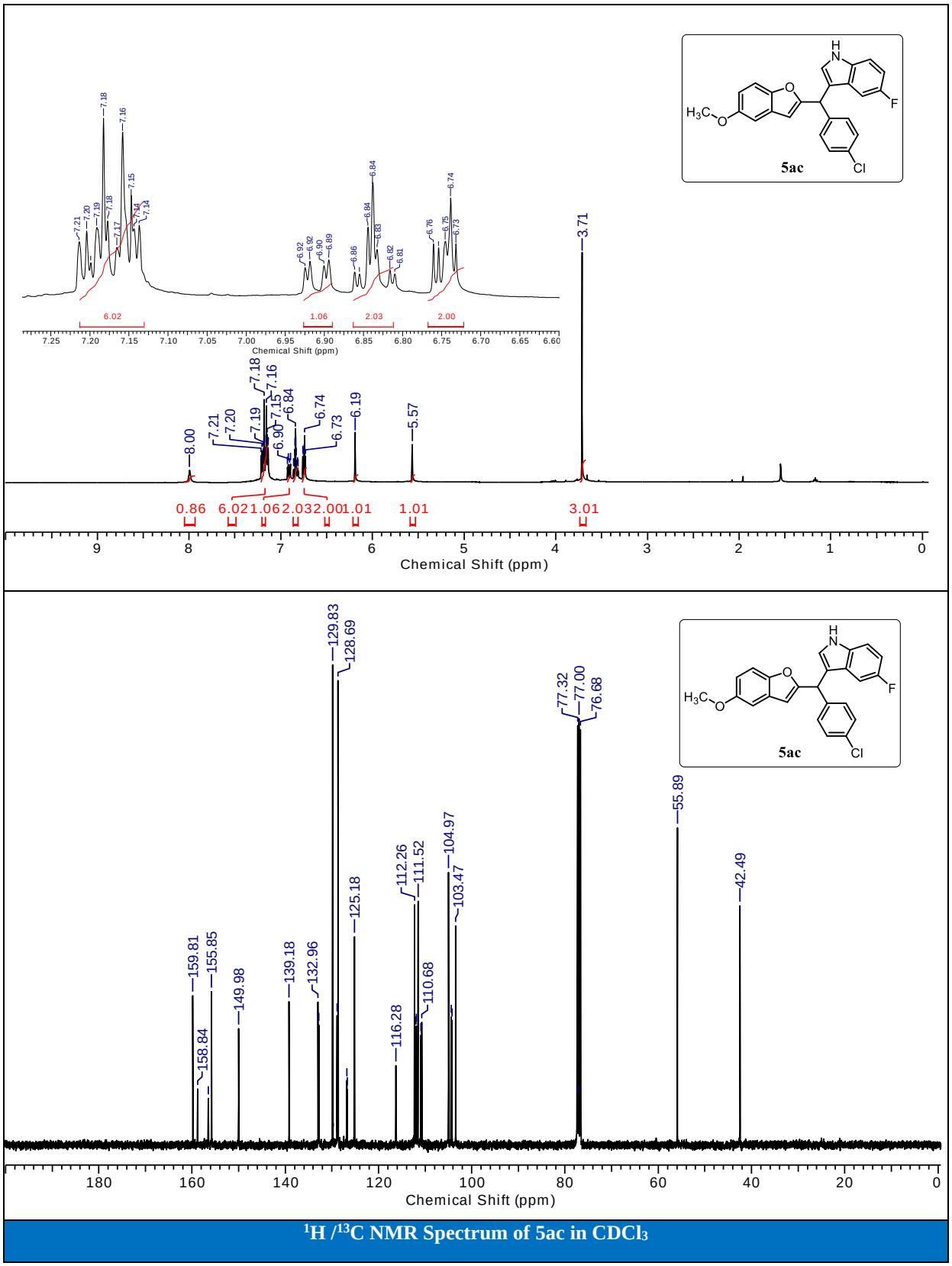

^{1}H /^{13}C NMR Spectrum of 5ac in $CDCl_3$

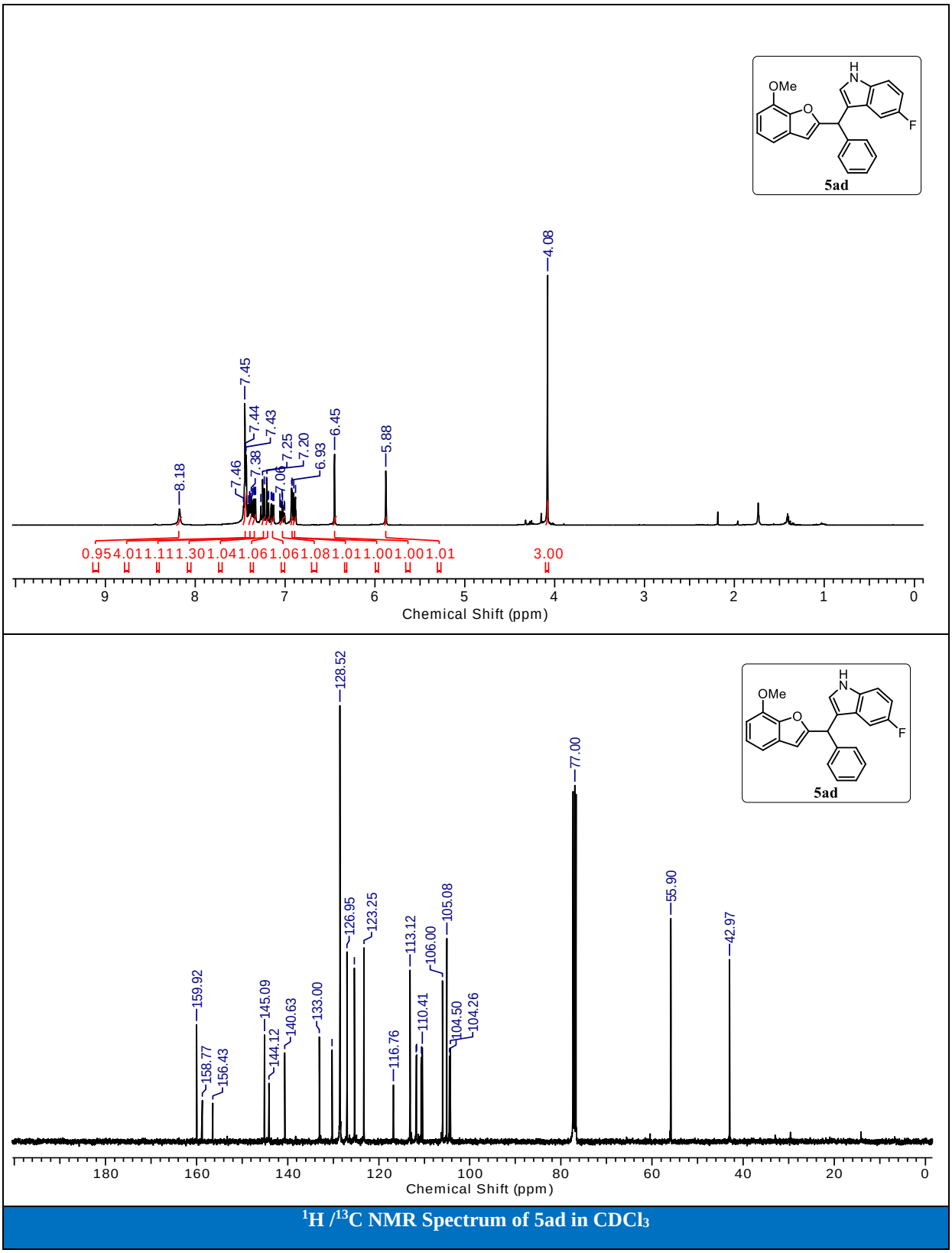

^{1}H /^{13}C NMR Spectrum of 5ad in $CDCl_3$

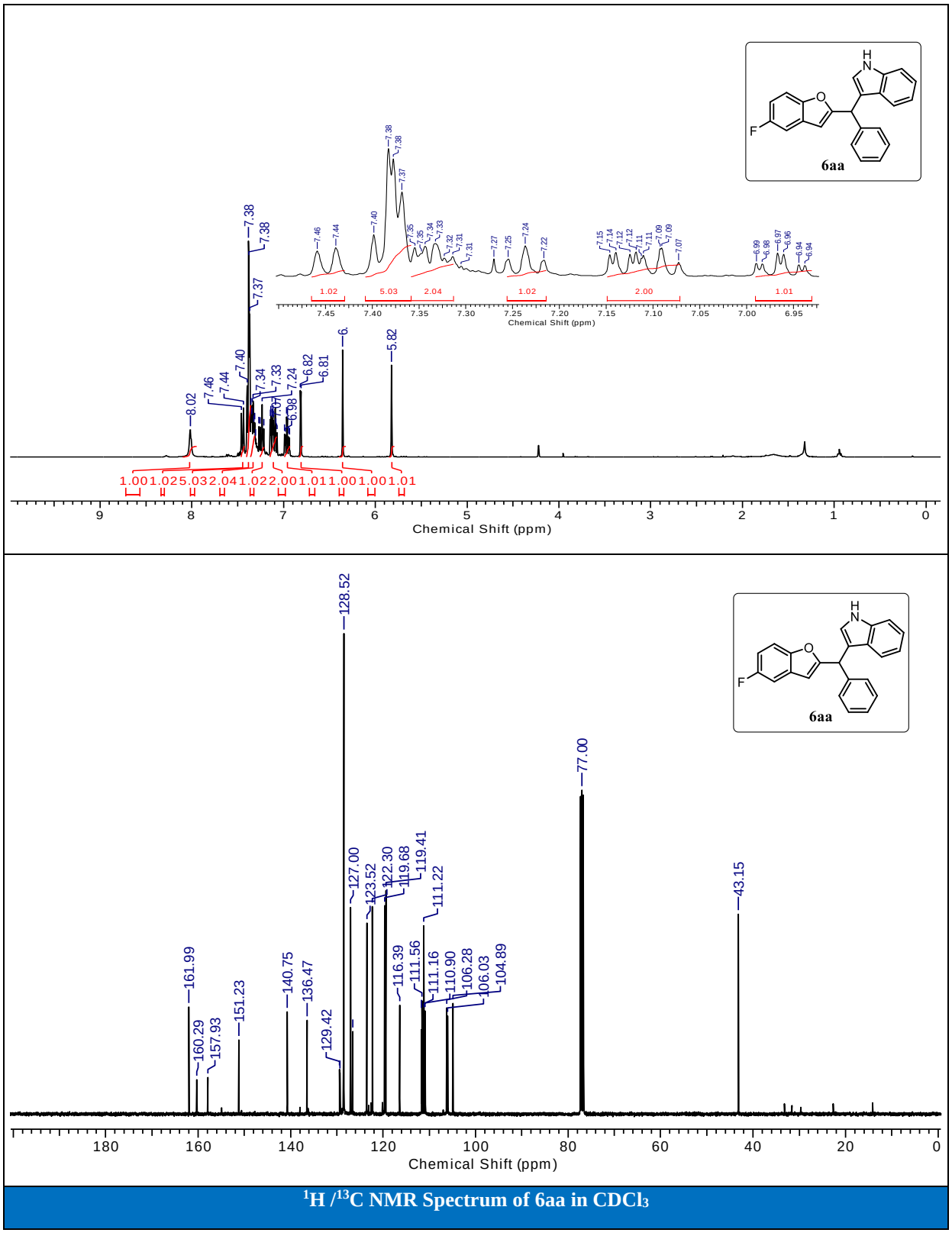

^{1}H /^{13}C NMR Spectrum of 6aa in $CDCl_3$

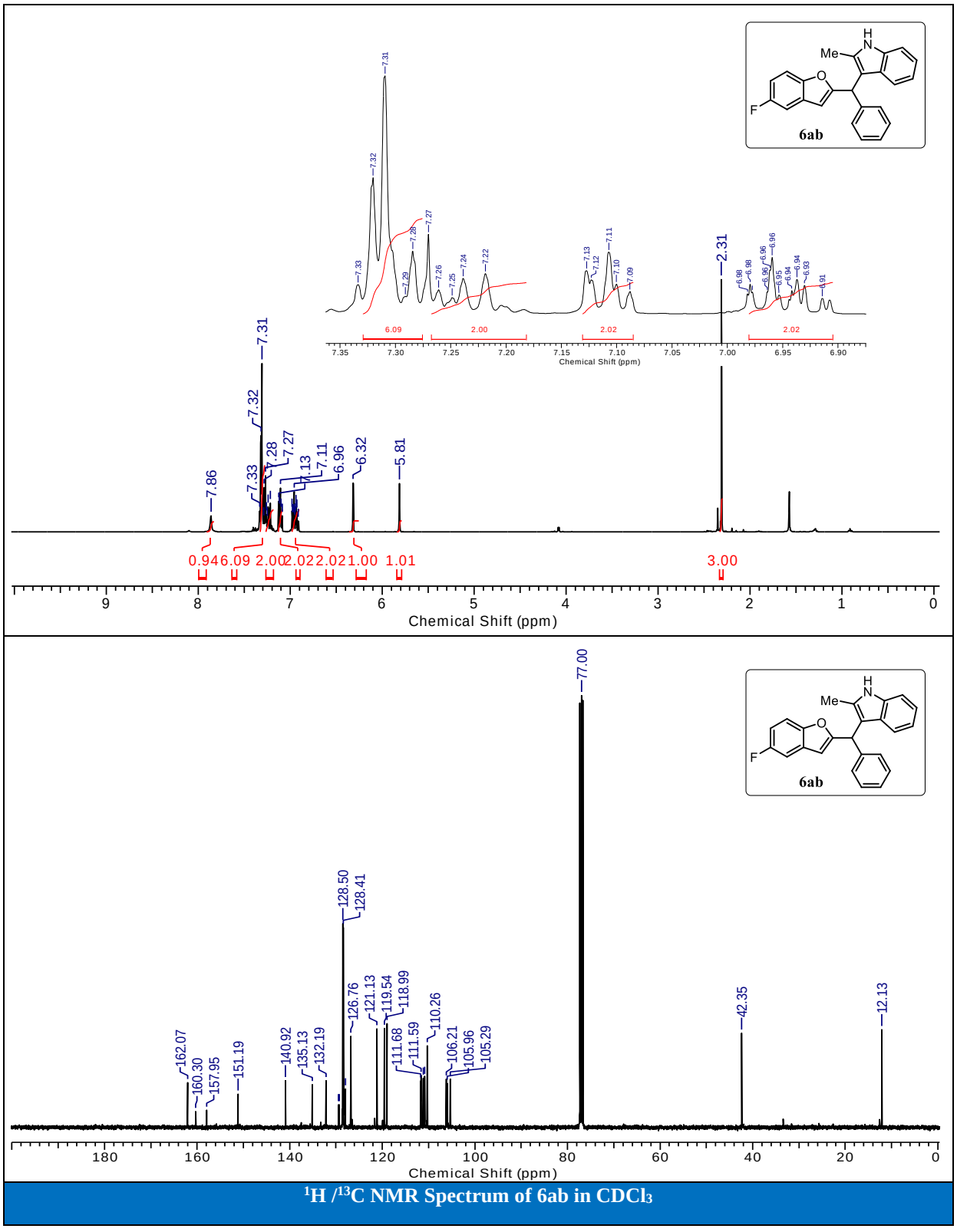

^{1}H /^{13}C NMR Spectrum of 6ab in $CDCl_3$

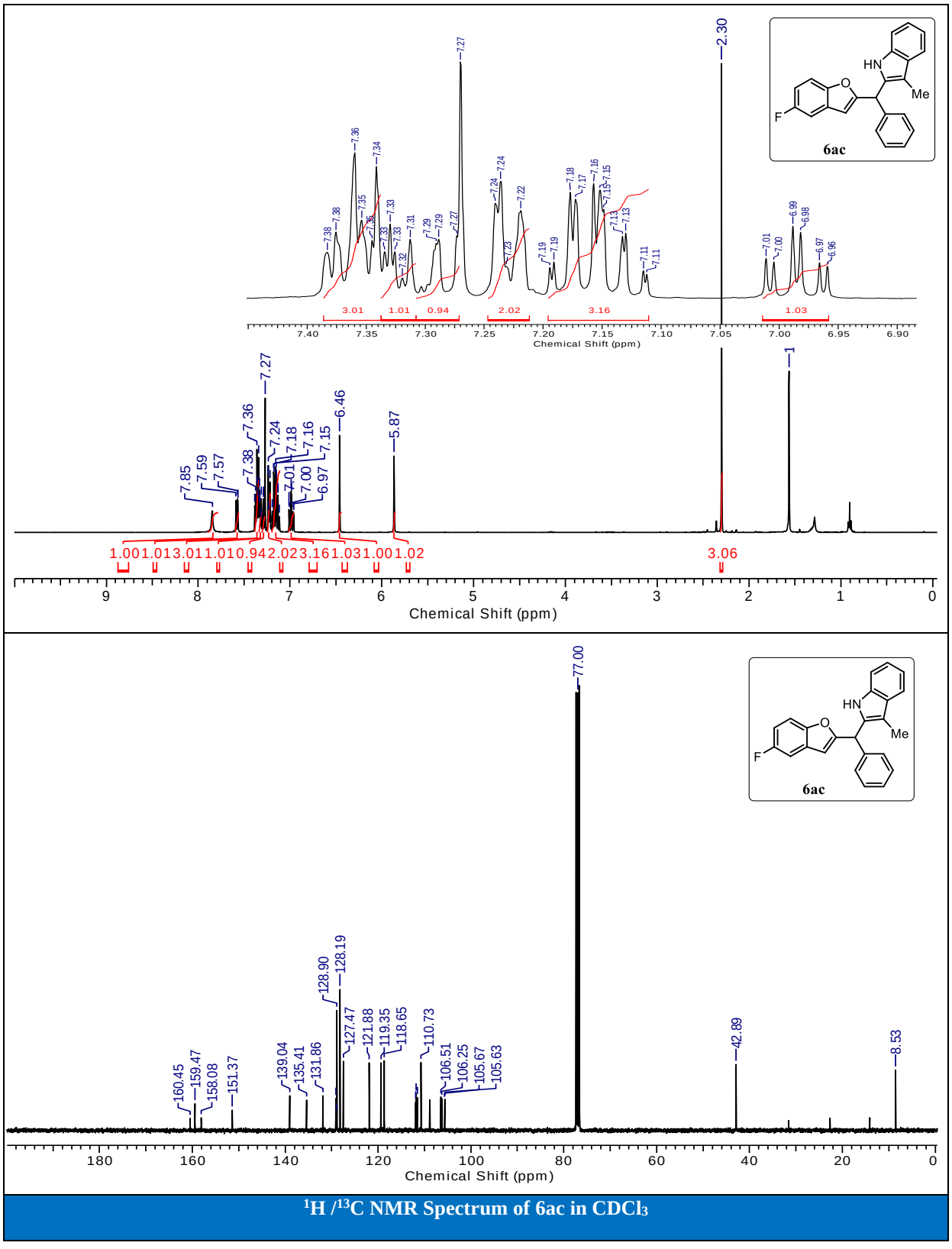

^{1}H /^{13}C NMR Spectrum of 6ac in $CDCl_3$

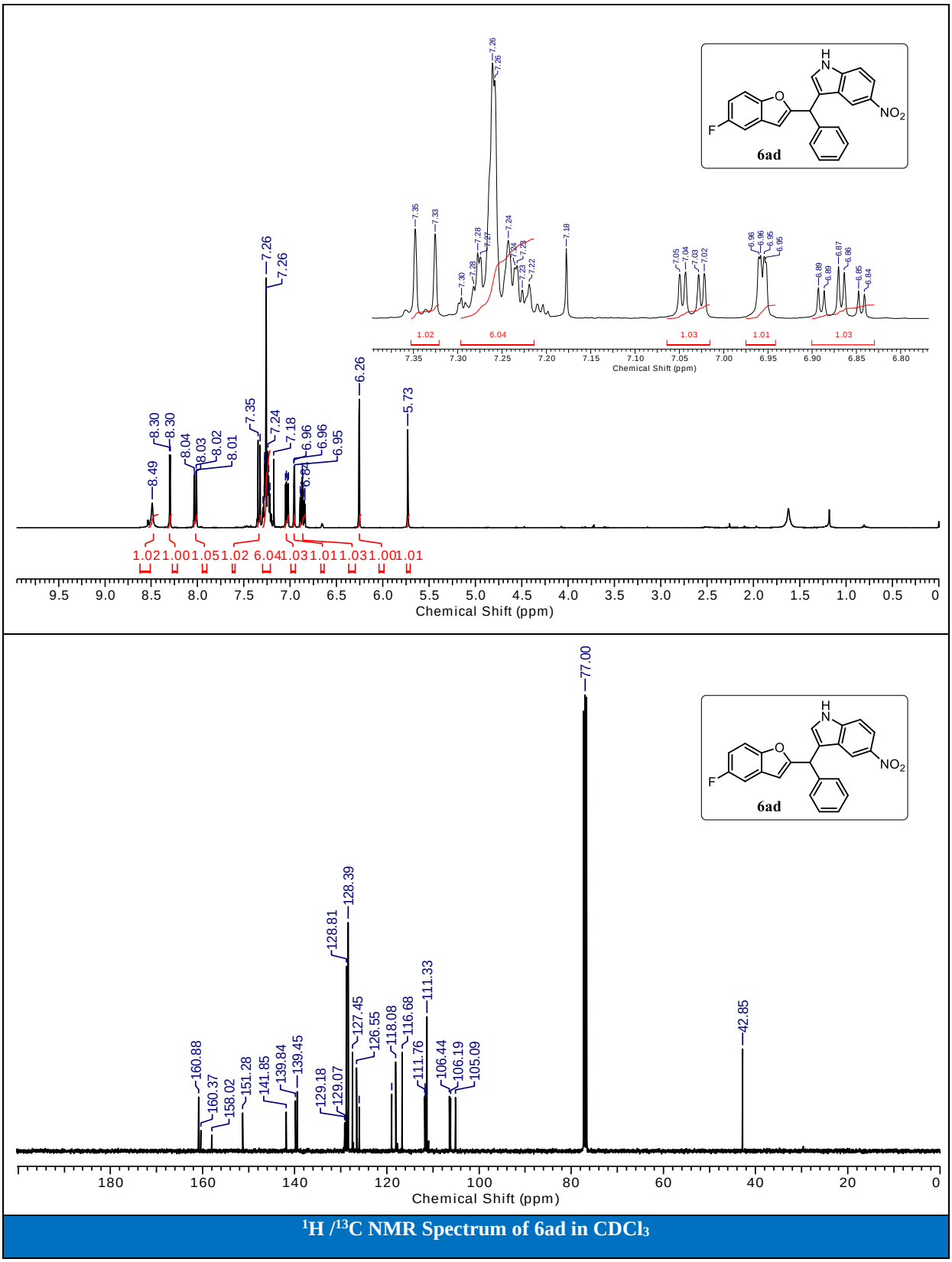

^{1}H /^{13}C NMR Spectrum of 6ad in $CDCl_3$

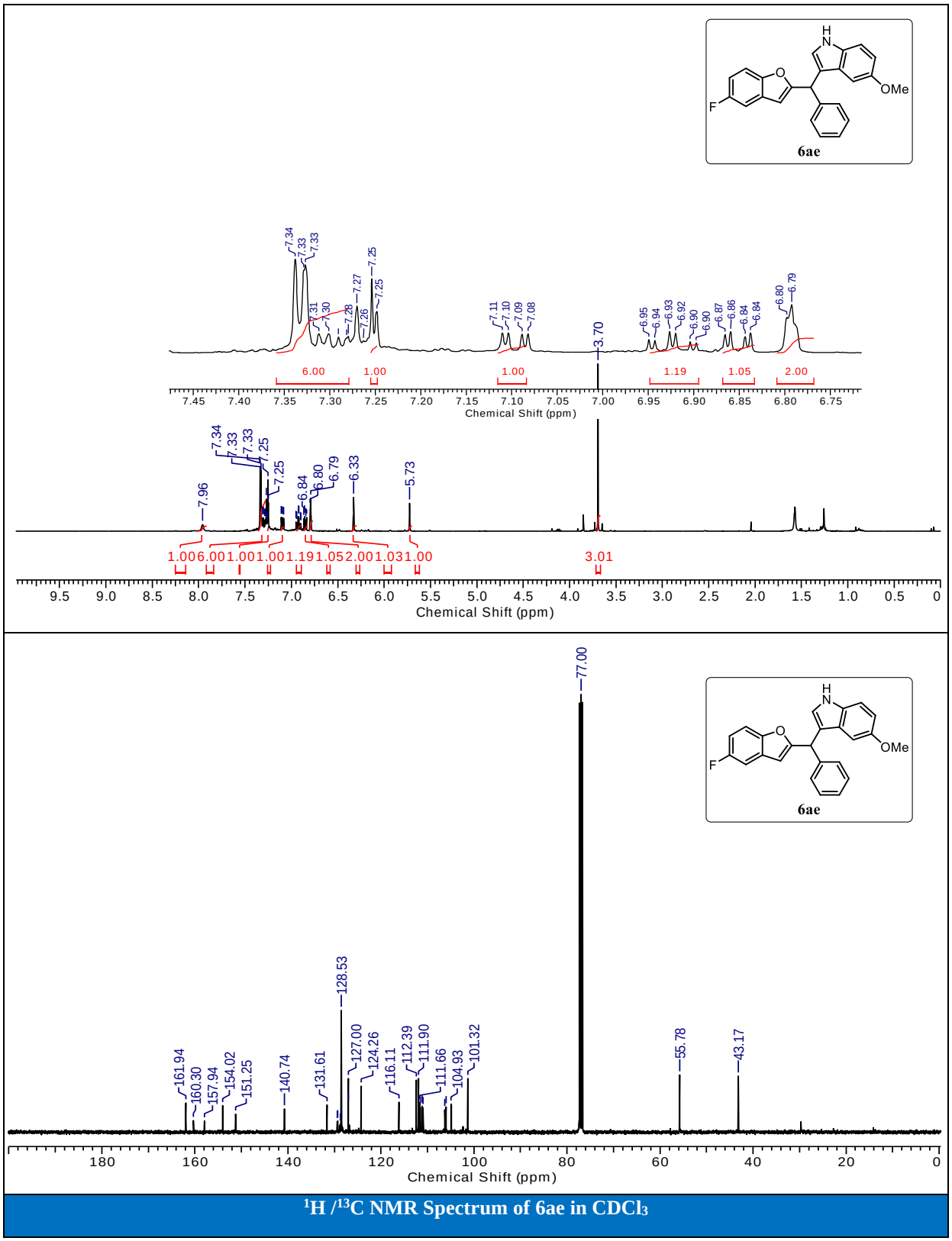

^{1}H /^{13}C NMR Spectrum of 6ae in $CDCl_3$

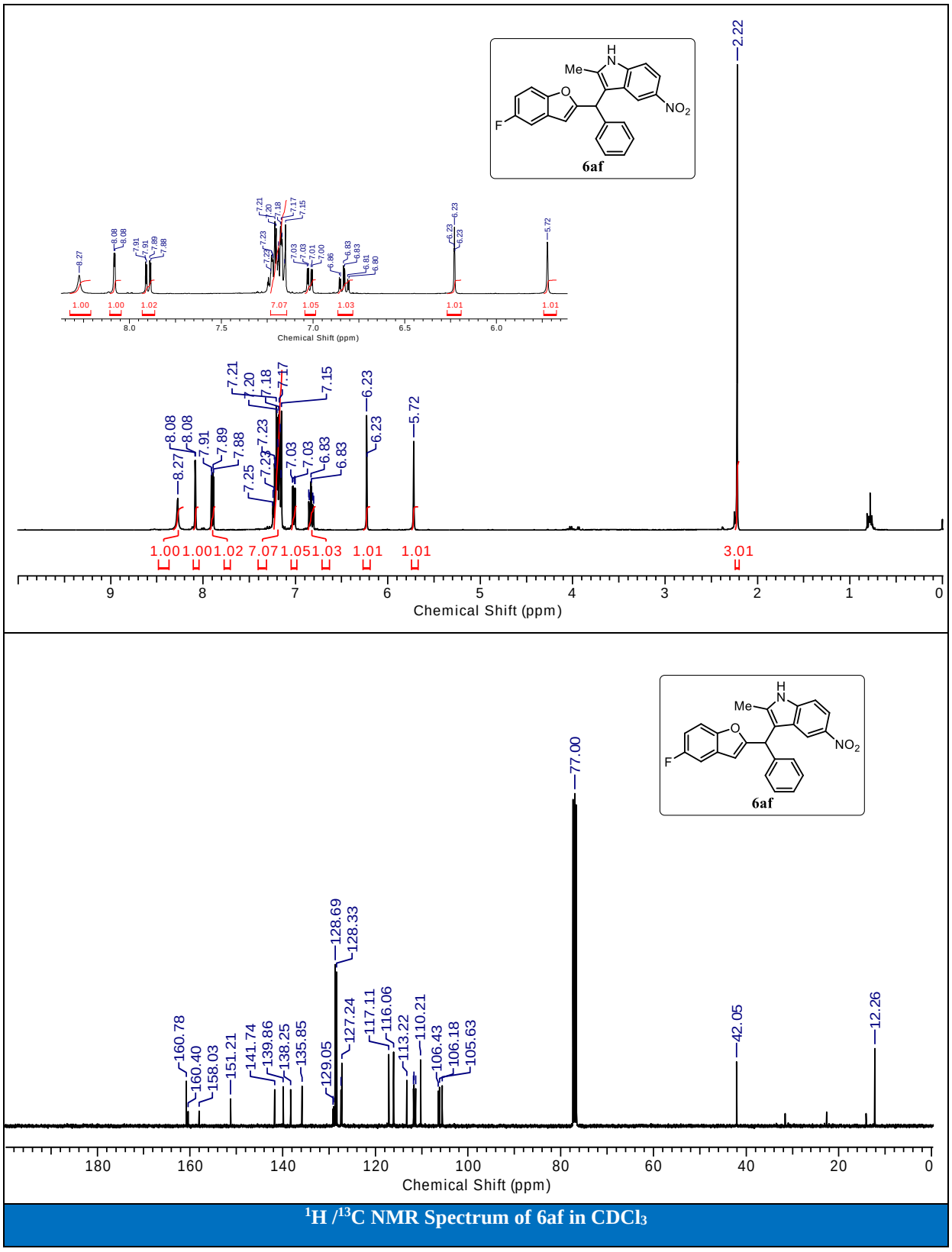

^{1}H /^{13}C NMR Spectrum of 6af in $CDCl_3$

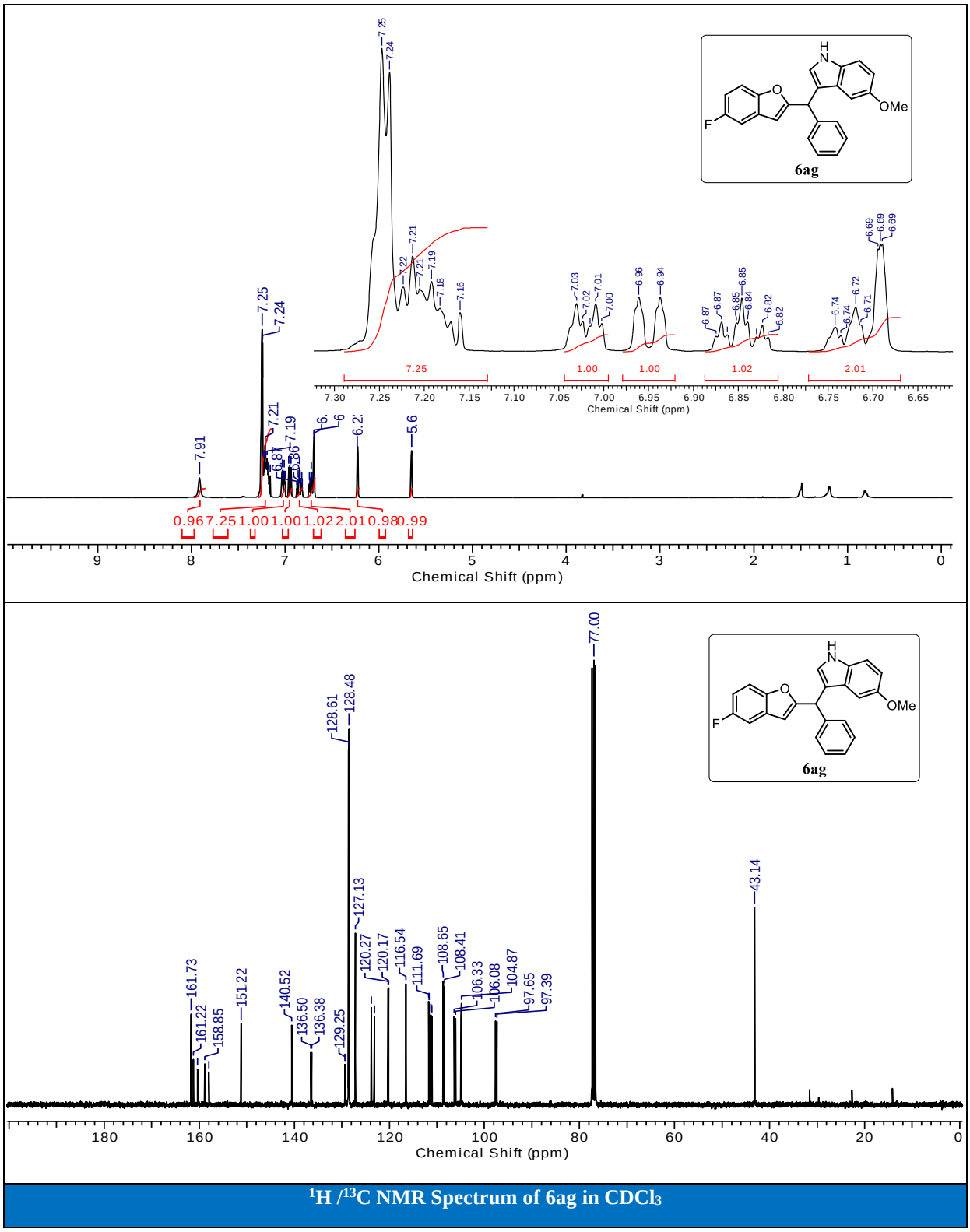

^{1}H /^{13}C NMR Spectrum of 6ag in $CDCl_3$

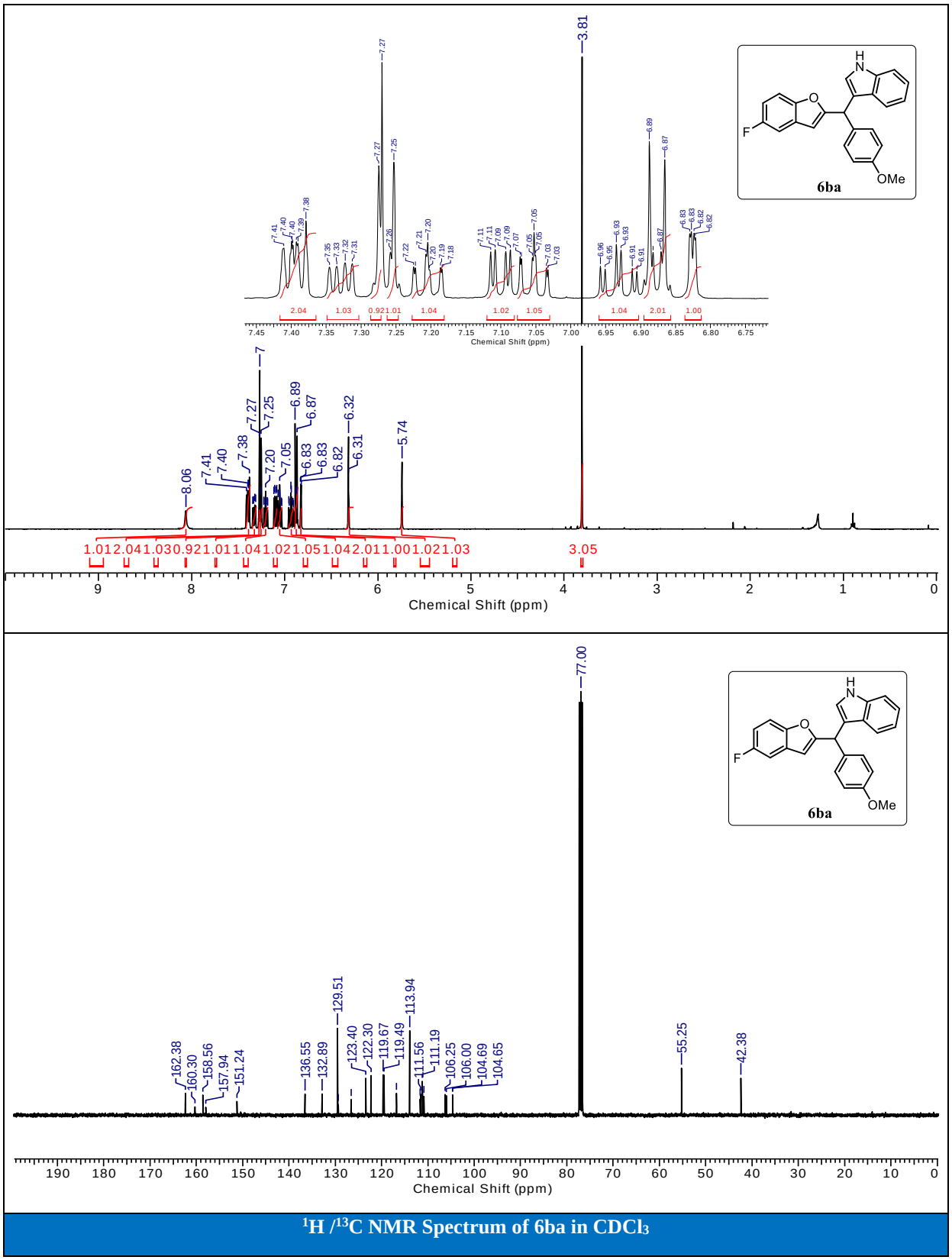

^{1}H /^{13}C NMR Spectrum of 6ba in $CDCl_3$

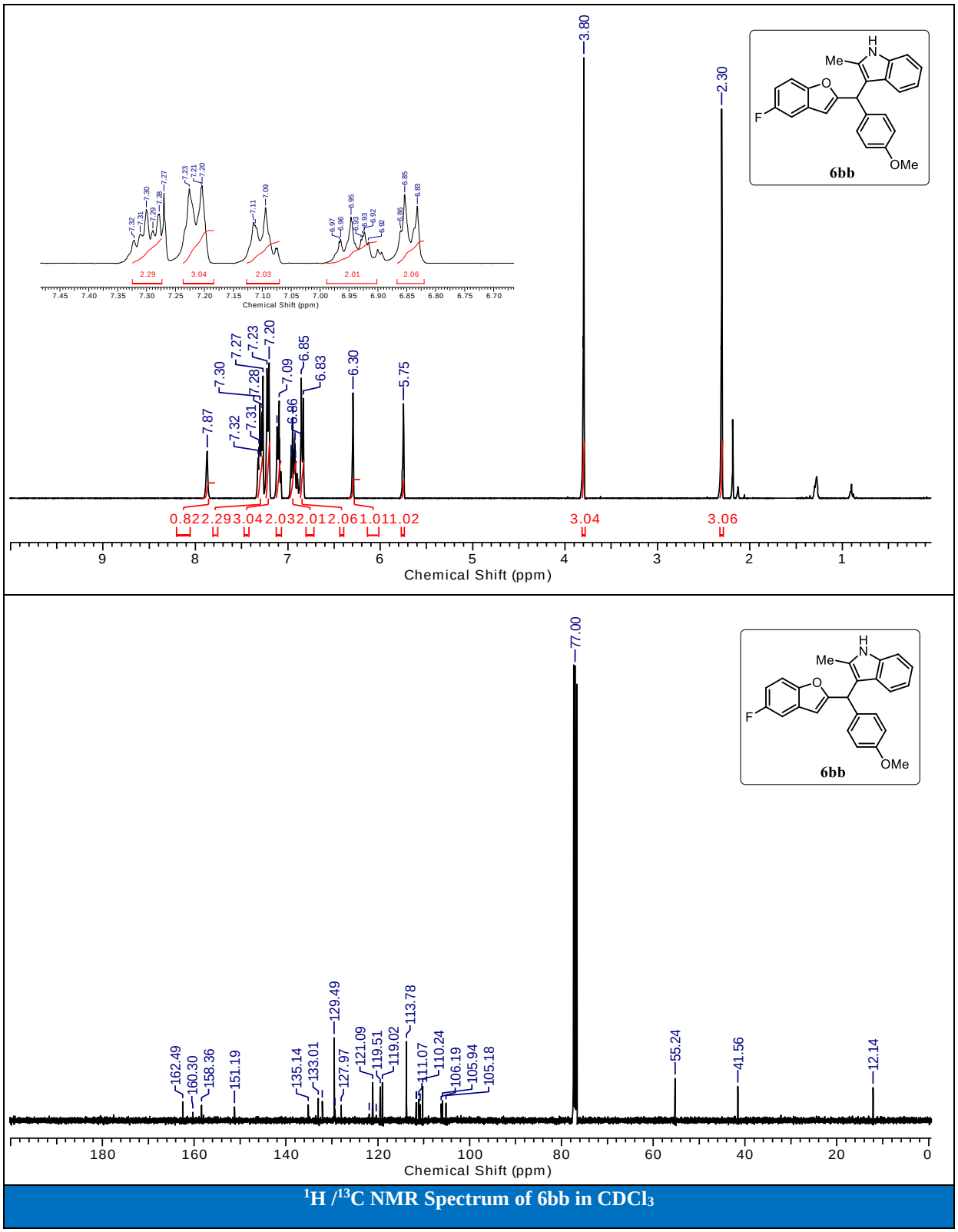

^{1}H /^{13}C NMR Spectrum of 6bb in $CDCl_3$

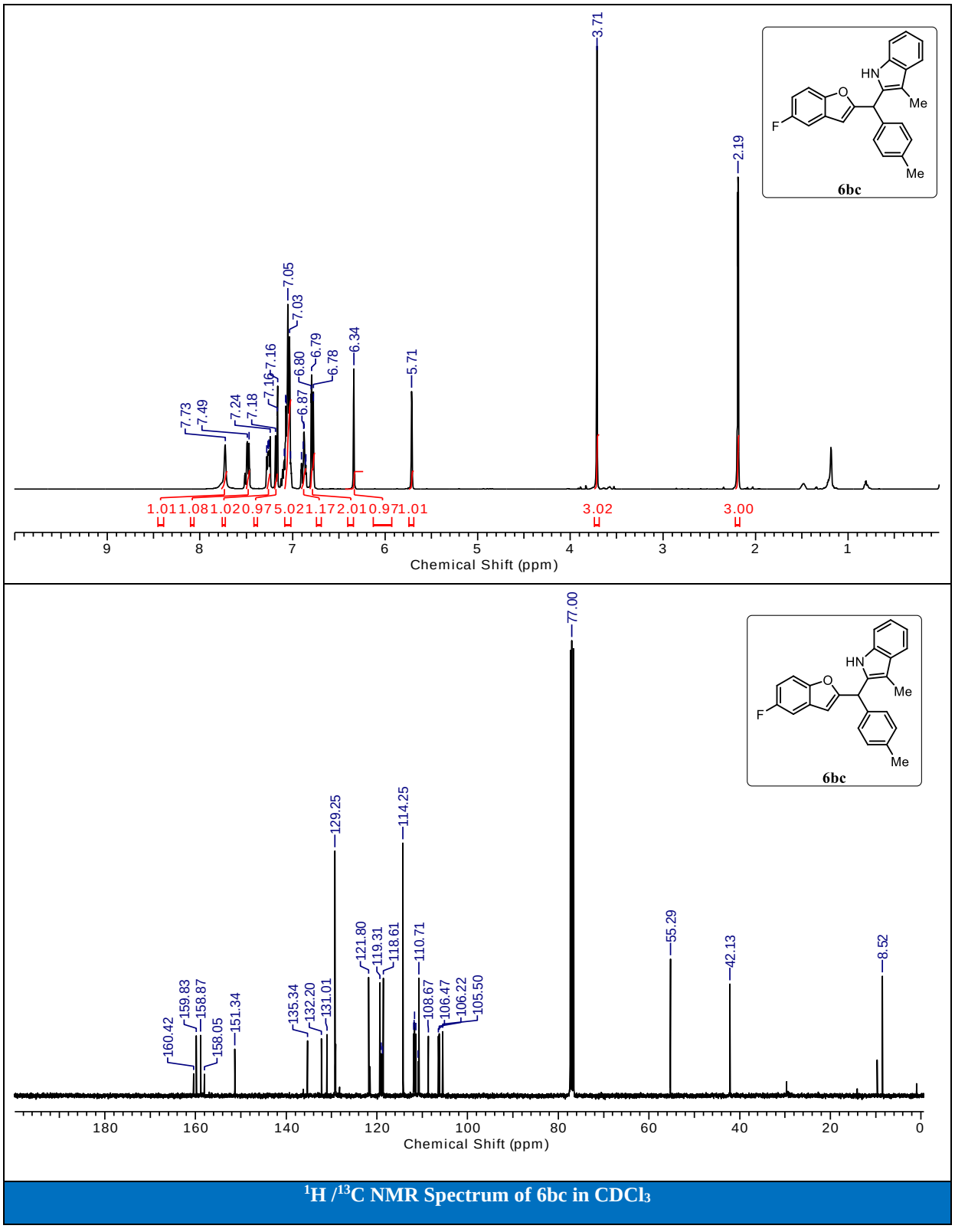

^{1}H /^{13}C NMR Spectrum of 6bc in $CDCl_3$

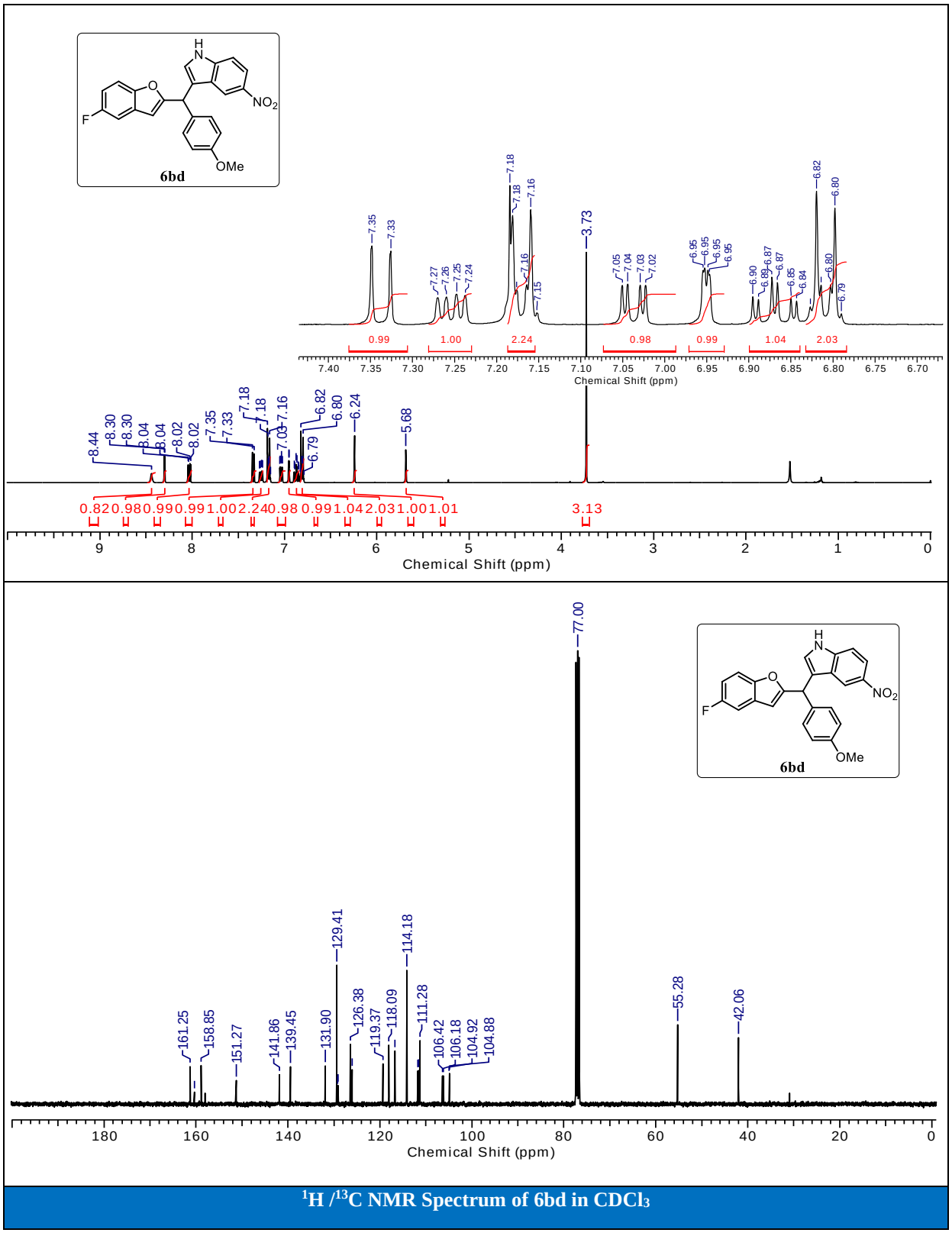

^{1}H /^{13}C NMR Spectrum of 6bd in $CDCl_3$

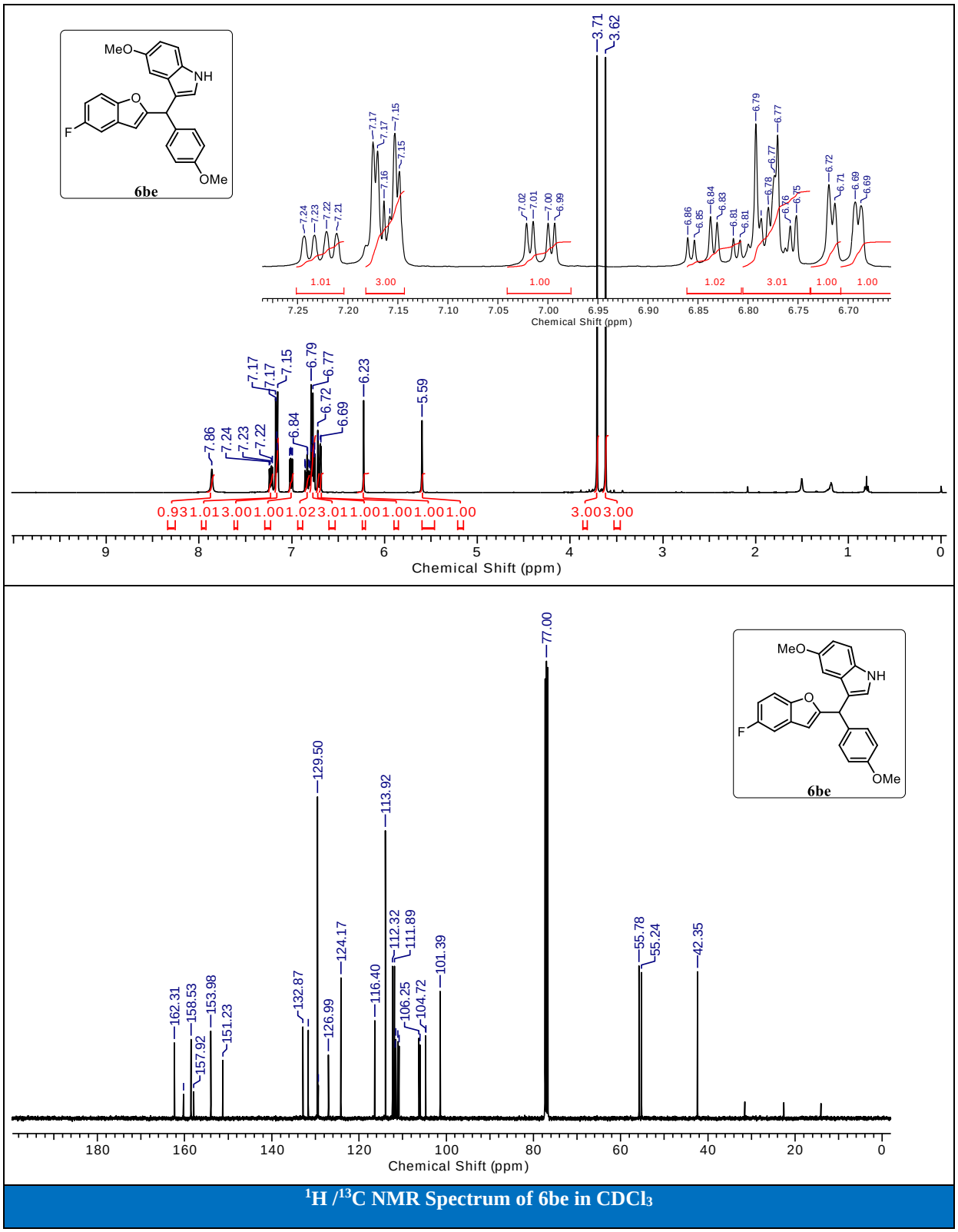

^{1}H /^{13}C NMR Spectrum of 6be in $CDCl_3$

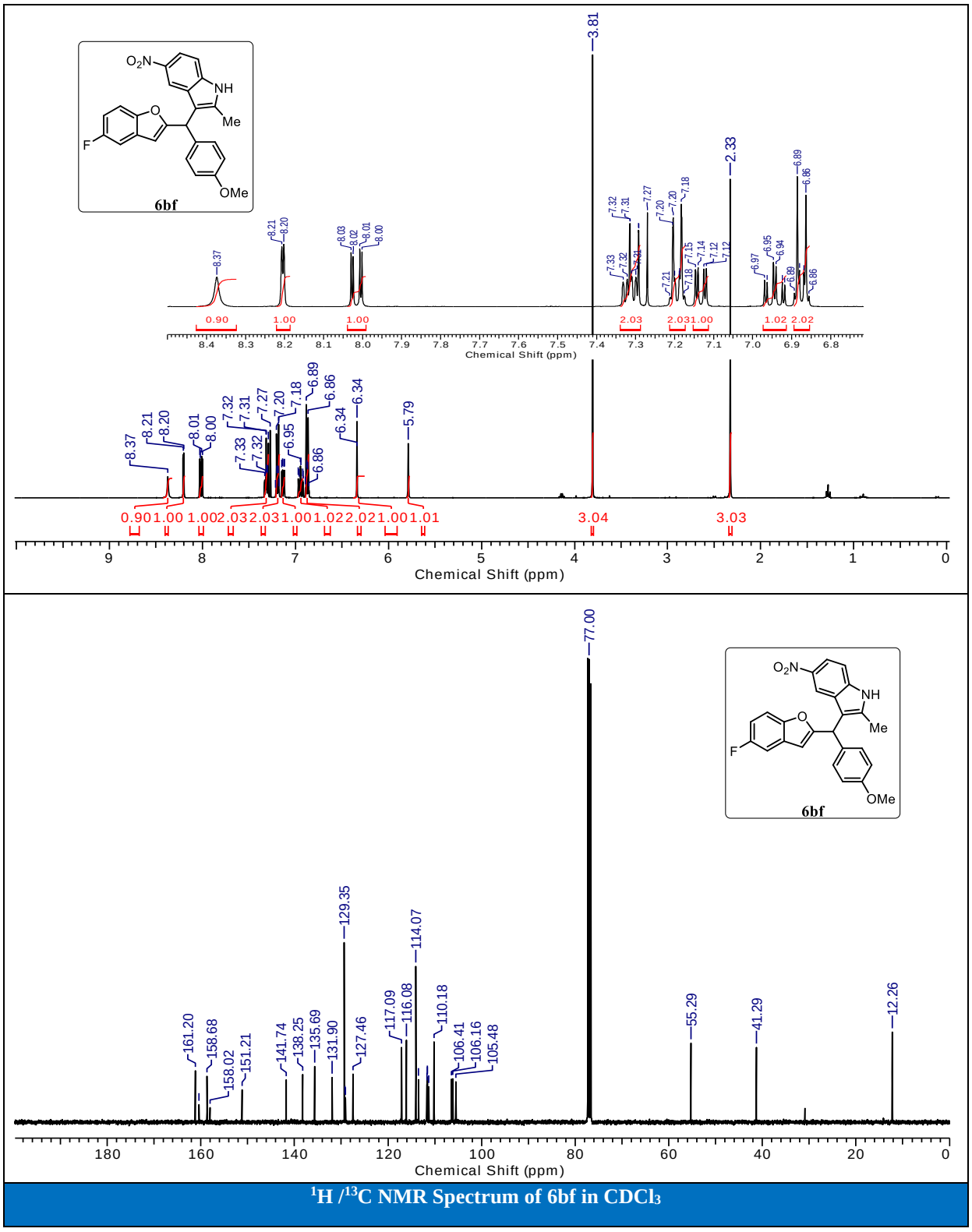

^{1}H /^{13}C NMR Spectrum of 6bf in $CDCl_3$

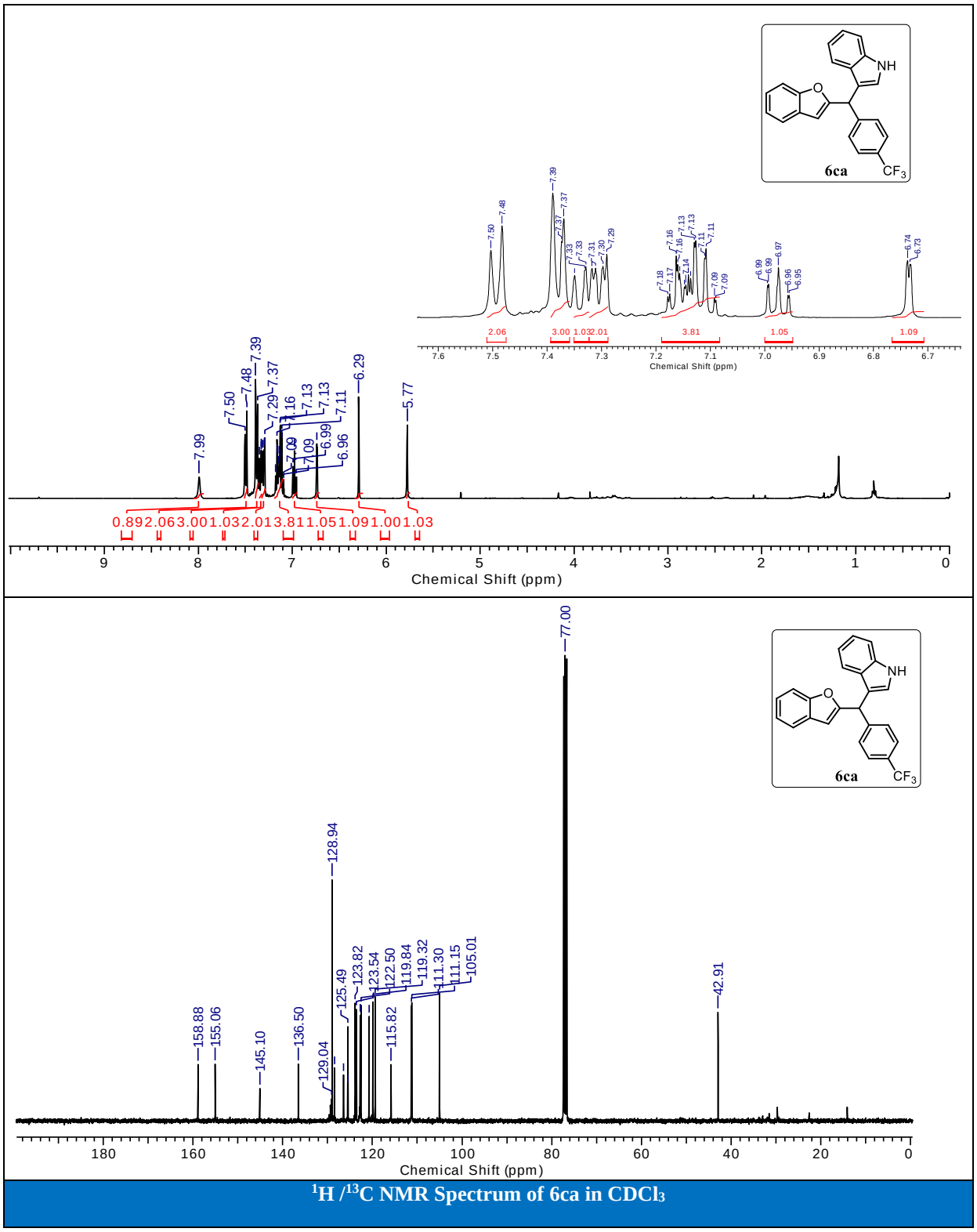

^{1}H /^{13}C NMR Spectrum of 6ca in $CDCl_3$

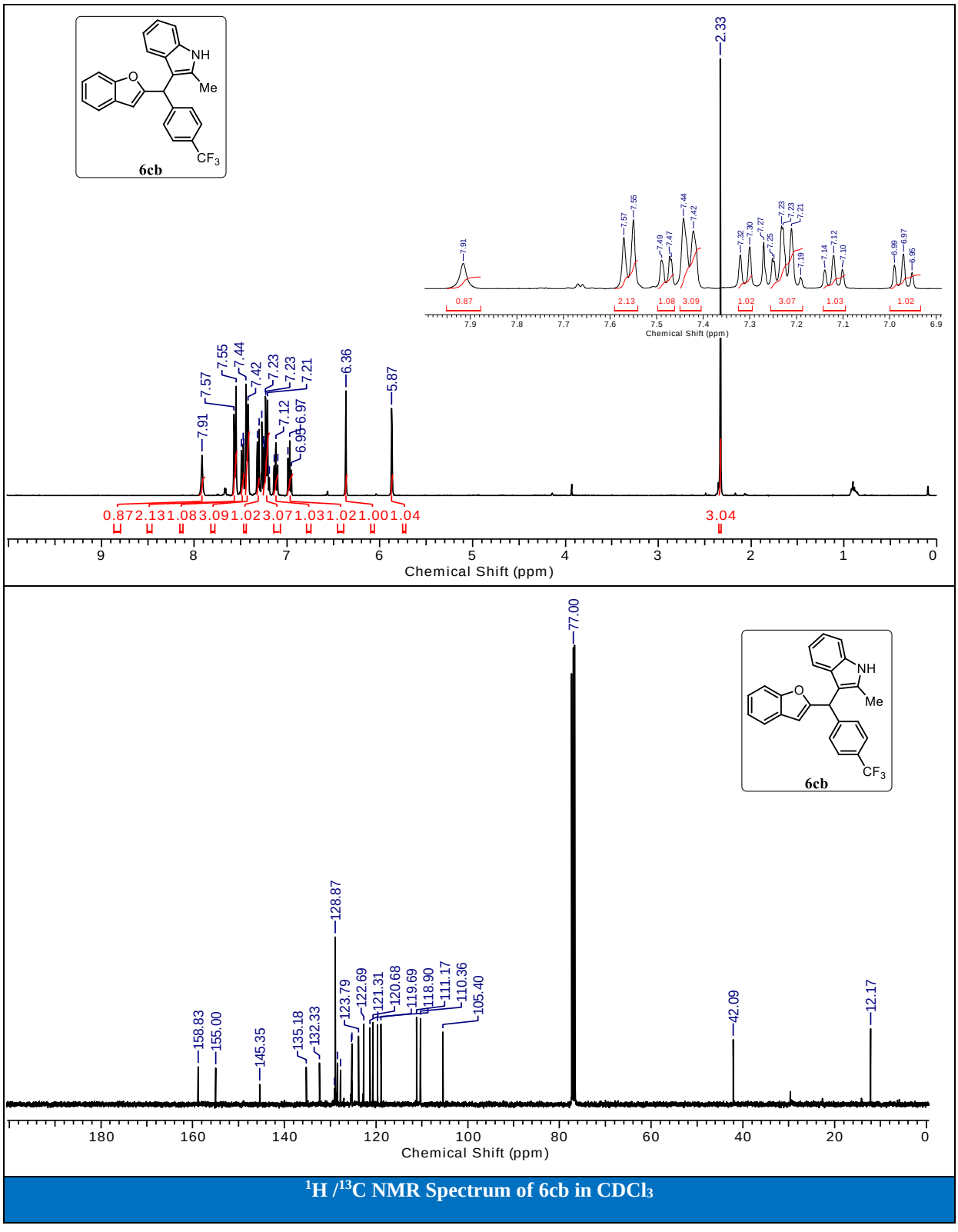

^{1}H /^{13}C NMR Spectrum of 6cb in $CDCl_3$

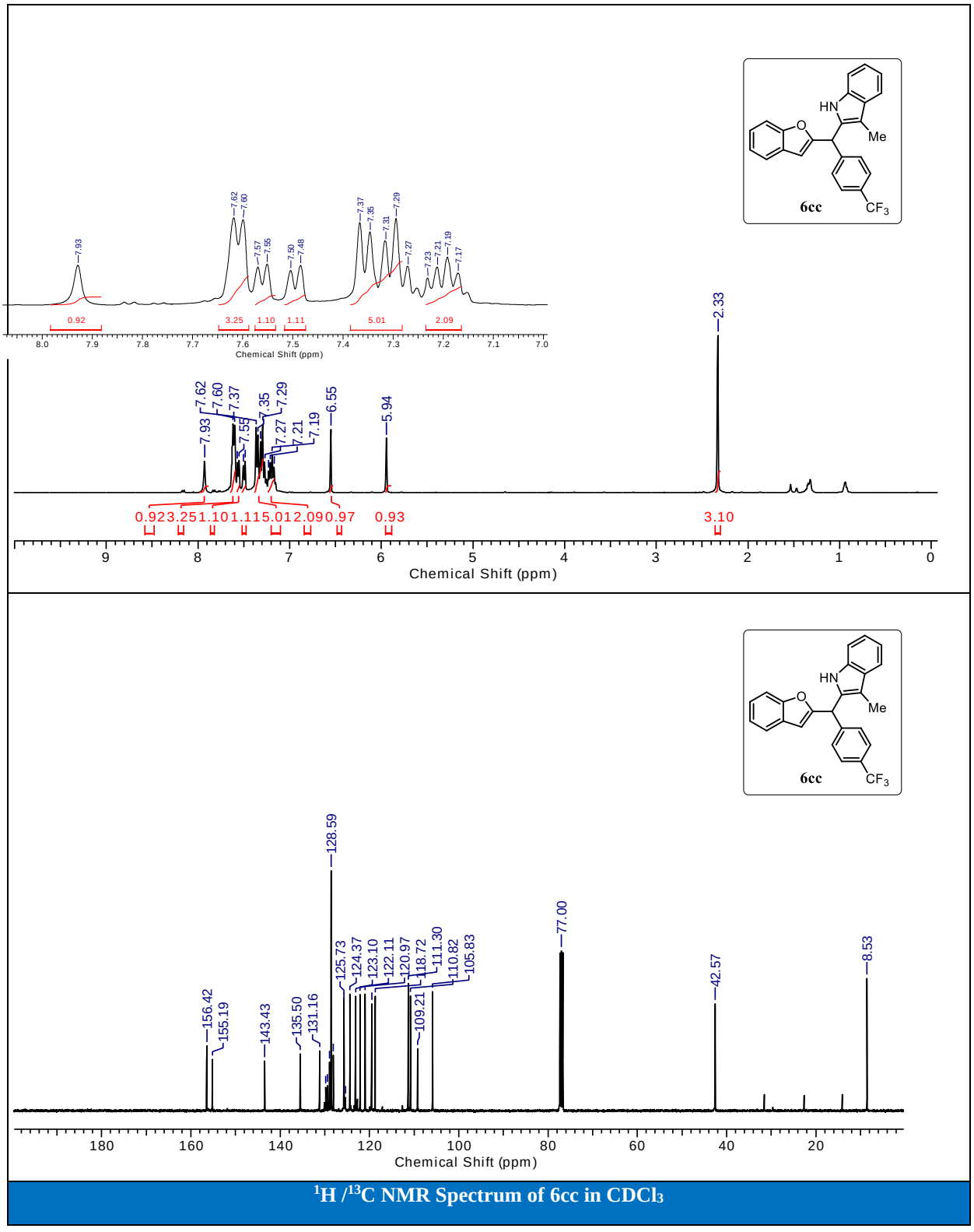

^{1}H /^{13}C NMR Spectrum of 6cc in $CDCl_3$

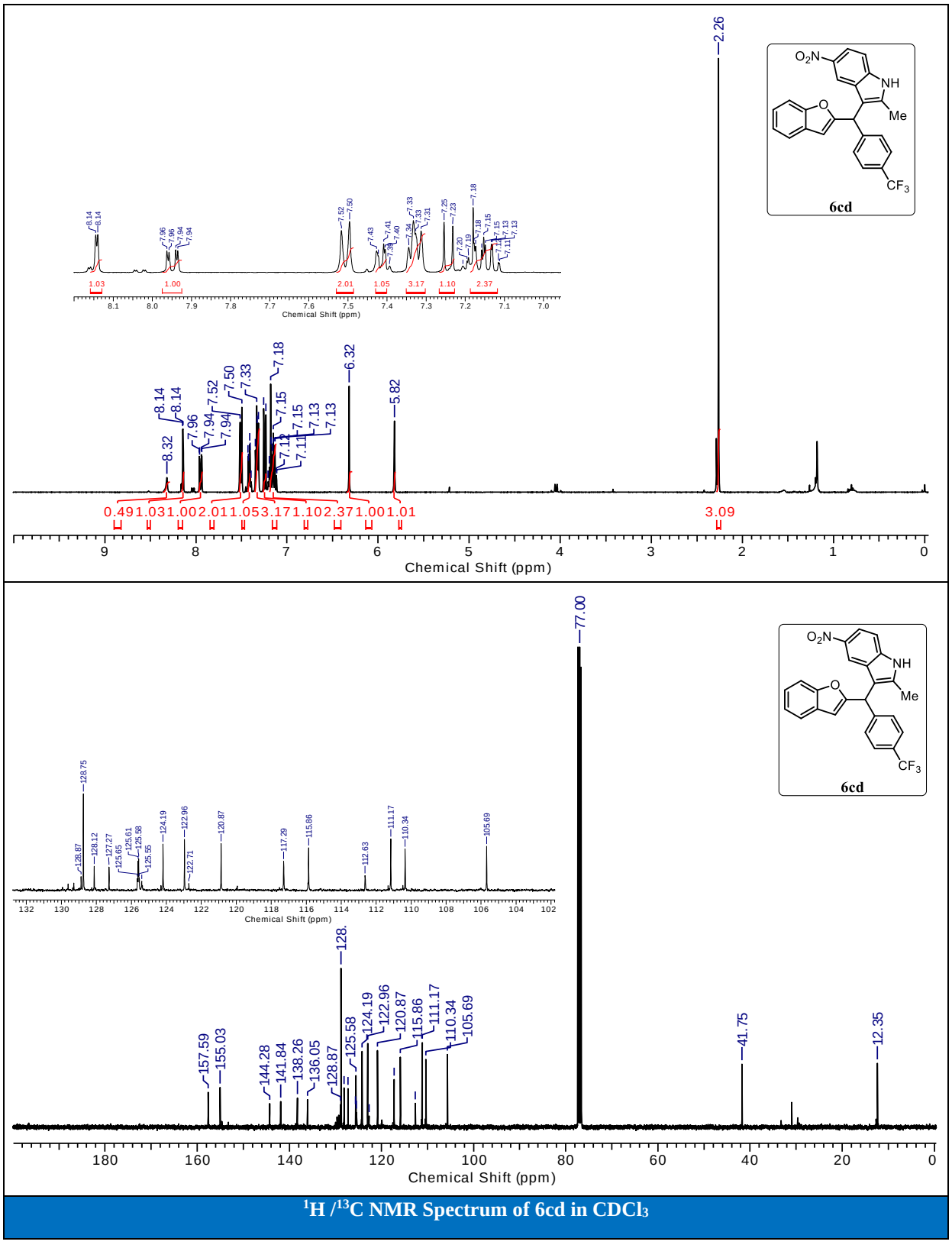

^{1}H /^{13}C NMR Spectrum of 6cd in $CDCl_3$

1) Wan, F.; Chen, F.; Fan, Y.; Chen, D. Clinical Significance of TET2 in Female Cancers. *Front. Bioeng. Biotechnol.* **2022**, *10*, 790605.

2) a) Saini, A.; Kumar, M.; Bhatt, S.; Saini, V.; Malik, A. Cancer Causes and Treatments. *IJPSR.* **2020**, *11* (7), 3109–3122. b) Blackadar, C. B. Historical Review of the Causes of Cancer. *WJCO.* **2016**, *7* (1), 54. c) Brennan, P.; Davey-Smith, G. Identifying Novel Causes of Cancers to Enhance Cancer Prevention: New Strategies Are Needed. *JNCI: J. Nat. Cancer Inst.* **2022**, *114* (3), 353–360.

3) Jemal, A.; Bray, F.; Center, M. M.; Ferlay, J.; Ward, E.; Forman, D. Global Cancer Statistics. *CA: A Cancer J. Clin.* **2011**, *61* (2), 69–90.

4) Sung, H.; Ferlay, J.; Siegel, R. L.; Laversanne, M.; Soerjomataram, I.; Jemal, A.; Bray, F. Global Cancer Statistics 2020: GLOBOCAN Estimates of Incidence and Mortality Worldwide for 36 Cancers in 185 Countries. *CA: Cancer J. Clin.* **2021**, *71* (3), 209–249.

5) Bray, F.; Ferlay, J.; Soerjomataram, I.; Siegel, R. L.; Torre, L. A.; Jemal, A. Global Cancer Statistics 2018: GLOBOCAN Estimates of Incidence and Mortality Worldwide for 36 Cancers in 185 Countries. *CA: Cancer J. Clin.* **2018**, *68* (6), 394–424.

6) Arruebo, M.; Vilaboa, N.; Sáez-Gutierrez, B.; Lambea, J.; Tres, A.; Valladares, M.; González-Fernández, Á. Assessment of the Evolution of Cancer Treatment Therapies. *Cancers* **2011**, *3* (3), 3279–3330.

7) Tsimberidou, A.-M. Targeted Therapy in Cancer. *Cancer Chemother. Pharmacol.* **2015**, *76* (6), 1113–1132.

8) a) Hansel, T. T.; Kropshofer, H.; Singer, T.; Mitchell, J. A.; George, A. J. T. The Safety and Side Effects of Monoclonal Antibodies. *Nat. Rev. Drug Discov.* **2010**, *9* (4), 325–338. b) Aghbash, P. S.; Hemmat, N.; Fathi, H.; Baghi, H. B. Monoclonal Antibodies in Cervical Malignancy-Related HPV. *Front. Oncol.* **2022**, *12*, 904790. c) Samaranayake, H.; Wirth, T.; Schenkwein, D.; Räty, J. K.; Ylä-Herttuala, S. Challenges in Monoclonal Antibody-Based Therapies. *Ann. Med.* **2009**, *41* (5), 322–331.

9) Zhong, L.; Li, Y.; Xiong, L.; Wang, W.; Wu, M.; Yuan, T.; Yang, W.; Tian, C.; Miao, Z.; Wang, T.; Yang, S. Small Molecules in Targeted Cancer Therapy:

Advances, Challenges, and Future Perspectives. *Sig. Transduct Target Ther.* **2021**, *6* (1), 201.

10) Bhat, P.; Kriel, J.; Shubha Priya, B.; Basappa; Shivananju, N. S.; Loos, B. Modulating Autophagy in Cancer Therapy: Advancements and Challenges for Cancer Cell Death Sensitization. *Biochem. Pharmacol.* **2018**, *147*, 170–182.

11) a) Klionsky, D. J. Autophagy Revisited: A Conversation with Christian de Duve. *Autophagy* **2008**, *4* (6), 740–743. b) Deter, R. L.; De Duve, C. INFLUENCE OF GLUCAGON, AN INDUCER OF CELLULAR AUTOPHAGY, ON SOME PHYSICAL PROPERTIES OF RAT LIVER LYSOSOMES. *J. Cell Biol.* **1967**, *33* (2), 437–449. c) Mizushima, N. A Brief History of Autophagy from Cell Biology to Physiology and Disease. *Nat. Cell Biol.* **2018**, *20* (5), 521–527.

12) Mizushima, N.; Komatsu, M. Autophagy: Renovation of Cells and Tissues. *Cell* **2011**, *147* (4), 728–741.

13) a) Yang, Y.; Hu, L.; Zheng, H.; Mao, C.; Hu, W.; Xiong, K.; Wang, F.; Liu, C. Application and Interpretation of Current Autophagy Inhibitors and Activators. *Acta. Pharmacol. Sin.* **2013**, *34* (5), 625–635. b) Mathew, R.; Karp, C. M.; Beaudoin, B.; Vuong, N.; Chen, G.; Chen, H.-Y.; Bray, K.; Reddy, A.; Bhanot, G.; Gelinas, C.; DiPaola, R. S.; Karantza-Wadsworth, V.; White, E. Autophagy Suppresses Tumorigenesis through Elimination of P62. *Cell* **2009**, *137* (6), 1062–1075. c) Lim, J.; Murthy, A. Targeting Autophagy to Treat Cancer: Challenges and Opportunities. *Front. Pharmacol.* **2020**, *11*, 590344.

14) a) Dice, J. F. Chaperone-Mediated Autophagy. *Autophagy* **2007**, *3* (4), 295–299. b) Li, W.; Yang, Q.; Mao, Z. Chaperone-Mediated Autophagy: Machinery, Regulation and Biological Consequences. *Cell. Mol. Life Sci.* **2011**, *68* (5), 749–763.

15) Li, W.; Li, J.; Bao, J. Microautophagy: Lesser-Known Self-Eating. *Cell. Mol. Life Sci.* **2012**, *69* (7), 1125–1136.

16) Klionsky, D. J.; Eskelinen, E.-L.; Deretic, V. Autophagosomes, Phagosomes, Autolysosomes, Phagolysosomes, Autophagolysosomes… Wait, I'm Confused. *Autophagy* **2014**, *10* (4), 549–551.

17) Kondapuram, S. K.; Sarvagalla, S.; Coumar, M. S. Targeting Autophagy with Small Molecules for Cancer Therapy. *JCMT* **2019**, *2019*.

18) He, S.; Li, Q.; Jiang, X.; Lu, X.; Feng, F.; Qu, W.; Chen, Y.; Sun, H. Design of Small Molecule Autophagy Modulators: A Promising Druggable Strategy. *J. Med. Chem.* **2018**, *61* (11), 4656–4687.

19) a)Saxton, R. A.; Sabatini, D. M. MTOR Signaling in Growth, Metabolism, and Disease. *Cell* **2017**, *168* (6), 960–976. b) Triola, G. Chemical Tools for Modulating Autophagy. *Tetrahedron* **2015**, *71* (3), 387–406. c) Hua, H.; Kong, Q.; Zhang, H.; Wang, J.; Luo, T.; Jiang, Y. Targeting MTOR for Cancer Therapy. *J. Hematol. Oncol.* **2019**, *12* (1), 71.

20) a) O'Farrell, F.; Rusten, T. E.; Stenmark, H. Phosphoinositide 3-Kinases as Accelerators and Brakes of Autophagy. *FEBS J.* **2013**, *280* (24), 6322–6337. b) Ahmed, A. R.; Candeo, A.; D'Abrantes, S.; Needham, S. R.; Yadav, R. B.; Botchway, S. W.; Parker, A. W. Directly Imaging the Localisation and Photosensitization Properties of the Pan-MTOR Inhibitor, AZD2014, in Living Cancer Cells. *Journal of Photochemistry and Photobiology B: Biology* **2020**, *213*, 112055.

21) a) Lazarus, M. B.; Novotny, C. J.; Shokat, K. M. Structure of the Human Autophagy Initiating Kinase ULK1 in Complex with Potent Inhibitors. *ACS Chem. Biol.* **2015**, *10* (1), 257–261. b) Martin, K. R.; Celano, S. L.; Solitro, A. R.; Gunaydin, H.; Scott, M.; O'Hagan, R. C.; Shumway, S. D.; Fuller, P.; MacKeigan, J. P. A Potent and Selective ULK1 Inhibitor Suppresses Autophagy and Sensitizes Cancer Cells to Nutrient Stress. *iScience* **2018**, *8*, 74–84.

22) Matsunaga, K.; Morita, E.; Saitoh, T.; Akira, S.; Ktistakis, N. T.; Izumi, T.; Noda, T.; Yoshimori, T. Autophagy Requires Endoplasmic Reticulum Targeting of the PI3-Kinase Complex via Atg14L. *J. Cell Biol.* **2010**, *190* (4), 511–521.

23) a) Honda, A.; Harrington, E.; Cornella-Taracido, I.; Furet, P.; Knapp, M. S.; Glick, M.; Triantafellow, E.; Dowdle, W. E.; Wiedershain, D.; Maniara, W.; Moore, C.; Finan, P. M.; Hamann, L. G.; Firestone, B.; Murphy, L. O.; Keaney, E. P. Potent, Selective, and Orally Bioavailable Inhibitors of VPS34 Provide Chemical Tools to Modulate Autophagy *in Vivo*. *ACS Med. Chem. Lett.* **2016**, *7* (1), 72–76. b)

Dowdle, W. E.; Nyfeler, B.; Nagel, J.; Elling, R. A.; Liu, S.; Triantafellow, E.; Menon, S.; Wang, Z.; Honda, A.; Pardee, G.; Cantwell, J.; Luu, C.; Cornella-Taracido, I.; Harrington, E.; Fekkes, P.; Lei, H.; Fang, Q.; Digan, M. E.; Burdick, D.; Powers, A. F.; Helliwell, S. B.; D'Aquin, S.; Bastien, J.; Wang, H.; Wiederschain, D.; Kuerth, J.; Bergman, P.; Schwalb, D.; Thomas, J.; Ugwonali, S.; Harbinski, F.; Tallarico, J.; Wilson, C. J.; Myer, V. E.; Porter, J. A.; Bussiere, D. E.; Finan, P. M.; Labow, M. A.; Mao, X.; Hamann, L. G.; Manning, B. D.; Valdez, R. A.; Nicholson, T.; Schirle, M.; Knapp, M. S.; Keaney, E. P.; Murphy, L. O. Selective VPS34 Inhibitor Blocks Autophagy and Uncovers a Role for NCOA4 in Ferritin Degradation and Iron Homeostasis in Vivo. *Nat. Cell Biol.* **2014**, *16* (11), 1069–1079. c) Pasquier, B.; El-Ahmad, Y.; Filoche-Rommé, B.; Dureuil, C.; Fassy, F.; Abecassis, P.-Y.; Mathieu, M.; Bertrand, T.; Benard, T.; Barrière, C.; El Batti, S.; Letallec, J.-P.; Sonnefraud, V.; Brollo, M.; Delbarre, L.; Loyau, V.; Pilorge, F.; Bertin, L.; Richepin, P.; Arigon, J.; Labrosse, J.-R.; Clément, J.; Durand, F.; Combet, R.; Perraut, P.; Leroy, V.; Gay, F.; Lefrançois, D.; Bretin, F.; Marquette, J.-P.; Michot, N.; Caron, A.; Castell, C.; Schio, L.; McCort, G.; Goulaouic, H.; Garcia-Echeverria, C.; Ronan, B. Discovery of (2 *S*)-8-[(3 *R*)-3-Methylmorpholin-4-Yl]-1-(3-Methyl-2-Oxobutyl)-2-(Trifluoromethyl)-3,4-Dihydro-2 *H* -Pyrimido[1,2- *a*]Pyrimidin-6-One: A Novel Potent and Selective Inhibitor of Vps34 for the Treatment of Solid Tumors. *J. Med. Chem.* **2015**, *58* (1), 376–400.

24) a) Xu, R.; Ji, Z.; Xu, C.; Zhu, J. The Clinical Value of Using Chloroquine or Hydroxychloroquine as Autophagy Inhibitors in the Treatment of Cancers: A Systematic Review and Meta-Analysis. *Medicine* **2018**, *97* (46), e12912. b) Chude, C.; Amaravadi, R. Targeting Autophagy in Cancer: Update on Clinical Trials and Novel Inhibitors. *IJMS* **2017**, *18* (6), 1279.

25) Surviladze, Z.; Sterk, R. T.; DeHaro, S. A.; Ozbun, M. A. Cellular Entry of Human Papillomavirus Type 16 Involves Activation of the Phosphatidylinositol 3-Kinase/Akt/MTOR Pathway and Inhibition of Autophagy. *J. Virol.* **2013**, *87* (5), 2508–2517.

26) Mattoscio, D.; Medda, A.; Chiocca, S. Human Papilloma Virus and Autophagy. *IJMS* **2018**, *19* (6), 1775.

27) a) Sung, H.; Ferlay, J.; Siegel, R. L.; Laversanne, M.; Soerjomataram, I.; Jemal, A.; Bray, F. Global Cancer Statistics 2020: GLOBOCAN Estimates of Incidence and Mortality Worldwide for 36 Cancers in 185 Countries. *CA Cancer J. Clin.* **2021**, *71* (3), 209–249. b) Peralta-Zaragoza, O.; Bermudez-Morales; Perez-Plasencia; Salazar-Leon; Gomez-Ceron; Madrid-Marina. Targeted Treatments for Cervical Cancer: A Review. *OTT* **2012**, 315.

28) Beddoe, A. M. Elimination of Cervical Cancer: Challenges for Developing Countries. *ecancer* **2019**, *13*.

29) a) Cohen, A. C.; Roane, B. M.; Leath, C. A. Novel Therapeutics for Recurrent Cervical Cancer: Moving Towards Personalized Therapy. *Drugs* **2020**, *80* (3), 217–227. b) Liu, L.; Wang, M.; Li, X.; Yin, S.; Wang, B. An Overview of Novel Agents for Cervical Cancer Treatment by Inducing Apoptosis: Emerging Drugs Ongoing Clinical Trials and Preclinical Studies. *Front. Med.* **2021**, *8*, 682366. c) Vora, C.; Gupta, S. Targeted Therapy in Cervical Cancer. *ESMO Open* **2018**, *3*, e000462.

30) Bevacizumab. In *Meyler's Side Effects of Drugs*; *Elsevier* **2016**; 963–965.

31) Monk, B. J.; Mas Lopez, L.; Zarba, J. J.; Oaknin, A.; Tarpin, C.; Termrungruanglert, W.; Alber, J. A.; Ding, J.; Stutts, M. W.; Pandite, L. N. Phase II, Open-Label Study of Pazopanib or Lapatinib Monotherapy Compared With Pazopanib Plus Lapatinib Combination Therapy in Patients With Advanced and Recurrent Cervical Cancer. *JCO* **2010**, *28* (22), 3562–3569.

32) Mackay, H. J.; Tinker, A.; Winquist, E.; Thomas, G.; Swenerton, K.; Oza, A.; Sederias, J.; Ivy, P.; Eisenhauer, E. A. A Phase II Study of Sunitinib in Patients with Locally Advanced or Metastatic Cervical Carcinoma: NCIC CTG Trial IND.184. *Gynecol. Oncol.* **2010**, *116* (2), 163–167.

33) Mirza, M.; Berton, D.; Vergote, I.; Depont Christensen, R.; Floquet, A.; Maenpaa, J.; Braicu, I.; Altintas, S.; Follana, P.; Ør Knudsen, A.; Ataseven, B.; Selle, F.; Lundgren, C.; Huober, J.; Fabbro, M.; Denys, H.; Heudel, P.; Magnusson, M.; Lindemann, K.; Sehouli, J. 1196 A Randomised Phase II Study of Combination

Chemotherapy with Nintedanib/Placebo in Advanced/Recurrent Endometrial Cancer. FANDANGO/ENGOT-EN1/FANDANGO. In *Late breaking abstracts*; BMJ Publishing Group Ltd, **2021**; A371.2-A372.

34) Chan, J. K.; Deng, W.; Higgins, R. V.; Tewari, K. S.; Bonebrake, A. J.; Hicks, M.; Gaillard, S.; Ramirez, P. T.; Chafe, W.; Monk, B. J.; Aghajanian, C. A Phase II Evaluation of Brivanib in the Treatment of Persistent or Recurrent Carcinoma of the Cervix: An NRG Oncology/Gynecologic Oncology Group Study. *Gynecol. Oncol.* **2017**, *146* (3), 554–559. b) Hofman, J.; Sorf, A.; Vagiannis, D.; Sucha, S.; Kammerer, S.; Küpper, J.-H.; Chen, S.; Guo, L.; Ceckova, M.; Staud, F. Brivanib Exhibits Potential for Pharmacokinetic Drug–Drug Interactions and the Modulation of Multidrug Resistance through the Inhibition of Human ABCG2 Drug Efflux Transporter and CYP450 Biotransformation Enzymes. *Mol. Pharm.* **2019**, *16* (11), 4436–4450.

35) Symonds, R. P.; Gourley, C.; Davidson, S.; Carty, K.; McCartney, E.; Rai, D.; Banerjee, S.; Jackson, D.; Lord, R.; McCormack, M.; Hudson, E.; Reed, N.; Flubacher, M.; Jankowska, P.; Powell, M.; Dive, C.; West, C. M. L.; Paul, J. Cediranib Combined with Carboplatin and Paclitaxel in Patients with Metastatic or Recurrent Cervical Cancer (CIRCCa): A Randomised, Double-Blind, Placebo-Controlled Phase 2 Trial. *Lancet Oncol.* **2015**, *16* (15), 1515–1524.

36) Goncalves, A.; Fabbro, M.; Lhommé, C.; Gladieff, L.; Extra, J.-M.; Floquet, A.; Chaigneau, L.; Carrasco, A. T.; Viens, P. A Phase II Trial to Evaluate Gefitinib as Second- or Third-Line Treatment in Patients with Recurring Locoregionally Advanced or Metastatic Cervical Cancer. *Gynecol. Oncol.* **2008**, *108* (1), 42–46.

37) *Critical Issues in Head and Neck Oncology: Key Concepts from the Seventh THNO Meeting*; Vermorken, J. B., Budach, V., Leemans, C. R., Machiels, J.-P., Nicolai, P., O'Sullivan, B., Eds.; Springer International Publishing: Cham, 2021.

38) Schilder, R. J.; Sill, M. W.; Lee, Y.-C.; Mannel, R. A Phase II Trial of Erlotinib in Recurrent Squamous Cell Carcinoma of the Cervix: A Gynecologic Oncology Group Study. *Int. J. Gynecol. Cancer* **2009**, *19* (5), 929–933.

39) a) Assad, D. X.; Elias, S. T.; Melo, A. C.; Ferreira, C. G.; De Luca Canto, G.; Guerra, E. N. S. Potential Impact of mTOR Inhibitors on Cervical Squamous Cell

Carcinoma: A Systematic Review. *Oncol. Lett.* **2016**, *12* (5), 4107–4116. b)De Melo, A. C.; Paulino, E.; Garces, Á. H. I. A Review of mTOR Pathway Inhibitors in Gynecologic Cancer. *Oxid. Med. Cell. Longev.* **2017**, *2017*, 1–8.

40) Tinker, A. V.; Ellard, S.; Welch, S.; Moens, F.; Allo, G.; Tsao, M. S.; Squire, J.; Tu, D.; Eisenhauer, E. A.; MacKay, H. Phase II Study of Temsirolimus (CCI-779) in Women with Recurrent, Unresectable, Locally Advanced or Metastatic Carcinoma of the Cervix. A Trial of the NCIC Clinical Trials Group (NCIC CTG IND 199). *Gynecol. Oncol.* **2013**, *130* (2), 269–274.

41) a) Sami, S.; Hoti, N.; Xu, H.-M.; Shen, Z.; Huang, X. Valproic Acid Inhibits the Growth of Cervical Cancer Both In Vitro and In Vivo. *J. Biochem.* **2008**, *144* (3), 357–362. b) Han, B. R.; You, B. R.; Park, W. H. Valproic Acid Inhibits the Growth of HeLa Cervical Cancer Cells via Caspase-Dependent Apoptosis. *Oncol. Rep.* **2013**, *30* (6), 2999–3005.

42) Thaker, P. H.; Salani, R.; Brady, W. E.; Lankes, H. A.; Cohn, D. E.; Mutch, D. G.; Mannel, R. S.; Bell-McGuinn, K. M.; Di Silvestro, P. A.; Jelovac, D.; Carter, J. S.; Duan, W.; Resnick, K. E.; Dizon, D. S.; Aghajanian, C.; Fracasso, P. M. A Phase I Trial of Paclitaxel, Cisplatin, and Veliparib in the Treatment of Persistent or Recurrent Carcinoma of the Cervix: An NRG Oncology Study (NCT#01281852). *Ann. Oncol.* **2017**, *28* (3), 505–511.

43) Gross, M.; Spencer, R. J. Recurrent Cervical Cancer Treated Successfully with Single-Agent PARP-Inhibitor, Olaparib. *Case Rep. Obstet. Gynecol.* **2022**, *2022*, 1–4.

44) Orbegoso, C.; Murali, K.; Banerjee, S. The Current Status of Immunotherapy for Cervical Cancer. *Rep. Pract. Oncol. Radiother.* **2018**, *23* (6), 580–588.

45) a) Colombo, N.; Dubot, C.; Lorusso, D.; Caceres, M. V.; Hasegawa, K.; Shapira-Frommer, R.; Tewari, K. S.; Salman, P.; Hoyos Usta, E.; Yañez, E.; Gümüş, M.; Olivera Hurtado De Mendoza, M.; Samouëlian, V.; Castonguay, V.; Arkhipov, A.; Toker, S.; Li, K.; Keefe, S. M.; Monk, B. J. Pembrolizumab for Persistent, Recurrent, or Metastatic Cervical Cancer. *N. Engl. J. Med.* **2021**, *385* (20), 1856–1867. b) Qi, L.; Li, N.; Lin, A.; Wang, X.; Cong, J. Efficacy and Safety of

Pembrolizumab on Cervical Cancer: A Systematic Review and Single-Arm Meta-Analysis. *Front. Oncol.* **2022**, *12*, 910486.

46) Weber, J. S.; O'Day, S.; Urba, W.; Powderly, J.; Nichol, G.; Yellin, M.; Snively, J.; Hersh, E. Phase I/II Study of Ipilimumab for Patients With Metastatic Melanoma. *JCO* **2008**, *26* (36), 5950–5956. b) Lheureux, S.; Butler, M. O.; Clarke, B.; Cristea, M. C.; Martin, L. P.; Tonkin, K.; Fleming, G. F.; Tinker, A. V.; Hirte, H. W.; Tsoref, D.; Mackay, H.; Dhani, N. C.; Ghatage, P.; Weberpals, J.; Welch, S.; Pham, N.-A.; Motta, V.; Sotov, V.; Wang, L.; Karakasis, K.; Udagani, S.; Kamel-Reid, S.; Streicher, H. Z.; Shaw, P.; Oza, A. M. Association of Ipilimumab With Safety and Antitumor Activity in Women With Metastatic or Recurrent Human Papillomavirus–Related Cervical Carcinoma. *JAMA Oncol.* **2018**, *4* (7), e173776.

47) Suzuki, H.; Nagai, K.; Yamaki, H.; Tanaka, N.; Umezawa, H. ON THE MECHANISM OF ACTION OF BLEOMYCIN : SCISSION OF DNA STRANDS IN VITRO AND IN VIVO. *J. Antibiot.* **1969**, *22* (9), 446–448.

48) Kurtz, J. E.; Hardy-Bessard, A.-C.; Deslandres, M.; Lavau-Denes, S.; Largillier, R.; Roemer-Becuwe, C.; Weber, B.; Guillemet, C.; Paraiso, D.; Pujade-Lauraine, E. Cetuximab, Topotecan and Cisplatin for the Treatment of Advanced Cervical Cancer: A Phase II GINECO Trial. *Gynecol. Oncol.* **2009**, *113* (1), 16–20.

49) a) Pandey, S.; Chandravati, C. Autophagy in Cervical Cancer: An Emerging Therapeutic Target. *Asian Pac. J. Cancer Prev.* **2012**, *13* (10), 4867–4871. b) Wu, L.; Shen, B.; Li, J.; Zhang, H.; Zhang, K.; Yang, Y.; Zu, Z.; Shen, D.; Luo, M. STAT3 Exerts Pro-Tumor and Anti-Autophagy Roles in Cervical Cancer. *Diagn. Pathol.* **2022**, *17* (1), 13.

50) Sharma, V.; Kumar, P.; Pathak, D. Biological Importance of the Indole Nucleus in Recent Years: A Comprehensive Review. *J. Heterocycl. Chem.* **2010**, *47* (3), 491–502.

51) a) Kamal, A.; Srikanth, Y. V. V.; Ramaiah, M. J.; Khan, M. N. A.; Kashi Reddy, M.; Ashraf, Md.; Lavanya, A.; Pushpavalli, S. N. C. V. L.; Pal-Bhadra, M. Synthesis, Anticancer Activity and Apoptosis Inducing Ability of Bisindole Linked Pyrrolo[2,1-c][1,4]Benzodiazepine Conjugates. *Bioorg. Med. Chem. Lett.*

2012, *22* (1), 571–578. b) Andreani, A.; Burnelli, S.; Granaiola, M.; Leoni, A.; Locatelli, A.; Morigi, R.; Rambaldi, M.; Varoli, L.; Landi, L.; Prata, C.; Berridge, M. V.; Grasso, C.; Fiebig, H.-H.; Kelter, G.; Burger, A. M.; Kunkel, M. W. Antitumor Activity of Bis-Indole Derivatives. *J. Med. Chem.* **2008**, *51* (15), 4563–4570. c) Safe, S.; Papineni, S.; Chintharlapalli, S. Cancer Chemotherapy with Indole-3-Carbinol, Bis(3′-Indolyl)Methane and Synthetic Analogs. *Cancer Lett.* **2008**, *269* (2), 326–338.

52) a) Mari, M.; Tassoni, A.; Lucarini, S.; Fanelli, M.; Piersanti, G.; Spadoni, G. Brønsted Acid Catalyzed Bisindolization of α-Amido Acetals: Synthesis and Anticancer Activity of Bis(Indolyl)Ethanamino Derivatives. *Eur. J. Org. Chem.* **2014**, *2014* (18), 3822–3830. b) Devi, N.; Kaur, K.; Biharee, A.; Jaitak, V. Recent Development in Indole Derivatives as Anticancer Agent: A Mechanistic Approach. *ACAMC* **2021**, *21* (14), 1802–1824. c) Chavan, K. A.; Shukla, M.; Chauhan, A. N. S.; Maji, S.; Mali, G.; Bhattacharyya, S.; Erande, R. D. Effective Synthesis and Biological Evaluation of Natural and Designed Bis(Indolyl)Methanes via Taurine-Catalyzed Green Approach. *ACS Omega* **2022**, *7* (12), 10438–10446. d) Pingaew, R.; Prachayasittikul, S.; Ruchirawat, S.; Prachayasittikul, V. Synthesis and Structure–Activity Relationship of Mono-Indole-, Bis-Indole-, and Tris-Indole-Based Sulfonamides as Potential Anticancer Agents. *Mol. Divers* **2013**, *17* (3), 595–604. e) Jamsheena, V.; Shilpa, G.; Saranya, J.; Harry, N. A.; Lankalapalli, R. S.; Priya, S. Anticancer Activity of Synthetic Bis(Indolyl)Methane-Ortho-Biaryls against Human Cervical Cancer (HeLa) Cells. *Chem. Biol. Interact.* **2016**, *247*, 11–21.

53) a) Zou, M.; Zeng, C. *3,3'-Diindolylmethane Inhibits Ovarian Cancer Cell Viability and Enhances Chemotherapy Sensitivity via STAT3 Pathway*; preprint; In Review, **2022**. b) Kandala, P. K.; Wright, S. E.; Srivastava, S. K. Blocking Epidermal Growth Factor Receptor Activation by 3,3′-Diindolylmethane Suppresses Ovarian Tumor Growth In Vitro and In Vivo. *J. Pharmacol. Exp. Ther.* **2012**, *341* (1), 24–32.

54) a) Majumder, I.; Paul, S.; Kundu, R. INDUCTION OF AUTOPHAGY IN HUMAN CERVICAL CANCER CELL LINE (SIHA) BY CHAETOMORPHA

LINUM (MULLER) KÜTZ. *Int. J. Pharm. Pharm. Sci.* **2018**, *10* (6), 74. b) Gao, J.; Yu, H.; Guo, W.; Kong, Y.; Gu, L.; Li, Q.; Yang, S.; Zhang, Y.; Wang, Y. The Anticancer Effects of Ferulic Acid Is Associated with Induction of Cell Cycle Arrest and Autophagy in Cervical Cancer Cells. *Cancer Cell Int.* **2018**, *18* (1), 102. c) Feng, X.; Zhou, J.; Li, J.; Hou, X.; Li, L.; Chen, Y.; Fu, S.; Zhou, L.; Li, C.; Lei, Y. Tubeimoside I Induces Accumulation of Impaired Autophagolysosome against Cervical Cancer Cells by Both Initiating Autophagy and Inhibiting Lysosomal Function. *Cell Death Dis.* **2018**, *9* (11), 1117.

55) a) Assad, D. X.; Elias, S. T.; Melo, A. C.; Ferreira, C. G.; De Luca Canto, G.; Guerra, E. N. S. Potential Impact of mTOR Inhibitors on Cervical Squamous Cell Carcinoma: A Systematic Review. *Oncol. Lett.* **2016**, *12* (5), 4107–4116. b) Movva, S.; Rodriguez, L.; Arias-Pulido, H.; Verschraegen, C. Novel Chemotherapy Approaches for Cervical Cancer. *Cancer* **2009**, *115* (14), 3166–3180.

56) a) Kitajima, M.; Takayama, H. Monoterpenoid Bisindole Alkaloids. In *The Alkaloids: Chemistry and Biology*; Elsevier, 2016; Vol. 76, pp 259–310. b)Pingaew, R.; Prachayasittikul, S.; Ruchirawat, S.; Prachayasittikul, V. Synthesis and Structure–Activity Relationship of Mono-Indole-, Bis-Indole-, and Tris-Indole-Based Sulfonamides as Potential Anticancer Agents. *Mol. Divers* **2013**, *17* (3), 595–604. c) Kamal, A.; Srikanth, Y. V. V.; Ramaiah, M. J.; Khan, M. N. A.; Kashi Reddy, M.; Ashraf, Md.; Lavanya, A.; Pushpavalli, S. N. C. V. L.; Pal-Bhadra, M. Synthesis, Anticancer Activity and Apoptosis Inducing Ability of Bisindole Linked Pyrrolo[2,1-c][1,4]Benzodiazepine Conjugates. *Bioorg. Med. Chem. Lett.* **2012**, *22* (1), 571–578. d) Kaushik, N.; Kaushik, N.; Attri, P.; Kumar, N.; Kim, C.; Verma, A.; Choi, E. Biomedical Importance of Indoles. *Molecules* **2013**, *18* (6), 6620–6662.

57) a) Stevenson, P. C.; Simmonds, M. S. J.; Yule, M. A.; Veitch, N. C.; Kite, G. C.; Irwin, D.; Legg, M. Insect Antifeedant Furanocoumarins from Tetradium Daniellii. *Phytochem.* **2003**, *63* (1), 41–46. b) Tanaka, H.; Oh-Uchi, T.; Etoh, H.; Sako, M.; Sato, M.; Fukai, T.; Tateishi, Y. An Arylbenzofuran and Four

Isoflavonoids from the Roots of Erythrina Poeppigiana. *Phytochem.* **2003**, *63* (5), 597–602.

58) Khanam, H.; Shamsuzzaman. Bioactive Benzofuran Derivatives: A Review. *Eur. J. Med. Chem.* **2015**, *97*, 483–504.

59) a) Shankar, B.; Jalapathi, P.; Saikrishna, B.; Perugu, S.; Manga, V. Synthesis, Anti-Microbial Activity, Cytotoxicity of Some Novel Substituted (5-(3-(1H-Benzo[d]Imidazol-2-Yl)-4-Hydroxybenzyl)Benzofuran-2-Yl)(Phenyl)Methanone Analogs. *Chem. Cent. J.* **2018**, *12* (1), 1. b) Koca, M.; Servi, S.; Kirilmis, C.; Ahmedzade, M.; Kazaz, C.; Özbek, B.; Ötük, G. Synthesis and Antimicrobial Activity of Some Novel Derivatives of Benzofuran: Part 1. Synthesis and Antimicrobial Activity of (Benzofuran-2-yl)(3-Phenyl-3-Methylcyclobutyl) Ketoxime Derivatives. *Eur. J. Med. Chem.* **2005**, *40* (12), 1351–1358.

60) Rao, GK.; Venugopala, KN.; Pai, PNS. Novel Schiff Bases of 4-Hydroxy 6-Carboxhydrazino Benzofuran Analogs: Synthesis and Pharmacological Study. *J. Pharmacol. Toxicol.* **2007**; *2*: 481–488.

61) Pieters, L.; Van Dyck, S.; Gao, M.; Bai, R.; Hamel, E.; Vlietinck, A.; Lemière, G. Synthesis and Biological Evaluation of Dihydrobenzofuran Lignans and Related Compounds as Potential Antitumor Agents That Inhibit Tubulin Polymerization. *J. Med. Chem.* **1999**, *42* (26), 5475–5481.

62) Dawood, K. M.; Abdel-Gawad, H.; Rageb, E. A.; Ellithey, M.; Mohamed, H. A. Synthesis, Anticonvulsant, and Anti-Inflammatory Evaluation of Some New Benzotriazole and Benzofuran-Based Heterocycles. *Bioorg. Med. Chem.* **2006**, *14* (11), 3672–3680.

63) Tsujihara, K.; Hongu, M.; Saito, K.; Kawanishi, H.; Kuriyama, K.; Matsumoto, M.; Oku, A.; Ueta, K.; Tsuda, M.; Saito, A. Na^+-Glucose Cotransporter (SGLT) Inhibitors as Antidiabetic Agents. 4. Synthesis and Pharmacological Properties of 4‘-Dehydroxyphlorizin Derivatives Substituted on the B Ring. *J. Med. Chem.* **1999**, *42* (26), 5311–5324.

64) Liao, Y.; Kozikowski, A. P.; Guidotti, A.; Costa, E. Synthesis and Pharmacological Evaluation of Benzofuran-Acetamides as “Antineophobic”

Mitochondrial DBI Receptor Complex Ligands. *Bioorg. Med. Chem. Lett.* **1998**, *8* (16), 2099–2102.

65) Wang, X.-Q.; Liu, L.-X.; Li, Y.; Sun, C.-J.; Chen, W.; Li, L.; Zhang, H.-B.; Yang, X.-D. Design, Synthesis and Biological Evaluation of Novel Hybrid Compounds of Imidazole Scaffold-Based 2-Benzylbenzofuran as Potent Anticancer Agents. *Eur. J. Med. Chem.* **2013**, *62*, 111–121.

66) Xu, K.; Liu, Y.; Wang, R.; Cai, P.; Fang, Y. Design, Synthesis, and Anticancer Activities of Benzofuran–Isatin Hybrids Tethered by Pentylene and Hexylene. *J. Heterocycl. Chem.* **2019**, *56* (7), 2052–2055.

67) Ma, Y.; Zheng, X.; Gao, H.; Wan, C.; Rao, G.; Mao, Z. Design, Synthesis, and Biological Evaluation of Novel Benzofuran Derivatives Bearing N-Aryl Piperazine Moiety. *Molecules* **2016**, *21* (12), 1684.

68) Hasima, N.; Ozpolat, B. Regulation of Autophagy by Polyphenolic Compounds as a Potential Therapeutic Strategy for Cancer. *Cell Death Dis.* **2014**, *5* (11), e1509–e1509.

69) Zhang, J.-Q. Antitumor Effect of Matrine in Human Hepatoma G2 Cells by Inducing Apoptosis and Autophagy. *WJG* **2010**, *16* (34), 4281.

70) Dan, V. M.; Muralikrishnan, B.; Sanawar, R.; J. S., V.; Burkul, B. B.; Srinivas, K. P.; Lekshmi, A.; Pradeep, N. S.; Dastager, S. G.; Santhakumari, B.; Santhoshkumar, T. R.; Kumar, R. A.; Pillai, M. R. Streptomyces Sp Metabolite(s) Promotes Bax Mediated Intrinsic Apoptosis and Autophagy Involving Inhibition of mTOR Pathway in Cervical Cancer Cell Lines. *Sci. Rep.* **2018**, *8* (1), 2810.

71) a) Surviladze, Z.; Sterk, R. T.; DeHaro, S. A.; Ozbun, M. A. Cellular Entry of Human Papillomavirus Type 16 Involves Activation of the Phosphatidylinositol 3-Kinase/Akt/mTOR Pathway and Inhibition of Autophagy. *J. Virol.* **2013**, *87* (5), 2508–2517. b) Tanida, I.; Ueno, T.; Kominami, E. LC3 and Autophagy. *Methods Mol. Biol*. **2008**, *445*, 77–88.

72) a) Bjørkøy, G.; Lamark, T.; Pankiv, S.; Øvervatn, A.; Brech, A.; Johansen, T. Chapter 12 Monitoring Autophagic Degradation of P62/SQSTM1. *Meth. Enzymol.* **2009**, *452*, 181–197. b) Mattoscio, D.; Medda, A.; Chiocca, S. Human Papilloma Virus and Autophagy. *IJMS* **2018**, *19* (6), 1775.

73) Mizushima, N. Chapter 2 Methods for Monitoring Autophagy Using GFP-LC3 Transgenic Mice. In *Meth. Enzymol.* **2009**, *452*, 13–23.

74) Edmondson, J. M.; Armstrong, L. S.; Martinez, A. O. A Rapid and Simple MTT-Based Spectrophotometric Assay for Determining Drug Sensitivity in Monolayer Cultures. *J. Tissue Cult. Methods* **1988**, *11* (1), 15–17.

Chapter II

Part I:

Design and Synthesis of Indene Fused Sugar Nucleosides as Potential Antiviral Agents for Covid-19

Part II:

Synthesis and Antiviral Activity of 7-[(2-Hydroxyethoxy)Methyl]Pyrrolo[2,3-d]Pyrimidine Nucleoside Derivatives

2.1.1 Introduction

In 2019, when the SARS-COVID (Novel Severe Acute Respiratory Syndrome Corona Virus Disease) outbreak occurred, everyone witnessed the huge disaster caused by a small virus, and ever since then, the whole world has been fighting against this deadly virus. The first case of COVID-19 was reported in China in December 2019 and after that, the Chinese government and researchers acted quickly to control the pandemic and conducted etiological studies.[1] On 31st December, China informed World Health Organization (WHO) about the cases of unknown etiology pneumonia discovered in Wuhan, Hubei Province, China. Then, on 23rd January 2020, the Chinese government announced a lockdown in Wuhan city (**Fig. F2.1**). After that, the World Health Organization (WHO) declared the severe acute respiratory syndrome coronavirus 2 (SARS-CoV-2) epidemic a public health emergency of international concern (PHEIC) on January 30, 2020. On February 11, 2020, the WHO formally designated the current coronavirus disease outbreak as Coronavirus Disease-2019 (COVID-19) and on the same day, COVID-19 was named as severe acute respiratory syndrome coronavirus 2 (SARS-CoV-2) by the international committee on taxonomy of viruses.[2] According to World Health Organization, as of 25th October 2023, there have been 771,549,718 confirmed cases of COVID-19, with 6,974,473 cumulative deaths. According to Gralinski and Menachery, SARS-COVID-19 is the third zoonotic human coronavirus of the century.[3]

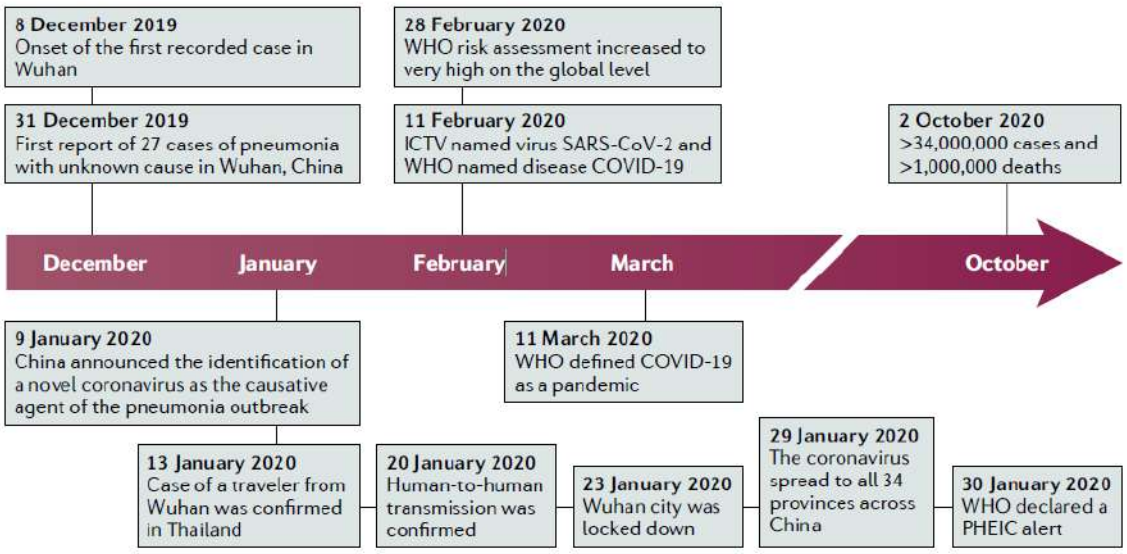

Figure F2.1: *A timeline of the important events in the COVID-19 epidemic*[2]

2.1.2 Origin of SARS-CoV-2

The origin of SARS-CoV-2, the virus that causes COVID-19, has been the focus of intense scientific investigation and studies. In order to identify the virus's origin, surveys and studies were carried out in China. Various techniques employed in the research are listed below.[13]

1) Sample collection
    a) Environmental samples
    b) Animal samples
    c) Sewage (silt) samples
2) Nucleic acid extraction
3) SARS-CoV-2 real-time PCR assay
4) Animal coronavirus test
5) Metagenomic sequencing of positive samples
6) Serological testing
    a) SARS-CoV-2-specific antibody screening
    b) SARS-CoV-2-specific antibody confirmation

Depending upon the results, the most accepted concept for SARS-Cov-2 origin is zoonotic spillover (natural origin). It's well-established that many emerging human infectious diseases have animal reservoirs, both in the wild and among domesticated animals. These diseases, known as zoonoses, are transmitted from animals to humans and can lead to significant public health challenges. Pathogens such as bacteria, viruses, parasites, and fungi that can move from animals to humans cause zoonotic diseases. Wildlife such as monkeys, bats, birds, and rodents can act as natural reservoirs for a variety of zoonotic diseases.[5] These pathogens can also be found in domesticated animals such as chickens, camels, and others.[6] Direct contact with infected animals or their body fluids, intake of contaminated animal products, or transmission via intermediary hosts are all possible modes of transmission.

In recent years, for example, A/H7N9, A/H5N6, A/H5N1, and other avian influenza viruses (bird flu) have infected humans following cross-species transmission from live birds, particularly from poultry to humans and according to recent publications,

the henipa viruses have emerged in humans via domesticated intermediate hosts (horses) after being transmitted from bat reservoir hosts. Rabies is frequently spread through the bite of an infected animal. Lyme disease is carried by ticks that prey on mammals such as deer. Some of the most serious emerging disease threats to human health and economic growth have been caused by these and other zoonotic viruses.

According to reports, it is possible that SARS-CoV-2 began in bats and spread to humans via an intermediate host species. It is believed that the virus spread from bats to another animal species, which then passed it on to humans, probably in China's seafood market in Wuhan. The intermediate host has not been discovered definitively, however, it could include species like pangolins. In the past, this zoonotic spillover scenario has been the source of other coronaviruses such as SARS and MERS (**Fig. F2.2**).[4]

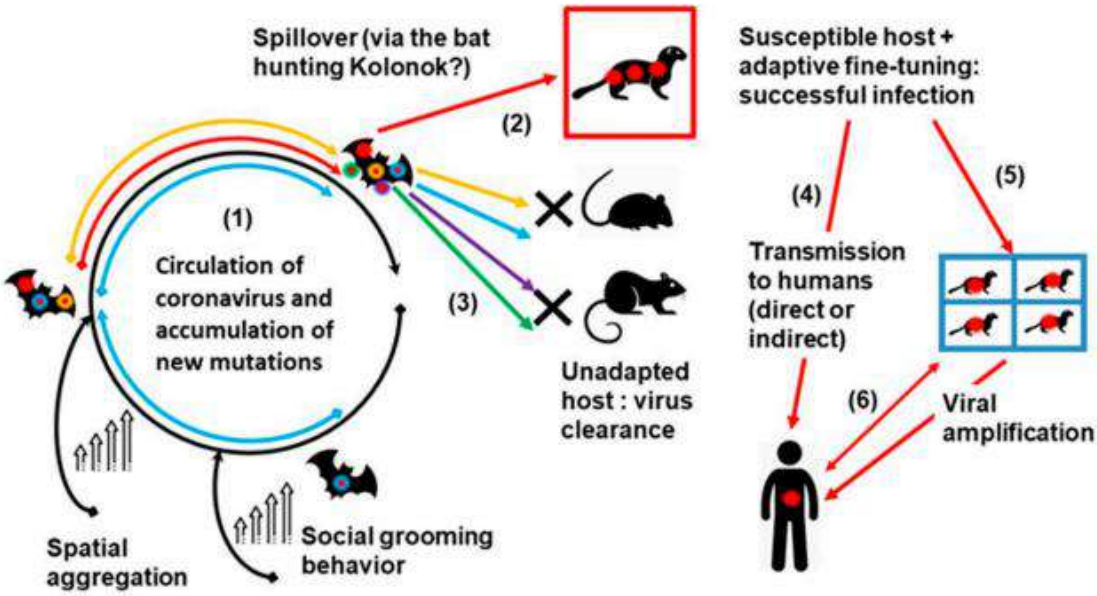

Figure F2.2 *Overall schema for various emergence paths, giving a conceptual framework for SARS-CoV-2 emergence route. The animals illustrated are animal species that have been addressed in regard to potential infection, but other species can be substituted.*[4]

While it is unknown how precisely individuals were exposed to the hypothesized wildlife reservoir or possible intermediary hosts of SARS-CoV-2, there are a number of plausible spillover paths that appear to be supported by circumstantial evidence. It's possible that bats directly transmitted the virus to people, or, as in the cases of MERS-CoV and probably SARS-CoV, there may have been an intermediary host involved.

domesticated cats, rabbits, pangolins, Mink, and raccoon dogs are examples of candidate intermediate host species that may harbor the SARS-CoV-2 virus [8] as well as species like civets, ferret badgers, and related musselids that have been shown to harbor the virus during the Guangdong Province, China outbreak.[7] Animal products, excrement, or intermediary hosts can all operate as direct or indirect vectors for the spread of viruses from infected animals to people.[7]

As a result, the research that has been done thus far has been limited to the Huanan market and has included a thorough sample plan that takes these transmission channels into consideration. These scientific tenets served as the foundation for the Huanan Market investigation. This describes the emphasis on animals and animal-derived products. The introduction of the virus by sick individuals elsewhere or exposure to tainted animal meat or food products that are refrigerated or frozen are two more possible pathways for the establishment of SARS-CoV-2 in individuals connected to the Huanan market in late 2019. Imported frozen or refrigerated fish products have been connected to three recent COVID-19 outbreaks in China.[9-13]

2.1.3 The structure of COVID-19

Coronaviruses are members of subfamily Coronavirinae. The four genera that make up the subfamily Coronavirinae of the Coronaviridae family are Deltacoronavirus, Gammacoronavirus, Betacoronavirus, and Alphacoronavirus. Compared to other RNA viruses, the genome of CoVs is the largest, measuring 27–32 kb. It is a singles-tranded positive-sense RNA (+ssRNA). According to Brian and Baric (2005), the nucleocapsid protein (N) forms the capsid outside the genome, and the envelope that surrounds it is packed with three structural proteins: envelope protein (E), spike protein (S), and membrane protein (M) (**Fig. F2.3**).[14] SARS-CoV-2 is composed of sixteen nonstructural proteins (nsp1–16) and four structural proteins (S, E, M, and N).

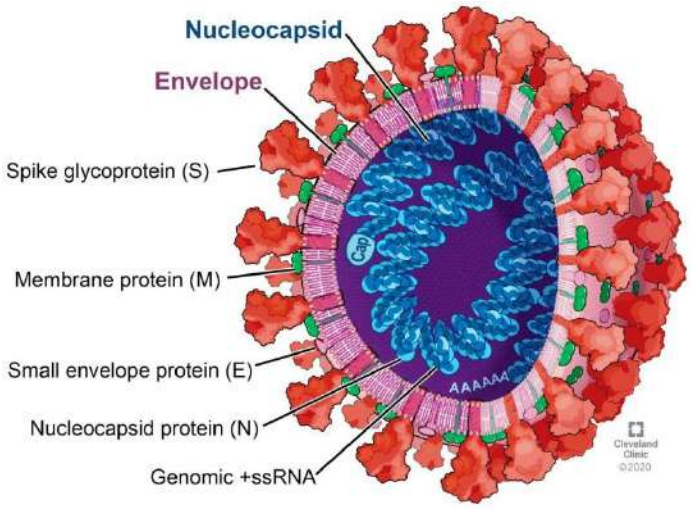

Figure F2.3: *Structure of Corona virus*[14]

a) **Spike Proteins (S)**: Under electron microscopy, these are the noticeable projections on the virus's surface that give it the appearance of a "crown" or "corona". For the virus to bind to and penetrate host cells,[1] the spike proteins are necessary. Neutralizing antibodies primarily target them, and the COVID-19 vaccine is based on them.

b) **Envelope (E) Proteins**: Essential membrane proteins involved in viral assembly and release are called envelope proteins.

c) **Membrane (M) proteins**: These are an additional class of structural proteins that are involved in the assembly and shape of the virus.

d) **Nucleocapsid (N) proteins**: The nucleocapsid (N) proteins are responsible for binding to the viral RNA and forming the genetic material-protein complex that forms the virus's core.

e) **Single-stranded RNA**: It is one strand of RNA that makes up the coronavirus genome, which contains all of the genetic information required for the virus to multiply and make viral proteins.

f) **Lipid Envelope**: The host cell membrane serves as the basis for the lipid bilayer that envelops the virus. The spike, envelope, and membrane proteins are embedded in this envelope.

g) **Genome**: The genes encoding different structural and non-structural proteins, such as those involved in transcription and replication, are found in the coronavirus genome.

Spike proteins are especially important because they form the crown-like structure on the surface of the virus. They engage with receptors on the host cell membrane to let the virus enter the cell more easily. For the antiviral therapies and development of vaccines, it is necessary to understand the nature and structure of spike proteins.

2.1.4 Mechanism of Infection of SARS-CoV-2:

Currently, the processes underlying the infection caused by SARS-CoV-2 remain unclear. However, they appear to resemble those put forth for other coronaviruses.[15] According to one concept, the virus attaches its S proteins to the host receptor ACE2, a membrane protein that is primarily expressed in the cells of the small intestine and lung. There are multiple phases in the mechanism of infection of SARS-CoV-2, which enable the virus to enter and multiply within host cells. The main steps in the infection process are summarized as follows:

1) **Binding and entry**:
    a) **Interaction with spike protein**: The angiotensin-converting enzyme 2 (ACE2) receptor on the surface of host cells, especially respiratory epithelial cells in the lungs and cells in the small intestine, is bound by the spike proteins (S proteins) on the surface of the virus.[16]
    b) **Activation of TMPRSS2 Protease**: Following binding, the virus can fuse with the host cell membrane and enter the cell for releasing viral gRNA into the cytoplasm and this process occurs due to cellular protease called TMPRSS2 (transmembrane serine protease 2) which cleaves the spike protein. Two different pathways are suggested for this process to occur: the early pathway through the plasma membrane or the late pathway through endosomes. S protein undergoes breakdown by endosomal proteases (e.g., cathepsin L) in the late path and by host plasma membrane proteases (e.g., TMPRSS2) in the early pathway. Availability of these proteases decides the route taken by the virus to enter the cell.
2) **Endocytosis or membrane fusion**: Using Direct Fusion with the host cell membrane (Endocytosis) or cellular absorption, the virus can enter the host cell.

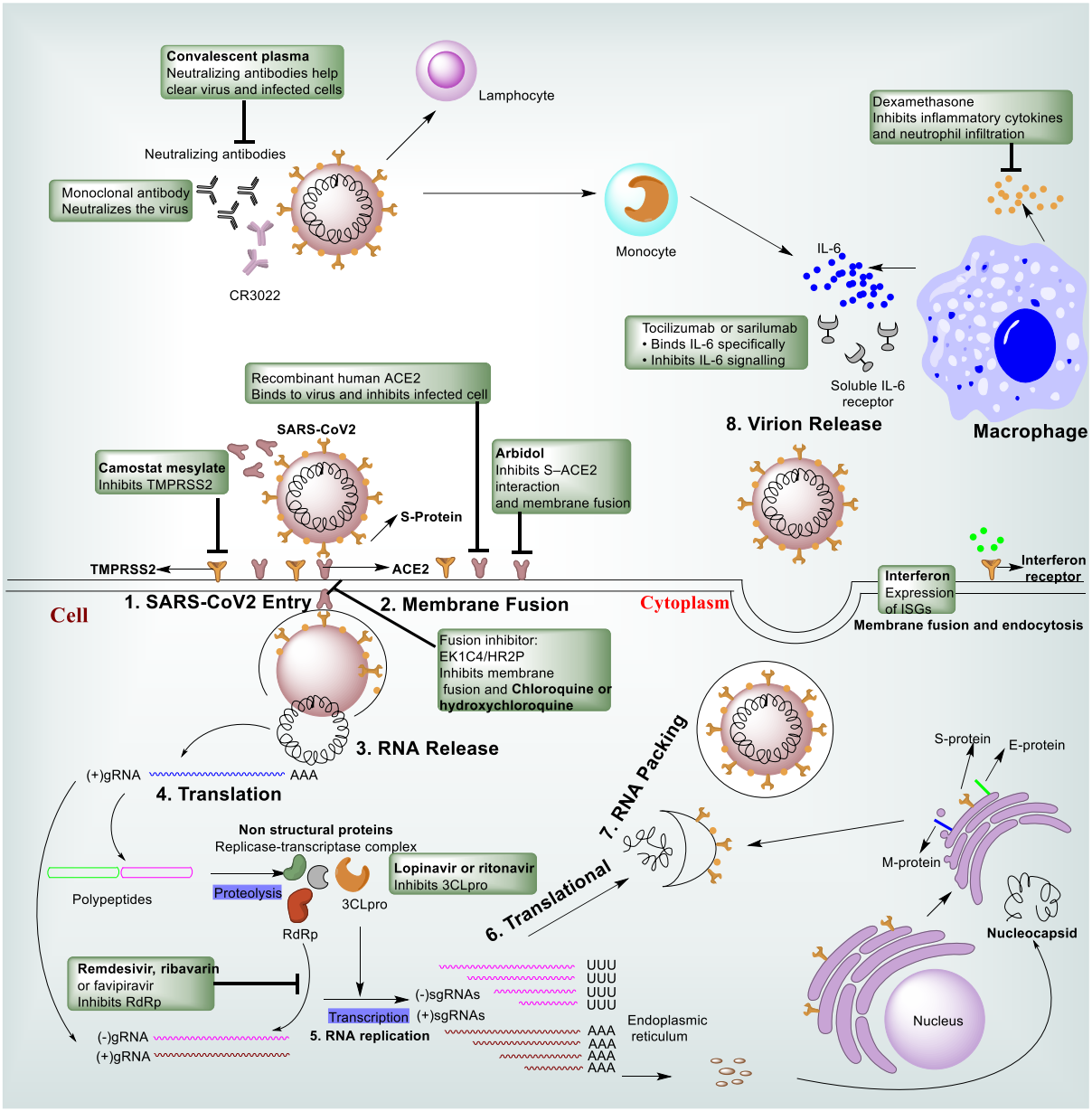

Figure F2.4: *The schematic illustration illustrating the process of COVID-19 entrance, replication, and packaging of viral RNA within the human cell and potential therapeutic targets.*

ACE2, angiotensin- converting enzyme 2; 3CLpro, 3C- like protease; CR3022, a SARS- CoV- specific human monoclonal antibody; E, envelope protein; EK1C4, lipopeptide derived from EK1 which is a pan-coronavirus fusion inhibitor targeting the HR1 domain of the spike protein; HR2P, heptad repeat 2- derived peptides of SARS- CoV-2 spike protein; IL-6, interleukin-6; ISG, interferon- stimulated gene; M, membrane protein; ER, endoplasmic reticulum; gRNA, genomic RNA; TMPRSS2, transmembrane protease serine protease 2; RdRp, RNA- dependent RNA polymerases; sgRNA, subgenomic RNA; S, spike protein.

3) **RNA release**: Once the virus enters the cytoplasm, it releases single-stranded gRNA (genome RNA).
4) **Translation and replication**: The viral polyproteins (pp1a/pp1ab) that are created when gRNA enters the cytoplasm are easily translated into individual Nsps that make up the RTCs (Fig. 2). When these complexes find transcriptional regulator sequences in gRNA, they start to transcribe a number of subgenomic RNAs that code for accessory and structural proteins; if they don't, the entire gRNA is duplicated.
5) **Assembly**: The structural proteins S, E, and M are transported to the ER-Golgi intermediate compartment (ERGIC) during translation, where they undergo post-translational changes such as proteolysis and N-glycosylation. A copy of the N proteins and gRNA bind in the cytoplasm simultaneously to form the nucleocapsid and transfer into the ERGIC. Within this compartment, the nucleocapsid and other viral proteins come together to form a virion.
6) **Release**: The virion then passes through the cytoplasm inside a vesicle and is released from the infected cell by exocytosis through cell lysis or cell bursting.

2.2 Various drugs explored for repurposing or the treatment of COVID-19:

The assessment of currently available medications for new therapeutic uses is known as "drug repurposing, repositioning, retasking, or reprofiling.[17] An existing drug (either investigational or approved), for repurposing efforts already has a safety and toxicity profile that is well-established, due to at least a few fruitful Phase I or Phase II clinical trials.[18] When taking into account the entire process, it has been calculated that the costs and time to bring a repurposed drug to market are ten times lower than those of a new drug, with the time being cut in half.[18] drug repurposing has many benefits over creating a new drug from scratch, even though the clinical phase III and regulatory requirements are still the same. These benefits include a shorter development period and lower development costs, a lower failure rate, and a centralized pharmaceutical supply chain for the production and delivery of effective drugs to the patients who actually need them.[19]

The coronavirus has been continuously evolving over the past three years, unleashing itself in mutated forms after certain intervals in the form of new variants, which have higher transmission capabilities thus causing a large number of deaths. The variants of COVID-19 include alpha, beta, gamma, delta, and omicron etc.[20] Many medications were investigated for possible repurposing in the treatment of the COVID-19 pandemic as it developed and Several host and viral molecular proteins have been investigated as possible therapeutic targets in the COVID-19 treatment search. Together with host metabolic pathways and the immunological response, they are involved in all major stages of the viral infection cycle, including cell entry and replication.[21] Here are some targeted drugs, that are under investigation for blocking the main steps of the SARS-Cov-2 virus replication cycle.

1) Viral entry inhibitors:

- **Angiotensin-converting enzyme 2 (ACE2) receptor inhibitor:** The enzyme ACE2 is a type I membrane protein. It is a functional receptor on cell surfaces by which SARS-CoV-2 penetrates host cells and is abundantly expressed in the kidneys, intestine, heart, and lungs before being shed into the bloodstream. It plays a crucial role in the prevention of the development of SARS in the SARS-CoV infection. ACE2 is a component of the renin-angiotensin-aldosterone system (RAAS), which controls blood pressure and fluid balance. The interaction between SARS-CoV-2 and ACE2 has the potential to disturb the regular operation of this system. Furthermore, viral internalization of ACE2 can reduce the availability of functional ACE2 on the cell surface, which may contribute to COVID-19 pathogenesis.

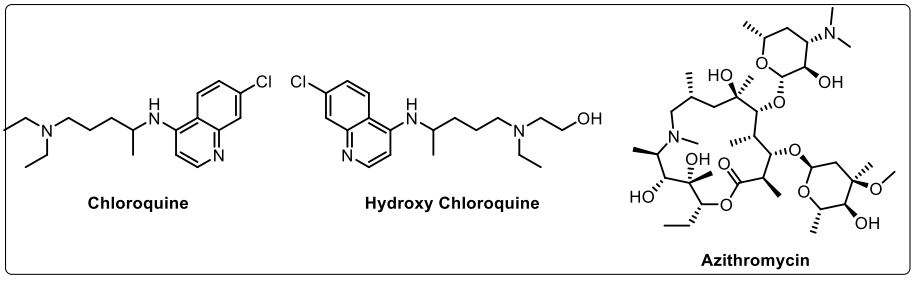

Figure F2.5: *ACE2 and spike binding complex, Endosomal acidification inhibitors*

There is no licensed medication for targeting the ACE2 receptor. Azithromycin, Chloroquine, and Hydroxychloroquine are among the medications that inhibit both ACE2 and the spike binding complex, as well as endosomal acidification.[22]

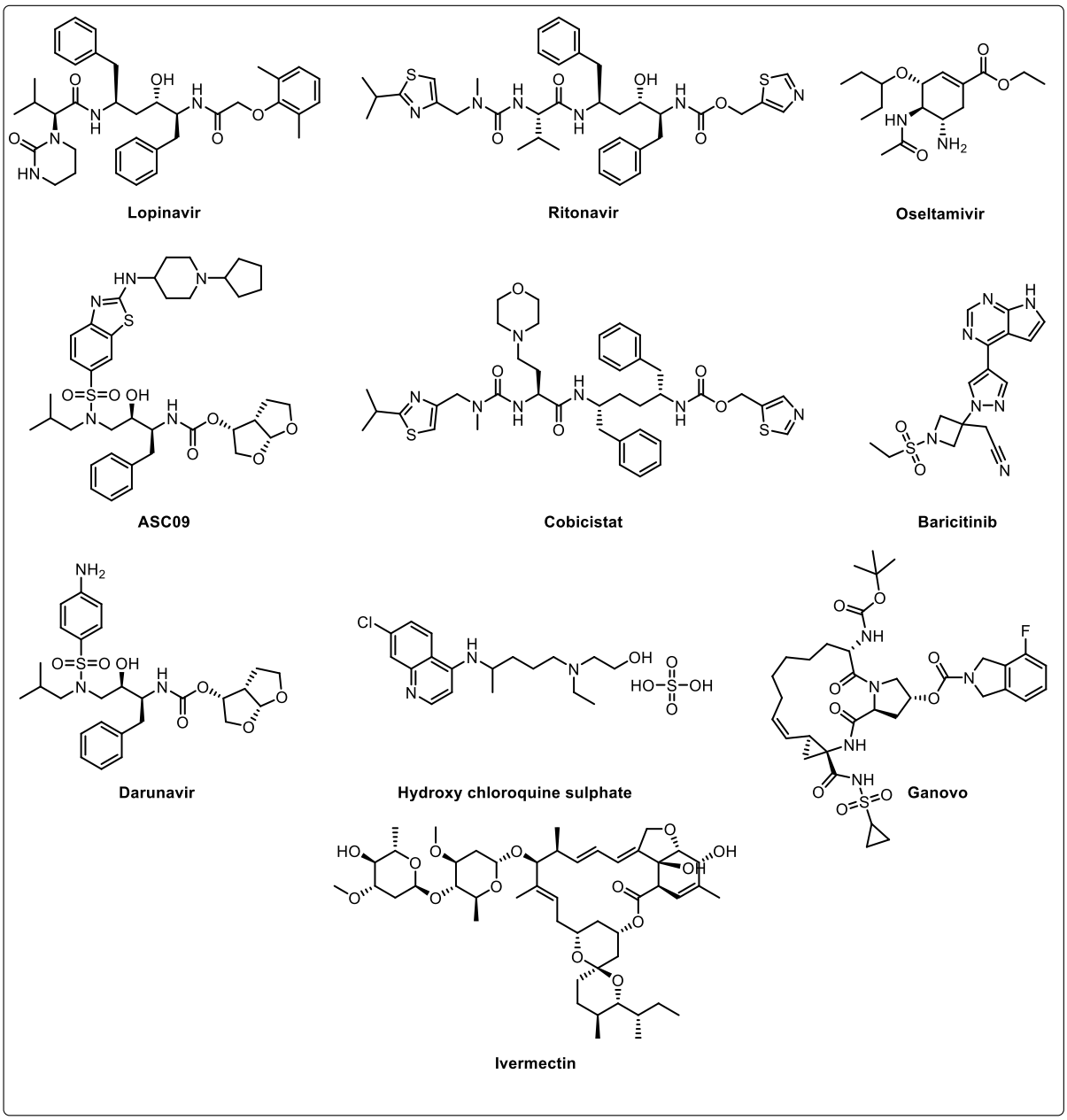

Figure F2.6: *3CLpro inhibitors*

2) Protease inhibitors:

- **3-chymotrypsin-like protease (3CLpro):**

One of the key enzymes in coronaviruses, such as SARS-CoV-2 (the virus that causes COVID-19), is 3-chymotrypsin-like protease (3CLpro), often referred to as the main protease (Mpro). It is a cysteine protease which has a three-domain structure. It has an active site that cleaves polyproteins made from the viral RNA, this protease contributes significantly to the viral life cycle by producing functional viral proteins. In the process of developing antiviral medications, it is important to comprehend and target 3CLpro. Targeting 3CLpro, a number of therapeutic candidates have been studied or are in development. These include novel medications that are made expressly to target the protease, as well as substances like lopinavir and ritonavir, which are protease inhibitors originally developed for the treatment of HIV.[23]

3) RNA-dependent RNA polymerases (RdRp) inhibitors: RNA-dependent RNA polymerase (RdRp) is an RNA viral enzyme that is required for both genome replication and transcription. Despite the variance in their sequences, the basic structural elements of RdRps are maintained. In the presence of divalent metal ions, they catalyze the formation of phosphodiester bonds between ribonucleotides using an RNA template.

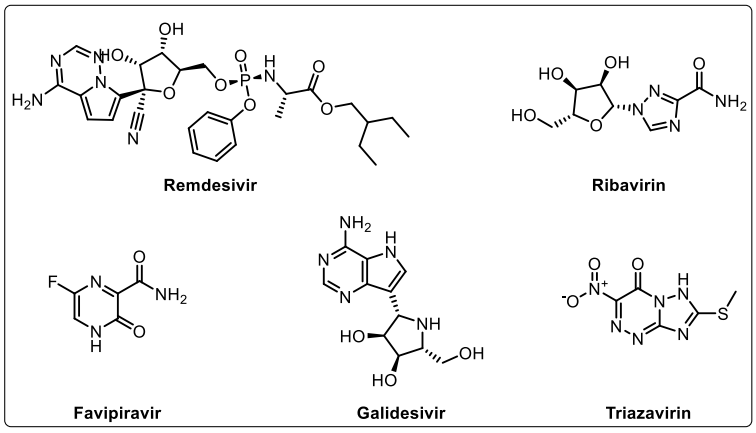

Figure F2.7: *RdRp inhibitors*

The therapeutic importance of inhibiting RdRp activity has led to the development of numerous inhibitors that have been used to treat a variety of RNA viruses, including Ebola, HIV, and the Zika virus. Although RdRp inhibitors can exert antiviral effects in a variety of ways, one significant manner in which these medicines impede RNA viral genome replication is by competing with adenosine triphosphate. When these RdRp inhibitors are metabolized, they compete with viral ATP molecules for inclusion into the nascent RNA strand. The RNA synthesis process is interrupted after the RdRp medication replaces ATP in the new strand, halting further virus multiplication. Tocilizumab, Remdesivir, Ribavirin, Galidesivir, Triazavirin, and Favipiravir are some well-known RdRp inhibitors.[24]

4) Helicase inhibitors: Helicases are enzymes that help unwind viral RNA during replication. Inhibiting helicase activity can disrupt viral propagation. Small compounds that serve as helicase inhibitors to impair the replication of RNA viruses, including coronaviruses like SARS-CoV-2, have been investigated by researchers. Preclinical research has found some substances with helicase inhibitory action. These include both synthetic and natural substances.[25]

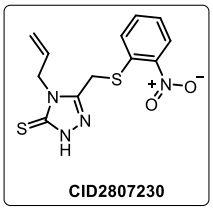

Figure F2.8: *Inhibitors of helicase-catalyzed DNA unwinding*

5) Endosome: Endosomes are important for the infection and growth of some viruses, such as the COVID-19-causing SARS-CoV-2 virus. The binding of the virus to the surface receptors of the host cell, specifically the angiotensin-converting enzyme 2 (ACE2) receptor, is the first stage of a SARS-CoV-2 infection. Following this binding, the virus can enter the host cell by invagining the cell's plasma membrane to generate vesicles known as endocytic vesicles, a process known as endocytosis. The virus is encased within these membrane-bound structures, referred to as early endosomes, once it has entered the endocytic vesicles. Thus, the virus enters the cell through these endosomes. MVBs, or

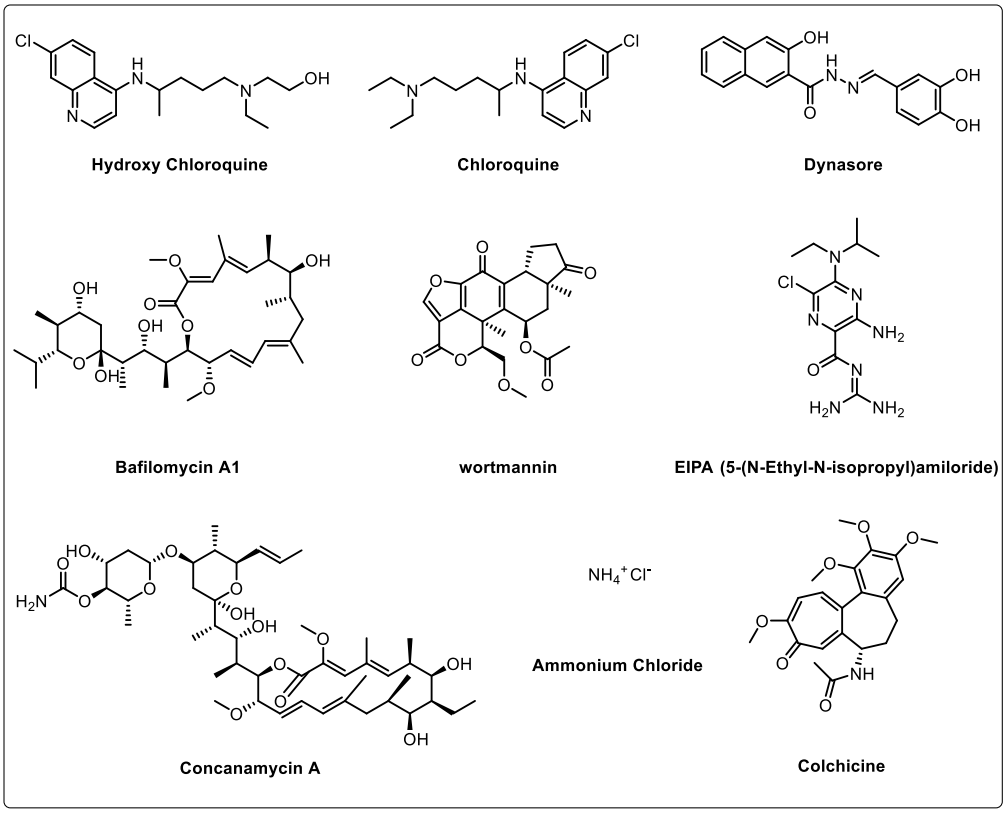

Figure F2.9: *Endosome inhibitors*

multivesicular bodies are late endosomes that develop from early endosomes during the endocytic process. The virus is further sorted and trafficked by these late endosomes. The fate of a virus within an endosome might change based on the type of virus and the cellular environment. Sometimes the virus-containing late endosomes might combine with lysosomes, which are organelles that have different enzymes for breakdown. The virus may be destroyed as a result of this fusion, stopping its spread. Alternatively, the virus can manage to break free from the endosome and evade destruction. SARS-CoV-2 is one of the viruses that can exit the endosome and enter the cytoplasm of the host cell, where it can multiply. For the infection process to continue, the virus can encourage its escape from the endosome. Research on possible antiviral medications that target the endocytic pathway and endosomal functions has been prompted by our growing understanding of the role of endosomes in viral infection, especially COVID-19. Potential treatment techniques that aim to limit viral entrance, restrict endosomal escape, or enhance viral breakdown in endosomes have been investigated by researchers.[24]

Substances and medications known as endosome inhibitors obstruct endosome functions, specifically endosomal trafficking, maturation, and endocytosis. These inhibitors have the potential to be applied in therapeutic or research settings, as they can interfere with endosomes' normal functioning.

6) Lysosome inhibitors: Lysosomes are membrane-bound organelles within cells that contain enzymes that break down and digest cellular trash, foreign particles, and infections. They are essential in cellular processes such as autophagy and cellular debris cleaning. The SARS-CoV-2 virus has been seen to interact with lysosomes during its life cycle in the context of COVID-19.

Endocytosed vesicles harboring the virus may then combine with lysosomes after the endocytosis process. Once the virus-containing endocytic vesicles merge with lysosomes, lysosomal enzymes have the potential to destroy the viral components. This fusion with lysosomes is part of the host cell's defense response to destroy and eradicate the invading virus. Autophagy is a cellular process that degrades and recycles cellular components. It can also help the host cell respond to viral infections. According to some research, SARS-CoV-2 infection may have an impact on autophagic processes, and the virus may utilize or modulate autophagy for its own reproduction. During COVID-19, the contact between the virus and lysosomes is a complicated part of the host-viral relationship. Understanding these pathways could help in the development of antiviral therapies. The precise mechanisms and consequences of lysosomal involvement in SARS-CoV-2 infection, however, remain a work in progress.

Lysosome inhibitors are compounds that prevent lysosomes, the cellular organelles responsible for breaking down and digesting cellular waste, foreign particles, and numerous cellular components, from working normally. In the case of virus infections such as COVID-19, lysosome inhibition may impair the virus's capacity to multiply or interact with host cells. It is crucial to highlight, however, that modifying lysosomal activity can have widespread effects on cellular processes, and the use of lysosome inhibitors in a medical context requires careful evaluation due to potential side effects and consequences on normal cellular function.[24]

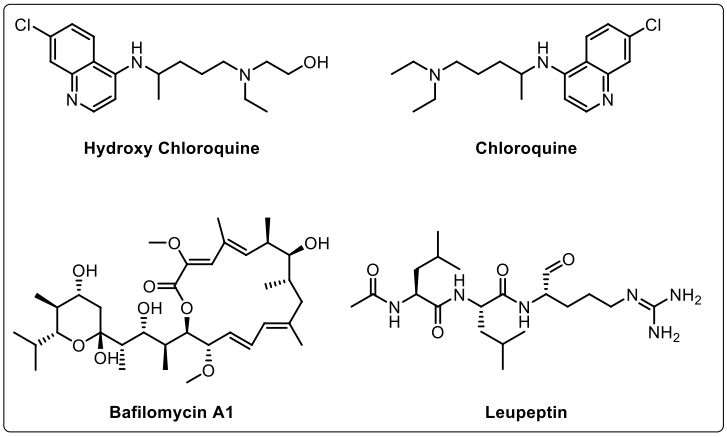

Figure F2.10: *Lysosome inhibitors*

7) Host immune response modulators: Host immune response modulators are a family of medications that try to modify the activity of the immune system. Modulation of the host immune response is a critical field of research in the context of viral infections such as COVID-19. The goal is to balance the immunological response, boosting the ability to combat the virus while limiting excessive inflammation and immune-mediated harm. Here are some techniques and drugs that come into the area of host immune response modulators:

- **Cytokine Inhibitors:**

They target pro-inflammatory cytokines such as tumor necrosis factor-alpha - TNF-, and interleukin-6 - IL-6. To minimize excessive inflammation, it inhibits the activity of particular cytokines. Tocilizumab and sarilumab, for example, target IL-6 and are used to treat severe COVID-19 instances.

- **Interferons:**

They target interferon-alpha and interferon-beta and promote the antiviral response by increasing the synthesis of interferons, which play an important role in the body's fight against viruses. Interferon-based therapy has been investigated in the context of COVID-19.

- **Janus Kinase (JAK) Inhibitors:** They inhibit Janus Kinase enzymes, which are important in cytokine signaling. JAK inhibitors such as baricitinib and tofacitinib have been studied for their ability to reduce the inflammatory response to COVID-19.

- **Modulators of the Bradykinin Receptor:**

They target bradykinin receptors and modulate the bradykinin pathway, which has been linked to inflammation and increased vascular permeability. Drugs such as icatibant have been investigated for their ability to manage the immune response to COVID-19.

- **Complement System Inhibitors:**

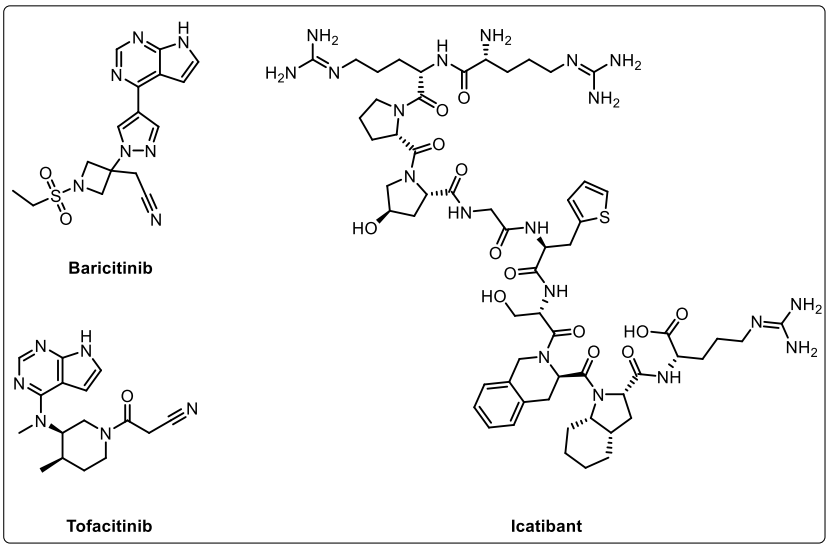

Figure F2.11: *Host immune response modulators*

They specifically target complement system components by inhibiting the complement system, which is involved in the immunological response. Complement inhibitors may be useful in preventing excessive inflammation. In COVID-19, research is being conducted to investigate their potential.[26]

8) Anti-inflammatory Agents:

Anti-inflammatory drugs have been the subject of substantial study and clinical trials in the context of COVID-19. The idea behind utilizing these medications is to control the immune response and lessen the excessive inflammation associated with severe forms of the condition. The following anti-inflammatory medications have been researched or used to treat COVID-19:

Corticosteroids:

Corticosteroids, such as Dexamethasone, are potent anti-inflammatory medications that inhibit the immune system. Which has been demonstrated to decrease mortality in

severe COVID-19 cases. It is advised to use it in hospitalized patients who require supplementary oxygen or mechanical breathing.

Inhibitors of Interleukin-6:

IL-6 is a cytokine that promotes inflammation. To combat the effects of high IL-6 activity, IL-6 inhibitors such as tocilizumab and sarilumab are utilized. They have been used in some cases with severe COVID-19, particularly when a cytokine storm is present.

Inhibitors of JAK:

Cytokine signaling is disrupted by Janus Kinase (JAK) inhibitors such as baricitinib. Baricitinib has been approved for use in specific situations after being studied for its possible anti-inflammatory properties in COVID-19.

Colchicine:

Colchicine is an anti-inflammatory medication that prevents microtubule polymerization. In COVID-19, it was evaluated for its prospective advantages and demonstrated some efficacy in lowering the risk of severe outcomes in some populations.

Non-steroidal anti-inflammatory Drugs (NSAIDs):

Ibuprofen and aspirin are examples of nonsteroidal anti-inflammatory drugs (NSAIDs). NSAIDs act by blocking enzymes that are involved in the generation of inflammatory mediators. Individuals are encouraged to follow healthcare instructions when using NSAIDs in COVID-19.[27]

9) Cellular Protease Inhibitors:

- **Transmembrane serine protease 2 (TMPRSS2) inhibitors**:

(TMPRSS2) is a cell surface protein that is mostly expressed throughout the respiratory and digestive systems by endothelial cells. A serine protease called TMPRSS2 is essential to the entry of some viruses such as SARS-CoV-2, the virus that causes COVID-19 into host cells. Reducing viral replication and infection may be possible by blocking TMPRSS2 entrance. TMPRSS2 participates in the proteolytic cleavage of some viruses' spike proteins, such as SARS-CoV-2. This cleavage is required for the virus to fuse with the membrane of the host cell and enter the cell. One possible COVID-19 therapy approach is the suppression of TMPRSS2. The degree of the infection can be decreased by preventing the virus from entering host cells by inhibiting TMPRSS2.

Numerous medications and substances have been studied for their potential to inhibit TMPRSS2. Nafamostat, gabexate, bromhexine, and camostat mesylate are a few of them.[28] Clinical investigations have evaluated the effectiveness of these medicines in lessening the severity of COVID-19. To increase the efficacy of COVID-19 treatment, some treatment approaches entail combining TMPRSS2 inhibitors with additional medications, such as remdesivir or monoclonal antibodies. To ascertain the safety and effectiveness of TMPRSS2 inhibitors in the context of COVID-19, investigations and clinical trials are being conducted.

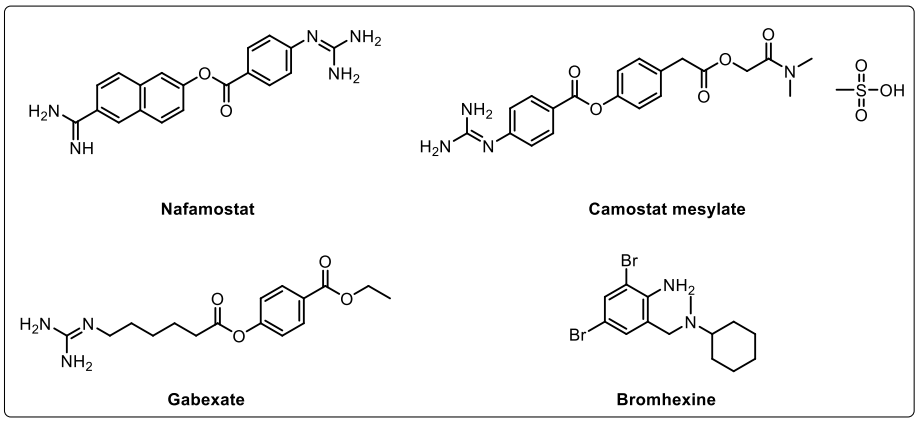

Figure F2.12: *TMPRSS2 inhibitors*

10) Papain-like protease (PLpro) Inhibitors: SARS-CoV-2, the virus that causes COVID-19, is one of the coronaviruses that encodes the papain-like protease (PLpro). One key enzyme in the digestion and replication of viral polyproteins is called PLpro. The PLpro is responsible for cleaving viral polyproteins at specific sites in coronaviruses like SARS-CoV-2. These huge precursor molecules, known as polyproteins, are first translated from the viral RNA and have several different functional domains. The release of specific functional viral proteins, including those required for viral replication, depends on the cleavage by PLpro. Viral transcription and replication depend on non-structural proteins that are released when PLpro cleaves polyproteins. The replication-transcription complex (RTC) and other viral processes are mediated by these proteins. The host immune response may be evaded in part via PLpro. As a component of the innate immune system's defense

against viral infections, it has the ability to cleave specific host cell proteins implicated in the interferon response.

Antiviral medication development may aim to target the papain-like protease. A method to impede the viral life cycle and possibly treat COVID-19 is the use of inhibitors that target the PLpro specifically. The purpose of these inhibitors is to prevent the protease from doing its job and hinder the spread of viruses. The papain-like protease's three-dimensional structure has been thoroughly defined, which has made it easier to design and create possible inhibitors. Targeting PLpro, inhibitors seek to obstruct this enzyme activity, which in turn prevents the spread of the virus. Chemical library screens have discovered certain natural products or chemicals, such as famotidine, GL0617, and ebselen are PLpro inhibitors.[29]

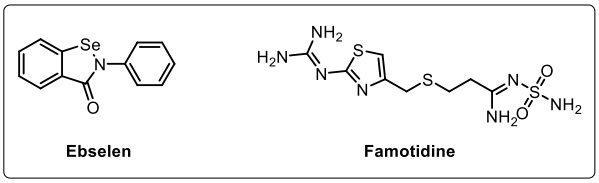

Figure F2.13: *Papain-like protease inhibitors*

11) Nucleocapsid N protein inhibitors: The key structural protein with multiple critical roles in the life cycle of the SARS-CoV-2 virus that causes COVID-19 is the nucleocapsid (N) protein. The complex of the N protein attached to the viral genomic RNA

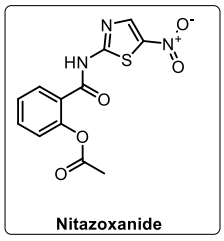

is called a nucleocapsid, and it is formed by the N protein. The virus's nucleocapsid structure gives it structural stability. The N protein encloses and shields the viral genome by binding to the SARS-CoV-2 viral RNA. The integrity of the viral RNA depends on this interaction. Both viral genome transcription and replication involve the N protein. In the course of the virus's replication cycle, it contributes to the production of new viral RNA. During the construction of the virus, the N protein helps pack the viral RNA into newly

formed virus particles. Infectious virus particles need this in order to be produced. The host's immune system may be triggered by the N protein, which could result in the development of antibodies. Because of this, the host's immune system targets the N protein, and COVID-19 diagnostic tests can identify antibodies directed against the N protein.

In order to comprehend the structure, reproduction, and immunological response of the virus, researchers are studying its N protein. It has also been investigated as a possible element in the creation of COVID-19 vaccinations. Compared to inhibitors that target other viral proteins like proteases or polymerases, those that target the nucleocapsid (N) protein of viruses are less frequent. The N protein lacks enzymatic activity that small compounds can directly target; instead, it functions primarily as a structural protein that encapsulates the viral DNA e.g. Nitazoxanide. Nonetheless, research is still being done to discover antiviral tactics that can subtly affect N protein functions or sabotage the viral life cycle.[30]

12) Monoclonal Antibodies:

- **Spike glycoprotein inhibitors**: Spike glycoprotein, also known as the spike protein, is an essential structural protein present on the surface of a variety of enveloped viruses, including as coronaviruses as the COVID-19-causing SARS-CoV-2. The characteristic spike-like projections on the viral surface are where the word "spike" originates. The immune system, the creation of vaccinations, and the development of antiviral treatments all target the spike protein, which is essential to viral infection. Facilitating the attachment of the virus to host cells is the primary function of the spike protein. The virus is capable of penetrating host cells and infecting them thanks to its receptor-binding domain (RBD), which binds to particular receptors on the cell's surface. The spike protein helps the viral envelope and host cell membrane fuse together, releasing the genetic material of the virus into the cytoplasm of the host cell, after it has bound to the host cell receptor.

The host immune system's response mostly targets the spike protein. The immune system interprets it as foreign, which triggers the creation of antibodies and T-cell reactions. The development of viral immunity depends on this immunological recognition. Distinct coronaviruses have distinct spike proteins, and research has focused on spike

protein alterations, especially during the COVID-19 pandemic. SARS-CoV-2 variants with particular mutations in the spike protein have been found such as fuzheng huayu tablet, n acetyl cysteine, and nitric oxide and their possible effects on transmissibility, vaccination effectiveness, and illness severity have been investigated.[31]

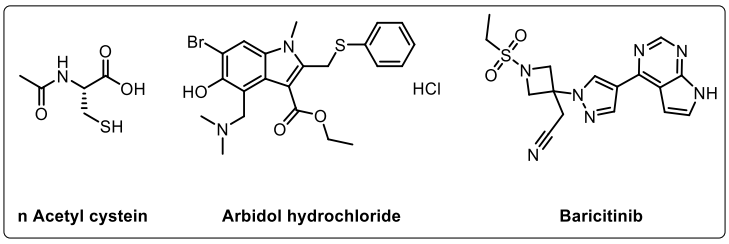

Figure F2.14: *Spike glycoprotein inhibitors*

13) Serotonin-reuptake inhibitors: Neurotransmitters are chemicals that act as messengers between nerve cells in the brain, and serotonin is one such molecule. It is believed to positively impact emotion, mood, and sleep. Serotonin is typically reabsorbed by the nerve cells after conveying a message (referred to as "reuptake").Serotonin transporters and σ-1 receptors are the sites of binding for SSRIs, which reduce inflammation and have anti-COVID actions. Viral entrance and virion assembly may be disrupted by SSRIs through their interaction with σ-1 and acid sphingomyelinase receptors. When compared to other SSRIs, fluvoxamine has a higher binding affinity to s-1 receptors, which has attracted significant scientific interest among the SSRIs under investigation.[28,32]

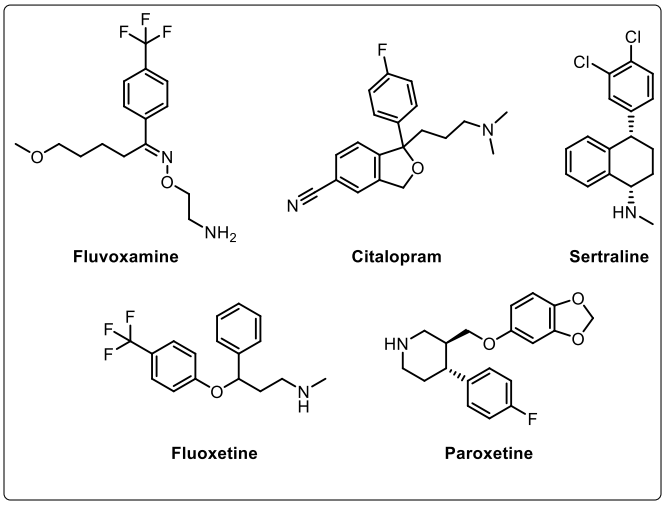

Figure F2.15: *Serotonin-reuptake inhibitors*

2.3 Approved Drugs For COVID-19:

In the COVID-19 drug development program, different preventative therapeutic drugs are being developed to reduce the intensity of COVID-19. Since the start of COVID-19, a number of biotechnology firms, pharmaceutical companies, and health organizations, and along with these, various academic research groups have been doing research to develop possible treatments for COVID-19. They conducted a preclinical and clinical evaluation of 506 candidates in April 2021, employing 419 possible COVID-19 medicines that were in clinical trials.

The process of drug development is a multistep process that normally takes more than five years to check the effectiveness and safety of a new compound. Several national regulatory authorities, including the EMA and the FDA, have approved protocols that accelerate clinical testing, and as a result, a number of medications are now in the third stage of clinical trials. To manage and treat COVID-19, the FDA has approved several drugs and therapeutics which are as follows.

Actemra (Tocilizumab): Tocilizumab is a cytokine inhibitor that targets IL-6 and is intended to reduce chronic inflammation. This drug has been authorized by the FDA for the treatment of COVID-19. It is used in hospitalized patients who are receiving systemic corticosteroids and require non-invasive or invasive mechanical breathing, extracorporeal membrane oxygenation (ECMO), or supplemental oxygen.

Veklury (Remdesivir): Gilead Sciences is a biopharmaceutical company, which developed Remdesivir as an antiviral agent. It is used to treat broad-spectrum antiviral diseases. After the outbreak of the COVID-19 pandemic, the FDA approved it for the treatment of COVID-19 adult patients and pediatric patients (infants 28 days of age and older with a weight of at least 3 kg) who may or may not be hospitalized and have mild COVID-19, as well as those patients who are at high risk of progression to severe COVID-19, which includes hospitalization or death.

Olumiant (baricitinib): It is used to treat rheumatoid arthritis, and the FDA approved it for the treatment of COVID adult patients who require extracorporeal membrane oxygenation

(ECMO), non-invasive or invasive mechanical ventilation, or supplemental oxygen following the COVID outbreak.

Paxlovid (nirmatrelvir and ritonavir): It works as a protease inhibitor. Ritonavir was approved by the FDA to treat mild-to-moderate COVID-19 in people who are at high risk of progressing to severe COVID 19, including hospitalization or death. It is not licensed for use as pre- or post-exposure prophylaxis for COVID-19 prevention.

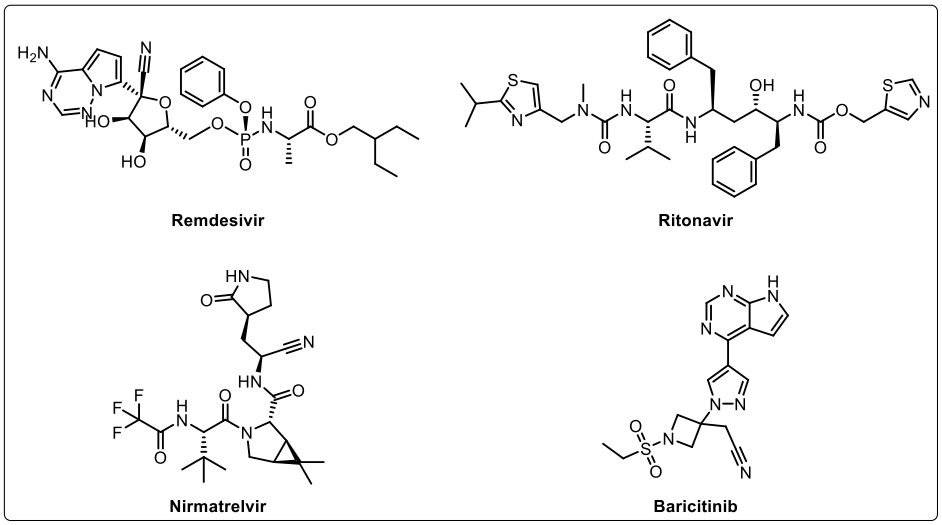

Figure F2.16: *Drugs approved for the treatment of COVID-19*

Even if various medications have been approved, there is still a need for new drugs due to limitations or adverse effects The coronavirus is constantly evolving with new variants. Thus, research in this field should be continued in order to identify a medicine with minimum side effects.

2.6 Results and discussion

In the initial phases of the COVID-19 pandemic, a lot of efforts have been focused on the development or the deployment of new and known nucleoside-based small molecules for identifying potential small molecules to target SARS-CoV-2. Nucleoside analogs are structural mimics of naturally occurring nucleosides and can interfere with viral replication by inhibiting the activity of viral polymerases. Remdesivir, a nucleoside analog, is one of the first drugs to be approved for the treatment of COVID-19 patients in some countries, but its efficacy and side effects warrant further investigation. Apart from this rapid evolution of SARS-CoV-2 mutants posed a significant challenge to the vaccination programs though they played a major role in containing this pandemic. Thus, the development of novel nucleoside analogs tailored specifically to target SARS-CoV-2 presents a significant opportunity to enhance antiviral therapy for COVID-19 and this constitutes as the second objective of this thesis.

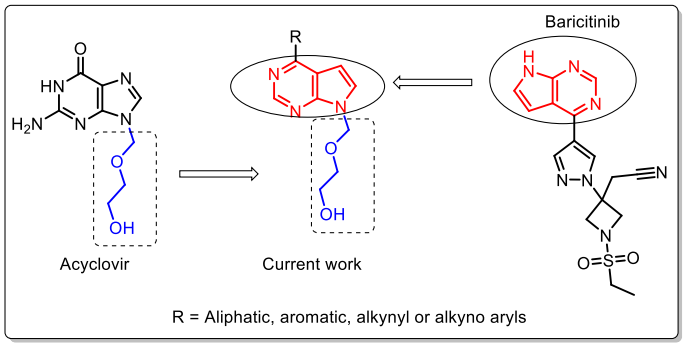

Figure F2.17: *Design of various acyclic pyrrolo(2,3-d)pyrimidine analogues*

In the context of COVID-19, and as a part of the newly initiated antiviral drug discovery program, we have come up with two different scaffolds (Series 1 and Series 2). The first series is funded upon integrating structural features of the acyclovir and JAK-2 kinase inhibitors Ruxolitinib and Baricitinib (**Fig. F2.17**). The basic structural core of baricitinib is pyrrolo[2,3-*d*] pyrimidine (7-deazapurine), which is a heterocyclic structure generated by the fusing of pyrrole and pyrimidine at the ortho position. The skeleton of Pyrrolo[2,3-*d*]pyrimidine is quite similar to that of purine. Thus, they are being used as substitutes for the canonical constituents of DNA and RNA and also engaged in nucleic acid sequencing. Pyrrolo[2,3-*d*]pyrimidine is also an important part of various biocides,

receptor antagonists, enzyme inhibitors, and antiviral nucleosides.[33] Recently various kinase inhibitors have appeared in literature with pyrrrolo[2,3-*d*]pyrimidine as a privileged scaffold.[34] Among them, Janus kinase inhibitors oclacitinib,[35] tofacitinib,[36] ruxolitinib[37] AZD5363,[38] and baricitinib[39] are mainly used for the treatment of myelofibrosis, Rheumatoid arthritis, psoriasis, atopic dermatitis and itchiness (**Fig. F2.18**). Similarly, the pyrrolo[2,3-*d*]pyrimidine acyclic nucleoside analogues exhibit antiviral efficacy against human cytomegalovirus which is the same or better than that of ganciclovir.[40] Especially the discovery of acyclovir[41] and (*S*)-DHPA[42] as anti-herpetic drugs, opened new avenues in the area of non-nucleosidic pyrrolopyrimidines. Thus, after taking inspiration from all of the preceding compounds, new small molecules containing pyrrole(2,3-*d*)pyrimidine have been designed by modifying substituents at the C4 position, and by keeping the acyclic nucleoside fixed at the nitrogen atom of the pyrrole ring. A number of antiviral analogues of 7-deazapurine acyclic nucleosides were produced and evaluated.

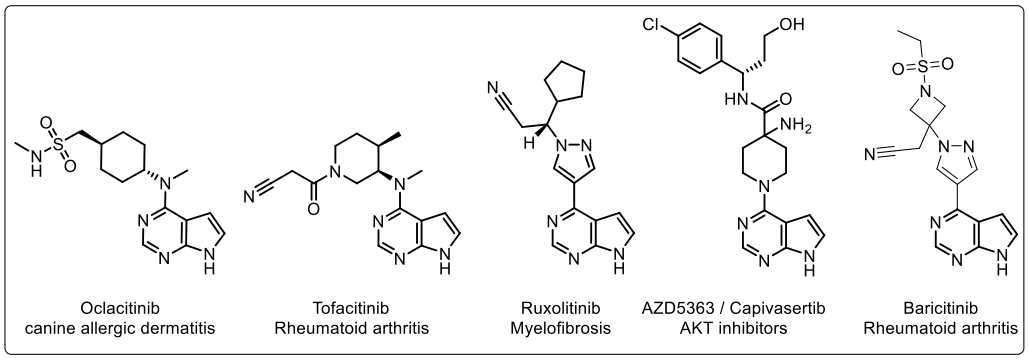

Figure F2.18: *JAK inhibitors composed of pyrrolo[2,3-d]pyrimidine as the primary structural core*

As this series was found to be not promising in terms of the anti-viral activity against SARS-CoV-2, we have come up with a new design and strategy that provided rapid access to the sugar-modified tricyclic nucleoside derivatives. For designing such molecules, we took the help of approved drugs, which are being used to treat COVID-19 with excellent outcomes.[43] These drugs mainly consist of sugar nucleosides, which are the structural subunits of nucleic acids such as DNA and RNA. A nucleoside is composed of nucleobases which is either a pyrimidine base (cytosine, thymine or uracil), a purine base (adenine or guanine), and a five-carbon sugar which is either ribose or a deoxyribose. The nucleoside analogues mimic natural nucleotides (**Fig. F2.19**) to be incorporated into

nascent viral RNA chains and due to structural differences, nucleoside analogues block the elongation of nascent RNA molecules by serving as chain terminators and thus inhibit virus replication. Due to their widespread applications, impressive potency and high barrier to resistance, some antiviral nucleoside analogues are under clinical trials such as remdesivir,[44] Ribavirin[45] and EIDD-1931 (**Fig. F2.19**). [46]

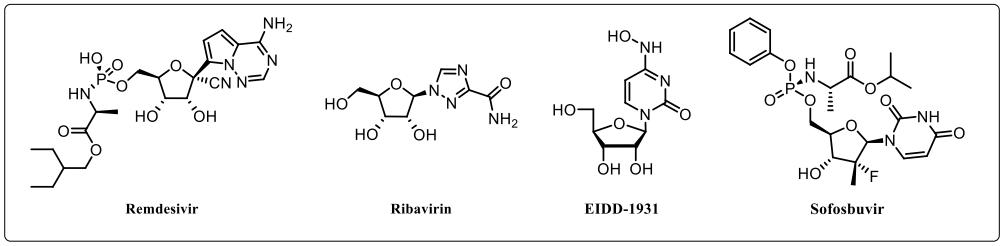

Figure F2.19. *Antiviral nucleosides used for the treatment of COVID-19*

The nucleosides which comprise modified structures, constitute an important class of therapeutic agents,[47] Especially, when we talk about anticancer and antiviral drugs, where the sugar-modified nucleosides are the point of attraction. So, with this frame of reference, certain compounds were designed with a modified carbohydrate part, where the furan ring is conjugated with the indene moiety because there are various Indene conjugated furan molecules that play an important role by exhibiting diverse biological activities such as antibacterial, antiviral, and anti-apoptotic. (**Fig. F2.20**).[48]

Uracil has also been frequently employed as a pyrimidine nucleobase since it is a distinctive component found in a wide range of commercial medications (**Fig. F2.19** and **F2.20**). The natural products having uridine scaffold show a number of biological activities such as antibiotic, antifungal, antiviral, and anticancer.[49] Also the derivatives of uracil, such as thymine and 5-fluoro uracil (5-FU) are broadly used as antiviral[50] and anticancer[51] agents in cytotoxic chemotherapy medication.

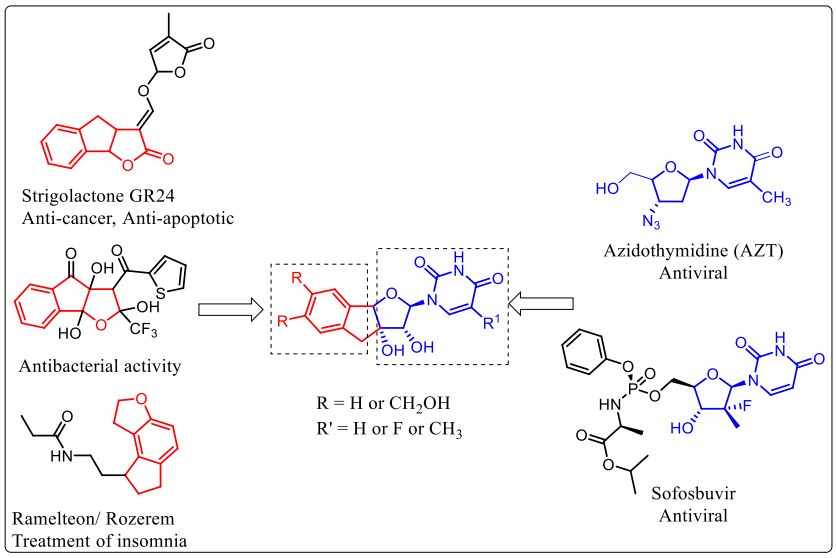

Figure F2.20. *Biologically active Indene and uracil based compounds*

When we compare the designed compound and remdesivir, the common thing is hydroxyl group present at the carbon 3 and according to theory, Remdesivir belongs to the class of non-obligate chain terminators since it should be possible to add more nucleotides to an RNA strand after remdesivir has been introduced because of the presence of the hydroxyl group that is located at the 3rd carbon in the sugar. This idea emphasizes the significance of the targeted molecule **(Fig. F2.21**).

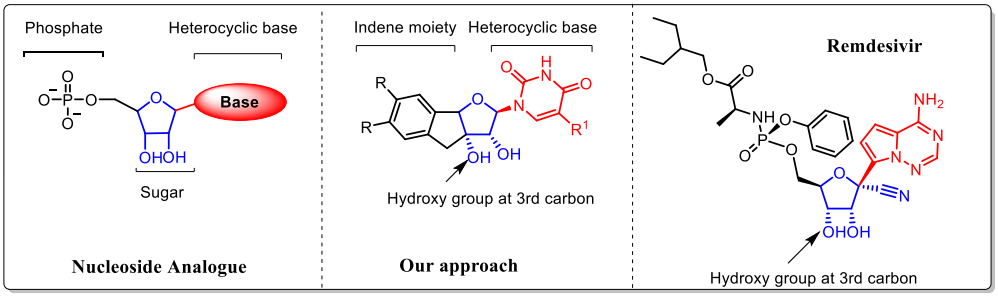

Figure F2.21: *Replacement of phosphate with indene moiety to synthesize new analogues of nucleoside*

2.7 Synthesis of Acyclovir Analogues

The key reactions for the synthesis of pyrrole[2,3-*d*]pyrimidin derivatives are Suzuki coupling for placing an aryl group and a Sonogashira coupling for placing an alkynyl group at the C4 position of pyrrolopyrimidine unit. The synthesis of coupling

partner **9** was carried out by the alkylation of 4-chloro-7*H*-pyrrolo[2,3-*d*]pyrimidine **7** with 2-(chloromethoxy)ethyl benzoate **8** employing NaH in DMF as a solvent (**Scheme S2.1**).

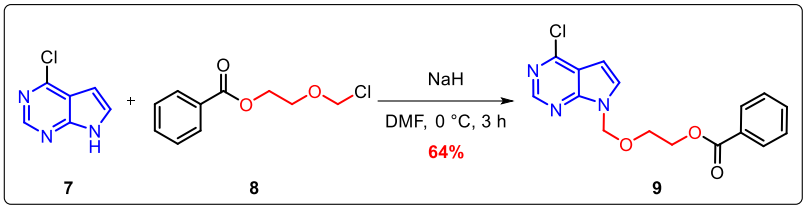

Scheme S2.1. *Synthesis of 2-((4-chloro-7H-pyrrolo[2,3-d]pyrimidin-7-yl)methoxy)ethyl benzoate*

As shown in **Scheme 2.2**, two distinct sets of analogs can be obtained by altering the substituents on the C4 position of pyrrole(2,3-*d*)pyrimidine. The general approach for the synthesis of compounds **13** and **15** is revealed in **Scheme 2.2**. In the first case, arylboronoic acids were intended for C4 coupling. Whereas in the second case, Sonogashira coupling of alkynes has been proposed. After getting the coupling partner **9** in hand, multiple conditions were tested for the Suzuki coupling, and the most favorable condition was utilized for the library synthesis. For the first step i.e. Suzuki coupling, boronic acid **10**, K_2CO_3, and $Pd(PPh_3)_4$ were added to a solution of 2-((4-chloro-1*H*-indol-1-yl)methoxy)ethyl benzoate **9** and toluene and the resulting reaction mixture was heated at 100 °C for 18 h to furnish the product **12** in good yields. For the confirmation of the product, ^1H, ^{13}C, and HRMS spectroscopic techniques were used. In the proton and carbon NMR of compound **12**, five aromatic protons and carbons appeared in the aromatic region. In the HRMS, the exact mass calculated for product **12** was $C_{22}H_{22}O_3N_3$ $[M+H]^+$: 374.1499, and it was found to be 374.1499. Thus, from ^1H, ^{13}C, and the HRMS spectrum, the formation of Suzuki coupling product **12** was confirmed. The compound **12** was then subjected to benzoyl deprotection by using K_2CO_3 in methanol to procure alcohol **13** in good yield. The structure of the final product was confirmed by ^1H, ^{13}C, and HRMS. In the proton spectroscopy, five protons were missing in the aromatic region, and in carbon spectroscopy, six carbons were missing in the aromatic region and one carbonyl carbon which appeared at δ 166 in compound **12** was missing. In the HRMS, the exact mass calculated for product **13** was $C_{15}H_{16}O_2N_3$ $[M+H]^+$: 270.1237, and it was found to be 270.1236. Thus, from ^1H, ^{13}C, and the HRMS spectrum, the formation of 2-((4-phenyl-7*H*-pyrrolo[2,3-*d*]pyrimidin-7-yl)methoxy)ethan-1-ol **13** was confirmed.

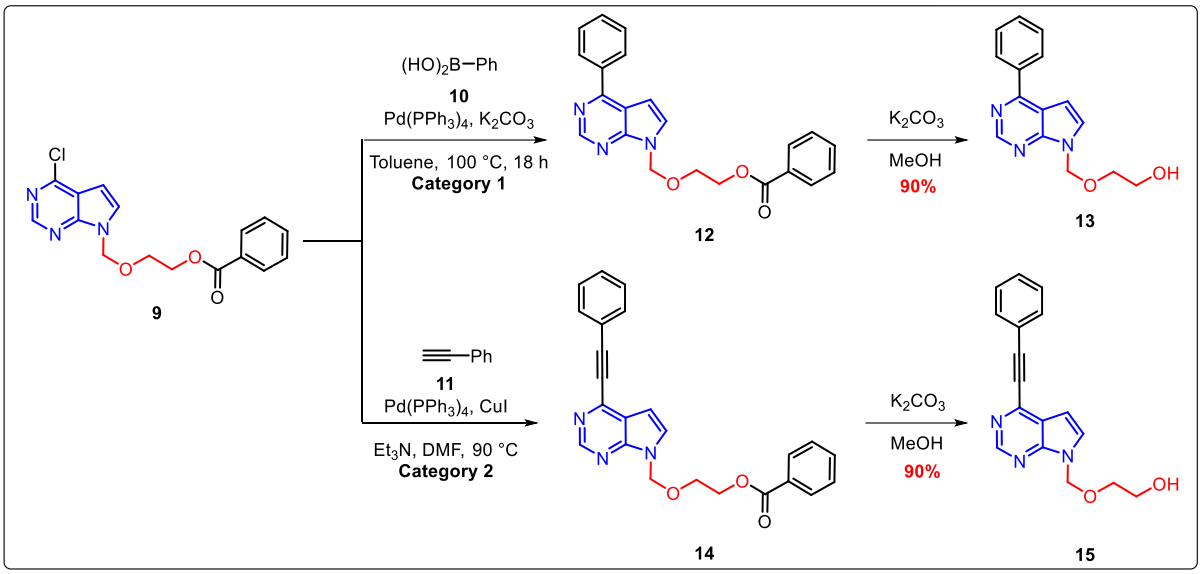

Scheme S2.2. *Synthesis of C4 substituted 2-((7H-pyrrolo[2,3-d]pyrimidin-7-yl)methoxy)ethan-1-ol*

In the second category, alkynyl derivatives were used as substituents at the C4 position. As shown in the **Scheme S2.2**, the first step is the Sonogashira coupling between halide **9** and alkyne **11**. Initial exploration of various conditions led to identify the optimized conditions that are given in **Scheme 2.2**. The employed conditions comprises of carrying the coupling with $Pd(PPh_3)_4$ complex as a catalyst in the presence of CuI as an additive and Et_3N as a base and in anhyd. DMF at 80 °C for 5–24 h depending upon substrate. The resulting compound **14** was then deprotected with K_2CO_3 in methanol to give alcohol **15**. The final product's structure was validated using ^{1}H, ^{13}C, and HRMS.

2.7.2 Exploring the scope of reaction:

As intended, collections of two categories of the molecules have been synthesized by exploring the scope of these reactions, employing different aryl boronic acids for the Suzuki coupling and alkynes for the Sonogashira coupling and subjecting the resulting coupled products for debenzoylation.

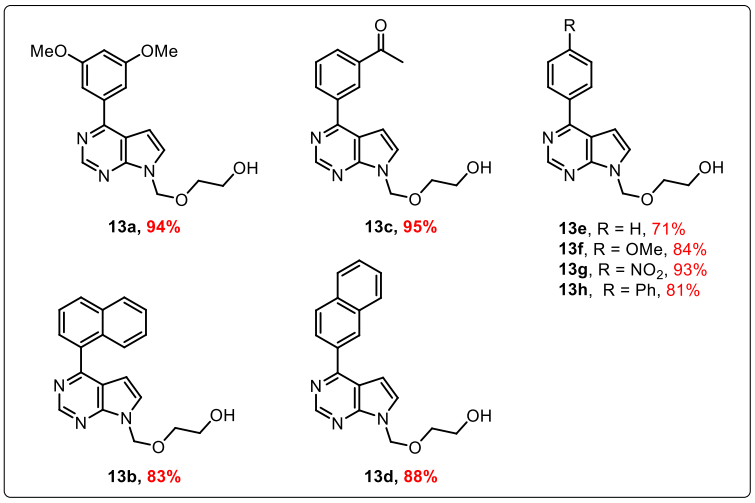

Figure F2.24: *Series 1: 7-[(2-Hydroxyethoxy)methyl]pyrrolo[2,3-d]pyrimidine Nucleosides with aryl substitution at C4 position*

Furthermore, in Category 2, we have investigated the possibility of pendant alkyl and aryl one the coupling alkyne (**Fig. F2.25**). To our delight, the reactions went effectively and the products were obtained in good to excellent yields of corresponding 7-[(2-Hydroxyethoxy)methyl]pyrrolo[2,3-*d*]pyrimidine nucleosides derivatives.

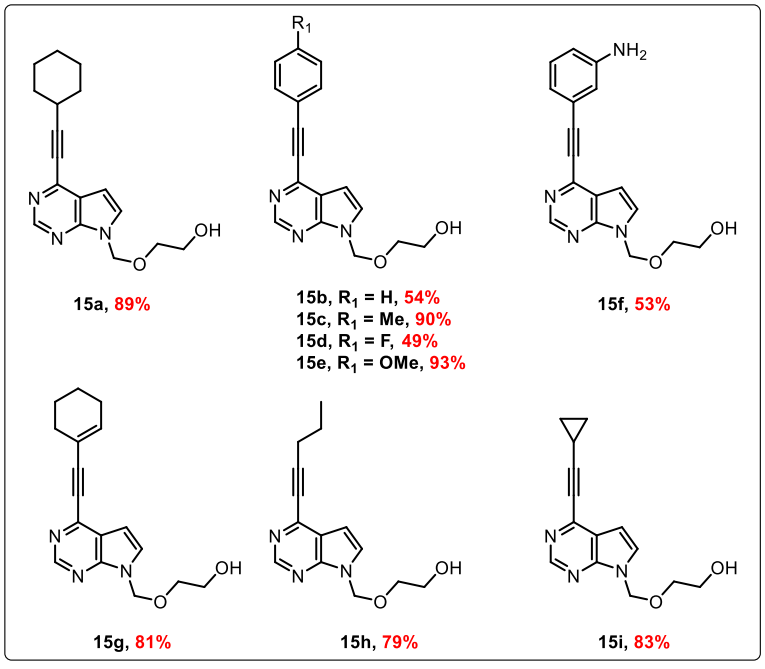

Figure F2.25: *Series 2: 7-[(2-Hydroxyethoxy)methyl]pyrrolo[2,3-d]pyrimidine Nucleosides with alkynyl or alkyno aryl substitution at C4 position*

2.8 Biology - Series 1

The antiviral screening has been carried out at CSIR-IMTech (Chandigarh) employing both RT-PCR Based and Cell Based ELISA for Screening in BSL-3 facility (see the experimental for complete details). Initial antiviral screening of the two series of compounds synthesized revealed they are not active and are non-cytotoxic. These results discouraged us from further exploring these series. However, in search of finding their utility, a brief literature study conducted revealed that the 7*H*-pyrrolo[2,3-*d*]pyrimidine analogues have been previously explored as potential candidates for antibacterial and antimicrobial activities (**Fig. F2.26**).[54]

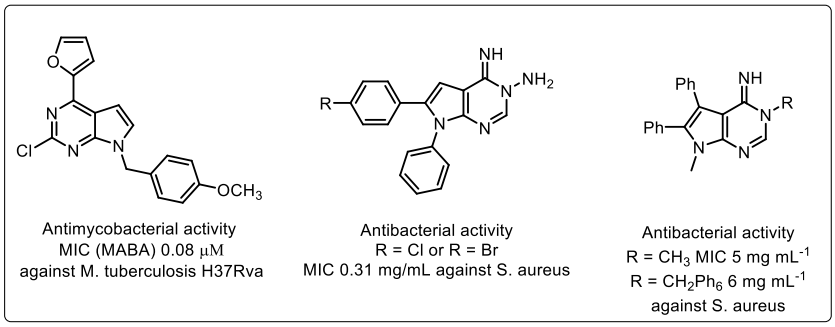

Figure F2.26: *Derivatives of pyrrolo[2,3-d]pyrimidine having antibacterial activity*

This prompted us to screen some of the selected compounds of these two series for their antibacterial activity. Amongst these, three compounds showed good antimicrobial activity against *Staphylococcus aureus* (gram positive bacteria), and the same compounds were not active against *Escherichia coli* (gram negative bacteria). The figures **(F2.27** and **Fig. F2.28)** shows the antimicrobial activity at 100 μg/ml against S. aureus and Escherichia coli.

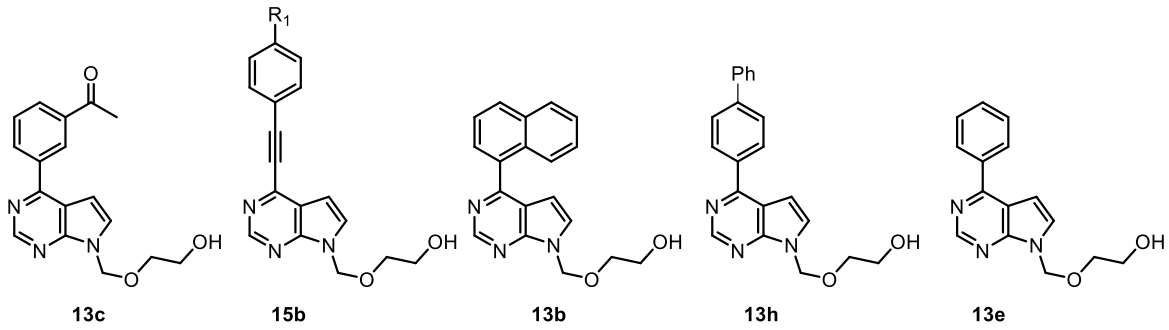

Figure F2.27. Selected compounds for the antimicrobial screening

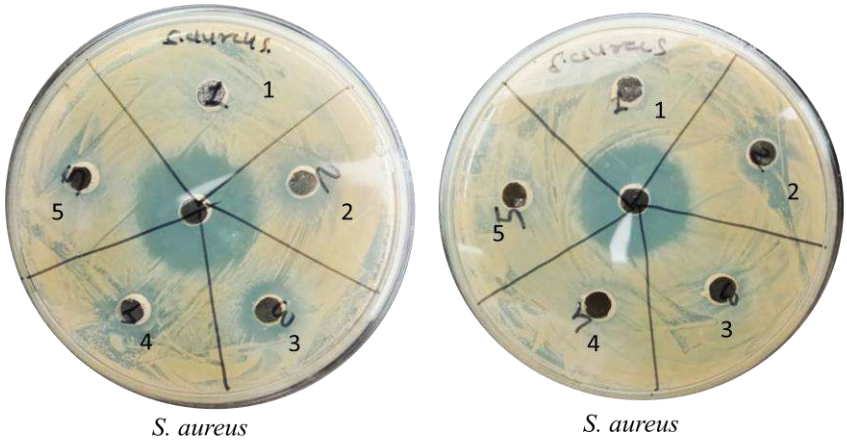

Test compound used: 100ul Test compound used: 50ul

Figure F2.27: *Antimicrobial Activity of **5 test compounds** against S. aureus at 100ug/ ml*

Test Compound	Zone of Inhibition in mm against *S. aureus*
13h	NA
13c	13
15b	14
13b	10
13e	NA

Table T2.1*: Antimicrobial activity of five synthesized compounds*

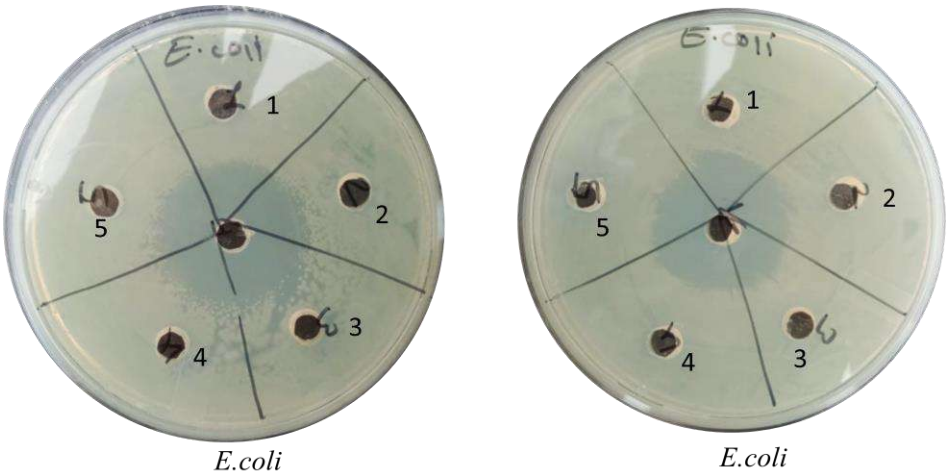

E.coli — Test compound used: 100ul

E.coli — Test compound used: 50ul

Figure F2.28: Antimicrobial Activity of **5 test compounds** against *E.coli*

Test Compoud	Zone of Inhibition in mm against E.coli
13h	NA
13c	NA
15b	NA
13b	NA
13e	NA

Table T2.2*: Antimicrobial activity five synthesized compounds against E.Coli*

2.8.1 Minimum Inhibitory Concentration of Compounds:

For the further study, we have chosen compound **13b** for the MIC. In this MIC study, Resorufin, a pink and highly red fluorescent substance, is used, that produced when oxidoreductase in active bacteria irreversibly reduces the blue dye resazurin (7-Hydroxy-3*H*-phenoxazin-3-one 10-oxide). Resorufin can then be further reduced to hydroresorufin, providing a direct and quantifiable indication of bacterial metabolic activity. (**Figure F2.29**) represents the conversion of Rosazurin to Resorufin.

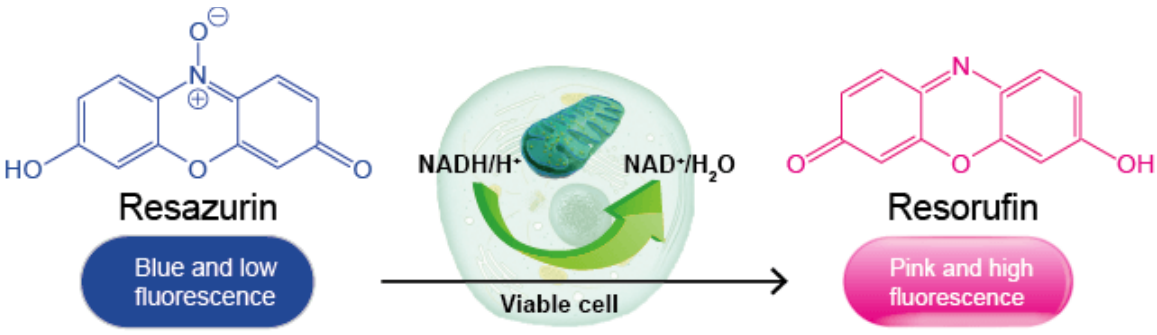

Figure F2.30*: Conversion of Rosazurin to Resorufin*

Observation:

Well No	1	2	3	4	5	6	7	8	9	10	11	12
Conc. (µg/ml)	1363	681	340	170	85	42	21	10	GC	SC	NC	PC
Abs.at 595 nm	0.112	0.111	0.120	0.374	0.364	0.355	0.326	0.476	0.983	0.108	0.357	0.120

Table T2.3: *MIC study for verifying the bacterial metabolic activity*

Pink Colour Indicate Presence of growth while blue colour indicates absence of growth GC: Growth Control, SC: Sterility Control, NC: Negative Control, PC: Positive Control

Percent Growth Inhibition:

Percent growth inhibition was found out using the formula, growth inhibition (%) = Ac− At/Ac×100, where Ac and At represent the absorbance of the control and test sample (compound or standard, respectively). Growth control: 0.983

1) ***S. aureus*** **Growth control**: 0.983

Conc.(µg/ml)	Absorbance at 600nm	Formula	Growth inhibition (%)
1363	0.112	= 0.983 -0.112/0.983×100	88.6
681	0.111	= 0.983-0.111/0.983×100	88.7

340	0.120	=0.983 -0.120/0.983×100	87.7
170	0.374	=0.983-0.374/0.983×100	61.9
85	0.364	=0.983-0.364/0.983×100	62.9
42	0.355	= 0.983 -0.355/0.983×100	63.8
21	0.326	= 0.983 -0.326/0.983×100	66.8
10	0.476	= 0.983 -0.476/0.983×100	51.5

2.8.2 Results:

Based on the absorbance and change in the color of the media it can be concluded that entry no.3 in **Table T2.3** shows 340 µg/ml minimal inhibitory conc. against *S. aureus.* Though the MIC is moderate, however, this provides a good starting point to further explore this scaffold by expanding the library and understand the SAR. Work in this direction is currently in progress.

2.9 Synthesis of Modified Sugar Nucleosides

Previously, our group published a modular strategy for the synthesis of a targeted collection of 4,5,6-trinems[52] and C3 isobenzfuran-spiroannulatedribo-configured nucleosides in furanose or pyranose forms.[53] As shown in the (**Figure F2.22**), the synthesis of the tricyclic core was done by using (2+2+2) cyclotrimerization as a key step.

After taking inspiration from these cyclotrimerization reactions, we intended to synthesize a group of novel modified sugar nucleoside compounds. In the synthesis of modified nucleosides, the (2+2+2) cyclotrimerization was taken as a key step, which forms a tricyclic ring system in a single step (**Fig. F2.23**).

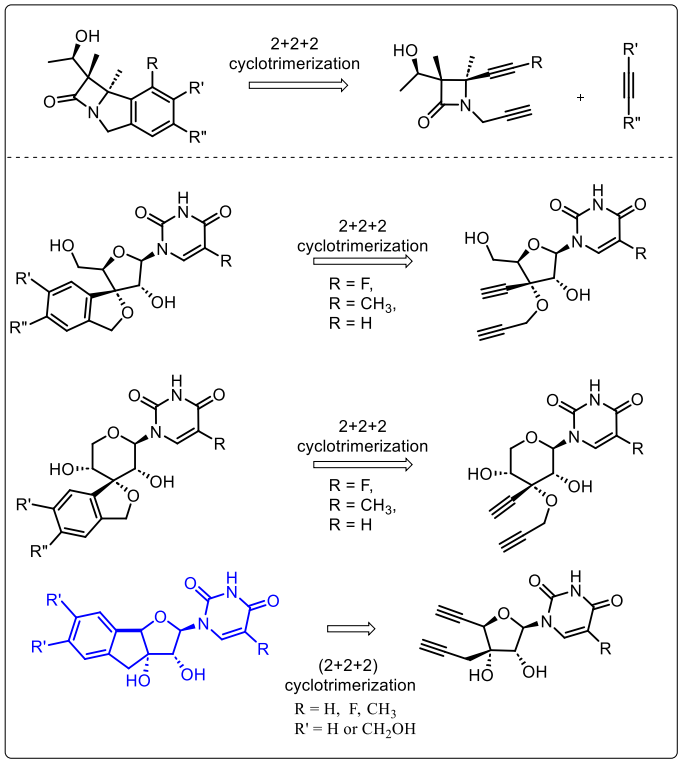

Figure F2.22: *(2+2+2) cyclotrimerization* & *Synthesis of modified nucleoside*

2.10 Retrosynthetic Strategy:

Our initial focus was on establishing a simple approach for the primary tricyclic core of nucleoside analogs. As shown in **Scheme S2.3**, we have employed cyclotrimerization of the diyne **22** as a key reaction at the penultimate stages to fuse the

indene ring and arrive at the modified nucleosides **24a**–**24f**. This type of reaction is a useful technique in organic synthesis since it allows for the production of complex molecules with specified structures. As shown in **Scheme S2.3**, to install the base unit in **20**, we decided to employ the glycosidation reaction of the corresponding diyne intermediate, which in turn, was planned from aldehyde **17** *via* the Ohira-bestmann reaction. Compound **17** was then planned to be synthesized by following the known literature condition.

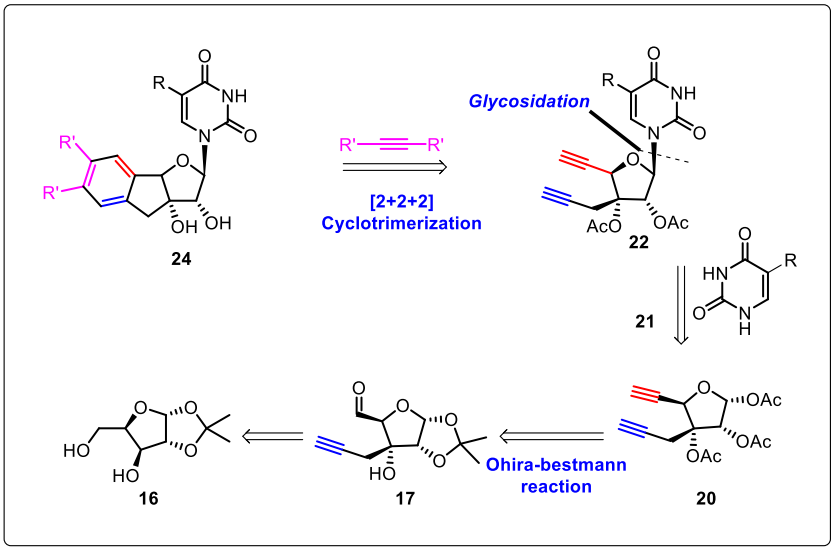

Scheme S2.3: *Retrosynthetic approach for indene conjugated nucleosides*

2.11 Synthesis of indene conjugated nucleoside derivatives:

Our work in this direction started with the synthesis of aldehyde **17** from D-Xylose **16** by following the reported literature procedure.[56] Compound **17** was then exposed to Ohira-Bestman reagent using K_2CO_3 in methanol solvent at 0 °C – rt for 9 h to afford **18** in 65% yield**.** Next, the acetonide group in compound **18** was subjected to deprotection in the presence of 70% AcOH at 110 °C for 5 h to give triol **19** in 79% of yield. The protection of 1,2,3 triol was carried out with Ac_2O, DMAP, and Et_3N in dichloromethane solvent at 0 °C – rt over night to afford triacetyl compound **20** in 87% yield. The ^{1}H NMR spectrum of diyne **20** exhibits a triplet at δ 2.99 (t, *J* = 2.7 Hz) and a doublet at δ 3.87 (*J* = 2.3 Hz), corresponding to two terminal alkyne groups. The acetyl protons appeared at δ 2.09, 2.07, 2.05. The ^{13}C NMR spectrum displayed three methyl groups from acetyl at δ 20.9 (q), 20.6

(q), and 20.2 (q) and the three carbonyls resonated at δ 169.1, 169.0, and 168.9. The exact mass calculated for product **20** in the HRMS was $C_{15}H_{16}O_7Na$ [M+Na]+: 331.0788, and it was determined to be 331.0782.

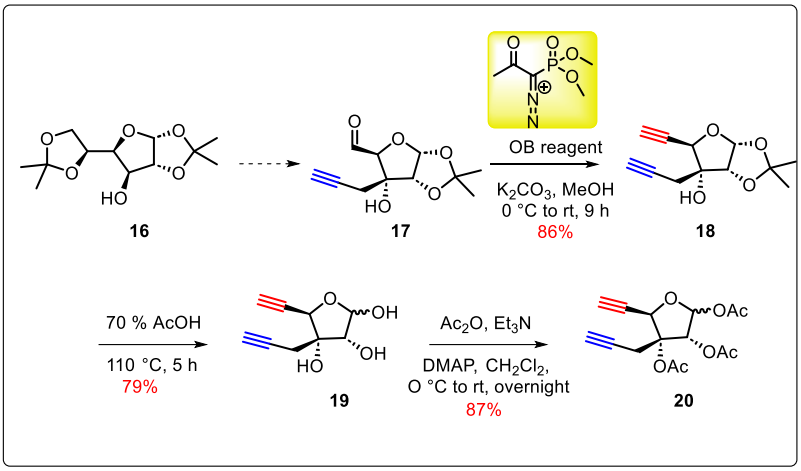

Scheme S2.4: *Synthesis of key diyne **20***

The modified Vorburggen condition was employed for the glycosidation of compound **20** in the presence of BSA and TMSOTf and acetonitrile solvent,[57] in which uracil, fluoro uracil, and thymine act as glycosyl acceptors to afford nucleosides **22a–22c** in 78% yield, it comprises the diyne required for the key step i.e. the (2+2+2) cyclotrimerization reaction. The structure of **22a** was confirmed by ^{1}H and ^{13}C spectrometry along with HRMS. In the proton NMR of **22a**, single corresponding to one of acetyl group was missing. The doublets corresponding to the two C–H of uracil unit were appeared at δ 6.34 (d, J = 7.8 Hz) and 5.54 (d, J = 7.8 Hz) and of N–H was seen to resonate at δ 9.40 as a singlet. In the ^{13}C NMR, two carbonyl carbons from uracil appeared at δ 162.8, 150.7. The exact mass calculated for product **22a** in the HRMS was $C_{17}H_{16}O_7N_2Na$ [M+Na]+: 383.0850, and it was determined to be 383.0840.

A similar spectral data pattern was observed for the compounds **22b** and **22c**. In the case of **22b**, in the ^{1}H NMR, one doublet corresponding to one C-H of fluorouracil was observed at δ 7.83, and in the ^{13}C, along with the disappearance of one acetyl carbon, two carbonyl carbons resonated at δ 171 and δ 171.2. Further confirmation of the compound was done by HRMS, in which the data acquired matched the exact mass of the compound**.** The exact mass calculated for product **22b** in the HRMS was $C_{17}H_{15}FO_7N_2Na$

[M+H]+: 401.0756, and it was determined to be 401.0746. Thus, confirming the structure of **22b**. In the ^{1}H NMR spectrum of **22c**, three CH_3 protons from thymine appeared at δ 1.93 and one C-H proton was observed at δ 7.47 and in the case of ^{13}C, two carbonyl carbons were resonated at δ 170.2 and δ 163.3 and one CH_3 carbon appeared at 12.8 as a quartet. The structure was further confirmed by HRMS data. The exact mass calculated for product **22c** in the HRMS was $C_{18}H_{18}O_7N_2Na$ [M+Na]+: 397.1006, and it was determined to be 397.0997.

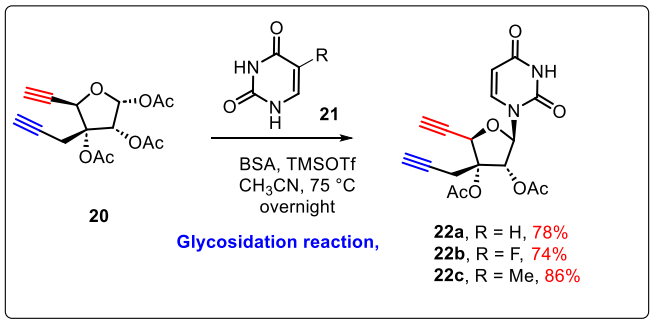

Scheme S2.5: *Glycosidation of Diyne 20 with Uracil, Flurouracil and Thymine*

Having the diynes **22a**–**22c**, our next concern was about the key cyclotrimerization. In this context, we have employed acetylene and 2-butyne-1,4-diol as the substrates along with the diynes. The trimerization reactions employing our previously established conditions [Wilkinson's catalyst [$Rh(PPh_3)_3$] in 4:1 toluene/ethanol solvents at 80 °C for 10 h] proceeded smoothly and provided the corresponding to give acetyl protected nucleosides **23aa–23ca** (with acetylene) and **23ab–23cb** (with butynediol) in very good yields.[56] Finally, the deacetylation of these compounds using liquid ammonia at −78 °C to completed the synthesis of the planned tricyclic nucleoside derivatives **24aa–24ca** (with acetylene) and **24ab–24cb** (with butynediol)**.** The structural characterization of all these compounds was carried out with the help of extensive NMR spectral data analysis and was further established with the help of single crystal X-ray diffraction studies of compound **24aa**.

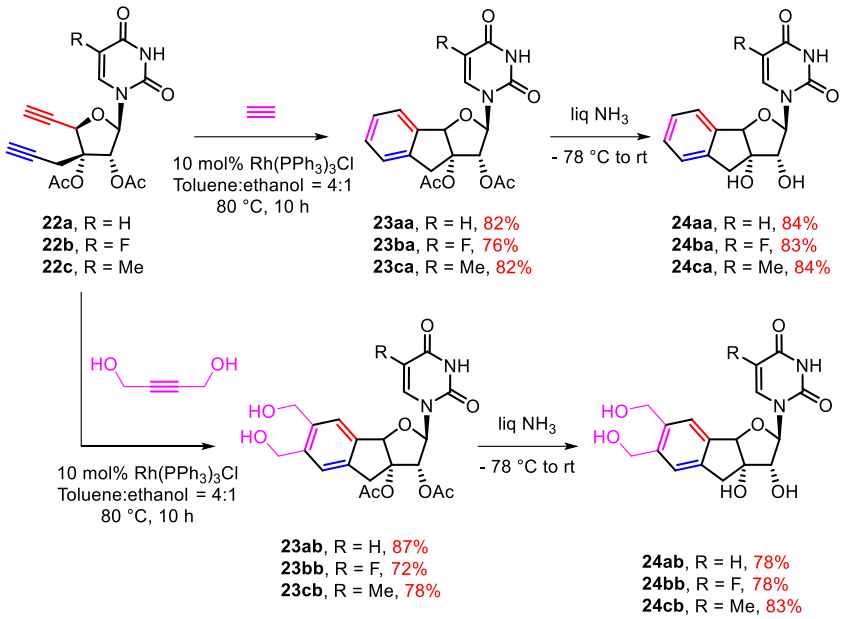

Scheme S2.6: *Synthesis of tricycic nucleosides*

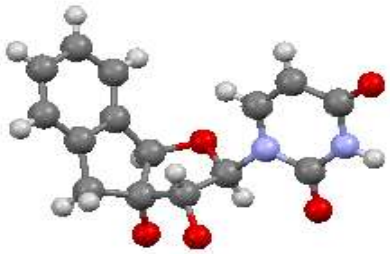

Figure F2.26: *Crystal structure of nucleoside analogue 24aa*

2.12 Biology

The nucleoside analogs, as mentioned in the introduction, act as antiviral drugs because they mimic natural nucleotides and can be incorporated into nascent viral RNA chains. Nucleoside analogs function as chain terminators to stop the elongation of nascent RNA molecules due to structural differences, which inhibits viral replication. As shown in Fig. **F2.28**, the nucleoside analogs were designed to terminate the viral replication by incorporating it into nascent viral RNA. The working of the designed molecule is shown in the following figure.

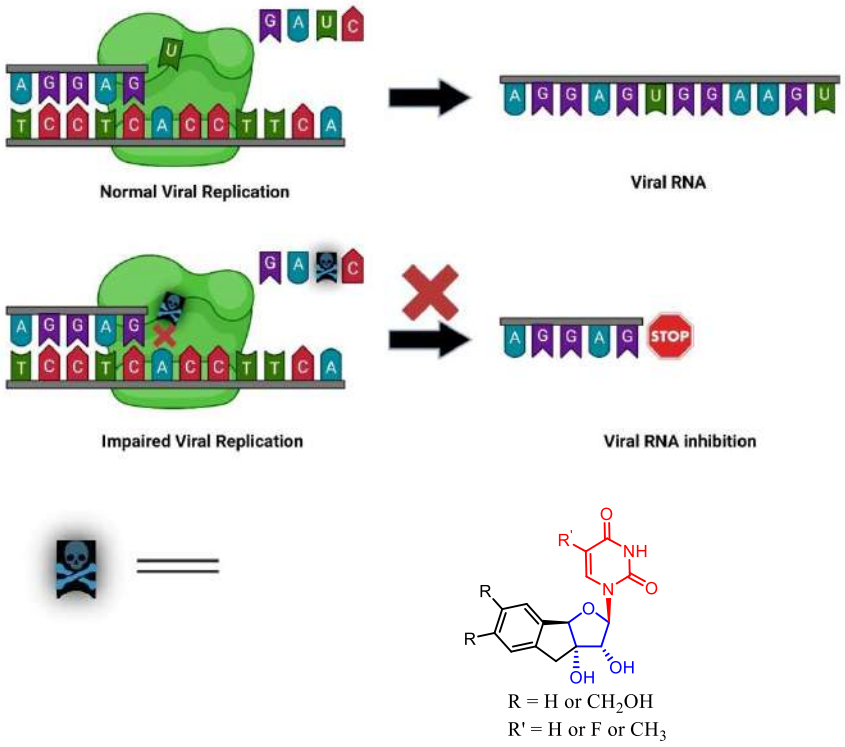

Figure F2.28. *Working of Antiviral Drugs*

2.12.1. Antiviral Activity

The antiviral screening has been carried out at CSIR-IMTech (Chandigarh) employing both RT-PCR Based and Cell Based ELISA for Screening in BSL-3 facility (see the experimental for complete details). To our delight, the synthesized compounds exhibit good to excellent results for % inactivation, % inhibition, and cytotoxicity when evaluated for antiviral activity.

	S. No.	**1**	**2**	**3**	**4**	**5**	**6**
	Sample Number	**24ab**	**24bb**	**24cb**	**24aa**	**24ba**	**24ca**
	ΔCt (10uM)						
Primary screening (RT-PCR)	**% inactivation (10uM)**	N/S	75	N/S	75	N/S	N/A

	ΔCt (1uM)						
	% inactivation (1uM)	<90	<90	N/S	N/S	<90	<90
Cytotoxicity		Non-cytotoxic	cytotoxic	cytotoxic	cytotoxic	Non-cytotoxic	Non-cytotoxic
Dose Response (RT-PCR)	**0.15uM**						N/S
	0.31uM						<90
	0.62uM						<90
	1.25uM						<90
	2.5uM						<90
	5uM						<90
EC50 (µM) (ELISA BASED)							
C-CAMP, Bengalore	**% Cell Viability (Vero E6 monolayer rescue) at 20uM**						
Assay Results @ 10 µM	**Virus RBD Spike protein-human ACE2**	-10.95	-13.34	-9.75	-5.89	-63.20	-6.07

	assay (% Inhibition)						

Table T2.1: *Antiviral Activity of six synthesized compounds*

2.12.2: % inactivation of SARS-CoV-2

The synthesized compounds were tested for their anti-SARS-CoV-2 activity and as per our consideration, the tested compounds have proven to show moderate activity.

Compounds	**SARS-CoV-2 inactivation 10uM (%)**		**SARS-CoV-2 inactivation 1uM (%)**	
	FAM	**HEX**	**FAM**	**HEX**
24ab	N/A	0	99.99	0
24ba	0	98	0	0
24bb	ND	ND	ND	ND

Table T2.2: *% inactivation of SARS-CoV-2 using FAM and HEX fluorescent dyes*

2.12.3: Cell viability assay

Four sugar nucleoside derivatives were investigated for cell viability at 50 and 20 μM on Vero cells. The cell viability was evaluated using the WST-1 reagent 48 hours after the chemical treatment. At 450 nm, the absorbance was measured, and the result was standardized against a blank that contained just the media and the WST-1 reagent. In addition to the single cell (positive control) and the cell treated with Triton X (negative control), various chemicals were also evaluated. Samples that were tested in triplicate are shown by the error bar.

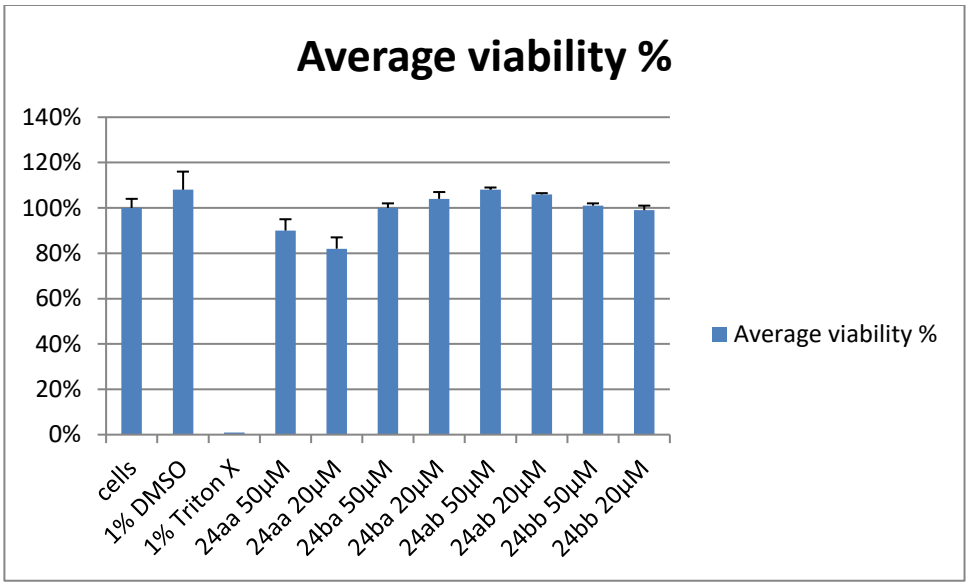

Figure F2.29. *Average % viability of 4 compounds*

Result: All the compounds were viable at 50 µM.

2.12.4: 1) Anti SARS-CoV-2 assay

Following the viability testing of the compounds, the antiviral activity of the viable compounds was evaluated. For one hour, VeroE6 cells were treated with 20 µM of each compound. Then, for an additional one hour, the plates were incubated at 37 °C with 5% CO_2 and infected with SARS-CoV-2 at 0.1 MOI. The infection was eradicated after one hour, and new media containing the compounds was added to each well. The plate was incubated in an incubator with 5% CO_2 for 48 h at 37 °C. The antiviral activity was evaluated using two readouts: (i) To ensure that CPE decreased, microscopic pictures were taken. (ii) The Cell Titer Glo technique was used to carry out the cell viability experiment.

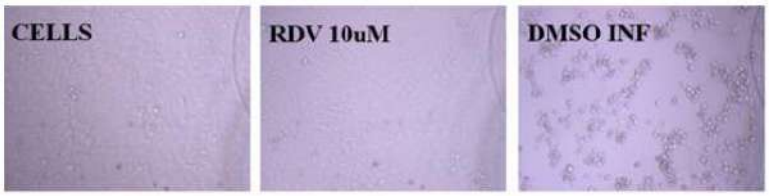

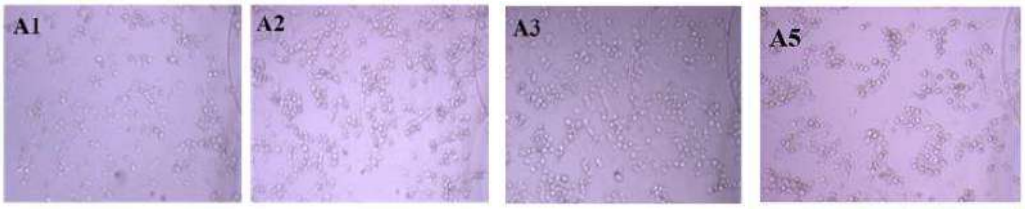

Figure F2.30: *Microscopic images showing cytopathic effect (CPE) of SARS-CoV-2 infection on VeroE6 under treatment conditions for compounds A1=24ab, A2= 24bb, A3= 24ba, A5=24aa. Images were captured at 10 X magnification after 48 hours post infection.*

(2) Cell viability assay under compound treatment and virus infection

To evaluate the antiviral activity, all drugs were evaluated at a concentration of 20 µM. After 48 hours of infection, the Cell Titer Glo technique was used to assess the cell viability of VeroE6.

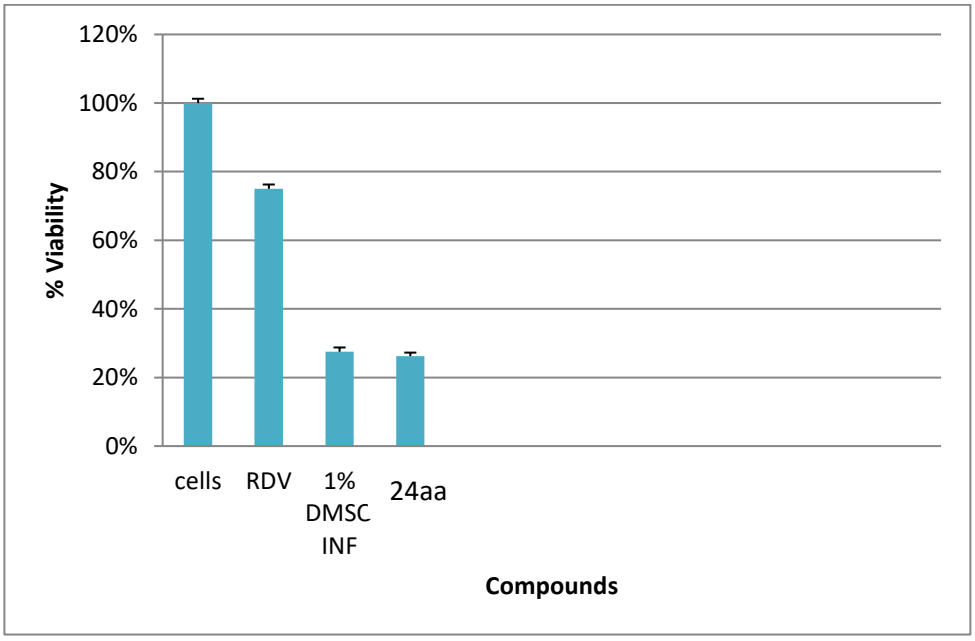

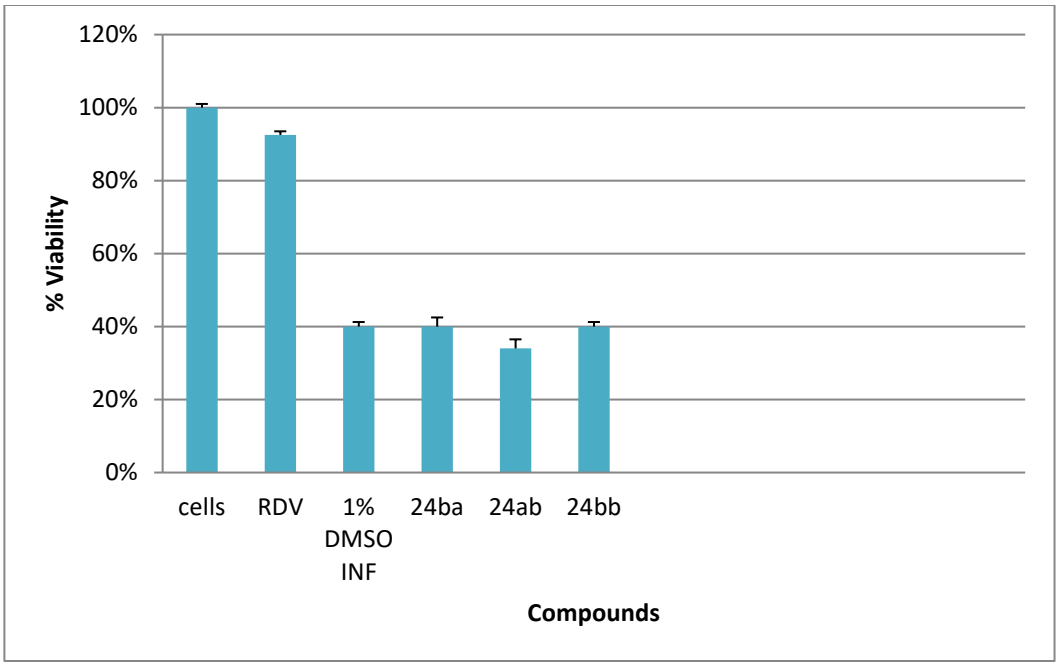

Result: Under a microscope, treatment with four compounds demonstrated the moderate viability of cells after the Cell Titer Glo assay.

2.13 Conclusions:

1) Six derivatives of Uracil, Fluoro uracil, and thymine with indeno-furan were designed and synthesized.

2) The cell viability assay of these compounds followed by anti-SARS-CoV-2 activity of compounds against Italian variant was performed by assessing the CPE by microscopic imaging and by cell viability test

3) 3 compounds (**24ba**, **24ab**, **24bb**) showed moderate activity under the microscope as well as cell viability after Cell Titer Glo assay.

Synthesis and Anmicrobial Activity of 7-[(2-Hydroxyethoxy)Methyl]Pyrrolo[2,3-d]Pyrimidine Nucleoside Derivatives:

2.14 Antimicrobial activity testing of compounds against *S. aureus,* and *E.coli:*

2.14.1 Materials and Methods:

A total of five samples were tested against two bacterial species *viz.*

1. *Staphylococcus aureus*
2. *Escherichia coli*

2.14.2 Inoculum Preparation:

1. Nutrient broth tubes were prepared.
2. Nutrient broth was inoculated using the bacterial cultures and were incubated overnight at 37 °C.

2.14.3 Well Diffusion Method:

a. Sterile Nutrient Agar plates were used for spread plate technique

b. 100 µl cultures having 0.1 O.D. which corresponds to 10^6 cfu/ml was inoculated and spread on the sterile plates.

c. Wells were created in the nutrient agar plates by using sterile borer.

d. 50 µl of each test samples were added in the well separately.

e. DMSO was used as a Negative control and for positive control streptomycin (100µg/ml) was used.

f. All the plates were incubated in Incubator at 37 ºC overnight.

g. Antimicrobial activity was detected by measuring the zone of inhibition (including the wells diameter) appeared after the incubation period.

2.14.4 Protocol to perform MIC experiment:

1) Before performing MIC experiment, check the antimicrobial activity (Qualitatively) of test compound by well diffusion assay.
2) Take sterile 96 well plate, add 200 µl of Mueller hinton broth in the each wells
3) Add testing compound in the wells in the decreasing conc., keep one well as sterility control (No addition) and one as a growth control (Without addition of any compound)
4) Take testing culture, set their O.D. to 0.1 which corresponds to 1×10^8 CFU mL−1
5) Add 20 µl of these cultures to each well except sterility control.
6) Incubate the plate at 37 °C at 90 rpm shaking condition. After the completion of 18 h, OD was taken at 600 nm using a multimode plate reader
7) Afterword's, add Resazurin dye (2.5 mg/ml) in well in the dark condition as resazurin dye is light sensitive
8) Keep the plate in dark condition for 3-5 h
9) Observe the change in the colour

2.15 General Experimental procedure for Suzuki coupling:

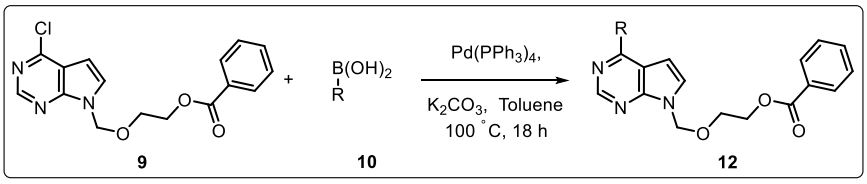

All reactions were conducted employing 100 mg of compound **9**. To a solution of 2-((4-chloro-1*H*-indol-1-yl)methoxy)ethyl benzoate **9** (1 eq.) in toluene (2 mL) in screw cap pressure tube was evacuated and back filled with argon. To this solution, boronic acid **10** (1.2 eq.), K_2CO_3 (2 eq.) and $Pd(PPh_3)_4$ (5 mol%) were added. The resulting reaction mixture was heated at 100 °C for 18 h. The tube was then cooled to room temperature and concentrated under reduced pressure. The resulting crude was purified by column chromatography to obtain the product **12**.

Experimental Data:

2-((4-(3,5-Dimethoxyphenyl)-7*H*-pyrrolo[2,3-*d*]pyrimidin -7-yl)methoxy)ethyl benzoate (12a): Yield: 60 mg (46%); R_f = 0.19 (30% EtOAc in petroleum ether); dark yellow semi solid; ^{1}H NMR (400 MHz, $CDCl_3$) δ 8.98 (s, 1H), 8.00 (dd, *J* = 8.3, 1.3 Hz, 2H), 7.54–7.58 (m, 1H), 7.40–7.44 (m, 3H), 7.25 (d, *J* = 2.4 Hz, 2H), 6.88 (d, *J* = 3.6 Hz, 1H), 6.64 (t, *J* = 2.3 Hz, 1H), 5.80 (s, 2H), 4.45 (dd, *J* = 5.9, 4.6 Hz, 2H), 3.90 (s, 6H), 3.87 (dd, *J* = 5.9, 4.6 Hz, 2H); ^{13}C NMR (101 MHz, $CDCl_3$) δ 166.4 (s), 161.0 (s), 157.7 (s), 151.8 (d), 139.8 (s), 133.1 (d), 129.8 (s), 129.6 (d, 2C), 128.6 (d), 128.3 (d, 2C), 115.8 (s), 106.8 (d, 2C), 102.5 (d), 102.1 (d), 77.3 (s), 77.2 (s), 73.5 (t), 67.1 (t), 63.5 (t), 55.6 (q, 2C); HRMS (ESI) calcd. for $C_{24}H_{24}N_3O_5$ $[M + H]^+$: 434.1710; found: 434.1706.

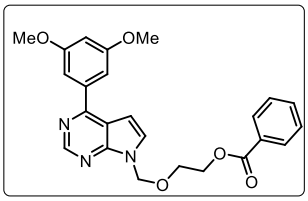

2-((4-(Naphthalen-1-yl)-7*H*-pyrrolo[2,3-*d*]pyrimidin-7-yl)methoxy)ethyl benzoate (12b): Yield: 110 mg (86%); R_f = 0.25 (20% EtOAc in petroleum ether); brown liquid; ^{1}H NMR (400 MHz, $CDCl_3$) δ 9.09 (s, 1H), 8.12 (d, *J* = 8.5 Hz, 1H), 8.00–8.04 (m, 3H), 7.96 (d, *J* = 7.8 Hz, 1H), 7.77 (dd, *J* = 7.1, 1.1 Hz, 1H), 7.62 (dd, *J* = 8.1, 7.2 Hz, 1H), 7.52–7.57 (m, 2H), 7.46–7.50 (m, 1H), 7.40–7.4 (m, 2H), 7.37 (d, *J* = 3.6 Hz, 1H), 6.46 (d, *J* = 3.6 Hz, 1H), 5.84 (s, 2H), 4.48–4.50 (m, 2H), 3.92 (m, 2H); ^{13}C NMR (101 MHz, $CDCl_3$) δ 166.4 (s), 159.2 (s), 152.2 (s), 151.9 (d), 135.0 (s), 134.0 (s), 133.0 (d), 130.9 (s), 129.9 (d), 129.8 (s), 129.6 (d, 2C), 128.4 (d), 128.3 (d), 128.3 (d, 2C), 128.1 (d), 126.6 (d), 126.1 (d), 125.7 (d), 125.1 (d), 118.3 (s), 102.2 (d), 73.5 (t), 67.1 (t), 63.5 (t); HRMS (ESI) calcd. for $C_{26}H_{22}N_3O_3$ $[M + H]^+$: 424.1661; found: 424.1662.

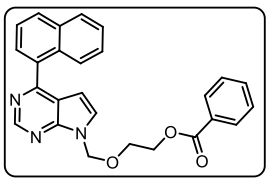

2-((4-(3-Acetylphenyl)-7*H*-pyrrolo[2,3-*d*]pyrimidin-7-yl)methoxy)ethyl benzoate (12c): Yield: 57 mg (45%); R_f = 0.25 (40% EtOAc in petroleum ether); brown solid; mp = 111 °C**;** ^{1}H NMR (400 MHz, $CDCl_3$) δ 9.00 (s, 1H), 8.70 (t, *J* = 1.6 Hz, 1H), 8.31 (dt, *J* = 7.8, 1.3 Hz, 1H), 8.12 (dt, *J* = 7.8, 1.3 Hz, 1H), 7.97–8.0 (m, 2H), 7.67 (t, *J* = 7.8 1H), 7.53 (tt, *J* = 7.0, 1.4 Hz, 1H), 7.46 (d, *J* = 3.6 Hz, 1H), 7.37–7.43 (m, 2H), 6.87 (d, *J* = 3.8 Hz, 1H), 5.81 (s, 2H), 4.41–4.46 (m, 2H), 3.84–3.89 (m, 2H), 2.71 (s, 3H); ^{13}C NMR (101

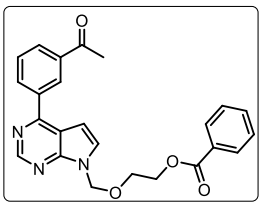

MHz, $CDCl_3$) δ 197.7 (s), 166.4 (s), 156.6 (s), 152.6 (s), 152.0 (d), 138.5 (s), 137.6 (s), 133.2 (d), 133.1 (d), 129.8 (s), 129.7 (d), 129.6 (d, 2C), 129.2 (d), 129.0 (d), 128.8 (d), 128.3 (d, 2C), 115.8 (s), 101.6 (d), 73.6 (t), 67.2 (t), 63.5 (t), 26.8 (q); HRMS (ESI) calcd. for $C_{24}H_{22}N_3O_4$ $[M + H]^+$: 416.1605; found: 416.1603.

2-((4-(Naphthalen-2-yl)-7*H*-pyrrolo[2,3-*d*]pyrimidin-7-yl)methoxy)ethyl benzoate (12d): Yield: 105 mg (82%); R_f = 0.25 (20% EtOAc in petroleum ether); brown solid; mp = 116 °C; ^{1}H NMR (400 MHz, $CDCl_3$) δ 9.08 (s, 1H), 8.11 (d, J = 8.5 Hz, 1H), 7.99–8.03 (m, 3H), 7.95 (d, J = 7.8 Hz, 1H), 7.76 (dd, J = 7.1, 1.1 Hz, 1H), 7.61 (dd, J = 8.1, 7.2 Hz, 1H), 7.51–7.56 (m, 2H), 7.45–7.49 (m, 1H), 7.39–7.43 (m, 2H), 7.36 (d, J = 3.6 Hz, 1H), 6.45 (d, J = 3.6 Hz, 1H), 5.83 (s, 2H), 4.48 (m, 2H), 3.91 (m, 2H); ^{13}C NMR (101 MHz, $CDCl_3$) δ 166.4 (s), 159.2 (s), 152.2 (s), 151.9 (d), 135.0 (s), 134.0 (s), 133.0 (d), 130.9 (s), 129.9 (d), 129.8 (s), 129.6 (d, 2C), 128.4 (d), 128.3 (d), 128.3 (d, 2C), 128.1 (d), 126.6 (d), 126.1 (d), 125.7 (d), 125.1 (d), 118.3 (s), 102.2 (d), 73.5 (t), 67.1 (t), 63.5 (t); HRMS (ESI) calcd. for $C_{26}H_{22}N_3O_3$ $[M + H]^+$: 424.1661 found: 424.1660.

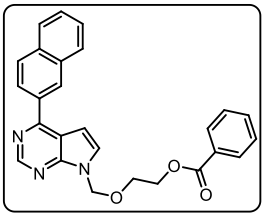

2-((4-Phenyl-7*H*-pyrrolo[2,3-*d*]pyrimidin-7-yl)methoxy)ethyl benzoate (12e):

Yield: 71 mg (63%); R_f = 0.25 (20% EtOAc in petroleum ether); dark yellow semi solid; ^{1}H NMR (400 MHz, $CDCl_3$) δ 8.99 (s, 1H), 8.09–8.12 (m, 2H), 7.98–8.00 (m, 2H), 7.52–7.59 (m, 4H), 7.39–7.43 (m, 3H), 6.87 (d, J = 3.8 Hz, 1H), 5.80 (s, 2H), 4.44–4.46 (m, 2H), 3.86–3.88 (m, 2H); ^{13}C NMR (101 MHz, $CDCl_3$) δ 166.4 (s), 157.9 (s), 152.6 (s), 152.1 (d), 138.0 (s), 133.1 (d), 130.2 (d), 129.8 (s), 129.7 (d, 2C), 128.9 (d, 2C), 128.8 (d, 2C), 128.6 (d), 128.3 (d, 2C), 115.8 (s), 102.0 (d), 73.6 (t), 67.2 (t), 63.6 (t); HRMS (ESI) calcd. for $C_{22}H_{20}N_3O_3$ $[M + H]^+$: 374.1499; found: 374.1499.

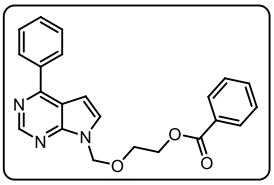

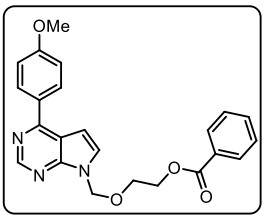

2-((4-(4-Methoxyphenyl)-7*H*-pyrrolo[2,3-*d*]pyrimidin-7-yl)methoxy)ethyl benzoate (12f): Yield: 105 mg (86%); R_f = 0.71 (40% EtOAc in petroleum ether); yellow semi solid; ^{1}H NMR (400 MHz, $CDCl_3$) δ 8.93 (s, 1H), 8.08–8.11 (m, 2H), 7.98 (d, J = 7.9 Hz, 2H), 7.53 (t, J = 7.5 Hz, 1H), 7.37–7.41 (m, 3H), 7.07 (d, J = 8.6 Hz, 2H), 6.85 (d, J = 3.6 Hz, 1H), 5.78 (s, 2H), 4.42–4.45 (m, 2H), 3.89 (s, 3H), 3.84–3.87 (m, 2H); ^{13}C NMR (101 MHz, $CDCl_3$) δ 166.3 (s), 161.3 (s), 157.4 (s), 152.4 (s), 151.9 (d), 133.0 (d), 130.5 (s), 130.3 (d, 2C), 129.8 (s), 129.6 (d, 2C), 128.3 (d, 2C), 128.1 (d), 115.1 (s), 114.2 (d, 2C), 102.0 (d), 73.5 (t), 67.1 (t), 63.5 (t), 55.4 (q); HRMS (ESI) calcd. for $C_{23}H_{22}N_3O_4$ $[M + H]^+$: 404.1610; found: 404.1603.

2-((4-(4-Nitrophenyl)-7*H*-pyrrolo[2,3-*d*]pyrimidin-7-yl)methoxy)ethyl benzoate (12g):

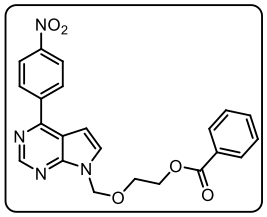

Yield: 108 mg (86%); R_f = 0.31 (40% EtOAc in petroleum ether); brown liquid; ^{1}H NMR (400 MHz, $CDCl_3$) δ 9.01 (s, 1H), 8.39–8.42 (m, 2H), 8.26–8.29 (m, 2H), 7.96–7.99 (m, 2H), 7.51–7.56 (m, 2H), 7.38–7.42 (m, 2H), 6.83 (d, J = 3.8 Hz, 1H), 5.82 (s, 2H), 4.43–4.46 (m, 2H), 3.86–3.89 (m, 2H); ^{13}C NMR (101 MHz, $CDCl_3$) δ 166.3 (s), 154.9 (s), 152.8 (s), 152.0 (d), 148.7 (s), 144.0 (s), 133.1 (d), 129.8 (s), 129.8 (s), 129.7 (d, 2C), 129.6 (d, 2C), 128.3 (d, 2C), 124.0 (d, 2C), 116.1 (s), 101.2 (d), 73.6 (t), 67.4 (t), 63.5 (t); HRMS (ESI) calcd. for $C_{22}H_{19}N_4O_5$ $[M + H]^+$: 419.1355; found: 419.1358.

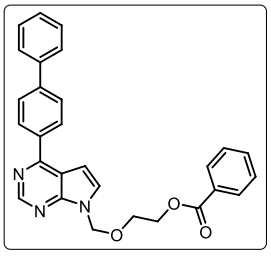

2-((4-([1,1'-Biphenyl]-4-yl)-7*H*-pyrrolo[2,3-*d*]pyrimidin-7-yl)methoxy)ethyl benzoate (12h): Yield: 69 mg (51%); R_f = 0.22 (25% EtOAc in petroleum ether); yellow solid; mp = 165 °C; ^{1}H NMR (400 MHz, $CDCl_3$) δ 9.01 (s, 1H), 8.19–8.22 (m, 2H), 8.00 (dd, J = 8.4, 1.3 Hz, 2H), 7.80–7.82 (m, 2H), 7.70–7.72 (m, 2H), 7.48–7.55 (m, 3H), 7.39–7.45 (m, 4H), 6.92 (d, J = 3.8 Hz, 1H), 5.82 (s, 2H), 4.46 (dd, J = 5.3, 4.1 Hz, 2H), 3.89 (dd, J = 5.4, 4.0 Hz, 2H); ^{13}C NMR (101 MHz, $CDCl_3$) δ 166.4 (s), 157.4 (s), 152.6 (s), 152.0 (d), 142.9 (s), 140.3 (s), 136.8 (s), 133.1 (d), 129.8 (s), 129.6 (d, 2C), 129.3 (d, 2C), 128.9 (d, 2C), 128.6 (d), 128.3 (d, 2C), 127.8 (d) 127.5 (d, 2C), 127.2

(d, 2C), 115.7 (s), 102.0 (d), 73.5 (t), 67.1 (t), 63.5 (t); HRMS (ESI) calcd. for $C_{28}H_{24}N_3O_3$ $[M + H]^+$: 450.1812: found: 450.1809.

General procedure for Sonogoshira coupling with 2-((4-chloro-1*H*-indol-1-yl)methoxy)ethyl benzoate (9) :

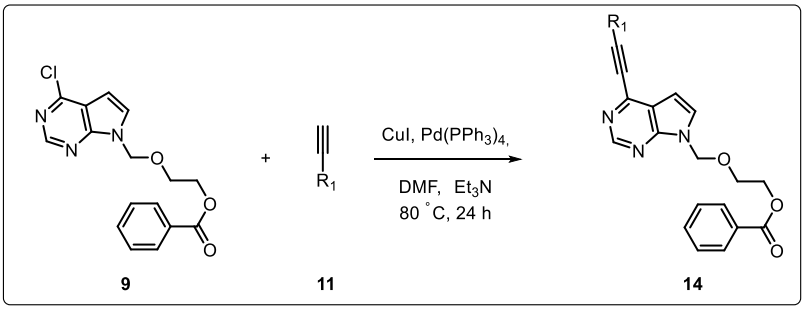

All reactions were carried out by employing 100 mg of substrate **9**. At rt, a degassed solution of compound **9** (1 eq.), terminal alkyne **11** (1.2 eq.) $Pd(PPh_3)_4$ (1 mol%) and CuI (2 mol%) in anhydrous DMF (1 mL) was treated with Et_3N (2 eq.). The reaction was heated to 80 °C for 5–24 h depending upon substrate. After the completion of reaction (as indicated by TLC), the solvent was evaporated under reduced presdsure and the residue was purified by flash silica gel column chromatography (ethyl acetate/petroleum ether) to afford the desired product **14**.

2-((4-(Cyclohexylethynyl)-7*H*-pyrrolo[2,3-*d*]pyrimidin-7-yl)methoxy)ethyl benzoate (14a): Yield: 39 mg (32%); R_f = 0.55 (5% EtOAc in DCM); yellow liquid;^{1}H NMR (400 MHz, $CDCl_3$) δ 8.81 (s, 1H), 7.95–7.97 (m, 2H), 7.54–7.58 (m, 1H), 7.41–7.45 (m, 2H), 7.35 (d, J = 3.6 Hz, 1H), 6.65 (d, J = 3.6 Hz, 1H), 5.73 (s, 2H), 4.40–4.42 (m, 2H), 3.80–3.82 (m, 2H), 2.73–2.79 (m, 1H), 1.94– 1.97(m, 2H), 1.79–1.83 (m, 2H), 1.70–1.62 (m, 4H), 1.38–1.44 (m, 2H); ^{13}C NMR (101 MHz, $CDCl_3$) δ 166.4 (s), 152.0 (d), 151.5 (s), 143.4 (s), 133.0 (d), 129.8 (s), 129.6 (d, 2C), 128.5 (d), 128.3 (d, 2C), 120.1 (s), 102.3 (s), 101.5 (d), 77.7 (s), 73.5 (t), 67.1 (t), 63.5 (t), 32.1 (t, 3C), 29.8 (d), 25.8 (t), 24.8 (t); HRMS (ESI) calcd. for $C_{24}H_{26}N_3O_3$ $[M + H]^+$: 404.1974; found: 404.1611.

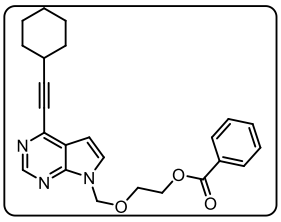

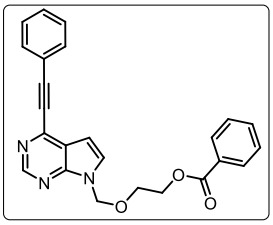

2-((4-(Phenylethynyl)-7*H*-pyrrolo[2,3-*d*]pyrimidin-7-yl)methoxy)ethyl benzoate (14b) : Yield: 24 mg (20%); R_f = 0.23 (20% EtOAc in petroleum ether); green semi solid; ^{1}H NMR (400 MHz, $CDCl_3$) δ 8.90 (s, 1H), 7.98–7.96 (m, 2H), 7.69 (dd, *J* = 7.8, 2.2 Hz, 2H), 7.54–7.58 (m, 1H), 7.40–7.45 (m, 6H), 6.76 (d, *J* = 3.6 Hz, 1H), 5.76 (s, 2H), 4.43 (dd, *J* = 4.7, 3.5 Hz, 2H), 3.84 (dd, *J* = 4.7, 3.3 Hz, 2H); ^{13}C NMR (101 MHz, $CDCl_3$) δ 166.3 (s), 152.0 (d), 151.6 (s), 142.4 (s), 133.1 (d), 132.4 (d, 2C), 129.7 (d), 129.6 (d, 2C), 129.1 (s), 128.5 (d, 2C), 128.4 (s), 128.3 (d, 2C), 121.5 (s), 120.0 (s), 101.4 (d), 95.8 (s), 85.6 (s), 73.5 (d), 67.2 (d), 63.4 (d); HRMS (ESI) calcd. for $C_{24}H_{20}N_3O_3$ $[M + H]^+$: 398.1499; found: 398.1497.

2-((4-(p-tolylethynyl)-7*H*-pyrrolo[2,3-*d*]pyrimidin-7-yl)methoxy)ethyl benzoate (14c):

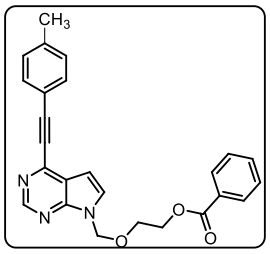

Yield: 51 mg (41%); R_f = 0.6 (20% EtOAc in petroleum ether); brown solid; mp = 65 °C; ^{1}H NMR (400 MHz, $CDCl_3$) δ 8.88 (s, 1H), 7.94–7.98 (m, 2H), 7.52–7.59 (m, 3H), 7.40–7.44 (m, 3H), 7.22 (d, *J* = 7.9 Hz, 2H), 6.74 (d, *J* = 3.6 Hz, 1H), 5.75 (s, 2H), 4.40–4.44 (m, 2H), 3.82–3.85 (m, 2H), 2.40 (s, 3H); ^{13}C NMR (101 MHz, $CDCl_3$) δ 166.3 (s), 152.0 (d), 151.5 (s), 142.7 (s), 140.1 (s), 133.0 (d), 132.3 (d, 2C), 129.7 (s), 129.6 (d, 2C), 129.3 (d, 2C), 128.8 (d), 128.3 (d, 2C), 119.9 (s), 118.5 (s), 101.4 (d), 96.1 (s), 85.3 (s), 73.4 (t), 67.2 (t), 63.4 (t), 21.6 (q); HRMS (ESI) calcd. for $C_{25}H_{22}N_3O_3$ $[M + H]^+$: 412.1661; found: 412.1667.

2-((4-((4-Fluorophenyl)ethynyl)-7H-pyrrolo[2,3-*d*]pyrimidin-7-yl)methoxy)ethyl benzoate (14d): Yield: 43 mg (34%); R_f = 0.6 (20% EtOAc in petroleum ether); dark brown solid; mp = 96 °C; ^{1}H NMR (400 MHz, $CDCl_3$) δ 8.88 (s, 1H), 7.96–7.98 (m, 2H), 7.65–7.70 (m, 2H), 7.53–7.57 (m, 1H), 7.41–7.45 (m, 3H), 7.08–7.14 (m, 2H), 6.73 (d, *J* = 3.6 Hz, 1H), 5.76 (s, 2H), 4.43 (dd, *J* = 5.3, 4.1 Hz, 2H), 3.84 (dd, *J* = 5.3, 4.1 Hz, 2H); ^{13}C NMR (101 MHz, $CDCl_3$) δ 166.3 (s), 164.6 (s), 162.1 (s), 152.0 (d), 151.6 (s), 142.3 (s), 134.5 (d, J_{C-F} = 9.2 Hz), 133.0 (d), 129.8 (s), 129.6 (d, 2C), 129.0 (d), 128.3 (d, 2C), 120.0 (s), 117.7 (d, J_{C-F} = 3.8 Hz), 116.1 (d), 115.9

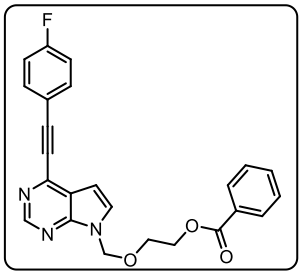

(d), 101.3 (d), 94.5 (s), 85.6 (s), 73.5 (t), 67.2 (t), 63.4 (t); HRMS (ESI) calcd. for $C_{24}H_{19}N_3O_3F$ $[M + H]^+$: 416.1410; found: 416.1404.

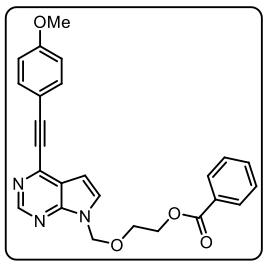

2-((4-((4-Methoxyphenyl)ethynyl)-7*H*-pyrrolo[2,3-*d*]pyrimidin-7-yl)methoxy)ethyl benzoate(14e): Yield: 33 mg (26%); R_f = 0.14 (30% EtOAc in petroleum ether); turmeric color solid; mp = 70 °C; ^{1}H NMR (400 MHz, $CDCl_3$) δ 8.86 (s, 1H), 7.87–8.02 (m, 2H), 7.59–7.67 (m, 2H), 7.51–7.57 (m, 1H), 7.43 (d, *J* = 7.9 Hz, 2H), 7.38–7.41 (m, 1H), 6.93 (d, *J* = 8.8 Hz, 2H), 6.73 (d, *J* = 3.6 Hz, 1H), 5.75 (s, 2H), 4.40–4.44 (m, 2H), 3.81–3.86 (m, 5H); ^{13}C NMR (101 MHz, $CDCl_3$) δ 166.3 (s), 160.8 (s), 152.0 (d), 151.5 (s), 142.9 (s), 134.0 (d, 2C), 133.0 (d), 129.8 (s), 129.6 (d, 2C), 128.7 (d), 128.3 (d, 2C), 119.8 (s), 114.2 (d, 2C), 113.6 (s), 101.4 (d), 96.3 (s), 85.0 (s), 73.4 (t), 67.2 (t), 63.4 (t), 55.3 (q); HRMS (ESI) calcd. for $C_{25}H_{22}N_3O_4$ $[M + H]^+$: 428.1610; found: 428.1606.

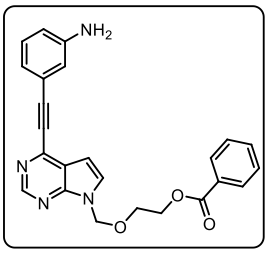

2-((4-((3-Aminophenyl)ethynyl)-7*H*-pyrrolo[2,3-*d*]pyrimidin-7-yl)methoxy)ethyl benzoate (14f): Yield: 38 mg (31%); R_f = 0.2 (40% EtOAc in petroleum ether); green semi solid; ^{1}H NMR (400 MHz, $CDCl_3$) δ 8.88 (s, 1H), 7.95– 7.98 (m, 2H), 7.53–7.57 (m, 1H), 7.39–7.44 (m, 3H), 7.18 (t, *J* = 7.8 Hz, 1H), 7.08 (dt, *J* = 7.6, 1.2 Hz, 1H), 6.99 (t, *J* = 2.3 Hz, 1H), 6.73–6.76 (m, 2H), 5.75 (s, 2H), 4.42 (dd, *J* = 5.3, 4.1 Hz, 2H), 3.84 (dd, *J* = 5.4, 4.1 Hz, 4H); ^{13}C NMR (101 MHz, $CDCl_3$) δ 166.3 (s), 152.0 (d), 151.6 (s), 146.4 (s), 142.6 (s), 133.0 (d), 129.7 (s), 129.6 (d, 2C), 129.4 (d), 128.9 (d), 128.3 (d, 2C), 122.7 (d), 122.2 (s), 120.0 (s), 118.3 (d), 116.7 (d), 101.4 (d), 96.2 (s), 85.1 (s), 73.5 (t), 67.2 (t), 63.5 (t); HRMS (ESI) calcd. for $C_{24}H_{21}N_4O_3$ $[M + H]^+$: 413.1614; found: 413.2612.

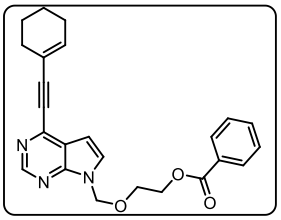

2-((4-(Cyclohex-1-en-1-ylethynyl)-7*H*-pyrrolo[2,3-*d*]pyrimidin-7-yl)methoxy)ethyl benzoate (14g): Yield: 48 mg (40%); R_f = 0.6 (20% EtOAc in petroleum ether); pale yellow semi solid; ^{1}H NMR (400 MHz, $CDCl_3$) δ 8.83 (s,1H), 7.96– 7.98 (m, 2H), 7.56 (tt, *J* = 7.4, 1.3 Hz, 1H), 7.41–7.45 (m, 2H), 7.36 (d, *J* = 3.6 Hz, 1H), 6.66 (d, *J* = 3.6

Hz, 1H), 6.48 (tt, *J* = 4.0, 1.9 Hz, 1H), 5.74 (s, 2H), 4.41–4.43 (m, 2H), 3.81–3.83 (m, 2H), 2.30–2.34 (m, 2H), 2.19–2.24 (m, 2H), 1.64–1.75 (m, 4H); ^{13}C NMR (101 MHz, $CDCl_3$) δ 166.4 (s), 152.0 (d), 151.5 (s), 143.4 (s), 133.0 (d), 129.8 (s), 129.6 (d, 2C), 128.5 (d), 128.3 (d, 2C), 120.1 (s), 102.3 (s), 101.5 (d), 77.7 (s), 77.3 (s), 73.5 (t), 67.1 (t), 63.5 (t), 32.1 (t, 2C), 29.8 (d), 25.8 (t), 24.8 (t); HRMS (ESI) calcd. for $C_{24}H_{24}N_3O_3$ $[M + H]^+$: 402.1817; found: 402.1820.

2-((4-(Pent-1-yn-1-yl)-7*H*-pyrrolo[2,3-*d*]pyrimidin-7-yl)methoxy)ethyl benzoate (14h)

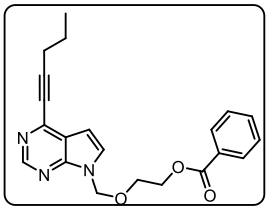

Yield: 35 mg (32%); R_f = 0.65 (20% EtOAc in petroleum ether); brown semi solid; ^{1}H NMR (400 MHz, $CDCl_3$) δ 8.82 (s, 1H), 7.94–8.00 (m, 2H), 7.56 (tt, *J* = 7.4, 1.3 Hz, 1H), 7.41–7.45 (m, 2H), 7.36 (d, *J* = 3.6 Hz, 1H), 6.66 (d, *J* = 3.6 Hz, 1H), 5.73 (s, 2H), 4.40–4.43 (m, 2H), 3.81–3.83 (m, 2H), 2.55 (t, *J* = 7.0 Hz, 2H), 1.72–1.78 (m, 2H), 1.12 (t, *J* = 7.4 Hz, 3H); ^{13}C NMR (101 MHz, $CDCl_3$) δ 166.3 (s), 151.9 (d), 151.5 (s), 143.3 (s), 133.0 (d), 129.8 (s), 129.6 (d, 2C), 128.5 (d), 128.3 (d, 2C), 120.0 (s), 101.4 (d), 98.2 (s), 77.9 (s), 73.4 (t), 67.1 (t), 63.5 (t), 21.7 (t), 21.6 (t), 13.6 (q); HRMS (ESI) calcd. for $C_{21}H_{22}N_3O_3$ $[M + H]^+$: .364.1661; found: 364.1654.

2-((4-(Cyclopropylethynyl)-7*H*-pyrrolo[2,3-*d*]pyrimidin-7-yl)methoxy)ethyl benzoate (14i): Yield: 42 mg (39%); R_f = 0.11 (20% EtOAc in petroleum ether); green solid; mp = 65 °C; ^{1}H NMR (400 MHz, $CDCl_3$) δ 8.78 (s,1H), 7.94–7.96 (m, 2H), 7.52–7.57 (m, 1H), 7.39–7.43 (m, 2H), 7.33 (d, *J* = 3.6 Hz, 1H), 6.62 (d, *J* = 3.6 Hz, 1H), 5.71 (s, 2H), 4.38–4.41 (m, 2H), 3.78–3.80 (m, 2H), 1.54–1.62 (m, 1H), 0.96–1.01 (m, 4H); ^{13}C NMR (101 MHz, $CDCl_3$) δ 166.3 (s), 151.9 (d), 151.4 (s), 143.1 (s), 133.0 (d), 129.8 (s), 129.6 (d, 2C), 128.5 (d), 128.3 (d, 2C), 119.9 (s), 101.7 (s), 101.4 (d), 73.4 (t), 73.0 (s), 67.1 (t), 63.4 (d), 9.4 (t, 2C), 0.4 (d); HRMS (ESI) calcd. for $C_{21}H_{20}N_3O_3$ $[M + H]^+$: 362.1505; found: 362.1500.

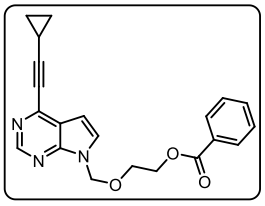

Benzoyl deprotection (13):

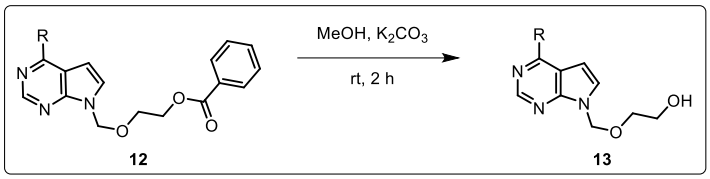

All reactions were conducted employing 50 mg of benzoate. In a typical reaction, aryl ester **12** (1.0 eq.), K_2CO_3 (1.2 eq.) methanol was stirred at room temperature until the complete consumption of starting material was noticed on TLC. After completion, the reaction mixture was concentrated under reduced pressure and the resulting crude was purified by flash silica gel column chromatography (ethyl acetate/petroleum ether) to afford the desired product **13**.

2-((4-(3,5-Dimethoxyphenyl)-7*H*-pyrrolo[2,3-*d*]pyrimidin-7-yl)methoxy)ethan-1-ol (13a) : Yield: 36 mg (94%); R_f = 0.1 (60% EtOAc in petroleum ether); brown solid; mp: 94 °C; ^{1}H NMR (400 MHz, $CDCl_3$) δ 8.97 (s, 1H), 7.40 (d, J = 3.6 Hz, 1H), 7.25 (d, J = 1.6 Hz, 2H), 6.89 (d, J = 3.5 Hz, 1H), 6.63 (s, 1H), 5.78 (s, 2H), 3.89 (s, 6H), 3.73–3.75 (m, 2H), 3.64–3.66 (m, 2H); ^{13}C NMR (101 MHz, $CDCl_3$) δ 161.1 (s, 2C), 157.8 (s), 152.4 (s), 151.8 (d), 139.8 (s), 128.7 (d), 116.0 (s), 106.8 (d, 2C), 102.6 (d), 101.9 (d), 74.0 (t), 70.3 (t), 61.8 (t), 55.5 (q, 2C); HRMS (ESI) calcd. for $C_{17}H_{20}N_3O_4$ $[M + H]^+$: 330.1448; found: 330.1447.

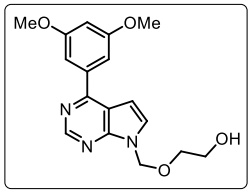

2-((4-(Naphthalen-1-yl)-7*H*-pyrrolo[2,3-*d*]pyrimidin-7-yl)methoxy)ethan-1-ol (13b): Yield: 31 mg (83%); R_f = 0.1 (50% EtOAc in petroleum ether); yellow semi solid; ^{1}H NMR (400 MHz, $CDCl_3$) δ 9.1 (s, 1H), 8.10 (d, J = 8.4 Hz, 1H), 8.01 (d, J = 8.3 Hz, 1H), 7.95 (d, J = 7.9 Hz, 1H), 7.77 (dd, J = 7.1, 1.1 Hz, 1H), 7.62 (dd, J = 8.1, 7.3 Hz, 1H), 7.54 (ddd, J = 8.4, 6.7, 1.3 Hz, 1H), 7.48 (ddd, J = 8.4, 6.7, 1.3 Hz, 1H), 7.36 (d, J = 3.6 Hz, 1H), 6.47 (d, J = 3.6 Hz, 1H), 5.8 (s, 2H), 3.76–3.79 (m, 2H), 3.70–3.73 (m, 2H), 2.78 (br. s., 1H); ^{13}C NMR (101 MHz, $CDCl_3$) δ 159.4 (s), 152.0 (s), 151.8 (d), 135.0 (s), 134.0 (s), 130.9 (s), 130.0 (d), 128.6 (d), 128.4 (d), 128.2 (d), 126.7 (d), 126.1 (d), 125.7 (d), 125.1 (d), 118.6 (s),

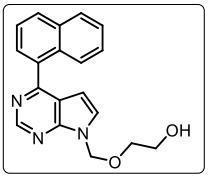

102.1 (d), 74.1 (t), 70.4 (t), 61.8 (t); HRMS (ESI) calcd. for $C_{19}H_{18}N_3O_2$ $[M + H]^+$: 320.1399; found: 320.1388.

1-(3-(7-((2-Hydroxyethoxy)methyl)-7*H*-pyrrolo[2,3-*d*]pyrimidin-4-yl)phenyl)ethan-1-one (13c): Yield: 36 mg (95%); R_f = 0.15 (60% EtOAc in petroleum ether); pink brown solid; mp: 107 °C; ^{1}H NMR (400 MHz, $CDCl_3$) δ 9.01 (s, 1H), 8.71 (t, J = 1.6 Hz, 1H), 8.33 (dt, J = 7.9, 1.4 Hz, 1H), 8.12 (dt, J = 7.9, 1.4 Hz, 1H), 7.67 (t, J = 7.8 Hz, 1H), 7.45 (d, J = 3.8 Hz, 1H), 6.90 (d, J = 3.8 Hz, 1H), 5.80 (s, 2H), 3.74–3.77 (m, 2H), 3.66–3.68 (m, 2H), 2.71 (s, 3H); ^{13}C NMR (101 MHz, $CDCl_3$) δ 197.7 (s), 156.8 (s), 152.5 (s), 151.9 (d), 138.4 (s), 137.7 (s), 133.2 (d), 129.8 (d), 129.2 (d, 2C), 128.8 (d), 116.0 (s), 101.5 (d), 74.0 (t), 70.4 (t), 61.8 (t), 26.8 (q); HRMS (ESI) calcd. for $C_{17}H_{18}N_3O_3$ $[M + H]^+$: 312.1343; found: 312.1342.

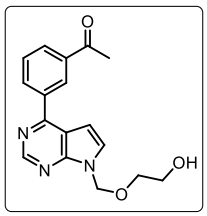

2-((4-(Naphthalen-2-yl)-7*H*-pyrrolo[2,3-*d*]pyrimidin-7-yl)methoxy)ethan-1-ol (13d) : Yield: 33 mg (88%); R_f = 0.1 (50% EtOAc in petroleum ether); white solid; mp: 117 °C; ^{1}H NMR (400 MHz, $CDCl_3$) δ 9.04 (s, 1H), 8.62 (s, 1H), 8.24 (dd, J = 8.5, 1.8 Hz, 1H), 8.01 (d, J = 9.0 Hz, 1H), 7.92–8.0 (m, 2H), 7.56–7.59 (m, 2H), 7.45 (d, J = 3.6 Hz, 1H), 7.0 (d, J = 3.6 Hz, 1H), 5.8 (s, 2H), 3.74–3.78 (m, 2H), 3.67–3.69 (m, 2H), 2.73 (br.s. 1H); ^{13}C NMR (101 MHz, $CDCl_3$) δ 158.0 (s), 152.5 (s), 152.0 (d), 135.3 (s), 134.2 (s), 133.24 (s), 129.1 (d), 128.9 (d), 128.8 (d), 128.6 (d), 127.8 (d), 127.2 (d), 126.5 (d), 125.8 (d), 116.2 (s), 101.9 (d), 74.0 (t), 70.4 (t), 61.9 (t); HRMS (ESI) calcd. For $C_{19}H_{18}N_3O_2$ $[M + H]^+$: 320.1378; found: 320.1387.

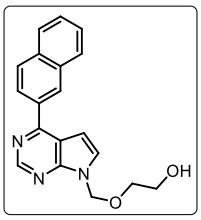

2-((4-Phenyl-7*H*-pyrrolo[2,3-*d*]pyrimidin-7-yl)methoxy)ethan-1-ol (13e) : Yield: 27 mg (71%); R_f = 0.2 (60% EtOAc in petroleum ether); yellow semi solid; ^{1}H NMR (400 MHz, $CDCl_3$) δ 8.99 (s, 1H), 8.11 (d, J = 7.3 Hz, 2H), 7.53–7.58 (m, 3H), 7.41 (d, J = 3.5 Hz, 1H), 6.89 (d, J = 3.5 Hz, 1H), 5.79 (s, 2H), 3.74–3.75 (m, 2H), 3.65–3.67 (m, 2H), 2.77 (br. s, 1H); ^{13}C NMR (101 MHz, $CDCl_3$) δ 158.0 (s), 152.3 (s), 151.9 (d), 137.9 (s), 130.2 (d), 128.8 (d, 2C),

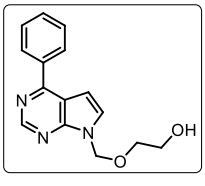

128.8 (d, 2C), 128.7 (d), 116.0 (s) 101.8 (d), 74.0 (t), 70.3 (t), 61.8 (t); HRMS (ESI) calcd. for $C_{15}H_{16}N_3O_2$ $[M + H]^+$: 270.1237; found: 270.1236.

2-((4-(4-Methoxyphenyl)-7*H*-pyrrolo[2,3-*d*]pyrimidin-7-yl)methoxy)ethan-1-ol (13f): Yield: 32 mg (85%); R_f = 0.25 (60% EtOAc in petroleum ether); light yellow solid; mp: 98 °C; ^{1}H NMR (400 MHz, $CDCl_3$) δ 8.94 (s, 1H), 8.12 (dt, J = 8.9, 2.1 Hz, 2H), 7.39 (d, J = 3.8 Hz, 1H), 7.08 (dt, J = 8.9, 2.1 Hz, 2H), 6.89 (d, J = 3.8 Hz, 1H), 5.78 (s, 2H), 3.91 (s, 3H), 3.74–3.76 (m, 2H), 3.65–3.67 (m, 2H), 2.74 (br. s. 1H); ^{13}C NMR (101 MHz, $CDCl_3$) δ 161.4 (s), 157.6 (s), 152.3 (s), 151.9 (d), 130.5 (s), 130.4 (d, 2C), 128.3 (d), 115.4 (s), 114.2 (d, 2C), 101.9 (d), 74.0 (t), 70.3 (t), 61.9 (t), 55.4 (q); HRMS (ESI) calcd. for $C_{16}H_{18}N_3O_3$ $[M + H]^+$:300.1348; found: 300.1345.

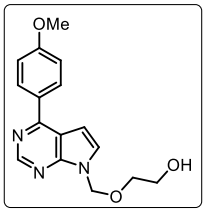

2-((4-(4-Nitrophenyl)-7*H*-pyrrolo[2,3-*d*]pyrimidin-7-yl)methoxy)ethan-1-ol (13g): Yield: 35 mg (93%); R_f = 0.2 (70% EtOAc in petroleum ether); dark yellow solid; mp: 105 °C; ^{1}H NMR (400 MHz, $CDCl_3$) δ 9.04 (s, 1H), 8.43 (d, J = 8.6 Hz, 2H), 8.31 (d, J = 8.9 Hz, 2H), 7.51 (d, J = 3.7 Hz, 1H), 6.88 (d, J = 3.7 Hz, 1H), 5.8 (s, 2H), 3.75–3.77 (m, 2H), 3.67–3.68 (m, 2H), 2.41 (b.s, 1H); ^{13}C NMR (101 MHz, $CDCl_3$) δ 155.1 (s), 152.7 (s), 152.0 (d), 148.7 (s), 144.0 (s), 129.9 (d), 129.7 (d, 2C), 124.0 (d, 2C), 116.3 (s), 101.1 (d), 74.1 (t), 70.5 (t), 61.8 (t); HRMS (ESI) calcd. for $C_{15}H_{15}N_4O_4$ $[M + H]^+$: 315.1093; found: 315.1082.

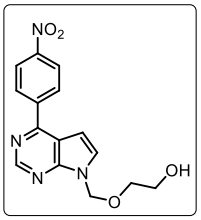

2-((4-([1,1'-Biphenyl]-4-yl)-7*H*-pyrrolo[2,3-*d*]pyrimidin-7-yl)methoxy)ethan-1-ol (13h): Yield: 31 mg (81%); R_f = 0.2 (50% EtOAc in petroleum ether); yellow solid; mp: 165 °C; ^{1}H NMR (400 MHz, $CDCl_3$) δ 9.01 (s, 1H), 8.21 (d, J = 8.3 Hz, 2H), 7.80 (d, J = 8.1 Hz, 2H), 7.69 (d, J = 7.6 Hz, 2H), 7.50 (t, J = 7.4 Hz, 2H), 7.39–7.43 (m, 2H), 6.93 (d, J = 3.5 Hz, 1H), 5.8 (s, 2H), 3.75–3.76 (m, 2H), 3.67–3.69 (m, 2H), 2.78 (br. s. 1H); ^{13}C NMR (101 MHz, $CDCl_3$) δ 157.5 (s), 152.4 (s), 151.9 (d), 143.0 (s), 140.3 (s), 136.8 (s), 129.3 (d, 2C), 128.9 (d, 2C), 128.7 (d), 127.8 (d), 127.5 (d, 2C), 127.2 (d, 2C),

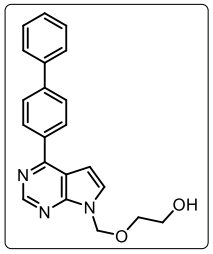

115.9 (s), 101.8 (d), 74.0 (t), 70.3 (t), 61.8 (t); HRMS (ESI) calcd. for $C_{21}H_{20}N_3O_2$ [M + H]$^+$: 346.1550; found: 346.1548.

Benzoyl deprotection (15):

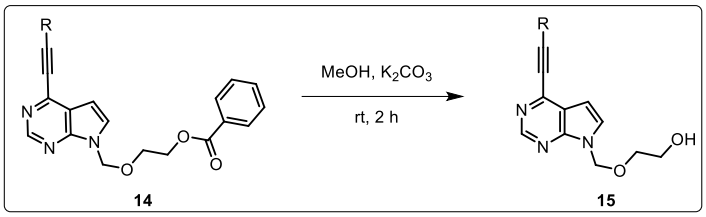

All reactions were conducted employing 50 mg of **14**. In a typical reaction, aryl ester (**14**) (1.0 equiv.), K_2CO_3 (1.2 equiv.), and the solvent methanol were charged in a 25 mL oven dried reaction tube. Reaction was carried out at room temperature under air condition. After, the reaction solution was evaporated in *vacuo*. The residue was purified by flash column chromatography (silica gel, ethyl acetate/petroleum ether) to afford the desired product **15**.

2-((4-(Cyclohexylethynyl)-7*H*-pyrrolo[2,3-*d*]pyrimidin-7-yl)methoxy)ethan-1-ol (15a) : Yield: 33 mg (90%); R_f = 0.3 (60% EtOAc in petroleum ether); yellow colour semisolid; ^{1}H NMR (500 MHz, $CDCl_3$) δ 8.83 (s, 1H), 7.35 (d, J = 3.4 Hz, 1H), 6.68 (d, J = 3.7 Hz, 1H), 5.73 (s, 2H), 3.71–3.73 (m, 2H), 3.59–3.61 (m, 2H), 2.77–2.79 (m, 1H), 2.48 (br. s, 1H), 1.95–1.97 (m, 2H), 1.80–1.82 (m, 2H), 1.65–1.69 (m, 2H), 1.57–1.58 (m, 2H), 1.41–1.43 (m, 2H); ^{13}C NMR (126 MHz, $CDCl_3$) δ 151.9 (d), 151.4 (s), 143.5 (s), 128.7 (d), 120.3 (s), 102.4 (s), 101.4 (d), 77.7 (s), 73.9 (t), 70.3 (t), 61.8 (t), 32.1 (t, 3C), 29.8 (d), 25.8 (t), 24.8 (t); HRMS (ESI) calcd. for $C_{17}H_{22}N_3O_2$ [M + H]$^+$: 300.1712; found: 300.1705.

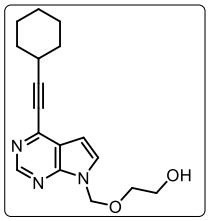

2-((4-(Phenylethynyl)-7*H*-pyrrolo[2,3-*d*]pyrimidin-7-yl)methoxy)ethan-1-ol (15b): Yield: 20 mg (54%); R_f = 0.2 (60% EtOAc in petroleum ether); green semi solid; ^{1}H NMR (400 MHz, $CDCl_3$) δ 8.90 (s, 1H), 7.68–7.70 (m, 2H), 7.41–7.45 (m, 4H), 6.80 (d, J = 3.8 Hz, 1H), 5.8 (s, 2H), 3.73–3.75 (m, 2H), 3.62–3.64 (m, 2H), 2.55 (br. s, 1H); ^{13}C NMR (101 MHz,

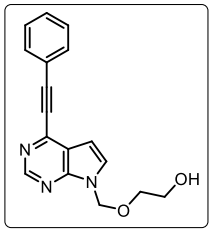

$CDCl_3$) δ 151.9 (d), 151.5 (s), 142.6 (s), 132.4 (d, 2C), 129.8 (d), 129.2 (d), 128.5 (d, 2C), 121.6 (s), 120.3 (s), 101.3 (d), 95.9 (s), 85.7 (s), 73.9 (t), 70.4 (t), 61.7 (t); HRMS (ESI) calcd. for $C_{17}H_{16}N_3O_2$ $[M + H]^+$: 294.1237; found: 294.1236.

2-((4-(p-tolylethynyl)-7*H*-pyrrolo[2,3-*d*]pyrimidin-7-yl)methoxy)ethan-1-ol (15c): Yield: 34 mg (90%); R_f = 0.2 (50% EtOAc in petroleum ether); yellow solid; mp: 117 °C; 1H NMR (400 MHz, $CDCl_3$) δ 8.89 (s, 1H) 7.58 (d, *J* = 8 Hz, 2H) 7.40 (d, *J* = 3.6 Hz, 1H) 7.22 (d, *J* = 8 Hz, 2H) 6.8 (d, *J* = 3.6 Hz, 1H), 5.8 (s, 2H) 3.73–3.75 (t, *J* = 4.7 Hz, 2H) 3.6 (t, *J* = 4.1 Hz, 2H) 2.41 (s, 3H), 1.76 (br. s, 1H); ^{13}C NMR (101 MHz, $CDCl_3$) δ 151.9 (d), 151.4 (s), 142.8 (s), 140.3 (s), 140.2 (s), 132.3 (d, 2C), 129.3 (d, 2C), 129.0 (d), 120.2 (s), 118.5 (s), 101.3 (d), 85.2 (s), 73.9 (t), 70.4 (t), 61.7 (t), 21.7 (q); HRMS (ESI) calcd. for $C_{18}H_{18}N_3O_2$ $[M + H]^+$: 308.1378; found: 308.1392.

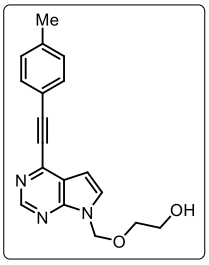

2-((4-((4-Fluorophenyl)ethynyl)-7*H*-pyrrolo[2,3-*d*]pyrimidin-7-yl)methoxy)ethan-1-ol (15d): Yield: 18 mg (49%); R_f = 0.2 (60% EtOAc in petroleum ether); yellow semi solid; ^{1}H NMR (500 MHz, $CDCl_3$) δ 8.9 (s, 1H), 7.68 (dd, *J* = 8.9, 5.2 Hz, 2H), 7.42 (d, *J* = 3.4 Hz, 1H), 7.12 (t, *J* = 8.8 Hz, 2H), 6.78 (d, *J* = 3.7 Hz, 1H), 5.76 (s, 2H), 3.73–3.75 (m, 2H), 3.63–3.64 (m, 2H) 2.45 (br. s, 1H); ^{13}C NMR (126 MHz, $CDCl_3$) δ 164.4 (s), 162.4 (s), 152.0 (d), 151.6 (s), 142.5 (s), 134.5 (d, $J_{C\text{-}F}$ = 8.5Hz), 129.2 (d), 120.2 (s), 116.1 (d), 115.9 (d), 101.2 (d), 94.6 (s), 85.5 (s), 77.2 (d), 74.0 (t), 70.4 (t), 61.8 (t); HRMS (ESI) calcd. for $C_{17}H_{15}FN_3O_2$ $[M + H]^+$: 312.1070; found: 312.1138.

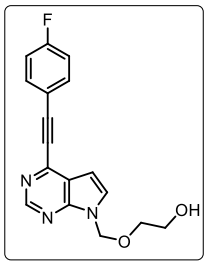

2-((4-((4-Methoxyphenyl)ethynyl)-7*H*-pyrrolo[2,3-*d*]pyrimidin-7-yl)methoxy)ethan-1-ol (15e): Yield: 35mg (94%); R_f = 0.2 (60% EtOAc in petroleum ether); brown semisolid; ^{1}H NMR (400 MHz, $CDCl_3$) δ 8.87 (s, 1H), 7.63 (dt, *J* = 9.0, 2.1 Hz, 2H), 7.4 (d, *J* = 3.6 Hz, 1H), 6.93 (dt, *J* = 9.0, 2.1 Hz, 2H), 6.76 (d, *J* = 3.6 Hz, 1H), 5.74 (s, 2H), 3.85 (s, 3H), 3.73–3.75 (m, 2H), 3.61–3.63 (m, 2H), 2.67 (s, 1H); ^{13}C NMR (101 MHz, $CDCl_3$) δ 160.8 (s), 151.9 (d), 151.4 (s), 143.0 (s), 134.1 (d, 2C), 128.9 (d), 120.0 (s), 114.2 (d,

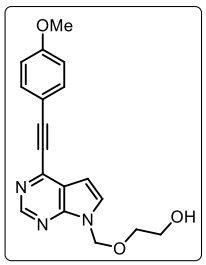

2C), 113.5 (s), 101.3 (d), 96.5 (s), 84.9 (s), 73.9 (t), 70.4 (t), 61.7 (t), 55.4 (q); HRMS (ESI) calcd. for $C_{18}H_{18}N_3O_3$ [M + H]$^+$: 324.1348; found: 324.1355.

2-((4-((3-Aminophenyl)ethynyl)-7*H*-pyrrolo[2,3-*d*]pyrimidin-7-yl)methoxy)ethan-1-ol (15f) : Yield: 19 mg (53%); R_f = 0.2 (60% EtOAc in petroleum ether); yellow semisolid; ^{1}H NMR (400 MHz, $CDCl_3$) δ 8.89 (s, 1H), 7.4 (d, *J* = 3.6 Hz, 2H), 7.19 (t, *J* = 7.8 Hz 1H), 7.07–7.10 (m, 1H), 6.99 (t, *J* = 1.5 Hz, 1H), 6.77 (d, *J* = 3.6 Hz, 2H), 6.74–6.76 (m, 1H), 5.75 (s, 2H), 3.73–3.75 (m, 2H), 3.62–3.64 (m, 2H), 1.77 (br. s, 1H); ^{13}C NMR (101 MHz, $CDCl_3$) δ 151.9 (d), 151.5 (s), 146.4 (s), 142.8 (s), 129.5 (d), 129.1 (d), 122.8 (d), 122.2 (s), 120.3 (s), 118.3 (d), 116.7 (d), 101.3 (d), 96.3 (s), 85.1 (s), 73.9 (t), 70.4 (t), 61.7 (t); HRMS (ESI) calcd. for $C_{17}H_{17}N_4O_2$ [M + H]$^+$: 309.1351; found: 309.1342.

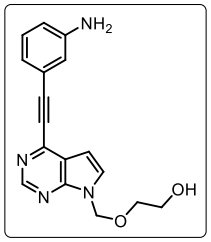

2-((4-(Cyclohex-1-en-1-ylethynyl)-7*H*-pyrrolo[2,3-*d*]pyrimidin-7-yl)methoxy)ethan-1-ol (15g): Yield: 30 mg (81%); R_f = 0.1 (50% EtOAc in petroleum ether); dark brown semisolid; ^{1}H NMR (400 MHz, $CDCl_3$) δ 8.85 (s, 1H), 7.35 (d, *J* = 3.6 Hz, 1H), 6.69 (d, *J* = 3.6 Hz, 1H), 6. 47–6.50 (m, 1H), 5.74 (s, 2H), 3.72–3.74 (m, 2H), 3.61–3.63 (m, 2H), 2.44 (br. s. 1H) 2.30–2.34 (m, 2H), 2.19–2.24 (m, 2H), 1.65–1.74 (m, 4H); ^{13}C NMR (101 MHz, $CDCl_3$) δ 151.9 (d), 151.4 (s), 143.3 (s), 139.4 (d), 128.7 (d), 120.0 (s), 101.3 (d), 98.3 (s), 83.5 (s), 73.9 (t), 70.3 (t), 61.8 (t), 29.7 (d), 28.8 (t), 26.0 (t), 22.1 (t), 21.3 (t); HRMS (ESI) calcd. for $C_{17}H_{20}N_3O_2$ [M + H]$^+$: 298.1555; found: 298.1552.

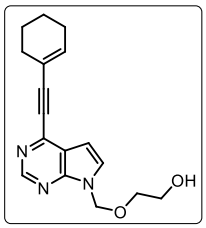

2-((4-(Pent-1-yn-1-yl)-7*H*-pyrrolo[2,3-*d*]pyrimidin-7-yl)methoxy)ethan-1-ol (15h) : Yield: 28 mg (79%); R_f = 0.1 (50% EtOAc in petroleum ether); dirty white semisolid; ^{1}H NMR (400 MHz, $CDCl_3$) δ 8.83 (s, 1H), 7.3 (d, *J* = 3.6 Hz, 1H), 6.68 (d, *J* = 3.6 Hz, 1H), 5.73 (s, 2H), 3.71–3.73 (m, 2H), 3.60–3.62 (m, 2H), 2.55 (t, *J* = 7.1 Hz, 2H), 1.69–1.78 (m, 3H), 1.1 (t, *J* = 7.4 Hz, 3H); ^{13}C NMR (101 MHz, $CDCl_3$) δ 151.9 (d), 151.4 (s), 143.4 (s), 128.7 (d), 120.3 (s), 101.3 (d), 98.4 (s), 77.9 (s), 73.9 (t), 70.3 (t), 61.8 (t), 21.7 (t), 21.6 (t), 13.6 (q); HRMS (ESI) calcd. for $C_{14}H_{18}N_3O_2$ [M + H]$^+$: 260.1399; found: 260.1382.

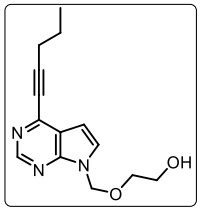

2-((4-(Cyclopropylethynyl)-7*H*-pyrrolo[2,3-*d*]pyrimidin-7-yl)methoxy)ethan-1-ol (15i) : Yield: 30 mg (83%); R_f = 0.1 (50% EtOAc in petroleum ether); brown solid; mp: 71 °C; ^{1}H NMR (400 MHz, $CDCl_3$) δ 8.80 (s, 1H), 7.34 (d, J = 3.6 Hz, 1H), 6.67 (d, J = 3.6 Hz, 1H), 5.72 (s, 2H) 3.71–3.75 (m, 2H) 3.60–3.62 (m, 2H), 2.43 (br. s, 1H), 1.57–1.64 (m, 2H) 1.26–1.31 (m, 2H), 1.01–1.03 (m, 1H); ^{13}C NMR (101 MHz, $CDCl_3$) δ 151.9 (d), 151.3 (s), 143.3 (s), 128.6 (d), 120.1 (s), 101.9 (s), 101.3 (d), 73.9 (t), 73.0 (s), 70.3 (t), 61.8 (t), 9.4 (t, 2C), 0.5 (d); HRMS (ESI) calcd. for $C_{14}H_{16}N_3O_2$ $[M + H]^+$: 258.1243; found: 258.1227.

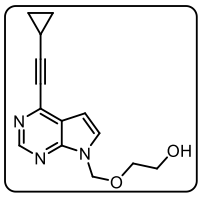

Design and Synthesis of Indene Fused Sugar Nucleosides as Potential Antiviral Agents for Covid-19:

Methodology for screening antiviral compounds:

RT-PCR Based method for Screening Antiviral Compounds

Vero E6 cells were seeded at a density of 50,000 cells/well in the 48-well plate. After ~ 16 h, cells were incubated in the presence of 2X concentrations of all compound dilutions at 37°C, 5% CO_2 for 15 min. After 15 min media with compounds was discarded and cells were incubated in the presence of the virus for 1.0 h. The virus culture being used (0.01 MOI) was diluted in the ratio of 1:1000 in DMEM + 5 % FBS media. After 1.0 h, the virus culture was discarded and cells were allowed to grow in the presence of 1X concentration of all the compound dilutions in 200 µL DMEM+ 5 % FBS media at 37 °C, 5% CO_2 for 48 h. After 48 h, the supernatant was collected and processed further for RNA extraction and RT-PCR.

Steps for RNA extraction and RT-qPCR

RNA extraction was done using a Gsure RNA isolation kit and RT-qPCR was further performed with GCC Diagsure RT-qPCR kit according to kit manufacturer's protocol. The test included Niclosamide at 1 µM and 5 µM concentrations as positive control and cells alone control besides positive and negative controls provided along with the kit. The experiments were performed twice in duplicates.

Analysis of RT-PCR data

ΔCt for all the samples was calculated using the Ct value difference between Virus control and test samples for the respective fluorophores used.

$$\Delta Ct = Ct\ (Virus\ Control) - Ct\ (Test\ Sample)$$

Cell Based ELISA for Screening Antiviral Compounds

The antiviral activity of compounds was evaluated using cell-based ELISA. Briefly, Vero E6 cells seeded at a density of 1.2×10^4 cells/well in 96-well plate were incubated for 16 h, at 37 °C with 5% CO_2. Then, cell monolayers were pretreated with serial double dilutions

of compounds from 0.001 to 10 µM (50 µL/well) for 15 min. After pretreatment, the compound-containing medium was aspirated from cell monolayers, and the virus was added at 0.01 MOI (multiplicity of infection) in 50 µL of DMEM supplemented with 2% FBS. After 1 h of viral adsorption at 37 °C, the inoculum was removed and replaced by 50 µL/well of the same pre-treatment dilutions and 50 µL/well of DMEM supplemented with 2% FBS. Finally, the plates were incubated at 37 °C, 5% CO_2 for 24 h. After 24 h, media with compounds was discarded, cells were fixed with formalin for 40 min, and further processed for cell-based ELISA.

For cell-based ELISA, cells were washed thrice with 1X PBS and blocked with 5 % BSA for 1 h. After washing thrice with 1X PBS, permeabilization of cells was done with 1 % w/v saponin for 30 min. The cells were then washed thrice with 1X PBS and incubated with HRP-Conjugated Nanobody against spike protein for 1 h, followed by washing thrice with 1X PBST. Thereafter, TMB substrate solution was added and incubated for 5 mins and the reaction was stopped by adding 2N H_2SO_4. The yellow color so obtained was quantified by taking absorbance at 450 nm and viral content (percentage of antigen) was calculated by following formula: Percent antigen = [(A) / (B) x 100], where A and B indicates the absorption of virus infected cells incubated with compound and virus infected cells, respectively. The test included Niclosamide at 1 µM and 5 µM concentrations as positive control and cells alone control besides positive and negative controls provided along with the kit. The experiments were performed twice in duplicates.

Controls used in cell-based ELISA

The validation of the antiviral efficacy of tested compounds was done by comparing the EC_{50} of test compounds concerning the EC_{50} of reported compounds being used against SARS CoV in Vero E6 cells. The EC_{50} obtained for Niclosamide and Remdesvir using ELISA-based assays were comparable to the reported studies.[58]

Compound	Reported EC_{50} in VERO E6 Cells against SARS CoV-2	EC_{50} from cell-based ELISA Assay
Niclosamide	< 0.1 µM (Wen *et al.*, 2007) PMID: 17663539	0.12 ± 0.03
Remdesivir	0.77 µM (Wang *et al.*, 2020) PMID: 32020029	0.87 ± 0.41

(3a*R*,5*R*,6*R*,6a*R*)-5-Ethynyl-2,2-dimethyl-6-(prop-2-yn-1-yl)tetrahydrofuro [2,3-d][1,3] dioxol-6-ol (18).

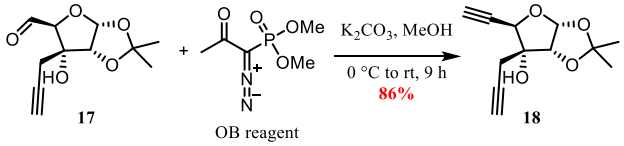

At 0 °C, to a solution of **17** (250 mg, 1.1 mmol) in MeOH (5 mL) was added K_2CO_3 (458 mg, 3.3 mmol) and Ohira Bestmann reagent (254 mg, 1.3 mmol) under an argon atmosphere and the resulting mixture was then stirred at room temperature for 9 h. After completion of reaction as indicated by TLC, MeOH was evaporated under reduced pressure followed by extraction using ethyl acetate (3x10 mL). The combined organic layer was dried (Na_2SO_4) and concentrated in vacuo. The residue was then purified by silica gel column chromatography (5→10% ethyl acetate in petroleum ether) to afford compound **18** (210 mg, 86%).

R_f = 0.8 (30% EtOAc in petroleum ether), white solid; mp: 84–86 °C; ^{1}H NMR (400 MHz, $CDCl_3$) δ 5.84 (d, J = 4.0 Hz, 1H),4.62 (d, J = 4.0 Hz, 1H), 4.56 (d, J = 2.1 Hz, 1H), 2.96 (d, J = 1.4 Hz, 1H), 2.92 (dd, J = 17.4, 2.7 Hz, 1H), 2.61 (d, J = 2.2 Hz, 1H), 2.47 (ddd, J = 1.1, 1.5, 17.4 Hz, 1H), 2.12 (t, J = 2.7 Hz, 1H), 1.60 (s, 3H), 1.40 (s, 3H); ^{13}C NMR (101 MHz, $CDCl_3$) δ 112.9 (s), 103.8 (d), 80.1 (d, 2C), 79.1 (s), 77.5 (s), 73.1 (d, 2C), 71.5 (s),

26.5 (q, 2C), 23.6 (t); HRMS (ESI) calcd. for $C_{12}H_{14}NaO_4$ $[M + Na]^+$: 245.0784; found: 245.0784.

(2*R*,3*R*,4*R*,5*R*)-5-Ethynyl-4-(prop-2-yn-1-yl)tetrahydrofuran-2,3,4-triyl triacetate (20)

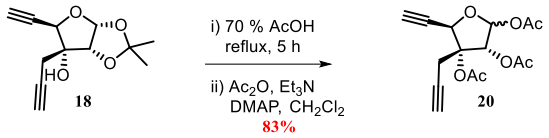

A solution of acetonide **18** (500 mg, 2.2 mmol) in 70% AcOH (5 mL) was refluxed at 110 °C for 5 h. After the completion of reaction (as indicated by TLC), acetic acid and water were evaporated under reduced pressure and the resulting crude residue (400 mg) was dissolved in CH_2Cl_2 (4 mL) and and treated with Et_3N (1.5 mL, 10.9 mmol) and DMAP (26.8 mg, 219 µmol) and cooled to 0 °C. To this mixture Ac_2O (2.1 mL, 21.9 mmol) was added slowly and the reaction mixture was allowed to warm to room temperature and stirring was continued for additional 8 h. The reaction mixture was diluted with CH_2Cl_2 (50 mL) and washed with water, brine, dried (Na_2SO_4) and concentrated under reduced pressure. The resulting crude was purified by silica gel column chromatography (5→10% ethyl acetate in petroleum ether) to afford compound **20** (603 mg, 87%).

R_f = 0.2 (30% EtOAc in petroleum ether); white solid; mp: 92–95 °C; ^{1}H NMR (500 MHz, DMSO-d_6) δ 6.30 (d, J = 4.6 Hz, 1H), 5.42 (d, J = 5.0 Hz, 1H), 4.98 (d, J = 2.3 Hz, 1H), 3.87 (d, J = 2.3 Hz, 1H), 3.1 (dd, J = 2.7, 17.2 Hz, 1H), 3.05 (dd, J = 2.7, 17.2 Hz, 1H), 2.99 (t, J = 2.7 Hz, 1H), 2.09 (s, 3H), 2.07 (s, 3H), 2.05 (s, 3H); ^{13}C NMR (126 MHz, DMSO-d_6) δ 169.1 (s), 169.0 (s), 168.9 (s), 92.6 (d), 81.7 (s), 81.2 (d), 77.6 (s), 76.7 (s), 74.2 (d), 74.0 (d), 72.9 (d), 23.5 (t), 20.9 (q), 20.6 (q), 20.2 (q); HRMS (ESI) calcd. for $C_{15}H_{16}NaO_7$ $[M + Na]^+$: 331.0788; found: 331.0782.

General procedure for glycosidation of diyne 20 to afford 22a, 22b and 22c.

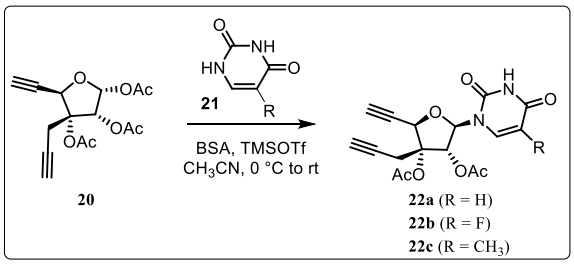

To a solution of **20** (500 mg, 1.6 mmol) in dry CH_3CN (5 ml) was added pyrimidine **21** (3.2 mmol) and BSA (8.1 mmol) at room temperature and then refluxed at 60 °C for 30 min. TMSOTf (3.2 mmol) was introduced at 0 °C and again refluxed overnight at 75 °C. After completion of reaction (as indicated by TLC), the reaction mixture was extracted using ethyl acetate (3 x15 mL). The combined organic layer was dried (Na_2SO_4) and then concentrated under reduced pressure. The residue was purified by silica gel column chromatography (ethyl acetate and petroleum ether) to afford glycosidation products **22a, 22b** and **22c**.

(2*R*,3*R*,4*R*,5*R*)-5-(2,4-Dioxo-3,4-dihydropyrimidin-1(2*H*)-yl)-2-ethynyl-3-(prop-2-yn-1-yl) tetrahydrofuran-3,4-diyl diacetate (22a): R_f = 0.8 (in EtOAc); yield: 456 mg (78%); white solid; mp: 107–110 °C; ^{1}H NMR (400 MHz, $CDCl_3$) δ 9.40 (s, 1H), 7.65 (d, J = 8.2 Hz, 1H), 6.34 (d, J = 7.8 Hz, 1H), 5.84 (dd, J = 8.2, 1.8 Hz, 1H), 5.54 (d, J = 7.8 Hz, 1H), 5.29 (d, J = 2.3 Hz, 1H), 3.41 (dd, J = 17.4, 2.7 Hz, 1H),3.13 (dd, J = 17.9, 2.7 Hz, 1H), 2.95 (d, J = 2.3 Hz, 1H), 2.21 (s, 3H), 2.11 (s, 3H), 2.02 (t, J = 2.7 Hz, 1H); ^{13}C NMR (101 MHz, $CDCl_3$) δ 170.2 (s), 169.9 (s), 162.8 (s), 150.7 (s), 139.1 (d), 103.9 (d), 85.7 (d), 84.7 (s), 80.5 (s), 77.5 (d), 76.7 (d), 76.6 (s), 73.7 (d), 71.6 (d), 22.6 (t), 21.6 (q), 20.6 (q); HRMS (ESI) calcd. for $C_{17}H_{16}N_2O_7Na$ $[M + Na]^+$: 383.0850; found: 383.0840.

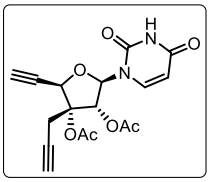

(2*R*,3*R*,4*R*,5*R*)-2-Ethynyl-5-(5-fluoro-2,4-dioxo-3,4-dihydropyrimidin-1(2*H*)-yl)-3-(prop-2-yn-1-yl)tetrahydrofuran-3,4-diyl diacetate (22b): Yield: 454 mg (74%); R_f = 0.6 (20% EtOAc in petroleum ether); yellowish brown solid; mp: 137-139 °C; ^{1}H NMR (500 MHz, CD_3OD) δ 7.83 (d, J = 6.1 Hz, 1H), 6.29 (dd, J = 1.5, 7.6 Hz, 1H), 5.57 (d, J = 7.6 Hz, 1H), 5.31 (d, J = 1.9 Hz, 1H), 4.23 (b. s., 1H), 3.340–3.44 (m, 2H), 3.18 (dd, J = 17.5, 2.3 Hz, 1H), 2.26 (s, 1H), 2.20 (s, 3H), 2.11 (s, 3H); ^{13}C NMR (126 MHz, CD_3OD) δ 171.3 (s), 171.0 (s), 150.4 (s), 148.8 (s), 140.9 (s), 124.3 (d, $J_{C–F}$ = 34.3 Hz), 87.0 (d), 85.7 (s, 2C), 82.3 (d), 77.6 (s), 77.3 (d), 74.7 (d), 72.7 (d), 23.4 (t), 21.8 (q), 20.9 (q); HRMS (ESI) calcd. for $C_{17}H_{15}FN_2O_7$ $[M + H]^+$: 401.0756; found: 401.0746.

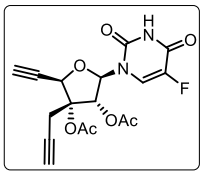

(3*R*,4*R*,5*R*)-2-Ethynyl-5-(5-methyl-2,4-dioxo-3,4-dihydropyrimidin-1(2*H*)-yl)-3-(prop-2-yn-1-yl)tetrahydrofuran-3,4-diyl diacetate (22c): Yield: 522 mg (86%); R_f = 0.6 (65% EtOAc in petroleum ether); white solid; mp: 188–191 °C; ^{1}H NMR (500 MHz, $CDCl_3$) δ 9.04 (s, 1H), 7.47 (s, 1H), 6.35 (d, *J* = 8.0 Hz, 1H), 5.55 (d, *J* = 7.6 Hz, 1H), 5.27 (d, *J* = 1.9 Hz, 1H), 3.42 (dd, *J* = 17.5, 2.7 Hz, 1H), 3.16 (dd, *J* = 17.5, 2.7 Hz, 1H), 2.96 (d, *J* = 1.9 Hz, 1H), 2.20 (s, 3H), 2.10 (s, 3H), 2.01–2.03 (m, 1H), 1.93 (s, 3H); ^{13}C NMR (126 MHz, $CDCl_3$) δ 170.2 (s), 169.9 (s), 163.3 (s), 150.8 (s), 134.8 (d, 2C), 112.4 (s), 85.5 (d), 84.8 (s), 80.3 (s), 77.8 (s), 76.5 (d), 73.8 (d), 71.5 (d), 22.7 (t), 21.6 (q), 20.7 (q), 12.8 (q); HRMS (ESI) calcd. for $C_{18}H_{18}N_2O_7Na$ $[M + Na]^+$: 397.1006; found: 397.0997.

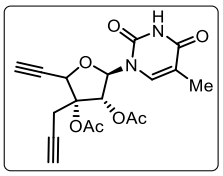

General procedure for (2+2+2) cyclotrimerization reactions of diyne 22 using acetylene gas:

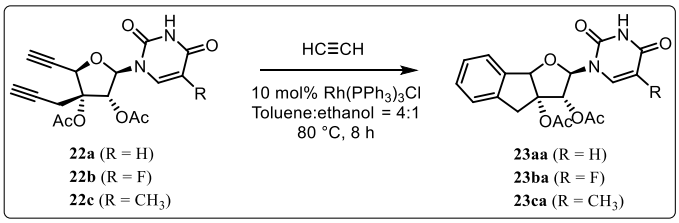

A solution of diyne (500mg, 1.4 mmol) in 4:1 toluene/ethanol (5 mL) in a screw cap pressure tube was evacuated and back filled with argon. To this solution Wilkinson's catalyst [$Rh(PPh_3)_3Cl$] (139µmol) was added. The resulting mixture was sealed with septum and copper wire and cooled to -78 °C. Acetylene gas was then condensed in reaction mixture by continuous bubbling for 25 min. The reaction mixture was stirred at 80 °C for 8 h and the screw cap pressure tube was cooled to room temperature. The resulting mixture was transferred to round bottom flask and solvents were evaporated under reduced pressure. The residue was purified by column chromatography using silica gel (ethyl acetate in petroleum ether) to afford cyclotrimerized products **23aa**, **23ba** and **23ca**.

(2*R*,3*R*,3a*R*)-2-(2,4-Dioxo-3,4-dihydropyrimidin-1(2*H*)-yl)-2,3,4,8b-tetrahydro-3a*H*-indeno [1,2-b]furan-3,3a-diyl diacetate (23aa): Yield: 440 mg (82%); R_f = 0.3 (50% EtOAc in petroleum ether); white solid; mp: 77–

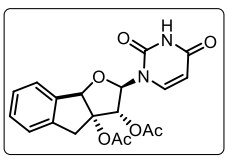

80 °C; ^{1}H NMR (500 MHz, $CDCl_3$) δ 9.24 (s, 1H), 7.36–7.45 (m, 3H), 7.29 (d, J = 6.7 Hz, 1H), 6.88 (d, J = 8.2 Hz, 1H), 6.48 (d, J = 7.9 Hz, 1H), 5.80 (s, 1H), 5.65 (dd, J = 8.2, 1.8 Hz, 1H),5.23 (d, J = 7.9 Hz, 1H), 3.81 (d, J = 17.4 Hz, 1H), 3.47 (d, J = 17.4 Hz, 1H), 2.22 (s, 3H), 2.12 (s, 3H); ^{13}C NMR (126 MHz, $CDCl_3$) δ 170.2 (s), 169.8 (s), 162.6 (s), 150.5 (s), 139.1 (s), 138.6 (d), 137.9 (s), 130.1 (d), 128.2 (d), 125.9 (d), 124.9 (d), 103.6 (d), 90.3 (s), 90.1 (d), 86.4 (d),77.0 (d), 39.7 (t), 21.4 (q), 20.5 (q); HRMS (ESI) calcd. for $C_{19}H_{18}N_2O_7Na$ [M + Na]$^+$: 409.1006; found:409.0998.

(2*R*,3*R*,3a*R*)-2-(5-Fluoro-2,4-dioxo-3,4-dihydropyrimidin-1(2*H*)-yl)-2,3,4,8b-tetrahydro-3a*H*-indeno[1,2-b]furan-3,3a-diyl diacetate (23ba):

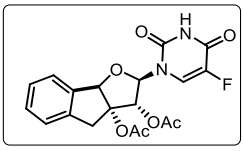

Yield: 406 mg (76%); R_f = 0.3 (80% EtOAc in petroleum ether); pale yellow solid; mp: 82–85 °C; ^{1}H NMR (500 MHz, $CDCl_3$) δ 9.07 (b. s., 1H), 7.35–7.43 (m, 3H), 7.27 (d, J = 6.9 Hz, 1H), 6.86 (d, J = 5.7 Hz, 1H), 6.42 (d, J = 7.2 Hz, 1H), 5.79 (s, 1H), 5.15 (d, J = 7.2 Hz, 1H), 3.75 (d, J = 17.2 Hz, 1H), 3.45 (d, J = 17.2 Hz, 1H), 2.19 (s, 3 H), 2.08 (s, 3H); ^{13}C NMR (126 MHz, $CDCl_3$) δ 170.1 (s), 169.8 (s), 149.1(s), 141.8(s), 139.0 (s, 2C), 137.7 (s, 2C), 130.4 (d), 128.4 (d), 126.0 (d), 124.9 (d), 122.8 (d, J_{C-F} = 34.3Hz), 90.4 (d), 87.2 (d), 77.3(d), 39.7 (t), 21.4 (q), 20.5 (q); HRMS (ESI) calcd. for $C_{19}H_{17}FN_2O_7Na$ [M + Na]$^+$: 427.0912; found: 427.0904.

2-(5-Methoxy-2,4-dioxo-3,4-dihydropyrimidin-1(2*H*)-yl)-2,3,8,8a-tetrahydro-3a*H*-indeno[2,1-b]furan-3,3a-diyl diacetate (23ca):

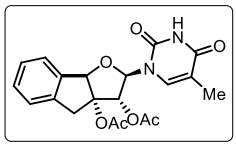

Yield: 438 mg (82%); R_f = 0.5 (65% EtOAc in petroleum ether); white solid; mp: 63–66 °C; ^{1}H NMR (400 MHz, $CDCl_3$) δ 8.77 (b. s., 1H), 7.33–7.43 (m, 3H), 7.28 (d, J =7.3 Hz, 1H), 6.58 (s, 1H), 6.45 (d, J = 7.3 Hz, 1H), 5.76 (s, 1H), 5.23 (d, J = 7.3 Hz, 1H), 3.81 (d, J = 17.7 Hz, 1H), 3.44 (d, J = 17.7 Hz, 1H), 2.18 (s, 3H), 2.08 (s, 3H), 1.71 (s, 3H); ^{13}C NMR (101 MHz, $CDCl_3$) δ 170.1 (s), 169.8 (s), 163.2 (s), 150.6 (s), 139.3 (s), 138.0 (s), 134.4 (d), 130.1 (d), 128.0 (d), 126.0 (d), 125.0 (d), 112.0 (s), 90.5 (s), 90.2 (d), 86.5 (d), 76.9 (d), 39.8 (t), 21.4 (q), 20.5 (q), 12.6 (q); HRMS (ESI) calcd. for $C_{20}H_{20}N_2O_7Na$: 423.1163 [M + Na]$^+$; found: 423.1153.

General procedure for (2+2+2) cyclotrimerization reactions of diyne 4–6 using but-2-yne-1,4-diol:

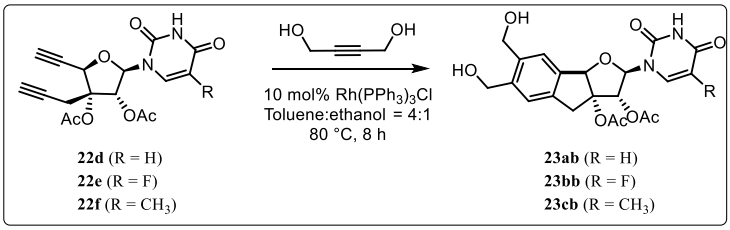

A solution of diyne (1.4 mmol) and 4:1 toluene/ethanol (5 mL) in screw cap pressure tube was evacuated and back filled with argon. To this solution Wilkinson's catalyst [$Rh(PPh_3)_3Cl$] (139µmol) and but-2-yne-1,4-diol (4.2 mmol) were added. The solution was then stirred at 80 °C for 8 h. The screw cap pressure tube was cooled to room temperature and the completion of reaction was confirmed by TLC. The solvents were evaporated under reduced pressure and the resulting residue was purified by column chromatography using silica gel (50→60 % ethyl acetate in petroleum ether) to afford **23d**, **23e** and **23f**.

(2*R*,3*R*,3a*R*)-2-(2,4-Dioxo-3,4-dihydropyrimidin-1(2*H*)-yl)-6,7-bis(hydroxymethyl)-2,3,4,8b-tetrahydro-3a*H*-indeno[1,2-b]furan-3,3a-diyl diacetate (23ab): Yield: 539 mg (87%); R_f = 0.3 (in EtOAc); white solid; mp: 82–84 °C; ^{1}H NMR (500 MHz, CD_3OD) δ 7.49 (s, 1H), 7.37 (s, 1H), 7.03 (d, *J* = 8.0 Hz, 1H), 6.39 (d, *J* = 7.6 Hz, 1H), 5.79 (s, 1H), 5.60 (d, *J* = 8.0 Hz, 1H), 5.28 (d, *J* = 7.2 Hz, 1H), 4.73 (s, 5H), 3.78 (d, *J* = 17.2 Hz, 1H), 3.44–3.48 (m, 1H), 3.19–3.23 (m, 1H), 2.19 (s, 3H), 2.09 (s, 3H); ^{13}C NMR (126 MHz, CD_3OD) δ 171.2 (s), 171.2 (s), 165.2 (s), 151.9 (s), 142.4 (s), 140.4 (d), 140.3 (s), 139.9 (s), 138.3 (s), 126.0 (d), 125.4 (d), 103.9 (d), 91.5 (s), 91.0 (d), 88.0 (d), 78.2 (d), 62.7 (t, 2C), 40.8 (t), 21.6 (q), 20.7 (q); HRMS (ESI) calcd. for $C_{21}H_{22}N_2O_9Na$ $[M + Na]^+$: 469.1218; found: 469.1210.

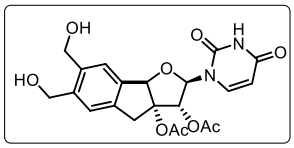

(2*R*,3*R*,3a*R*)-2-(5-Fluoro-2,4-dioxo-3,4-dihydropyrimidin-1(2*H*)-yl)-6,7-bis(hydroxymethyl) -2,3,4,8b-tetrahydro-3a*H*-indeno[1,2-b]furan-3,3a-diyl diacetate (23bb): Yield: 441 mg (72%); R_f = 0.3 (in EtOAc); yellow liquid; mp: 84–86 °C; ^{1}H NMR (200 MHz, DMSO-d_6) δ 7.49 (s, 1H), 7.36 (s, 1H), 7.09 (d, *J* = 6.1 Hz, 1H), 6.35 (dd, *J* = 7.5, 1.6 Hz, 1H), 5.77 (s, 1H), 5.25 (d, *J* = 7.5 Hz, 1H), 4.78 (s, 4H), 4.71 (s, 3H), 3.77 (d, *J* = 17.6 1H), 3.40–3.48 (m, 1H), 2.17 (s, 3H), 2.07 (s, 3H); ^{13}C NMR (126 MHz, DMSO-d_6) δ 161.7 (s),

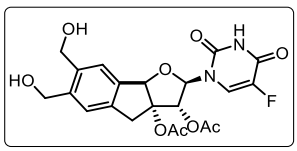

161.6 (s), 141.0 (s), 149.0 (s), 132.9 (s), 131.3 (s), 130.8 (s), 130.5 (s), 128.6 (s), 116.3 (d), 115.7 (d), 114.7 (d, J_{C-F} = 34.33 Hz), 81.8 (s), 81.6 (d), 78.8 (d), 68.6 (d), 53.0 (t), 53.0 (t), 31.5 (t), 11.9 (q), 11.0 (q); HRMS (ESI) calcd. for $C_{21}H_{21}FN_2O_9Na$ $[M + Na]^+$: 487.1123; found: 487.1114.

5,6-Bis(hydroxymethyl)-2-(5-methyl-2,4-dioxo-3,4-dihydropyrimidin-1(2*H*)-yl)-2,3,8,8a-tetrahydro-3a*H*-indeno[2,1-b]furan-3,3a-diyl diacetate (23cb): Yield: 480 mg (78%); R_f = 0.4 (50% EtOAc in petroleum ether); yellow liquid; ^{1}H NMR (500 MHz, CD_3OD) δ 7.46 (s, 1H), 7.33 (s, 1H), 6.71 (s, 1H), 6.36 (d, J = 7.6 Hz, 1H), 5.74 (s, 1H), 5.24 (d, J = 7.6 Hz, 1H), 4.69 (d, J = 2.3 Hz, 4H), 3.78 (d, J = 17.5 Hz, 1H), 3.43 (d, J = 17.5 Hz, 1H), 2.16 (s, 3H), 2.06 (s, 3H), 1.68 (s, 3H); ^{13}C NMR (126 MHz, CD_3OD) δ 171.0 (s), 171.0 (s), 165.1 (s), 151.8 (s), 142.2 (s), 140.1 (s), 139.8 (s), 138.1 (s), 135.5 (d), 126.1 (d), 125.6 (d), 112.5 (s), 91.2 (s), 90.8 (d), 87.4 (d), 77.8 (d), 62.8 (t), 62.7 (t), 40.7 (t), 21.6 (q), 20.8 (q), 12.6 (q); HRMS (ESI) calcd. for $C_{22}H_{24}N_2O_9Na$ $[M + Na]^+$: 483.1374; found: 483.1365.

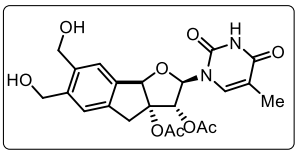

General procedure for acetyl deprotection.

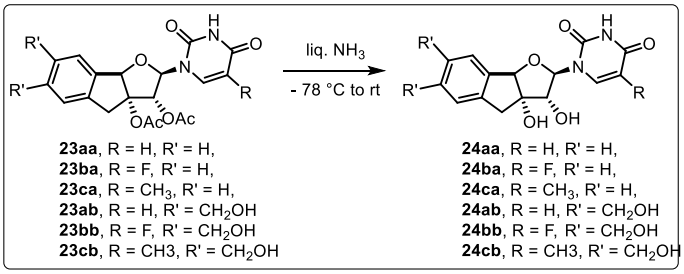

Acetyl protected compound **23** (500 mg) was taken in two-neck flask and cooled to –78 °C followed by condensation of ammonia. After the condensation of ammonia, the solution was stirred overnight and the temperature increased from –78 °C to rt. After completion of reaction (as indicated by TLC), Ethyl acetate was added to the solution and the solvent was evaporated on rota vapour at reduced pressure for complete removal of ammonia gas. The residue was then washed with diethyl ether and purified by column chromatography using silica gel (MeOH in DCM) to afford acetyl deprotection product **24**.

1-((2*R*,3*R*,3a*S*)-3,3a-Dihydroxy-3,3a,4,8b-tetrahydro-2*H*-indeno[1,2-b]furan-2-yl) pyrimidine-2,4(1*H*,3*H*)-dione (24aa): Yield: 328 mg (84%); R_f = 0.4 (in EtOAc); white solid; mp: 245–247 °C; $[\alpha]_D^{27}$: +37.3 (c = 0.22, MeOH);^{1}H NMR (400 MHz, CD_3OD) δ 7.37 (d, *J* = 8 Hz, 1H), 7.27–7.34 (m, 2H), 7.23 (d, *J* = 7 Hz, 1H), 6.93 (d, *J* = 8.1 Hz, 1H), 6.22 (d, *J* = 7.5 Hz, 1H), 5.55 (d, *J* = 8.1 Hz, 1H), 5.35 (s, 1H), 3.80 (d, *J* = 7.5 Hz, 1H), 3.25 (d, *J* = 16.3 Hz, 1H), 3.03 (d, *J* = 16.4 Hz, 1H); ^{13}C NMR (101 MHz, CD_3OD) δ 152.3 (s), 141.4 (s), 140.8 (s, 2C), 140.8 (d), 130.4 (d), 128.6 (d), 126.7 (d), 126.0 (d), 103.4 (d), 91.9 (d), 89.9 (d), 85.6 (s), 79.1 (d), 41.8 (t); HRMS (ESI) calcd. for $C_{15}H_{14}N_2O_5Na$ $[M + Na]^+$: 325.0795; found: 325.0786.

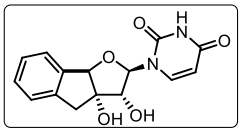

1-((2*R*,3*R*,3a*S*)-3,3a-Dihydroxy-3,3a,4,8b-tetrahydro-2*H*-indeno[1,2-b]furan-2-yl)-5-fluoropyrimidine-2,4(1*H*,3*H*)-dione (24ba): Yield: 328 mg (83%); R_f = 0.4 (EtOAc); white solid; mp: 125–127 °C; $[\alpha]_D^{27}$: +99.59 (c 0.31, MeOH); ^{1}H NMR (400 MHz, DMSO-d_6) δ 7.75 (s, 1H), 7.74–7.75 (m, 2H), 7.23–7.30 (m, 3H), 7.17 (d, *J* = 6.4 Hz, 1H), 6.76 (d, *J* = 4.9 Hz, 1H), 5.26 (s, 1H), 3.72 (d, *J* = 7.5 Hz, 1H), 3.21 (d, *J* = 16.5 Hz, 1H), 2.97 (d, *J* = 16.4 Hz, 1H); ^{13}C NMR (101 MHz, DMSO-d_6) δ 140.1 (s, 2C), 139.6 (s, 2C), 128.8 (d), 127.0 (d), 125.3 (d), 124.5 (d), 90.2 (d), 88.2 (d, J_{C-F} = 2.2 Hz) 84.1 (s, 2C), 77.9 (d), 77.2 (d), 40.8 (t); HRMS (ESI) calcd. for $C_{15}H_{13}FN_2O_5Na$ $[M + Na]^+$: 343.0701; found: 343.0692.

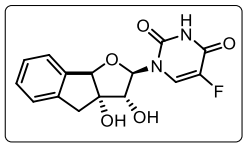

1-(3,3a-Dihydroxy-3,3a,8,8a-tetrahydro-2*H*-indeno[2,1-b]furan-2-yl)-5-methylpyrimidine-2,4(1*H*,3*H*)-dione (24ca): Yield: 332 mg (84%); R_f = 0.4 (80% EtOAc); white solid; mp: 260–262 °C; $[\alpha]_D^{27}$: +45.61 (c 0.94, MeOH); ^{1}H NMR (400 MHz, CD_3OD) δ 7.39–7.41 (m, 1H), 7.35 (td, *J* = 1.6, 7 Hz, 2H), 7.28 (d, *J* = 7Hz, 1H), 6.75 (d, *J* = 1.1 Hz, 1H), 6.21 (d, *J* = 7.5 Hz, 1H), 5.34 (s, 1H), 3.87 (d, *J* = 7.5 Hz, 1H), 3.27 (d, *J* = 16.5Hz, 1H), 3.04 (d, *J* = 16.4 Hz, 1H), 1.65 (s, 3H); ^{13}C NMR (101 MHz, CD_3OD) δ 166.2 (s), 153.0 (s), 142.2 (s), 141.7 (s), 137.1 (d), 130.8 (d), 128.8 (d), 127.1 (d), 126.5 (d), 112.1 (s), 92.5 (d), 90.4 (d), 86.1 (s), 79.2 (d), 42.4 (t), 12.5 (q); HRMS (ESI) calcd. for $C_{16}H_{16}N_2O_5Na$ $[M + Na]^+$: 339.0951; found: 339.0941.

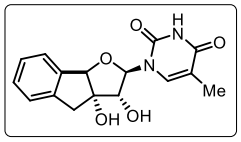

1-((2*R*,3*R*,3a*S*)-3,3a-Dihydroxy-6,7-bis(hydroxymethyl)-3,3a,4,8b-tetrahydro-2*H*-indeno[1,2 -b]furan-2-yl)pyrimidine-2,4(1*H*,3*H*)-dione (24ab):

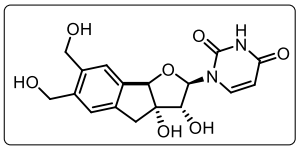

Yield: 317 mg (78%); R_f = 0.7 (in EtOAc); white solid; mp: 216–218 °C; $[\alpha]_D^{27}$: +139.89 (c = 0.09, MeOH); ^{1}H NMR (500 MHz, DMSO-d_6) δ 11.37 (s, 1H), 7.30 (s, 1H), 7.26 (s, 1H), 7.00 (d, *J* = 8.0 Hz, 1H), 6.02 (d, *J* = 8.0 Hz, 1H), 5.69 (b.s, 1H), 5.64 (s, 1H), 5.56 (d, *J* = 8.4 Hz, 1H), 5.15–5.17 (m, 3H), 4.48–4.54 (m, 4H), 3.72 (d, *J* = 7.6 Hz, 1H), 3.19 (d, *J* = 16.4 Hz, 1H), 2.88 (d, *J* = 16.4 Hz, 1H); ^{13}C NMR (126 MHz, DMSO-d_6) δ 166.3 (s), 152.7 (s), 142.2 (d), 141.5 (s), 140.8 (s), 140.2 (s), 139.5 (s), 126.5 (d), 125.8 (d), 104.0 (d), 91.9 (d), 89.7 (d), 85.9 (s), 78.1 (d), 62.1 (t, 2C), 42.0 (t); HRMS (ESI) calcd. for $C_{17}H_{19}N_2O_7$ $[M + H]^+$: 363.1187; found: 363.1176.

1-((2*R*,3*R*,3a*S*,8b*R*)-3,3a-Dihydroxy-6,7-bis(hydroxymethyl)-3,3a,4,8b-tetrahydro-2*H*-indeno [1,2-b]furan-2-yl)-5-fluoropyrimidine-2,4(1*H*,3*H*)-dione (24bb): Yield: 318 mg (78%); R_f = 0.3 (10% MeOH in DCM); white solid; mp: 188–190 °C; $[\alpha]_D^{27}$: +104.23 (c = 0.15, MeOH); ^{1}H NMR (400 MHz, CD_3OD) δ 7.46 (s, 1H), 7.34 (s, 1H), 7.07 (d, *J* = 6.5 Hz, 1H), 6.20 (dd, *J* = 7.7, 1.8 Hz, 1H), 5.32 (s, 1H), 4.71 (s, 4H), 3.83 (d, *J* = 7.6 Hz, 1H), 3.26 (d, *J* = 5.3 Hz, 1H), 3.02 (d, *J* = 16.6 Hz, 1H); ^{13}C NMR (101 MHz, CD_3OD) δ 142.2 (s), 141.1 (s), 140.9 (s, 2C), 140.4 (s, 2C), 126.5 (d), 125.8 (d), 125.1 (d, J_{C-F} = 33.6 Hz), 92.4 (d), 90.5 (d), 86.1 (s, 2C), 79.0 (d), 62.9 (t), 62.8 (t), 42.3 (t); HRMS (ESI) calcd. for $C_{17}H_{17}FN_2O_7Na$ $[M + Na]^+$: 403.0912; found: 403.0912.

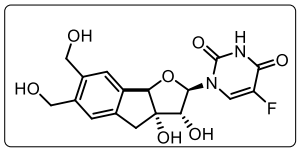

1-(3,3a-Dihydroxy-5,6-bis(hydroxymethyl)-3,3a,8,8a-tetrahydro-2*H*-indeno[2,1-b]furan-2-yl)-5-methylpyrimidine-2,4(1*H*,3*H*)-dione (24cb):

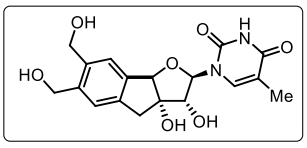

Yield: 339 mg (83%); R_f = 0.4 (10% MeOH in DCM); white solid; mp: 126–128 °C; $[\alpha]_D^{27}$: +71.83 (c 0.24, MeOH); ^{1}H NMR (400 MHz, CD_3OD) δ 7.44 (s, 1H), 7.31 (s, 1H), 6.74 (d, *J* = 1.1Hz, 1H), 6.19 (d, *J* = 7.5 Hz, 1H), 5.34 (s, 1H), 4.70(d, *J* = 1.5, 4H), 3.82 (d, *J* = 7.5 Hz, 1H), 3.25 (d, *J* = 16.5 Hz, 1H), 3.03 (d, *J* = 16.5 Hz, 1H), 1.67 (s, 3H); ^{13}C NMR (101 MHz, CD_3OD) δ 165.8 (s), 152.6 (s), 141.8 (s), 140.8 (s), 140.5 (s), 139.9 (s), 136.6 (d), 126.4 (d), 125.9 (d), 112.0 (s),

91.9 (d), 89.9 (d), 85.9 (s), 79.0 (d), 62.8 (t), 62.8 (t), 41.9 (t), 12.6 (q); HRMS (ESI) calcd. for $C_{18}H_{20}N_2O_7Na$ $[M + Na]^+$: 399.1163; found: 399.1160.

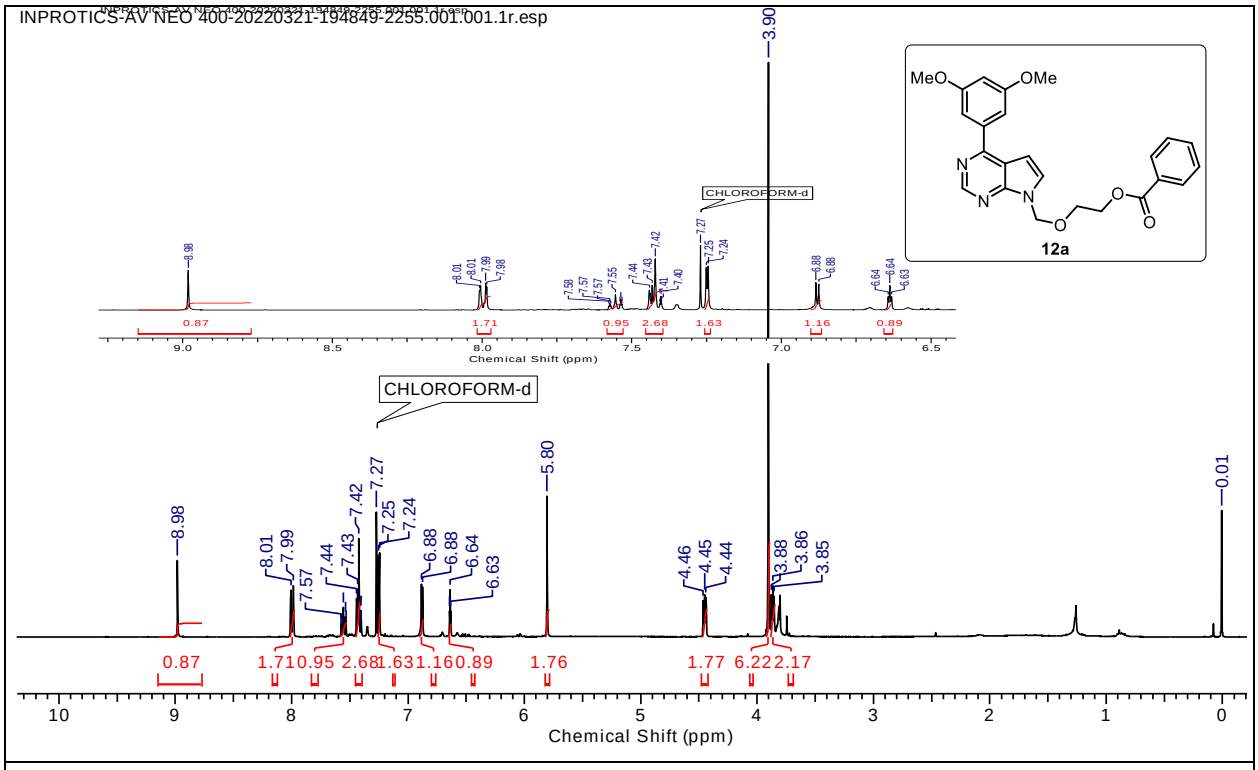

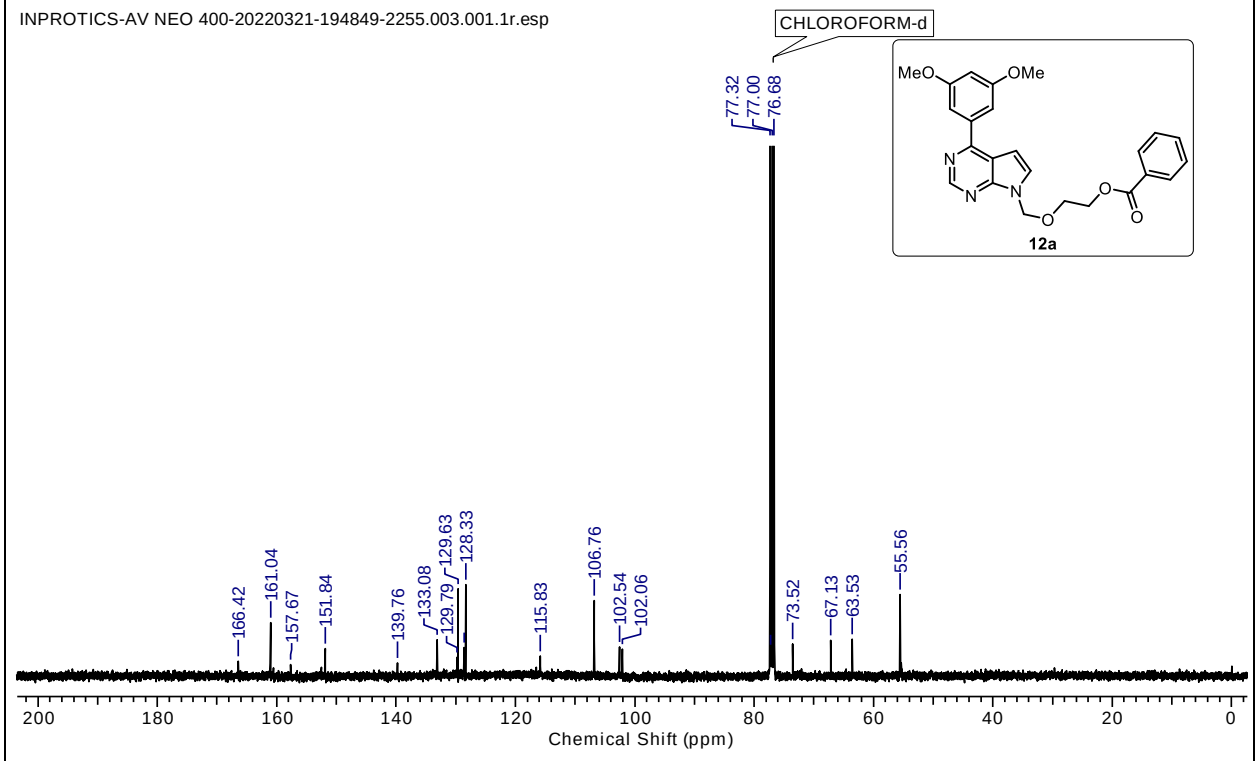

^{1}H /^{13}C NMR Spectrum of 12a in $CDCl_3$

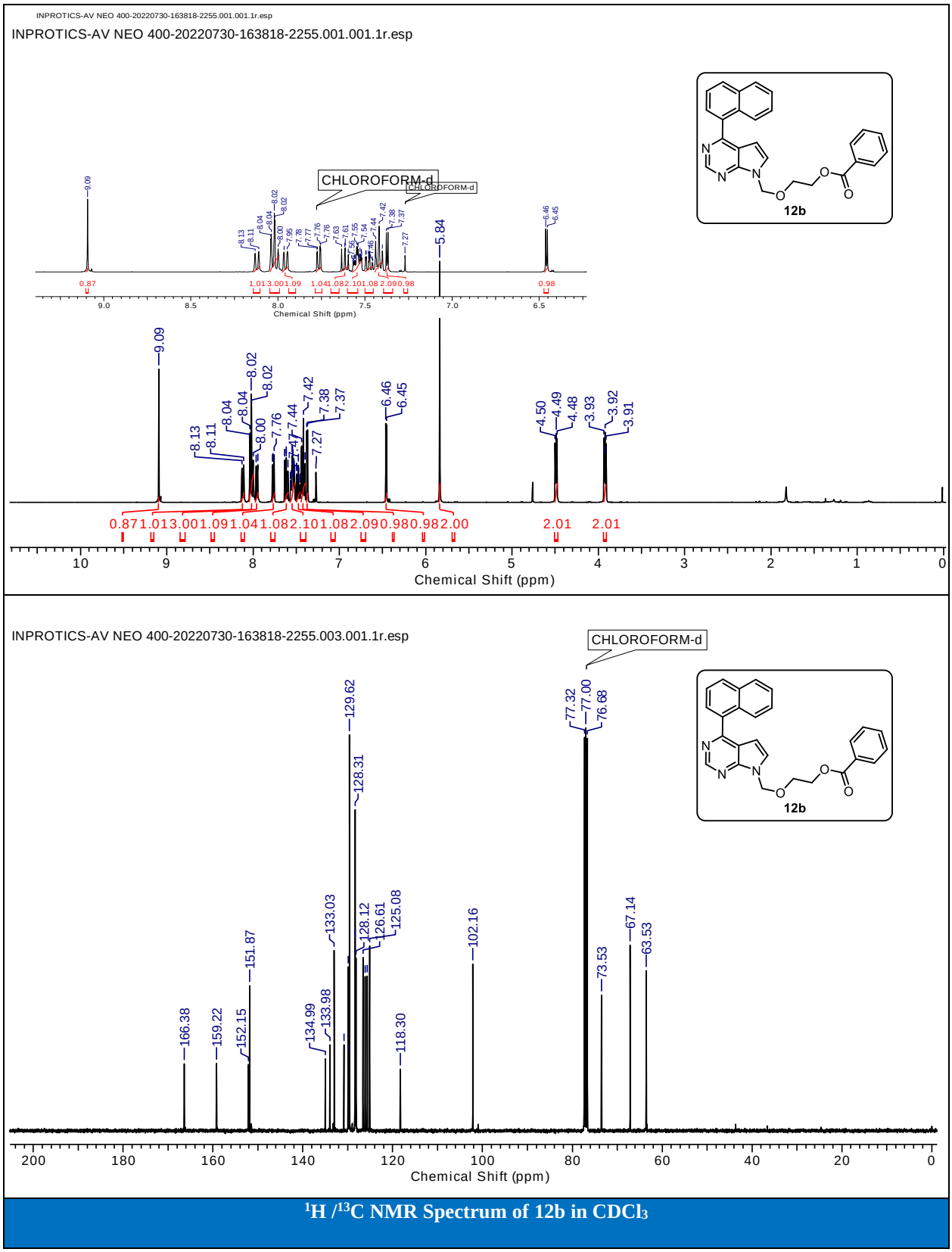

^{1}H /^{13}C NMR Spectrum of 12b in $CDCl_3$

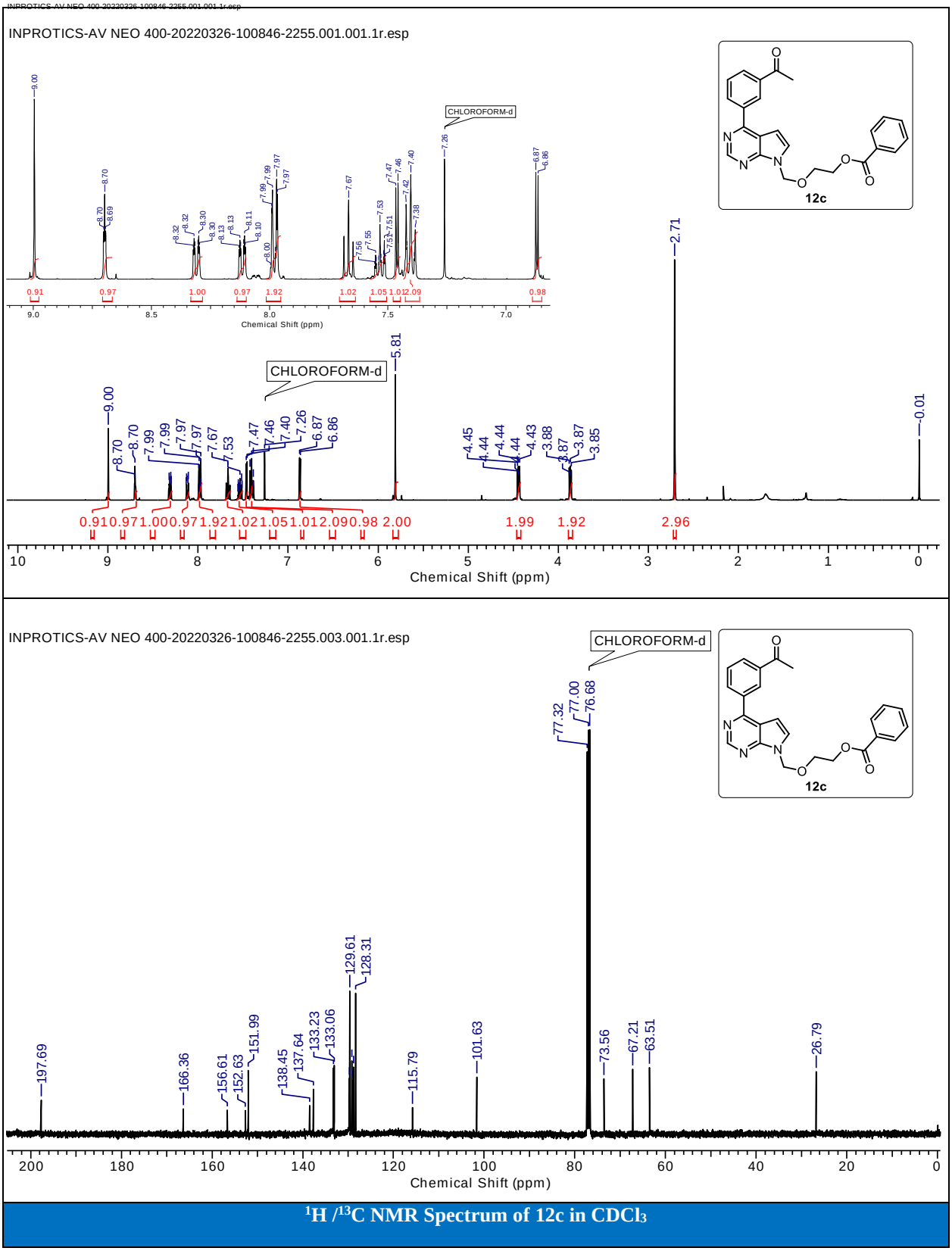

^{1}H /^{13}C NMR Spectrum of 12c in $CDCl_3$

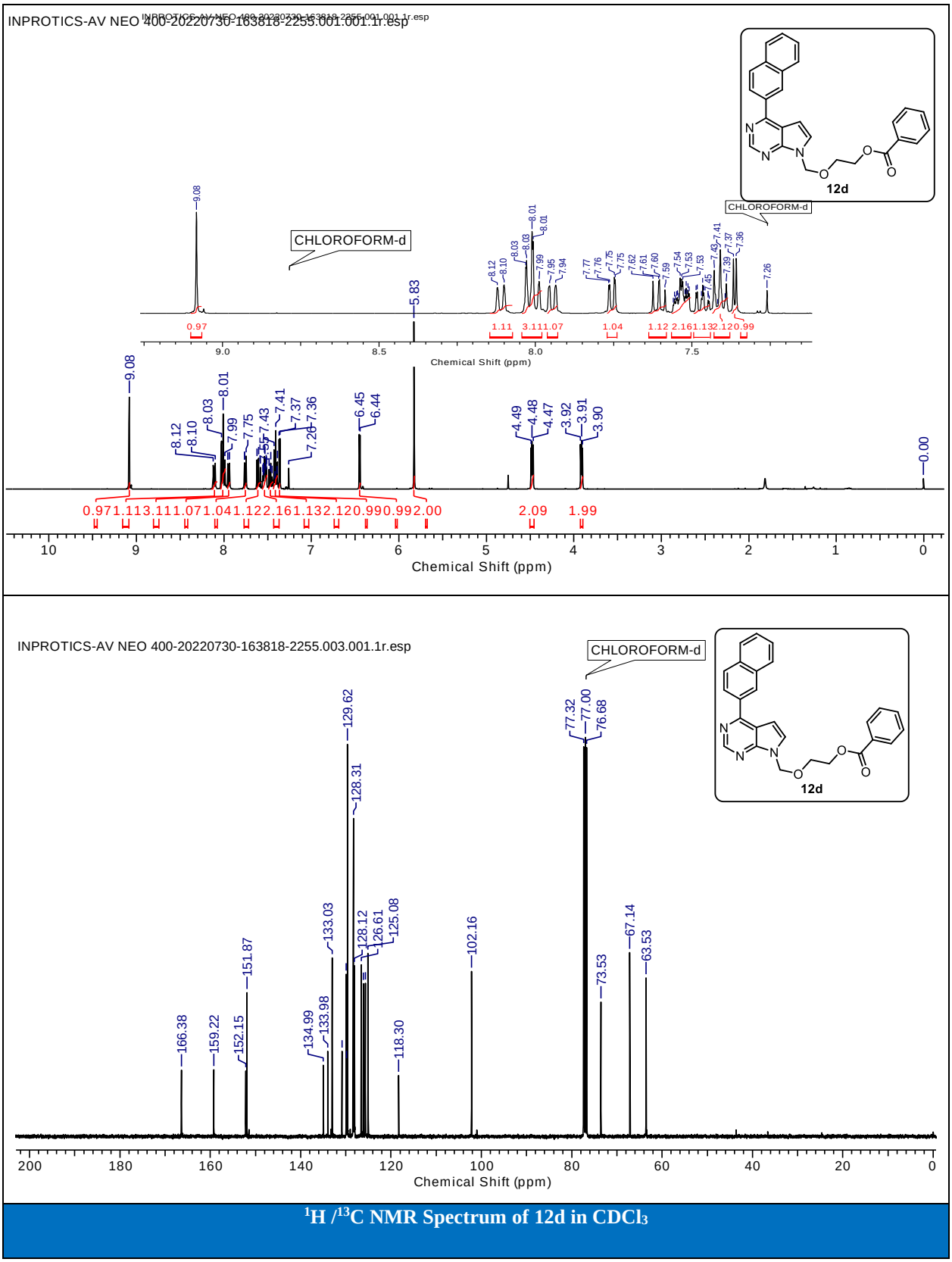

^{1}H /^{13}C NMR Spectrum of 12d in $CDCl_3$

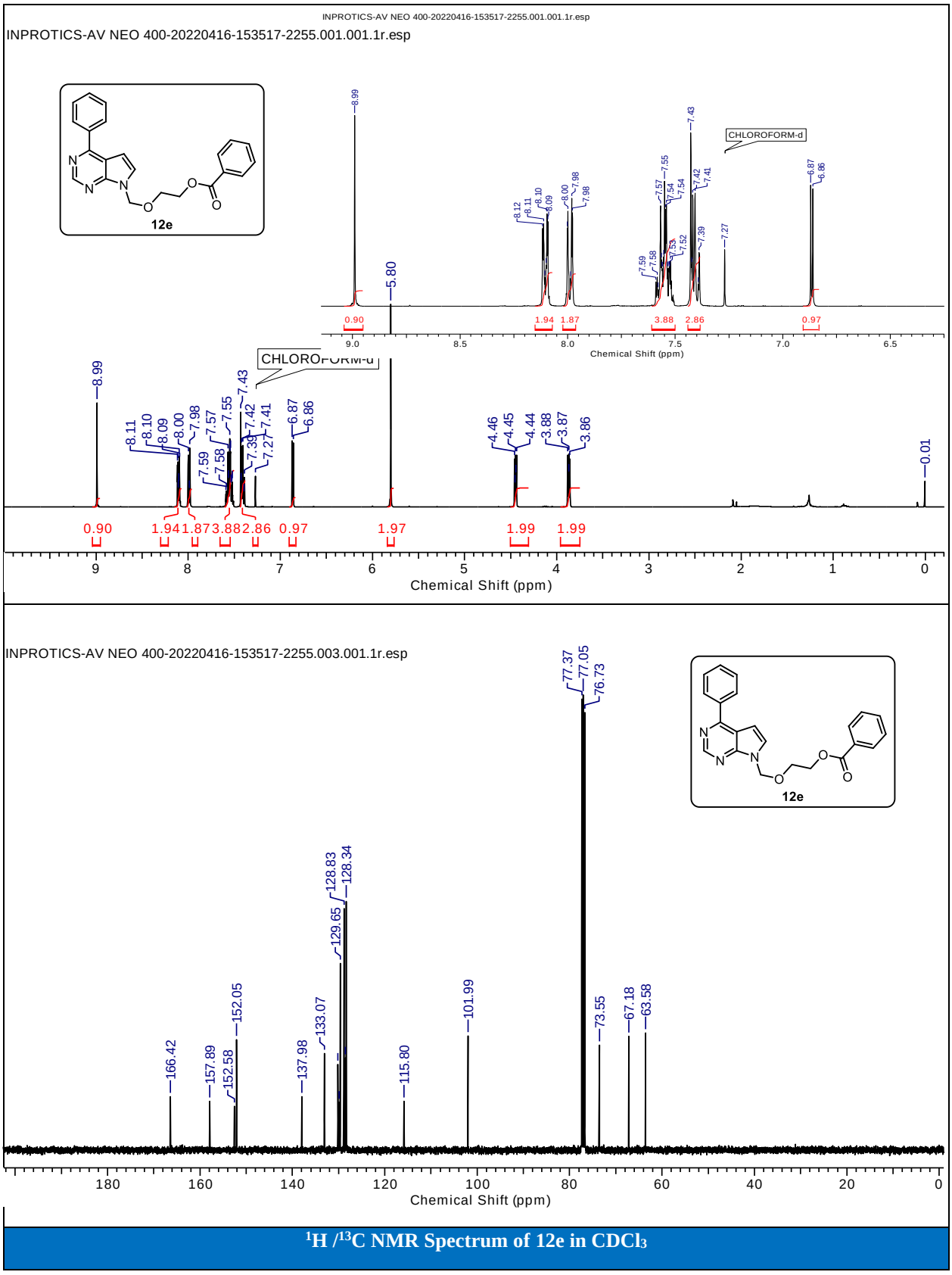

^{1}H /^{13}C NMR Spectrum of 12e in $CDCl_3$

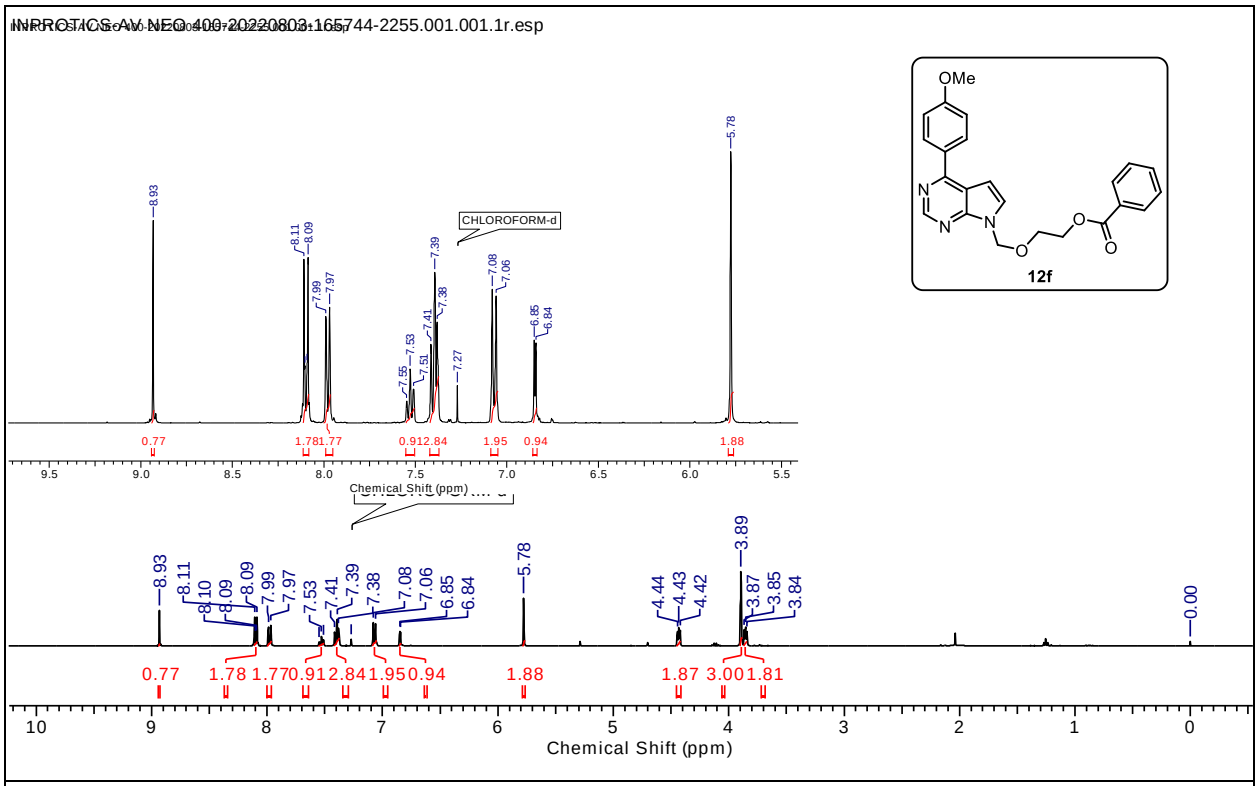

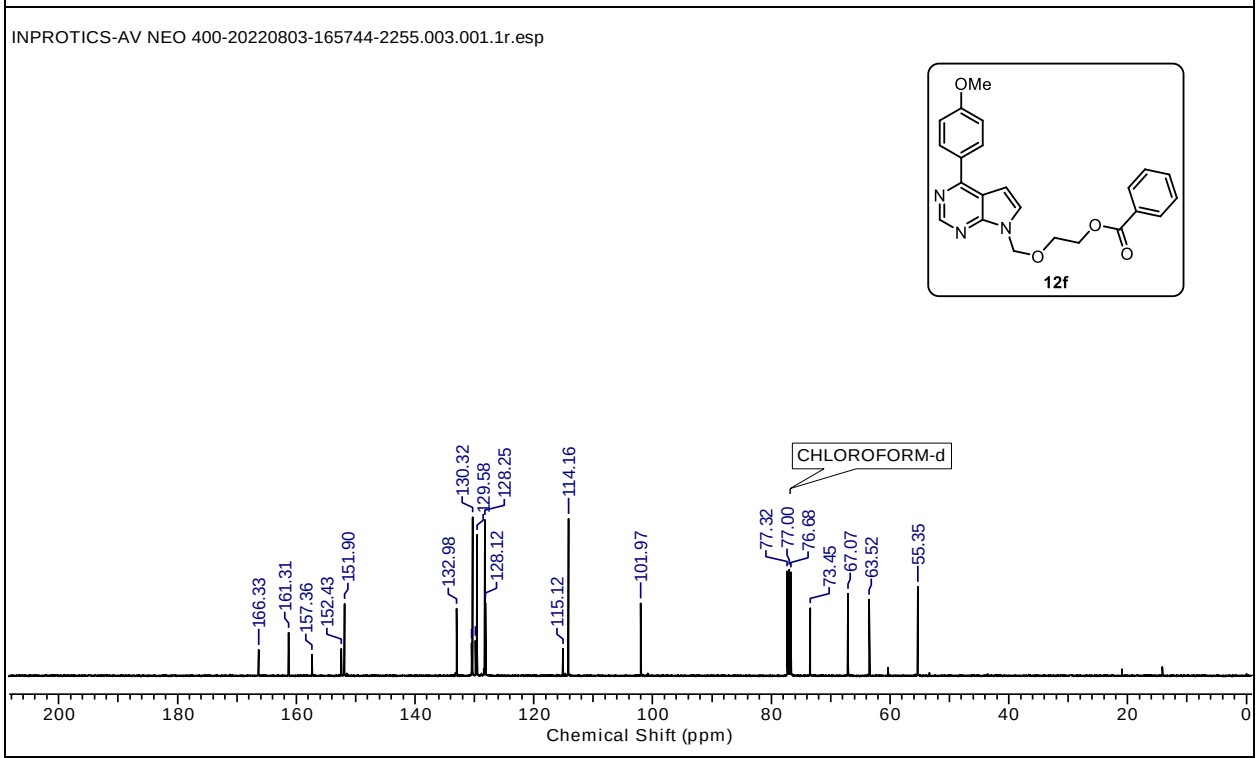

^{1}H /^{13}C NMR Spectrum of 12f in $CDCl_3$

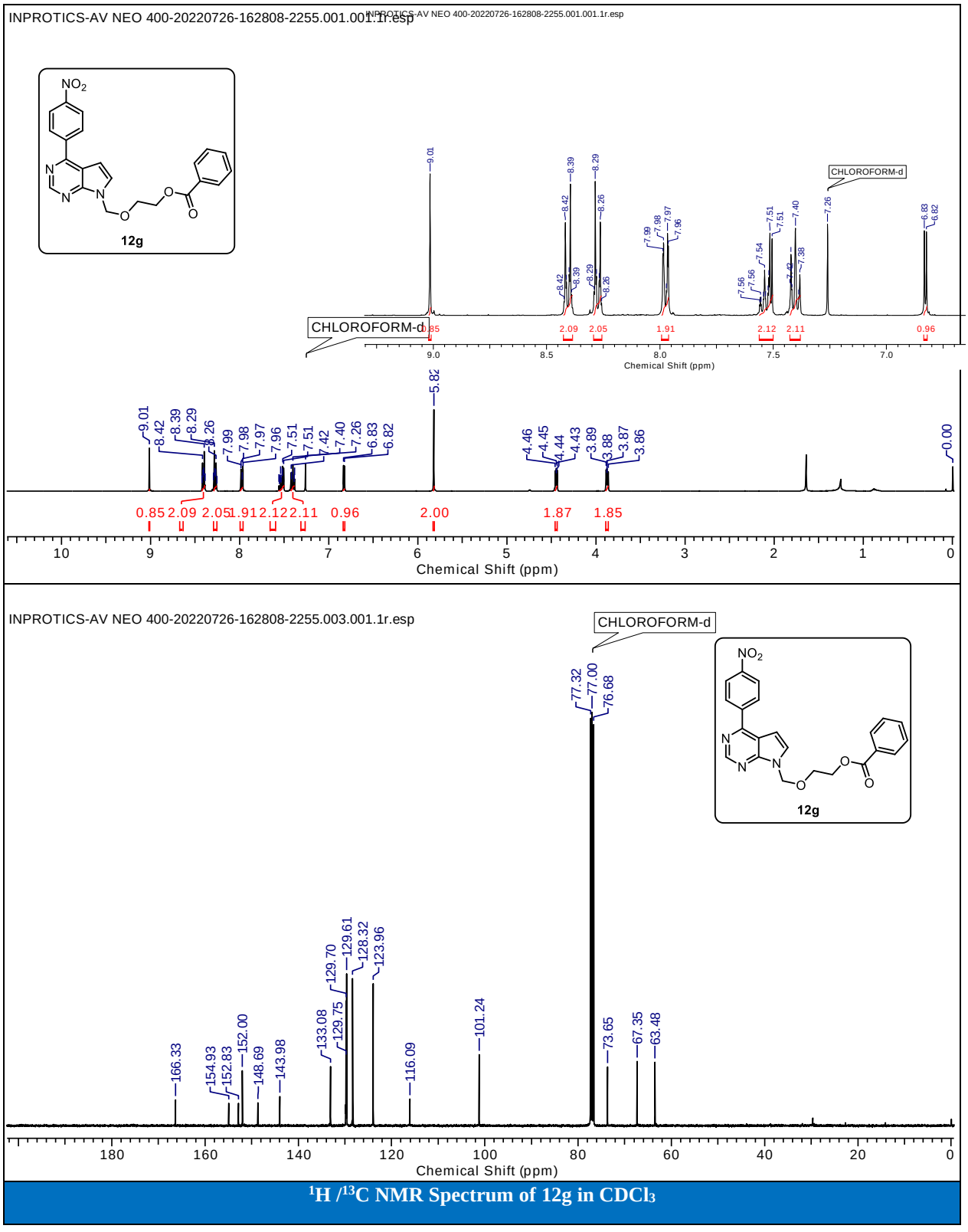

^{1}H /^{13}C NMR Spectrum of 12g in $CDCl_3$

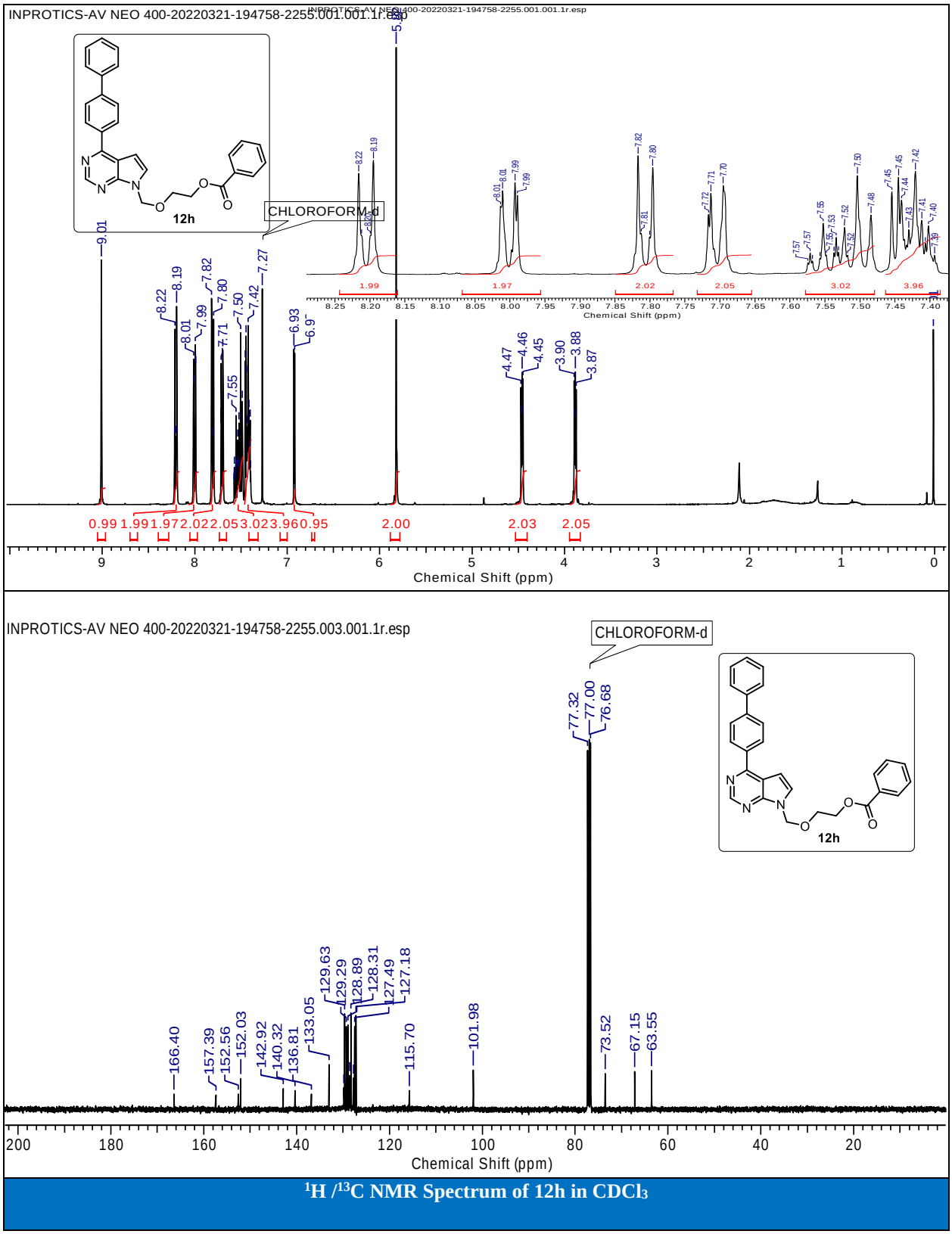

^{1}H /^{13}C NMR Spectrum of 12h in $CDCl_3$

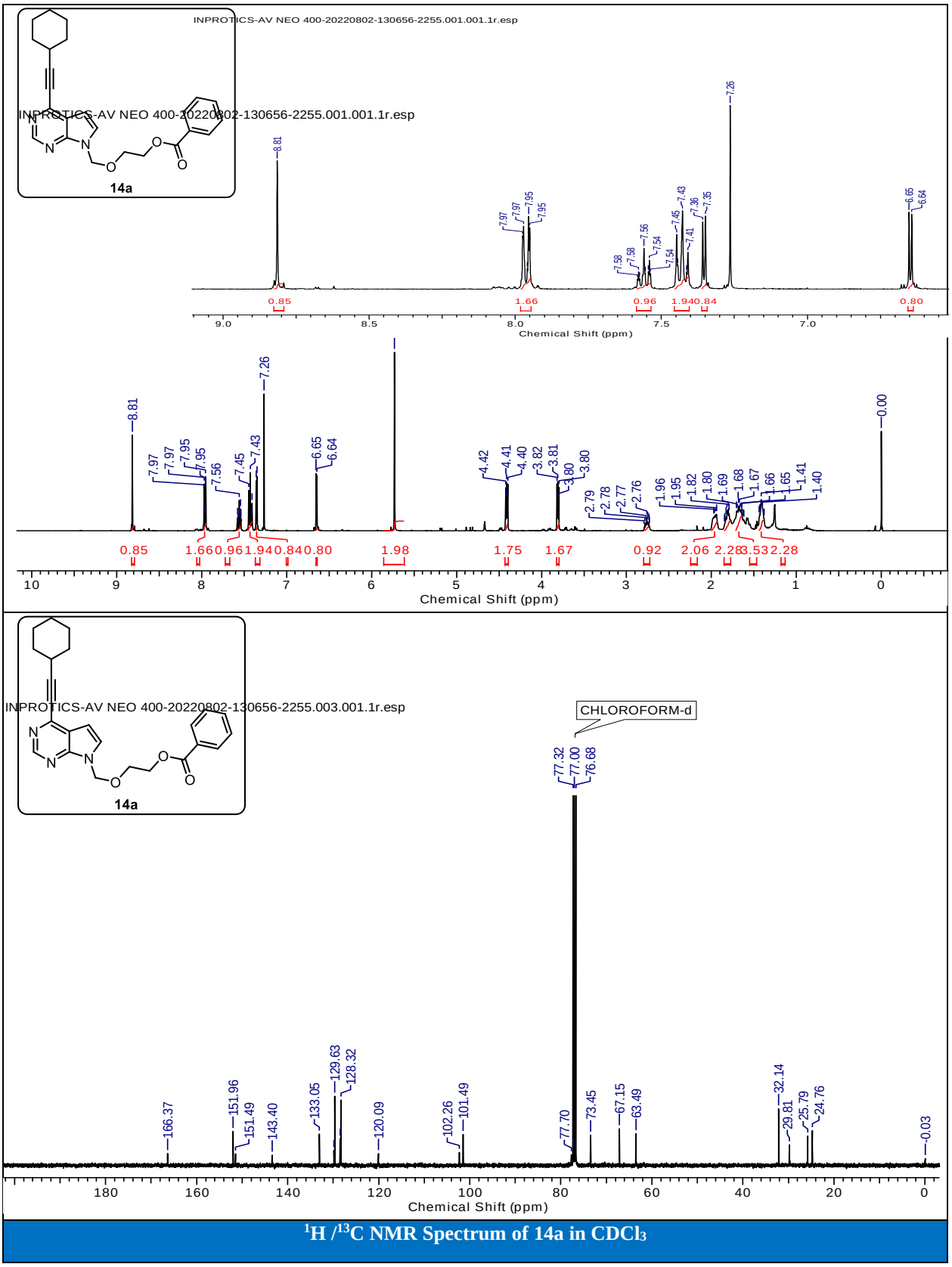

^{1}H /^{13}C NMR Spectrum of 14a in $CDCl_3$

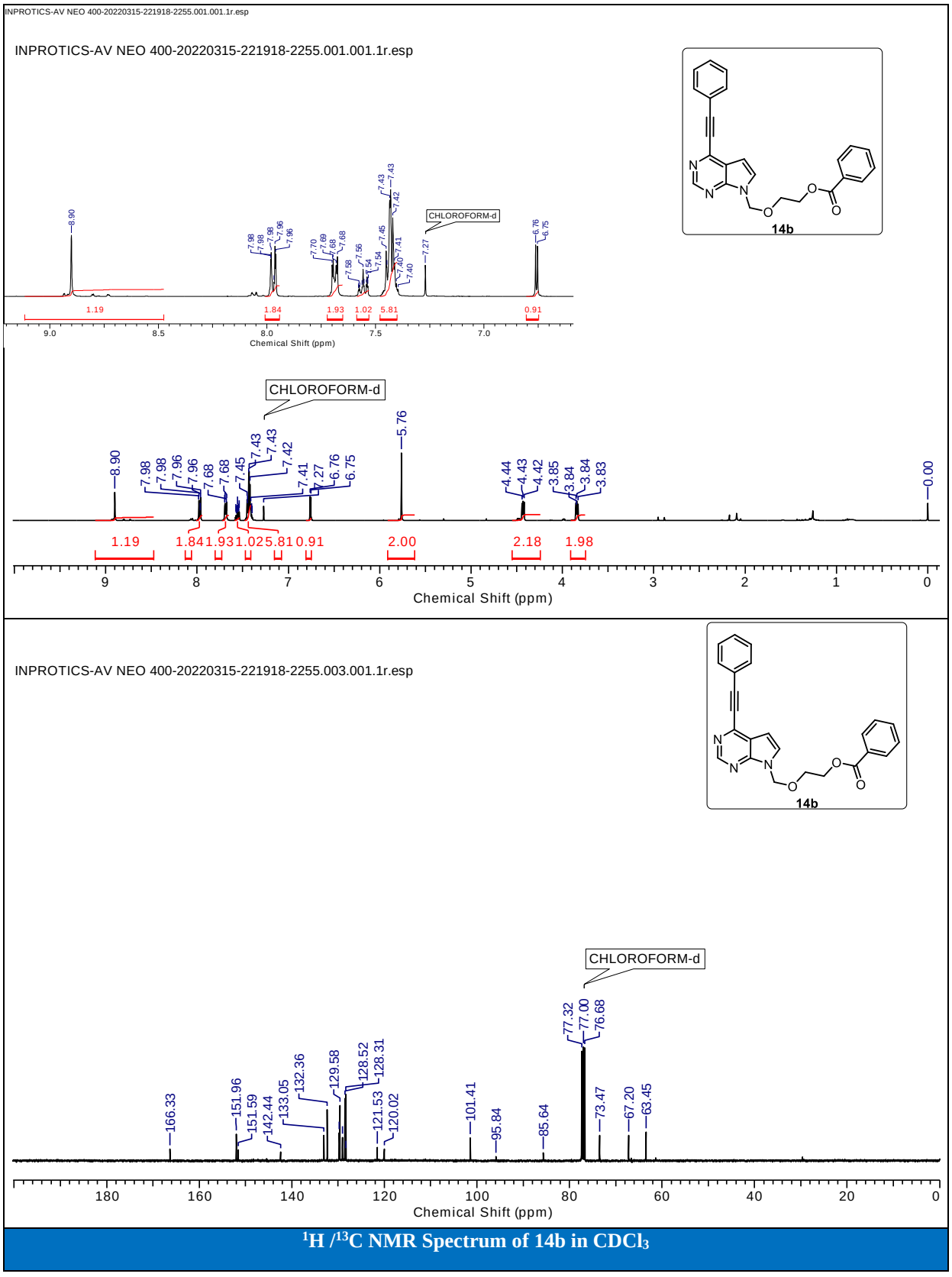

^{1}H /^{13}C NMR Spectrum of 14b in $CDCl_3$

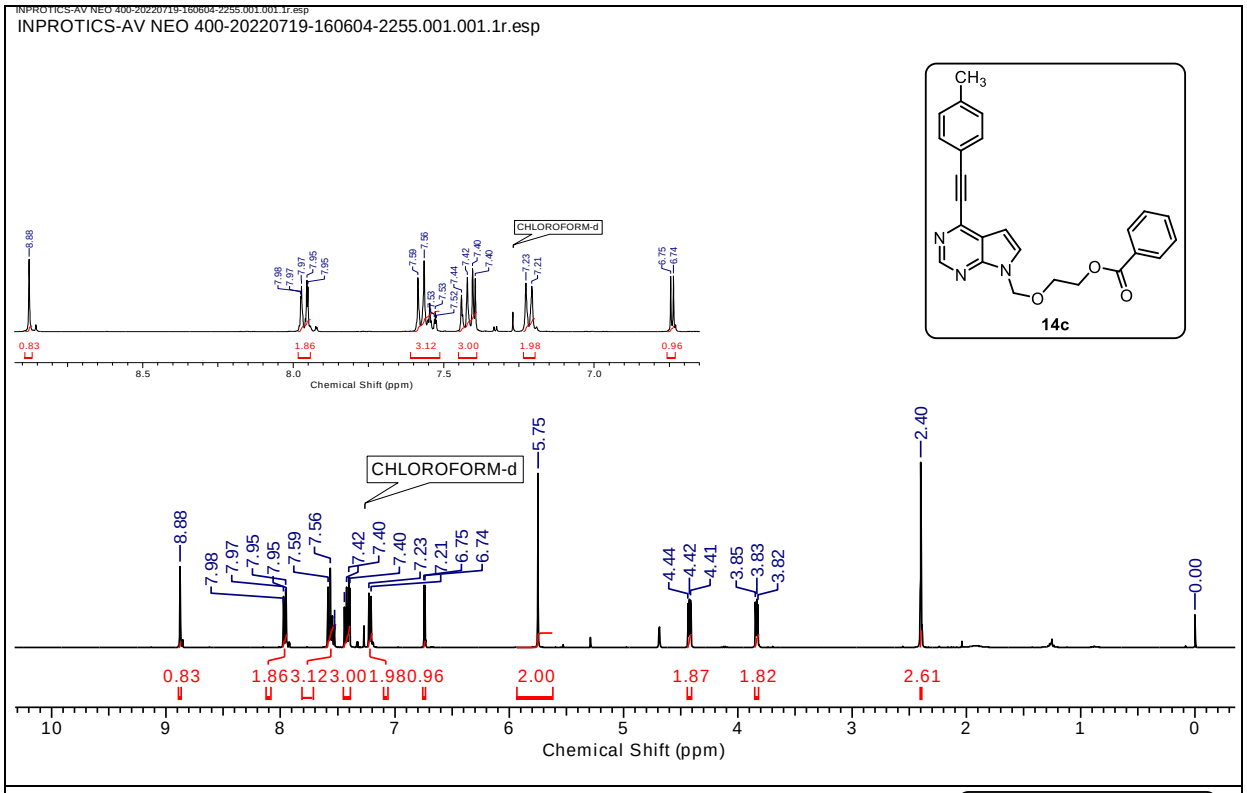

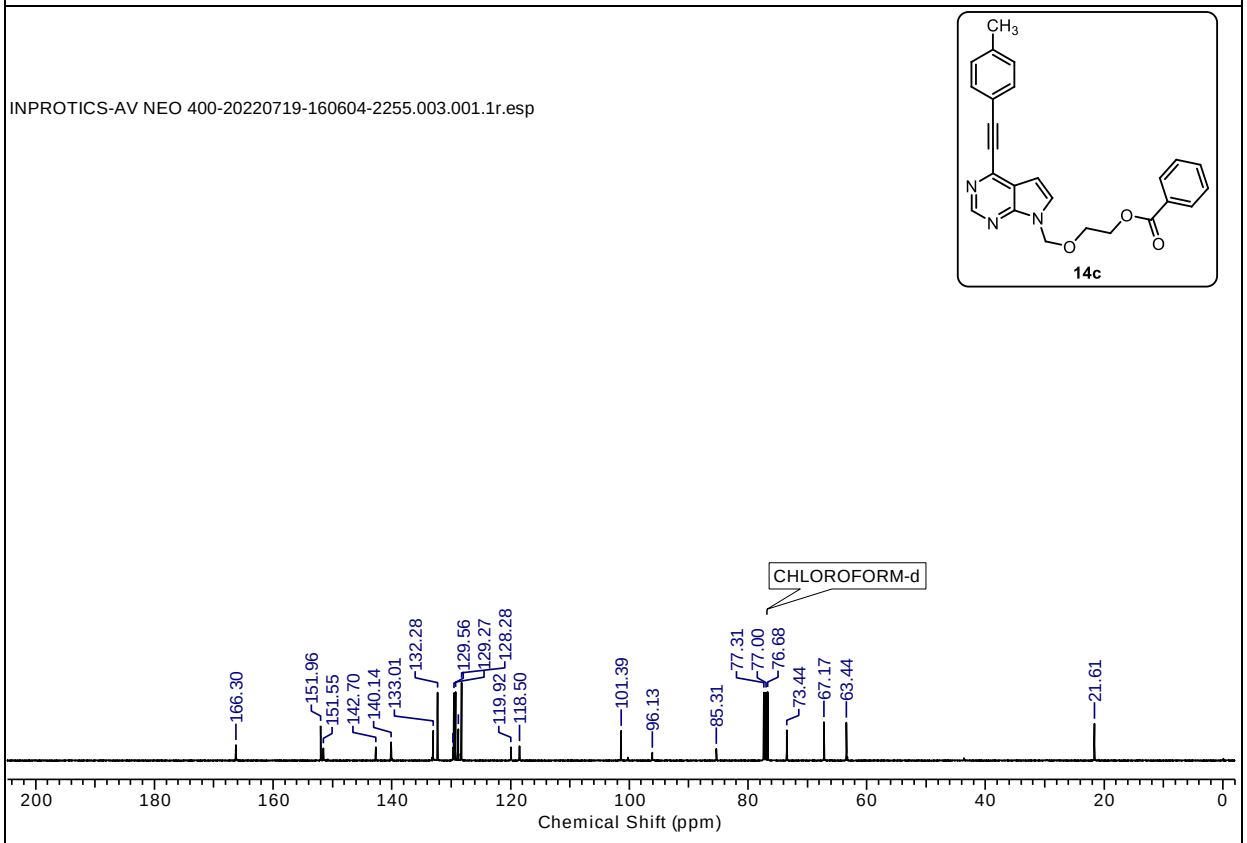

^{1}H /^{13}C NMR Spectrum of 14c in $CDCl_3$

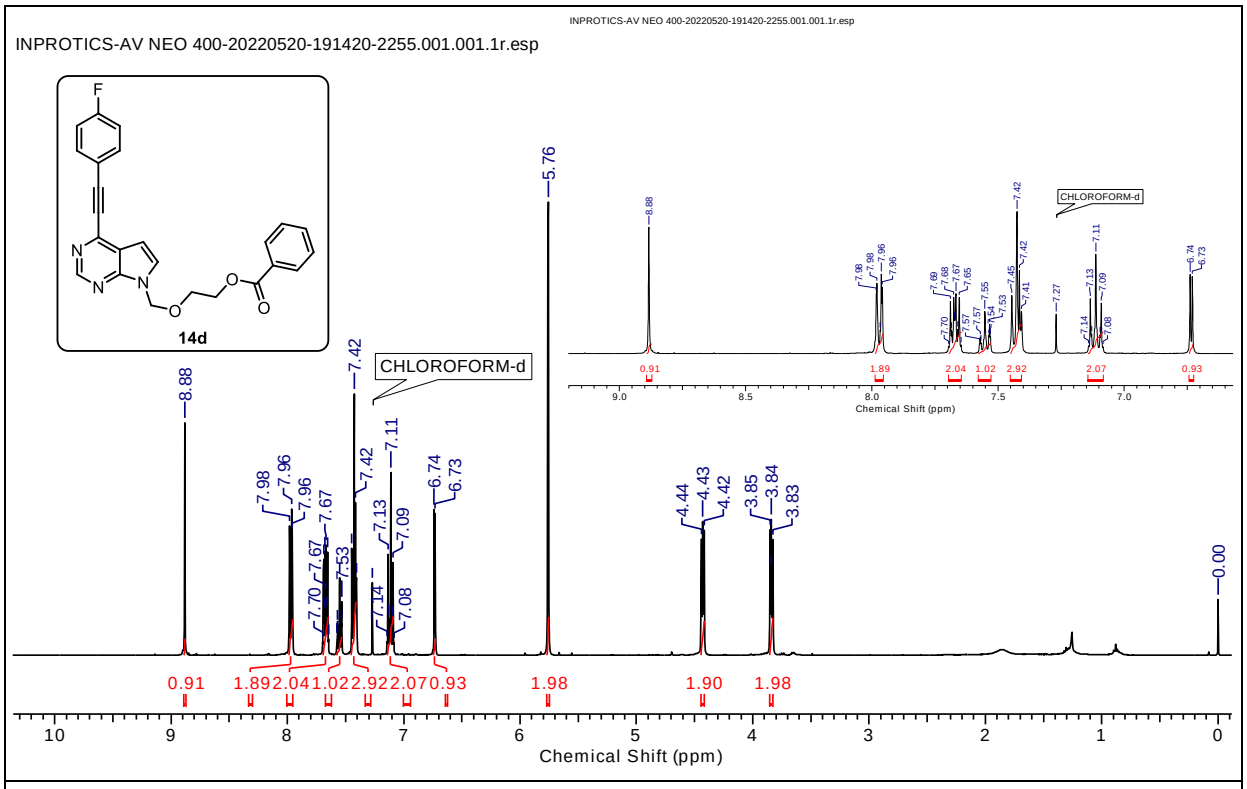

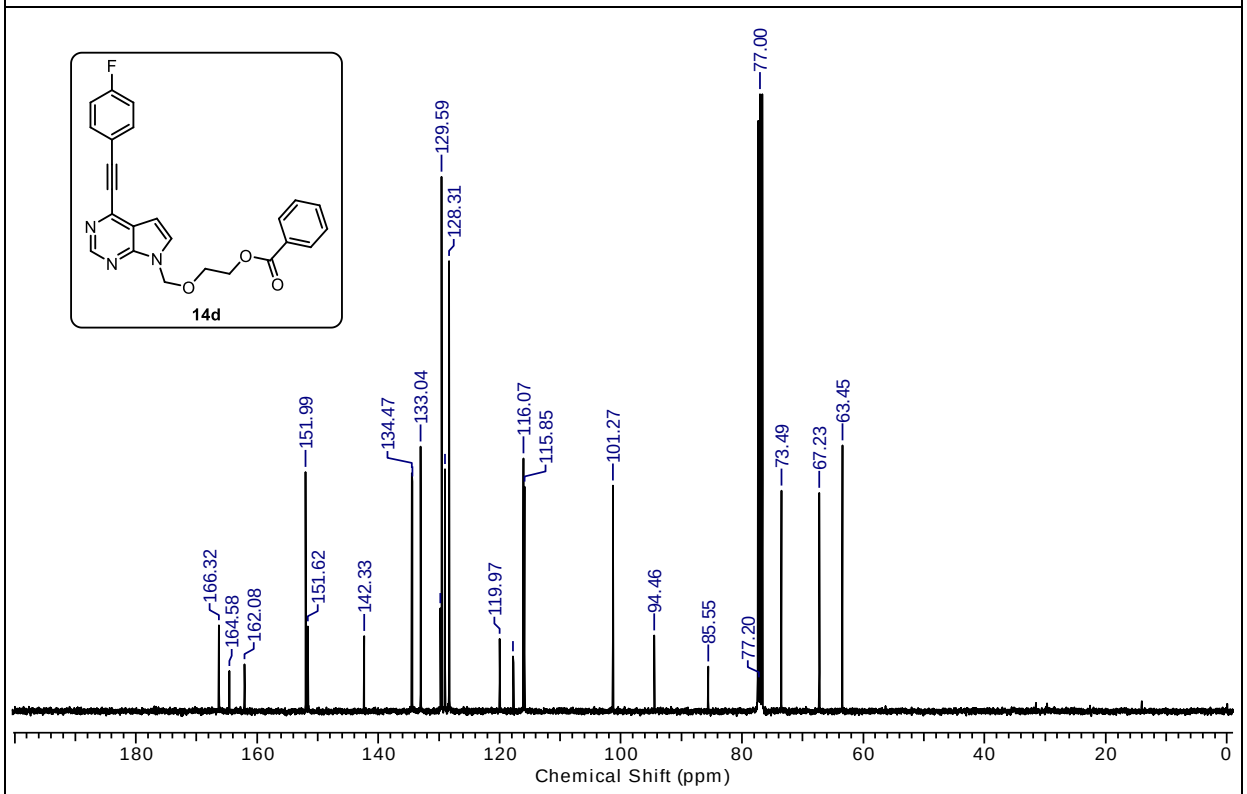

^{1}H /^{13}C NMR Spectrum of 14d in $CDCl_3$

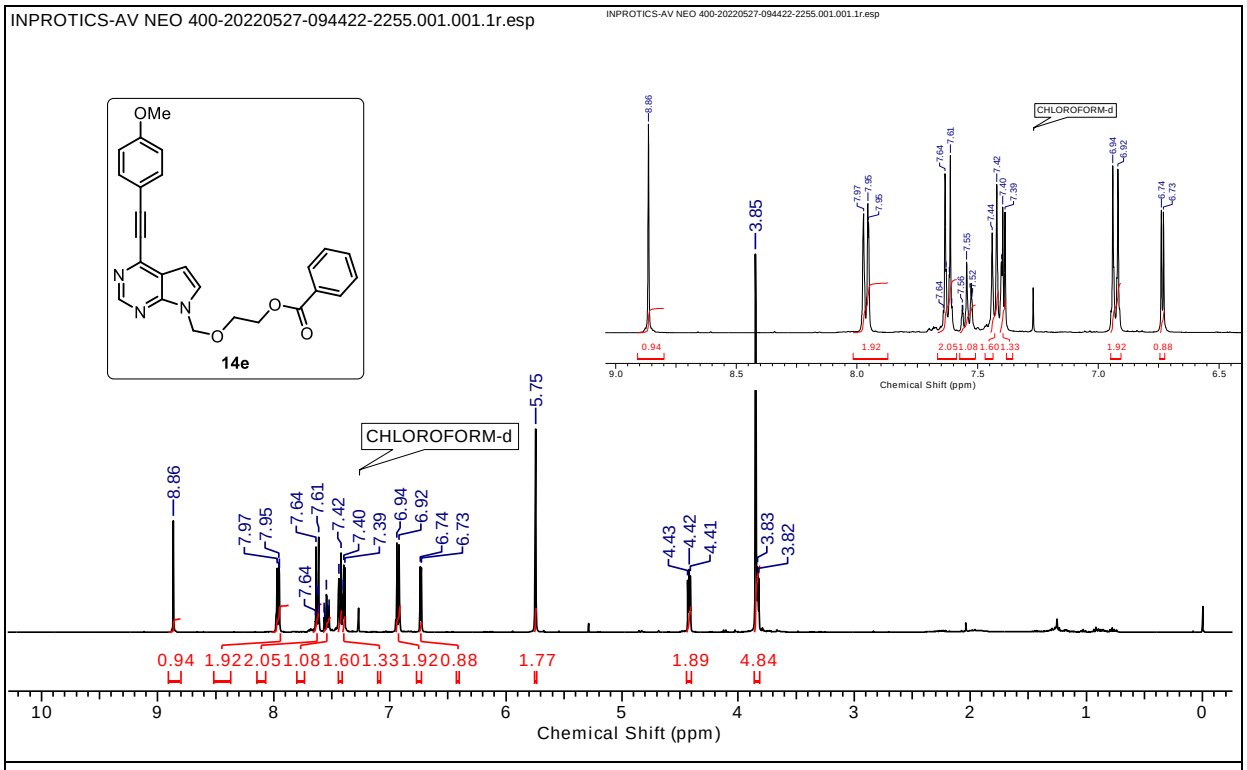

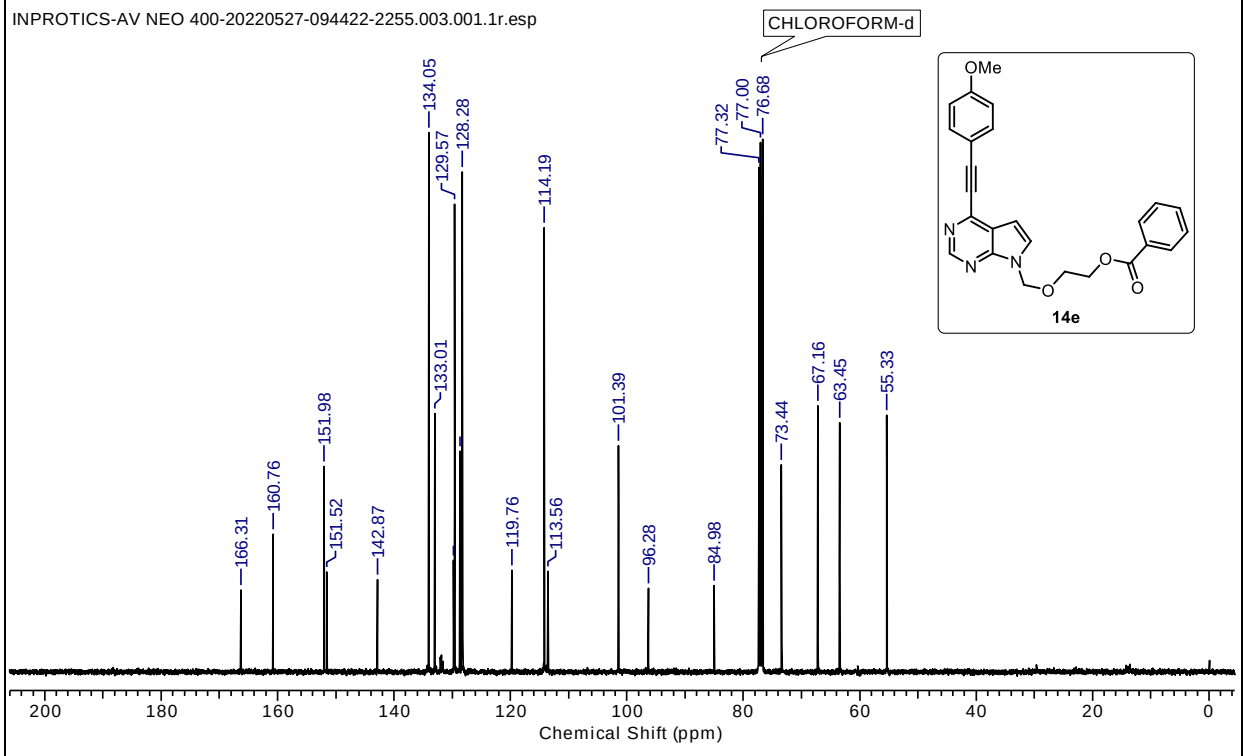

^{1}H /^{13}C NMR Spectrum of 14e in $CDCl_3$

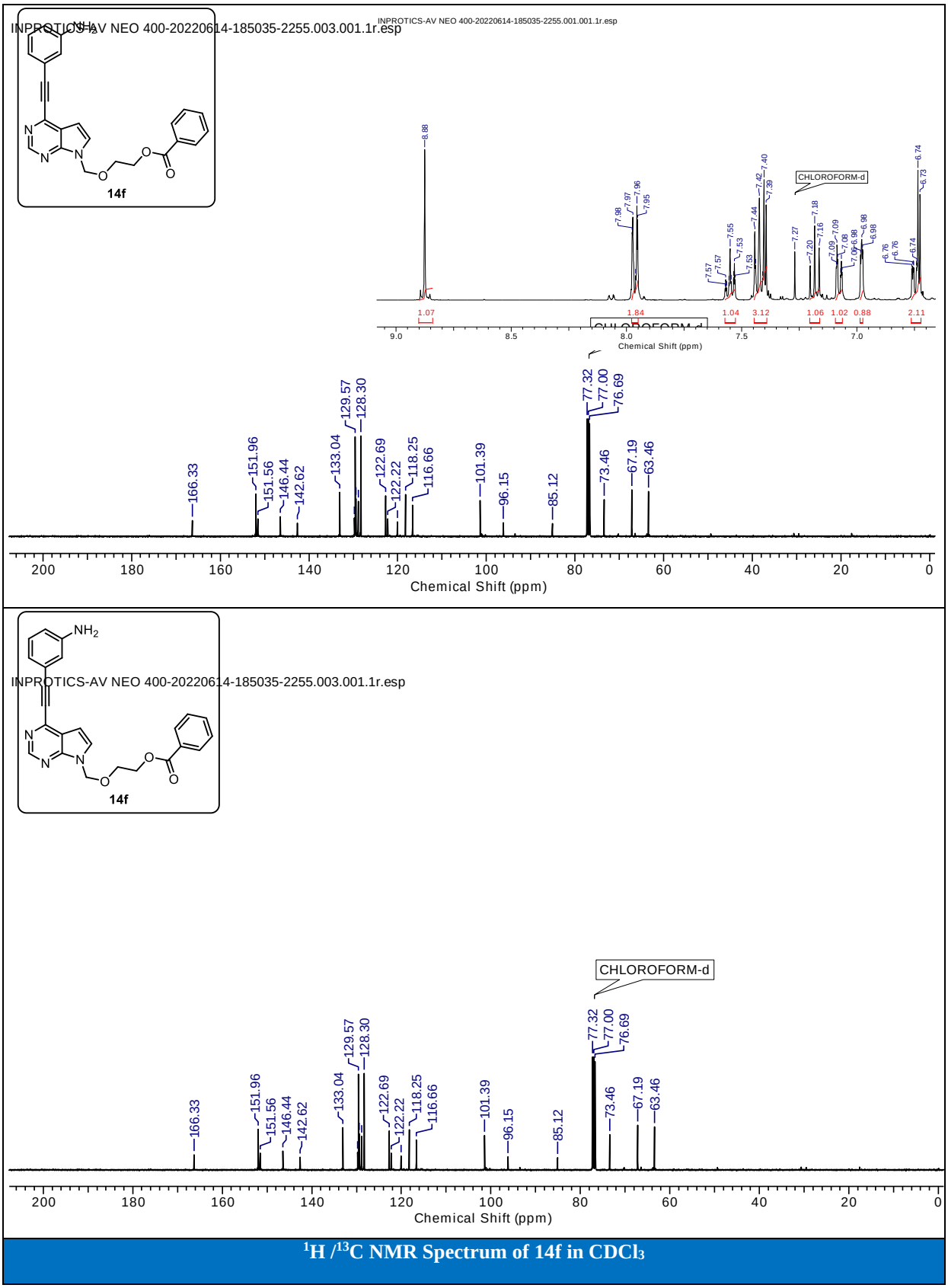

^{1}H /^{13}C NMR Spectrum of 14f in $CDCl_3$

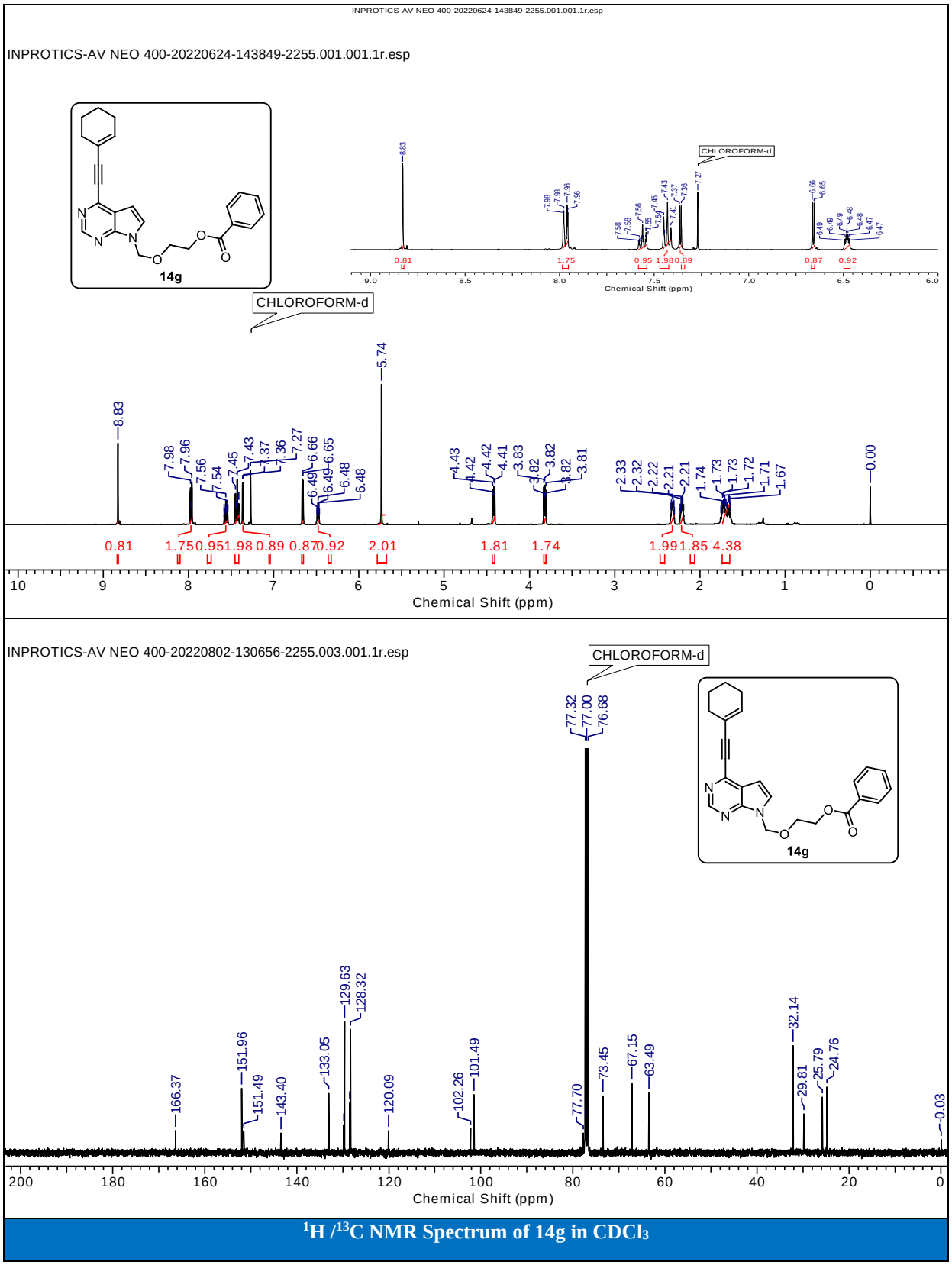

^{1}H /^{13}C NMR Spectrum of 14g in $CDCl_3$

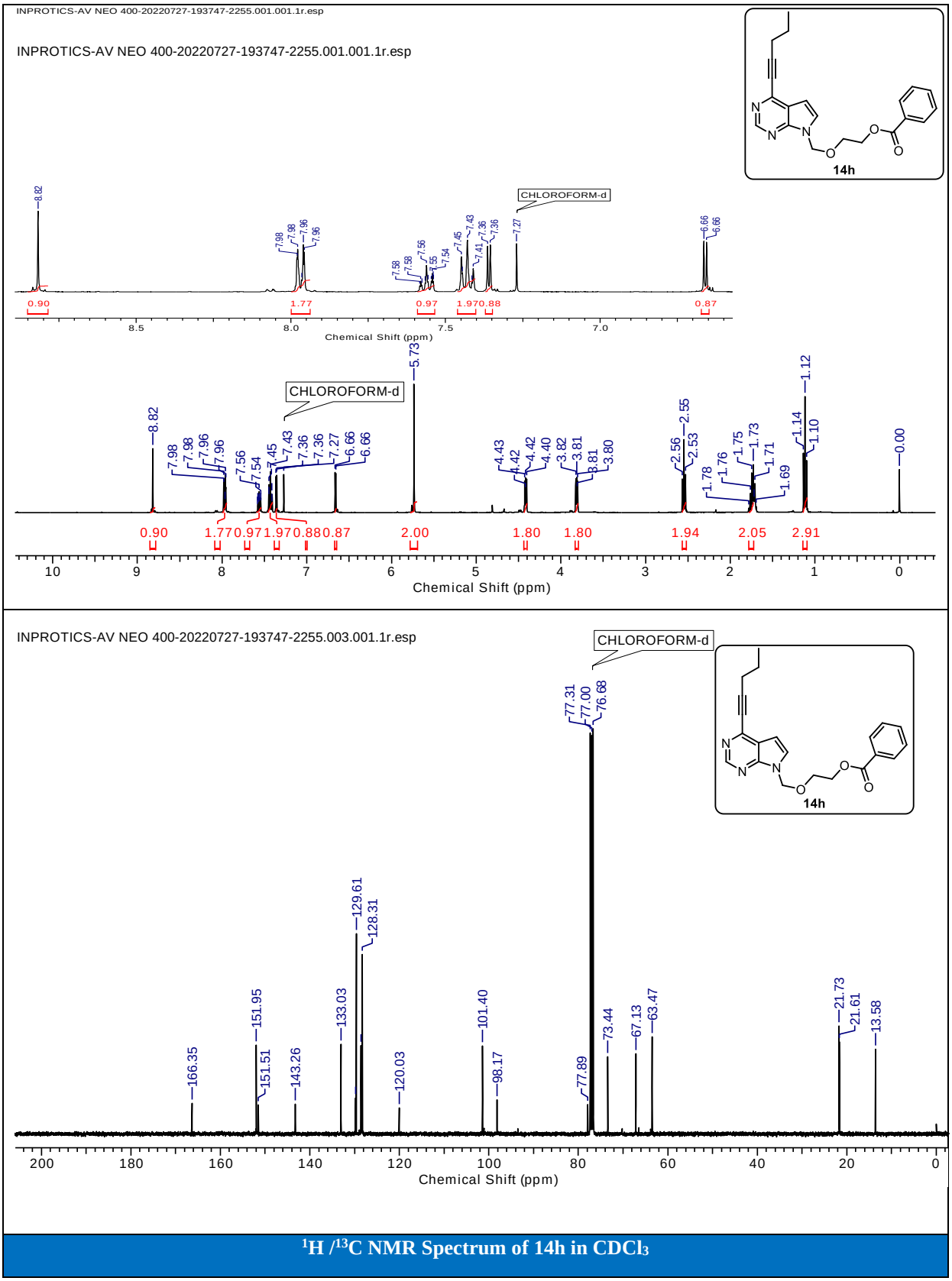

^{1}H /^{13}C NMR Spectrum of 14h in $CDCl_3$

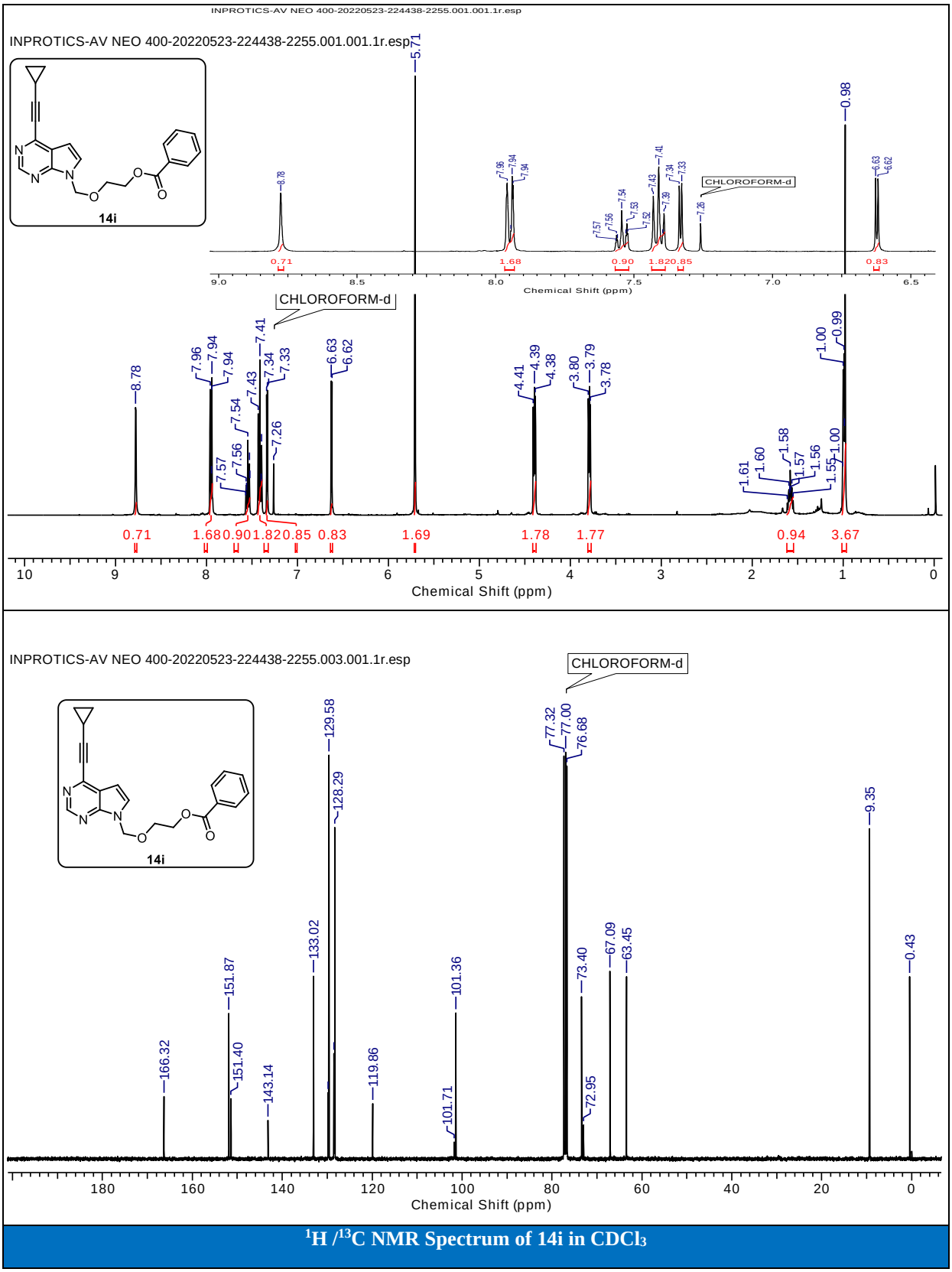

^{1}H /^{13}C NMR Spectrum of 14i in $CDCl_3$

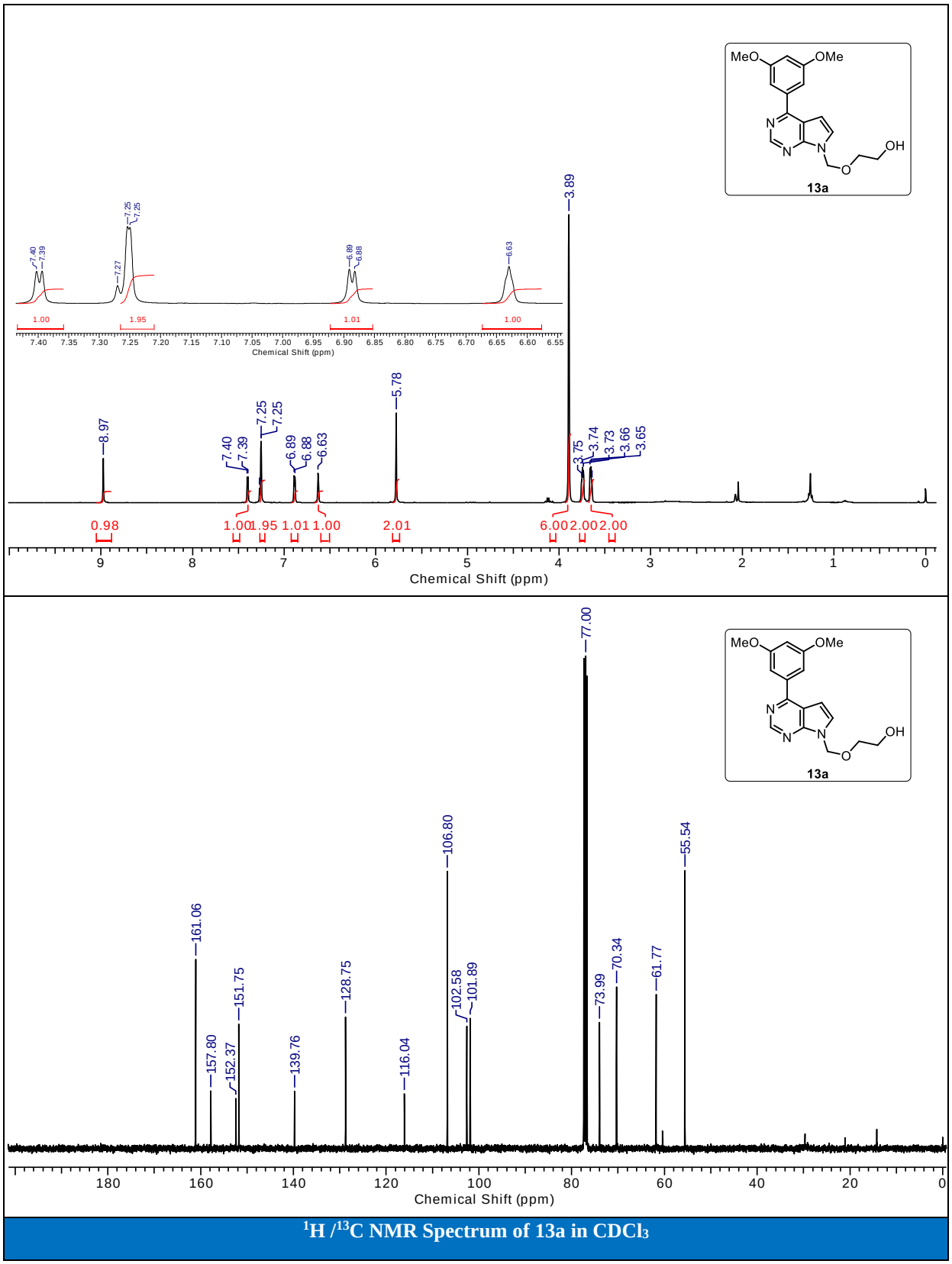

^{1}H /^{13}C NMR Spectrum of 13a in $CDCl_3$

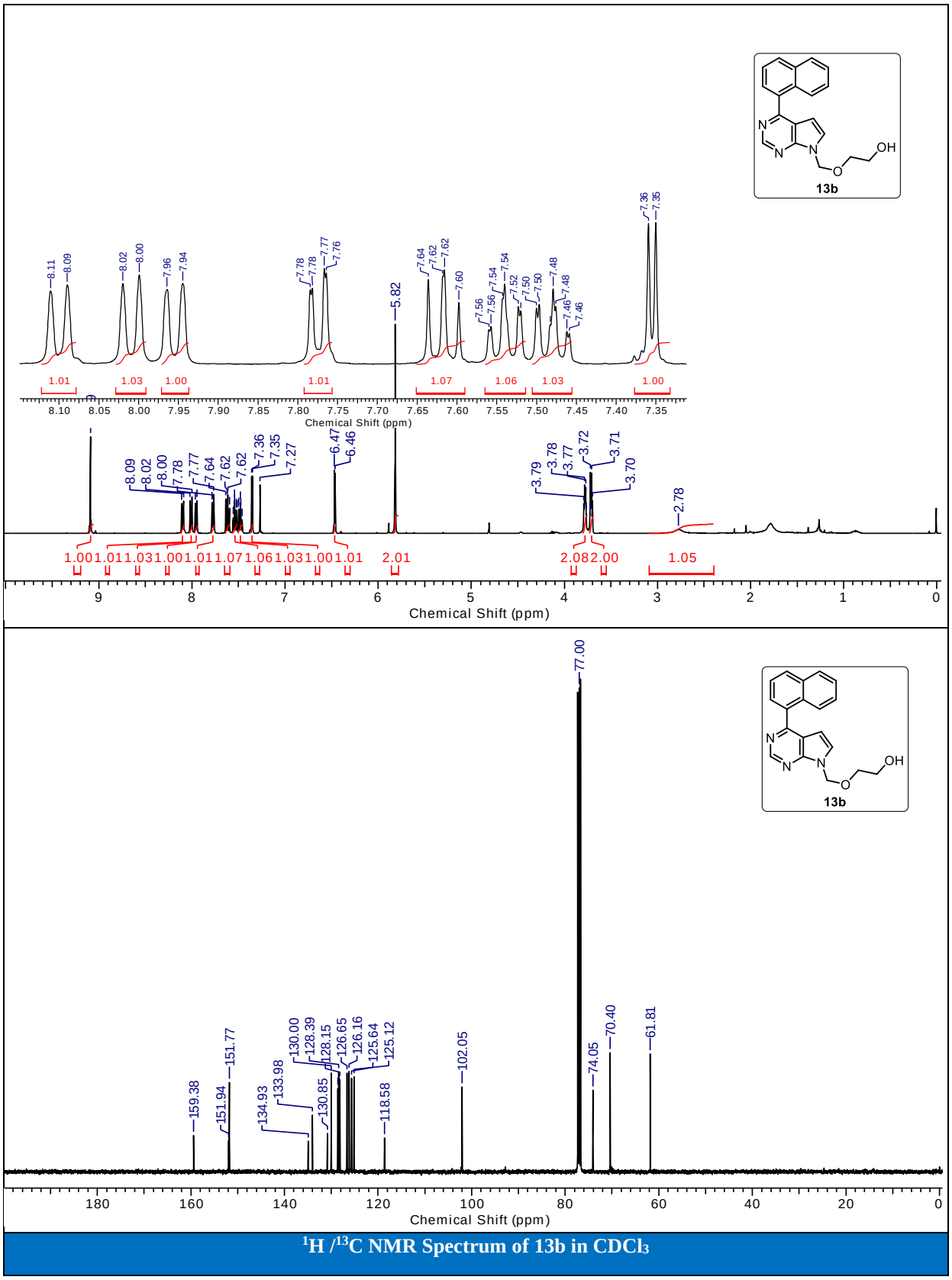

^{1}H /^{13}C NMR Spectrum of 13b in $CDCl_3$

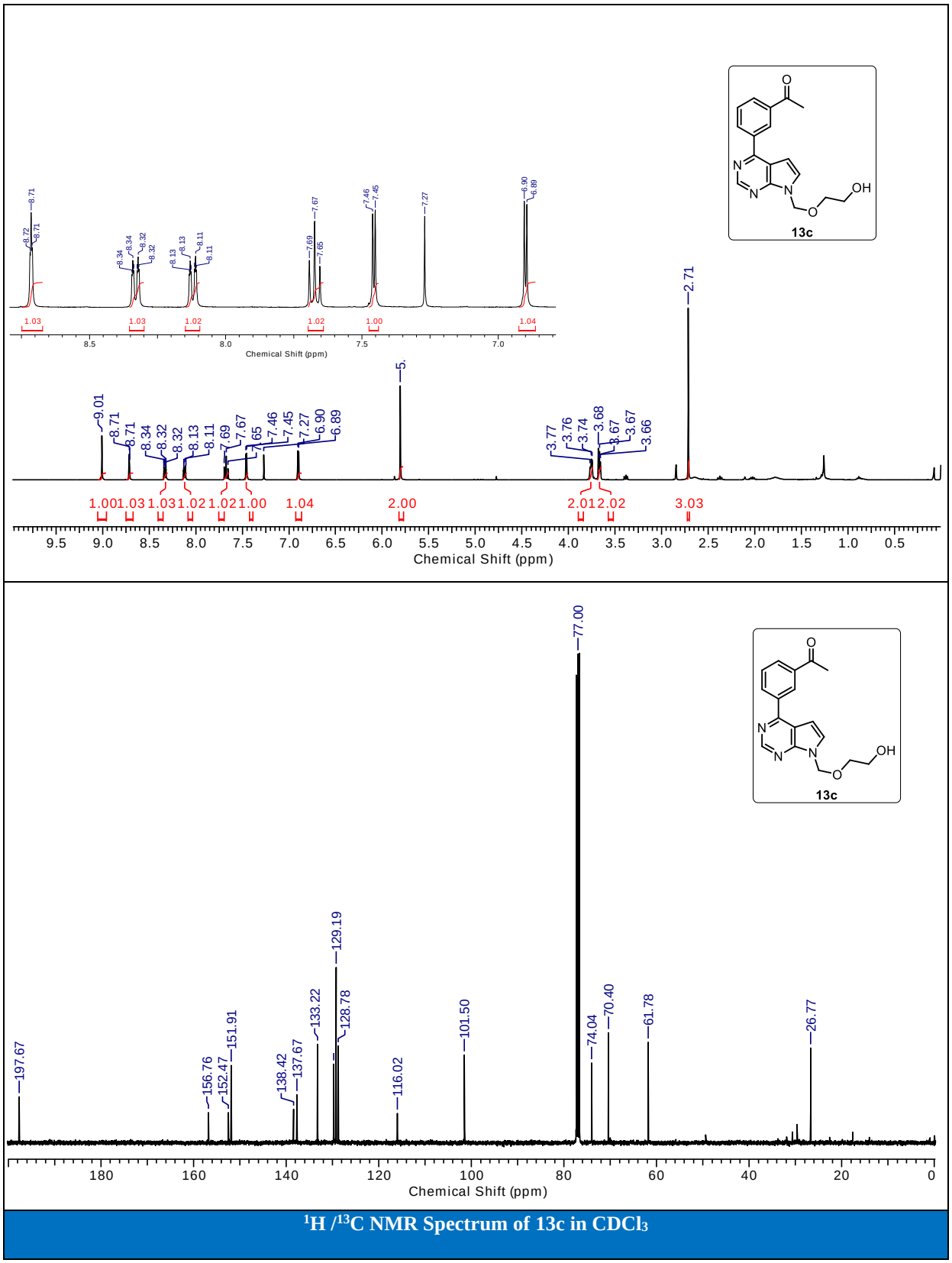

^{1}H /^{13}C NMR Spectrum of 13c in $CDCl_3$

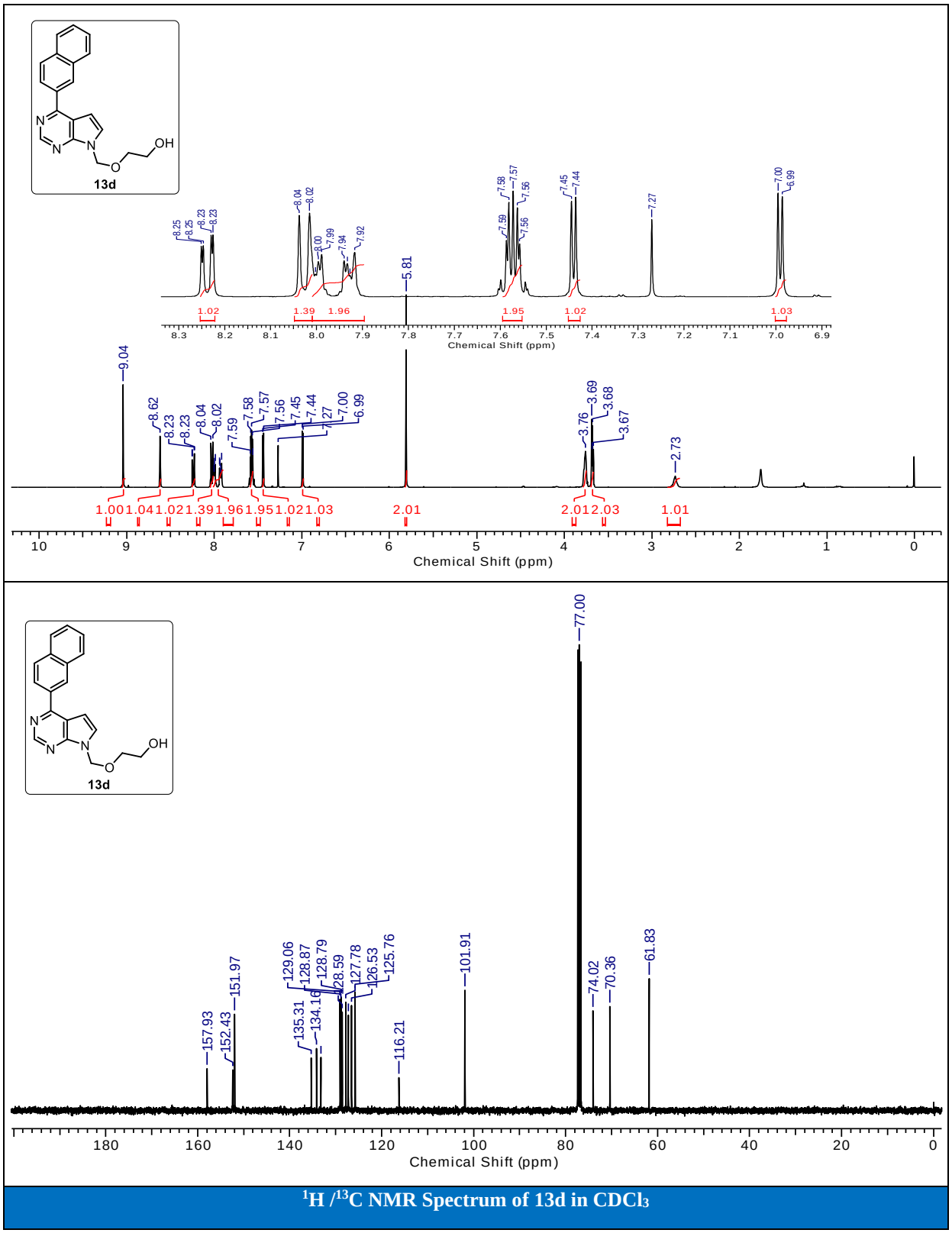

^{1}H /^{13}C NMR Spectrum of 13d in $CDCl_3$

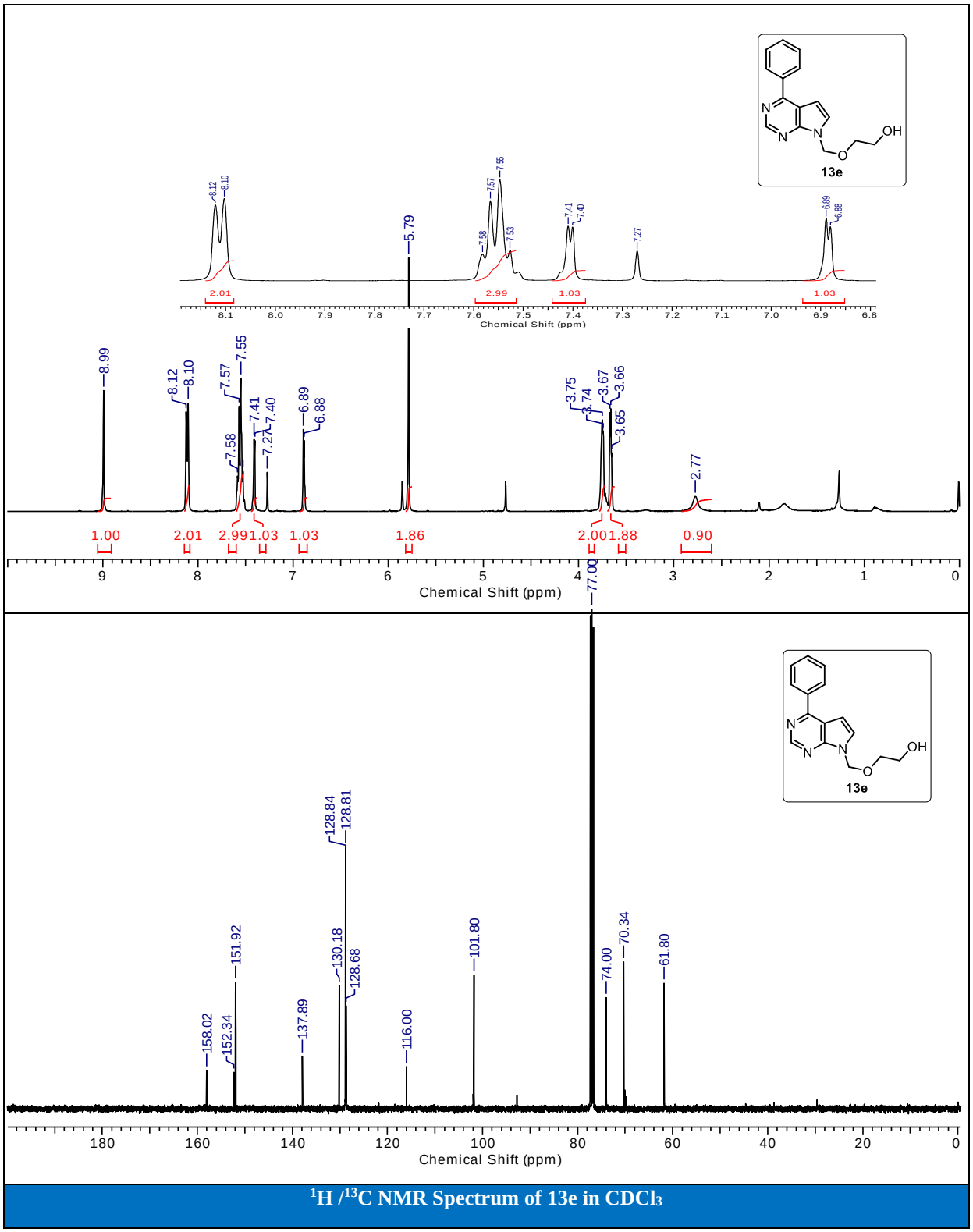

^{1}H /^{13}C NMR Spectrum of 13e in $CDCl_3$

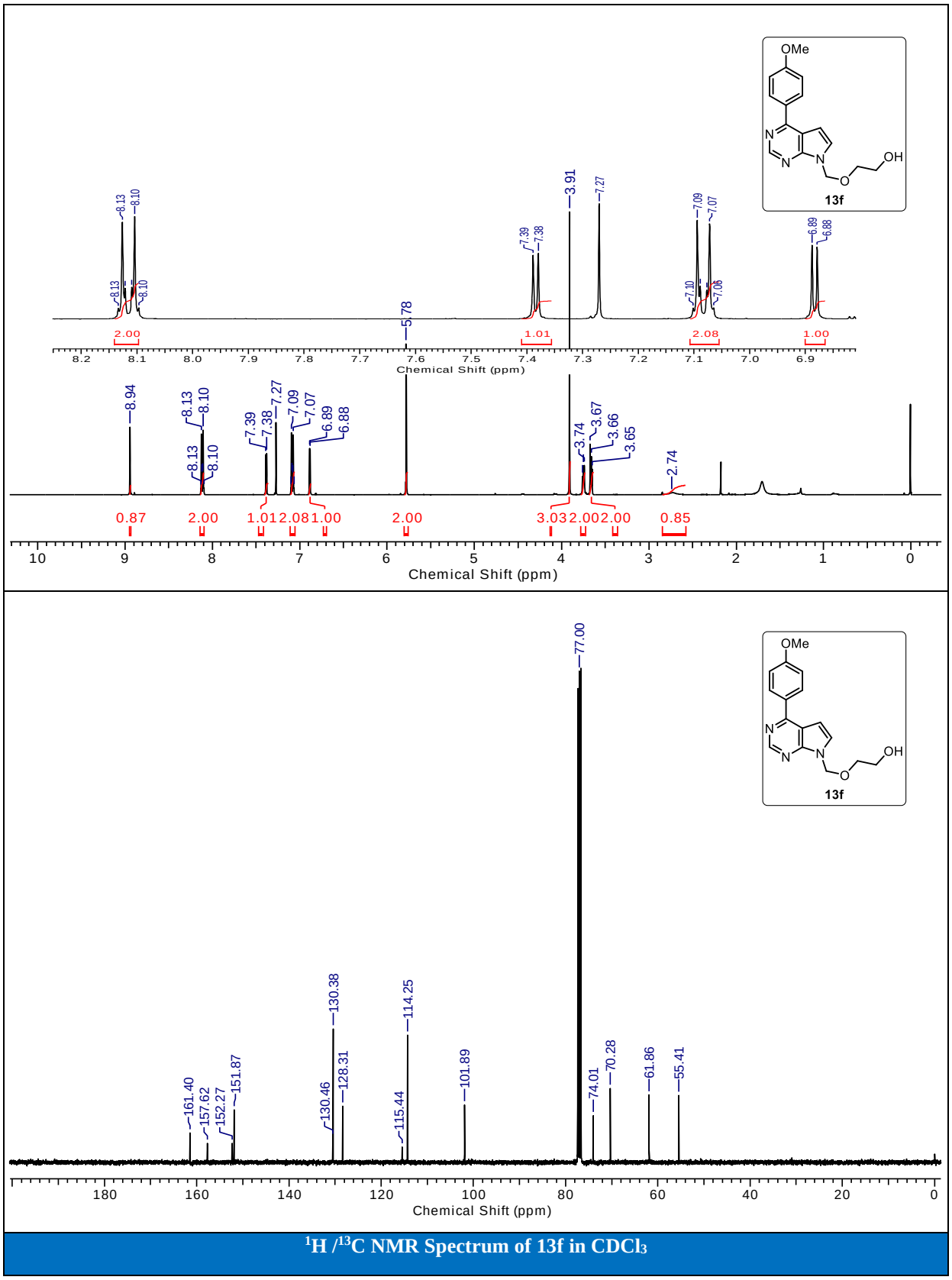

^{1}H /^{13}C NMR Spectrum of 13f in $CDCl_3$

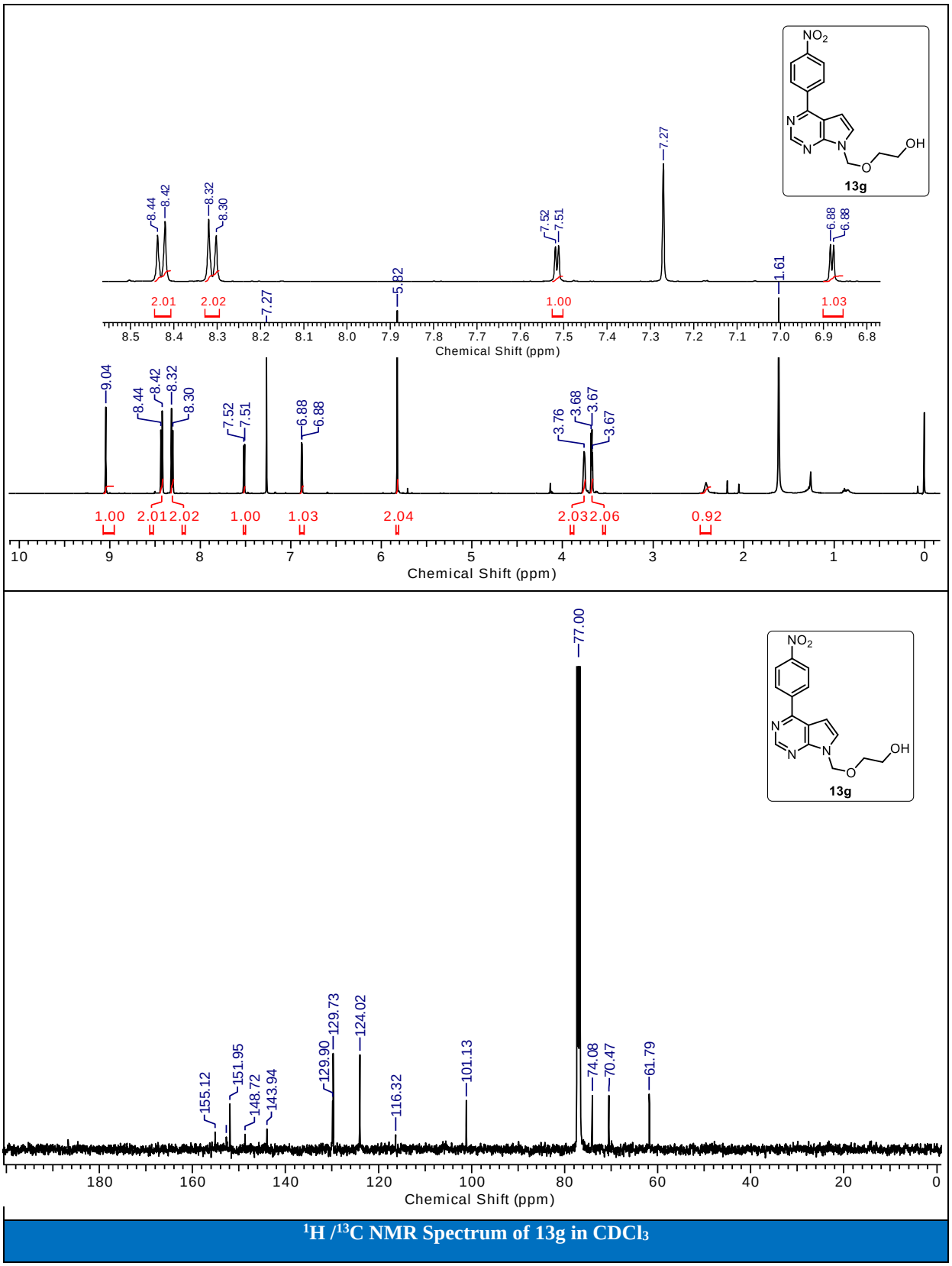

^{1}H /^{13}C NMR Spectrum of 13g in $CDCl_3$

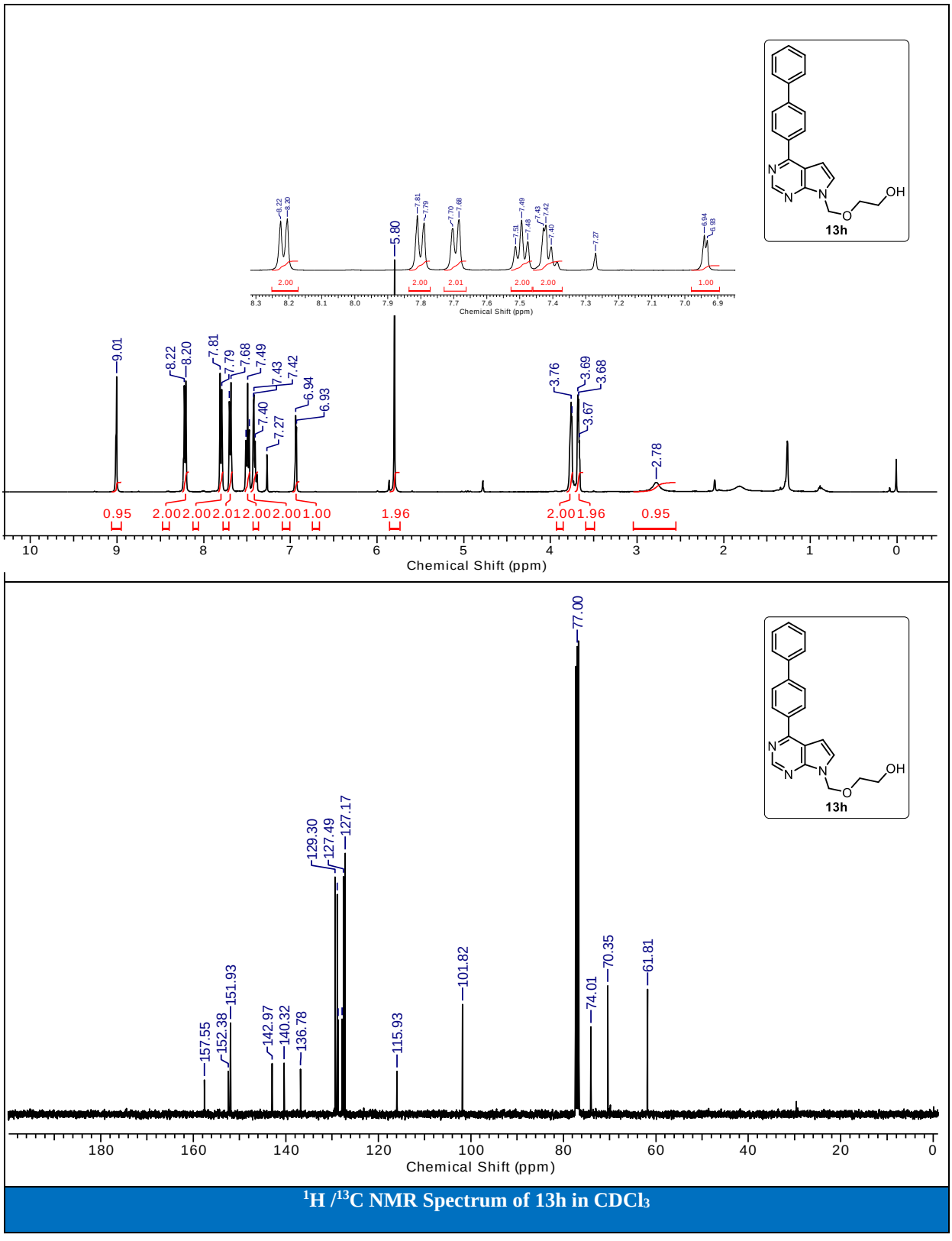

^{1}H /^{13}C NMR Spectrum of 13h in $CDCl_3$

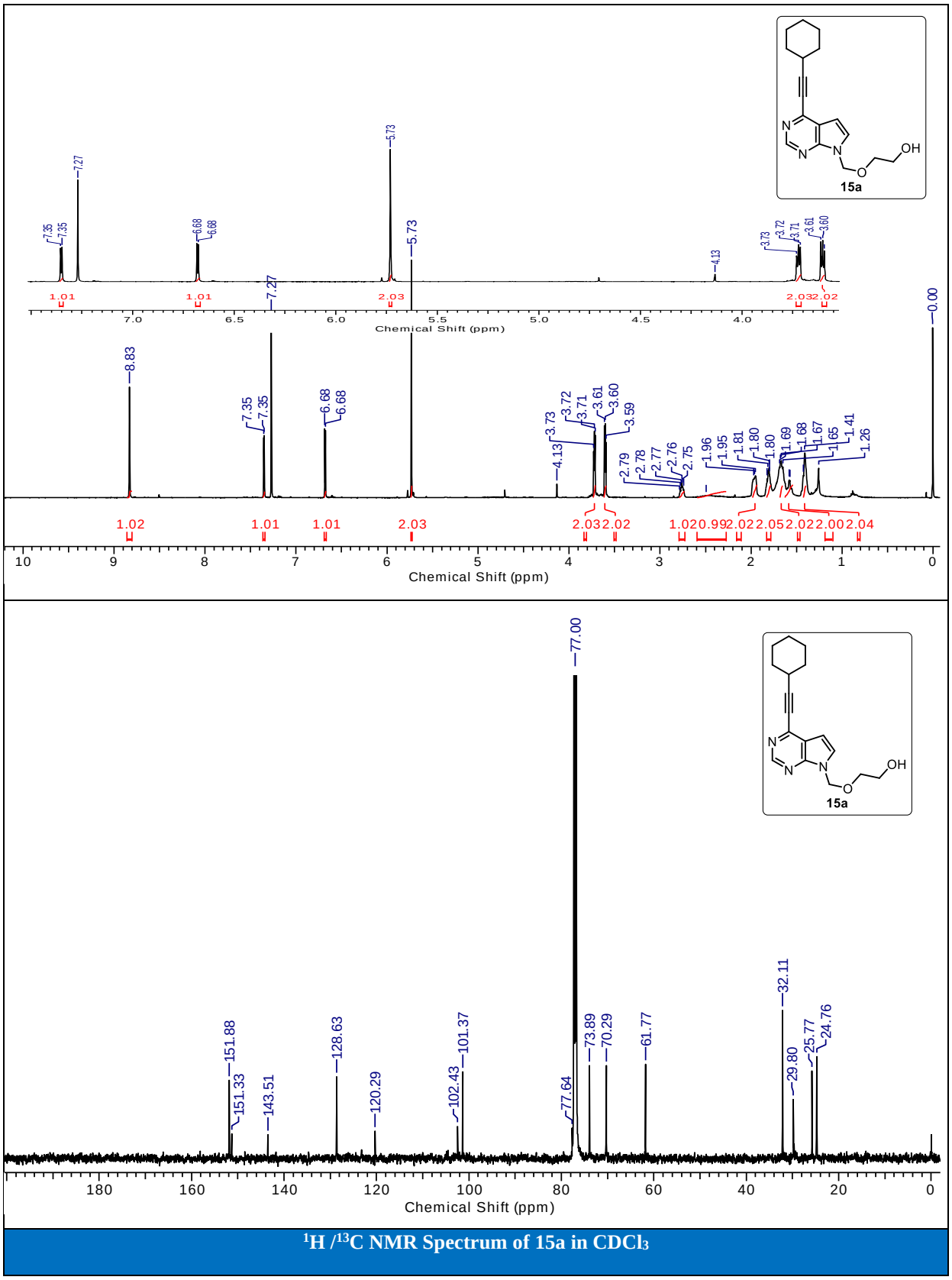

^{1}H /^{13}C NMR Spectrum of 15a in $CDCl_3$

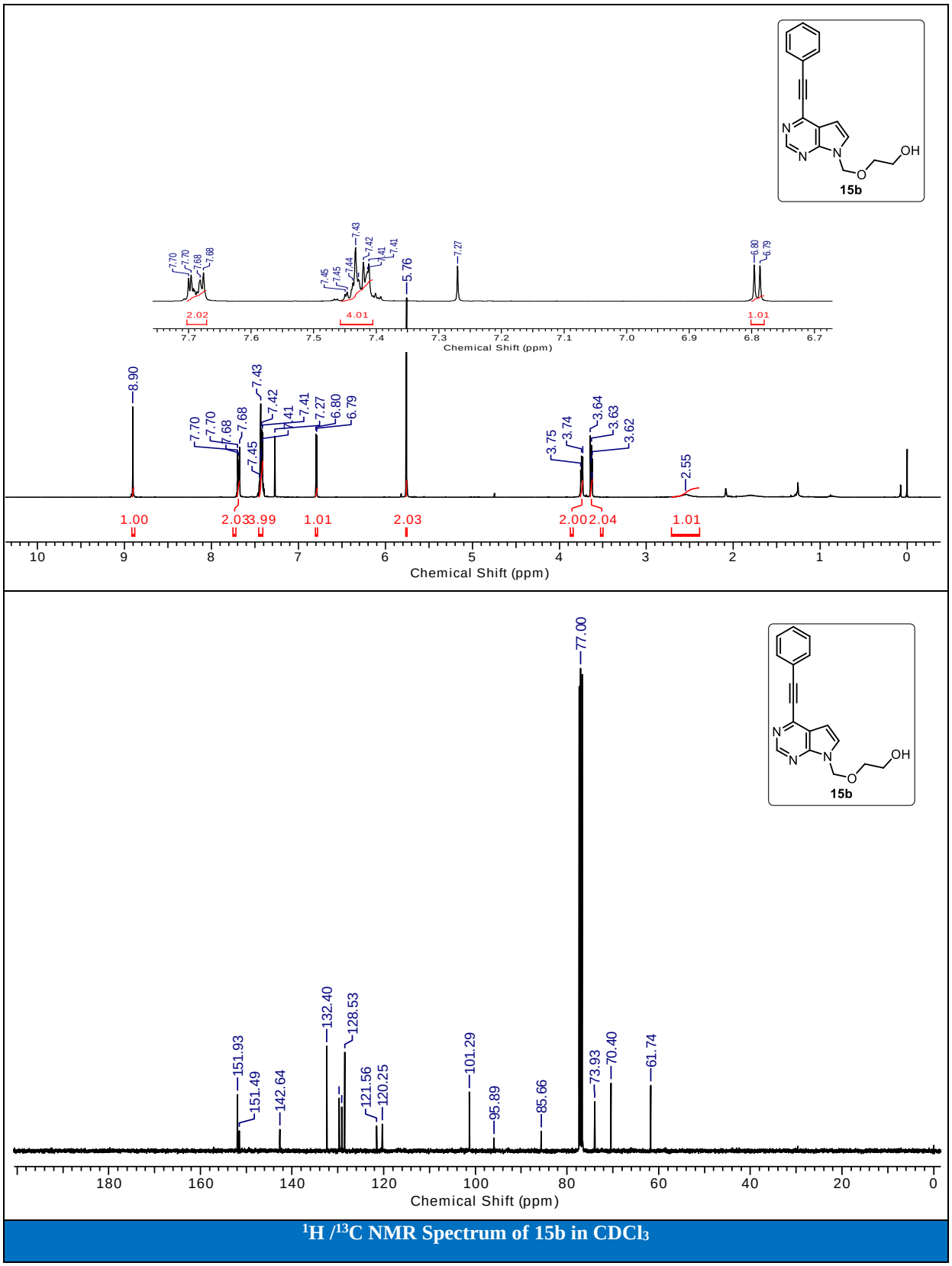

^{1}H /^{13}C NMR Spectrum of 15b in $CDCl_3$

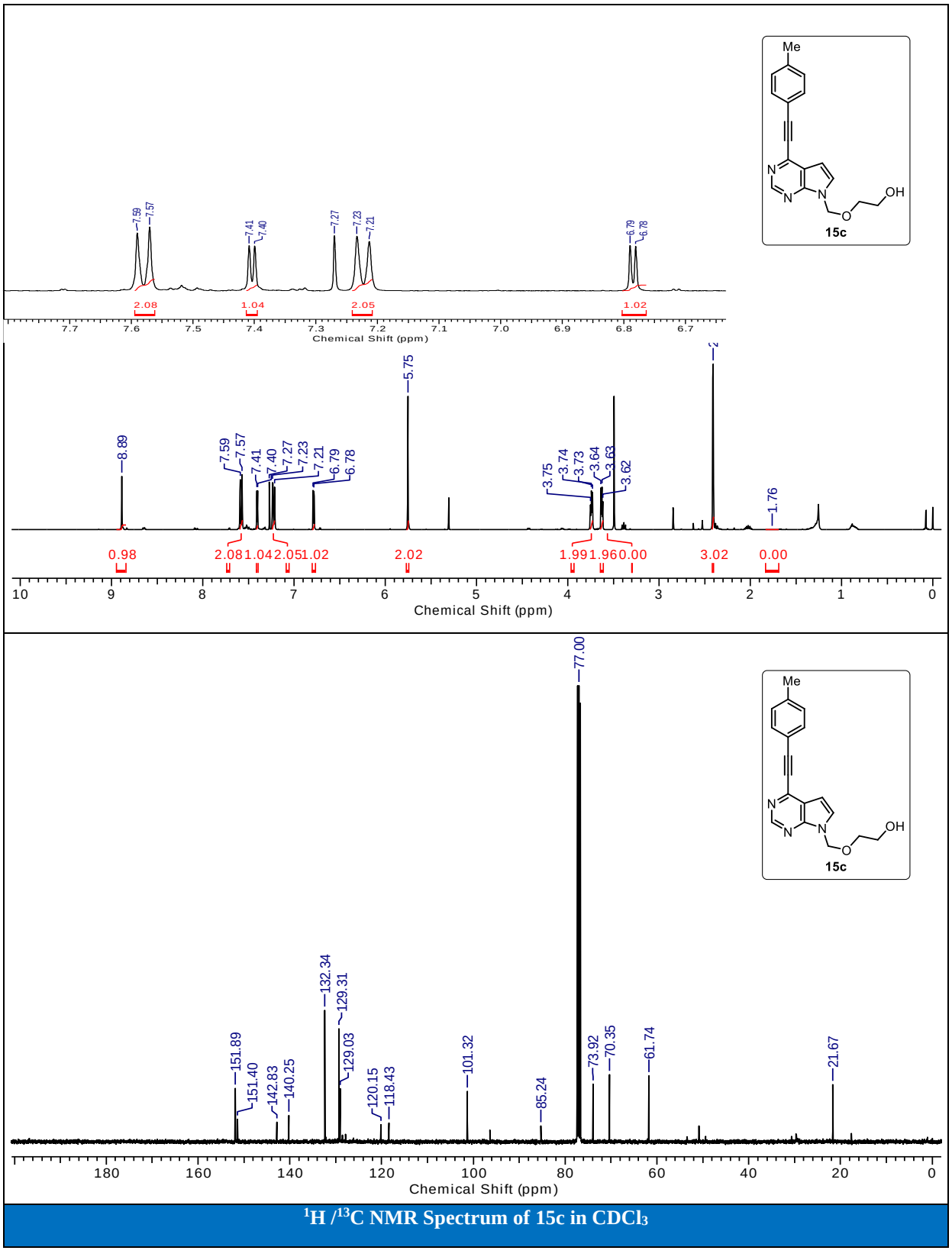

^{1}H /^{13}C NMR Spectrum of 15c in $CDCl_3$

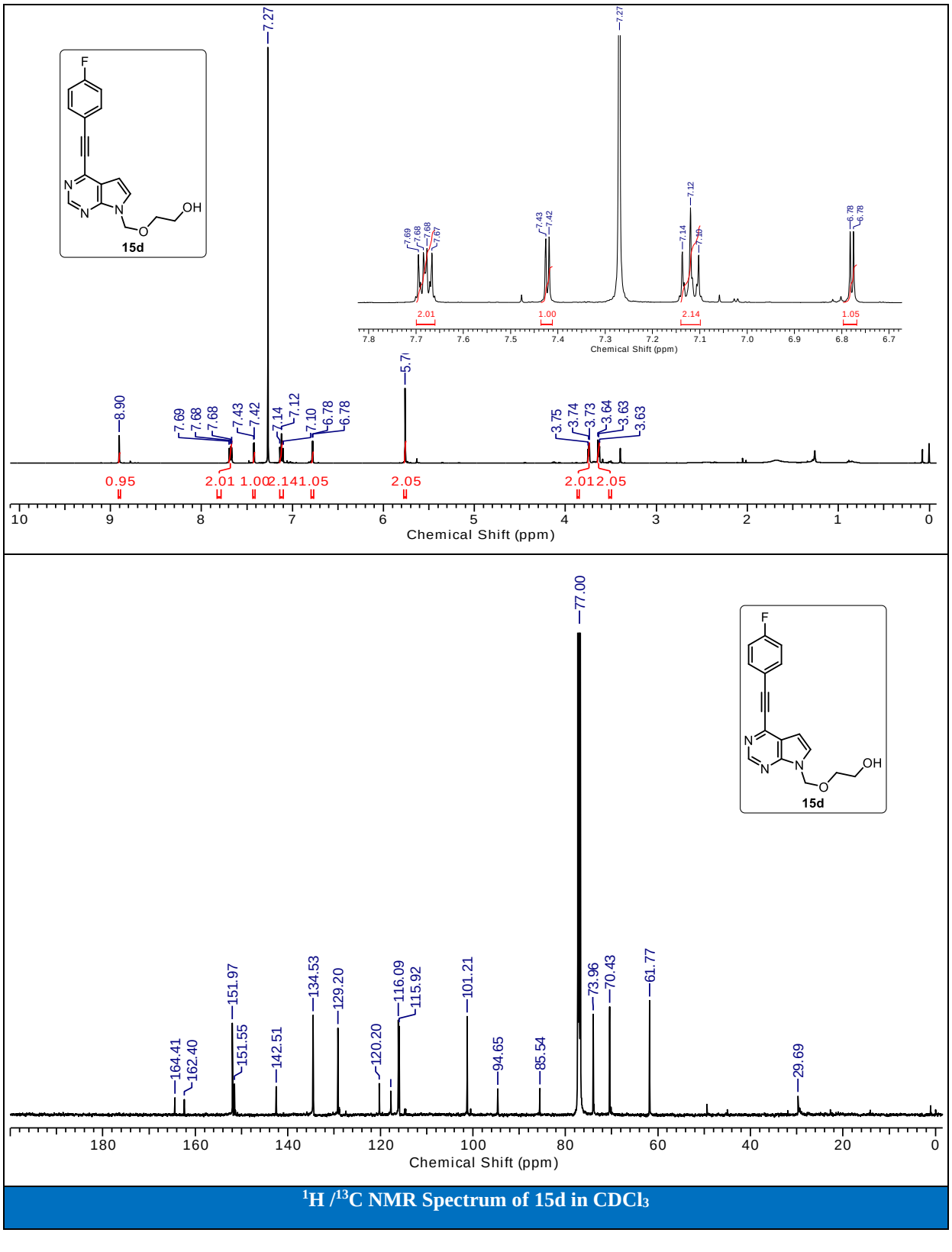

^{1}H /^{13}C NMR Spectrum of 15d in $CDCl_3$

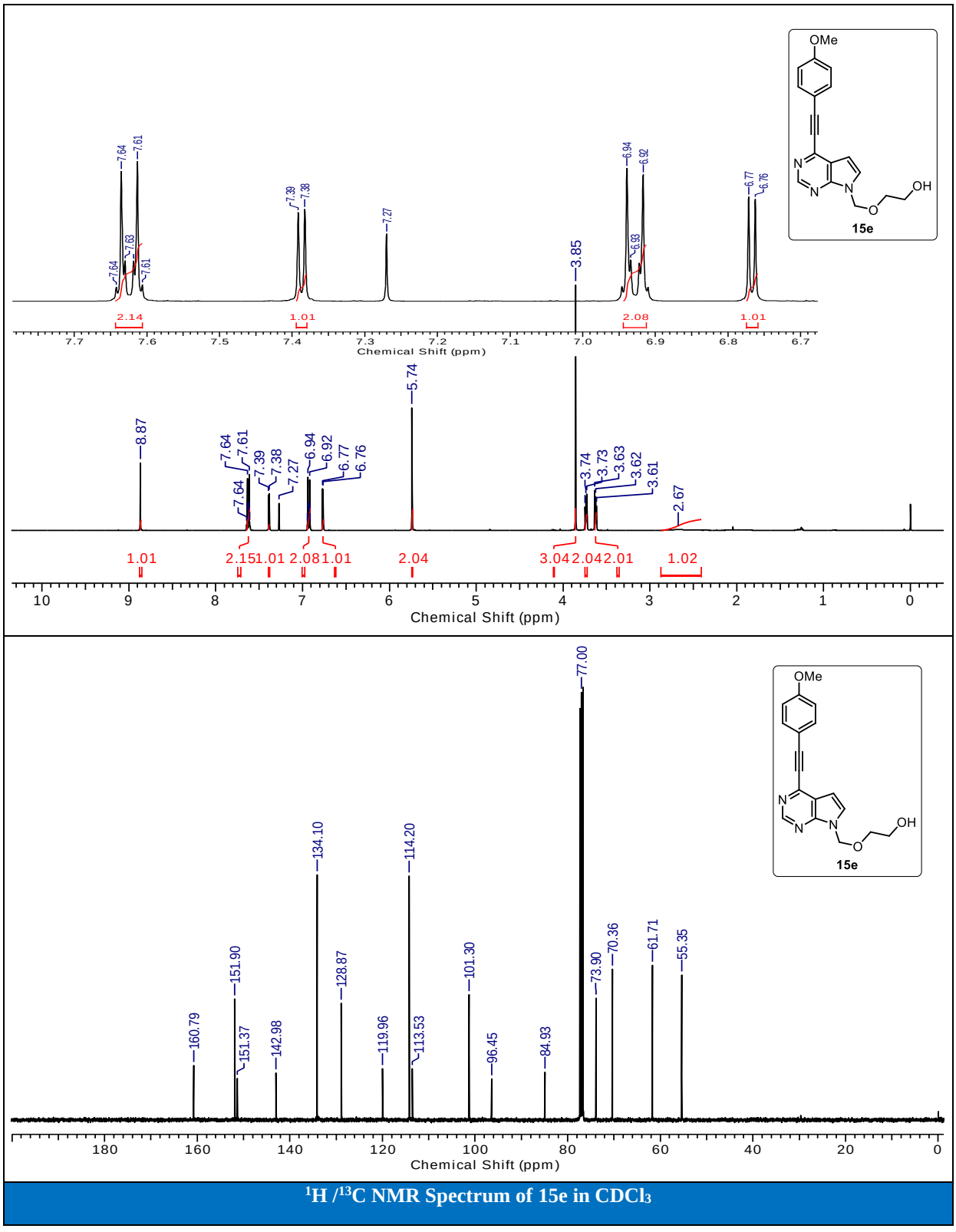

^{1}H /^{13}C NMR Spectrum of 15e in $CDCl_3$

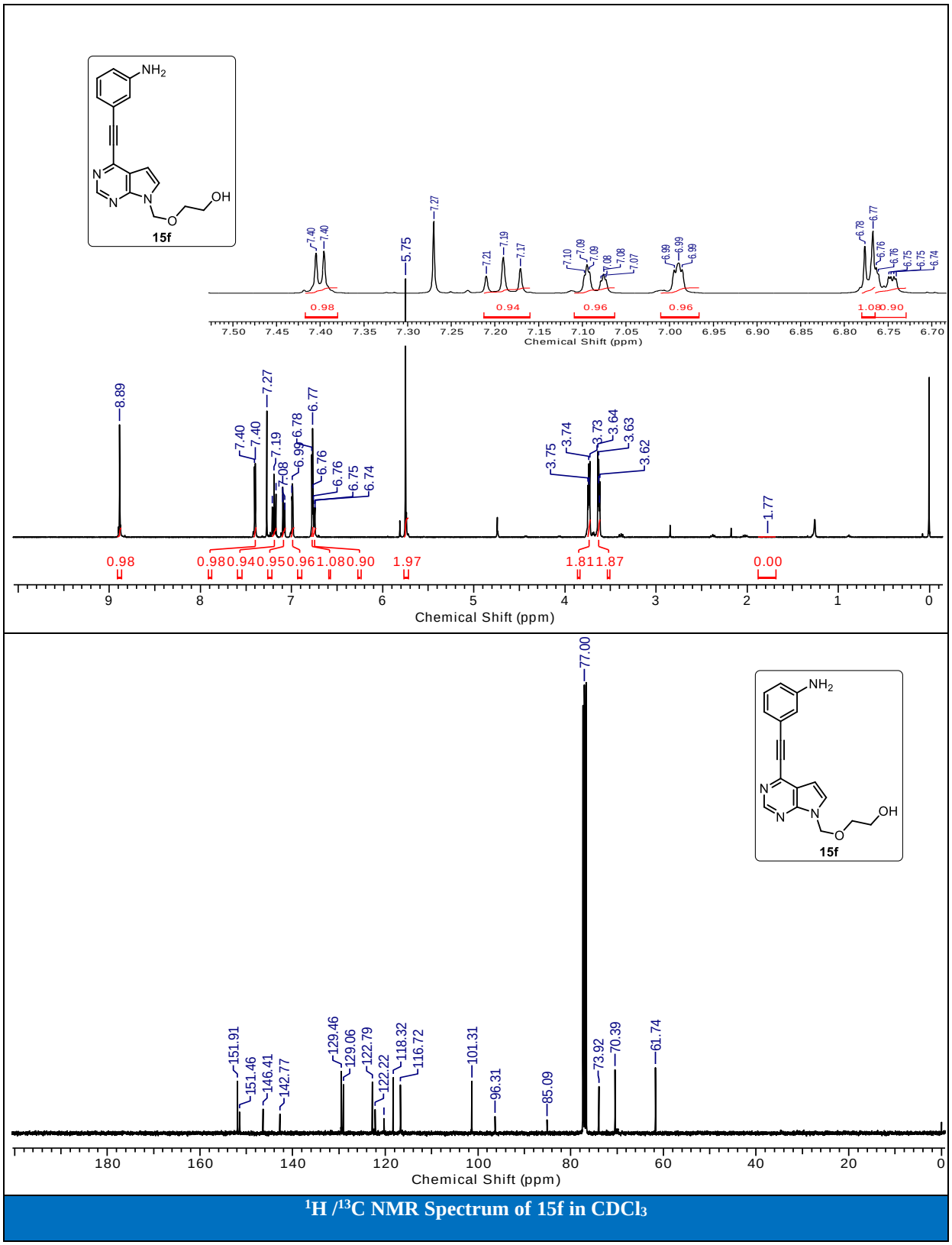

^{1}H /^{13}C NMR Spectrum of 15f in $CDCl_3$

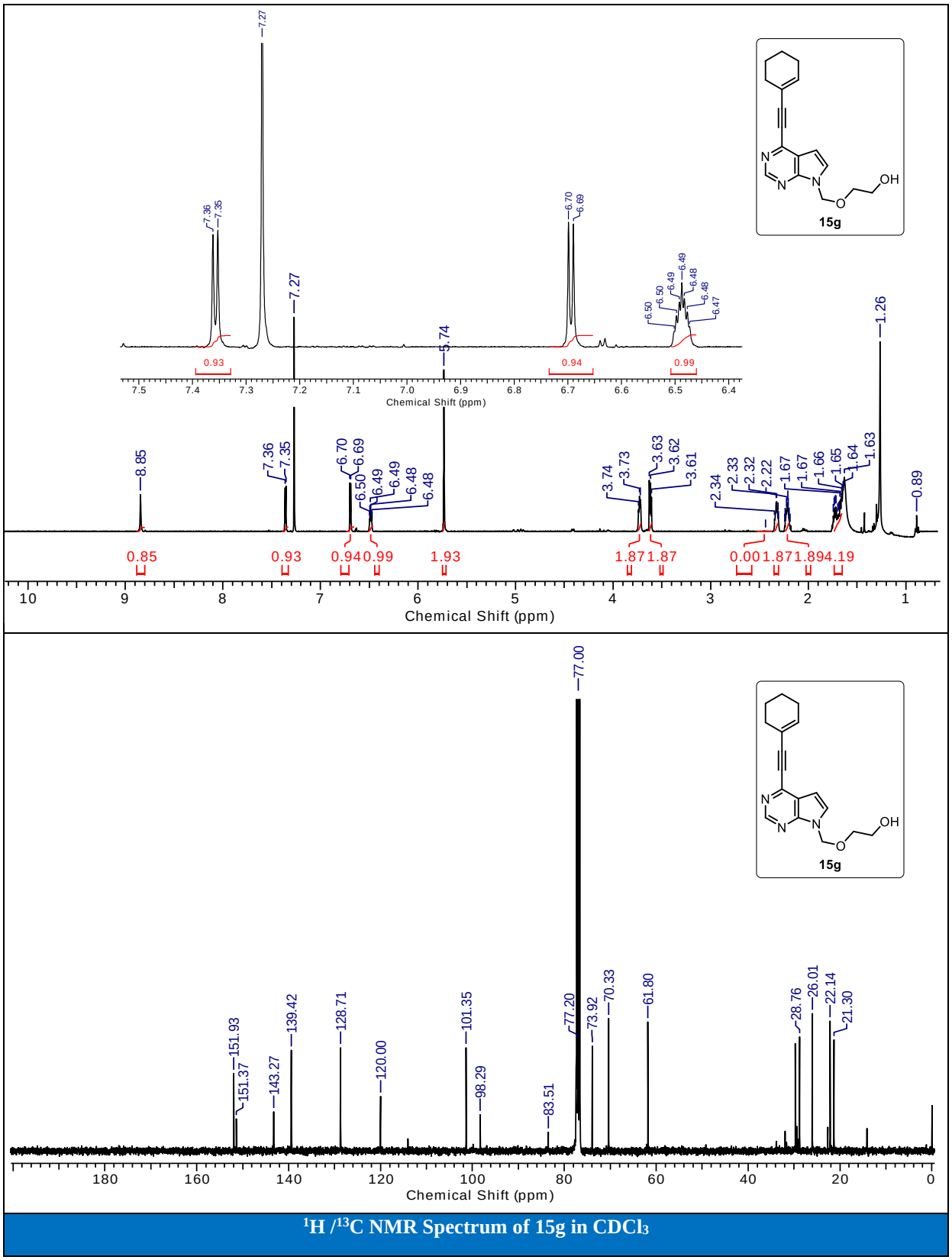

^{1}H /^{13}C NMR Spectrum of 15g in $CDCl_3$

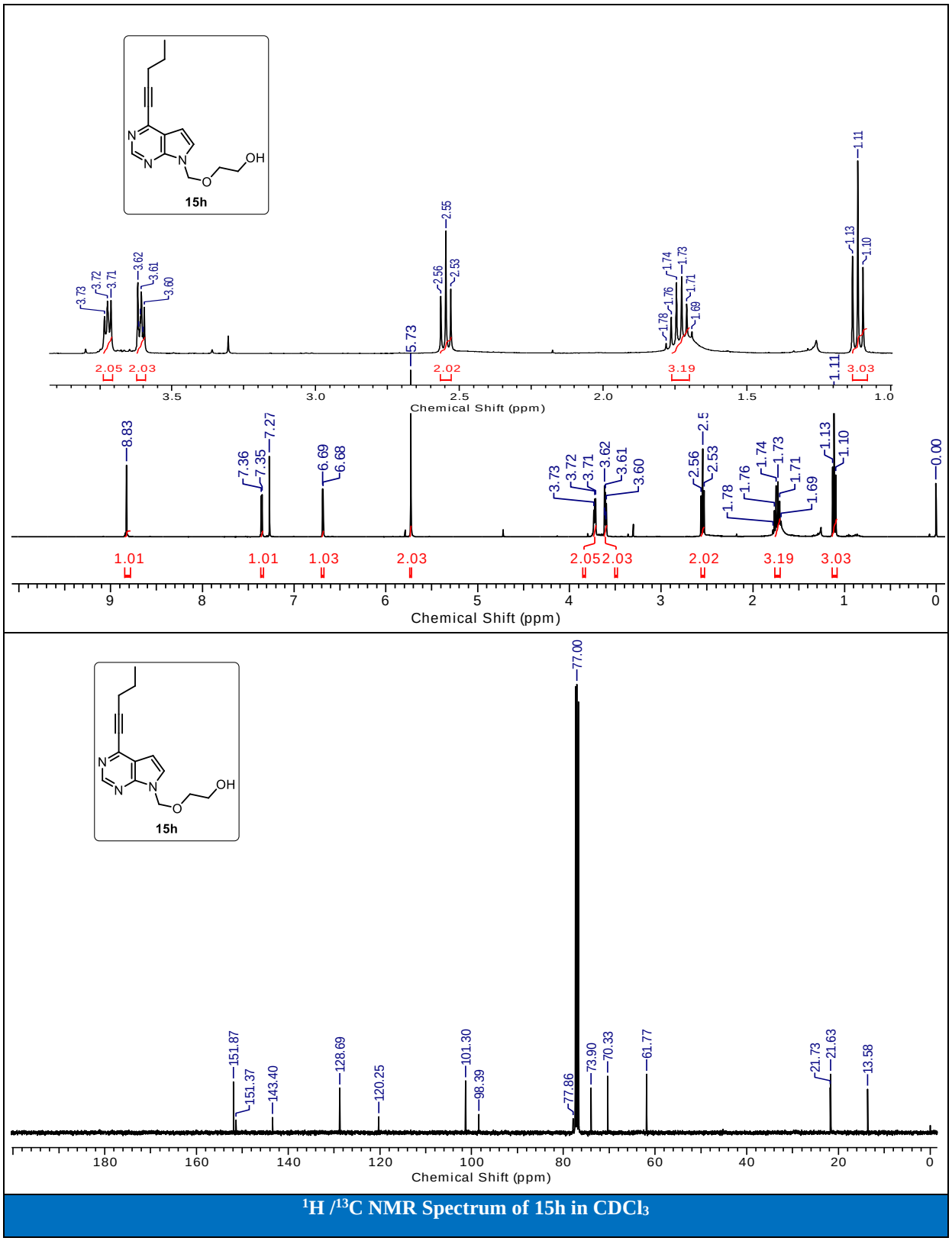

^{1}H /^{13}C NMR Spectrum of 15h in $CDCl_3$

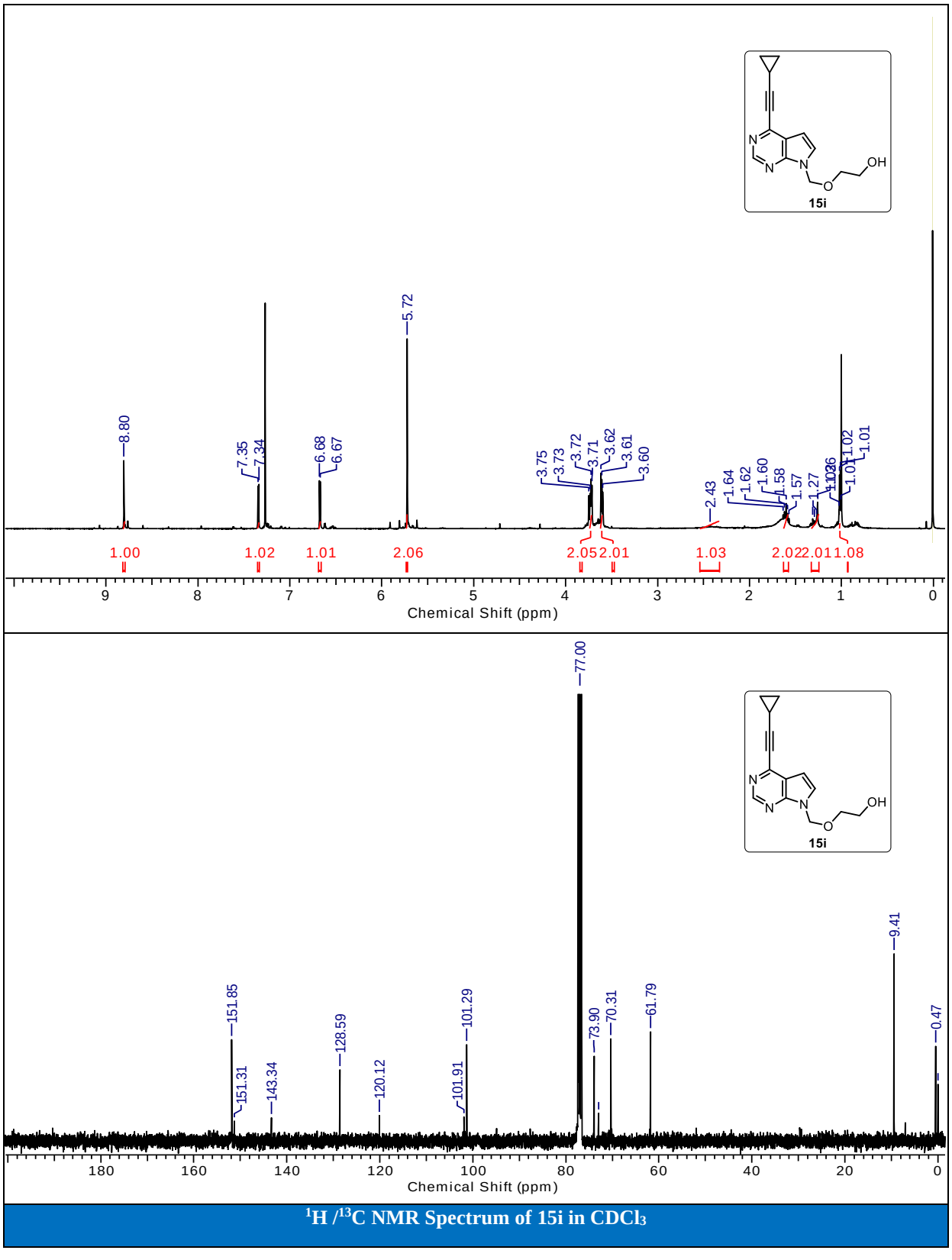

^{1}H /^{13}C NMR Spectrum of 15i in $CDCl_3$

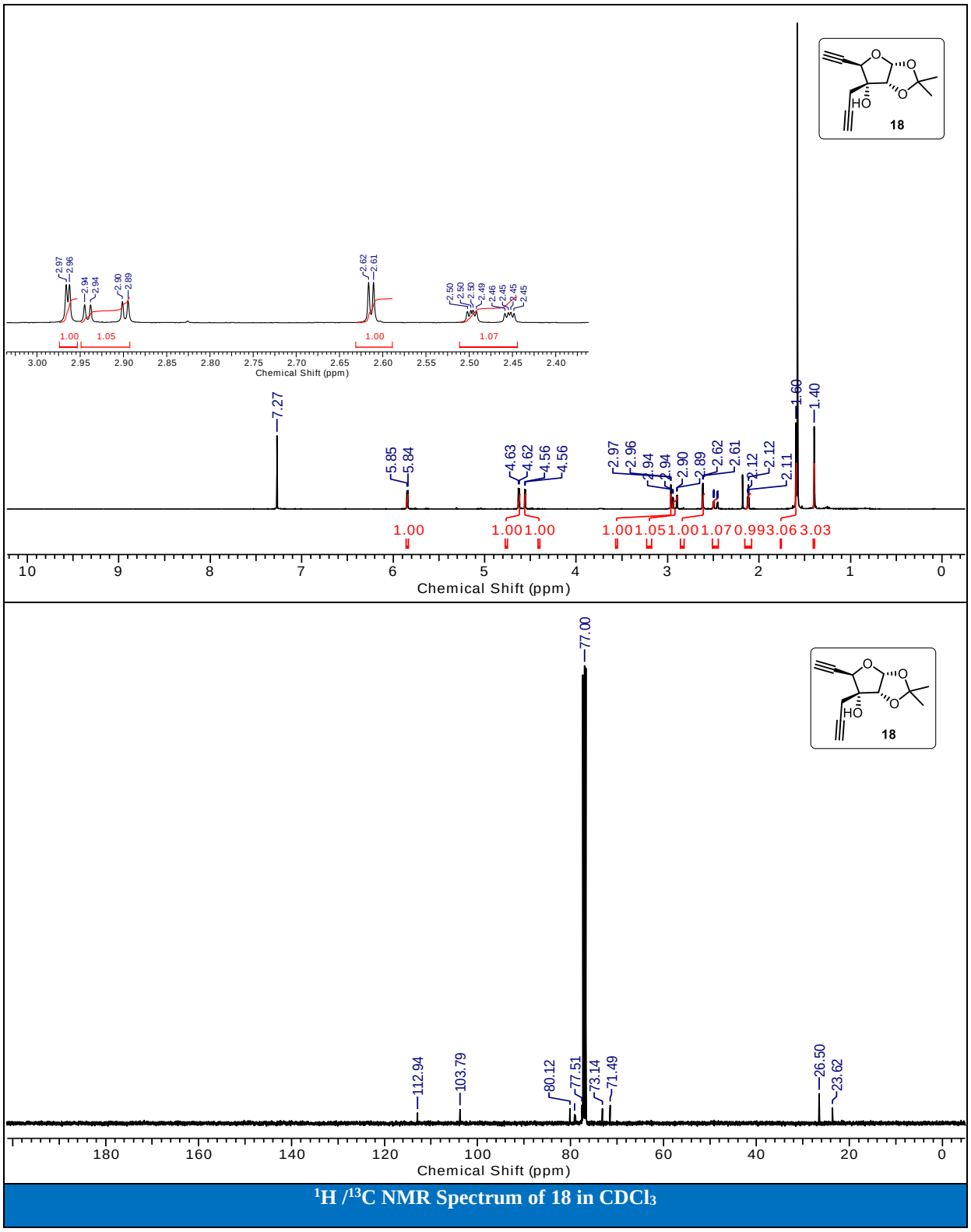

^{1}H /^{13}C NMR Spectrum of 18 in $CDCl_3$

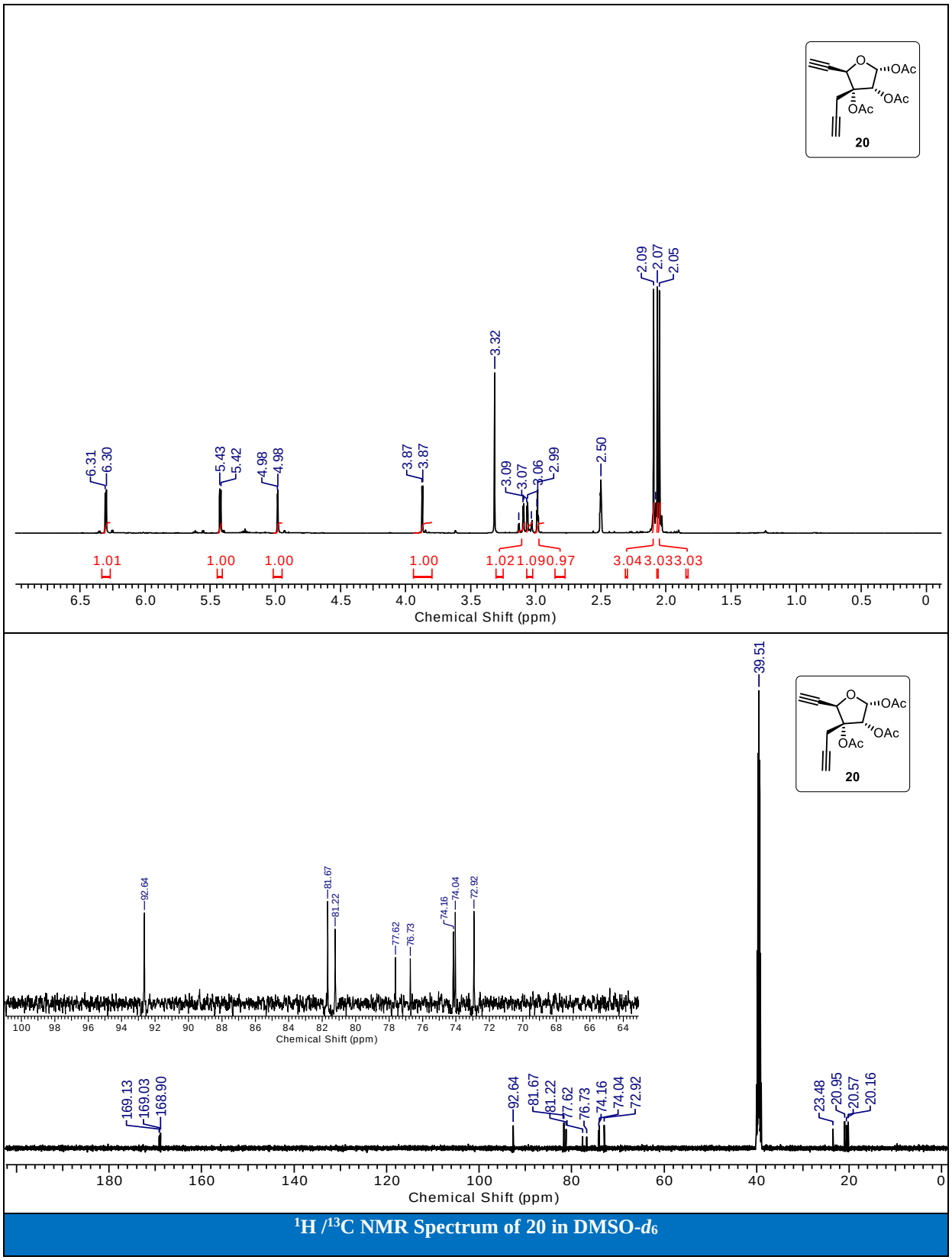

^{1}H /^{13}C NMR Spectrum of 20 in DMSO-d_6

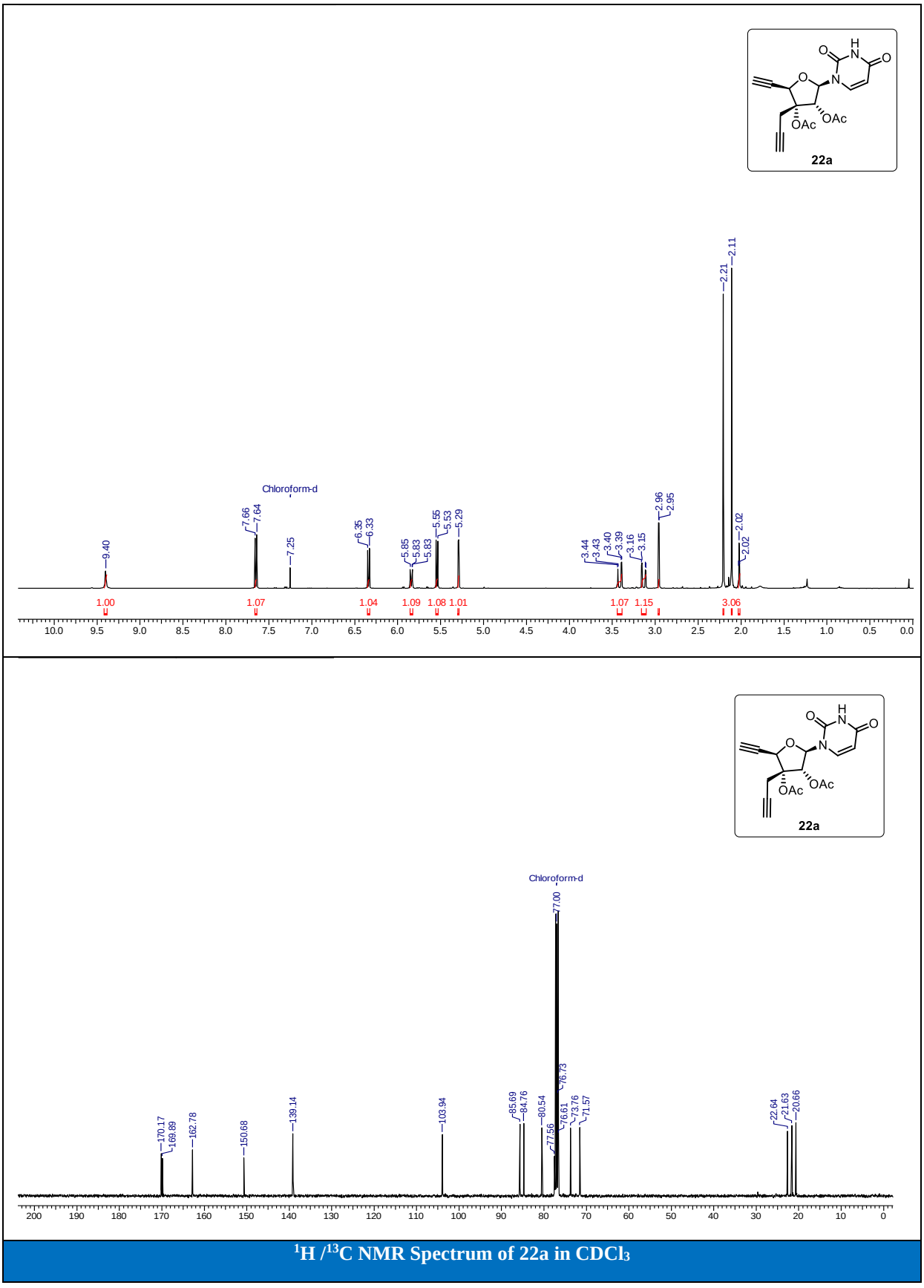

^{1}H /^{13}C NMR Spectrum of 22a in $CDCl_3$

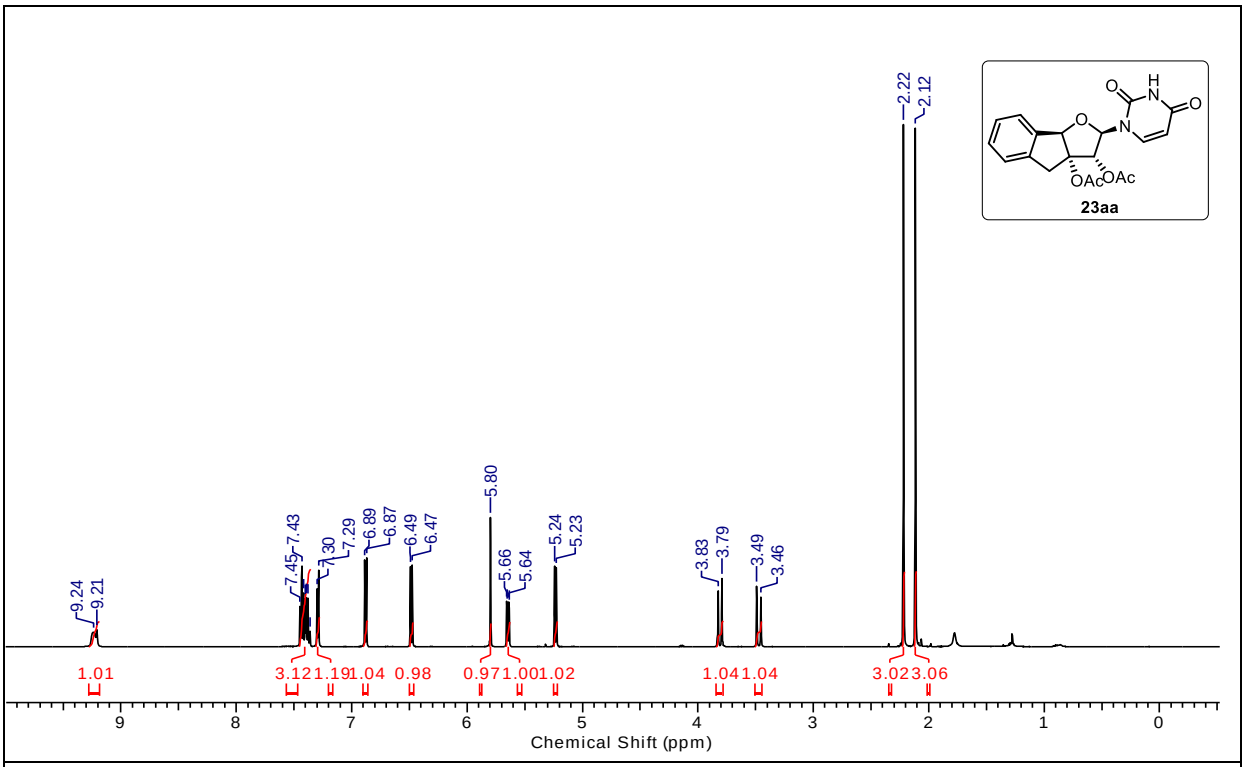

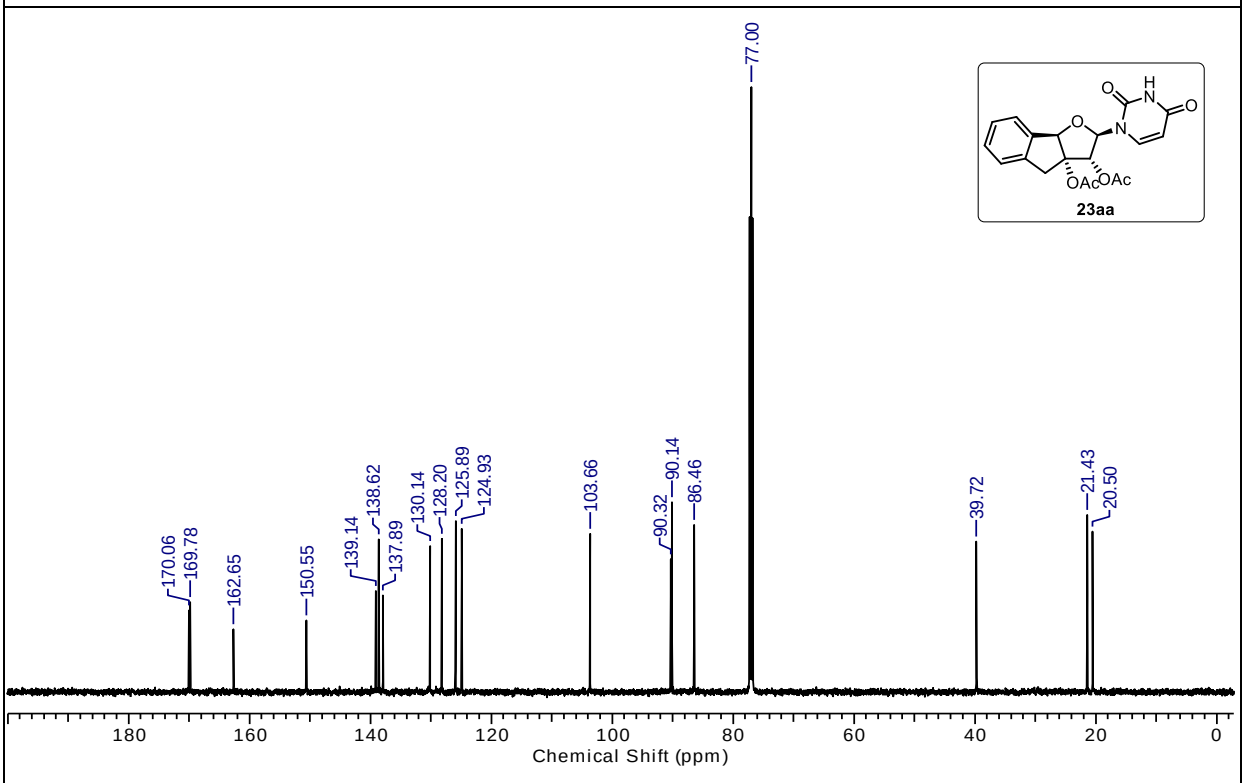

^{1}H /^{13}C NMR Spectrum of 23aa in $CDCl_3$

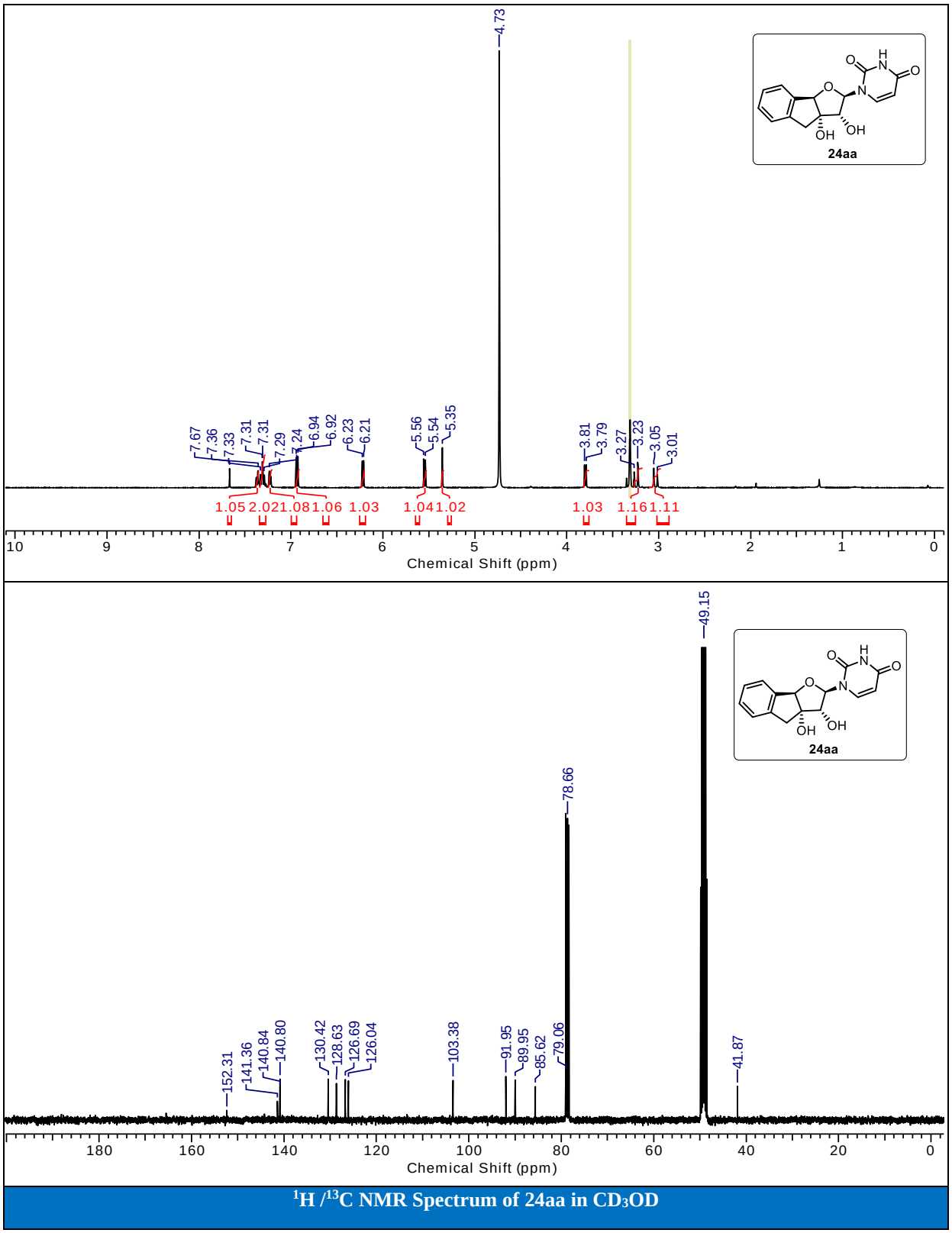

^{1}H /^{13}C NMR Spectrum of 24aa in CD_3OD

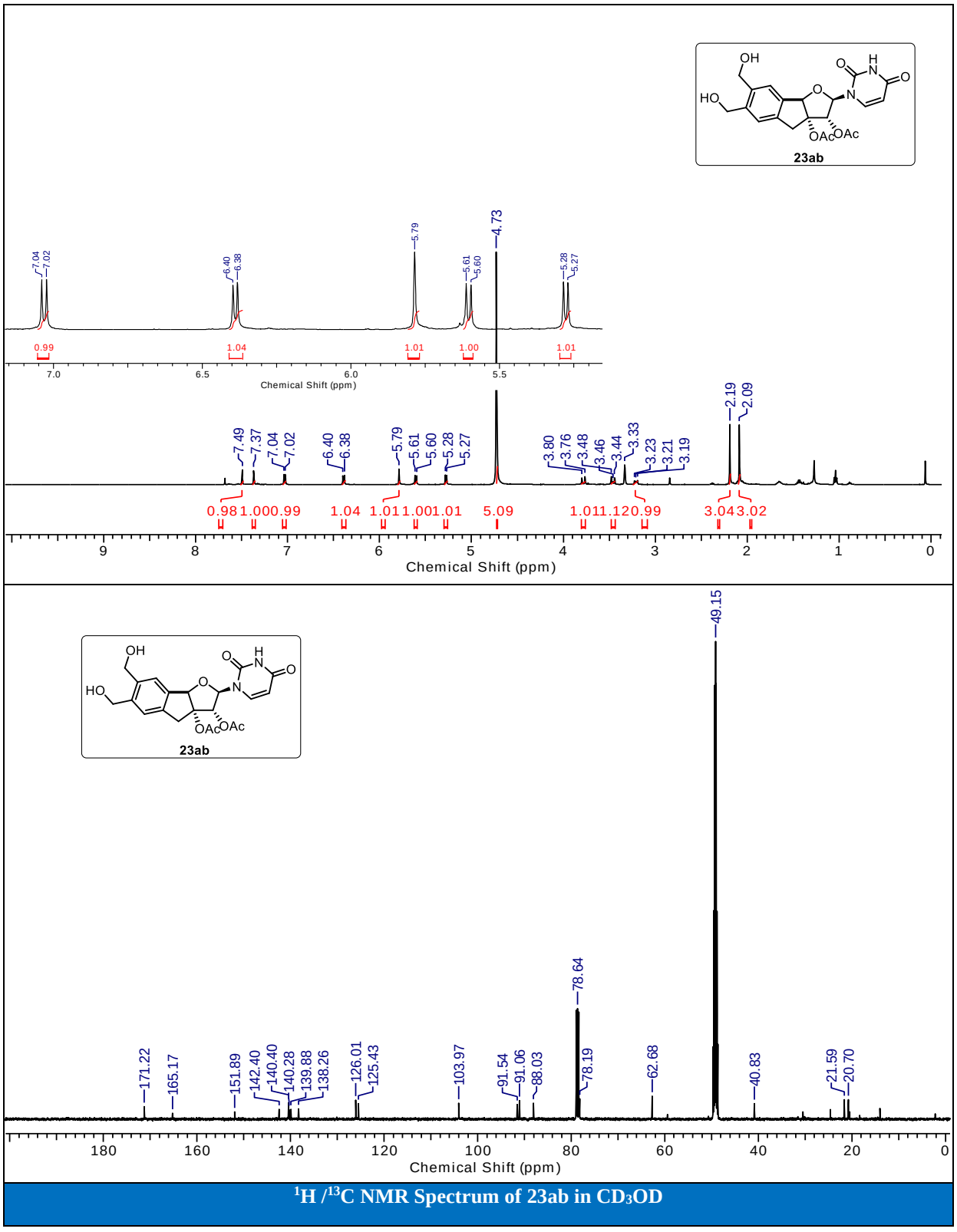

^{1}H /^{13}C NMR Spectrum of 23ab in CD_3OD

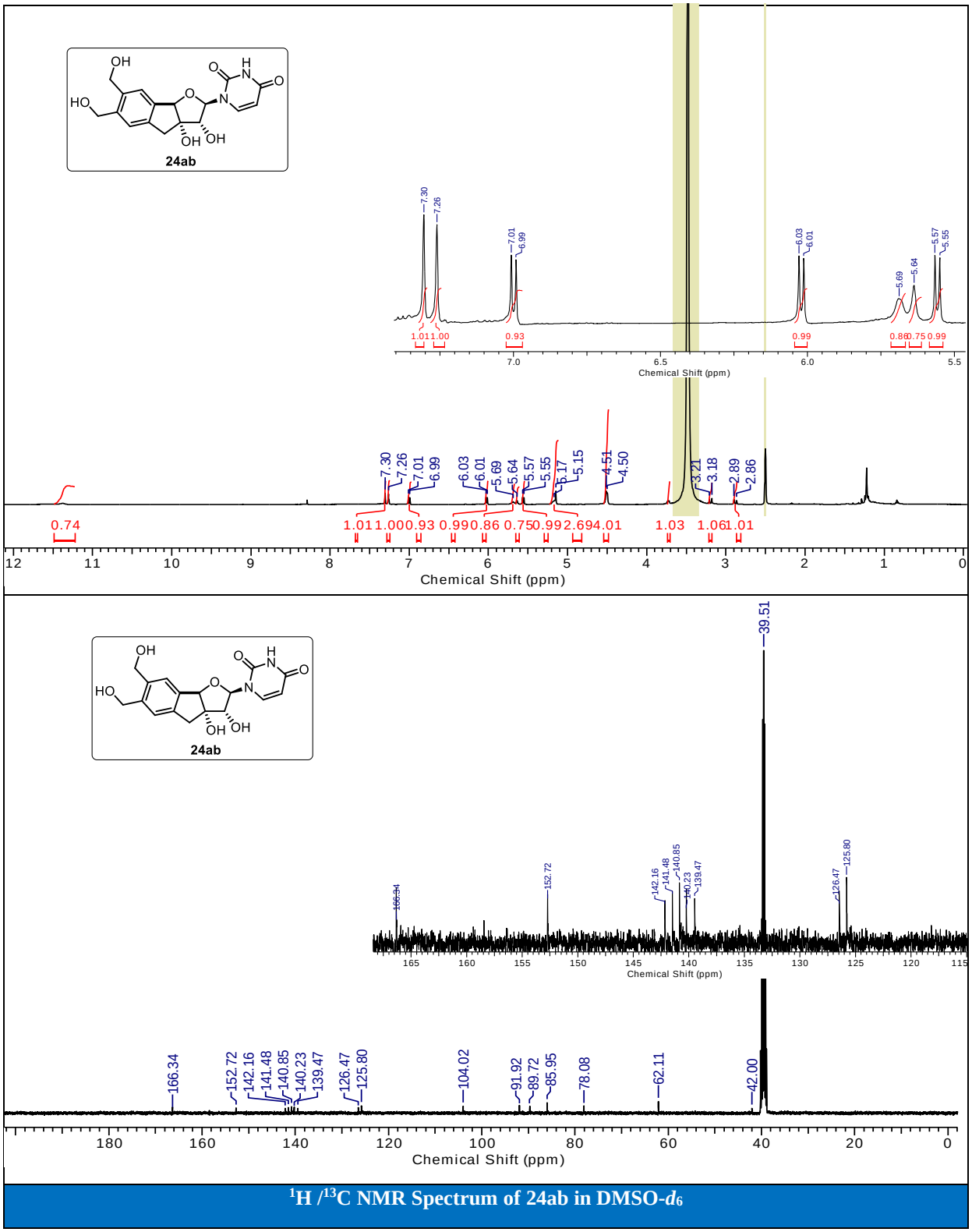

^{1}H /^{13}C NMR Spectrum of 24ab in DMSO-d_6

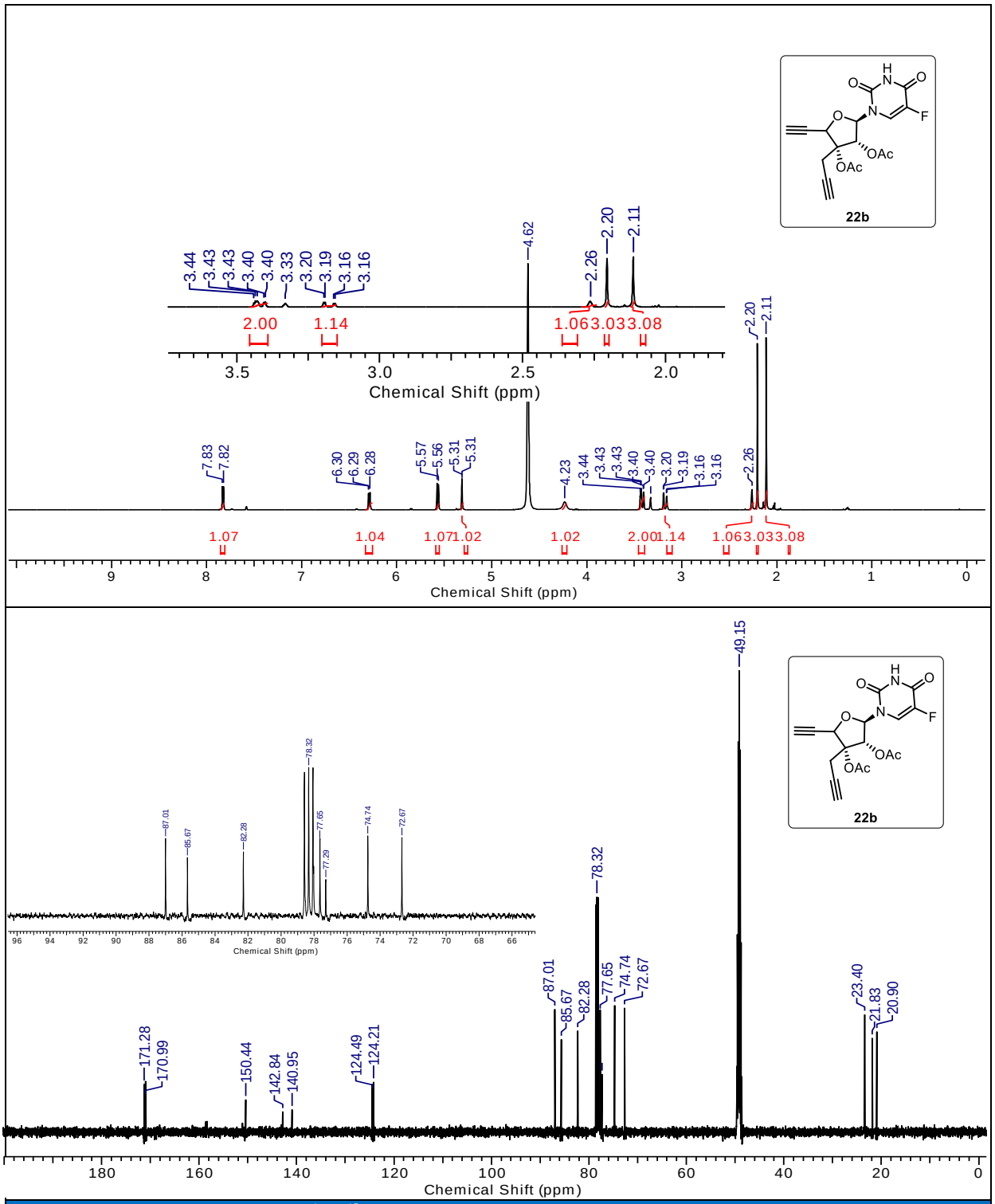

^{1}H /^{13}C NMR Spectrum of 22b in CD_3OD

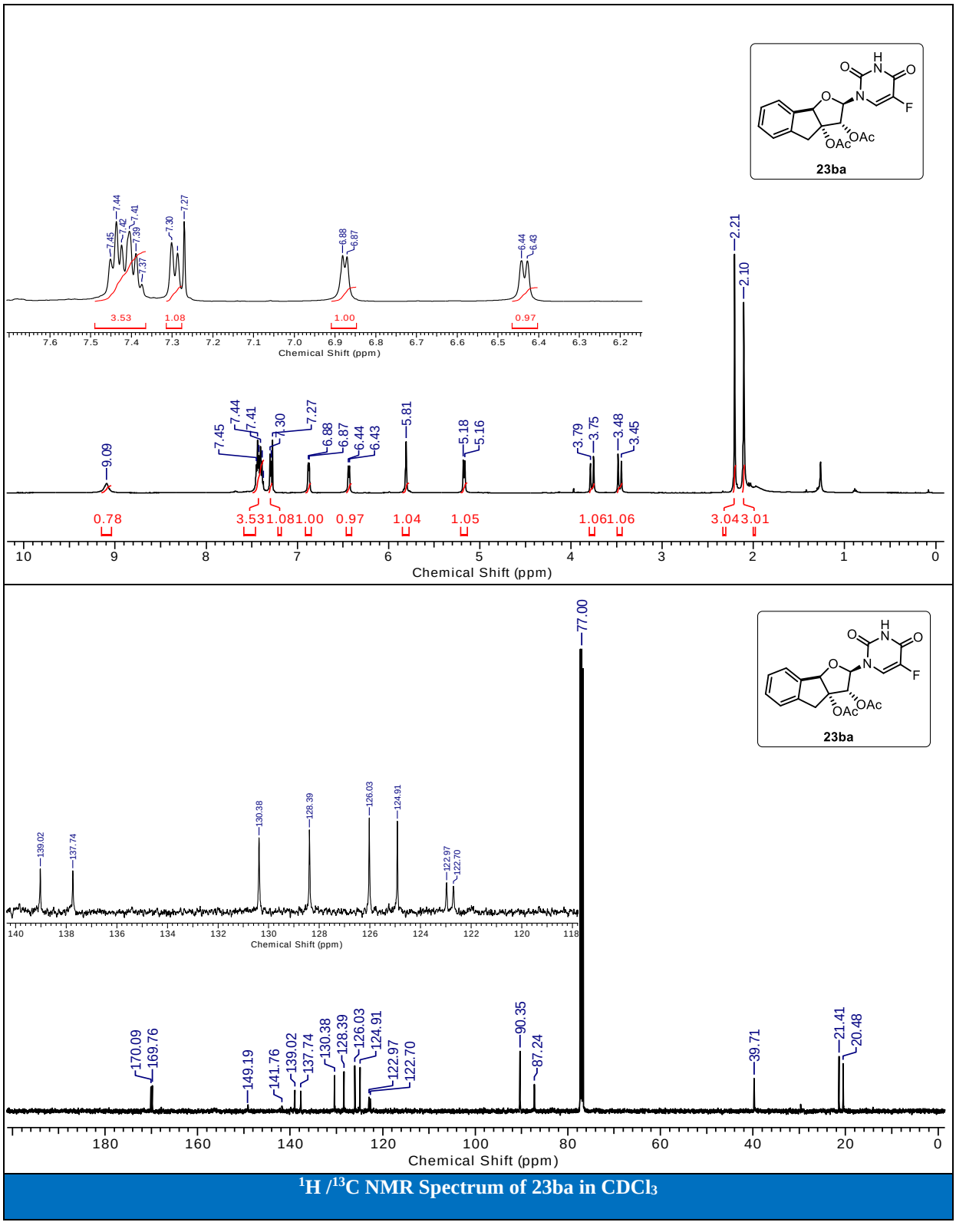

^{1}H /^{13}C NMR Spectrum of 23ba in $CDCl_3$

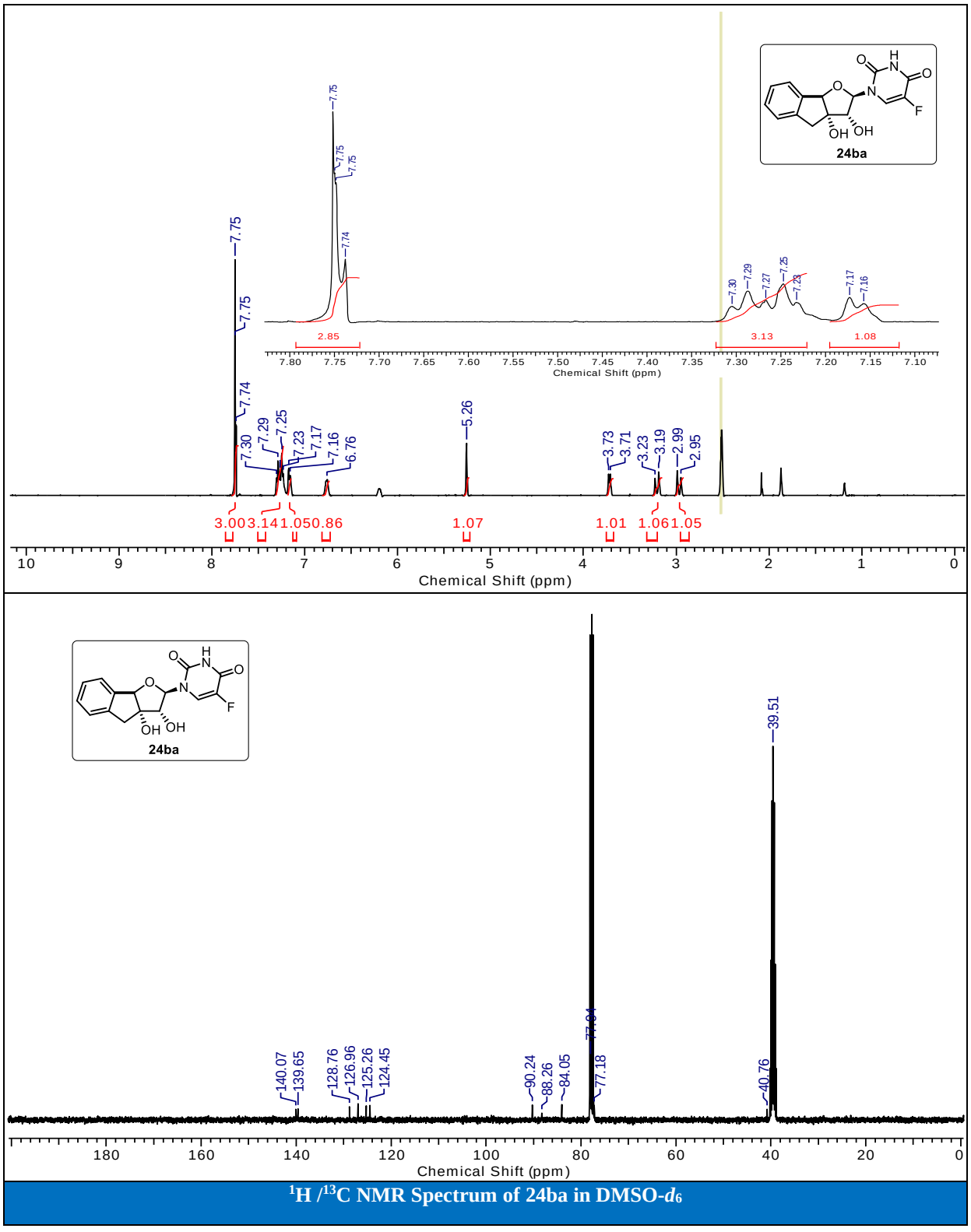

^{1}H /^{13}C NMR Spectrum of 24ba in DMSO-d_6

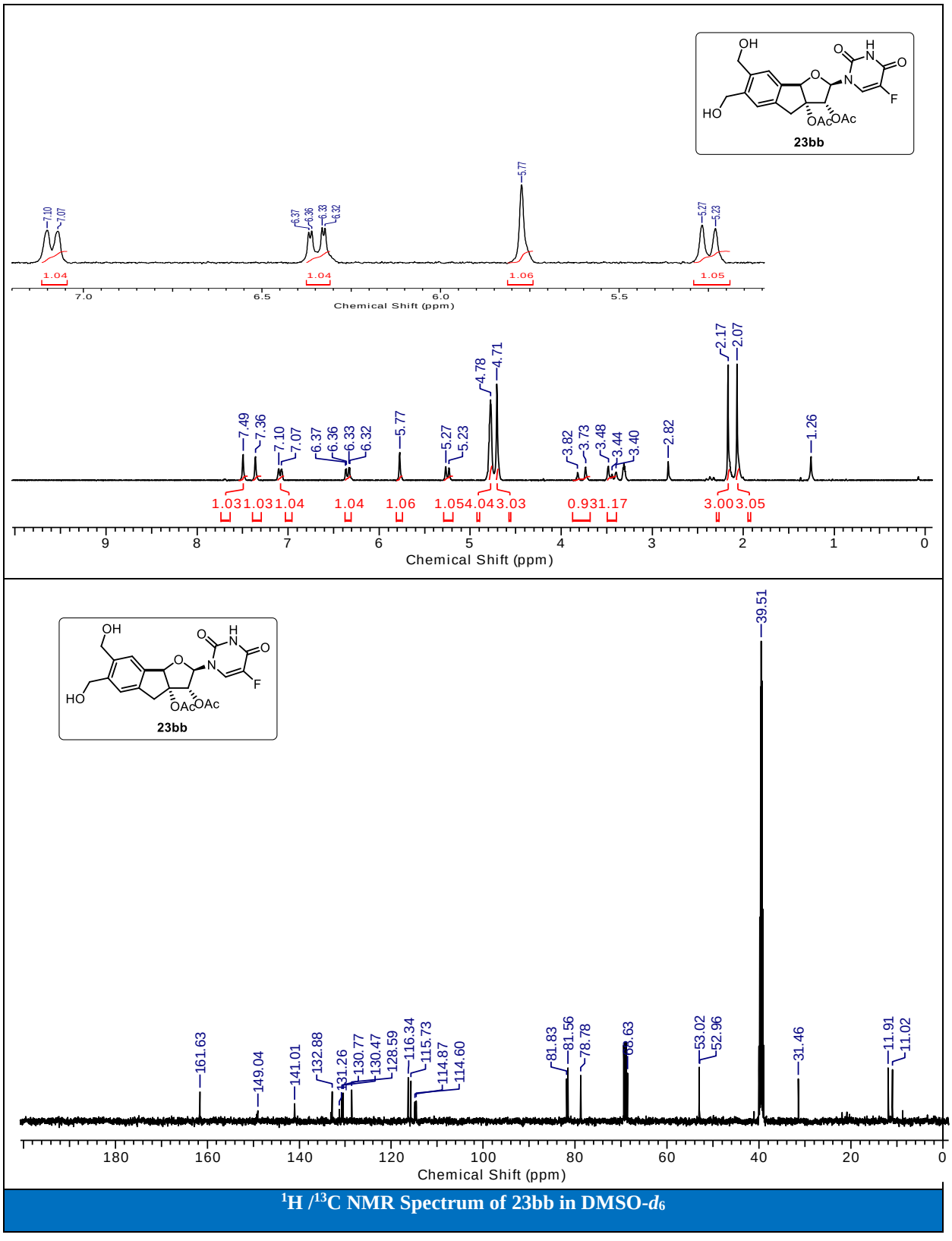

^{1}H /^{13}C NMR Spectrum of 23bb in DMSO-d_6

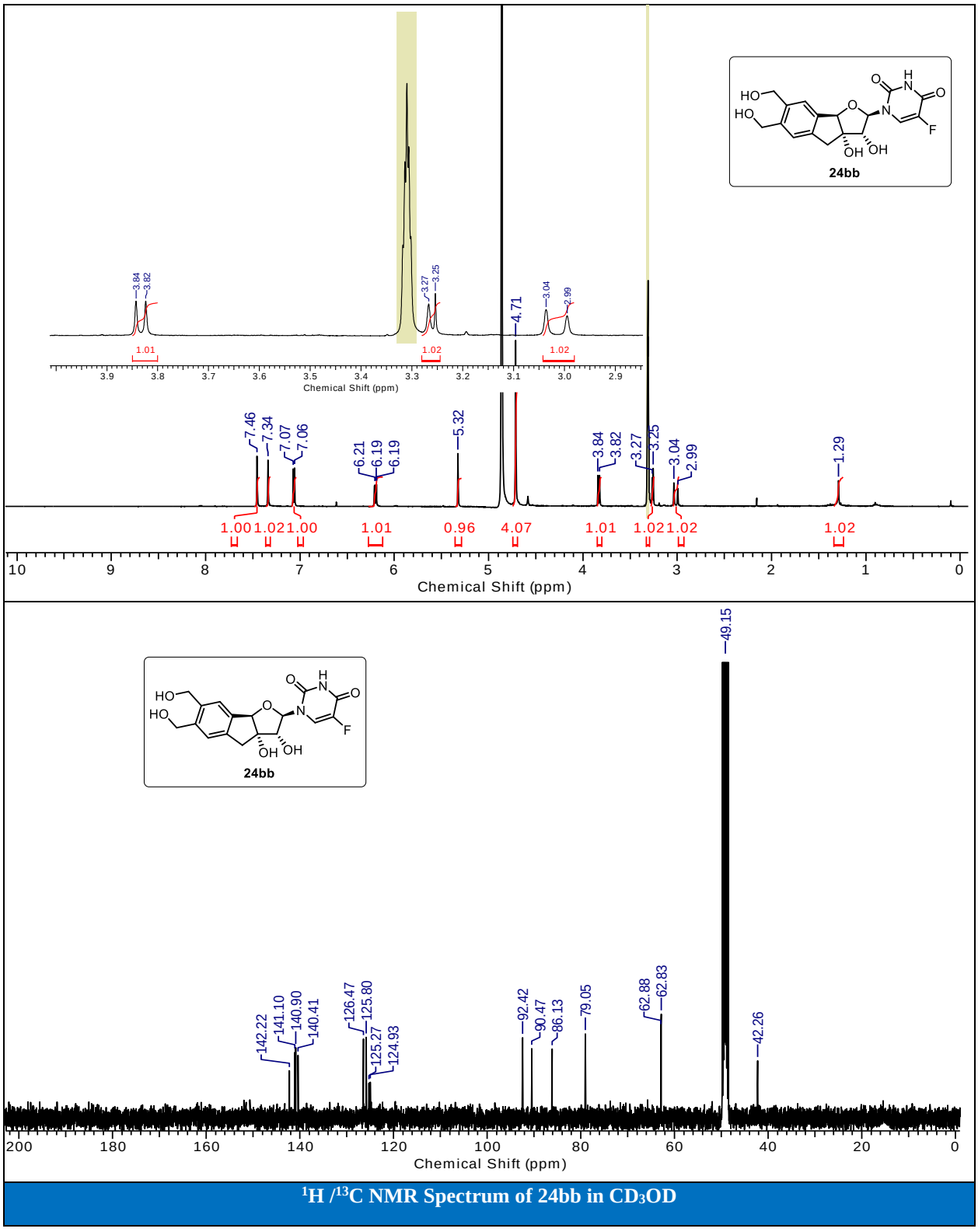

^{1}H /^{13}C NMR Spectrum of 24bb in CD_3OD

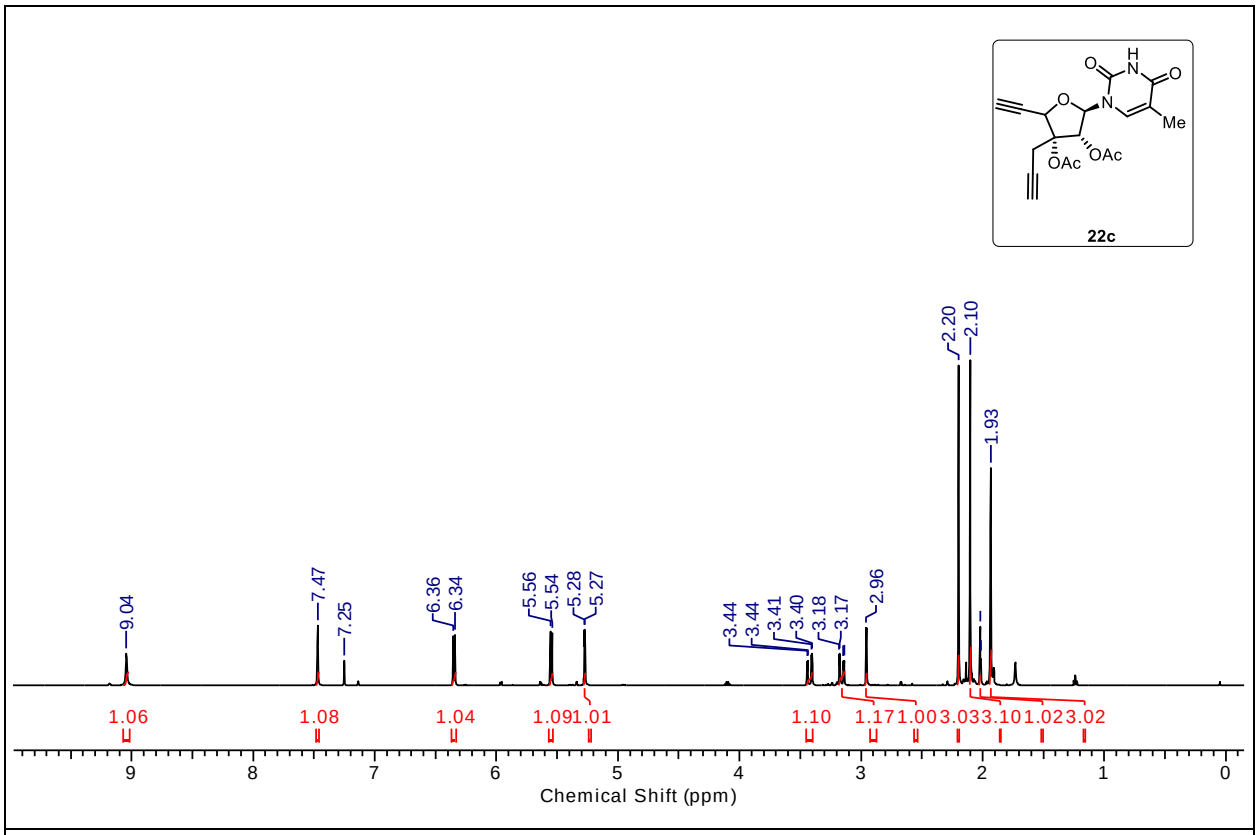

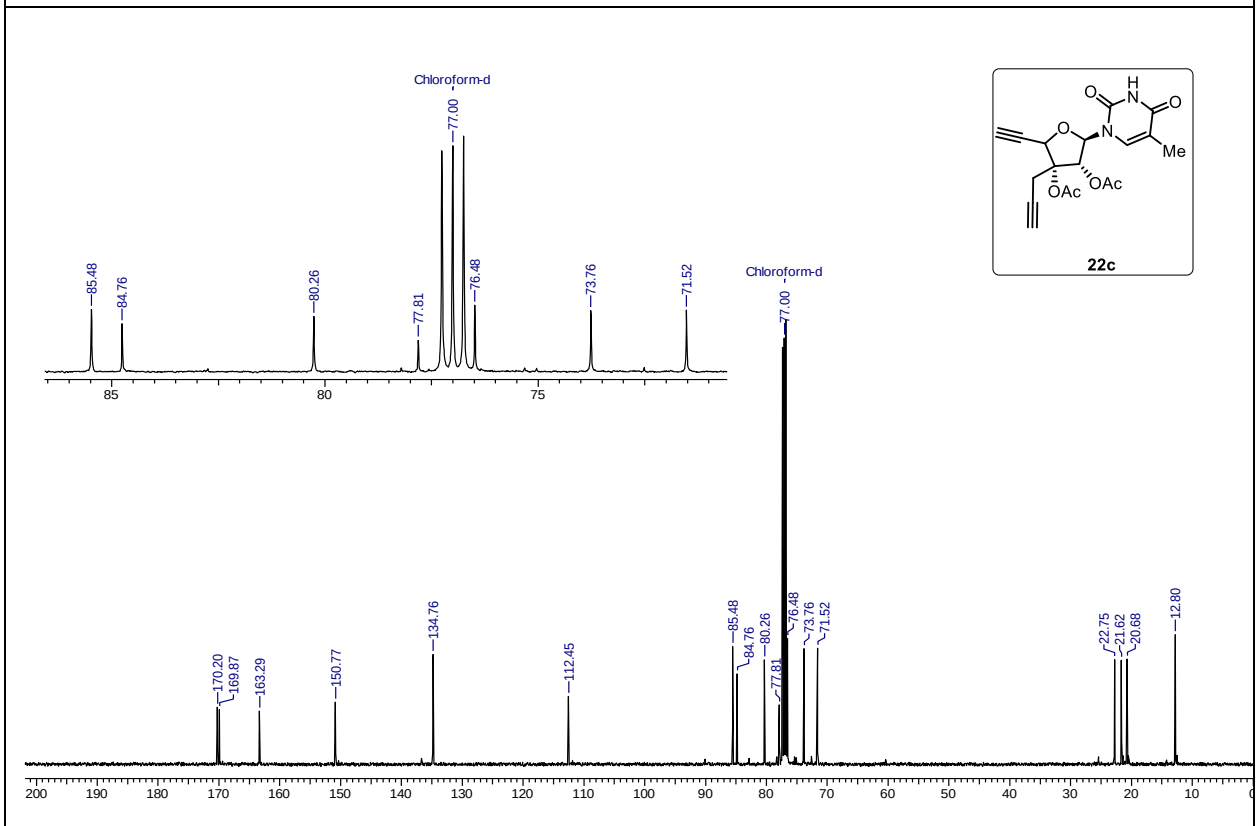

^{1}H /^{13}C NMR Spectrum of 22c in $CDCl_3$

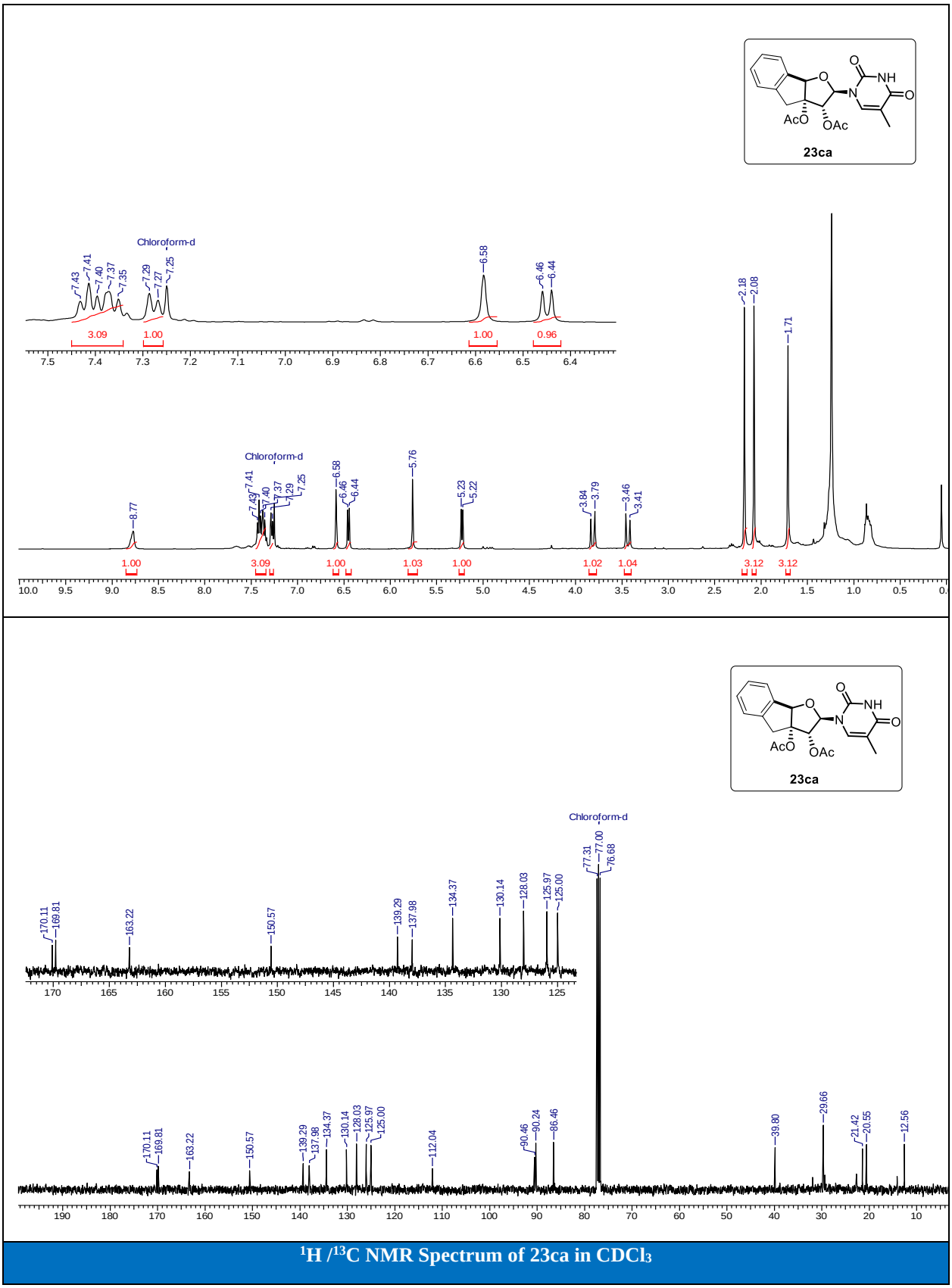

^{1}H /^{13}C NMR Spectrum of 23ca in $CDCl_3$

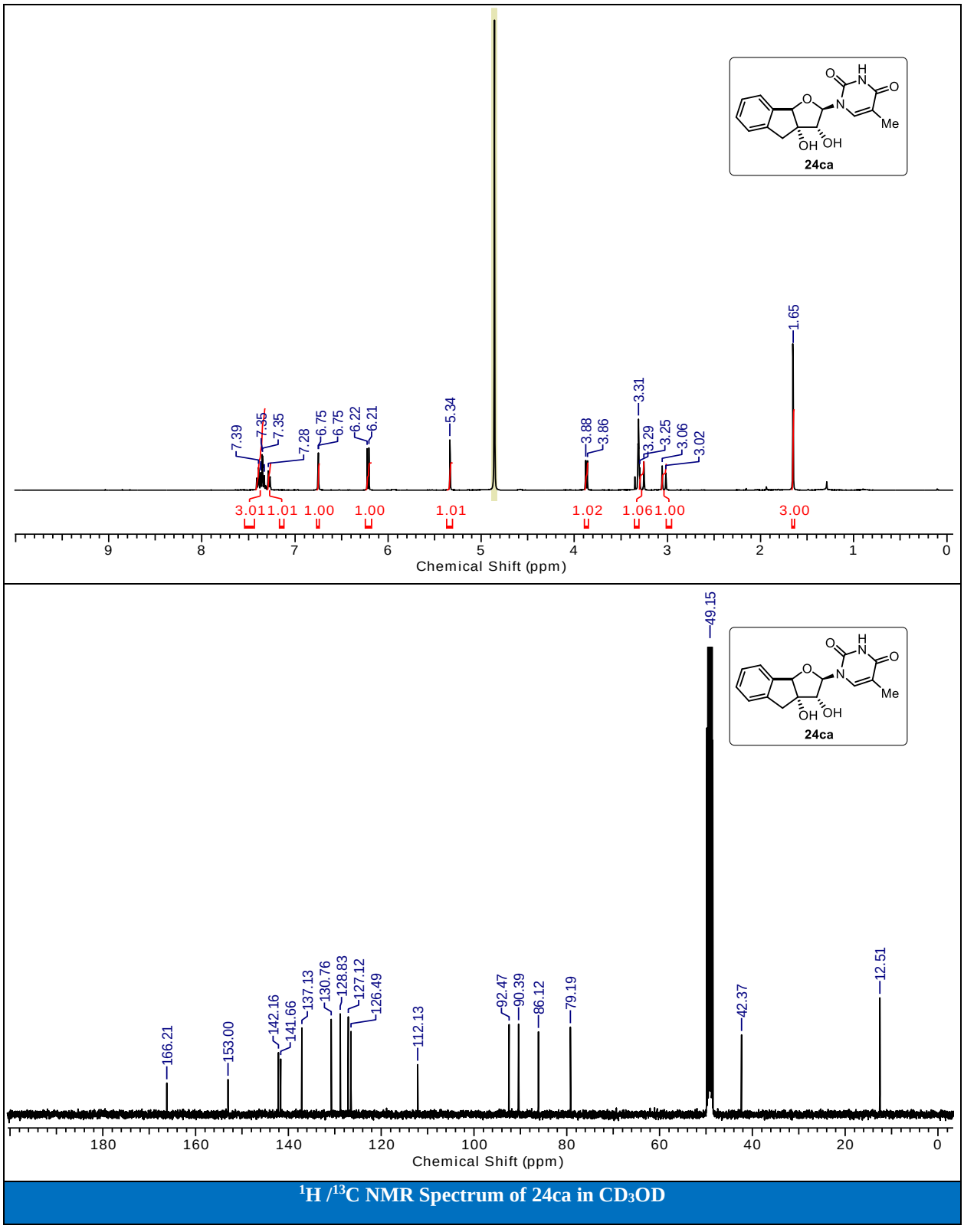

^{1}H /^{13}C NMR Spectrum of 24ca in CD_3OD

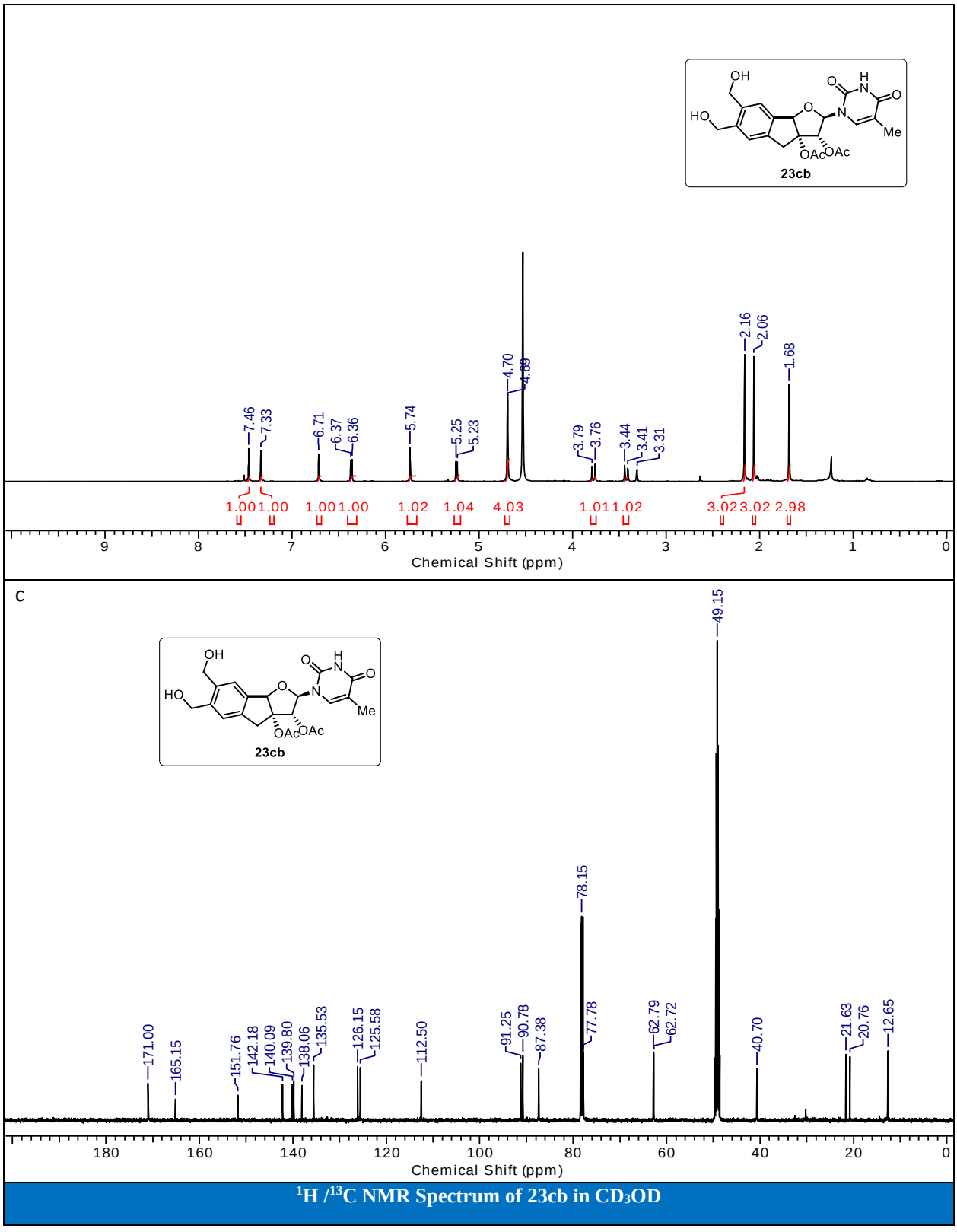

^{1}H /^{13}C NMR Spectrum of 23cb in CD_3OD

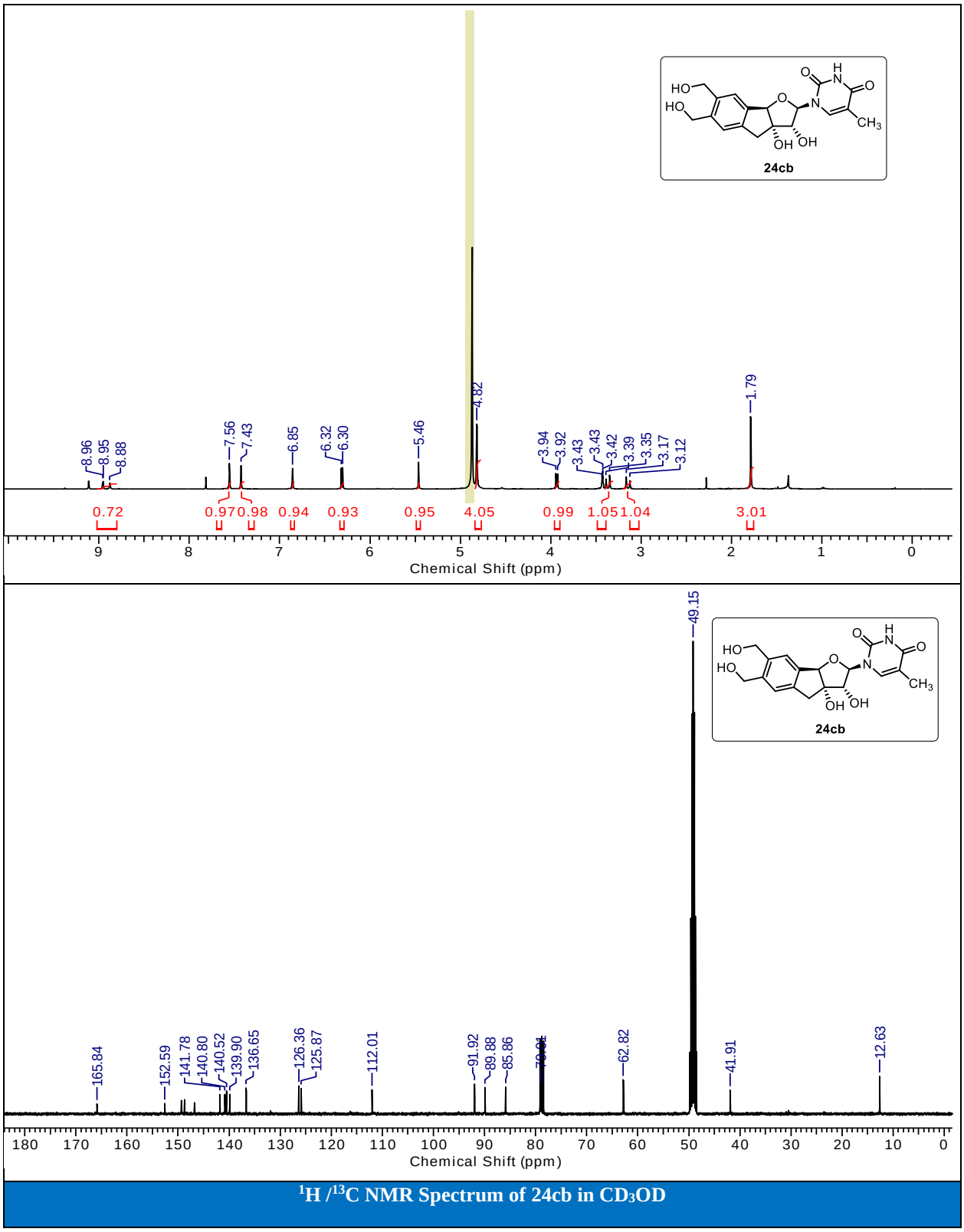

^{1}H /^{13}C NMR Spectrum of 24cb in CD_3OD

1) a) Sun, P.; Lu, X.; Xu, C.; Sun, W.; Pan, B. Understanding of COVID-19 Based on Current Evidence. *J. Med. Virol.* **2020**, *92* (6), 548–551. b) Wang, M.-Y.; Zhao, R.; Gao, L.-J.; Gao, X.-F.; Wang, D.-P.; Cao, J.-M. SARS-CoV-2: Structure, Biology, and Structure-Based Therapeutics Development. *Front. Cell. Infect. Microbiol.* **2020**, *10*, 587269. c) Platto, S.; Wang, Y.; Zhou, J.; Carafoli, E. History of the COVID-19 Pandemic: Origin, Explosion, Worldwide Spreading. *Biochem. Biophys. Res. Commun.* **2021**, *538*, 14–23. e) Liu, Y.-C.; Kuo, R.-L.; Shih, S.-R. COVID-19: The First Documented Coronavirus Pandemic in History. *Biomed. J.* **2020**, *43* (4), 328–333.

2) Hu, B.; Guo, H.; Zhou, P.; Shi, Z.-L. Characteristics of SARS-CoV-2 and COVID-19. *Nat. Rev. Microbiol.* **2021**, *19* (3), 141–154.

3) Gralinski, L.; Menachery, V. D. Return of the Cornavirus: 2019-nCoV. Viruses **2020**, *12*, 135.

4) a) Maurin, M.; Fenollar, F.; Mediannikov, O.; Davoust, B.; Devaux, C.; Raoult, D. Current Status of Putative Animal Sources of SARS-CoV-2 Infection in Humans: Wildlife, Domestic Animals and Pets. *Microorganisms* **2021**, *9* (4), 868. b) Zhang, C.; Zheng, W.; Huang, X.; Bell, E. W.; Zhou, X.; Zhang, Y. Protein Structure and Sequence Reanalysis of 2019-nCoV Genome Refutes Snakes as Its Intermediate Host and the Unique Similarity between Its Spike Protein Insertions and HIV-1. *J. Proteome. Res.* **2020**, *19* (4), 1351–1360.

5) a) Jones, K. E.; Patel, N. G.; Levy, M. A.; Storeygard, A.; Balk, D.; Gittleman, J. L.; Daszak, P. Global Trends in Emerging Infectious Diseases. *Nature* **2008**, *451* (7181), 990–993. b) Taylor, L. H.; Latham, S. M.; Woolhouse, M. E. J. Risk Factors for Human Disease Emergence. *Phil. Trans. R. Soc. Lond.* **2001**, *356*, 983–989.

6) Smith, I.; Wang, L.-F. Bats and Their Virome: An Important Source of Emerging Viruses Capable of Infecting Humans. *Curr. Opin. Virol.* **2013**, *3* (1), 84–91.

7) Guan, Y.; Zheng, B. J.; He, Y. Q.; Liu, X. L.; Zhuang, Z. X.; Cheung, C. L.; Luo, S. W.; Li, P. H.; Zhang, L. J.; Guan, Y. J.; Butt, K. M.; Wong, K. L.; Chan, K. W.; Lim, W.; Shortridge, K. F.; Yuen, K. Y.; Peiris, J. S. M.; Poon, L. L. M. Isolation

and Characterization of Viruses Related to the SARS Coronavirus from Animals in Southern China. *Science* **2003**, *302* (5643), 276–278.

8) INFECTION WITH SARS-COV-2 IN ANIMALS https://www.woah.org/fileadmin/Home/MM/EN_Factsheet_SARS-CoV-2.pdf.
9) Bai, L.; Wang, Y.; Wang, Y.; Wu, Y.; Li, N.; Liu, Z.; National Health Commission Key Laboratory of Food Safety Risk Assessment, Food Safety Research Unit (2019RU014) of Chinese Academy of Medical Science, China National Center for Food Safety Risk Assessment, Beijing, China. Controlling COVID-19 Transmission Due to Contaminated Imported Frozen Food and Food Packaging. *China CDC Weekly* **2021**, *3* (2), 30–33.
10) Pang, X.; Ren, L.; Wu, S.; Ma, W.; Yang, J.; Di, L.; Li, J.; Xiao, Y.; Kang, L.; Du, S.; Du, J.; Wang, J.; Li, G.; Zhai, S.; Chen, L.; Zhou, W.; Lai, S.; Gao, L.; Pan, Y.; Wang, Q.; Li, M.; Wang, J.; Huang, Y.; Wang, J.; COVID-19 Field Response Group; COVID-19 Laboratory Testing Group. Cold-Chain Food Contamination as the Possible Origin of COVID-19 Resurgence in Beijing. *Natl. Sci. Rev.* **2020**, *7* (12), 1861–1864.
11) Zhao, X.; Mao, L.; Zhang, J.; Zhang, Y.; Song, Y.; Bo, Z.; Wang, H.; Wang, J.; Chen, C.; Xiao, J.; Ji, T.; Yang, Q.; Xu, W.; Wang, D.; Yao, W.; National Institute for Viral Disease Control and Prevention, Chinese Center for Disease Control and Prevention, Beijing, China; Liaoning Province Center for Disease Control and Prevention, Shenyang, Liaoning, China; Dalian Municipal Center for Disease Control and Prevention, Dalian, Liaoning, China. Reemergent Cases of COVID-19 — Dalian City, Liaoning Province, China, July 22, 2020. *China CDC Weekly* **2020**, *2* (34), 658–660.
12) Yuan, Q.; Kou, Z.; Jiang, F.; Li, Z.; Zhang, L.; Liu, H.; Zhao, X.; Kang, D.; Gao, R.; Lei, J.; Shandong provincial Center for Disease Control and Prevention, Jinan, Shangdong, China; Qingdao prefecture Center for Disease Control and Prevention, Qingdao, Shangdong, China; Chinese Center for Disease Control and Prevention, Beijing, China; National Institute for Viral Disease Control and Prevention, China CDC, Beijing, China. A Nosocomial COVID-19 Outbreak

Initiated by an Infected Dockworker at Qingdao City Port — Shandong Province, China, October, 2020. *China CDC Weekly* **2020**, *2* (43), 838–840.

13) https://www.who.int/publications-detail-redirect/who-convened-global-study-of-origins-of-sars-cov-2-china-part

14) a) *Coronavirus Replication and Reverse Genetics*; Enjuanes, L., Ed.; Current topics in microbiology and immunology; Springer: Berlin ; New York, 2005. b) Li, F. Structure, Function, and Evolution of Coronavirus Spike Proteins. *Annu. Rev. Virol.* **2016**, *3* (1), 237–261. c) Huang, Y.; Yang, C.; Xu, X.; Xu, W.; Liu, S. Structural and Functional Properties of SARS-CoV-2 Spike Protein: Potential Antivirus Drug Development for COVID-19. *Acta Pharmacol Sin* **2020**, *41* (9), 1141–1149. d) Boopathi, S.; Poma, A. B.; Kolandaivel, P. Novel 2019 Coronavirus Structure, Mechanism of Action, Antiviral Drug Promises and Rule out against Its Treatment. *J. Biomol. Struct. Dyn.* **2020**, 1–10. e) Bergmann, C. C.; Silverman, R. H. COVID-19: Coronavirus Replication, Pathogenesis, and Therapeutic Strategies. *CCJM*. **2020**, *87* (6), 321–327.

15) Wang, S.; Zhang, Y.; Liu, S.; Peng, H.; Mackey, V.; Sun, L. Coronaviruses and the Associated Potential Therapeutics for the Viral Infections. **2020**, *8* (2). b) Nishiga, M.; Wang, D. W.; Han, Y.; Lewis, D. B.; Wu, J. C. COVID-19 and Cardiovascular Disease: From Basic Mechanisms to Clinical Perspectives. *Nat. Rev. Cardiol.* **2020**, *17* (9), 543–558.

16) Tang, T.; Bidon, M.; Jaimes, J. A.; Whittaker, G. R.; Daniel, S. Coronavirus Membrane Fusion Mechanism Offers a Potential Target for Antiviral Development. *Antivir. Res.* **2020**, *178*, 104792.

17) Wu, C.; Liu, Y.; Yang, Y.; Zhang, P.; Zhong, W.; Wang, Y.; Wang, Q.; Xu, Y.; Li, M.; Li, X.; Zheng, M.; Chen, L.; Li, H. Analysis of Therapeutic Targets for SARS-CoV-2 and Discovery of Potential Drugs by Computational Methods. *Acta Pharmaceutica Sinica B* **2020**, *10* (5), 766–788. b) Senger, M. R.; Evangelista, T. C. S.; Dantas, R. F.; Santana, M. V. D. S.; Gonçalves, L. C. S.; De Souza Neto, L. R.; Ferreira, S. B.; Silva-Junior, F. P. COVID-19: Molecular Targets, Drug Repurposing and New Avenues for Drug Discovery. *Mem. Inst. Oswaldo Cruz.* **2020**, *115*, e200254.

18) Cha, Y.; Erez, T.; Reynolds, I. J.; Kumar, D.; Ross, J.; Koytiger, G.; Kusko, R.; Zeskind, B.; Risso, S.; Kagan, E.; Papapetropoulos, S.; Grossman, I.; Laifenfeld, D. Drug Repurposing from the Perspective of Pharmaceutical Companies. *Br. J. Pharmacol.* **2018**, *175* (2), 168–180.

19) a) Pushpakom, S.; Iorio, F.; Eyers, P. A.; Escott, K. J.; Hopper, S.; Wells, A.; Doig, A.; Guilliams, T.; Latimer, J.; McNamee, C.; Norris, A.; Sanseau, P.; Cavalla, D.; Pirmohamed, M. Drug Repurposing: Progress, Challenges and Recommendations. *Nat. Rev. Drug Discov.* **2019**, *18* (1), 41–58. b) Senger, M. R.; Evangelista, T. C. S.; Dantas, R. F.; Santana, M. V. D. S.; Gonçalves, L. C. S.; De Souza Neto, L. R.; Ferreira, S. B.; Silva-Junior, F. P. COVID-19: Molecular Targets, Drug Repurposing and New Avenues for Drug Discovery. *Mem. Inst. Oswaldo Cruz*. **2020**, *115*, e200254. c) Krumm, Z. A.; Lloyd, G. M.; Francis, C. P.; Nasif, L. H.; Mitchell, D. A.; Golde, T. E.; Giasson, B. I.; Xia, Y. Precision Therapeutic Targets for COVID-19. *Virol. J.* **2021**, *18* (1), 66. d) Poduri, R.; Joshi, G.; Jagadeesh, G. Drugs Targeting Various Stages of the SARS-CoV-2 Life Cycle: Exploring Promising Drugs for the Treatment of Covid-19. *Cell. Signl.* **2020**, *74*, 109721.

20) Rambaut, A.; Holmes, E. C.; O'Toole, Á.; Hill, V.; McCrone, J. T.; Ruis, C.; Du Plessis, L.; Pybus, O. G. A Dynamic Nomenclature Proposal for SARS-CoV-2 Lineages to Assist Genomic Epidemiology. *Na.t Microbiol.* **2020**, *5* (11), 1403–1407.

21) Drożdżal, S.; Rosik, J.; Lechowicz, K.; Machaj, F.; Szostak, B.; Przybyciński, J.; Lorzadeh, S.; Kotfis, K.; Ghavami, S.; Łos, M. J. An Update on Drugs with Therapeutic Potential for SARS-CoV-2 (COVID-19) Treatment. *Drug Resist. Updat.* **2021**, *59*, 100794. b) Omolo, C. A.; Soni, N.; Fasiku, V. O.; Mackraj, I.; Govender, T. Update on Therapeutic Approaches and Emerging Therapies for SARS-CoV-2 Virus. *Eur. J. Pharmacol.* **2020**, *883*, 173348.

22) Ahmad, I.; Pawara, R.; Surana, S.; Patel, H. The Repurposed ACE2 Inhibitors: SARS-CoV-2 Entry Blockers of Covid-19. *Top Curr. Chem. (Z)* **2021**, *379* (6), 40.

23) a) Nukoolkarn, V.; Lee, V. S.; Malaisree, M.; Aruksakulwong, O.; Hannongbua, S. Molecular Dynamic Simulations Analysis of Ritronavir and Lopinavir as

SARS-CoV 3CLpro Inhibitors. *J. Theor. Biol.* **2008**, *254* (4), 861–867. b) He, J.; Hu, L.; Huang, X.; Wang, C.; Zhang, Z.; Wang, Y.; Zhang, D.; Ye, W. Potential of Coronavirus 3C-like Protease Inhibitors for the Development of New Anti-SARS-CoV-2 Drugs: Insights from Structures of Protease and Inhibitors. *Int. J. Antimicrob. Agents* **2020**, *56* (2), 106055. c) Bryant, A.; Lawrie, T. A.; Dowswell, T.; Fordham, E. J.; Mitchell, S.; Hill, S. R.; Tham, T. C. Ivermectin for Prevention and Treatment of COVID-19 Infection: A Systematic Review, Meta-Analysis, and Trial Sequential Analysis to Inform Clinical Guidelines. *Am. J. Ther.* **2021**.

24) Sohag, A. A. M.; Hannan, M. A.; Rahman, S.; Hossain, M.; Hasan, M.; Khan, M. K.; Khatun, A.; Dash, R.; Uddin, M. J. Revisiting Potential Druggable Targets against SARS-CoV -2 and Repurposing Therapeutics under Preclinical Study and Clinical Trials: A Comprehensive Review. *Drug Dev. Res.* **2020**, *81* (8), 919–941.

25) Shadrick, W. R.; Ndjomou, J.; Kolli, R.; Mukherjee, S.; Hanson, A. M.; Frick, D. N. Discovering New Medicines Targeting Helicases: Challenges and Recent Progress. *SLAS Discovery* **2013**, *18* (7), 761–781.

26) Singh, L.; Bajaj, S.; Gadewar, M.; Verma, N.; Ansari, M. N.; Saeedan, A. S.; Kaithwas, G.; Singh, M. Modulation of Host Immune Response Is an Alternative Strategy to Combat SARS-CoV-2 Pathogenesis. *Front. Immunol.* **2021**, *12*, 660632.

27) Gilzad-Kohan, H.; Jamali, F. Anti-Inflammatory Properties of Drugs Used to Control COVID-19 and Their Effects on the Renin-Angiotensin System and Angiotensin-Converting Enzyme-2. *J. Pharm. Pharm. Sci.* **2020**, *23*, 259–277. b) Kushner, P.; McCarberg, B. H.; Grange, L.; Kolosov, A.; Haveric, A. L.; Zucal, V.; Petruschke, R.; Bissonnette, S. The Use of Non-Steroidal Anti-Inflammatory Drugs (NSAIDs) in COVID-19. *npj Prim. Care Respir. Med.* **2022**, *32* (1), 35.

28) Shapira, T.; Monreal, I. A.; Dion, S. P.; Buchholz, D. W.; Imbiakha, B.; Olmstead, A. D.; Jager, M.; Désilets, A.; Gao, G.; Martins, M.; Vandal, T.; Thompson, C. A. H.; Chin, A.; Rees, W. D.; Steiner, T.; Nabi, I. R.; Marsault, E.; Sahler, J.; Diel, D. G.; Van De Walle, G. R.; August, A.; Whittaker, G. R.; Boudreault, P.-L.; Leduc, R.; Aguilar, H. C.; Jean, F. A TMPRSS2 Inhibitor Acts as a Pan-SARS-CoV-2 Prophylactic and Therapeutic. *Nature* **2022**, *605* (7909), 340–348. b) Hu, X.;

Shrimp, J. H.; Guo, H.; Xu, M.; Chen, C. Z.; Zhu, W.; Zakharov, A. V.; Jain, S.; Shinn, P.; Simeonov, A.; Hall, M. D.; Shen, M. Discovery of TMPRSS2 Inhibitors from Virtual Screening as a Potential Treatment of COVID-19. *ACS Pharmacol. Transl. Sci.* **2021**, *4* (3), 1124–1135.

29) Báez-Santos, Y. M.; St. John, S. E.; Mesecar, A. D. The SARS-Coronavirus Papain-like Protease: Structure, Function and Inhibition by Designed Antiviral Compounds. *Antivir. Res.* **2015**, *115*, 21–38. b) Jiang, H.; Yang, P.; Zhang, J. Potential Inhibitors Targeting Papain-Like Protease of SARS-CoV-2: Two Birds With One Stone. *Front. Chem.* **2022**, *10*, 822785. c) Osipiuk, J.; Azizi, S.-A.; Dvorkin, S.; Endres, M.; Jedrzejczak, R.; Jones, K. A.; Kang, S.; Kathayat, R. S.; Kim, Y.; Lisnyak, V. G.; Maki, S. L.; Nicolaescu, V.; Taylor, C. A.; Tesar, C.; Zhang, Y.-A.; Zhou, Z.; Randall, G.; Michalska, K.; Snyder, S. A.; Dickinson, B. C.; Joachimiak, A. Structure of Papain-like Protease from SARS-CoV-2 and Its Complexes with Non-Covalent Inhibitors. *Nat. Commun.* **2021**, *12* (1), 743.

30) Al-kuraishy, H. M.; Al-Gareeb, A. I.; Elekhnawy, E.; Batiha, G. E.-S. Nitazoxanide and COVID-19: A Review. *Mol. Biol. Rep.* **2022**, *49* (11), 11169–11176.

31) Liu, X.-H.; Cheng, T.; Liu, B.-Y.; Chi, J.; Shu, T.; Wang, T. Structures of the SARS-CoV-2 Spike Glycoprotein and Applications for Novel Drug Development. *Front. Pharmacol.* **2022**, *13*, 955648.

32) a) Visos-Varela, I.; Zapata-Cachafeiro, M.; Piñeiro-Lamas, M.; Carracedo-Martínez, E.; Saez, M.; Herdeiro, M. T.; Figueiras, A.; Salgado-Barreira, Á. Repurposing Selective Serotonin Reuptake Inhibitors for Severity of COVID-19: A Population-Based Study. *Eur. Neuropsychopharmacol.* **2023**, *71*, 96–108. b) Deng, J.; Rayner, D.; Ramaraju, H. B.; Abbas, U.; Garcia, C.; Heybati, K.; Zhou, F.; Huang, E.; Park, Y.-J.; Moskalyk, M. Efficacy and Safety of Selective Serotonin Reuptake Inhibitors in COVID-19 Management: A Systematic Review and Meta-Analysis. *Clin. Microbiol. Infect.* **2023**, *29* (5), 578–586.

33) De Coen, L. M.; Heugebaert, T. S. A.; García, D.; Stevens, C. V. Synthetic Entries to and Biological Activity of Pyrrolopyrimidines. *Chem. Rev.* **2016**, *116* (1), 80–139.

34) a) Musumeci, F.; Sanna, M.; Grossi, G.; Brullo, C.; Fallacara, A. L.; Schenone, S. Pyrrolo[2,3-d]Pyrimidines as Kinase Inhibitors. *CMC* **2017**, *24* (19). b) Thapa, K.; Verma, N.; Singh, T. G.; Kaur Grewal, A.; Kanojia, N.; Rani, L. COVID-19-Associated Acute Respiratory Distress Syndrome (CARDS): Mechanistic Insights on Therapeutic Intervention and Emerging Trends. *Int. Immunopharmacol.* **2021**, *101*, 108328.

35) a) Erickson, S.; Heul, A. V.; Kim, B. S. New and Emerging Treatments for Inflammatory Itch. *Ann. Allergy Asthma Immunol.* **2021**, *126* (1), 13–20. b) Gonzales, A. J.; Bowman, J. W.; Fici, G. J.; Zhang, M.; Mann, D. W.; Mitton-Fry, M. Oclacitinib (APOQUEL ®) Is a Novel Janus Kinase Inhibitor with Activity against Cytokines Involved in Allergy. *Vet. Pharmacol. Ther.* **2014**, *37* (4), 317–324.

36) Dhillon, S. Tofacitinib: A Review in Rheumatoid Arthritis. *Drugs* **2017**, *77* (18), 1987–2001.

37) Wade, R.; Hodgson, R.; Biswas, M.; Harden, M.; Woolacott, N. A Review of Ruxolitinib for the Treatment of Myelofibrosis: A Critique of the Evidence. *PharmacoEconomics* **2017**, *35* (2), 203–213.

38) a) Zhang, Y.; Zheng, Y.; Faheem, A.; Sun, T.; Li, C.; Li, Z.; Zhao, D.; Wu, C.; Liu, J. A Novel AKT Inhibitor, AZD5363, Inhibits Phosphorylation of AKT Downstream Molecules, and Activates Phosphorylation of mTOR and SMG-1 Dependent on the Liver Cancer Cell Type. *Oncol. Lett.* **2016**, *11* (3), 1685–1692. b) Zhu, K.; Liu, X.; Liu, C.; Xu, Y.; Fu, Y.; Dong, W.; Yan, Y.; Wang, W.; Qian, C. AKT Inhibitor AZD5363 Suppresses Stemness and Promotes Anti-Cancer Activity of 3,3′-Diindolylmethane in Human Breast Cancer Cells. *Toxicol. Appl. Pharmacol.* **2021**, *429*, 115700. Mogul, A.; Corsi, K.; McAuliffe, L. Baricitinib: The Second FDA-Approved JAK Inhibitor for the Treatment of Rheumatoid Arthritis. *Ann. Pharmacother.* **2019**, *53* (9), 947–953.

39) Mogul, A.; Corsi, K.; McAuliffe, L. Baricitinib: The Second FDA-Approved JAK Inhibitor for the Treatment of Rheumatoid Arthritis. *Ann. Pharmacother.* **2019**, *53* (9), 947–953.

40) a) Jacobson, J. G.; Renau, T. E.; Nassiri, M. R.; Sweier, D. G.; Breitenbach, J. M.; Townsend, L. B.; Drach, J. C. Nonnucleoside Pyrrolopyrimidines with a Unique Mechanism of Action against Human Cytomegalovirus. *Antimicrob. Agents Chemother.* **1999**, *43* (8), 1888–1894. b) Gupta, P. K.; Nassiri, M. R.; Coleman, L. A.; Wotring, L. L.; Drach, J. C.; Townsend, L. B. Synthesis, Cytotoxicity, and Antiviral Activity of Certain 7-[(2-Hydroxyethoxy)Methyl]Pyrrolo[2,3-d]Pyrimidine Nucleosides Related to Toyocamycin and Sangivamycin. *J. Med. Chem.* **1989**, *32* (7), 1420–1425.

41) O'Brien, J. J.; Campoli-Richards, D. M. Acyclovir: An Updated Review of Its Antiviral Activity, Pharmacokinetic Properties and Therapeutic Efficacy. *Drugs* **1989**, *37* (3), 233–309.

42) Clercq, E. D.; Holy, A. Antiviral Activity of Aliphatic Nucleoside Analogues: Structure-Function Relationship. *J. Med. Chem*. **1979**, *22* (5), 510–513.

43) Pruijssers, A. J.; Denison, M. R. Nucleoside Analogues for the Treatment of Coronavirus Infections. *Curr. Opin. Virol.* **2019**, *35*, 57–62.

44) a) Brown, A. J.; Won, J. J.; Graham, R. L.; Dinnon, K. H.; Sims, A. C.; Feng, J. Y.; Cihlar, T.; Denison, M. R.; Baric, R. S.; Sheahan, T. P. Broad Spectrum Antiviral Remdesivir Inhibits Human Endemic and Zoonotic Deltacoronaviruses with a Highly Divergent RNA Dependent RNA Polymerase. *Antivir. Res.* **2019**, *169*, 104541. b) Vangeel, L.; Chiu, W.; De Jonghe, S.; Maes, P.; Slechten, B.; Raymenants, J.; André, E.; Leyssen, P.; Neyts, J.; Jochmans, D. Remdesivir, Molnupiravir and Nirmatrelvir Remain Active against SARS-CoV-2 Omicron and Other Variants of Concern. *Antivir. Res.* **2022**, *198*, 105252.

45) Khalili, J. S.; Zhu, H.; Mak, N. S. A.; Yan, Y.; Zhu, Y. Novel Coronavirus Treatment with Ribavirin: Groundwork for an Evaluation Concerning COVID-19. *J. Med. Virol.* **2020**, *92* (7), 740–746.

46) Sheahan, T. P.; Sims, A. C.; Zhou, S.; Graham, R. L.; Pruijssers, A. J.; Agostini, M. L.; Leist, S. R.; Schäfer, A.; Dinnon, K. H.; Stevens, L. J.; Chappell, J. D.; Lu, X.; Hughes, T. M.; George, A. S.; Hill, C. S.; Montgomery, S. A.; Brown, A. J.; Bluemling, G. R.; Natchus, M. G.; Saindane, M.; Kolykhalov, A. A.; Painter, G.; Harcourt, J.; Tamin, A.; Thornburg, N. J.; Swanstrom, R.; Denison, M. R.; Baric,

R. S. An Orally Bioavailable Broad-Spectrum Antiviral Inhibits SARS-CoV-2 in Human Airway Epithelial Cell Cultures and Multiple Coronaviruses in Mice. *Sci. Transl. Med.* **2020**, *12* (541), eabb5883.

47) Ami, E.; Ohrui, H. Intriguing Antiviral Modified Nucleosides: A Retrospective View into the Future Treatment of COVID-19. *ACS Med. Chem. Lett.* **2021**, *12* (4), 510–517.

48) a) Prandi, C.; Kapulnik, Y.; Koltai, H. Strigolactones: Phytohormones with Promising Biomedical Applications. *Eur. J. Org. Chem.* **2021**, *2021* (29), 4019–4026. b) Kuriyama, A.; Honda, M.; Hayashino, Y. Ramelteon for the Treatment of Insomnia in Adults: A Systematic Review and Meta-Analysis. *Sleep Med.* **2014**, *15* (4), 385–392. c) Obafemi, C. A.; Adelani, P. O.; Fadare, O. A.; Akinpelu, D. A.; Famuyiwa, S. O. Synthesis, Crystal Structure and in Vitro Antibacterial Activity of 2,3a,8b-Trihydroxy-3-(Thiophen-2-Ylcarbonyl)-2-(Trifluoromethyl)-2,3,3a,8b-Tetrahydro-4H-Indeno[1,2-b]Furan-4-One. *J. Mol. Struct.* **2013**, *1049*, 429–435.

49) a) Serpi, M.; Ferrari, V.; Pertusati, F. Nucleoside Derived Antibiotics to Fight Microbial Drug Resistance: New Utilities for an Established Class of Drugs? *J. Med. Chem.* **2016**, *59* (23), 10343–10382. b) Winn, M.; Goss, R. J. M.; Kimura, K.; Bugg, T. D. H. Antimicrobial Nucleoside Antibiotics Targeting Cell Wall Assembly: Recent Advances in Structure–Function Studies and Nucleoside Biosynthesis. *Nat. Prod. Rep.* **2010**, *27* (2), 279–304. c) Shelton, J.; Lu, X.; Hollenbaugh, J. A.; Cho, J. H.; Amblard, F.; Schinazi, R. F. Metabolism, Biochemical Actions, and Chemical Synthesis of Anticancer Nucleosides, Nucleotides, and Base Analogs. *Chem. Rev.* **2016**, *116* (23), 14379–14455. d) Nizhenkovska, I.; Gorchakova, N.; Zaychenko, G.; Narokha, V. Uracil as the Basis for Medication Creation. *Curr. Top. Pharmacol.* **2018**, *22*, 19–26. e) Messina, V.; Nevola, R.; Izzi, A.; De Lucia Sposito, P.; Marrone, A.; Rega, R.; Fusco, R.; Lumino, P.; Rinaldi, L.; Gaglione, P.; Simeone, F.; Sasso, F. C.; Maggi, P.; Adinolfi, L. E. Efficacy and Safety of the Sofosbuvir/Velpatasvir Combination for the Treatment of Patients with Early Mild to Moderate COVID-19. *Sci. Rep.* **2022**, *12* (1), 5771.

50) a) Messina, V.; Nevola, R.; Izzi, A.; De Lucia Sposito, P.; Marrone, A.; Rega, R.; Fusco, R.; Lumino, P.; Rinaldi, L.; Gaglione, P.; Simeone, F.; Sasso, F. C.; Maggi, P.; Adinolfi, L. E. Efficacy and Safety of the Sofosbuvir/Velpatasvir Combination for the Treatment of Patients with Early Mild to Moderate COVID-19. *Sci. Rep.* **2022**, *12* (1), 5771. b) Bozzi, A.; D'Andrea, G.; Brisdelli, F. AZT: An Old Drug with New Perspectives. *CCP* **2008**, *3* (1), 20–37. c) Cragg, G. M.; Newman, D. J. Natural Product Sources of Drugs: Plants, Microbes, Marine Organisms, and Animals. In *Comprehensive Medicinal Chemistry II*; Elsevier, 2007; pp 355–403.

51) Zhang, N.; Yin, Y.; Xu, S.-J.; Chen, W.-S. 5-Fluorouracil: Mechanisms of Resistance and Reversal Strategies. *Molecules* **2008**, *13* (8), 1551–1569.

52) Ramana, C. V.; Dushing, M. P.; Mohapatra, S.; Mallik, R.; Gonnade, R. G. Target Cum Flexibility: An Alkyne [2+2+2]-Cyclotrimerization Strategy for Synthesis of Trinem Library. *Tetrahedron Lett.* **2011**, *52* (1), 38–41.

53) Suryawanshi, S. B.; Dushing, M. P.; Gonnade, R. G.; Ramana, C. V. The Isochroman- and 1,3-Dihydroisobenzofuran-Annulation on Carbohydrate Templates via [2+2+2]-Cyclotrimerization and Synthesis of Some Tricyclic Nucleosides. *Tetrahedron* **2010**, *66* (32), 6085–6096.

54) a) Hassan Hilmy, K. M.; Khalifa, M. M. A.; Allah Hawata, M. A.; AboAlzeen Keshk, R. M.; El-Torgman, A. A. Synthesis of New Pyrrolo[2,3-d]Pyrimidine Derivatives as Antibacterial and Antifungal Agents. *Eur. J. Med. Chem.* **2010**, *45* (11), 5243–5250. b) Vazirimehr, S.; Davoodnia, A.; Beyramabadi, S. A.; Nakhaei-Moghaddam, M.; Tavakoli-Hoseini, N. Two New Pyrrolo[2,3- *d*]Pyrimidines (7-Deazapurines): Ultrasonic-Assisted Synthesis, Experimental and Theoretical Characterizations as Well as Antibacterial Evaluation. *Zeitschrift für Naturforschung B* **2017**, *72* (7), 481–487. c) Khoje, A. D.; Kulendrn, A.; Charnock, C.; Wan, B.; Franzblau, S.; Gundersen, L.-L. Synthesis of Non-Purine Analogs of 6-Aryl-9-Benzylpurines, and Their Antimycobacterial Activities. Compounds Modified in the Imidazole Ring. *Bioorg. Med. Chem.* **2010**, *18* (20), 7274–7282.

55) Bartoli, A.; Gabrielli, F.; Alicandro, T.; Nascimbeni, F.; Andreone, P. COVID-19 Treatment Options: A Difficult Journey between Failed Attempts and Experimental Drugs. *Intern. Emerg. Med.* **2021**, *16* (2), 281–308.

56) Chevallier, O. P.; Migaud, M. E. Investigation of Acetyl Migrations in Furanosides. *Beilstein J. Org. Chem.* **2006**, *2*. b) Dushing, M. P.; Ramana, C. V. Target Cum Flexibility: Synthesis of C(3′)-Spiroannulated Nucleosides. *Tetrahedron Lett.* **2011**, *52* (36), 4627–4630.

57) a) Ramana, C. V.; Induvadana, B.; Srinivas, B.; Yadagiri, K.; Deshmukh, M. N.; Gonnade, R. G. The Influence of Electronic Factors on Pd-Mediated Cycloisomerization: A Systematic Investigation of Competitive 6-Exo-Dig versus 7-Endo-Dig Cyclizations of Sugar Alkynols. *Tetrahedron* **2009**, *65* (47), 9819–9832. b) Suryawanshi, S. B.; Dushing, M. P.; Gonnade, R. G.; Ramana, C. V. The Isochroman- and 1,3-Dihydroisobenzofuran-Annulation on Carbohydrate Templates via [2+2+2]-Cyclotrimerization and Synthesis of Some Tricyclic Nucleosides. *Tetrahedron* **2010**, *66* (32), 6085–6096.

58) a) Wen, C.-C.; Kuo, Y.-H.; Jan, J.-T.; Liang, P.-H.; Wang, S.-Y.; Liu, H.-G.; Lee, C.-K.; Chang, S.-T.; Kuo, C.-J.; Lee, S.-S.; Hou, C.-C.; Hsiao, P.-W.; Chien, S.-C.; Shyur, L.-F.; Yang, N.-S. Specific Plant Terpenoids and Lignoids Possess Potent Antiviral Activities against Severe Acute Respiratory Syndrome Coronavirus. *J. Med. Chem.* **2007**, *50* (17), 4087–4095. b) Wang, M.; Cao, R.; Zhang, L.; Yang, X.; Liu, J.; Xu, M.; Shi, Z.; Hu, Z.; Zhong, W.; Xiao, G. Remdesivir and Chloroquine Effectively Inhibit the Recently Emerged Novel Coronavirus (2019-nCoV) in Vitro. *Cell Res.* **2020**, *30* (3), 269–271.

Abstract

Name of the Student: Shaziyaparveen Khairunnasar Siddiqui. **Registration No. :** 10CC17A26009
Faculty of Study: Chemical Science **Year of Submission:** 2024

AcSIR academic centre/CSIR Lab: National Chemical Laboratory (NCL), Pune

Name of the Supervisor(s): Dr.C.V.Ramana

Title of the thesis: "The Development of Small Molecule Autophagy Inducers in Cervical Cancer Cells and Antiviral Modified Nucleosides Against COVID-19."

Cervical cancer is a leading cause of cancer-related deaths in women and is one of the global health concerns. Amongst the various cellular processes of the cervical cancer cells, the autophagy has been shown to play a crucial role in cervical cancer cell survival and resistance to therapy. Thus, in this context, we document the design and development of 3-(benzofuran-2-ylmethyl)-1*H*-indole derivatives as potential autophagy inducers in cervical cancer cells. The design of targeted compounds was based on the natural products having bisindolylmethane and benzofuran scaffolds with diverse biological activities. A focused small molecule library designed around this scaffold has been synthesized and screening against various cancer cells led to the identification of **2** synthesized molecules with a promising inhibition against the Siha cell line.

In the initial phases of COVID-19 pandemic, lot of efforts have been focused on the development or the deployment of new and known nucleoside based small molecules for identifying potential small molecules to target SARS-CoV-2. Remdesivir, a nucleoside analogue, is one of the first drugs to be approved for the treatment of COVID-19 patients in some countries, but its efficacy and side effects warrant further investigation. Thus, the development of novel nucleoside analogues tailored specifically to target SARS-CoV-2 presents a significant opportunity to enhance antiviral therapy for COVID-19 and this constitutes as the second objective of this thesis. In the context of Covid-19, we have come up with two different scaffolds. The first series is funded upon integrating structural feature of the acyclovir and JAK-2 kinase inhibitors Ruxolitinib and Baricitinib. As this series was found to be not promising in terms of the anti-viral activity against SARS-CoV-2, we have come up with a new design and strategy that provided a rapid access to the sugar-modified tricyclic nucleoside derivatives in which, cyclotrimerization was employed as a key reaction.

5. Publications:

List of Publications Emanating from the Thesis Work

1. Siddiqui, S. K.; Ramana, C. V.; Gonnade, R. G. Crystal structure of 1-(4-bromophenyl)but-3-yn-1-one. *Acta Crystallogr. E.* **2023**; 79(7):633-636.
2. Siddiqui, S. K.; SahayaSheela, V. J.; Kolluru, S.; Pandian, G. N.; Santhoshkumar, T. R.; Dan, V. M.; Ramana, C. V. Discovery of 3-(Benzofuran-2-Ylmethyl)-1H-Indole Derivatives as Potential Autophagy Inducers in Cervical Cancer Cells. *Bioorg. Med. Chem. Lett.* **2020**, *30* (19), 127431.
3. Design and Synthesis of Indene Fused Sugar Nucleosides as Potential Antiviral Agents for Covid-19 (Manuscript under preparation).
4. Synthesis and Antiviral Activity of 7-[(2-Hydroxyethoxy)Methyl]Pyrrolo[2,3-d]Pyrimidine Nucleoside Derivatives (Manuscript under preparation).

List of Publications Non-Emanating from the Thesis Work

5. Srinivas, K.; Siddiqui, S. K.; Mudaliar, J. K.; Ramana, C. V. Ru(II)-Catalyzed C–H Activation/Alkylation of 3-Formylbenzofurans with Conjugated Olefins: Product Divergence. *J. Org. Chem.* **2019**, *84* (9), 5056–5066.

6. Poster prenentation:

National Science Day at CSIR-NCL, Feb-2019

Name:- "Design and Synthesis of Indene Fused Sugar Nucleosides as Potential Antiviral Agents for Covid-19."

Acta Cryst E CRYSTALLOGRAPHIC COMMUNICATIONS

ISSN 2056-9890

Crystal structure of 1-(4-bromophenyl)but-3-yn-1-one

Shaziyaparveen K. Siddiqui,[a,b] C. V. Ramana[a,b] and Rajesh G. Gonnade[c,b]*

[a]Division of Organic Synthesis, CSIR-National Chemical Laboratory, Dr. Homi, Bhabha Road, Pashan, Pune-411008, India, [b]Academy of Scientific and Innovative Research (AcSIR), Sector 19, Kamla Nehru Nagar, Ghaziabad, Uttar Pradesh 201002, India, and [c]Physical & Materials Chemistry Division, CSIR-National Chemical Laboratory, Dr. Homi Bhabha Road, Pune-411008, India. *Correspondence e-mail: rg.gonnade@ncl.res.in

Received 12 May 2023
Accepted 7 June 2023

Edited by D. Chopra, Indian Institute of Science Education and Research Bhopal, India

Keywords: crystal structure; intermolecular interactions; Hirshfeld surface analysis.

CCDC reference: 2268276

Supporting information: this article has supporting information at journals.iucr.org/e

The title compound, 1-(4-bromophenyl)but-3-yn-1-one, $C_{10}H_7BrO$, crystallizes in the monoclinic space group $P2_1/n$ with one molecule in the asymmetric unit. The structure displays a planar geometry. The crystal structure is consolidated by C—H···O hydrogen bonding and a short C═O···C≡C (acetylene) contacts. Hirshfeld surface analysis indicates that H···H, C···H/H···C and H···Br/Br···H interactions play a more important role in consolidating the crystal structure compared to H···O/O···H and C···C contacts.

1. Chemical context

The title compound 1-(4-bromophenyl)but-3-yn-1-one (**1**) was obtained as a side product during the synthesis of 5-(4-bromophenyl)isoxazole-3-carboxylic acid (**2**) from the NaOH-mediated hydrolysis of ethyl 5-(4-bromophenyl)isoxazole-3-carboxylate (**3**). These arylisoxazole carboxylic acids have been identified as potential isosteres of aryl diketo acid in the design of novel HIV-1 integrase inhibitors (Zeng *et al.*, 2008). The presence of three distinct functional groups, viz. alkyne, bromo, and carbonyl, offers an intriguing opportunity to explore how intermolecular interactions contribute to the cohesion of the crystal structure.

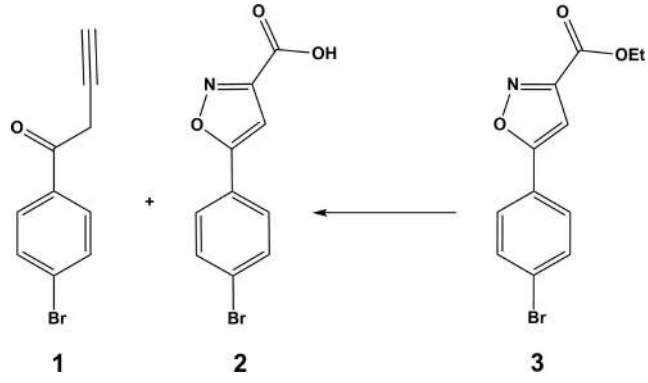

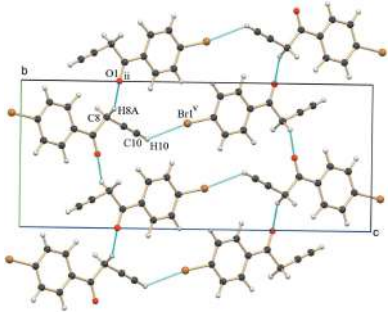

2. Structural commentary

The title compound crystallizes in the monoclinic $P2_1/n$ centrosymmetric space group with one molecule of **1** in the asymmetric unit (Fig. 1). The structure displays a planar geometry [torsion angle C5—C1—C8—C9 = 175.4 (3)°, only the C5 atom of phenyl ring is considered and not the full fragment]. The phenyl ring makes a dihedral angle of 5.4 (2)°

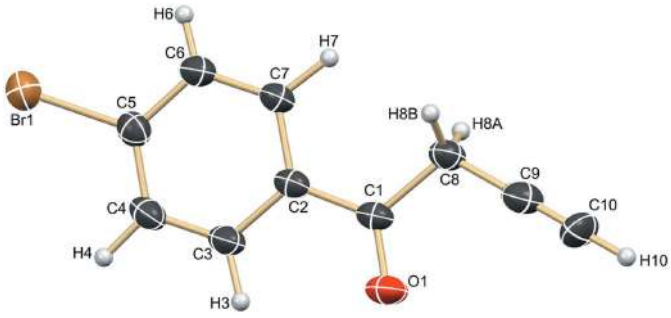

Figure 1
The asymmetric unit of **1** with the atom labelling. Displacement ellipsoids represent 30% probability levels.

with the least-squares plane through the O1/C1/C8–C10 fragment.

3. Supramolecular features

In the crystal, the closely associated molecules of **1** generate two different helical assemblies across the crystallographic 2_1-screw axis (*b*-axis). The helical assembly generated using C1═O1···C9^{i}≡C10^{i} (acetylene, C=O···π) contacts [symmetry code: (i) $-x+\frac{1}{2}, y+\frac{1}{2}, -z+\frac{3}{2}$] (Li *et al.*, 2019; Mooibroek, *et al.*, 2008) has a sheet structure (Fig. 2, Table 1), while the helical assembly created using C—H···O (C8—H8*A*···O1^{ii}) contacts [symmetry code: (ii) $-x+\frac{3}{2}, y-\frac{1}{2}, -z+\frac{3}{2}$] (Desiraju & Steiner, 2001) has a proper helical structure (Fig. 3, Table 1). The helical assembly created using the short C1═O1···C9≡C10 contacts is further supported by marginal C—H···π [symmetry code: (iii) $-x+\frac{1}{2}, y-\frac{1}{2}, -z+\frac{3}{2}$] contacts involving the phenyl ring (C7—H7) and the π cloud of the acetylene moiety. Both helices are intertwined and form a two-dimensional sheet structure roughly along the *a*-axis direction. Along the longer *c*-axis, molecules are loosely connected using weak C—H···Br (C10—H10···Br1^{iv} contacts [symmetry code: (iv) $x-\frac{3}{2}, -y+\frac{1}{2}, z-\frac{1}{2}$] (van den Berg & Seddon, 2003), generating the extended assembly (Figs. 2 and 3, Table 1).

Table 1
Hydrogen-bond geometry (Å, °).

D—H···*A*	*D*—H	H···*A*	*D*···*A*	*D*—H···*A*
C1—O1···C9^{i}		3.13 (1)		154 (1)
C8—H8*A*···O1^{ii}	1.02 (4)	2.31 (4)	3.259 (5)	156 (3)
C7—H7···C10^{iii}	1.06 (3)	2.71 (4)	3.626 (5)	144 (3)
C10—H10···Br1^{iv}	0.93	2.68	3.305 (5)	126

Symmetry codes: (i) $-x+\frac{1}{2}, y+\frac{1}{2}, -z+\frac{3}{2}$; (ii) $-x+\frac{3}{2}, y-\frac{1}{2}, -z+\frac{3}{2}$; (iii) $-x+\frac{1}{2}, y-\frac{1}{2}, -z+\frac{3}{2}$; (iv) $x-\frac{3}{2}, -y+\frac{1}{2}, z-\frac{1}{2}$.

In order to visualize and quantify intermolecular interactions in **1**, a Hirshfeld surface analysis (Spackman & Jayatilaka, 2009) was performed using *Crystal Explorer 21.5* (Spackman *et al.*, 2021), and the associated two-dimensional fingerprint plots (McKinnon *et al.*, 2007) were generated. The Hirshfeld surfaces for the molecule in **1** are shown in Fig. 4 in which the two-dimensional fingerprint plots of the most dominant contacts are also presented. H···H (27.4%), H···C/C···H (22.3%) and H···Br/Br···H (22.0%) contacts are responsible for the largest contributions to the Hirshfeld surface. Besides these contacts, H···O/O···H (11.8%) and C···C (7.8%) interactions contribute significantly to the total Hirshfeld surface. The contributions of further contacts are only minor and amount to C···Br/Br···C (4.5%) and C···O/O···C (3.6%).

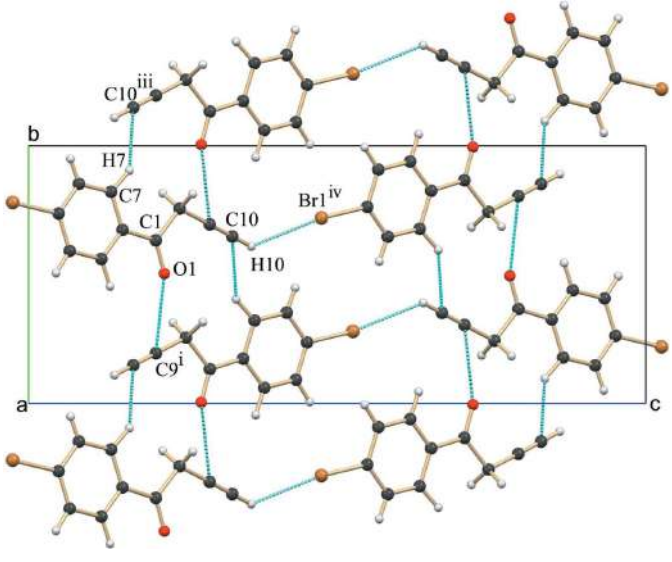

Figure 2
A view of the molecular packing of **1** along the helical *b*-axis showing the association of closely linked molecules by C═O···C≡C (acetylene, C═O···π) and marginal C—H···π (π-cloud of acetylene molecules) contacts. Neighbouring helices along the longer *c* axis are linked by C—H···Br contacts. Symmetry codes as in Table 1.

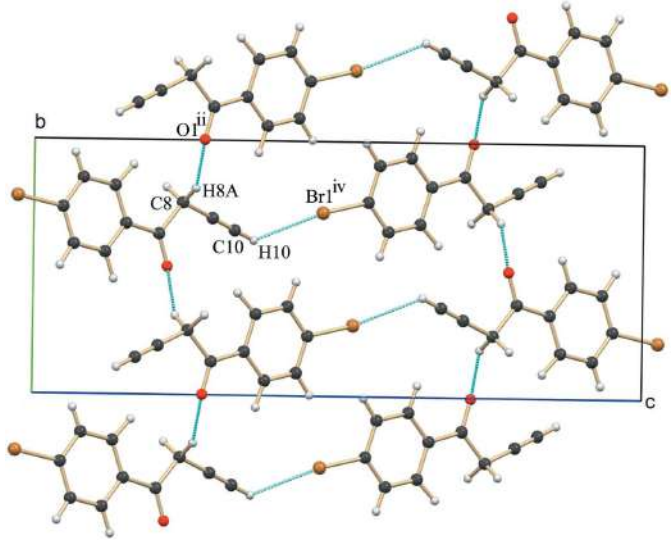

Figure 3
A view of the molecular packing of **1** along the helical *b*-axis showing the association of closely linked molecules by C—H···O contacts. Neighbouring helices along the longer *c* axis are linked by C—H···Br contacts. Symmetry codes as in Table 1.

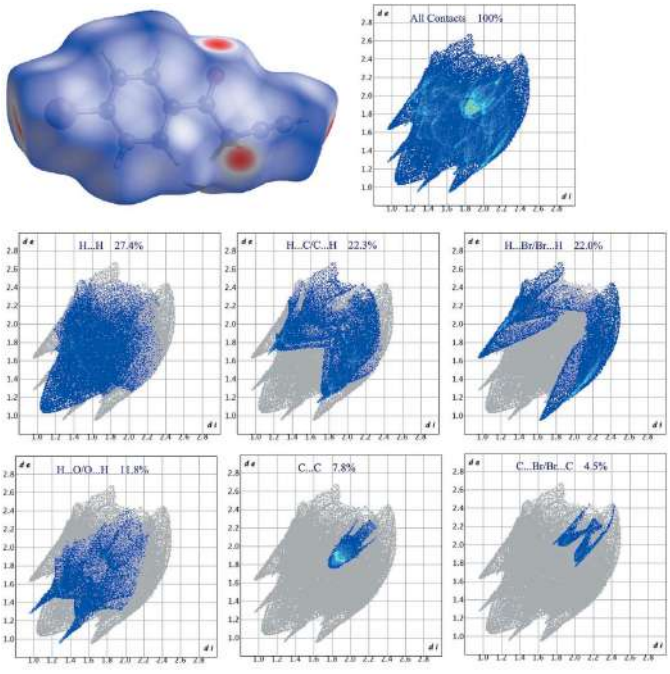

Figure 4
Three-dimensional Hirshfeld surfaces of compound **1** plotted over d_{norm} in the range −0.2760 to 0.9829 a.u., and Hirshfeld fingerprint plots for all contacts and those decomposed into H···H, H···C/C···H, H···Br/Br···H, H···O/O···H, C···C and C···Br/Br···C contacts. d_i and d_e denote the closest internal and external distances (in Å) from a point on the surface.

4. Database survey

A survey of the Cambridge Structural Database (version 5.43, update 4, November 2022; Groom *et al.*, 2016) revealed that no crystal structure of compound **1** has been reported. Moreover, no crystal structure similar to that of compound **1** has been reported. However, focusing only on the 1-phenylbut-3-yn-1-one unit yielded 24 hits with not much similarity with the title compound. The most similar structure with respect to compound **1** is 3-phenyl-2-(phenylethynyl)-1*H*-inden-1-one (FEGDOO; Kumar *et al.*, 2022).

5. Synthesis and crystallization

A solution of methyl ester **3** (100 mg, 0.35 mmol) and 1*N* NaOH (3 mL) and methanol (3 mL) was heated to reflux for 3 h. After completion of the reaction as indicated by TLC, the reaction mixture was cooled to room temperature and neutralized with a solution of 3N HCl and then extracted with dichloromethane (3 × 10 mL). The combined organic layer was washed with brine and concentrated. The resulting crude was purified by column chromatography (30% ethyl acetate in petroleum ether) to afford the acid **2** (70 mg, 74% yield) and an alkyne, the title compound **1** (8 mg, 11% yield) as colourless solids. Colourless crystals of the title compound **1** suitable for single crystal X-ray diffraction analysis were obtained by slow evaporation of an ethanol solution.

Table 2
Experimental details.

Crystal data	
Chemical formula	$C_{10}H_7BrO$
M_r	223.07
Crystal system, space group	Monoclinic, $P2_1/n$
Temperature (K)	297
a, b, c (Å)	4.471 (2), 9.032 (4), 21.652 (11)
β (°)	92.252 (8)
V (Å^3)	873.7 (7)
Z	4
Radiation type	Mo $K\alpha$
μ (mm^{-1})	4.65
Crystal size (mm)	0.35 × 0.28 × 0.13
Data collection	
Diffractometer	Bruker SMART APEX
Absorption correction	Multi-scan (*SADABS*; Bruker 2016)
T_{min}, T_{max}	0.293, 0.583
No. of measured, independent and observed [$I > 2\sigma(I)$] reflections	4994, 1965, 1397
R_{int}	0.043
(sin $\theta/\lambda)_{max}$ (Å^{-1})	0.664
Refinement	
$R[F^2 > 2\sigma(F^2)]$, $wR(F^2)$, S	0.048, 0.140, 1.02
No. of reflections	1965
No. of parameters	133
H-atom treatment	H atoms treated by a mixture of independent and constrained refinement
$\Delta\rho_{max}$, $\Delta\rho_{min}$ (e Å^{-3})	0.40, −0.62

Computer programs: *APEX3* and *SAINT-Plus* (Bruker, 2016), *SHELXS97* (Sheldrick, 2008), *SHELXL2014/7* (Sheldrick, 2015), *ORTEP-3 for Windows* (Farrugia, 2012), *Mercury* (Macrae *et al.*, 2020), *SHELXTL* (Sheldrick, 2008), *PLATON* (Spek, 2020) and *publCIF* (Westrip, 2010).

6. Refinement

Crystal data, data collection and structure refinement details are summarized in Table 2. All H atoms (except the acetylene H atom) were located in difference-Fourier map and refined isotropically. The acetylene (—C≡C—H) H atom was placed in a geometrically idealized position using HFIX 163. It was constrained to ride on its parent atom, with U_{iso}(H) = 1.2U_{eq}(C) for acetylene. The long C8—H8*A* distance [1.02 (4) Å] could be the result of its involvement in the directional C— H···O hydrogen-bond formation with O1.

Acknowledgements

SKS thanks the DST–INSPIRE program for a research fellowship.

References

Berg, J. van den & Seddon, K. R. (2003). *Cryst. Growth Des.* **3**, 643–661.
Bruker (2016). *APEX3*, *SAINT-Plus* and *SADABS*. Bruker AXS Inc., Madison, Wisconsin, USA.
Desiraju, G. R. & Steiner, T. (2001). *The Weak Hydrogen Bond in Structural Chemistry and Biology*. Oxford University Press.
Farrugia, L. J. (2012). *J. Appl. Cryst.* **45**, 849–854.
Groom, C. R., Bruno, I. J., Lightfoot, M. P. & Ward, S. C. (2016). *Acta Cryst.* B**72**, 171–179.
Kumar, S., Nunewar, S., Sabbi, T. K. & Kanchupalli, V. (2022). *Org. Lett.* **24**, 3395–3400.

Li, P., Vik, E. C., Maier, J. M., Karki, I., Strickland, S. M. S., Umana, J. M., Smith, M. D., Pellechia, P. J. & Shimizu, K. D. (2019). *J. Am. Chem. Soc.* **141**, 12513–12517.
Macrae, C. F., Sovago, I., Cottrell, S. J., Galek, P. T. A., McCabe, P., Pidcock, E., Platings, M., Shields, G. P., Stevens, J. S., Towler, M. & Wood, P. A. (2020). *J. Appl. Cryst.* **53**, 226–235.
McKinnon, J. J., Jayatilaka, D. & Spackman, M. A. (2007). *Chem. Commun.* pp. 3814–3816.
Mooibroek, T. J., Gamez, P. & Reedijk, J. (2008). *CrystEngComm*, **10**, 1501–1515.
Sheldrick, G. M. (2008). *Acta Cryst.* A**64**, 112–122.
Sheldrick, G. M. (2015). *Acta Cryst.* C**71**, 3–8.
Spackman, M. A. & Jayatilaka, D. (2009). *CrystEngComm*, **11**, 19–32.
Spackman, P. R., Turner, M. J., McKinnon, J. J., Wolff, S. K., Grimwood, D. J., Jayatilaka, D. & Spackman, M. A. (2021). *J. Appl. Cryst.* **54**, 1006–1011.
Spek, A. L. (2020). *Acta Cryst.* E**76**, 1–11.
Westrip, S. P. (2010). *J. Appl. Cryst.* **43**, 920–925.
Zeng, L.-F., Zhang, H.-S., Wang, Y.-H., Sanchez, T., Zheng, Y.-T., Neamati, N. & Long, Y.-Q. (2008). *Bioorg. Med. Chem. Lett.* **18**, 4521–4524.

supporting information

Acta Cryst. (2023). E**79**, 633-636 [https://doi.org/10.1107/S205698902300508X]

Crystal structure of 1-(4-bromophenyl)but-3-yn-1-one

Shaziyaparveen K. Siddiqui, C. V. Ramana and Rajesh G. Gonnade

Computing details

Data collection: *APEX3* (Bruker, 2016); cell refinement: *SAINT-Plus* (Bruker, 2016); data reduction: *SAINT-Plus* (Bruker, 2016); program(s) used to solve structure: *SHELXS97* (Sheldrick, 2008); program(s) used to refine structure: *SHELXL2014/7* (Sheldrick, 2015); molecular graphics: *ORTEP-3 for Windows* (Farrugia, 2012), *Mercury* (Macrae *et al.*, 2020); software used to prepare material for publication: *SHELXTL* (Sheldrick, 2008), *PLATON* (Spek, 2020) and *publCIF* (Westrip, 2010).

1-(4-Bromophenyl)but-3-yn-1-one

Crystal data

$C_{10}H_7BrO$
$M_r = 223.07$
Monoclinic, $P2_1/n$
$a = 4.471$ (2) Å
$b = 9.032$ (4) Å
$c = 21.652$ (11) Å
$\beta = 92.252$ (8)°
$V = 873.7$ (7) Å^3
$Z = 4$
$F(000) = 440$
$D_x = 1.696$ Mg m^{-3}
Mo $K\alpha$ radiation, $\lambda = 0.71073$ Å
Cell parameters from 1876 reflections
$\theta = 2.4$–$24.9°$
$\mu = 4.65$ mm^{-1}
$T = 297$ K
Block, colourless
0.35 × 0.28 × 0.13 mm

Data collection

Bruker SMART APEX diffractometer
Radiation source: fine-focus sealed tube
Graphite monochromator
Phi and ω Scan scans
Absorption correction: multi-scan (SADABS; Bruker 2016)
$T_{min} = 0.293$, $T_{max} = 0.583$
4994 measured reflections
1965 independent reflections
1397 reflections with $I > 2\sigma(I)$
$R_{int} = 0.043$
$\theta_{max} = 28.2°$, $\theta_{min} = 2.4°$
$h = -4 \rightarrow 5$
$k = -11 \rightarrow 11$
$l = -27 \rightarrow 27$

Refinement

Refinement on F^2
Least-squares matrix: full
$R[F^2 > 2\sigma(F^2)] = 0.048$
$wR(F^2) = 0.140$
$S = 1.02$
1965 reflections
133 parameters
0 restraints
Primary atom site location: structure-invariant direct methods
Hydrogen site location: mixed
H atoms treated by a mixture of independent and constrained refinement
$w = 1/[\sigma^2(F_o^2) + (0.0812P)^2 + 0.1069P]$ where $P = (F_o^2 + 2F_c^2)/3$
$(\Delta/\sigma)_{max} = 0.002$
$\Delta\rho_{max} = 0.40$ e Å^{-3}
$\Delta\rho_{min} = -0.62$ e Å^{-3}

Special details

Geometry. All esds (except the esd in the dihedral angle between two l.s. planes) are estimated using the full covariance matrix. The cell esds are taken into account individually in the estimation of esds in distances, angles and torsion angles; correlations between esds in cell parameters are only used when they are defined by crystal symmetry. An approximate (isotropic) treatment of cell esds is used for estimating esds involving l.s. planes.

Fractional atomic coordinates and isotropic or equivalent isotropic displacement parameters (Å²)

	x	*y*	*z*	U_{iso}*/U_{eq}
C1	0.5990 (7)	0.3666 (3)	0.79382 (16)	0.0508 (8)
Br1	1.37959 (10)	0.22006 (5)	1.02549 (2)	0.0743 (2)
C2	0.7972 (7)	0.3261 (3)	0.84766 (16)	0.0488 (7)
C3	0.9384 (9)	0.4391 (4)	0.88181 (17)	0.0581 (9)
H3	0.887 (9)	0.545 (5)	0.8679 (19)	0.080 (12)*
C4	1.1186 (9)	0.4079 (4)	0.93323 (18)	0.0615 (9)
H4	1.217 (9)	0.494 (5)	0.9555 (19)	0.077 (11)*
C5	1.1578 (9)	0.2628 (4)	0.95122 (18)	0.0556 (8)
C6	1.0233 (9)	0.1475 (4)	0.91808 (18)	0.0609 (9)
H6	1.065 (9)	0.051 (5)	0.9319 (19)	0.070 (11)*
C7	0.8439 (9)	0.1783 (4)	0.86619 (17)	0.0560 (8)
H7	0.752 (8)	0.096 (4)	0.8364 (15)	0.054 (9)*
C8	0.4544 (9)	0.2439 (4)	0.7551 (2)	0.0555 (9)
H8B	0.342 (9)	0.184 (4)	0.7824 (18)	0.056 (10)*
C9	0.2564 (10)	0.3048 (4)	0.7064 (2)	0.0666 (11)
H8A	0.617 (10)	0.187 (5)	0.734 (2)	0.068 (12)*
C10	0.1011 (10)	0.3516 (5)	0.6698 (2)	0.0783 (12)
H10	−0.0283	0.3905	0.6393	0.094*
O1	0.5514 (7)	0.4954 (2)	0.77985 (13)	0.0718 (8)

Atomic displacement parameters (Å²)

	U^{11}	U^{22}	U^{33}	U^{12}	U^{13}	U^{23}
C1	0.0553 (18)	0.0353 (15)	0.0622 (19)	−0.0025 (13)	0.0097 (15)	−0.0018 (14)
Br1	0.0827 (4)	0.0702 (3)	0.0688 (3)	−0.00322 (18)	−0.0116 (2)	−0.00504 (18)
C2	0.0542 (18)	0.0368 (14)	0.0563 (18)	−0.0031 (13)	0.0125 (15)	−0.0051 (14)
C3	0.076 (2)	0.0382 (16)	0.061 (2)	−0.0070 (15)	0.0057 (18)	−0.0033 (15)
C4	0.074 (2)	0.0484 (19)	0.062 (2)	−0.0152 (17)	0.0072 (18)	−0.0110 (17)
C5	0.060 (2)	0.0547 (19)	0.0524 (19)	−0.0042 (15)	0.0068 (15)	−0.0065 (16)
C6	0.077 (2)	0.0415 (18)	0.064 (2)	−0.0030 (17)	0.0016 (18)	−0.0003 (16)
C7	0.069 (2)	0.0386 (15)	0.060 (2)	−0.0030 (15)	0.0009 (17)	−0.0053 (15)
C8	0.057 (2)	0.0396 (15)	0.069 (2)	0.0016 (15)	−0.0034 (19)	−0.0029 (16)
C9	0.067 (2)	0.0464 (18)	0.087 (3)	−0.0048 (17)	0.002 (2)	−0.0019 (19)
C10	0.084 (3)	0.060 (2)	0.088 (3)	0.005 (2)	−0.032 (2)	0.017 (2)
O1	0.0875 (18)	0.0377 (12)	0.0895 (19)	0.0002 (12)	−0.0066 (16)	0.0024 (13)

Geometric parameters (Å, º)

C1—O1	1.218 (4)	C5—C6	1.388 (5)
C1—C2	1.482 (5)	C6—C7	1.383 (5)
C1—C8	1.518 (5)	C6—H6	0.93 (4)
Br1—C5	1.895 (4)	C7—H7	1.06 (3)
C2—C3	1.397 (5)	C8—C9	1.458 (7)
C2—C7	1.407 (5)	C8—H8B	0.96 (4)
C3—C4	1.378 (6)	C8—H8A	1.02 (4)
C3—H3	1.03 (5)	C9—C10	1.117 (6)
C4—C5	1.377 (5)	C10—H10	0.9300
C4—H4	1.01 (5)		
O1—C1—C2	121.6 (3)	C7—C6—C5	119.7 (3)
O1—C1—C8	119.6 (3)	C7—C6—H6	123 (3)
C2—C1—C8	118.8 (3)	C5—C6—H6	117 (3)
C3—C2—C7	118.9 (3)	C6—C7—C2	119.8 (3)
C3—C2—C1	118.7 (3)	C6—C7—H7	123.5 (18)
C7—C2—C1	122.4 (3)	C2—C7—H7	116.4 (18)
C4—C3—C2	121.1 (3)	C9—C8—C1	110.9 (3)
C4—C3—H3	123 (2)	C9—C8—H8B	110 (2)
C2—C3—H3	116 (2)	C1—C8—H8B	107 (2)
C5—C4—C3	119.2 (3)	C9—C8—H8A	107 (2)
C5—C4—H4	123 (2)	C1—C8—H8A	109 (2)
C3—C4—H4	117 (3)	H8B—C8—H8A	113 (3)
C4—C5—C6	121.3 (4)	C10—C9—C8	178.8 (6)
C4—C5—Br1	119.4 (3)	C9—C10—H10	180.0
C6—C5—Br1	119.2 (3)		
O1—C1—C2—C3	−1.9 (5)	C3—C4—C5—Br1	−175.1 (3)
C8—C1—C2—C3	177.7 (3)	C4—C5—C6—C7	−0.6 (6)
O1—C1—C2—C7	177.0 (3)	Br1—C5—C6—C7	175.5 (3)
C8—C1—C2—C7	−3.4 (5)	C5—C6—C7—C2	−0.5 (6)
C7—C2—C3—C4	−0.7 (5)	C3—C2—C7—C6	1.1 (6)
C1—C2—C3—C4	178.3 (3)	C1—C2—C7—C6	−177.8 (3)
C2—C3—C4—C5	−0.4 (6)	O1—C1—C8—C9	−3.3 (6)
C3—C4—C5—C6	1.0 (6)	C2—C1—C8—C9	177.1 (3)

Hydrogen-bond geometry (Å, º)

D—H···*A*	*D*—H	H···*A*	*D*···*A*	*D*—H···*A*
C1—O1···C9^{i}		3.13 (1)		154 (1)
C8—H8*A*···O1^{ii}	1.02 (4)	2.31 (4)	3.259 (5)	156 (3)
C7—H7···C10^{iii}	1.06 (3)	2.71 (4)	3.626 (5)	144 (3)
C10—H10···Br1^{iv}	0.93	2.68	3.305 (5)	126

Symmetry codes: (i) −*x*+1/2, *y*+1/2, −*z*+3/2; (ii) −*x*+3/2, *y*−1/2, −*z*+3/2; (iii) −*x*+1/2, *y*−1/2, −*z*+3/2; (iv) *x*−3/2, −*y*+1/2, *z*−1/2.